Amariei, Anca Elena (2024) *Gas phase pyrolytic approach for stable isotope analysis of hopanoids lipids*. PhD thesis.

Gas phase pyrolytic approach for stable isotope analysis of hopanoids lipids

Anca Elena Amariei

BSc University of Glasgow

MSc (Res) University of Glasgow

School of Engineering

University of Glasgow

A thesis submitted in fulfilment of the requirements for the degree of

Doctor of Philosophy

February 2024

University of Glasgow

School of Engineering

Statement of Originality to Accompany Thesis Submission

Name: Anca Elena Amariei

Registration Number:

I certify that the thesis presented here for examination for a PhD degree of the University of Glasgow is solely my own work other than where I have clearly indicated that it is the work of others (in which case the extent of any work carried out jointly by me and any other person is clearly identified in it) and that the thesis has not been edited by a third party beyond what is permitted by the University's PGR Code of Practice.

The copyright of this thesis rests with the author. No quotation from it is permitted without full acknowledgement.

I declare that the thesis does not include work forming part of a thesis presented successfully for another degree.

I declare that this thesis has been produced in accordance with the University of Glasgow's Code of Good Practice in Research.

I acknowledge that if any issues are raised regarding good research practice based on review of the thesis, the examination may be postponed pending the outcome of any investigation of the issues.

Signature: …………………………………………………….

Date: ………………………25/02/2024…………..……………

Acknowledgements

Abstract

Methanotrophs are known for their role in mitigating CH_4 emissions, with aerobic methanotrophs adapted to a wide range of environments. In oxic settings, they are able to utilise this high global warming potential molecule as a source of energy, oxidising it to CO_2, or as a source of carbon, incorporating the CH_4-carbon's (C-CH_4) isotopic signature into the *intra*molecular structure of the membrane-located hopanoid lipids. Being decay-resistant, hopanoids can be used to study past CH_4 cycles.

Compound-specific isotope analysis (CSIA) of diploptene, a hopanoid biomarker, has been initially employed in this work to identify the advantages and limitations of this technique to assess past CH_4 consumption within three peatlands of Pastaza-Marañón Foreland Basin (PMFB). This study thus provides the first multi-biomarker, yet low-resolution, isotopic reconstruction of the three peatlands, with CSIA values of hopanoids, as well as of n-alkanes and fatty acids interpreted in conjunction with previously measured biomarker concentrations and a wide range of palaeoenvironmental data from the same peatlands or area. Isotopic values of n-alkanes and diploptene reflect the CH_4-producing conditions of the area, fluctuating with past changes in each peatland's history. It was however found that methanotrophs were not the sole producers of hopanoids and, due to source dilution and the fact that the three aerobic methanotroph types can also incorporate different amounts of C-CO_2, via distinctive pathways, diploptene's methanotrophic isotopic signature can become muted in these (palaeo)environmental samples at the CSIA level.

These limitations, together with low compound concentrations and co-elution, were also encountered in simplified, one-diploptene source methanotrophic lab cultures conducted in this work to study diploptene's CSIA evolution in relationship to isotopically known CH_4 and CO_2 sources. Even when the bio-producer is known, diploptene's CSIA was influenced by the varying quantities of C-CH_4 and C-CO_2 incorporated by type I and II methanotrophs. New tools are thus required to assess methanotrophic processes in natural environments and increase confidence in source attribution. This work develops theoretical and analytical methodologies for the gaseous pyrolysis of diploptene that could enable the detection of methanotrophy at the *intra*molecular (or position-specific) level through isotopic analyses.

Analytical instruments capable of accessing this information are currently restricting these new isotopic applications through complex setups, molecule-specific uses and high costs. Gaseous pyrolysis is demonstrated in this thesis on a bespoke GC-FID instrument (prep-GC) adapted to overcome these limitations. The development of the prep-GC instrument and methodology took place in a step-like fashion, with experiments aimed at increasing and

testing its capacities on compounds such as methanol, MTBE, 2,3 DMN, squalene and diploptene, and their multiple pyrolysates. The prep-GC is demonstrated to be able to analyse compounds with molecular masses between 32 - 410 g/mol and at least up to 850°C pyrolytic temperatures, making it a universal analytical instrument for the pyrolysis of volatile and semi-volatile compounds. Experiments presented in this thesis demonstrate the ability of the prep-GC to heart-cut and concentrate, within a trap, compounds of interest, release, pyrolyse and transfer the pyrolysates to a second detector for quantification and identification. The analytical pyrolytic methodologies were further adapted and the results were confirmed through *in-silico* pyrolysis, using Reaction Mechanism Generator (RMG, Gao et al., 2016).

Diploptene, and hopanoids in general, have never been subjected to pyrolysis to investigate if the C-CH_4 moieties can be accessed and their relationship to the CH_4 cycle. The pyrolytic breakdown mechanism of diploptene was assessed first on RMG and the results were experimentally studied. On RMG, for the simulated pyrolytic temperature of 750°C, isoprene was the main pyrolytic fragment, produced from squalene, which occurs as an unstable intermediate. During pyrolysis, the diploptene backbone therefore unfolded, undoing the action of the squalene-hopene cyclase, and was broken down into isoprene units. Theoretical and experimental evidence of diploptene, squalene and isoprene pyrolysis are presented to support isoprene as the main diploptene pyrolysis fragment between 550°C-625°C. Isoprene however is demonstrated to not provide new isotopic evidence when compared to diploptene, as it does not allow a direct isotopic investigation of the C-CH_4 and C-CO_2 incorporated through the different methanotroph bio-cycles. Isoprene ozonolysis is proposed as a future tool that could access this *intra*molecular information, post diploptene (and squalene) pyrolysis. Finally, although produced from the same predecessor (squalene), RMG simulations indicate that other hopanoids present different breakdown mechanisms, requiring individual breakdown pyrolytic assessments for future PSIA studies.

The development of the prep-GC instrument for gaseous pyrolysis biomarkers at low environmental concentrations and the exploration of hopanoid pyrolysis mechanisms in this thesis contribute to advancing the understanding of methanotrophy and its detection via isotopic studies, paving the way for new *intra*molecular isotopic investigations.

Conferences

1. **Amariei, A.E**., Stillings, M., Toney, J, Gauchotte-Lindsay, C – **RSC 2022**, *Theoretical and analytical pyrolysis: diploptene biomarker application*

2. **Amariei, A.E**., Stillings, M., Knapp, M., Toney, J, Gauchotte-Lindsay, C. – **JESIUM 2022**, *Position-Specific Isotope Analysis in hopanoid lipids*

3. **Amariei, A.E**., Toney, J.L. and Gauchotte-Lindsay, C. - *Modelling and analytical pyrolysis of methanotroph biomarkers,* **BOGS 2021**

4. **Amariei, A.E**., Stillings, M. Toney, J.L., Gauchotte-Lindsay, C. – *Pyrolysis on a prep-GC for PSIA*, **RSC Scotland**, **Dec. 2020**

5. **Amariei, A.E**., Stillings, M., Toney, J.L., Graham, D. and Gauchotte-Linsday, C., - **RSC 2020, Aberdeen**, *Type II methanotrophs: understanding metabolic pathways and isotopic signatures in palaeoenvironments.*

6. **Amariei, A.E**., Toney, J.L., Graham, D. and Gauchotte-Linsday, C. – **SIMSUG 2019** – poster presentation - *Methanotrophy through biomarkers-do we know how to recognize its full extend?*

Table of contents

Symbols and abbreviations

OM	Organic matter
GHG	Greenhouse gas
BSIA	Bulk-specific isotope analysis
CSIA	Compound-specific isotope analysis
PSIA	Position-specific isotope analysis
prep-GC	preparational GC-FID referring to main thesis instrument
C-CH4	CH_4-provided carbon
RMG	Reaction mechanism generator software
CBC	Calvin-Benson cycle
MMO	Methane monooxygenase
p, s MMO	particulate, soluble MMO
QT peatland	Quistococha peatland
SJO peatland	San Jorge peatland
BVA peatland	Buena Vista peatland
PMFB	Pastaza-Marañón Foreland Basin
LPS	Lipopolysaccharides
PLFA	Phospho Lipid Fatty Acid
FA	Fatty Acid
MEP	Methylerythriol phosphate
RuMP pathway	Ribulose monophosphate pathway
CF	Continuous flow
GC	Gas chromatography
FID	Flame Ionizing Detector
MS	Mass Spectrometer
IRMS	Isotope Ratio Mass Spectrometer
RT	Retention time
LOD	Limit of detection
MSD	Mass Spectrometer Detector
TOF-MS	Time-of-flight MS
EI	Electron ionisation
CI	Chemical ionisation
TIC mode	Total Ion Chromatogram
SIM	Selected Ion Mode chromatograms
cal yr BP	Calibrated years before present
RPM	Rotation per minute
StDev	Standard deviation
HMW	High molecular weight

List of Figures

List of Tables

1. Introduction and thesis objectives

1.1. Background

Methane (CH_4), is the second most significant greenhouse gas, with a global warming potential 27 times higher than that of CO_2 when assessed over a period of 100 years, and with a total lifetime of 9.26 ± 06 years (i.e., CO_2 GWP-100=1; IPCC, 2021). While there is consensus among models regarding the increasing trends of CH_4 in the future, there is still considerable uncertainty on a global scale about its cycle and its relationship with future warming scenarios (IPCC, 2021). This uncertainty can be reduced by re-evaluating impacting factors and refining CH_4 sinks and sources in global models (Kirschke *et al.*, 2013). For this, new analytical tools and frameworks are required, that can provide further evidence of the driving factors for increased levels of CH_4 production in past ecosystems.

Lipid biomarkers, analysed via gas chromatography (GC) techniques, have become reliable tools for investigating ancient ecosystems and past climates, adding, from an evolutionary perspective, important dimensions to our understanding of life on Earth (Briggs and Summons, 2014). Advances in the GC field have enabled the analysis of reduced sample sizes, the effective separation and identification of lipids, leading to increased sensitivities and providing detailed and accurate insights into the composition of complex organic mixtures (Peters *et al.*, 2005). Isotope analysis can enhance the understanding of the environmental setting, by providing details of the operating biological cycles. It can be performed at the sample's bulk level (BSIA) and, when used in conjunction with GC systems, it can yield more insight into the source and composition of organic matter by conducting compound-specific isotope analysis (CSIA) or position-specific isotope analysis (PSIA), which examines isotopic variations at the *intra*molecular level.

The emergence of PSIA (Abelson and Hoering, 1961b; Brenna *et al.*, 1997) has opened up new avenues for research, with promising applications in all fields in which CSIA is currently carried out. PSIA is however an application that has been used in a limited number of studies to extract detailed isotopic information, aiding the investigation of biosynthetic pathways and probing, at the *intra*molecular level, the complex relationship between living organisms, their metabolism and environments. This analysis is relatively uncommon compared to CSIA, and even more challenging to conduct on environmental samples, due to several limitations. Firstly, the low concentration of the compounds selected for PSIA can

become an issue when trying to obtain accurate isotopic measurements. Secondly, complex matrices and co-elution of compounds can make it difficult to isolate specific compounds for this analysis. Additionally, the high cost of the instrumental and complex setup required for PSIA can also limit its use, highlighting a current gap in analytical capabilities.

Hopanoids have been employed to study the carbon cycle in past environments via CSIA. Diploptene, a hopanoid-class lipid, has been widely used to understand the CH_4 cycle via its methanotroph bio-producers and has been successful in assessing CH_4 consumption (and implicit, production) through its depleted isotopic signatures across a wide range of environments and geologic timescales (see Appendix A.3.1.). However, methanotrophs are not the sole bio-producers of diploptene. It is bio-synthesised by a wide range of aerobic and anaerobic bacteria, as well as by several trees and ferns, that can contribute to the diploptene pool. Thus, one gap in knowledge is that, although methanotrophy detection is approached by CSIA, diploptene's isotopic signatures can be muted with increased input from non-methanotroph producers, making it less reliable in assessing methanotrophy. Furthermore, methanotrophs can assimilate CO_2, which has a more enriched signature in the atmosphere compared to CH_4 (Table 2.1), and incorporate the C-CO_2 into diploptene at various points within the metabolic pathway (Hanson and Hanson, 1996; Jahnke et al., 1999), thus further diluting the methanotrophic signal. Although a strongly negative $\delta^{13}C_{diploptene}$ indicates CH_4 incorporation and oxidation, a less negative isotopic signature does not necessarily indicate the absence of methanotrophy or that of an active methanotroph community. Conducting PSIA on targeted moieties may provide isotopic measurements that reflect the CH_4-provided carbon (C-CH_4) isotopic signature.

Pyrolysis is a technique that has been previously employed to perform PSIA, via the production of molecular fragments. It can be further coupled online with GC-IRMS systems to provide accurate isotopic measurements of the breakdown molecular components (Gauchotte-Lindsay and Turnbull, 2016). Research on hopanoid molecules using PSIA could provide important insights into the biochemistry of these molecules, linking them more accurately to CH_4 consumption. However, the gaps in knowledge regarding diploptene PSIA, are significant and should be addressed. Firstly, diploptene has never been subjected to direct pyrolysis, thus the produced fragments and the breakdown mechanism are not known. Secondly, it is unclear if the produced fragments are of PSIA value, if the C-CH_4 position-specific atoms can be reached within this compound and how this information can aid (palaeo)environmental reconstructions. Lastly, PSIA is limited by GC instrumental methodologies, and the system setup should be able to analyse a wide range of samples, expanding this analysis to high molecular weight compounds and unknown pyrolysates.

1.2. Research Aim and Objectives

To address the highlighted gaps in knowledge and limitations of the emerging PSIA field, this thesis aims to investigate theoretically and instrumentally the potential of pyrolysis-based PSIA of diploptene as a proxy for methanotrophy assessment. The objectives are as follows:

- The isotopic investigation of hopanoids (and *n*-alkane) biomarkers extracted from 3 recently discovered peatlands from Pastaza-Marañón Foreland Basin (PMFB), Peru to evaluate the advantages and limitations of diploptene as a proxy for methanotrophy assessment, achieved in Chapter 3;

- To calculate the CSIA fractionation factors between diploptene and CH_4 source in pure cultures of type I and type II aerobic methanotrophs, achieved in Chapter 4;

- To develop the instrumental methodology for online pyrolysis by employing a modified GC-FID, a GC-MS and *in-silico* validation, achieved in Chapter 5;

- To further extend the application range of the developed analytical instrument for low concentration and high molecular weight compounds, demonstrated in Chapter 6 via the heart-cut, compound concentration, pyrolysis and pyrolysate identification of a DMN compound;

- To pyrolyse diploptene, assess its breakdown mechanisms and potential for PSIA through *in-silico* and experimental pyrolysis coupled with GC-MS and GC-FID analysis of the produced fragments, achieved in Chapter 7.

1.3. Thesis outline

This thesis is structured in 5 main work chapters, one for each outlined objective. The literature review focuses on concepts and instrumentation used for the overall thesis aim and for achieving the main objectives. This is followed by Chapter 3 which examines a complex palaeoenvironment in which diploptene is found. In Chapter 4, the system from which diploptene is analysed, is simplified. Pure methanotroph cultures are analysed, providing a one-source diploptene pool to investigate further the advantages and limitations at the CSIA level. Thus, in Chapters 5 and 6, the work is focused on the development of the analytical instrument (prep-GC) and methodologies aimed at online pyrolysis and identification of produced pyrolysates. Finally, in Chapter 7, diploptene's *intra*molecular links to the CH_4 cycle are discussed, together with its pyrolytic breakdown mechanism and its PSIA potential and significance.

2. Literature review

2.1. Methane – a driving factor of global warming

CH_4 has approximately a global warming potential 27 times greater (IPCC, 2021) than that of CO_2, meaning that over a period of 100 years (i.e., GWP-100), the radiative forcing for the release of 1 Tg of CH_4 is 27 times higher than the equivalent amount of CO_2. This figure has been recently revised to highlight the uncertainty associated with the reaction rate coefficients between $CH_4 + OH$, $CH_3O_2 + HO_2$, $CH_3O_2 + NO$, and terpene $+ O_3$ and the GWP-100 of CH_4 was proposed to be 37 ± 10 Tg of CO_2 (Derwent, 2020).

The global budgets of atmospheric gases take into account both sources and sinks. For CH_4, sources differ significantly in terms of geographical extent (Melton *et al.*, 2013) and GHG input amount (Bridgham *et al.*, 2013), with varying emissions quantities and uncertainty levels depending on the methods used. Despite disagreements on the overall global estimates, all published results show increasing trends of CH_4 levels since early monitoring (i.e., 1983, Global Monitoring Laboratory, Mauna Lao; Lan *et al.*, 2022, Lan *et al.*, 2024). By incorporating the 1% annual increase in CH_4 concentrations (Lelieveld *et al.*, 1993) and comparing it to palaeorecords, which display nature-driven increases and decreases of CH_4

and CO_2 levels (i.e., ice cores, Petit *et al.*, 1999), the current trend is expected to lead to a rapid runaway climatic effect. There is a consensus that an increase in atmospheric CH_4 concentration is linked to increasing global temperatures (Lelieveld *et al.*, 1998; Kirschke et al., 2013; Nisbet *et al.*, 2014), responsible for a fifth of the global warming since pre-industrial times, with anthropogenic sources being a major factor (e.g., rice agriculture, land use, Eusufzai *et al.*, 2010). These records are also in agreement that present-day concentrations are unprecedented in the last thousands of years (i.e., last 5 kyrs, Ruddiman and Thomson, 2001; last 420 kyrs, Petit et al., 1999), with current values above 1700 ppb, following the warmest scenario described by the Intergovernmental Panel on Climate Change (IPCC), and predicted to reach concentrations of 2550 ppm by 2050 (Lelieveld et al., 1998).

Wetlands (e.g., peatlands, flooded soils) are defined as natural environments with a constant water table at or close to the surface, which differ in terms of soil conditions and proprieties from upland neighbouring environments, harbouring vegetation adapted to waterlogged conditions, and placed at the interface between terrestrial and aquatic systems. Their ability to sequester large amounts of carbon under anaerobic conditions is widely recognised (Mitsch and Gosselink, 2015). They are however also considered the primary natural sources of CH_4, with the IPCC (2022) reporting top-down estimates as high as 83% and bottom-up estimates of 40% of the natural CH_4 emissions, representing 31% and 20%, respectively, of the total CH_4 global emissions. At the global scale, it has been recognised that anaerobic conditions facilitated by high water tables, promote the breakdown of organic matter (OM)
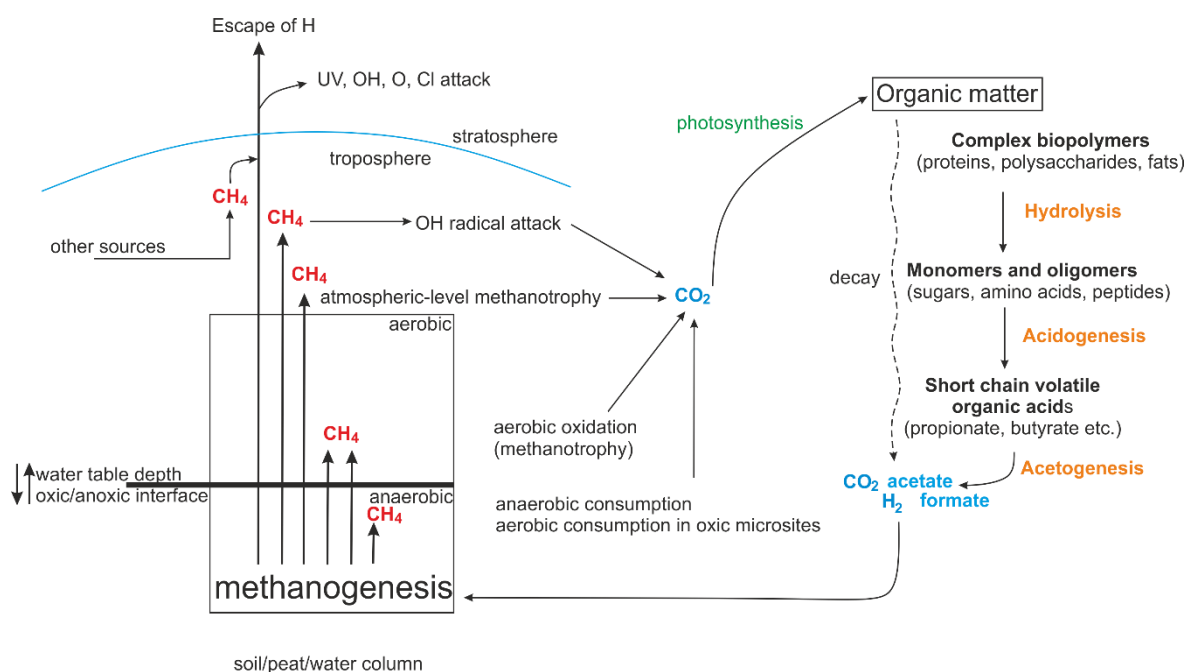
Figure 2.1 Summarised CH_4 cycle depicting main sources and sinks (edited from Cicerone and Oremland, 1988, Nazaries et al., 2013 and Fermoso et al., 2019).

by methanogenic microbes, leading to the release of CH_4 (i.e., Conrad, 2007; Figure 2.1). This process is considerably reduced under oxic conditions, with vegetation and substrate quality, temperature (and latitude), *in-situ* aeration potential, pH, microbial assemblage and competitive relationships also influencing the methanogenic activity (Segers, 1998; Williams and Yavitt, 2010). Methanogens have thus been extensively studied (Blaut, 1994; Hanson and Hanson, 1996; Enzmann *et al.*, 2018), with a general consensus that understanding the environmental conditions under which they occur, as well as their diversity and metabolism, can help constrain CH_4 sources and global budgets.

During decay, specialised micro-organisms alter fresh OM in the aerobic part of the system, followed by further breakdown via intricate anaerobic food webs via hydrolysis, acidogenesis, acetogenesis and finally, methanogenesis. Hydrolysis of polysaccharides leads to the formation of sugars which are then processed (i.e., fermented) by specialised microbial groups to lower weight molecules such as low molecular weight fatty acids and alcohols, acetate, H_2 and CO_2 (Cicerone and Oremland, 1988; Conrad *et al.*, 2011; Figure 2.1). Methanogenesis is considered the final step of OM decomposition, conducted by a subgroup of specialised archaea that can utilise only a small number of substrates for energy and growth. This takes place where reducing and anaerobic conditions prevail, such as in wetlands, flooded soils, sediments in marine or freshwater systems, geothermal systems, and the digestive tracts of animals. Specialised archaea, such as methanogens, produce CH_4 mainly by the reduction of CO_2 with H_2 (Eq. 1) and via the fermentation of acetate (Eq. 2). Methylated compounds such as methanol, methylamines, formate, and dimethylsulphur account for less than 5% to the overall CH_4 production (Conrad, 2007). At the final step of decay, CH_4 is the ideal non-toxic product, with low water solubility, transported to the surface via bubble ebullition, diffusion or plant transport (Chanton, 2005).

$$CO_2 + 4H_2 \rightarrow CH_4 + 2H_2O \text{ (hydrogenotrophic methanogens)} \qquad \text{Eq. 1}$$

$$CH_3COOH \rightarrow CH_4 + CO_2 \text{ (acetoclastic methanogens)} \qquad \text{Eq. 2}$$

The major CH_4 sink is the troposphere, via OH radical attack which is approximated to account for over 90% of the global removal, followed by stratospheric loss (3%) and by CH_4 oxidising bacteria, known as **methanotrophs**, which is approximated at only 4% removal (Kirschke et al., 2013; Figure 2.1). However, in many environments, the rate of methanotroph CH_4 oxidation exceeds that of methanogen production (with respect to its volume; Fritz *et al.*, 2011; Kip *et al.*, 2012) indicating that this is an *in-situ* limiting factor of

CH_4 reaching the atmosphere. Methanotrophs have been thus proposed as low-cost CH_4 emissions mitigators, able to combat global warming, amongst other bioremediation benefits (Pandey *et al.*, 2014a).

Methanotrophy can take place both in the presence or absence of O_2, leading to the classification of anaerobic or aerobic methanotrophy. CH_4 oxidation is now also recognised to occur in strictly and facultative anaerobic microbes and denitrifying bacteria (e.g., Ettwig *et al.*, 2008), particularly in marine environments (Party *et al.*, 2001), further limiting the flux of CH_4 emissions when it operates in peatlands. This however takes place at a lower rate, with consumption being exceeded by aerobic methanotrophs (Smemo and Yavitt, 2011), making this process of greater interest. This thesis thus explores new means of detecting **aerobic methanotrophy** within past environments via CH_4 incorporation mechanisms and metabolic pathways within the different divisions of the *Proteobacteria* (i.e. α- and γ-*Proteobacteria*), *Verrucomicrobia* and NC10 phyla, focusing on the three types of aerobic methanotrophs (i.e. type I, II and X).

2.2. Aerobic methanotrophs

Aerobic methanotrophs are microbes capable of incorporating and oxidising CH_4 and its conjugated forms as a carbon and energy source (Hanson and Hanson, 1996). Since their discovery in the early 1900s (Kaserer, 1905) and with the isolation of the first CH_4-oxidising organisms (*Bacillus methanicus,* Söhngen, 1906), methanotrophs have provided a subject of study and debate, with the understanding of this widely diverse group and the environments in which it occurs, rapidly expanding. They represent key components of the CH_4 cycle (Figure 2.1) due to their ability to act as a sink, limiting effluxes to the atmosphere of CH_4 produced under anaerobic conditions via *in-situ* consumption, or further removing CH_4 at atmospheric concentrations (Anthony, 1982; Anthony, 1982; Knief *et al.*, 2003; Dedysh *et al.*, 2005). They have been further exploited in bio-remediation and toxic organic compounds removal and were shown, for example, to co-metabolise trichloroethylene pollutant (i.e., Smith and Dalton, 2004; Pandey *et al.*, 2014b). Given their complex nature, they are found across diverse environments (see Appendix A.3.1.), present a wide range of morphological, physiological and metabolic features and can be grouped based on different proprieties.

Various schemes of classification are used when describing methanotrophic bacteria, implying the wide variety and adaptations of these microbes. They are part of the *Proteobacteria*, further divided based on 16S rRNA sequencing into *Alphaproteobacteria*

and *Gammaproteobacteria* (Hanson and Hanson, 1996). *Verrucomicrobia* phylum was added later, with the isolation of genus *Methylacidiphilum* (i.e. V4 isolate; Dunfield *et al.*, 2007) containing thermophilic and acidophilic representants with three methanotrophs grouped under the single name of "*Methylacidiphilum infernorum*", able to grow at 65°C, in a pH as low as 1.5 (Semrau *et al.*, 2008). Finally, the NC10 phylum was included to this classification (Op den Camp *et al.*, 2009; Ettwig *et al.*, 2010), with the first known species *M. oxyfera*, that can produce its own O_2 from nitric oxide (NO), and it is thus capable of anaerobic CH_4 oxidation alike methanotroph representants within the *Proteobacteria* and *Verruomicrobia* (Ettwig et al., 2010; He et al., 2016).

Physiologically, aerobic methanotrophs are a sub-group of methylotrophs, which are able to use one-carbon units such as CH_4, its conjugated forms and methylated compounds. However, they are defined by the presence of methane monooxygenase (MMO), an enzyme that allows the initial oxidation of CH_4 into methanol under oxic conditions (Hanson and Hanson, 1996; Murrell and Smith, 2010; Kang *et al.*, 2019; Eq. 3; Chapter 7, Figures 7.6, 7.7, 7.8 and 7.9). From an evolutionary point of view, the two types of MMO in methanotrophs, particulate and soluble (pMMO, sMMO), were mostly likely inherited by lateral gene transfer at a later evolutionary stage than the acquisition of methanol dehydrogenase enzymes, MeDH and Xox-MeDH (Kang et al., 2019).

$$CH_4 + O_2 \text{ (via MMO enzyme)} \rightarrow CH_3\text{-}OH + H_2O \qquad \text{Eq. 3}$$

The two biochemically different types of MMO vary in terms of distribution among aerobic methanotrophs, location within the microorganism and relationship to copper. pMMO is membrane-bound and wider-spread among aerobic methanotrophs while sMMO is a cytoplasmic enzyme and it is less abundant (Hanson and Hanson, 1996). Only a small number of methanotrophs are known to contain both enzymes (Kang et al., 2019). For these methanotrophs, copper presence within the environment or culture medium appears to be the main indicator of whether pMMO or sMMO will be expressed. sMMO is typically expressed when less copper is available (Hanson and Hanson, 1996). The biochemical mechanisms of sMMO can be found reviewed in Lawton and Rosenzweig (2016). Methanotrophs which exhibit the pMMO enzyme require copper for its expression (Murrell *et al.*, 2000). The presence or absence of copper in wetland environments is influenced by the hydrological regime and can influence the distribution of methanotroph types, both on a spatial and temporal scale (Hanson and Hanson, 1996).

2.2.1. Type I, II and X methanotroph classification

The most common classification of aerobic methanotrophs is based on the two main types, I and II, with type X viewed as a subcategory of the former, yet containing elements of both (Hanson and Hanson, 1996; Trotsenko and Murrell, 2008). This classification encompasses multiple distinctions at the genera level, including C assimilation pathways further detailed in Chapter 7 and phospholipid fatty acid profiles, making it ideal for the study of C incorporation into biomarkers and their identification in palaeoenvironments in this thesis.

Based on 5S and 16S rRNA analysis, type I methanotrophs belong to the *Gamma* subdivision of the *Proteobacteria*, together with type X, while type II belongs to the *Alpha* subdivision. Genera included in these types are reviewed by Murrell (2010) and Hanson and Hanson (1996). The type I selected for this work is *Methylomonas methanica*, type II – *Methylosinus trichosporium* (OB3b) and type X – *Methylococcus capsulatus* (Aberdeen(IIA)).

Type I intracytoplasmic membrane arrangement is in bundles of vesicular disks, containing mainly fatty acids with 16 carbon atoms, and can assimilate formaldehyde as part of the ribulose monophosphate (RuMP) pathway (Murrell et al., 2000; detailed further in Chapter 7). It can only express pMMO, it is incapable of nitrogen fixation (Hanson and Hanson, 1996), and can incorporate a small amount of CO_2, relative to type II and X (Anthony, 1982; Jahnke et al., 1999).

Type II has paired peripheral layers within the intracytoplasmic membrane, produces mainly fatty acids with 18 carbon atoms and can incorporate both formaldehyde and formate via the serine cycle (Chistoserdova and Lidstrom, 1994; see Chapter 7). It can express both pMMO and sMMO, has the ability to fix nitrogen and, as part of its metabolic pathway, is able to incorporate a larger amount of CO_2 and metabolise a wider range of substrates when compared to type I (Hakobyan and Liesack, 2020).

Type X has the same intracytoplasmic membrane arrangement as type I, produces mainly saturate and monosaturated fatty acids with 16 carbon atoms, yet can assimilate carbon via a combination of RuMP with enzymes specific to Calvin-Benson cycle (CBC) and serine pathway (Hanson and Hanson, 1996). Similar to type II, type X can fix nitrogen and as part of the serine and CBC pathways, and is able to incorporate CO_2.

Environmental preferences are also considered with respect to this classification, mainly referring to types I and II, with several studies observing the prevalence of a certain type within distinctive environments. Although this classification is not widely applicable,

adaptations and competitive relationships between methanotrophs allow them to thrive in different niches even within the same environment.

Type I appears to occur in some studies in freshwater sediments or shallower terrestrial settings, where oxygen availability is higher (Bender and Conrad, 1992; Bender and Conrad, 1993; Bull *et al.*, 2000), and CH_4 concentrations are similar to atmospheric ones (i.e. low affinity; Bull et al., 2000), outcompeting type II in these conditions. In general, type I will grow more effectively when copper is found in higher concentrations, favouring pMMO expression (Graham *et al.*, 1993) and it was also observed to occur in environments where the pH is less acidic to borderline-neutral (Dedysh, 2009). Within the studied peatlands in this work, it was inferred at the surface of BVA peatland (Amariei, 2018), with reported pHs of 6.31 and 5.88 between the dry and wet seasons, respectively (Teh *et al.*, 2017).

Type II was reported in deeper settings within the environment, where O_2 concentration is lower or when CH_4 concentration is above atmospheric levels (i.e. high affinity; Bull et al., 2000). Type II methanotrophs were also found in acidic peatlands, within *Sphagnum*, bearing a symbiotic relationship with the moss (Dedysh, 2002; Murrell, 2010). When inferred within (palaeo)environments, they appear to prefer more acidic pHs than type I such as, within Pastaza-Marañón Foreland Basin (PMFB), type II was inferred based on the presence of C18:1 fatty acids (Amariei, 2018) and was later confirmed by Finn *et al.* (2020), in QT and SJO peatlands where the depth calibrated pH was between 3.1 and 5.4 (Amariei, 2018).

Apart from type I, II and X, two more types have been proposed (Murrell, 2010), a type III containing the acidophilic *Methylocapsa* and type IV, containing the three Verrucomicrobia representants, together known as *Methylacidiphilum infernorum*. The ability to recognize their presence in past environments is based on their lipid profiles such as fatty acids discussed below, and their stable isotope composition.

2.3. Lipid biomarkers

Biomarkers can be regarded as ubiquitous "chemical fossils" (Eglinton and Calvin, 1967), with specific biomarkers recognised for all three domains of life (Brocks and Pearson, 2005; Briggs and Summons, 2014), serving thus as proxies and past life fingerprints when direct evidence is not available. The first link between a molecular fossil, porphyrins, and its source, chlorophyll, was made in the 1930s (Treibs, 1934; Treibs, 1936). Since then, biomarkers have been linked to numerous bio-producers and their lipid remains can be used

to characterise wetlands and their (palaeo) vegetation assemblages, microbial communities and environmental parameters such as temperatures, pH, oxygen levels, water table levels via proxy calibration, biochemical cycles, the presence or absence of certain organisms, on time scales and under conditions that are not suitable for DNA investigations (Briggs and Summons, 2014).

In organic geochemistry, biomarkers are defined as decay-resistant organic molecules produced by, and linked to past living organisms' bio-synthetic pathways. They are preserved in the geological record, serving as evidence of past life, environmental conditions at the time of formation and diagenetic processes that occurred since their deposition (Brocks and Pearson, 2005; Brocks and Summons, 2005). These encompass a wide range of compounds (i.e., steroids, pigments, waxes, hopanoids, fatty acids), are insoluble in water, yet can be extracted with specific organic solvents.

Methanogens and methanotrophs, and microbes in general, are known to produce specific hopanoid and fatty acid biomarkers that enable their identification across a wide range of environments. These biomarkers, when coupled with carbon isotopic studies, aid in the reconstruction of the CH_4 cycle on the geological time scale. Biomarkers associated with vegetation, including *n*-alkanes, fatty acids, and sterols, have applications in diverse environments to describe changes in vegetation assemblages, discernible through their relative input and preservation conditions. Their combined study, coupled with isotope analysis, has aided in determining periods of high and low water table (Nichols *et al.*, 2006), vegetation type shifts (Ficken *et al.*, 2000), altitude profiles (Feakins *et al.*, 2018).

The main biomarkers used in this work, hopanoids and *n*-alkanes, are reviewed below, providing the current knowledge and studies based on which they have aided previous palaeoenvironmental interpretations (Amariei, 2018).

2.3.1.   Methanotroph cell membranes

Methanotrophs are Gram-negative bacteria, distinguishable from Gram-positives primarily through their cell walls and membrane structure, which, ultimately, allows crystal violet Gram staining and their easy detection as developed by Christian Gram (1884). Beveridge (1999) summarised the Gram-negative membrane as "strong, tough and elastic", relating the long life-span and ubiquitous nature of bacteria to these proprieties. Unsurprisingly, their membrane contains lipids as resistant to decay: phospholipid fatty acids (PLFA) and hopanoids, employed frequently as bacteria biomarkers.

The gram-negative bacteria cell is composed of an outer and inner membrane, two bi-layered structures, separated by the periplasm (peptidoglycan, Figure 2.2). The outer membrane is composed of lipopolysaccharides (LPS; Figure 2.2), proteins, phospholipid fatty acids (PLFA) and porins. Within the outer membrane, LPS molecules are located towards the exterior (Figure 2.2) having a protective, structural and mobility role and are reviewed in detail in Zhang *et al.* (2013) while PLFA are located in both layers of the outer membrane.

The lipids (PLFA and LPS) are in constant movement around the cell (Beveridge, 1995). The periplasm, the area separating the outer and inner membrane, contains proteins that facilitate nutrients and external compounds to be bonded to the cell as they are incorporated through porins, contains vesicles and is in constant chemical change as a response to the environment (Beveridge, 1999). The inner membrane is in contact with the cytoplasm, and it is composed of two layers of phospholipids, both containing proteins (Ruiz *et al.*, 2006; Figure 2.2).
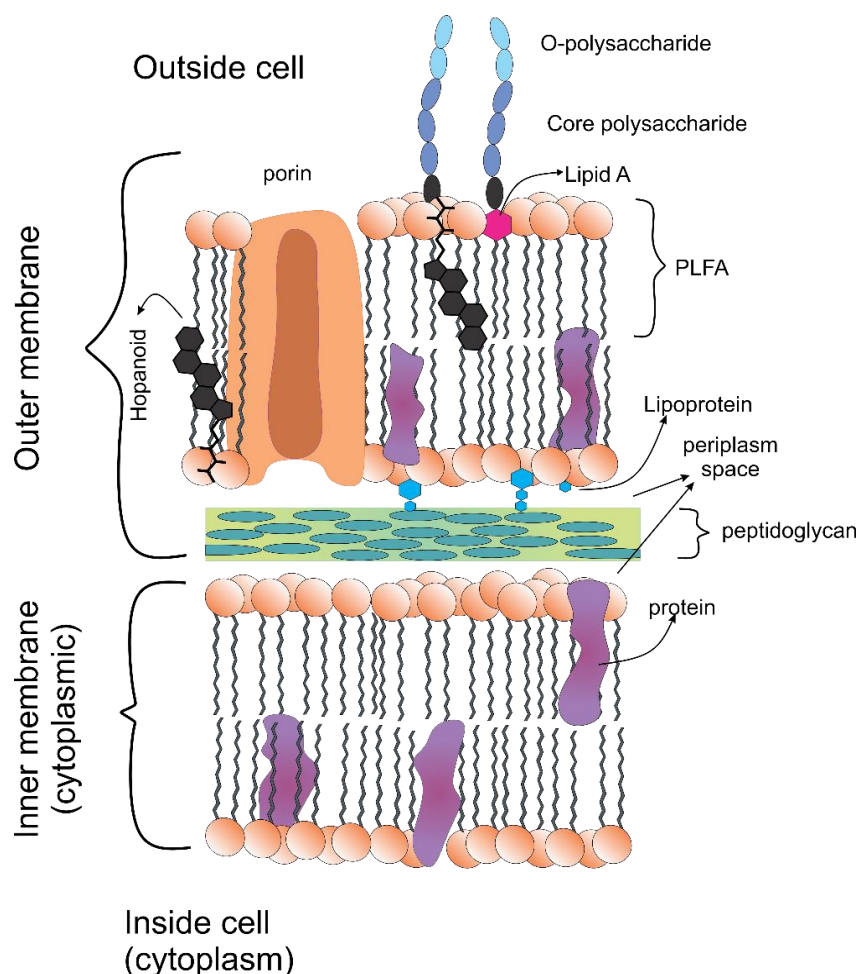
Figure 2.2 Membrane structure in Gram-negative bacteria (edited from Naloka, 2024).

Within the membrane, hopanoids are believed to occur between PLFA lipids and to regulate the fluidity of the outer membrane, providing increased rigidity and reducing permeability,

similar to the role of sterol in eukaryotes (Figure 2.3). In some bacteria, hopanoids have been observed to increase in concentrations with increased stress caused by temperature or acidity (Kannenberg and Poralla, 1999). Sáenz et al., (2015) further showed in a study on *Methylobacterium extorquens* and its *shc*-lacking mutant that the role of hopanoids is also related to multidrug resistance, with function in outer membrane ordering and interactions with glycolipids at that level.

2.3.1.1. Hopanoid overview

Hopanoids or pentacyclic triterpenoids are referred to and viewed as "sterol surrogates" of eukaryotes, exhibiting similar chemical, structural and functional proprieties, both displaying decay-resistant molecular backbones. Hopanoids display impressive characteristics, with over 200 structures identified in 1992 and classified as the most abundant natural multi-carbon compound, with approximations of a total global mass in the order of 10^{12} tons (Ourisson and Albrecht, 1992). The term hopanoid is used here to refer to molecules containing the pentacyclic triterpenoid backbone structure, acknowledging terms such as biohopanoids (i.e. produced *de novo*, unaltered), including bacteriohopanopolyols (BHPs), and geohopanoids, modified by diagenetic processes, and containing degradation products of the former, and their distinction in literature (Ourisson and Rohmer, 1992). Hopanoids attributed to purple sulphur bacteria have been further found in marine sediments as old as 1.64 Ba, with evidence of sterols and hopanoids such as 2α-methylhopanes, C_{27}-, C_{29}- and C_{30}-hopanes displaying evidence of eukaryote early life and oxic conditions (Brocks *et al.*, 2003; Brocks *et al.*, 1999; Summons *et al.*, 1999).

The need to understand hopanoid producers was initiated by their abundance in petroleum studies which led to their wide discovery in bacteria (Ourisson and Rohmer, 1992) and, most importantly, to a new pathway for isoprenoid biosynthesis, the methylerythriol phosphate (MEP) pathway (Rohmer et al., 1993), further discussed in Chapter 7.

Hopanoids have been detected in cyanobacteria (Sanez et al., 2012), obligate methylotrophs, non-sulphur bacteria (Rohmer et al., 1984), planctomycetes (Sinninghe Damste et al., 2004; Talbot et al., 2008a and references therein). The squalene-hopane cyclase (*sch*) which leads to the cyclisation of squalene and the synthesis of diploptene and diplopterol (Figure 2.3), was found in approximately 10% of both aerobic and anaerobic bacteria (Belin et al., 2018; Fischer et al., 2005; Ourisson et al., 1979). Sterol formation from squalene occurs via the action of oxidosqualene cyclase (*osc*; Figure 2.3) and they are characteristic of eukaryotes. Furthermore, hopanoids have been also reported in ferns, fungi, lichens and tropical tree

resins (Ageta and Arai, 1983; Rohmer et al., 1992; Volkman, 2005 and references therein; Ourisson et al., 1987), all encoding the SCH enzyme (Belin et al., 2018) and are discussed further in Subsection 7.3.1. under sources of diploptene, the main hopanoid of interest for this thesis.

2.3.1.2. *Hopanoids skeleton and nomenclature*

Hopanoids are hydrophobic planar molecules containing a 5-ring backbone (Figure 2.3). They form through the fusion of 6 isoprene units and belong to the isoprenoid group or cyclic triterpenoid subclass (Belin et al., 2018). This nomenclature leads to the encompassing name of pentacyclic triterpenoids, a name denoting their C_{30} skeleton, and 5 hexane ring structures in chair configurations (Kannenberg and Poralla, 1999).
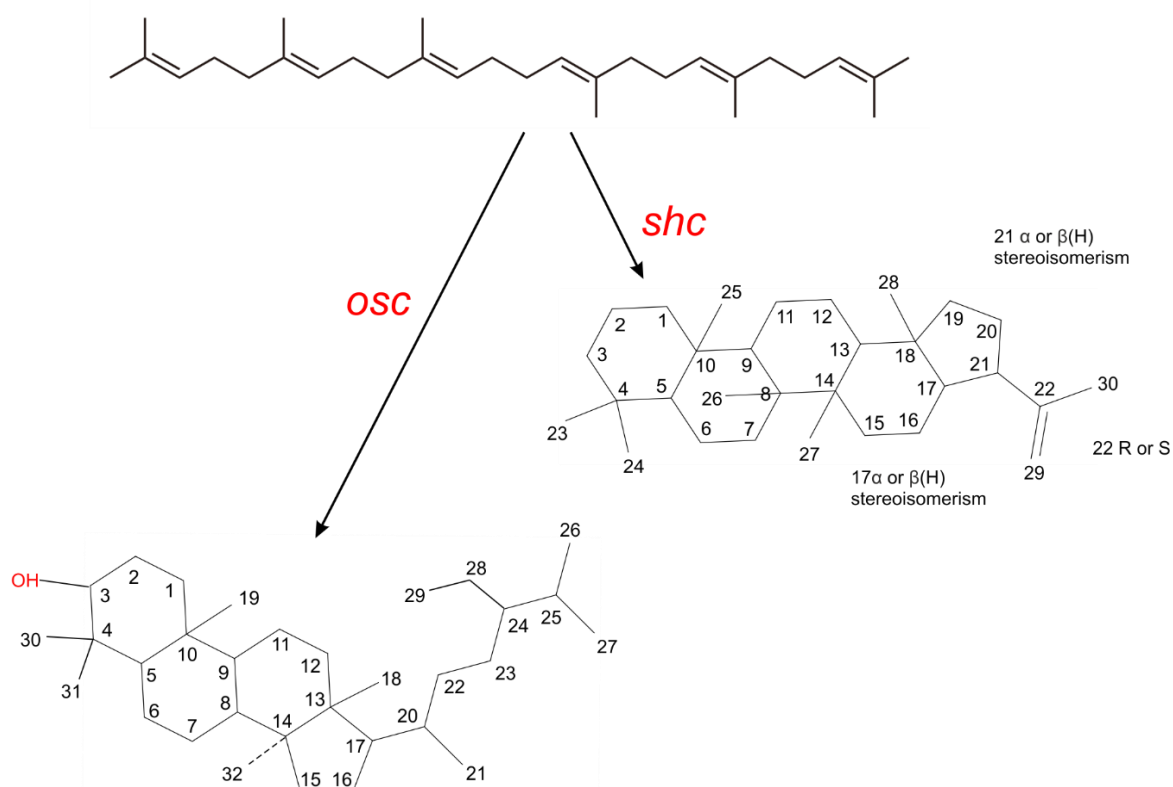
Figure 2.3 The conversion of squalene into diploptene and sterol skeleton, cholestane, via the action of two different enzymes: osc=oxidosqualene cyclase; shc=squalene-hopene cyclase. Molecular structures generated using RMG (Green and West, 2023), diploptene numbering taken from The Summons Lab (2024) and cholesterol numbering from Volkman (2005).

2.3.2. *n*-Alkanes - plant waxes

n-Alkanes are linear hydrocarbons present in plant cuticles and waxes and serve as important biomarkers in palaeoenvironmental reconstructions due to their stable and well-preserved nature over geological timescales (Jansen and Wiesenberg, 2017). They are key lipids in analysing the developmental history of the three peatlands reviewed in the following subsection and analysed in Chapter 3 of this work, as they provide valuable information on the past environments and transitions, as recorded through vegetation.

On their surface, leaves contain epicuticular waxes composed of aliphatic compounds, mainly of long chain *n*-alkanes and fatty acids (Kunst and Samuels, 2003), that act as a protective barrier against external factors. Their decay-resistant nature in sedimentary samples has been used to discern between relative percentages of vegetation and microbial input, between different vegetation sources and degrees of organic matter preservation (Jansen and Wiesenberg, 2017). The demonstrated generalisation is that long chain *n*-alkanes, with a strong odd-over-even distribution of the carbon numbers (i.e., $n\text{-}C_{27}$, $n\text{-}C_{29}$, $n\text{-}C_{31}$…), are produced as leaf waxes by terrestrial higher plants (Eglinton and Hamilton, 1967), $n\text{-}C_{23}$ and $n\text{-}C_{25}$ by aquatic plants, with the $P_{aquatic}$ (P_{aq}) ratio used to discern between input of terrestrial, emergent or submerged and floating macrophytes (Ficken et al., 2000). Shorter chains, with an even carbon distribution (i.e., $n\text{-}C_{16}$ and $n\text{-}C_{18}$), have been associated with thermal biomass degradation (Eckmeier and Wiesenberg, 2009), while lipid profiles with a high abundance of $n\text{-}C_{17}$ to $n\text{-}C_{21}$ are considered evidence of marine algae input (Cranwell *et al.*, 1987). In degraded OM, there is an overall decrease in the concentration of *n*-alkanes and a loss of the odd-over-even preference, with a decrease in the Carbon Preference Index (CPI) as long chain *n*-alkanes are preferentially degraded (Thomas *et al.*, 2021). *n*-Alkanes have been successfully employed across a wide range of environments to describe vegetation shifts based on their relative input and preservation conditions (i.e., forests-Norris *et al.*, 2013; peatlands-Baker *et al.*, 2016; marine-Bird *et al.*, 1995; mountain or altitude profiles-Feakins et al., 2018; lacustrine or marine-Feakins *et al.*, 2007).

Biomarker analysis coupled with stable isotopic techniques can provide further information on the prevalent environmental conditions at the time of their formation, preferred carbon sources and incorporation pathways to reinforce the links with the proposed bio-producers. Rieley *et al.* (1991) used carbon stable isotope signatures in correlation with the *n*-alkane distribution to define sedimentary sources by comparison to 'present-day' lake-side vegetation assemblage and values. Krull *et al.* (2007) have determined the different inputs of C_3 (trees) and C_4 (grasses) plants via stable isotope analysis, developing the I_{dec} index to

monitor changes over long time scales. Hydrological changes have also been investigated using hydrogen stable isotopes of *n*-alkanes (Xiong *et al.*, 2005) alongside wide climatic changes recorded within the C and H isotopes of these lipids (Saini *et al.*, 2017). Furthermore, carbon isotopes of hopanoids and FAs have been successful at detecting methanotrophy in the environment (Appendix A.3.1.)

2.4. Pastaza-Marañón Foreland Basin – previous work and literature review

Extensive palaeoenvironmental records exist for Pastaza-Marañón Foreland Basin (PMFB), with the current set of isotopic values for *n*-alkanes, hopanoids and fatty acids produced in this thesis (Chapter 3) adding to records such as **pollen** (Roucoux *et al.*, 2013; Kelly *et al.*, 2017), **geochemical and hydraulic conductivity** (Lawson *et al.*, 2014; Kelly *et al.*, 2014), **carbon storage** (Lawson *et al.*, 2015; Draper *et al.*, 2014; Lähteenoja *et al.*, 2012), **aerial carbon-pool and emission mapping** (Webb *et al.*, 2016), peatland on-site **GHG emissions measurements and controls** (van Lent *et al.*, 2019; Teh et al., 2017; Van Haren and Cadillo-Quiroz, 2016), **hydrological changes** (Aniceto *et al.*, 2014), **vegetation diversity** (Draper *et al.*, 2018; Valderrama, 2013) and **anthropogenic records and impact**s (Kelly *et al.*, 2018). The current biomarker dataset was thus aided by a wide range of existing data, and biomarkers were compared to pollen records which were previously used to describe the palaeoenvironmental shifts at QT and SJO. The MSc work of the author (Amariei, 2018) provided the first biomarker record for the three peatlands, containing *n*-alkanes, hopanoids, fatty acids, alcohols, GDGTs, and also the first overall palaeoenvironmental assessment for BVA peatland which even currently lacks a pollen record interpretation. Biomarkers were also used to calibrate palaeotemperatures and past peatland pHs for the first time in PMFB for the three cores (Amariei, 2018) after good correlations with present-day measurements (Teh et al., 2017). Within the three peatlands, diploptene was present in different concentrations within all sampled zones. As this biomarker can have multiple bio-producers, the correlations to methanotrophy and methanotroph community size were assessed through a suite of biomarkers (hopanoids, fatty acids, GDGTs), as direct isotopic evidence was not available at the time. In past studies (see diploptene CSIA review in Appendix A.3.1.), diploptene's isotopic signature could inform on the presence or absence of aerobic methanotrophs in environments where CH_4 production was expected. CSIA of this compound conducted in Chapter 3, will thus support previous assessments of the three

peatlands to act as CH_4 sinks or sources in the studied zones (Amariei, 2018), confirming the presence of aerobic methanotrophs and their relative activity.

The discovery of thick and undisturbed peat deposits in PMFB allowed new lines of investigation into pristine peatland (and overall, wetland) environments. Their addition to the global methane map and incorporation into global carbon budgets means that carbon cycles and dynamics must be further studied at these sites, and that assessments of past carbon incorporation pathways should be understood for future conservation and habitat rehabilitation. The studies which followed (i.e., post Amariei, 2018) investigated in deeper detail the impact of **vegetation** (Bhomia *et al.*, 2019; Kallweit, 2020; van Haren *et al.*, 2021; Soosaar *et al.*, 2022), **hydrology** (Quintana-Cobo *et al.*, 2018; van Lent et al., 2019), **microbiology** (Finn et al., 2020; Buessecker *et al.*, 2021) and **human presence** (Kelly et al., 2018; Hastie *et al.*, 2022; Hidalgo Pizango *et al.*, 2022) on local and regional carbon stores (Zhuang *et al.*, 2019; Coronado *et al.*, 2021; Bourgeau-Chavez *et al.*, 2022; Melton *et al.*, 2022) and GHG emissions (Brewer and Cadillo-Quiroz, 2020; Murphy, 2020; Treat *et al.*, 2021), providing data for the assessment of climate change impact on PMFB and its behaviours under predicted warming scenarios (i.e., IPCC, 2021, Chapter 4).

Modelling has already indicated that a potential shift of PMFB from a current carbon sink to a carbon source is likely under warmer and wetter climate scenarios (Wang *et al.*, 2018). Assessment of palaeotemperature, past precipitation regimes (indirectly via palaeo-pH biomarker calibration) and hydrology-vegetation assessments have, and can provide further details when coupled with vegetation-related biomarkers or pollen records. Furthermore, the Amazonia contains co-existing ombrotrophic (i.e., rainfed) and minerotrophic peatlands (i.e., flood-water fed; Lähteenoja *et al.*, 2009a), which is unusual compared to their Asian counterparts which are ombrotrophic in nature (Page *et al.*, 2006; Dommain *et al.*, 2015). This feature makes the PMFB peatlands important for further research, as they could provide valuable knowledge about the climate response in a region of significant ecological diversity.

More recent studies (Finn et al., 2020; Buessecker et al., 2021) have investigated the microbial community assemblage and functions in several peatlands from PMFB at the surface and in the top 100 cm. As expected, the hydrological regime which divides the peatlands into ombrotrophic (SJO), minerotrophic (BVA) and mixed (QT) has an impact on microbial distribution and roles with the water table depth governing the oxygen levels, while the water source (i.e., river flood-water or rain) controlling the acidity and mineral content of each peatland. Methanogen and methanotroph communities have been described via DNA and RNA markers (Finn et al., 2020; Buessecker et al., 2021) for the three peatlands

investigated here, and CH$_4$ fluxes have been related to their activity and peatland characteristics. In this chapter, this will allow previous methanotroph-related biomarker concentrations (i.e., hopanoids and fatty acids) to be compared to present-day microbial assemblages at the surface of QT, SJO and BVA, and correlations extrapolated to core-depths.

Previously, the potential of each peatland zone (i.e., sample) to act as a CH$_4$ sink or source was assessed based on a suite of biomarkers (Amariei, 2018). However, biomarkers (i.e., C$_{16:1}$ and C$_{18:1}$ fatty acids and hopanoids) used to assess microbial communities and to infer the presence of methanotrophs are known to be produced by a wider range of bacteria, which leads to ambiguity in interpretation and is further discussed in Subsection 3.3.4. CSIA has been widely applied to understand carbon sources and incorporation pathways into bacteria, and to confirm the presence of methanotrophs (see for example Appendix A.3.1.) yet only a limited set of CSIA data exist currently from PMFB (Inglis *et al.*, 2019), which cannot be used alone in providing down-core palaeoenvironmental interpretations. Given the broad range of data already existing for these peatlands and the proposed CH$_4$-sink or -source peatland assessments (Amariei, 2018), the same samples will be used in this work to investigate further the CH$_4$ cycle in PMFB via CSIA and the use of diploptene and associated hopanoids as proxies for past CH$_4$ consumption. The palaeoenvironmental setting and evolution of the 3 peatlands are described next, offering a compressive summary of the current studies that will support the newly produced isotopic values and their contextualization.

2.4.1. QT peatland – palaeoenvironmental summary

The Quistococha (QT) peatland is defined as mixed (i.e., van Lent et al., 2019), with a complex hydrological regime, receiving input from atmospheric precipitations, with an annual mean discharge of 3097 mm/yr (Marengo, 1998; Roucoux et al., 2013), from the Itaya River, a tributary of Amazon (Roucoux et al., 2013) and groundwater. The waterlogged, high humidity (80-90%), nutrient-poor and acidic conditions allow the present-day development of closed-canopy palm swamp vegetation (Roucoux et al., 2013). This vegetation type accounts for 78% (Draper et al., 2018) of the vegetation at PMFB, containing species such as *Mauritiella armata*, *Tabebuia insignis* and, the most abundant by basal area, *Mautitia flexuosa (M. flexuosa)* (Roucoux et al., 2013), which may have an impact on later discussed isotopic values.

Seasonality is poorly marked by the precipitation regime, with a wet season between June and September and a drier one between November and December (Marengo, 1998; Roucoux et al., 2013), conditions which also occur in the remaining two peatlands. The peat cores and surface samples were collected during the dry season when, within the *M. flexuosa* vegetation type peatlands, the peat temperatures recorded by Teh et al. (2017) during four field campaigns were averaged at 25.3°C and the air temperatures at 26.4°C. During sample collection, the peat's pH was subacidic at 5.49 and the water table just above the surface, at 6 cm (±1.3cm), with recorded dissolved oxygen values of 17.3%, slightly lower than those recorded during the wet season (Teh et al., 2017).

The pollen record was analysed by Roucoux et al. (2013) and the biomarker record by Amariei (2018). As an overview of the recent ($\leq$ 2280 cal yr BP) transitions experienced at this core location (Roucoux et al., 2013), the site was initially part of the Amazon River channel which deposited sandy sediments. The channel was then cut from the Amazon's direct influence, and inorganic clays, characteristic of lake-like settings, were deposited in a calmer environment (QT-1; 2280-2200 cal yr BP; Roucoux et al. (2013). As vegetation colonised the exposed terrain and the area experienced flooding conditions, peat started to accumulate (QT-2, 2200-2100 cal yr BP), with lake-specific vegetation developing at the core site. The pollen record indicates the next transition was to a permanently waterlogged forest (QT-3a 2100-1990 cal yr BP; Roucoux et al., 2013), yet the biomarker record still indicates the presence of a pool and macrophytes at the site (Amariei, 2018). Above this, *M. flexuosa* appears at QT for the first time (QT-3b; 2100-1990 cal yr BP; Roucoux et al., 2013), yet there are no samples from this core section for biomarker analysis, and the palm trees disappear in the following section (QT-4a), which is characterised by a closed canopy. The forested vegetation appears then to retreat from the site (QT-4b) and the pollen record suggests either herbaceous vegetation colonizing the site or the formation of a pool with fen and/or floating mat vegetation (Roucoux et al., 2013). For QT-4b, the biomarker record did not show a P_{aq} value (=0.11) to indicate a strong presence of a lake-like setting as in the previous depths (i.e., QT-2) and, coupled with both low brGDGTs and hopanoids concentrations previously interpreted as caused by the lack of root exudates or required microbial substrate, this depth was interpreted as an expansion of herbaceous taxa through the biomarker evidence (Amariei, 2018). The following sample from QT-4c represents a return to seasonally flooded wetland vegetation with a closed canopy (Roucoux et al., 2013), supported by the biomarker record, and QT-4d to herbaceous taxa, although no sample from this interval is available. The site becomes permanently waterlogged in QT-5a (120-128 cm; 1010-360 cal yr BP) and the canopy remains closed across QT-6 (20-28 cm; 360 cal yr BP)

with the reappearance of *Mauritia* t. which persisted until the present day (Roucoux et al., 2013).

2.4.2.   SJO peatland – palaeoenvironmental summary

San Jorge (SJO) is an ombrotrophic peatland characterised by a domed aspect, with the peat accumulating under acidic and nutrient-poor conditions (Lähteenoja et al., 2009a; Teh et al., 2017). In PMFB, this type of peatland sustains the most carbon-dense environment yet with a low tree diversity. SJO peat developed in the dome centre under short-pole forest vegetation, and is surrounded by palm swamp forest (Kelly et al., 2017). The dome morphology is mainly rainfed (Lähteenoja et al., 2009a) with thicker peat depths in the centre area of the peatland, making it at the same time more susceptible to water table depth changes (Kelly et al., 2017).

The samples analysed in this subsection were previously subjected to pollen and radiocarbon (Kelly et al., 2017), and biomarker analysis (Amariei, 2018). Several further carbon isotope values are available for *n*-alkanes and hopanoids from 3 samples collected between 70-100 cm from the same peatland Inglis et al. (2019), which will be integrated here as auxiliary measurements to the overall interpretation.

Similarly to QT, SJO has seen several palaeoenvironmental shifts, with both the pollen and biomarker data recording these changes. As an overview, radiocarbon dating of the core indicates that peat started forming at the site 2160-2370 cal yr BP (Kelly et al., 2017). Up to 240 cm, SJO is composed of sands, silts and clays which accumulated under the influence of the Amazon river.

Peat started to accumulate above 240 cm (sample SJO-1), indicating high water tables and anoxic conditions. The following available sample (SJO-2) is from a pollen zone dominated by herbaceous taxa, with an open canopy and the possibility of a lake development in the proximity of the core (i.e., floating mat vegetation pollen; Kelly et al., 2017). SJO-3 sample recorded higher input from aquatic plants, floating mat vegetation, freshwater algae indicating the formation or further expansion of the previous marginal lake. Specific aquatic taxa led to the observation that the lake waters were nutrient-rich and well-oxygenated (Kelly et al., 2017). SJO-4 sample sees the lake retreating from the core site, with peat input from terrestrial vegetation yet with lower accumulation rates and a hiatus in peat deposition around 100 cm. Finally, the surface of the domed peatland indicates ombrotrophic present-day conditions, mainly fed by precipitations, with the current vegetation possibly

establishing 200-150 cal yr BP as flood amplitudes reduced and the topography domed (Kelly et al., 2017).

2.4.3. BVA peatland – palaeoenvironmental summary

BVA was assessed as a peat-harbouring area in 2009 (Lähteenoja *et al.*, 2009b; Lähteenoja et al., 2009a), together with the previous two peatlands discussed above (QT, SJO). However, less is known about this peatland in terms of vegetation succession and palaeoenvironmental shifts as no pollen records have been produced to date. The previous biomarker study (Amariei, 2018) was the first to discuss the peatland's development, based on biomarkers assessed and confirmed against pollen records in the other two peatlands. Down-core carbon isotopic data is now provided for the 10 samples from this location (i.e., 6 core, 4 surface) and their interpretation is linked to the biomarker record, on-site surface measurements (Teh et al., 2017; Murphy, 2020; Kelly et al., 2014), and novel studies on DNA and rRNA on surface and subsurface microbial assemblages (Finn et al., 2020; Buessecker et al., 2021).

As an overview, BVA is considered a minerotrophic peatland due to its above rain-water nutrient content, higher Ca/Mg (Lähteenoja et al., 2009a) and a pH close to neutral values (Teh et al., 2017). As it has developed on a flat topography, it is annually flooded by nutrient-rich waters (Lähteenoja et al., 2009a), with the water table below the surface during the dry seasons (Teh et al., 2017) when, unlike in the previous two discussed peatlands, CH_4 fluxes are higher than in the wet seasons (Teh et al., 2017). These conditions allow peat to accumulate under present-day forested vegetation, with overall higher diversity than at QT or SJO (Kelly et al., 2014).

As in QT, a pale silty-clay sample is available from below the peat record (BVA-1) yet P_{aq} did not have values high enough to indicate a lake-like setting, with lipids considered to be allochthonous in nature. Higher plants dominated the vegetation at the core location, with a CPI below 10, yet a strong odd-over-even *n*-alkane distribution. There is no biomarker indication of a lake or herbaceous taxa development in the BVA succession, at least for the analysed zones. Hopanes peak twice in concentrations (BVA-2 and BVA-5) indicating higher palaeo-oxygen concentrations. Importantly, the detection of FAs indicative both of type I and II methanotrophs at BVA (Amariei, 2018) was recently confirmed by DNA surface studies (Finn et al., 2020).

Carbon stable isotope analysis can provide, within the context of previously analysed data, further certainty on lipid-inferred (palaeo)environmental shifts and processes, providing

certainty in biomarker attributed bio-producers. As isotopic measurements are scarce within PMFB, *n*-alkanes and hopanoids can be employed to understand better vegetation successions and the links between the inferred CH_4-production and methanotroph CH_4 consumption.

2.5. Carbon stable isotopes and processes

Carbon has two stable isotopes: ^{12}C which occurs in approximatively 98.93% and ^{13}C, bearing a natural percentage of 1.07% (Hoefs, 2015) and, in order to measure their ratios at natural abundance levels on an Isotope Ratio Mass Spectrometer (IRMS), they need to be converted first to CO_2 or CO (Valley and Cole, 2018), and calibrated against a standard ($^{13}C/^{12}C_{PDB}$=0.0112372). The delta value (i.e., $\delta^{13}C$) thus measures the relative abundance of the carbon isotopes in a sample compared to a standard. A negative isotopic value of a compound, such as -40‰, indicates that its $^{13}C/^{12}C$ is 40‰ (i.e., 40/1000) lower than that of the used standard. If sample A has a $\delta^{13}C$ that has a lower ^{13}C to ^{12}C ratio relative to sample B, A is referred to as being more depleted, or lighter, displaying a more negative value relative to B, while B is relatively more enriched, or heavier, in regards to the amount of ^{13}C to ^{12}C compared to A. The carbon isotopic signature (‰) of a compound can be calculated after Eq. 4:

$$\delta^{13}C = \frac{\left(^{13}C/_{12C}\right)_{sample} - \left(^{13}C/_{12C}\right)_{standard}}{\left(^{13}C/_{12C}\right)_{standard}} \qquad \text{Eq. 4}$$

At the final step in OM decomposition, methanogenesis leads to the production of isotopically depleted CH_4 (Rosenfeld and Silverman, 1959; Whiticar *et al.*, 1986). The enhanced depletion in the ^{13}C relative to the ^{12}C has been early on recognised in all the pathways that lead to microbial-mediated CH_4 production, via acetoclastic fermentation (Gelwicks *et al.*, 1994), reduction of CO_2 (Games *et al.*, 1978), reduction of methanol (Rosenfeld and Silverman, 1959). This process is mass-dictated. The bond between two lighter isotopes (i.e., ^{12}C-^{12}C) is weaker and more reactive than a bond between heavier isotopes (i.e., ^{12}C-^{13}C), an effect that arises from the potential energy surfaces, used to

describe the harmonic oscillator approximation and vibrations between two atoms through quantum mechanics (Valley and Cole, 2018). At the CH_4-producing reaction level, a lower vibration frequency is characteristic of heavy isotopes, while higher vibration frequencies are characteristic of lighter isotopes with higher ionic potential (Tiwari *et al.*, 2015). From here on, the lighter isotopes will form weaker bonds and thus, will react more readily, giving a faster reaction rate than the heavier isotopes, leading to the observed **isotopic effects** or **fractionation** (Boschker and Middelburg, 2002; Valley and Cole, 2018), based on mass discrepancies. A faster reaction rate will favour lighter isotopes and thus, weaker bonds will lead to the product of a reaction enriched in lighter isotopes, while the reactant, in heavier isotopes (Melander *et al.*, 1980).

The isotopic <u>fractionation factor</u> (α) is a quantification of the partitioning of isotopes (Eq. 5), with k-the <u>rate constant</u> and n-the number of exchanged atoms (i.e. if n=1, only one atom exchanged, α=k). For a unidirectional reaction (A→B; Eq. 6), it indicates the extent of fractionation or, in other words, how much the lighter isotope was preferred to the heavier one (Blaser and Conrad, 2016; Eq. 6). This mass discrimination process is a consequence of the <u>isotope effect</u> discussed above.

$$\alpha = k^{\frac{1}{n}}$$ Eq. 5

$$\alpha_{A,B} = (\delta^{13}C_A + 10^3)/(\delta^{13}C_B + 10^3) = R_A/R_B = (^{13}C/^{12}C)_A / (^{13}C/^{12}C)_B$$ Eq. 6

The <u>enrichment factor/isotopic fractionation factor</u> (ε), is caused by the **isotopic effects** and indicates the degree of fractionation during a reaction (i.e. conversion of substrate→product) and can inform on the degree that heavier isotopes were discriminated during a biochemical reaction (Eq. 7). The α can be replaced by ε, as ε is also expressed in ‰ as δ value in Eq. 4 (Valley and Cole, 2018).

$$\varepsilon = (1 - \alpha) \times 10^3$$ Eq. 7

ε is temperature dependent (Urey, 1947), with a general assumption that isotopic fractionation increases with decreasing temperature, with α inverse proportional to T^2 (Tiwari et al., 2015).

Different processes involved in the CH_4 production and consumption cycle have characteristic isotopic signatures and fractionation factors, discriminating between lighter, biologically-produced CH_4 and the prevailing reactions and substrates (Conrad, 2005), thermogenically-produced CH_4 resulted from degradation of OM in sedimentary rocks during burial and abiogenic CH_4, formed by chemical reactions that do not involve OM (i.e., mantle activity, gas-water-rock interactions, Etiope and Sherwood Lollar, 2013; pyrogenic).

The latter two are non-discriminatory processes, with isotopic fractionation affected by the produced amount and diffusion processes (Zhang and Krooss, 2001), leading to relatively enriched CH_4 isotopic signatures. At the atmospheric level, the different sources and isotopic signatures are mixed, with a global bulk $\delta^{13}C_{CH4}$ of -53‰ (Chanton *et al.*, 2005). Isotopic fractionation takes place during CH_4 destruction via OH, with the molecules containing the lighter carbon reacting faster, leading to a $\delta^{13}C_{CH4}$ signature for ambient air of approximative -47‰, with latitudinal or regional scale differences (Cicerone and Oremland, 1988; Brownlow *et al.*, 2017; Schroll *et al.*, 2020).

Conversely, CH_4 aerobic (and anaerobic) oxidation by bacteria has its own biologic isotopic fractionation effect, favouring reactions that involve the lighter isotope of carbon (Silverman and Oyama, 1968; Chanton et al., 2005), leading to a depletion of their biomass on the expense of an ^{13}C-enriched surrounding atmosphere. The three types of methanotrophs discussed will incorporate CH_4 either as formaldehyde or formate (see Subsection 7.3.1.), leading to a depletion in the dissimilated CO_2 or in the intracellular carbon-pool available for growth.

Methanotroph biomarkers reported in the literature, such as fatty acids and hopanoids discussed previously, have highly depleted isotopic signatures when compared to non-methanotroph lipids produced by e.g., plants, chemotrophs, heterotrophs within the same environment. This occurs as isotopic fractionation takes place between the *in-situ*, already depleted methanogen-produced CH_4 pool (or less depleted CH_4 when available at atmospheric concentrations; Bull et al., 2000) and intracellular space, as mediated by the MMO enzyme. The initial, MMO-mediated, step is followed by a series of further isotopic fractionation factors associated with biological reactions which lead to the formation of a specific biomarker. For example, as discussed earlier, the MMO enzyme can have two forms, with the pMMO leading to higher CH_4 pool fractionation factors than sMMO. Expression of one of the two enzymes was not seen to have an effect on the distribution of lipids, yet lipids of type I utilising the RuMP cycle and pMMO were less depleted (by 1-3‰) than those of the serine cycle (12‰) relative to the biomass bulk isotopic signature (Jahnke et al., 1999).

Similarly to how CH_4 fractionation occurs during methanotroph incorporation, plant organic matter (including biomarkers) exhibits a carbon isotopic composition that is related to the photosynthetic pathway responsible for its fixation. The atmospheric $\delta^{13}C_{CO2}$ has remained constant over the geological time, shifting only recently towards more depleted values due to anthropogenic fossil fuel burning (i.e., from -6.5‰ to -8‰; NOAA, 2024). Plant CO_2

incorporation fractionates against the heavier $^{13}CO_2$ based on their own metabolism, via CO_2 diffusion into the leaf, enzymatic isotopic fractionation and available carbon pools used for synthesis, preferentially using $^{12}CO_2$ (Park and Epstein, 1961; O'Leary, 1981). C_3 plants (e.g., rice, grass, oak trees) draw from the CO_2 atmospheric pool via the carboxylation of ribulose biphosphate, with the Rubisco fractionation accounting for 29‰ during CO_2 fixation (Park and Epstein, 1960; Roeske and O'Leary, 1984), while C_4 plants (e.g., maze, sugarcane; drier climates) use CO_2 via the carboxylation of phosphoenolpyruvate (Kortschak et al., 1965). These two processes have different fractionation factors, with C_3 plants displaying more negative bulk $\delta^{13}C$ values than C_4 which can also fixate enriched bicarbonate (Table 2.1), with CAM plants displaying a value between the two types. Currently, known fractionation factors (α) for enzymatic plant processes are summarised in Tcherkez et al. (2011). A detailed database of global CH_4 isotopic signatures from different processes can be found in Schwietzke et al. (2016), and a summary of isotopic values relevant for this work, in Table 2.1.

Different plant metabolites display varying $\delta^{13}C$ values. At the leaf level, epicuticular wax components such as *n*-alkanes have relatively depleted values when compared to carbohydrates and bulk plant material (Park and Epstein, 1961; Collister et al., 1994). Leaf wax fatty acids also display relatively depleted values relative to the fixed CO_2 (Hobbie and Werner, 2004). Furthermore, isotopic variations were observed between *n*-alkanes of different lengths, varying between 0.1‰ to 6‰, indicating that isotopic variations within this range between different homologues in sedimentary records may not have different sources (Collister et al., 1994). This is due to primary isotope effects which favours the selection of ^{12}C during the formation of a bond, leading to non-homogenous isotopic distribution with metabolites (Hobbie and Werner, 2004;). At the position-specific level, in one phytology study, glucose intramolecular distribution was shown to differ between C_3 and C_4 plants, with C-1 and C-3 carbon positions able to distinguish between the two metabolic pathways (Rossmann et al., 1991). Carbon biosynthetic fluxes of different types of plants were also observed to have different fractionation patterns, such that woody C_3 plants lipids and lignin have more carbon allocation than those in herbaceous plants (Hobbie and Werner, 2004). The partition of carbons within a pathway is isotopically-dependent on the size and isotopic value of the substrate pool, and its replenishment. Isotopic fractionation is thus associated with biological reactions such as those which lead to the formation of *n*-alkanes, fatty acids and hopanoids as the isotope flux is incomplete and unidirectional.

To access biomarkers for identification, quantification, isotopic analysis and pyrolysis, they have to be extracted from the bacteria culture or sediment sample via organic solvents, and

separated into classes based on the polarity of the solvent (see Subsection 3.2.2.). Gas chromatography (GC) methods are then employed to separate a class of compounds into individual molecules, with different detectors allowing more fine-tuned analysis.

Table 2.1 Summary of literature reported isotopic values relevant to this work.

Environmental pool	Isotopic values	Reference
Atmospheric CH$_4$	-47‰	Cicerone and Oremland (1988); Brownlow et al., 2017; Schroll et al., 2020
Atmospheric CO$_2$ present	-8‰	NOAA, 2024
Methanogenic CH$_4$		
Aceticlastic α	α=1.007 to 1.027	Goevert and Conrad, 2009
CO$_2$ reduction α	α=1.002 to 1.079	Botz *et al.*, 1996
Wetlands	-61.5 ±0.6‰	Schroll et al., 2020
Tropical wetlands	-61.5± 2.9‰ to -53 ±0.4‰	Brownlow et al., 2017
	-40‰ to -70‰	Schroll et al., 2020
Boreal wetlands	-50‰ to -85‰	Schroll et al., 2020
CH$_4$ from biomass burning	-24‰ to -32‰	Cicerone and Oremland, 1988
Animal emissions with a C3-plant diet	-60‰ to -75‰; -69.4±3.1‰	Cicerone and Oremland, 1988; Schroll et al., 2020
Animal emissions with a C4-plant diet	-47‰ to -55‰; -54.6±3.1‰	Cicerone and Oremland, 1988; Schroll et al., 2020
Thermogenic CH$_4$	-25‰ to -50‰	Cicerone and Oremland, 1988
C stored in C3 plants	-22‰ to -37‰	Cicerone and Oremland, 1988
C stored in C4 plants	-10‰ to -20‰	Cicerone and Oremland, 1988
C stored in CAM plants	-27‰ light; -13‰ dark	O'Leary, 1981
Leaf wax n-alkanes of C3 (n-C$_{24}$ to n-C$_{35}$)	-31‰ to -39‰	Collister et al., 1994
Leaf wax n-alkanes of C4	-18‰ to -25‰	Collister et al., 1994

2.6.   Gas chromatography and associated techniques

Gas chromatography (GC) techniques coupled with Flame Ionization Detector (FID), Mass Spectrometer Detector (MSD), and Isotope Ratio Mass Spectrometry (IRMS), prove indispensable in the study of semi-volatile compounds such as *n*-alkanes, fatty acids and hopanoids from (palaeo)environmental samples, with a focus in this thesis on peatlands and microbial cultures. FID is valuable for its sensitivity to hydrocarbons, making it apt for detecting and quantifying *n*-alkanes in complex mixtures. The versatile MSD provides enhanced specificity by identifying individual compounds based on their mass spectra, allowing for precise characterization of hopanoids, *n*-alkanes and fatty acids. IRMS, on the other hand, facilitates the assessment of isotopic signatures, enabling the determination of carbon isotope ratios in these compounds. In palaeoenvironmental studies, GC techniques aid in reconstructing past environmental conditions by analysing biomarkers preserved in peat cores. The unique fingerprinting capabilities of FID and MSD contribute to compound identification, while IRMS provides insights into the sources and cycling of organic matter. These techniques, when integrated, offer a comprehensive approach to unravelling the complexities of peatland ecosystems and their historical dynamics, shedding light on climate, vegetation, and microbial interactions over time.

2.6.1. Gas chromatography principles

The term *chromatography*, composed of the Greek words *chromos* and *graphein* (colour and write) was first used by M.S. Tswett (1872-1919) in the study of leaf pigment separation using liquid chromatography techniques, with suggestions in the 1960s for the term to be changed to Tswettography (tswett = (ru) colour; Smolková-Keulemansová, 2000). Professor Erika Cremer conducted the first scientific work in the field of GC at the University of Innsbruck in the second part of 1944. She replaced the solvent mobile phase in liquid chromatography with an inert carrier gas phase to separate compounds, and further pioneered the principles of relative retention time and peak area calculation. Due to the historical context, this chromatographic advancement was not published at the time (Ettre, 1990) and the first description that set the scene of GC lies in two papers by Martin and Synger (Martin and Synge, 1941a, Martin and Synge, 1941b). The studies still employed liquid-liquid

extraction and partitioning of amino-acids, yet mentioned the separation of volatile compounds in a column through which a gas flow is supplied over a gel treated with non-volatile solvents (Bartle and Myers, 2002). In 1952, their work received the Nobel prize and was described in Nature as "likely (…) one of the most important milestones in the development of chemical sciences" (Smolková-Keulemansová, 2000). In the same year, Gerhard Hesse presented the absorption GC in gas-solid systems and published a book based on this principle in 1943. In the early 1950s the first GC system was built outside England and the petrochemical industry (i.e., Shell and British Petroleum) became interested in the further development of early technology. This technique has grown in popularity over the years due to its improved selectivity and resolution, reproducibility, precision, sample amount and types that it can accurately process.

IUPAC defines chromatography as "a physical method of separation in which the components to be separated are distributed between two phases, one of which is stationary (stationary phase) while the other (the mobile phase) moves in a definite direction" (Ettre, 1993). There are numerous types of chromatography methods, including column chromatography, ion-exchange, molecular sieve chromatography, affinity and pseudo-affinity, paper and thin layer chromatography, dye-ligand, hydrophobic interaction, liquid and gas chromatography (Coskun, 2016). The role of a GC system is the separation of volatiles and semi-volatile analytes. The separation is due to the two interacting heterogeneous phases (i.e. non-miscible), one stationary and one mobile, that are in contact with each other close enough to interact, yet do not mix. In this thesis the focus is on capillary
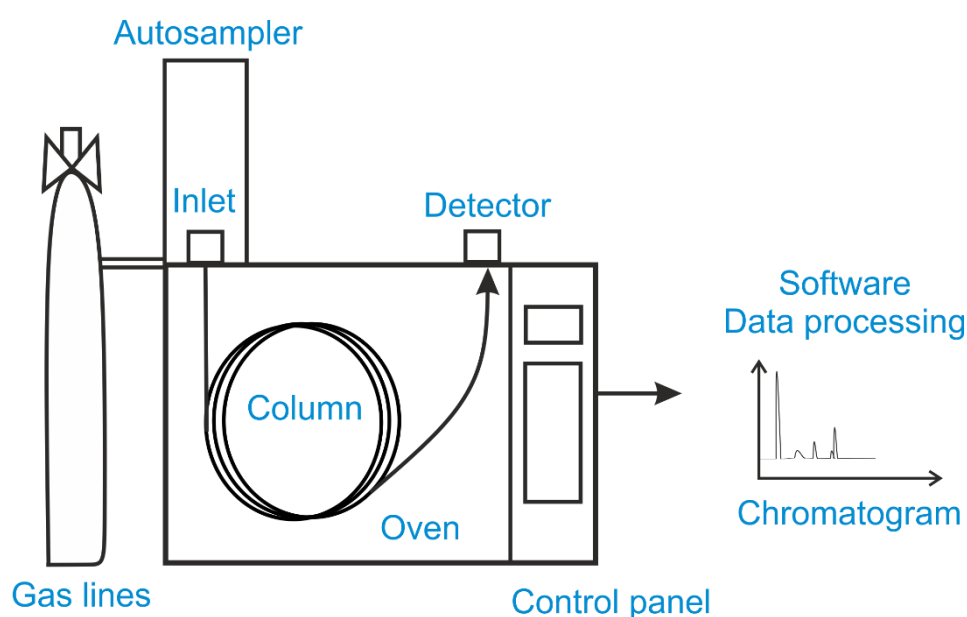
Figure 2.4 Schematic view of a simple GC system (edited from Dettmer-Wilde and Engewald, 2014).

gas chromatography, and the functioning principles of a simple GC system (Figure 2.4) are briefly described next.

For GC systems, the mobile phase is a pure and inert carrier gas, usually helium, that carries the vaporized analytes through a thin yet long glass/fused silica column, and the stationary phase is the internal coating in the column (Dettmer-Wilde and Engewald, 2014). The sample (gas or liquid) is loaded into a microliter syringe and injected manually or automatically into the GC inlet. The **inlet** is usually heated, transforming the liquid sample into vapor, mixing it with the carrier gas and transferring the constituting molecules to the head of the column in a controlled and repeatable fashion (Figure 2.5). During separation, equilibrium is formed between the mobile and stationary phase in segments of the column, with the remaining mobile phase being transported to the next segment of the column (i.e., plate; de Coning and Swinley, 2019). The **oven**, in which the column is enclosed, is usually heated to a set temperature, following a heating gradient (°C/min) or is held isothermal at a constant temperature, usually up to 350°C or as indicated by the column manufacturer (i.e., based on internal coating proprieties). Thus, as the compounds move through the **column** (stationary phase), multiple solute-vaporisation or absorption-desorption reactions are taking place. The carrier gas flow rate has an effect on the hold-up time, the time the compound spends in gas phase and moving through the system, while the oven's temperature or ramp has an effect on the retention time, the time the compound spends retained or sorbed onto the column (McCann *et al.*, 2020). This leads to different compounds with various proprieties and boiling points to be retained differently, resulting ideally in a reproducible dwell time (retention time) which leads to their separation and can be used for relative identification. The end of the column is connected to a **detector** (Dettmer-Wilde and Engewald, 2014), which receives and records the eluting compound signal in real time, transferring and translating it via a software for the user to interpret. The operation principles
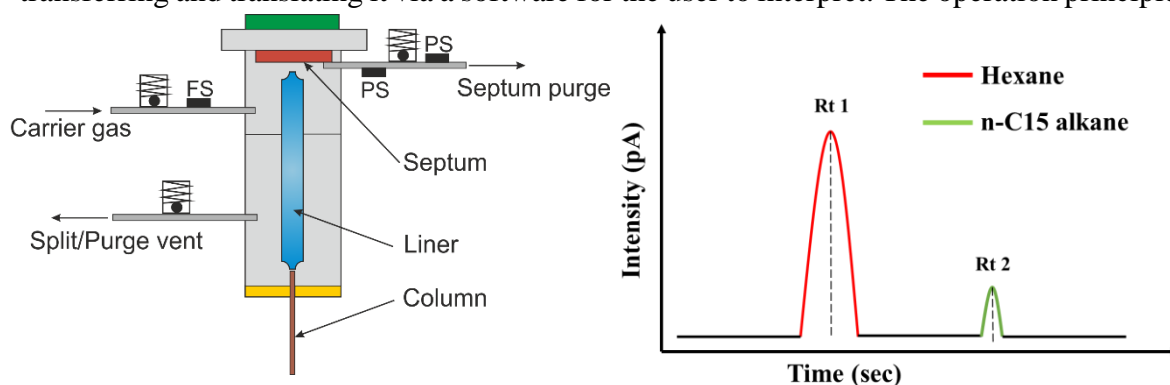
Figure 2.5 Reproduced schematic view of a Split/less Agilent inlet and chromatogram. PS=pressure sensor; FS=flow sensor. Notice the different intensities and retention times of the two molecules.

of the detectors used in this work are described next. The plotted signal is called a **chromatogram** and it is described by its retention time on the *x* axis and usually by its intensity or abundance on the *y* axis (Figure 2.5).

2.6.2. Detectors

2.6.2.1. Flame Ionizing Detector (FID)

The GC-**Flame Ionizing Detector** (GC-FID) was first introduced in 1958 (William and Dewar, 1958; Holm, 1999) and consists of a hydrogen-air flame to which the analytes are directed. As the analytes within the carrier gas reach the flame, they are burned (destructive analysis), leading to the formation of ions (e$^-$; Figure 2.6). The ions make up an electric current proportional to the number of carbons within a compound, which is redirected by a polarising voltage to a collector (i.e., a circular metal electrode) that converts the small signal (picoamps; 10^{-12} A order) into a digital reading, done by an electrometer.

At the flame point, the chemical bonds are broken via hydrogen atom attack and bond fission, and the molecules are step-wise converted to CH_4, which exhibits the strongest C-H bonds (Figure 2.6; Holm, 1999). A very small number of carbon atoms will become ionised (around
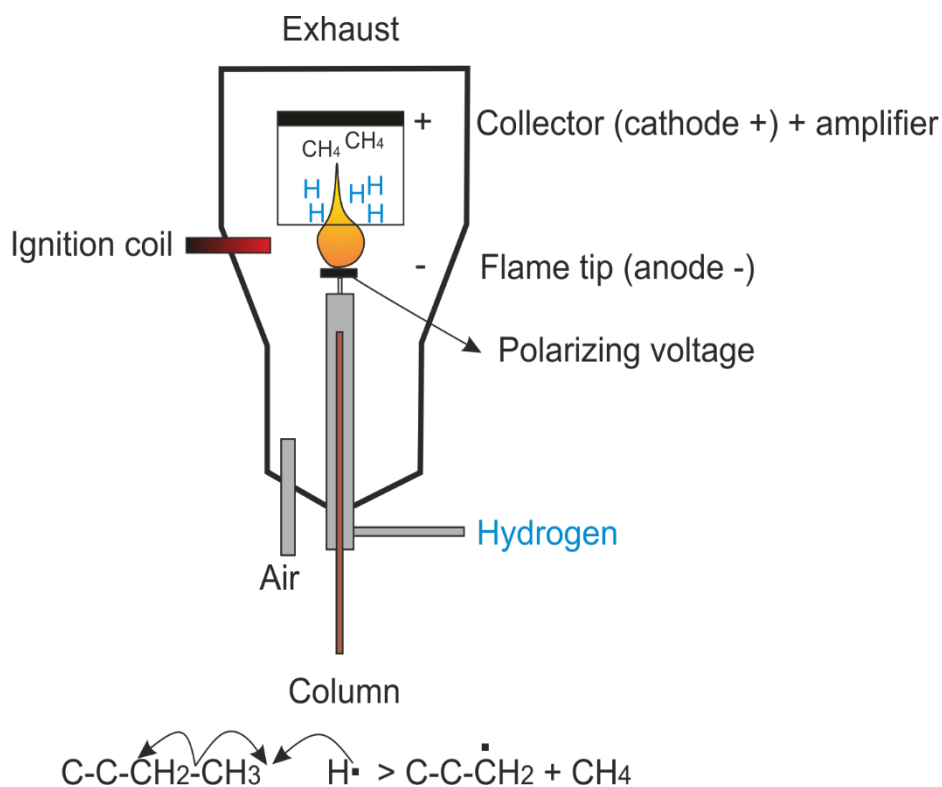
Figure 2.6 Schematic of an FID. Notice the position of the anode, at the flame's tip, and the cathode, at the flame's end, where the ion collector and amplifier are located. The chemo-ionisation process below shows the H atom attack and CH_4 formation as described and shown in Holm (1999).

61

1:1.000.000), with the ion number proportional to the amount of compound burned (mass), making the FID a robust carbon-counting detector (Holm, 1999). This detector is thus set to analyse carbon-containing samples able to produce CH_4 moieties during bond-breaking at the flame point, making it an almost universal detector as it only excludes a few analytes such as CO, CO_2, CS_2, CH_2O, CH_2O_2. The limit of detection (LOD) is 10^{-12} g of carbon/second (Dettmer-Wilde and Engewald, 2014). The background noise of an FID is related to the purity of the flame hydrogen or carrier gas, and can approach zero. Background increases at higher oven temperatures as a result of column "bleed", as the stationary phase degrades and releases small amounts of compounds into the mobile phase (Holm, 1999). The GC-FID utilised in this study was a 7890A Agilent.

2.6.2.2. Mass Spectrometer (MS)

The FID working principle of chem-ionisation was actually understood via the use of a mass spectrometer (MS) (Holm, 1997) by the direct probing of the flame and analysis of the molecule resulting during hydrogen burning. This occurred over 40 years after the FID was introduced. The MS working principle was first demonstrated in 1959 (Gohlke, 1959) when molecules separated via a GC system were introduced into a time-of-flight MS (TOF-MS); a timeline of pre-dating scientific events are available in De Hoffmann and Stroobant (2007).

The **GC coupled** with a **Mass Spectrometer detector** (GC-MSD) operates under high vacuum conditions, limiting the interactions between sample molecules and atmospheric contaminants. The hyphenation of the GC and MSD occurs via a heated interface where the
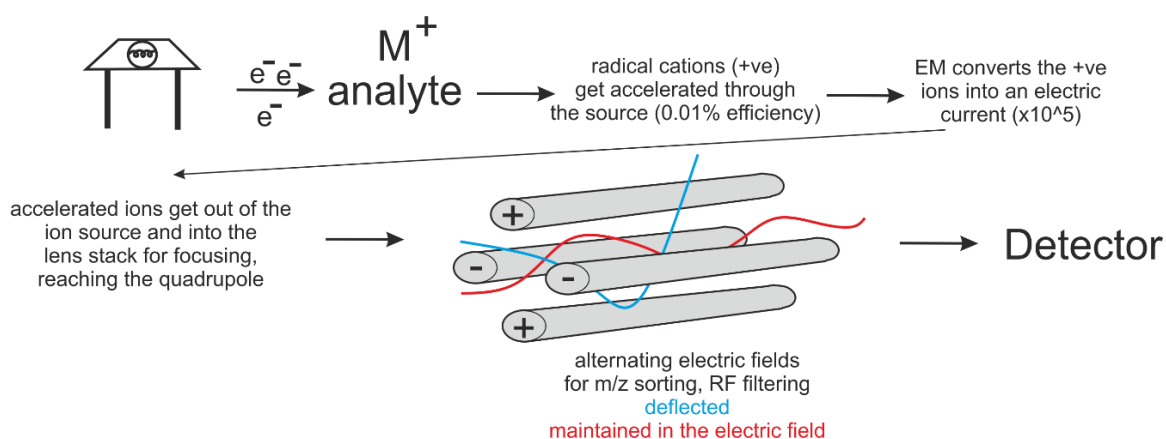
Figure 2.7 Operating principle of the MSD, ion generation, sorting and detection through the quadrupole. The unstable molecular ion fragments further, forming ions, radicals and neutral charged smaller molecules. These secondary particles are then converted into electrons, and are amplified to an order of 10^5-10^6 within the electron multiplier (EM), producing a current. They are then focused by lenses, accelerated by a dynode and sent, in the case of the MSD used in this thesis, to the quadrupole analyser, where they are screened.

high flow of the carrier gas is reduced before analytes reach the MSD and ion source. **Electron ionisation** (EI) is the most common ion source to form ions and is the method employed in this work for qualitative identification of molecules. In the ion source (Figure 2.7), electrons emitted from a filament are able to ionise the analytes, leading to a loss of an electron (e⁻). This is termed the **molecular ion (M⁺),** and it indicates the total mass of an analyte (i.e., mass of compound minus 1). The quadrupole consists of 4 rods, to which an AC current is applied, together with an DC and an alternating RF (radio frequency), used to select and focus ions only of a certain, pre-selected mass to charge ratio (*m/z*) to the detector, producing a 'fingerprint' of the analyte (Figure 2.7). This consists of the molecular ion and further peaks of different intensities that provide information on the structure of fragments and that of the analyte as a whole. This fingerprint is termed a **mass spectrum** and it is used for analyte identification (and quantification) (De Hoffmann and Stroobant, 2007). EI however, does not always produce a molecular ion due to extensive fragmentation, and chemical ionisation (CI) is sometimes preferred due to its "soft ionisation" potential (De Hoffmann and Stroobant, 2007). For dataset and library correlations, and to assure that gas phase molecules are ionised to the same degree, for EI the voltage is set in most MSD at 70 eV, an energy able to convert 0.001% of a compound into ions. For each compound, a mass spectrum is generated containing the molecular ion and other ionised fragments of the compounds, presented as their **mass-to-charge ratio (*m/z*)** and their abundance. The mass spectra are compared with existing records within software libraries (i.e. NIST, Wiley) for compound identification. The GC-MS instrument used in this study is an Agilent 5975C inlet XL EL/CL MSD with a triple axis detector.

2.6.2.3. Isotope Ratio Mass Spectrometer (IRMS) – stable carbon isotope application

The use of hyphenation to integrate GC instrumentation with a combustion unit and an IRMS detector is prevalent in many scientific fields (Preston and Owens, 1983; Lichtfouse, 2000), including, but not limited to: geochemistry, (palaeo)environmental chemistry and monitoring, archaeology, (bio)degradation, food and beverages, forensic science and drugs, astrobiology and biology, arts and history, sports and competitions. When a question arises regarding the origin or fate of molecules present within a sample at natural abundances, stable isotope measurements provide in-depth information at the intermolecular level. Being such a versatile analytical tool with wide applications, an extensive literature has been published on stable isotopes and IRMS techniques, with the references provided above constituting sub-field reviews.

Unlike the dual-inlet IRMS, commonly used for very accurate and repeated measurements at natural abundance levels, where the sample and reference gas are measured (almost) simultaneously, under the same conditions (Barrie and Prosser, 1996), the continuous flow (CF) systems couples the power of GC separation, online combustion and delivery of CO_2 molecules to an IRMS. Dual-inlet IRMS measurements were possible prior to 1950 (Nier, 1947; Dunn and Carter, 2018), while the first paper which utilised a CF-IRMS for CSIA was published in 1978 by Matthews and Hayes, and later, the system was optimized in 1983 and 1985 by Preston and Owens.

Following GC separation, the compounds have to be converted into simple gas molecules to allow for the quantitative measurement of the molecule and scan range of the IRMS detector (i.e., for CO_2, scan m/z 44, 45 and 46). They enter a combustion reactor set at temperatures usually between 900°C-1000°C for carbon isotopes, made out of quartz or ceramic material and packed with CuO/Pt or CuO/NiO/Pt fine wires (Eakin et $al.$, 1992). In the presence of high temperatures, organic compounds are converted into CO_2, which, if quantitative combustion takes place, they represent the isotopic signature of the original molecule, retaining thus the isotopic provenance. Over time, the combustion reaction depletes the reactor's packing of oxygen. The reactor is routinely conditioned by passing pure O_2 to restore its combustion efficiency. A semi-permeable membrane, such as Nafion®, is used to remove water produced during the combustion reaction, ensuring that only the targeted gases are measured, while the combustion products are kept in the carrier gas and directed to the ion source which operates under vacuum (Figure 2.8).

In the case of carbon stable isotope measurements, the produced CO_2 can have three isotopomers: $^{12}C^{16}O^{16}O$ (m/z 44), $^{13}C^{16}O^{16}O$ (m/z 45) or $^{12}C^{18}O^{16}O$ (m/z 46). Water removal in the previous step is essential due to the interaction with CO_2 which could lead to HCO_2^+ generation (i.e. protonation), leading to a false increase in the m/z 45 signal. The Craig correction is also applied to correct for the presence of O_2 in the sample, which can interfere with the accurate measurement of the carbon isotope ratio through isobaric interferences. It takes into account the abundance of O_2 isotopes (^{17}O and ^{18}O), and their impact on the measured carbon isotope ratio (Hoffmann and Roksandic, 1989). The CO_2 molecules are then introduced by the carrier gas into the ion source via an open-split interface. The open-split also allows the introduction of a standard gas directly from an independent static volume (i.e., CO_2 calibrated cylinder), facilitating external calibration in the GC-IRMS. For accurate isotopic measurements, and as bottled CO_2 changes its isotopic signature over time as the liquid content is transformed into gas within the bottle due to consumption and

pressure changes, cylinder calibration is routinely required. This is done by measuring the CO_2 against compounds with known isotopic values.

Similarly to an MSD, in the IRMS ion source (Figure 2.8), the ionisation of CO_2 molecules takes place through electron ionisation (EI) as electrons are produced by the filament. Focusing lenses divert the electrons through a magnetic analyser, where their trajectory is bent due to their mass and momentum, and are thus directed to a specific Faraday collector cup (Figure 2.8). For CO_2 measurements, 3 Faraday cups are employed, each connected to an amplifier with different gains, adjusted for compounds at natural concentration levels. The signals is recorded simultaneously on the Faraday cups, producing an accurate measurement of the abundance of each isotope (Dunn and Carter, 2018). The IRMS is thus a detector that records, with high accuracy and at natural concentration levels, the abundance of heavier and lighter carbons from a compound, reporting a ratio ($^{13}C/^{12}C$). This ratio is then calibrated by the software against a reference standard, usually the CO_2 "working gas" cylinder if its isotopic value has been adjusted to the PDB standard, for inter-lab value reporting.

For CSIA, chromatographic resolution should ensure that the compounds are well separated prior to combustion, with one isotopic measurement characterising one compound. To achieve PSIA, one compound of interest should be chromatographically separated from other molecules (i.e., heart-cut) and the bonds within the compound of interest should be first broken, with the produced fragments chromatographically separated prior to combustion. For complex samples which contain more than one compound, this implies a double separation achieved usually through the use of two capillary columns.
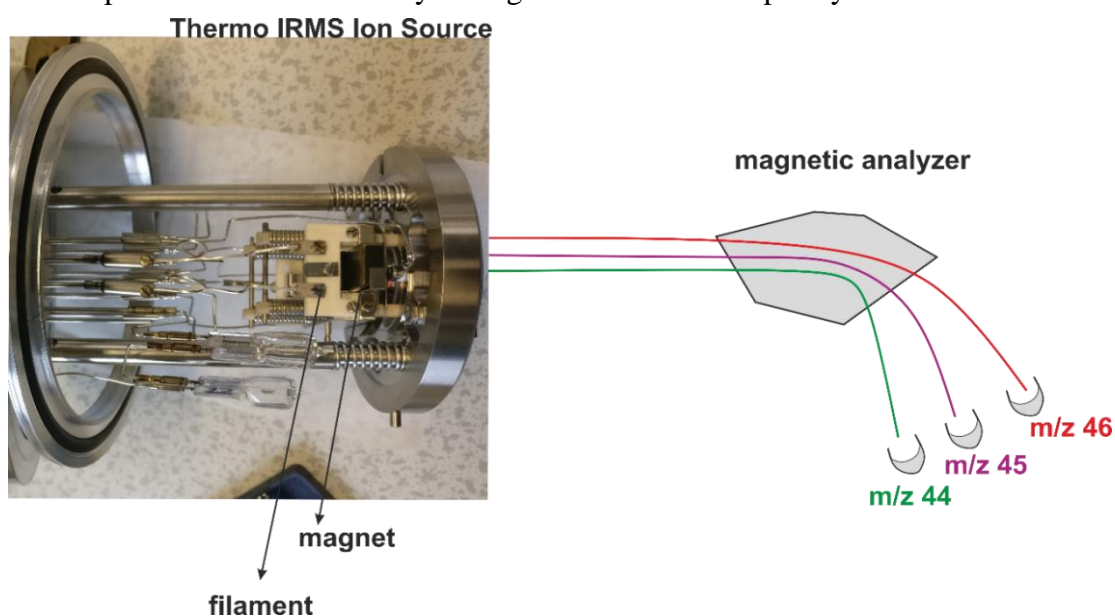
Figure 2.8 Thermo GC Ultra IRMS ion source (University of Strathclyde) and ion trajectory into carbon Faraday cups.

2.7. Position-specific isotope analysis

2.7.1. Offline position-specific isotope analysis

Position-specific isotope investigations look at the *intra*molecular differences within the molecule, between various constituting atoms, employed based on the knowledge that the constituting atom isotopes are not homogeneously distributed (Hobbie and Werner, 2004). The procedure can take place **offline**, with the molecular breakdown process done separately from the analytical instrument (i.e., pyrolysis, ozonolysis, chemolysis). The products are collected, introduced and separated via GC means, followed by identification and isotopic measurement or **online**, with a pyrolyser hyphenated to the GC system (GC-Pyr-MS, GC-Pyr-IRMS). The studies reviewed in this subsection were focused on offline PSIA, with the molecules of interest chemically broken down and the resulting moieties analysed separately on an IRMS (Figure 2.9). The studies employing online PSIA are reviewed further in Subsection 2.7.2. This review division has been done to highlight first the increased level of information PSIA can provide and the broad range of compounds that can be subjected to this technique through offline means, while the focus on the analytical requirements for online PSIA and pyrolysis are reviewed together to be taken forward during the prep-GC system development work (Figure 2.9).

Yankwich and Promislow (1953) described isotopic variations between two different carbons within a molecule (i.e., *intra*molecular or sub-molecular variations) produced via the same synthetic processes by two different manufacturers. Two commercially available acetic acids were broken down into methylamine and CO_2. Within one sample, no significant isotopic difference was found between the methylamine-derived CO_2 and the original carboxyl carbon (i.e., difference was explained through contamination with small amounts of external CO_2) yet a different sample showed that methylene (i.e., methyl-carbon) was enriched with more than 10‰ compared to the carboxyl-carbon.

Similarly, Meinschein *et al.* (1974) looked at the isotopic differences between the methyl and carboxyl carbon of acetic acids. When purified from cider vinegar, the methyl was isotopically depleted compared to the parent molecule (and carboxyl counterpart). The synthetically produced glacial acetic acid displays the opposite trend, with the methyl radical relatively enriched compared to the overall molecule and carboxyl moiety, highlighting the different synthesis pathways used to produce the latter.

Abelson and Hoering (1961a) were the first to specifically study the isotopic variations between carbons of a molecule and the associated implications when discussing bio-synthetic pathways. The study analysed the amino acids from 6 algae species to understand the fractionation processes taking place in photosynthetic organisms. The molecules of interest (i.e., amino acids) were separated into two fractions, one being combusted as a whole and transformed into CO_2 and the other fraction was subjected to the nihydrin reaction which detached the carboxyl moiety from the rest of the amino acid, trapped it in a ℓN_2 cooled trap and reintroduced it in an dual-inlet IRMS. Compared to the total $\delta^{13}C$ of the algae (BSIA), extracted lipid fractions were more isotopically depleted pointing to an important isotopic fractionation step in the synthesis of lipids (CSIA). Amino acids fractions were slightly enriched, comparable to the provided CO_2. Furthermore, the carboxyl radicals were found to be relatively enriched in all 6 species, compared to the corresponding amino acids and corresponding amino acid moiety (PSIA; Table 3 in Abelson and Hoering, 1961a).
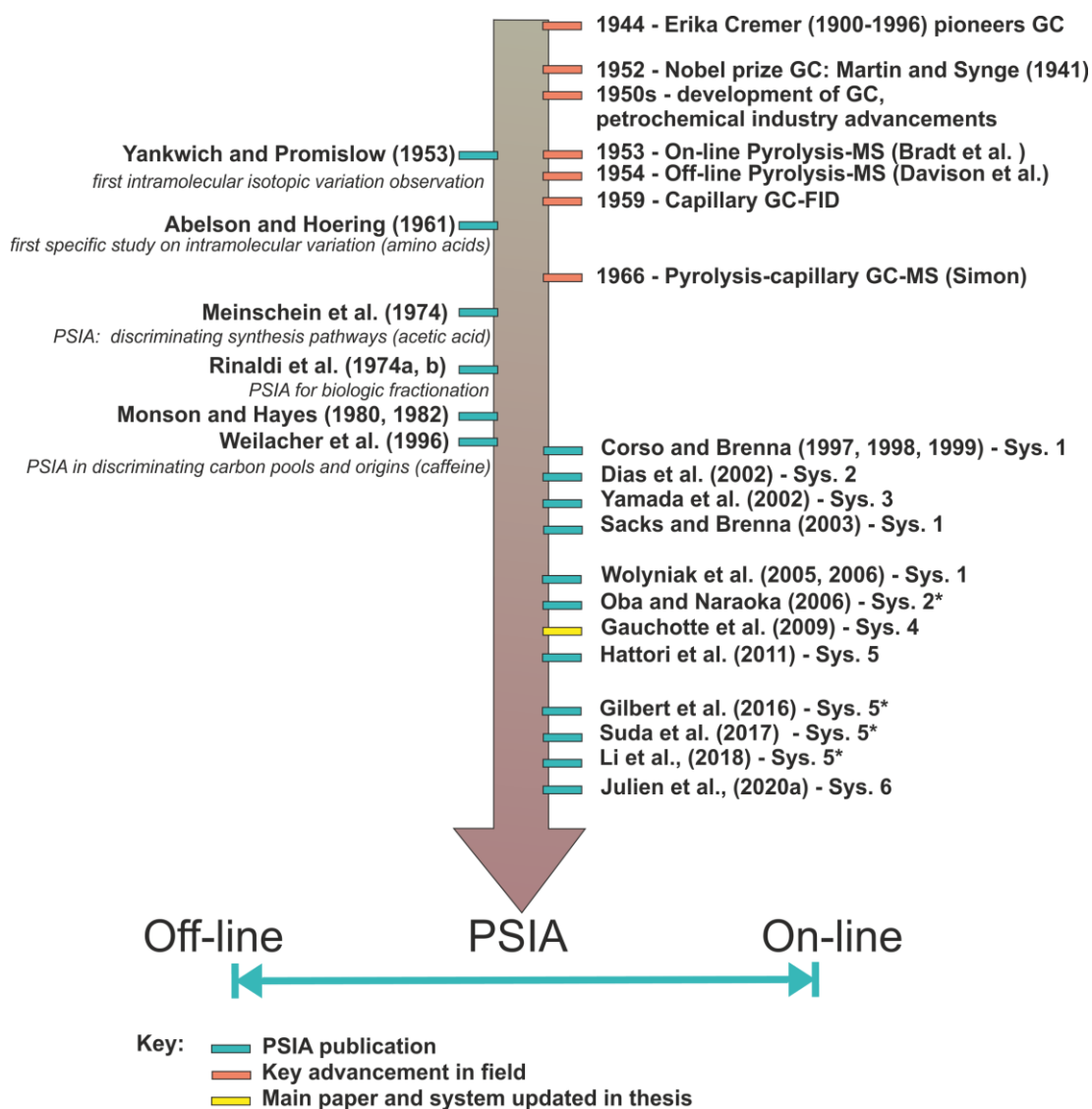
Figure 2.9 PSIA field moments and important publications. Online studies reviewed in Chapter 5.

Monson and Hayes (1980) looked at the intramolecular variations in PLFA of *E. coli* and proposed a carbon flow branching point to explain the relatively depleted signatures of the carboxyl moiety when compared to the acyl-ACP's precursor. The Schmidt reaction was quantitatively used to access the carboxyl moieties of the FAs and for unsaturated FA, the isotopic value of the olefinic carbon closest to the carboxyl moiety was obtained via oxidative ozonolysis. In a similar study, Monson and Hayes (1982) used ozone to oxidisethe double bond of fatty acids produced by *E. coli* grown on glucose, followed by silver oxide bond cleavage and a modified Schmidt decarboxylation reaction to produce CO_2 prior to IRMS analysis. The FAs were on average 3‰ depleted relative to the glucose source, with alternating positions of acetyl-CoA building blocks showing a kinetic isotope effect of 2.3‰ compared to the neighbouring carbon.

Rinaldi *et al.* (1974a) investigated the biological fractionation associated with ethanol oxidation to acetic acid by *Acetobacter suboxydans*. The provided ethanol showed intramolecular differences, with the methyl-carbon relatively enriched by 4.6 ‰ compared to the methoxy-carbon. This however translated to the methyl-carbon of the produced acetic acid being 3.8‰ depleted compared to the methoxy-carbon (i.e., former methanol-carbon), following the general rule that during bio-synthesis the more reduced carbons are isotopically lighter compared to the more oxidised carbons (i.e., Meinschein et al., 1974; Rinaldi *et al.*, 1974b). Furthermore, as the acetylation reaction proceeded, the remaining ethanol with the culture was more enriched (by 2‰), in agreement with biological fractionation processes that prefer carbon-depleted compounds over enriched. When utilised as acetyl-CoA in the biosynthesis of lipids, the isotopic order between carboxyl and methyl groups should be conserved. In a similar study, Rinaldi et al. (1974b) studied the isotopic ordering in acetoin extracted from apple cider vinegar and confirmed the previous observations of Meinschein et al. (1974), that carbon enrichment takes place in the direction of more oxidised species. Acetoin was transformed into two acetic acid molecules. As it forms from two molecules of pyruvate, the two methyl radicals in acetoin have similar isotopic values as they both originate from pyruvate-methyls. When comparing the remaining two carbons of acetoin at the position-level, the carbonyl-carbon is enriched compared to the hydroxy-carbon, the less oxidised specie.

Weilacher *et al.* (1996) looked at the intramolecular variations in caffeine and bromine extracted from natural products and compared the isotopic signatures of natural alkaloids with that of synthetic purine alkaloids, noticing different isotopic patterns. The core (backbone) of caffeine originates from glycine and the remaining carbons from tetrahydrofolic acid (THF), formate or formaldehyde and bicarbonate, with the methyl

groups having their origins in S-adenosylmethionine (SAM). The different carbon pools allow discriminations between natural and synthetic products, with the synthetic counterparts being more depleted. Furthermore, various moieties show isotopic differences that can be coupled to the country of origin (e.g., $\delta^{13}C$ of C-4 and C-5 from glycine produced in Sri Lanka and Assam).

A number of important lessons from offline PSIA studies were taken forward during the development of online PSIA methods, some of which are reviewed and discussed in the next subsections. The first and possibly most obvious lesson in this field of investigation is that, in a biological system, atoms within a molecule are heterogenous, displaying non-statistical *intra*molecular variations (i.e., natural glucose, Rossmann et al., 1991). It is also required to obtain isotopic knowledge at the compound-specific level to explain (and calculate) position-specific variations. Isotopic distribution is controlled by reacting molecules (or raw materials), reactions, reaction rates and equilibria conditions. In closed and un-branched systems, for example, the isotopic composition of reactants needs to match the isotopic composition of products (Monson and Hayes, 1980). At a branching point, isotope effects favour depletion of ^{13}C on one side of the branch and enrichment in the other. Biological and non-biological processes can be thus studied and defined using *intra*molecular isotopic differences (Meinschein et al., 1974; Rinaldi et al., 1974b). It was also observed that isotopic enrichment takes place in the direction of more oxidised species (Rinaldi et al., 1974b). Finally, reactions need to be quantitative (Abelson and Hoering, 1961a; Monson and Hayes, 1982; Meinschein et al., 1974; Rinaldi et al., 1974b) or the isotopic fractionation that takes place needs to be studied for isotopic corrections (Vogler and Hayes, 1979; Vogler, 1979; Monson and Hayes, 1982), leading to the use of Rayleigh equation. The importance and wide molecular range applicability of PSIA is also reflected in the variety of techniques available for its implementation, including offline and online methods, as well as nuclear magnetic resonance (NMR) and Fourier transform infrared (FTIR) spectroscopy.

2.7.2. Online position-specific isotope analysis – systems and field advancements

The development of online PSIA systems started with the hyphenation of a GC to a pyrolyser and an IRMS detector in 1997 by Corso and Brenna (1997), marking the first automated application for online continuous flow of PSIA (System 1, Table 2.2; Figure 2.10). The *intra*molecular study of an isotopically labelled methyl palmitate with a compound specific isotopic value of $\delta^{13}C_{MePal}=4.06‰$ was done through pyrolysis. Exposed to high pyrolytic

temperatures, the compound produced two series of peaks – grouped as α-Olefins and Fatty Acid Methyl Esters (FAMEs), corresponding to the two halves of the molecule, depending on the position of the broken C-C bond along the molecular chain. Isotopic labelling of the [1-^{13}C] positions and the mass spectra of the fragments indicated that no rearrangement took place, and providing a position-specific isotopic value of 457‰ for the labelled position, allowing the calculation of the olefin correspondent at -27.46‰ through mass balance equations. In their system, a straight deactivated fused silica capillary (25 cm x 0.25 mm) was placed in the pyrolyser and eluting pyrolysates were cryo-focused at -40°C before injection in the second GC system. The second GC system was used to separate the fragments and transfer them to either an FID, an Ion Trap MS or an IRMS through the use of a valve. The system was ideal for the study of pyrolysates, reactions that are taking place and compile, from one analysis, several lines of evidence to support PSIA. The degree of isotopic fractionation was studied by subjecting the Methyl Palmitate to two pyrolytic temperatures (i.e., 550°C and 600°C) which varied the amounts of produced pyrolysates and found that no significant isotopic fractionation occurred between each experiment. Overall, this PSIA setup is capable of analysing a wide variety of molecules due to the presence of the heated transfer line, with the only drawback being the lack of a cryo-trapping unit to concentrate compounds prior to pyrolysis, that may be required for environmental samples.

The same system setup was used in a series of PSIA studies including: a) the pyrolysis at 600°C and analysis of palmitic acid fragments (C16:0) which was converted to methyl palmitate (Me-C16:0) via the derivatizing addition of one methyl which was then
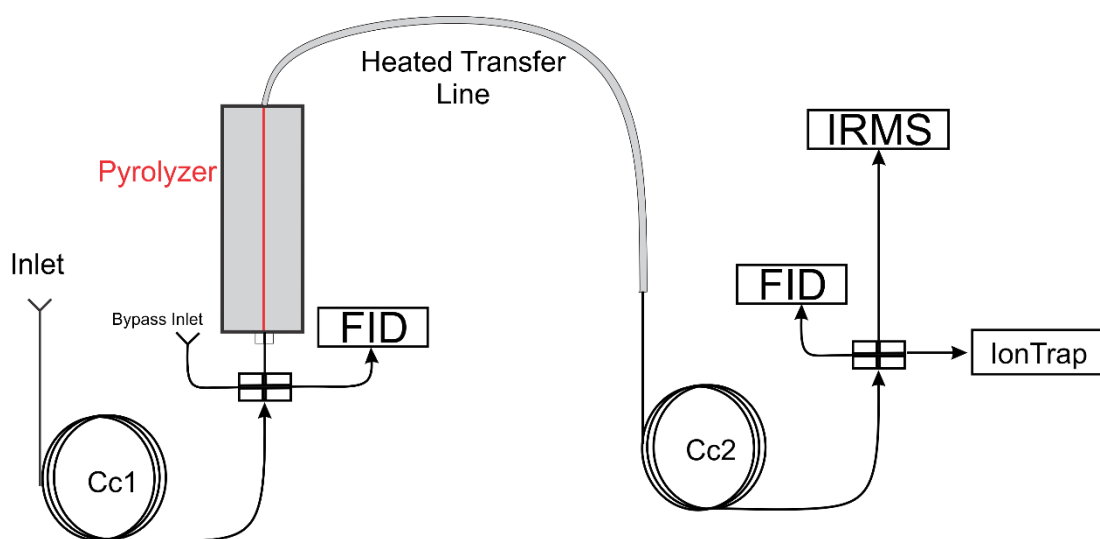
Figure 2.10 System 1: The first online PSIA system (Corso and Brenna, 1997).

quantitatively transformed to hexadecanol via the LiAlH$_4$ reaction to eliminate isotopic uncertainties attributed to derivatization (Corso *et al.*, 1998); b) to study the *intra*molecular values of fragments of toluene (i.e., methane and benzene) and of *n*-alkanes between *n*-C$_5$

and n-C$_{10}$ (i.e., methane and corresponding α-olefins) (Corso and Brenna, 1999); c) to study the pyrolysis behaviour of two analogues of amino acids, 3-methylthiopropylamine and isoamylamine, yet in this case study, low pyrolysate efficiencies led to an increase in the amount of sample required prior to pyrolysis (Sacks and Brenna, 2003); d) for PSIA studies of alaninol, phenethyl amine (Wolyniak *et al.*, 2005) and of lactic acid (Wolyniak *et al.*, 2006).

A similar system was developed by Hattori et al. (2011), which made use of two thermally-controlled ovens, each equipped with a capillary column, separated by a pyrolytic unit (ceramic tube; Figure 5.2). An overall similar system was utilised by Nimmanwudipong *et al.* (2015) for the study of acetic acid. Hattori et al. (2011)'s first GC was used to separate the compound of interest (acetic acid) from a complex mixture (commercial vinegar) using an oven ramp between 60°C-200°C, to send them to the pyrolyser, while the second GC system was used to separate the pyrolysates and was operated isothermally at 30°C. A deactivated fused silica (FS) capillary was used as a transfer line between the pyrolyser and GC-systems, similar to System 3 (Yamada et al., 2002). It was observed that, overall, the methyl position is isotopically depleted compared to the carboxyl position for a wide variety of starting raw materials used in the production of the vinegar. Furthermore, the study successfully discriminates one artificially produced vinegar sample from a set of 14 tested based on the inverse isotopic relationship between the two moieties of acetic acid, highlighting the use of PSIA in quality control (Hattori et al., 2011). The main drawback of this system is the unheated transfer line in contact with the atmosphere, which limits the molecular size of fragments that can be transferred to the second GC oven.
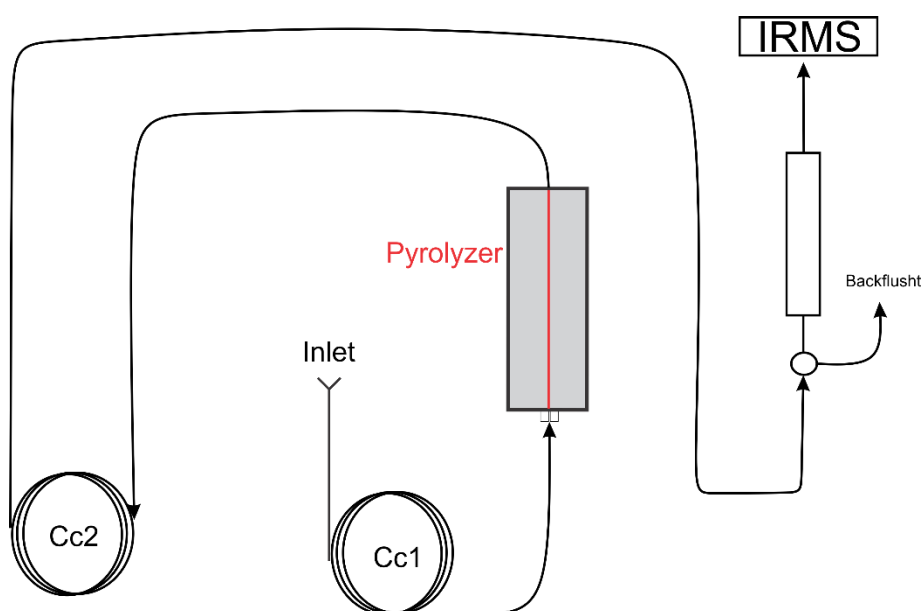
Figure 2.11 Schematic diagram of PSIA system 5 used by Hattori et al. (2011).

Dias et al. (2002) utilised a CF-PSIA system limited to one GC system (and oven; Figure 5.3) and, through the use of a valve and a modified pyrolysis tube containing palladium wires heated at 600°C, they determined the isotopic composition of the carboxyl-moiety carbon from a series of C_2-C_8 organic acids found in a mixture (System 2, Table 2.2). While the system is a more simplified and robust setup than System 1 (Corso and Brenna, 1997), it is application-specific yet can be easily adapted to analyse a greater variety of compounds.
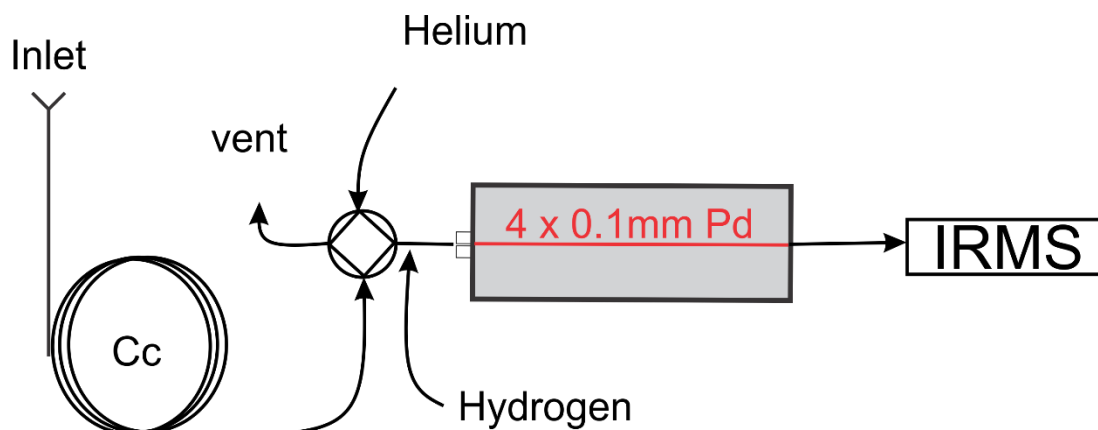
Figure 2.12 System 2 for the PSIA of organic acids of the carboxyl-moiety developed by Dias et al. (2002).

Yamada et al. (2002) proposed a system capable of analysing nanomolar amounts of pure samples, with an application on acetic acid (System 3; Figure 5.4). Acetic acid was injected and transferred directly via a deactivated FS capillary to an online pyrolyser, with the produced pyrolysates, CH_4 and CO_2, separated by a capillary column within the GC oven before transfer to a combustion furnace and introduced into an IRMS. A deactivated FS capillary was again placed in the pyrolyser (a resistively heated ceramic tube), and the remaining section of the capillary was used as a transfer line to the IRMS. The acetic acid was pyrolysed between 800°C and 1000°C. This system setup is however unfit for analysing
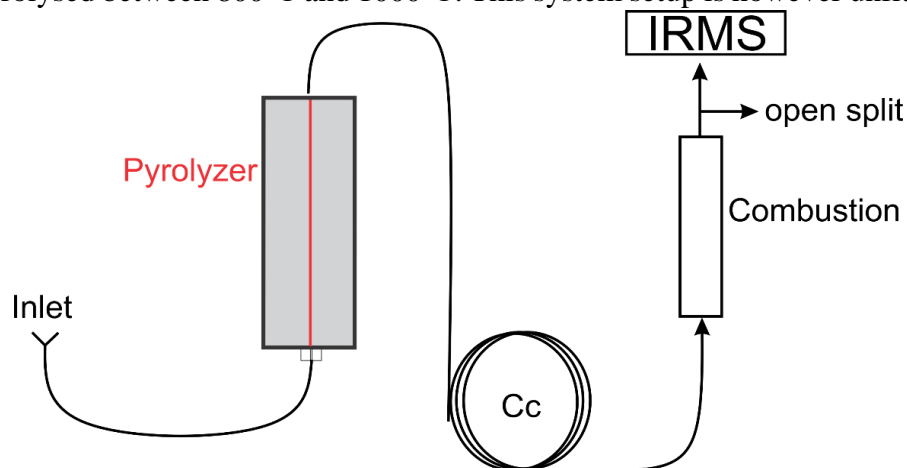
Figure 2.13 Schematic of PSIA system used by Yamada et al. (2002).

larger molecular weight compounds due to the generation of a cold-spot before the IRMS detector.

System 4 was used to study MTBE online pyrolysis by Gauchotte-Lindsay et al. (2009) and it was used as a reference when designing the prep-GC system presented in this chapter. The system was well fitted to understand the pyrolysis mechanisms given its capacity to alter residence time of molecules within the pyrolysis furnace through the use of an auxiliary helium pressure (Figure 5.5). Furthermore, a temperature-controlled cryo-focusing unit was placed after the pyrolyser. The cryo-unit consisted of a capillary fed through a nickel tube which was submersed in liquid N_2 prior and after pyrolysis to trap and contain the products of MTBE pyrolysis. Through the means of heated tape that was placed around the nickel tube, the pyrolysates and MTBE were remobilized and focused prior to injection in a second GC-system for separation. The presence of the cryo-focusing unit within an online PSIA-GC-setup allows pyrolysates concentration. The pyrolysis took place in a temperature-controlled unit in which an unpacked 0.7 mm ID quartz tube was placed. A switching valve was placed after the second GC-system, which could redirect the flow and eluting compounds either to a Time of Flight Mass Spectrometer for identification or to a combustion furnace and then to an IRMS for isotopic measurements at position-level. Given that the distance between the cyro-focusing unit and the second GC is small enough, or that the heated tape can remove cold spots, system 4 would be able to deal with a wider range of molecular weight compounds.
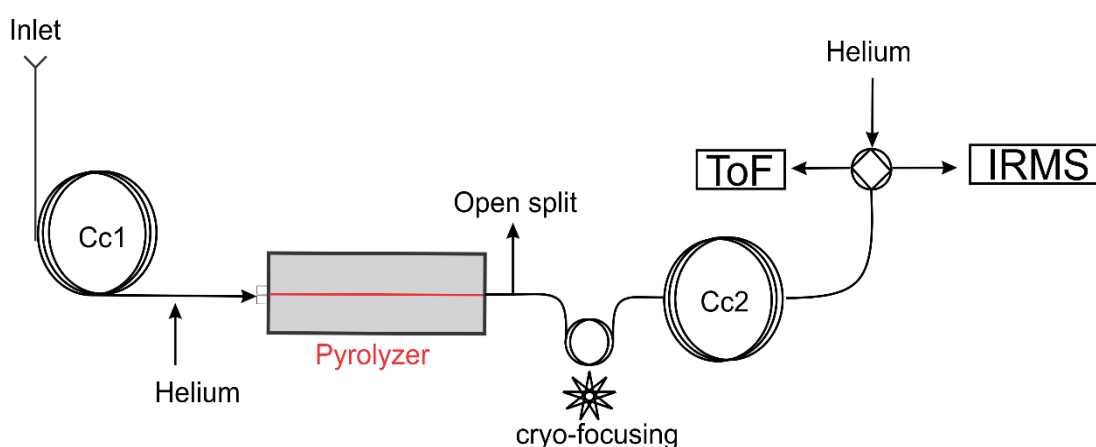
Figure 2.14 System of Gauchotte-Lindsay et al. (2009) with open-split placed after the furnace to avoid the risk of backflushing.

Li et al., 2018 (System 5*, Figure 5.6.) presents a more advanced prep-GC system, utilised in the analysis of propane at position-specific levels, based on the PSIA-propane work of Gilbert *et al.* (2016) (system diagram not provided). The system setup involved two GC systems, each equipped with a capillary column with identical proprieties. The first GC system was used for injection and sample purification. Propane was purified and isolated from a complex mixture with the use of a valve, and the compound was sent to a laboratory-made pyrolysis unit which again utilised a deactivated FS capillary for pyrolysis and as a transfer line, with subsequent pyrolysates separation in the second GC-system. This system incorporates some of the characteristics of System 1 (Corso and Brenna, 1997), implementing a second oven for the separation of pyrolysates, and more importantly, having the capacity of quantifying the pyrolysates and unpyrolysed parent molecule through the means of the FID. Identification and quantification of pyrolysates was however done using standards. The system is however unfit for the analysis of high molecular weight compounds given the cold spot generation between the two GCs and oxidation furnace.
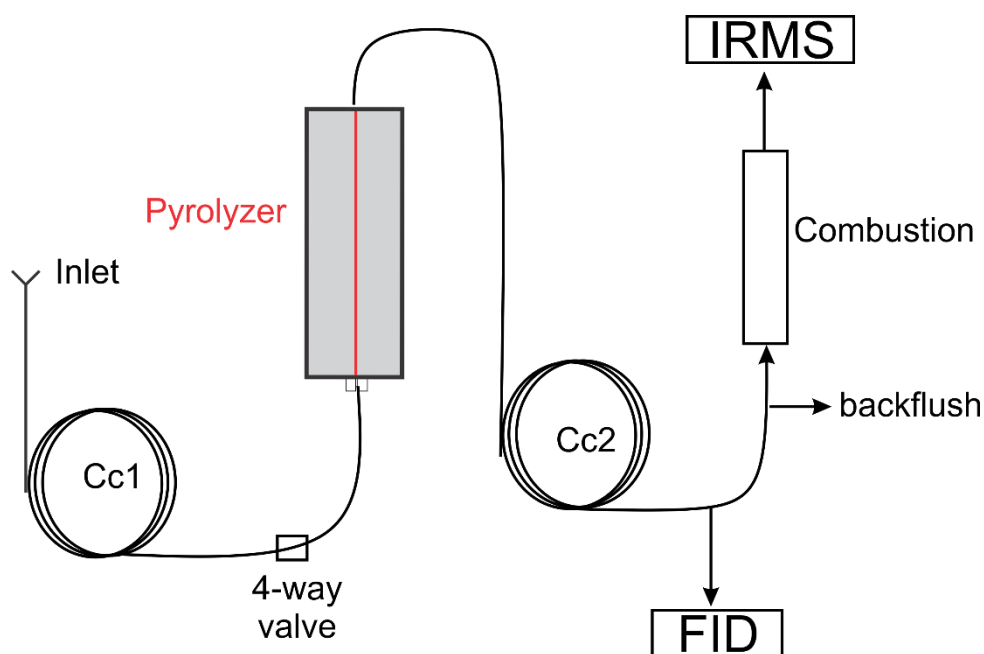
Figure 2.15 System 5* used by Li et al. (2018).

Finally, the system employed by Julien et al. (2020) for the study of butane from natural samples makes use of two GC systems, yet through the means of a switching valve, the molecule of interest can be either directed to a combustion furnace for CSIA, or to a pyrolyser connected to a second capillary column for compound separation followed by combustion and IRMS analysis (Figure 5.7.). As the system was not equipped with an MSD, Reaction Mechanism Generator (RMG) software was used to determine the pyrolytic

reactions and carbon rearrangement, a software further tested in this chapter and used in this thesis.
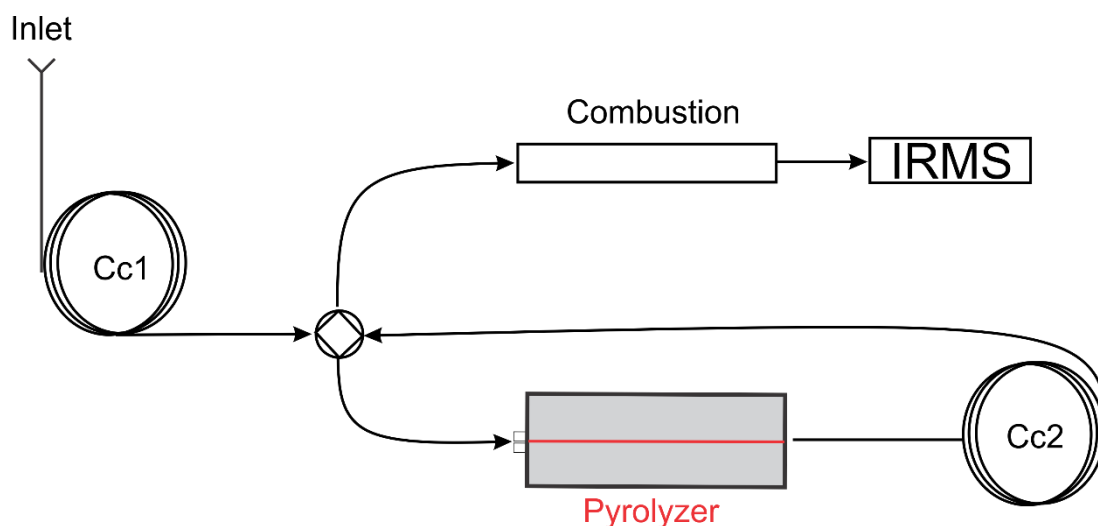
Figure 2.16 Schematic of system used by Julien et al., 2020

Online PSIA systems thus combine insights from offline studies, integrating GC system robustness with detectors' sensitivity. While modern online systems require less pure sample, drawbacks exist, influencing their applicability and warranting consideration in prep-GC system design. These limitations are highlighted here and were taken into account when designing the prep-GC system for diploptene pyrolysis, and future PSIA.

Instrumental constrains Hyphenations of the type GC-pyrolysis-GC-MS/FID/IRMS detectors add constrains on laboratory equipment availability and costs. The separation of a compound from a complex mixture in one GC oven, was followed in several prep-GC systems by pyrolysis and reinjection in a second GC oven in which fragment separation took place before they were delivered to a MSD or IRMS detector (e.g., Corso and Brenna, 1997; Li et al., 2018; Gauchotte-Lindsay et al., 2009; Julien et al., 2020). This system setup would not allow the independent use of the second GC system or of the available detectors, making PSIA less attractive due to increased costs as it required two GC ovens, an MSD and IRMS only for this analysis type.

Cold spots generation Several PSIA-systems (Yamada et al., 2002, Hattori et al., 2011, Li et al., 2018) utilised a deactivated FS capillary threaded through the pyrolyser, linking the two GC systems and acting as a transfer line. The molecules used have low molecular weights (i.e., propane and acetic acid), leading to even lower molecular weight pyrolysates, capable of being transported in the stream of helium at room temperature. However, for higher molecular weights, the deactivated FS capillary would form a long cold spot, and

Table 2.2 Summary of online PSIA studies and system used (→ representing direct moiety correspondence from parent molecule).

Study	Parent molecules	Pyr T°C	Pyrolysates	Sys.
Corso and Brenna, 1997	Methyl Palmitate	550°C 600°C	Series of α-Olefins and FAMEs	1
Corso et al., 1998	Hexadecanol (initial Palmitic acid)	600°C	Series C_x:1-ol, α-Olefins & 1-hexadecene	1
Corso and Brenna, 1999	Toluene → nC5-nC10 →	800°C-1050°C 550°C	→CH_4 and benzene →CH_4 and α-Olefin	1
Dias et al., 2002	Acetic acid Octanoic acid C2-C8 organic acids→		CH_4 and CO_2 →Carboxyl-derived CO_2	2
Yamada et al., 2002	Acetic acid	800°C-1000°C	CH_4 and CO_2	3
Sacks and Brenna, 2003	3-MeThiopropylamine and isoamylamine	620°C-900°C	Multiple (propylene, isobutylene, H-cyanide)	1
Wolyniak et al., 2005	Alaninol, phenethyl amine	900°C	multiple	1
Wolyniak et al., 2006	Lactic acid		multiple	1
Oba and Naraoka, 2006	Acetic acid	1000°C	CH_4 and CO_2	2* 3*
Gauchotte-Lindsay et al., 2009	MTBE	500°C-750°C	MeOH and isobutylene	4
Hattori et al., 2011	Acetic acid: carboxyl-Carbon→ methyl-Carbon→	1000°C	 →CO_2 →CH_4	5
Nimmanwudipong et al., 2015	Acetic acid		CH_4 and CO_2	
Gilbert et al., 2016	Propane	750°C-950°C	CH_4, C_2H_6, C_2H_4	5*
Suda *et al.*, 2017				5*
Li et al., 2018	Propane	800°C-840°C	CH_4, C_2H_4, C_3H_6, C_2H_6	5*
Julien et al., 2020	Butane	850°C	multiple	6

Notes: * – system follows work presented in above unmarked system number.

molecules would condense along the capillary without a source of heat. Furthermore, as discussed later, FS capillary becomes highly brittle after pyrolysis above 500°C, making the transfer line prone to frequent replacements.

Application or molecule type-specific In the case of System 2 (Dias et al., 2002), the pyrolyser consists of heated palladium wires and H_2 as a reaction gas capable of analysing organic acids and reach PSIA at the carboxyl moiety for a series of organic acids from complex mixtures. In this application, the corresponding *n*-alkanes are not transformed into CO_2 for isotopic quantification, and it lacks a detector capable of identifying other compounds which could have pyrolysed at 600°C, the temperature at which the palladium wires were heated to produce the carboxyl-derived CO_2. System 3 of Yamada et al. (2002) also presents a limited application range, capable of analysing only pure compounds, albeit in very low concentrations (i.e., nanomolar range). Although PSIA can be studied on a wide range of pure standards, the presence of only one capillary column aimed to separate the pyrolysates makes this system incompatible with more complex samples and limitations also occur in the investigation of produced pyrolysates and reactions, requiring pure standards for their identification or prior knowledge of the molecule's pyrolytic behaviour.

Compound concentration System 1 of Corso and Brenna (1997) involved a -40°C cryo-focusing step at the head of the second column, with an example of oven ramp of 3°C/min applied between -40°C and 260°C (Corso et al., 1998). While for the analysis of Methyl Palmitate the cryo-focusing temperature may be low enough to trap pyrolysates, there is no means to concentrate this compound ahead of pyrolysis. Apart from Gauchotte-Lindsay et al. (2009), system 4, which utilises liquid N_2 to trap methanol and isobutylene after pyrolysis, the remaining reviewed systems for PSIA do not involve a cryo-focusing or a parent molecule concentration step, restricting the range of analysis of low concentrated compounds from natural samples or requiring an increased amount of material for one analysis (Sacks and Brenna, 2003). Thus, the prep-GC system for PSIA used in this work contains a temperature-controlled trap that can be connected with ease either prior or after the pyrolysis step, depending on the pattern of molecular fragmentation and can concentrate the compound or resulting pyrolysate(s).

Compound heart-cutting The coupling of GC-Pyr system with a switching valve would enable targeted compound concentration which would make PSIA possible in complex and natural-abundance samples, enhancing either the amount of parent compound prior to pyrolysis, or that of pyrolysates. Separating a compound of interest from a complex sample via a GC run via the mechanical action of a valve switching (either manually or automatically) is called heart-cutting and is a technique frequently used in multidimensional gas chromatography (MDGC) (De Alencastro et al., 2003). The principle of MDGC involves two capillary columns, usually of different polarities that are used to separate co-eluting peaks. As compounds of interest elute from the first-dimension column, they may not be

fully resolved, hence they are introduced directly or via trapping or cryo-focusing in a second dimension, where a column with a different polarity is used to further separate co-eluting peaks (De Alencastro et al., 2003). Furthermore, IRMS response is directly proportional to the amount of carbon of the combusted compound, requiring between 10-100s of nmols (Dunn and Carter, 2018). Pyrolysates of interest will have less carbon than the parent compound (i.e., MTBE (5C) breaking down into methanol (1C) and isobutylene (4C)), reducing the sensitivity for this analysis. Targeted and quantitative compound trapping and concentration would increase the amount of carbon available for combustion and IRMS measurement, leading to increased precision.

The current prep-GC used in this work was built based on a previous generation version of Gauchotte-Lindsay et al. (2009), that could be used to study the pyrolytic breakdown and *intra*molecular isotopic variation of a wide range of molecular weight compounds and was validate for MTBE. The same molecule was thus use to achieve pyrolysis and pyrolysate transfer in order to validate and calibrate the prep-GC in Chapter 4. The prep-GC system presented in this thesis was however designed to analyse environmental complex samples, where peaks of interests are present in low concentration and can co-elute with other compounds, making them unsuitable for PSIA.

2.7.3. Site specific natural isotope fractionation nuclear magnetic resonance

Site specific natural isotope fractionation nuclear magnetic resonance (SNIF-NMR or irm-NMR) is a parallel IRMS technique used to determine the distribution of isotopes within molecules, widely applied in food and drinks industries for quality control (i.e. Commission Regulation (EC), 2000; Martin *et al.*, 1985; Reid *et al.*, 2006), with the added advantage of being non-destructive. One of the disadvantages of online pyrolysis PSIA (Py-GC/IRMS) is that it only allows a maximum of 4 carbons to be analysed at the position's level (Jézéquel *et al.*, 2017). Analysing molecules with a larger number of carbons at the position-specific level becomes challenging due to the complexity of the spectra and the difficulty in resolving individual carbon positions beyond the 4th carbon (Hoffman and Rasmussen, 2019). However, trapping alternatives coupled with mass balance equations and identification of reactions that are leading to produced fragments allow multiple pyrolysates to be quantified during the same analysis.

SNIF-NMR has been also employed in the study of chemical and biochemical pathways (reviewed in Martin *et al.*, 2008). For example, in deciphering plant's regime and climate of

growth (i.e. meteoric water in vine leaves from grape cultures from different regions). Since SNIF-NMR analysis became possible in the 1980s, the instrumental sensitivity has increased, with this analysis being achieved at natural abundance levels, yet with isotopic accuracies of 1‰ for carbon isotopes (Jézéquel et al., 2017).

2.8. Pyrolysis and isotope fractionation

2.8.1. Pyrolysis

Unlike the combustion reaction, which is done in the presence of oxygen, producing CO_2 and H_2O molecules as seen in the case of GC-C-IRMS, the pyrolytic reaction is conducted under an inert atmosphere, usually helium, at low pressures and over a range of temperatures which are application dependent, usually above 400°C. During pyrolysis, the thermal energy is absorbed, breaking the chemical bonds in a molecule (i.e., C-C or C-O; endothermic), leading to bond rearrangements and, usually, to the formation of **pyrolysates**, fragment moieties cleaved from a parent molecule (Moldoveanu, 2019a). **Primary pyrolysates** have a direct provenience from the parent molecule, while **secondary pyrolysates** are formed during the further breakdown of primary fragments or rearrangement.

The energy required to break (dissociation; endothermic) or that is released during the formation (exothermic) of a bond between two adjacent atoms is called **bond energy**. The enthalpy required for a given X-Y bond to homolytically break is referred to as **bond dissociation energy** (Gold, 2019). During a reaction, bonds can be simultaneously broken and formed. The dissociation energy between two atoms is however different to that attributed to the bond itself when calculated at the entire molecule level (i.e., average value vs dissociation value; Sanderson (1975)).

The energy required for the formation of a bond is known as **standard enthalpy of formation** (H_{298}) and it is expressed in **kcal/mol** (or kJ/mol). During pyrolysis, the energy required for bond breaking equals the negative energetic value required to form the same bond. Bonds requiring less energy will break first, and at lower temperatures, followed by those which present higher values (Moldoveanu, 2019b). Molecular dissociation (after a bond breaks), leads to the reorganisation of energies within a (previous parent) molecule. As the bonds break in a step-like fashion, the sum of dissociation energies across all bonds within the molecule is defined as the heat of atomisation for the entire molecule, while the heat of reaction is the difference between the sum of dissociation energies of the formed

bonds and the broken bonds (Szwarc, 1950). The role of pyrolysis is, however, to produce lower molecular weight compounds, amiable with the intended analytical technique.

Analytical pyrolysis takes place within controlled laboratory studies, in the presence or absence of catalysts or reagents (Akalın and Karagöz, 2014), on small amounts of analytes, with the aim of experimentally determine reactions that are taking place and produce pyrolysates or identification of the starting material (Moldoveanu, 2019a). Experimental design can target pyrolysis temperature or rate of heating (if not isothermal), residence time of molecules in the pyrolysis reactor, chemical analytes and amounts. This work employs pyrolysis and GC techniques to study the breakdown patterns of molecules of interest (i.e., **online pyrolysis**). The coupling of GC with a pyrolyser (Py-GC) and subsequent identification of the produced fragments by an MSD (GC-Py-MS) outputs a **pyrogram**, a representation of the pyrolysis process, indicating the formed moieties due to C-C cleavage reaction and their abundances. The C-C cleavage reactions are specific to each molecule's intramolecular strengths and each applied temperature, making the analysis reproducible (Wampler, 1999; Gauchotte-Lindsay et al., 2009).

2.8.2. Isotopic fractionation during pyrolysis

The formation of free carbon-containing radicals (methyls, carboxyls) due to C-C cleavage reactions promoted by high temperatures in the pyrolyser is the fundamental working principle of position-specific isotope analysis (PSIA), with the subsequent goal of their online analysis on an MS/IRMS detector. The pyrolyser used in this work is a previous GC-IRMS temperature-controlled combustion furnace (i.e., VG ISOCHROM-GC) in which a fused silica capillary column was threaded (i.e., "on-column" pyrolysis), allowing the analysis of small amounts of sample (µg to ng) to be analysed online.

Through PSIA, isotopic effects can be studied at an *intra*molecular level (Gauchotte-Lindsay and Turnbull, 2016) as it is now known that biogenic compounds do not display a homogeneous isotopic distribution at the molecular level (Rossmann et al., 1991; Hayes, 2001; Hobbie and Werner, 2004). Bond formation which led to targeted lipids and bond breaking, achieved in this study through pyrolysis, will be thus affected by kinetic fractionation due to the non-homogenous isotopic distribution at the compound level, resulted from previous metabolic isotopic effects and if the reactant is not fully pyrolysed (non-quantitative). This process is associated with an isotopic fractionation effect, based on the bond's vibrational energy discussed above. Bonds involving lighter carbons or hydrogens have weaker vibrational energy, leading to their selective breakage over bonds

involving a heavier isotope, which require a higher amount of energy to break and will proceed slower (Werner and Cormier, 2022). During bond forming or breaking, the atoms that are not directly involved in bond forming or breaking will experience a neglectable or no change in their isotopic signature (i.e., secondary isotope effects).

Furthermore, the quantitative consumption via pyrolysis of the parent molecule in this work, was associated with the production of secondary pyrolysates, as further bonds were broken in primary fragments, introducing thus further fractionation factors. Quantitative breakdown of the parent molecule may however lead to polymerisation and isotopic scrambling (Gauchotte-Lindsay and Turnbull, 2016), with atoms losing their isotopic fidelity and relationship with the parent compound, as long as their new position within secondary pyrolysates is uncertain. In instances when parent molecule pyrolysis is not quantitative, a Rayleigh plot can be constructed, taking into account the initial isotopic signature of the parent molecule, fraction of the reacted molecule and the isotopic signature of the remaining parent molecule, leading to the calculation of the enrichment factor associated with the reaction (Gauchotte-Lindsay et al., 2009; Fischer *et al.*, 2009). For these measurements to provide reliable results, the pyrolysis breakdown mechanism, formed pyrolysates and conditions under which they form need to be first understood. *In-silico* models enable the exploration of a wide range of reaction conditions, including temperature, residence time, and pressure, with minimum costs, offering insights into the impact of these parameters on reaction outcomes.

2.9. Reaction Mechanism Generator (RMG) – *in-silico* pyrolysis

Taking into consideration the online pyrolytic conditions (i.e., temperature, residence time within the reactor, system pressure), a reaction may not run to completion (quantitative), leading to products which are isotopically lighter, and reactants relatively enriched than the starting isotopic composition. However, these methodology parameters can also help in the modelling of the pyrolytic breakdown of compounds if the reaction mechanism is known, aiding the understanding of isotopes partitioning between reactants and products. The Reaction Mechanism Generator (RMG) used in this work is the open-source software developed in Python syntax and accessible at https://rmg.mit.edu/, used to automatically build complex kinetic models for a wide range of reacting gas- or liquid-phase systems, able to handle molecules containing C, H, O, S and N atoms (West *et al.*, 2012; Gao *et al.*, 2016). Since its launch (Green *et al.*, 2001), RMG has so far been employed to study chemical

processes and kinetic models for combustion (e.g., Magoon *et al.*, 2010; Blondal *et al.*, 2019), oxidation (e.g., Zhao *et al.*, 2018; Lee, 2021), bio-oil gasification (e.g., Khanshan and West, 2016), cracking (e.g., Van Geem *et al.*, 2006) and, most importantly for this work, pyrolysis (e.g., Harper *et al.*, 2011; Dong *et al.*, 2020). New features have been recently added to RMG, with the software able to perform heterogeneous catalysis, uncertainty analysis, a SurfaceReactor was introduced alongside the Liquid and Simple reactor (gas phase) (Liu *et al.*, 2021), with an added functionality to be employed in position-specific isotope analysis (PSIA, e.g., Goldman *et al.*, 2019; Julien et al., 2020).

RMG was built to understand chemical reactions, as it relies on a thermochemical and kinetic database to predict hundreds of species and their associated reactions (Gao et al., 2016; Liu et al., 2021). It further has the advantage of generating mechanisms compatible with CHEMKIN, Cantera, ANSYS (Gao et al., 2016) – software able to handle further gas-phase chemical kinetics, thermodynamics and transport processes. Thermodynamics are represented by trees, estimated using Benson group additivity formulas (Benson and Buss, 1958; Gao et al., 2016) and further improved by "on-the-fly quantum calculations" for less well constrained cyclic and polycyclic molecules (Gao et al., 2016). The thermodynamics of each species are defined as:

- H_{298} (Kcal/mol or kJ/mol) - the standard enthalpy of formation at 298⁰K (ΔH_f^0)
- S_{298} (J/mol*K) which is defined as the standard entropy at 298⁰K
- $C_p^0(T)$ -standard heat capacity as a function of T, temperature, for multiple T values (taken from RMG documents).
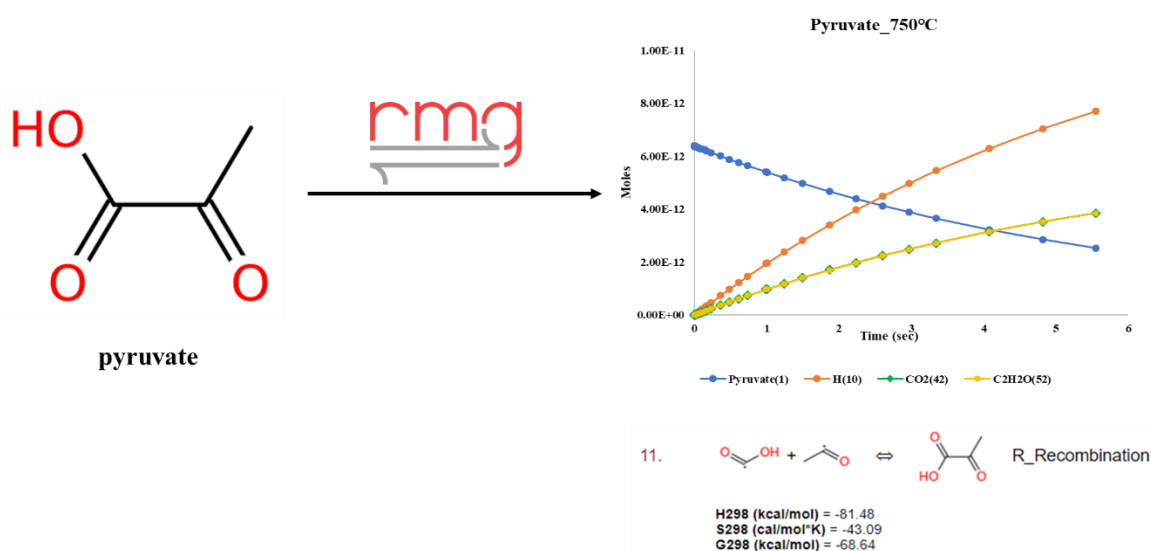
Figure 2.17 Example of RMG reaction mechanisms for pyruvate pyrolysis at 750℃. Notice the reaction time axis provided in seconds, oY axis in moles and provided mechanisms of main pyrolysate formation, with the associated thermodynamic values.

82

The main mechanism steps are shown in Figure 2.11, with an example of the output in Figure 2.10. To summarise the background process, RMG uses templates of functional groups, defined as graphs, and a set of 45 reaction families, to understand a reaction and generate a product. Details of rate reaction rules are associated with each reaction family, followed by kinetics between reaction sites that indicate how a bond will change. The reaction rate coefficients (i.e., k(T, P)) are calculated based on known rate rules and previously inputted reaction pathways and templates (i.e., trees). All reactions and rate trees are provided within the RMG database and can be individually accessed and investigated. At each iteration step, RMG takes into account reaction rates and uses a flux-based algorithm to enlarge the model and decide which reaction and species to use in the next step (Gao et al., 2016).

User-defined input.py: reactor type, library, reactants, starting concentrations, operating conditions (temperature, pressure, reaction time), and constrains

Creates all possible reactions between reactants based on templates of reaction families (core/edge; iterative enlargement)

For each reaction → RMG generates reaction rate constant (k) and the thermodynamic properties of newly products

Quantification of concentration of all species in the mechanism as a function of time and importance evaluation of newly products

Iterative procedure continues until no new products that are kinetically important are introduced to the core mechanism

Figure 2.18 Based on Gao et al. (2016) and Goldman et al. (2019).

The RMG code for performing reactor pyrolysis is ideal for the work conducted in this thesis as it can fully model the conditions of the GC system and dimensions of the online pyrolyser. Similar to the RMG code, the prep-GC methodology was designed to perform pyrolysis on individual, heart-cut compounds. GC parameters such as system pressure, carrier gas flow (i.e., for calculating the volumetric flow) and initial concentration of compound can be provided in the code, together with the pyrolytic temperatures and a terminationTime, defined as the time the molecule experiences the pyrolytic temperatures. The reaction time

(i.e., terminationTime, τ) was calculated for each simulated molecule following Eq. 8 below (Goldman et al., 2019):

$$\tau = \frac{V}{\sqrt{}} = \frac{T}{T_o}\frac{V}{\sqrt{}_o}$$

Eq. 8

where τ is the calculated residence time of molecules within the pyrolysis tube; V is the volume of the pyrolysis tube; $\sqrt{}$ is the volumetric flow rate for the system's pressure, P_o, and T_o, the oven temperature (Goldman et al., 2019– Supplementary information). The volume of the reactor was calculated using cylinder volume $= \pi *$ radius^2 *length, taking into account the internal diameter (ID) of the capillary used and the length over which pyrolysis occurred.

RMG provides a useful tool for understanding molecular breakdown of new compounds and, by adjusting the reaction mechanism to the prep-GC system and methods, it offers an auxiliary line of evidence for this work. Furthermore, as diploptene, and hopanoids in general, were never subject to pyrolysis, RMG will be used to study their pyrolytic fragments and temperatures at which they occur. Coupling of *in-silico* and experimental pyrolytic results, CSIA of environmental and pure methanotroph culture lipids, and theoretical frameworks of C-CH$_4$ incorporation within diploptene, will inform on the potential of online pyrolysis of this molecule and its subsequent pyrolytic fragments to be used as a proxy for aerobic methanotrophy detection.

3. CSIA of Pastaza-Marañón Foreland Basin peatland lipids

3.1. Introduction

Discovered in 2009 (Lähteenoja et al., 2009a; Lähteenoja et al., 2009b), PMFB represents the perfect site to study the isotopic signatures of diploptene biomarker in a natural environment, given its recently confirmed CH_4 source potential (Lähteenoja et al., 2009b; van Lent et al., 2019; Teh et al., 2017;Winton *et al.*, 2017) and vast extent of pristine tropical peatlands with undisturbed palaeoenvironmental records that span back at least ~8900 years (i.e., Aucayacu peatland; Swindles, 2018). An extensive biomarker investigation (*n*-alkanes, fatty acids, hopanoids, GDGTs) for surface and core samples from 3 peatlands, Quistococha (QT), Buena Vista (BVA) and San Jorge (SJO), was conducted between 2017-2018, during the author's MSc by Research study entitled "*The potential of biomarkers for reconstructing long-term ecohydrological and microbial community changes in newly discovered Amazonian peatlands*" (Amariei, 2018) and confirmed the presence of diploptene, in varying concentrations. The findings of this thesis, together with a literature review of the existing data sets for the three peatlands explored in the chapter, are found in Subsection 2.4.

This chapter focuses on three peatlands situated in the Pastaza-Marañón Foreland Basin (PMFB), Peru, in order to understand the natural conditions under which methanotroph-produced diploptene occurs in association with diverse other diploptene bio-producers. The previous assessment conducted by the author of this thesis assessed the occurrence of methanotrophs and each peatland's (palaeo)potential to act as a CH_4 sink or source. Given that isotopic measurements are scarce within PMFB, hopanoids, diploptene included, *n*-alkanes and fatty acids are investigated, aiding the understanding of the palaeoenvironmental evolution of the area. This allows to understand the advantages and limitations of the CSIA analytical tool when it is employed to assess the main diploptene bio-producers in a complex (palaeo)environment.

3.2. Materials and methods

3.2.1. Sample collection and nomenclature

Surface and core samples were collected in 2010 during the dry season by Dr Katherine Roucoux, University of St Andrews, UK, and the associated research group. From each peatland, surface and core samples were provided for biomarker analysis which was conducted by Amariei (2018). Full details of peat sampling methodology and location are provided in Amariei (2018). Lipid aliquots of the same samples were re-extracted following the BECS protocol (Figure 3.1-courtesy of BECS Laboratory, University of Glasgow) and used for isotope analysis in this work. The pollen intervals provided here are based on research done by Roucoux et al. (2013). The nomenclature of each sample is kept the same as in Roucoux et al. (2013), as it was used as well in Amariei (2018). Each isotopic value refers to a zone, or depth, and is described by one peatland sample, usually representing an 8 cm depth section of the core.

3.2.2. ASE extraction

The samples were frozen as soon as they were received, freeze-dried and the dried peat was homogenised using a mortar and pestle. New aliquots of each sample were weighed and added into stainless steel cells which were loaded to the Accelerated Solvent Extractor (ASE 350, Thermo Fisher Scientific, Waltham, Massachusetts, US). The Total Lipid Extract (TLE) was obtained from 0.5 g of peat that was extracted for each sample, apart from samples 2389 and 2409 which came from a silty-clay organic-poor horizon for which 2 g were used.

The ASE was used to extract the TLE using DCM:MeOH (9:1, vol:vol), heated 6°C/min to 120°C (5 min) over 2 cycles, with a purge time of 100 sec. Once extracted, the TLE was dried over a gentle steam of N_2 and split into fractions using silica gel column chromatography as summarised below.

3.2.3. Lipid extraction and clean-up

A more in-depth description of the lipid clean-up and extraction protocol can be found in Amariei (2018) and a summary is provided here and in Figure 3.1. Samples were separated into a neutral (TNF) and acid (TAF) fractions over an LC-NH_3 silica gel column, by eluting with DCM:isopropyl (1:1, vol:vol) and Ether with 4% acetic acid, respectively. The neutral

fraction was further separated into 4 fractions, using a 230-400 mesh/35-70 micron silica powder (standard silica) loaded onto a Pasteur pipette through which the following solvents were added to obtain each fraction: hexane → aliphatic hydrocarbons (N1); DCM → ketones, esters and other aromatic compounds (N2); ethyl acetate:hexane (1:3, vol:vol) → alcohols (N3); methanol → polar compound (GDGTs; N4). The acid fraction was further cleaned over a standard silica column using hexane and DCM. The DCM fraction contained the fatty acids of interest (A2), while the hexane fraction was discarded. The N1 fraction was analysed on the GC-IRMS for all three peatlands, whereas the A2 fraction was only analysed from QT and BVA, following Figure 3.1 protocol.
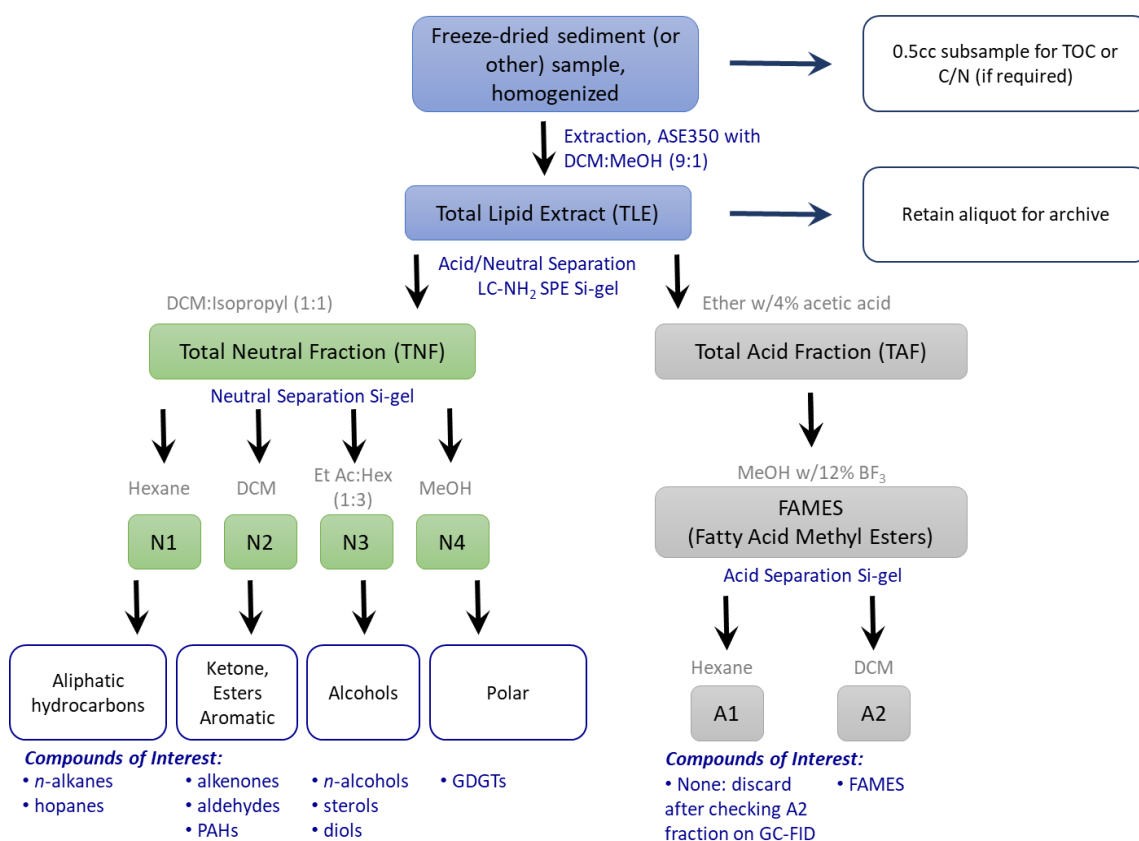
Figure 3.1 BECS laboratory, University of Glasgow, protocol for lipid separation into compound classes prior to GC analysis.

3.2.4. GC-MS and GC-IRMS methods

Several underivatized samples were previously analysed on a GC-MS system at the University of Glasgow, to aid with GC-IRMS lipid identification. Samples were loaded into 150 µL inserts in GC vials and lipids were identified on a 7890 Agilent GC coupled with a 5977 MS (**GC-MS**) and equipped with an HP-1-MS column (60 m × 0.25 mm × 0.25 µm). 1 µL of sample was injected from each vial. The inlet was set at 315°C in splitless mode and

the He flow at 1.5 mL/min. The oven method was: 60°C (2 min), 30°C/min to 120°C (0 min) followed by 5°C/min to 310°C (33 min); total run time was 75 min. Solvent delay time was set at 10 min into the run. The GC-MS acquired the data in Total Ion Extract (TIC) mode over a scan range of *m/z* 40-650. Lipids were identified using Agilent Mass Hunter Workstation, Qualitative Analysis Version B.07.00 coupled with NIST library 2.0. A diploptene external standard (Sigma-Aldrich, 04626) was used to confirm the identity of the compound while the BECS calibration standard, to identify *n*-alkanes (Appendix A.3.2).

The underivatized N1 and the derivatized A2 (see below) fractions were analysed on a continuous flow Isoprime 100 **GC-IRMS** at the University of Bristol, OGU, on a HP-1 column (50 m × 0.32 mm × 0.17 µm). The polarity of the column was the same as the one used on the GC-MS at the University of Glasgow employed for compound identification, ensuring the same compound elution order. The same in-lab external standard was further used on both instruments (Appendix A.3.2.). Single injections of each sample were conducted and 1 µL of sample was injected from each vial. The inlet was set at 325°C splitless mode and the flow to 2 mL/min. The oven method program was set isothermal for 2 min at 60°C, followed by 30°C/min until 120°C and a 5°C/min until 320°C, where it was kept isothermal for 10 minutes; the total run time was 55 min, making 1 min equal to 605 scans. The instrument was set to back flush the solvent peak while two CO_2 pulses were provided for isotopic stability assessment. The CO_2 cylinder carbon isotopic value was previously calculated and reported to be -23.93‰. The instrument reproducibility was ≤ 0.5‰ and the reported instrumental long-term precision was 0.3‰ (Inglis et al., 2019). The stability of the instrument was further monitored by injecting the OGU FAME external standard every 4 samples during the sequence, with an average SD of 0.14‰ (n=18; Appendix A.3.3.). *n*-Alkanes were analysed in 50 µL hexane, while FAs were further diluted and run in 150 µL to be within the range of the CO_2 calibration peaks (Figure 3.2) and external OGU FAME standard (Figure 3.2., Appendix A.3.3 for isotopic values).

3.2.5. FAME correction to FA CSIA

The acid fraction containing fatty acids (FA; A2 fraction) had to be derivatised given the high polarity of compounds, set to be analysed on a non-polar column. This work was conducted at the OGU, University of Bristol. Approximatively 150 µL MeOH-BF_3 derivatizing agent with a lab-provided value (-31.42‰) was added to each 8 mL vial, and the vials were heated at 70°C for 1 h. The derivatised samples were allowed to cool to room temperature and were dried under a gentle stream of N_2. Silica columns were pre-cleaned

using hexane (~ 4 mL) and the samples were loaded onto the columns using DCM. Approximatively 4 mL of DCM were further used to elute the FAs fraction, which were dried under N_2 and then transferred into GC vial inserts using 150 µL hexane.

The derivatization process leads to the addition of an external carbon atom to the FA structure, transforming them into fatty acid methyl esters (FAMEs). The isotopic value of the added carbon atom (from the MeOH-BF_3, methyl moiety) has to be mathematically subtracted post-IRMS analysis of FAMEs for accurate isotopic results of environmentally-produced FAs. The isotopic value of the methyl carbon of MeOH-BF_3 was provided by the lab, at -31.42‰. Assuming that the derivatization reaction was quantitative (i.e., ran to completion, with MeOH-BF_3 in excess), an assumption which can be made for low concentration environmental samples, the calculation is done following Eq. 9 (Rieley, 1994):

$$\delta^{13}C_{FA} = \frac{n_{FAME} \times \delta^{13}C_{FAME} - n_{MeOH} \times \delta^{13}C_{MeOH}}{n_{FA}}, \qquad \text{Eq. 9}$$

where n_{FAME}, n_{FA} and n_{MeOH} - the number of carbon atoms in each molecule (i.e., 1 for MeOH), $\delta^{13}C_{FA}$ is the corrected value to be calculated, $\delta^{13}C_{FAME}$ the isotopic values of the analysed lipids given by the GC-IRMS and $\delta^{13}C_{MeOH}$ was -31.42‰.

3.2.6. Software and parameters

IRMS data was processed on IonOS software using the reported isotopic values of the FAMEs compounds within the external standard and CO_2 cylinder and using the following parameters for the monitoring peak integration: max flat top deviation = 5 (% height), peak width = 50 (% FWHM), minimum peak height = 100000 (fA). The peak limits were set to ignore 30% of the peak start and 10% of the peak end. The baseline was calculated using the Ratio-Offset method in the Before and After mode, with the horizontal option selected. For sample peaks, the relative height was set to 4%, and absolute height to 0.0008 nA, with automatic peak-to-peak baseline noise and peak width at 5% height scans selected. The baseline start threshold was set at 0.1% and the end threshold at 0.2%. The same options were kept for the baseline calculation. Craig (CO_2) correction was applied and the values are reported on the VPDB scale. IRMS chromatograms were plotted using Microsoft Excel using the scatter graph option with smooth lines to allow chromatogram display aspect and text standardization between chapters, and add zoomed-in chromatograms within the same plot.

3.2.7. Peak identification

Beam *m/z* 44 was plotted in all IRMS graphs, representing the signal intensity (nA). The FAs were identified based on the FAME external standard containing saturated FAMEs with
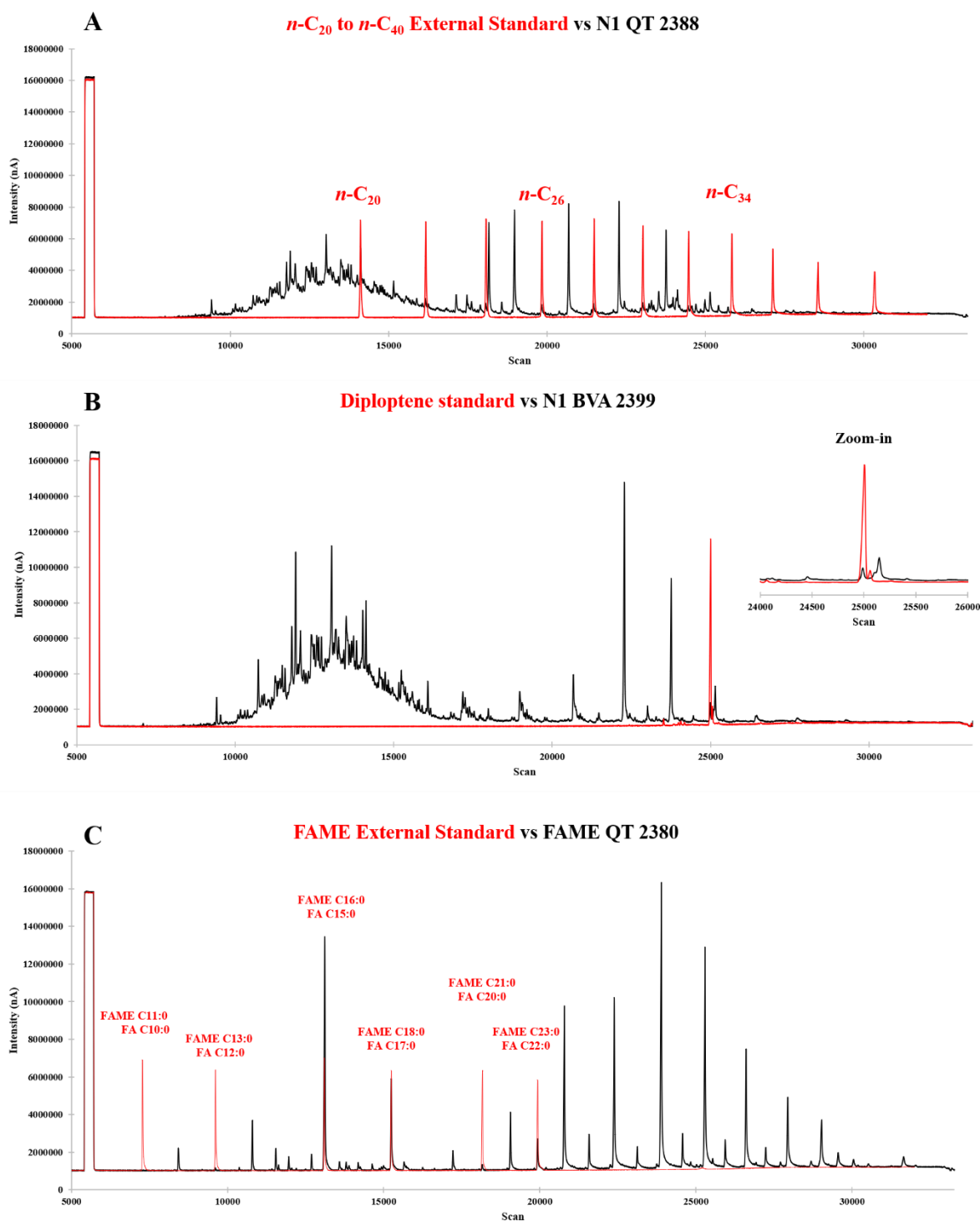
Figure 3.2 A: n-Alkane analytical standard IRMS chromatogram overlaid on a QT sample for lipid identification. B: Diploptene analytical standard used to identify the retention times and diploptene biomarker within a BVA sample. C: FAME external standard (red chromatogram) overlaid on a QT surface sample for lipid identification. X axis represents scan time.

11, 13, 16, 18, 21 and 23 carbons used for isotopic calibrations at OGU, University of Bristol. To determine the corresponding FAs, the chain lengths of FAMEs were decreased by one carbon number (Figure 3.2.C). *n*-Alkanes were identified by injecting an external standard containing even carbon atom number n-alkane chains in the range of *n*-C_{20} to *n*-C_{40} (Sigma-Aldrich; 67444; Figure 2.3.A). Finally, a diploptene standard (0.1mg/mL hop-21(29)-ene in isooctane; Sigma-Aldrich, 04626-1mL) was injected to determine its retention time for sample compound identification (Figure 2.3.B). As it was purchased, this standard did not have a known (pre-calculated) isotopic values, thus it was considered a sample.

To aid with GC-IRMS peak identifications, several samples were analysed on the GC-MS. C_{29}-hopane and hop-17(21)-ene were present in a few samples across all three peatlands. Their characteristic *m/z* are provided in Table 3.1. Multiple other hopanoids such as βα and αβ C_{27}-hopane, C_{29}-hopane and C_{31}-hopane were also identified first on the GC-MS based on characteristic *m/z* (e.g., 191, Sessions *et al.*, 2013) and elution order, yet they did not have high enough concentrations for isotopic analysis. The *n*-alkanes were identified using the retention times of the external in-lab (BECS) and *n*-alkane mix standards, which contained *n*-alkanes in the range of *n*-C_{20} to *n*-C_{40} (even carbon chain lengths) and molecular ions. Odd carbon length chains of n-alkanes had the highest concentrations given the type of samples analysed (peat) and were evenly spaced in terms of retention times.

Table 3.1 Fragment m/z used for GC-MS lipid identification.

Lipid	Mass (M+)	Characteristic m/z	Proxy for
n-alkanes	Various	57, 71, 85, 99, 113…	Vegetation
fatty acids	Various	74, 87, 101, 115, 129…	Vegetation and Bacteria
FAMEs	Various	(+TMS): 117, 132, 145…	Vegetation and Bacteria
C_{27}-hop	370	149, 191	Bacteria
Diploptene	410	189, 191, 395, 95	Bacteria
C_{29}-hop	398	191, 177	Bacteria
hop-17(21)-ene	424	313, 205, 189, 191, 95	Bacteria
C_{31}-hop	426	191, 205	Bacteria
Squalene	410	69, 81, 136, 341	Multiple
Isoprene	68	27, 39, 53	Multiple
Archaeol	426	130, 131, 341, 369, 412	Archaea

3.3. Results

3.3.1. Main findings

This chapter presents the first downcore and surface multi-biomarker isotopic analysis of QT, BVA and SJO peatlands. Isotopic values of *n*-alkanes and hopanoids are analysed and discussed in the context of previously analysed biomarker concentrations and interpretations, summarized in Amariei (2018) and in Subsection 2.4 of this thesis. Fatty acids isotopic data is provided in Appendixes A.3.4 and A.3.6. Diploptene isotopic values, the main biomarker of interest for this thesis, were measured between the wide range of -65.6‰ to -28.7‰, indicating a strong methanotroph signal in some of the studied zones, with input from non-methanotrophic sources. The most depleted value in this dataset was measured in QT-2 at -65.6‰, representing the most depleted value across present and ancient peatlands to date. Furthermore, the isotopic analysis pointed towards the existence of C_4 plants in PMFB, depicted through highly enriched *n*-C_{23} isotopic values. If confirmed by future pollen records, this would be the first time within PMFB that C_4 plants are identified through means of CSIA.

Through the wide range of isotopic values that diploptene displays, this Chapter highlights the limitations of attributing, with high confidence, methanotrophs as the bio-producers as most of the CSIA values do not reflect a strong methanotrophy signal. New analytical tools that enable isotopic analysis at the *intra*molecular levels (position-specific level) are thus required.

3.3.2. QT lipid isotopic signatures

8 core samples and 5 surface samples (Table 3.2) were analyzed for QT, with *n*-alkanes spanning *n*-C_{23} to *n*-C_{33} odd carbon chain lengths. Diploptene had high enough concentrations for IRMS measurements in 8 of the 13 samples. Single injections of each sample were analysed, which does not allow to calculate the reproducibility of the results, on a GC-IRMS instrument with a reported long-term precision of ± 0.3‰ (Inglis et al., 2019).

Table 3.2 QT core and surface n-alkanes and diploptene isotopic values (± 0.3‰, 1σ). QT6 is considered an auxiliary sample from the same peatland, taken from Inglis et al., (2019).

ID	Depth	*n*-C_{23}	*n*-C_{25}	*n*-C_{27}	*n*-C_{29}	*n*-C_{31}	*n*-C_{33}	*Diploptene*
2377	0	-32.19	-33.84	-34.52	-38.60	-40.73	-38.28	-44.24
2378	0	-36.12	-35.11	-34.16	-37.65	-40.32	-34.74	-43.12
2379	0	-36.33	-35.52	-38.19	-40.01	-40.93	-37.91	-45.29
2380	0	-33.23	-34.27	-34.33	-40.88	-41.77	-35.24	-45.50
2381	0	-34.49	-36.62	-36.51	-42.12	-40.60	-35.99	-44.46
2382	24 QT-6		-37.09	-35.99	-37.35	-34.91	-39.59	-48.04
QT6	90-100		-33.3	-33.1	-34.1	-35.9	-36.7	-29.2 (αβ C_{31}-hop)
2383	124 QT-5a		-31.12	-32.34	-36.68	-37.79	-43.10	
2384	174 QT-4c		-34.79	-42.77	-39.19	-37.52	-43.77	
2385	244 QT-4b	-23.46	-27.22	-32.51	-37.29	-34.95	-36.17	-48.76
2386	290 QT-4a			-38.29	-40.13	-39.12	-41.32	
2387	352 QT-3		-34.68	-36.51	-40.12	-36.41		
2388	384 QT-2	-36.47	-36.67	-37.73	-39.96	-39.01	-39.47	-65.59
2389	415 QT-1			-23.27	-26.99	-30.02	-30.53	

One set of isotopic data is available for the 90-100 cm depth (i.e., QT-5b, Roucoux et al., 2013) of QT from Inglis et al. (2019). The values are provided in a different colour within Table 3.2, associated with the sample QT6. Only samples anaylzed within this thesis were plotted in Figure 3.3, displaying the downward trend of each measured *n*-alkane.

An isotopic shift is seen in the surface samples (n=5) between n-C_{23}, n-C_{25}, and n-C_{27}, with values between -32.19‰ and -38.19‰, and n-C_{29}, n-C_{31}, n-C_{33}, with isotopic values between -34.75‰ and -42.12‰. The averaged isotopic values (n=5) are most depleted for n-C_{29} and n-C_{31}, with -39.85‰ and -40.87‰, respectively (Table 3.2).
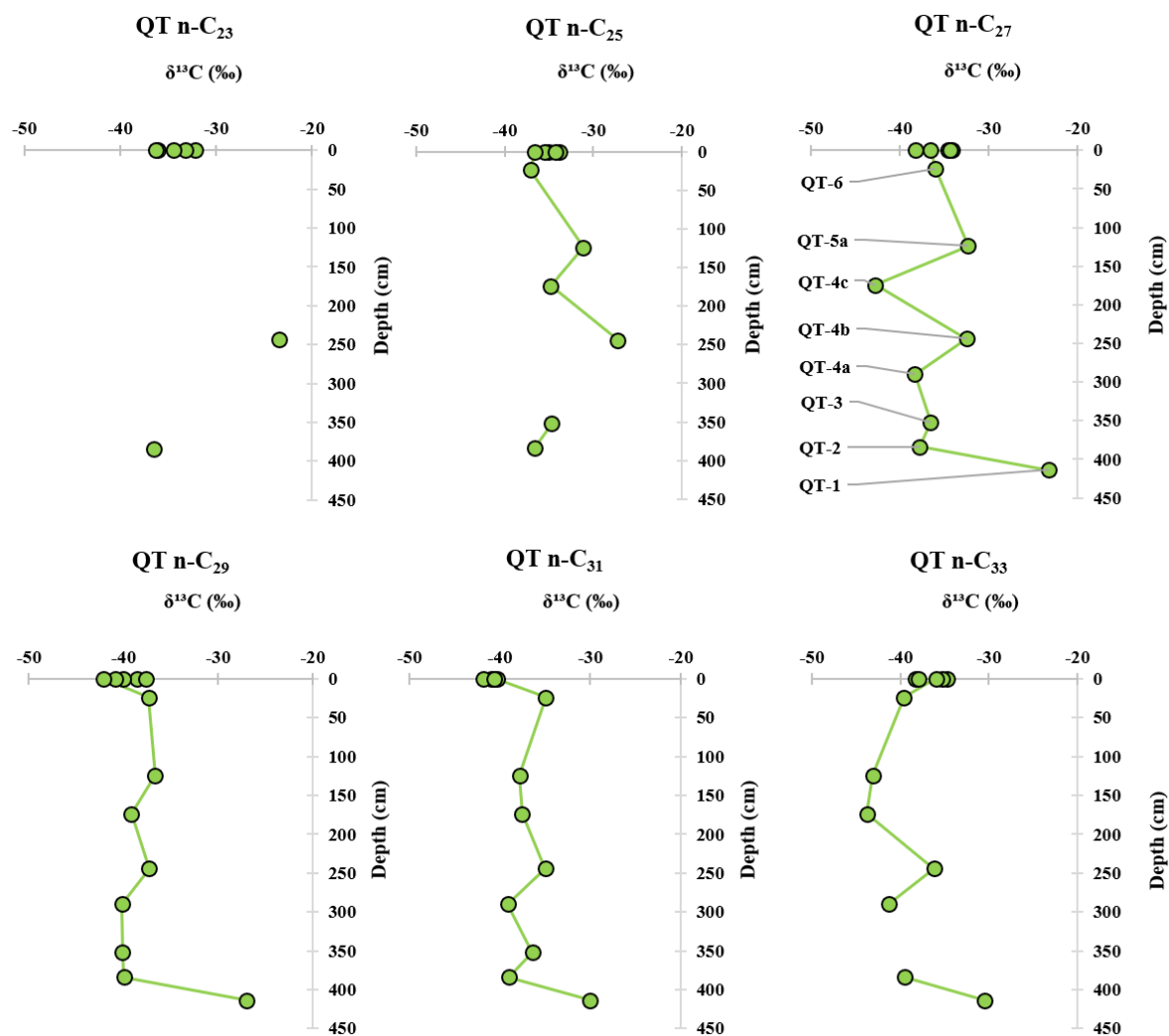
Figure 3.3. Isotopic profiles of n-alkanes from QT peatland. The zones discussed in this chapter are provided for n-C27, linking them to their corresponding depths; they are consistent for the remaining n-alkanes.

3.3.3. SJO lipid isotopic signatures

From SJO, 4 core and 5 surface samples were measured, with 3 auxiliary samples, from 90-70 cm depth from the same peatland added to Table 3.3. Although the auxiliary samples were not part of the same core, Inglis et al. (2019) provides a series of isotopic measurements from depths that were unavailable for the current work (Table 3.3). These samples are within the isotopic range of the values measured in this work.

n-C_{23} and n-C_{25} had overall low concentrations, with isotopic measurements possible in only 2, and respectively 3 core samples. Only n-C_{29} had high enough concentrations and could be measured in all available SJO samples.
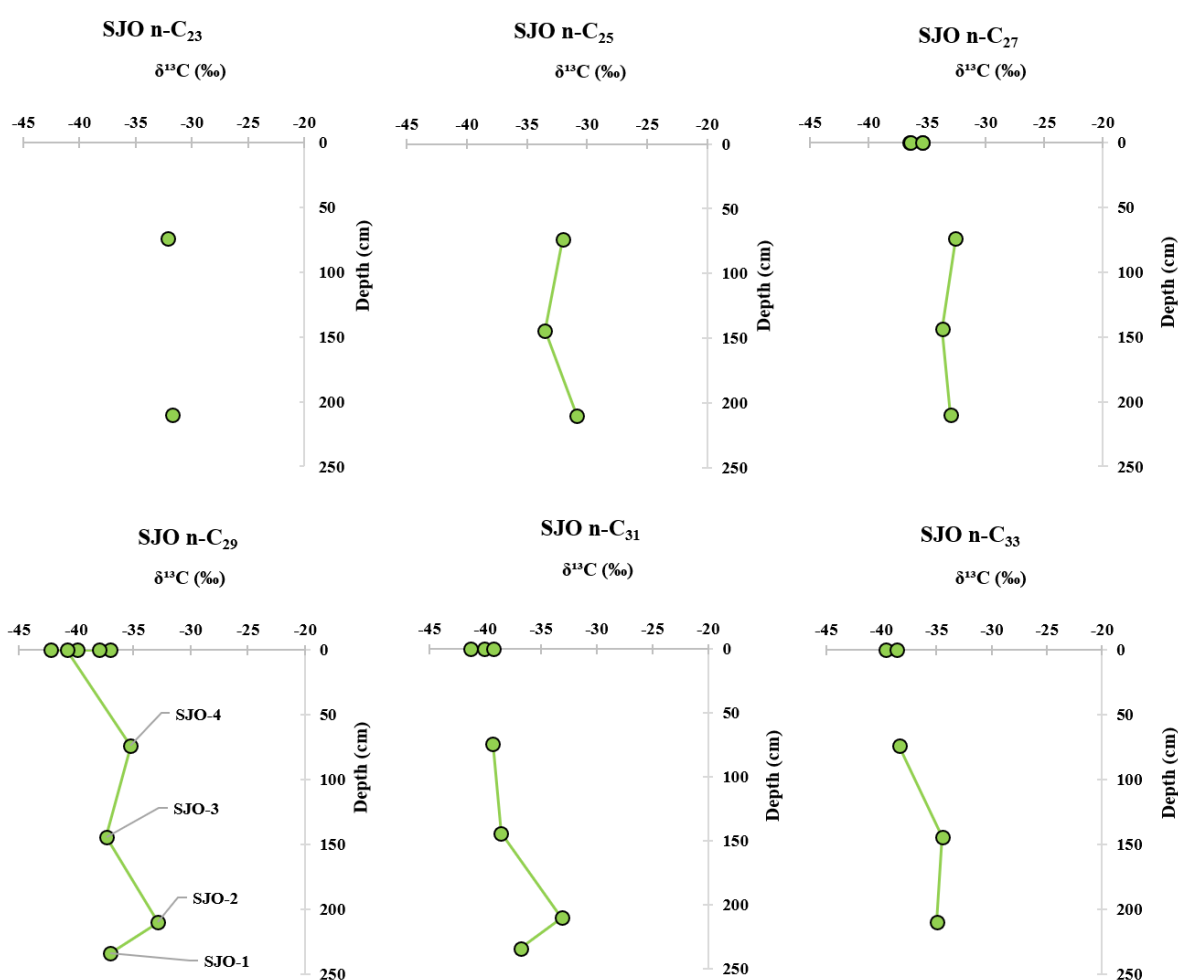
Figure 3.3 Isotopic profiles of n-alkanes from SJO peatland. The zones discussed in this chapter are provided for n-C₂₉, linking them to their corresponding depths; they are consistent for the remaining n-alkanes.

n-Alkanes become more depleted in the surface samples, with n-C_{29} displaying the most depleted value, at -42.19‰ in the sample associated with the BECS id 2392 (Figure 3.4).

Diploptene was measured in 3 out of the 9 available samples, ranging between -28.76‰ and -37.59‰ with the auxiliary diploptene value being part of this range, at -33.9‰.

Table 3.3 SJO core n-alkanes and diploptene CSIA values (± 0.3‰, 1σ). SV24, SV18 and SV6 are considered auxiliary samples from the same peatland, taken from Inglis et al., (2019).

BECS id	Depth-cm	n-C_{23}	n-C_{25}	n-C_{27}	n-C_{29}	n-C_{31}	n-C_{33}	Diploptene
2390	0			-35.43	-37.02	-41.30	-39.58	
2391	0			-36.46	-39.91	-40.08	-38.57	
2392	0			-36.39	-42.19			
2393	0			-35.38	-38.00	-39.22		-34.89
2394	0				-40.81			
2395	74 SJO-4	-32.11	-32.01	-32.55	-35.23	-39.32	-38.36	-37.59
SV24	70-80		-32.1	-32.1	-33.4	-35.0		-33.9
SV18	80-90				-34.4	-35.4		
SV6	80-90				-34.9	-35.5		
2396	144 SJO-3		-33.51	-33.69	-37.37	-38.58	-34.46	
2397	210 SJO-2	-31.72	-30.83	-33.02	-32.86	-33.14	-34.96	-28.76
2398	234 SJO-1				-37.02	-36.80		

3.3.4. BVA lipid isotopic signatures

Finally, CSIA values are available for *n*-alkanes, diploptene and FAs for BVA. The lipids had high enough concentrations, and isotopic data is available for most depths. FAs values and profiles are available in Appendix A.3.6., and *n*-alkanes and diploptene CSIA values are presented in Table 3.4 and Figure 3.5. No auxiliary values are available for this peatland.

Table 3.4 BVA core CSIA values of n-alkanes and diploptene ($\pm 0.3‰$, 1σ).

BECS	Depth	n-C_{23}	n-C_{25}	n-C_{27}	n-C_{29}	n-C_{31}	n-C_{33}	Diploptene
2399	0	-19.92	-21.90	-24.19	-34.22	-33.57	-30.71	-42.07
2400	0	-19.44	-21.32	-24.54	-35.93	-34.49	-28.19	
2401	0			-30.50	-39.18	-37.77	-35.97	
2403	0			-33.73	-38.70	-39.93	-42.14	
2404	4		-31.01	-30.27	-39.42	-36.36	-36.36	-50.87
2405	64		-30.26	-30.73	-37.10	-34.86	-36.36	
2406	128		-28.34	-28.55	-36.74	-35.83	-37.86	
2407	208		-28.22	-26.50	-35.86	-33.75	-36.41	-59.17
2408	270			-25.64	-36.86	-34.58	-36.38	-54.41
2409	336	-19.40	-22.17	-25.84	-31.42	-32.96	-31.74	-55.99

For BVA, n-C_{23} and n-C_{25} had the most enriched isotopic values across the 3 peatlands, with values of -19.4‰ and -21.32‰, respectively (Table 3.4). n-Alkanes become more depleted with increasing carbon numbers in the chain length, with the most depleted value measured for n-C_{33} at -42.14‰ at the surface of the peatland.
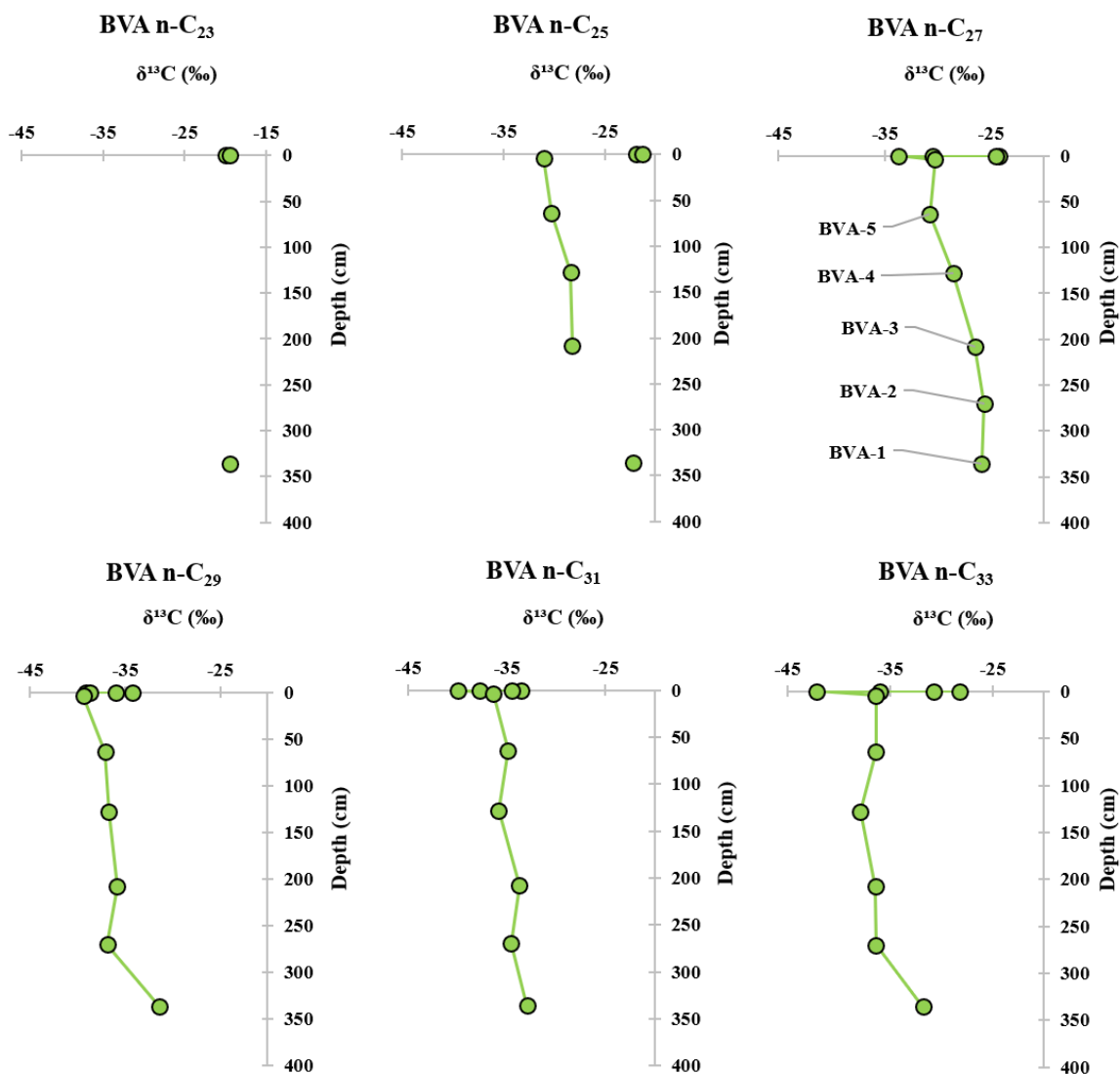
Figure 3.4 Isotopic profiles of n-alkanes from BVA peatland. The zones discussed in this chapter are provided for n-C27, linking them to their corresponding depths; they are consistent for the remaining n-alkanes.

3.3.5. Diploptene isotopic signatures

Diploptene was measured in 5 out of the 10 samples available from BVA for this study. The biomarker becomes more enriched towards the surface, recording values as depleted as -59.17‰ at the averaged depth of 208 cm, and -42.07‰ at the surface. QT and BVA are similar in terms of isotopic depth profiles, with diploptene displaying more depleted values towards the bottom of the core. Interestingly, at both core locations, diploptene values from samples just below the surface (i.e., QT-6 at 20-28 cm and BVA-6 at 0-8 cm) are more depleted compared to those occurring at the surface. Both peatlands have similar diploptene isotopic values at the surface, -42‰ to -45.5‰ (Figure 3.5).
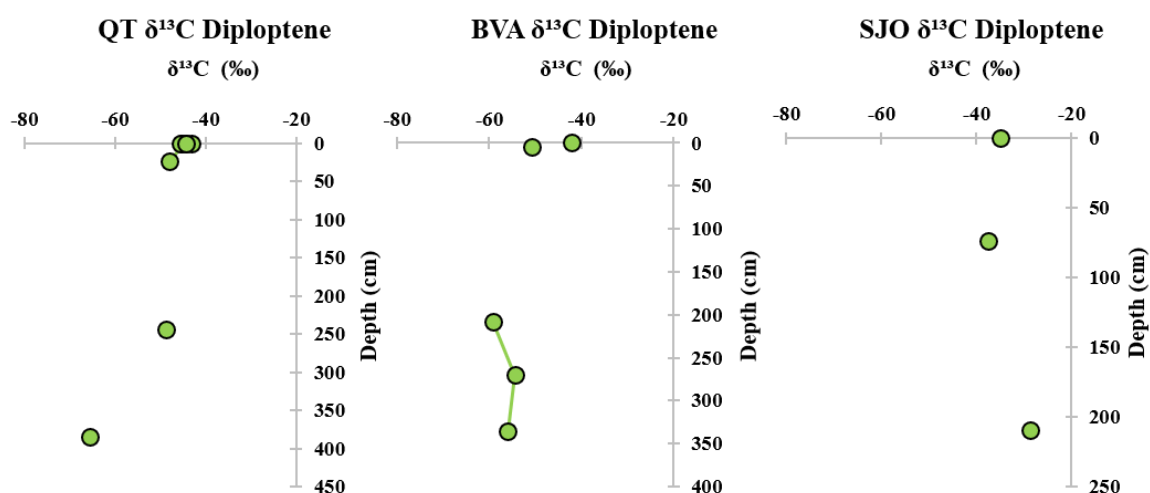
Figure 3.5 Diploptene isotopic profiles from the three peatlands.

3.4. Discussions

The new isotopic values are discussed in the context of previously analysed lipid concentrations and assessments (Amariei, 2018), as they provide auxiliary information on the basis of which, microbial communities and palaeoenvironmental transitions can be further interpreted.

3.4.1. QT lipid isotopic signatures in the wider peatland context

The first available sample (Zone QT-1; 2280- 2200 cal yr BP), from 410-420 cm, contains the most enriched isotopic values from QT, across all analysed n-alkanes (Table 3.2) and FAs (Appendix A.3.4.). This silty-clay horizon was deposited before peat accumulation started at the site of the QT core, when the location was still part of the Amazon river flood plain (Roucoux et al., 2013). The pollen records (Roucoux et al., 2013), P_{aq} (Amariei, 2018) and sediments indicate the presence of a lake, with water input mainly from atmospheric precipitations and less from repeated flooding events. It is thus difficult to assess which lipids are allochthonous (i.e., from remote locations) and which are autochthonous (i.e., produced *in-situ*), yet the site is dominated by the input of short chain n-alkanes, most likely indicating local emergent macrophyte vegetation, yet extending to n-C_{39}, with an odd-over-even preference, suggesting the presence of higher plants in the area (Amariei, 2018). The $\Delta_{nC27\text{-}nC33}$=7.62‰ indicates a mixed source input for the two n-alkanes, potentially from both C_3 and C_4 plants, given the more enriched short-chain isotopic values (Cicerone and Oremland, 1988). For the depth of 410-420 cm, diploptene and other hopanoids did not have high enough concentrations for CSIA.

Around 2200-2100 cal yr BP, in a peat section labelled QT-2 from 380-388 cm, there is evidence of the establishment of waterlogged and oxygen-deprived conditions, leading to the accumulation of organic matter (OM). The analysis of n-alkanes suggests input from higher plants, with pollen and biomarker records indicating open-water vegetation in a lake-like setting. Isotopic values of n-alkanes reveal the onset of OM accumulation, followed by decay processes and likely CH_4 production. Such as, diploptene, which had high enough concentrations for CSIA, also presented the most negative value from the aliphatic fraction from QT, at -65.59‰. Significantly, diploptene's isotopic values are also the most depleted across the entire dataset presented in this work, the most depleted value of diploptene from the T-GRES peatland database and the 2nd most depleted value across all hopanoid biomarkers from the same database (Inglis et al., 2019). Within the database, one sample

from Cobham peatland, UK, contained diploptene as depleted as -75.69‰, deposited at the onset of the Paleocene-Eocene Thermal Maximum which took place approximately 55 Ma (PETM; Inglis et al., 2019 and references in SI). Within the literature, more depleted diploptene values have been recorded across a wide spread range of environments such as in the Ace thermokarst lake (i.e., -68.2‰; Davies *et al.*, 2016), marine sediments (-66‰; Yamada and Ishiwatari, 1999), surface sediments above a CH_4-emitting mud volcano (-70‰ to -75‰; Elvert and Niemann, 2008), at Lake Rotsee (-60‰ to -43‰, Naeher *et al.*, 2014), and have in all cases been associated with CH_4 consumption by methanotrophs. Appendix A.3.1. compiles a more widespread review of the isotopic values of diploptene from literature, coupled with their inferred bio-producers. Diploptene, a compound with the most negative isotopic value in the aliphatic fraction, indicates strong CH_4 incorporation by methanotrophs.

Sample QT-3a (2100-1990 cal yr BP) from 348-356 cm, depicts a zone dominated by short-chain *n*-alkanes (i.e., *n*-C_{18} and *n*-C_{19}), with a P_{aq} ratio indicating the presence of a pool and emerging macrophytes. No isotopic values of the short chain *n*-alkanes were extracted due to co-elution. No major fluctuations in the isotopic composition of the available *n*-alkane is recorded, and diploptene concentrations were too low for CSIA.

In zone QT-4a (294-286 cm), a strong odd-over-even preference of long-chain *n*-alkanes indicates input from higher vascular plants, coinciding with the retreat of the previous pool and closure of the canopy. Isotopic values of *n*-C_{31} and *n*-C_{27} show a relative depletion compared to the previous depth, suggesting environmental conditions similar to Zone QT-4c discussed below. Previous biomarker analysis indicates that, at that time, the peatland acted as a CH_4 source, supported by the presence of certain fatty acids and archaeol. Diploptene concentration was however too low for isotopic measurements to provide further evidence.

Zone QT-4b (240-248 cm) lacks indicators of pool development and shows enriched values in *n*-alkanes and fatty acids, suggesting a shift to herbaceous taxa. CH_4 production is assessed as reduced, supported by current isotopic records which indicate limited methanogenic/methanotroph activity and a change experienced in the microbial community. The herbaceous species likely provided less available OM substrate and root exudates to sustain microbes (Whiting and Chanton, 1993; Girkin *et al.*, 2018; Hoyos-Santillan *et al.*, 2019). Diploptene's isotopic value is relatively enriched, possibly due to contributions from type II and X methanotrophs capable of incorporating higher amounts of CO_2 (Handson and Handson, 1996) and input from non-methanotrophic bacteria.

In <u>Zone QT-4c</u> (170-178 cm), a shift to higher plants is observed, aligning with pollen records and canopy closure. Isotopic values of *n*-alkanes and fatty acids, particularly *n*-C_{25} and *n*-C_{27}, show significant depletion, indicative of underlying methanogenesis and methanotrophy processes. The closed canopy likely led to a less well-mixed atmosphere below the treeline (i.e. "canopy effect" highlighted in literature for Amazonia regions, Van der Merwe and Medina, 1991; Inglis et al., 2019), leading to the incorporation of depleted CO_2 through photosynthesis and biosynthetic cycles. If some of the CH_4 was oxidised *in-situ* by the methanotroph community, depleted CO_2 would have been emitted from the surface of the peatland and incorporated within vegetation. Ambiental CH_4-derived CO_2 incorporation was also observed in Lake Qualluuraq, a thermokarst lake in Alaska (Elvert *et al.*, 2016) and in *Sphagnum* mosses where symbiotic methanotrophs convert CH_4 into CO_2 which is readily available and incorporated into plant lipids (Raghoebarsing *et al.*, 2005; Kip *et al.*, 2010).

<u>Zone QT-5a</u> (1010-360 cal yr BP), from 120-128 cm depth, is characterised by the reappearance of *Mauritia*, with the canopy closing under permanently waterlogged and anoxic conditions (Roucoux et al., 2013). From previous biomarker analysis, there appears to be a shift or disturbance experienced in both the bacterial and archaeal communities, possibly due to the shift in vegetation. Biomarkers linked to methanogenesis (i.e., isoGDGT-0, archaeol) decrease in concentrations, leading to the interpretation of a reduced CH_4 production, which led in turn to the decrease of the methanotroph community. *n*-Alkane isotopic values are overall more enriched compared to the previous depth, indicating less depleted CO_2 incorporation and, although the canopy was similarly closed as in QT-4a and QT-4c, different tree species with different adaptations could have caused the less depleted values seen in this zone. However, the shift in the microbial community is most likely the dominant cause for the enriched *n*-alkanes isotopic values as (Amariei, 2018): i) biomarkers linked to methanogenesis (i.e., isoGDGT-0, archaeol) are seen to decrease in concentrations; ii) due to a possible lack of substrate, isoGDGTs 1-3 liked to anaerobic methanotrophs are also seen to have lower concentrations yet iii) there is a spike in the concentrations of hopanoids (i.e., αβ C_{27}-hopane, αβ C_{31}-hopane, diplopterol) and FAs indicative of bacteria (i.e., $C_{18:1;}$ Amariei, 2018). The apparition of *Mauritia*, with its associated adaptation to waterlogged conditions, could have favoured this microbial structure. It is likely that less CH_4 was produced (as indicated by methanogen biomarkers) with some amount still being oxidised within the peatland. Under the closed-canopy, less atmospheric mixing is expected. While CO_2 incorporation by plants takes place, one possibility can be the enrichment of the CO_2 available under the tree-line, leading to the enrichment seen in the *n*-alkanes in this

zone. Although not in high enough concentrations for CSIA, the isotopic values of diploptene are expected to be relatively enriched compared to the rest of the QT core samples.

One set of auxiliary isotopic data is available for the 90-100 cm depth (i.e., QT-5b, Roucoux et al., 2013) of QT from Inglis et al. (2019). Isotopic values for n-C$_{29}$, n-C$_{31}$ and n-C$_{33}$ are enriched compared to other depths (Table 3.2). The isotopic signature of αβ C$_{31}$-hopane was measured at -29.2‰, highly enriched compared to diploptene values measured in this work. It should be however noted that, within the T-GRES peatland database, this hopanoid is always enriched when compared to the diploptene from the same sample. Similarly, another hopanoid, βα C$_{29}$-hopane, was measured in 5 QT samples in this work (Appendix A.3.5) and displayed overall enriched isotopic signatures when compared to diploptene from the same sample, indicating different bio-producers or bio-synthetic cycles.

Sample QT-6 (360 cal yr BP) from 20-28 cm, is characterised by a closed canopy, under *Mauritia t.* (Roucoux et al., 2013). n-Alkanes show different isotopic trends, with odd n-C$_{25}$ to n-C$_{29}$ displaying more depleted values compared to the previous depth, and n-C$_{31}$ and n-C$_{33}$ displaying relatively enriched values. It is likely that different bio-producers (species) led to the formation of these n-alkanes. Specific lipid-producers, utilising CO_2 from different levels (i.e., height distribution) within the environment, can lead to different isotopic signatures of the plant wax composition. For example, it was previously observed in this zone and at SJO via biomarker and pollen record correlation, that n-C$_{32}$ can be linked to the expansions of Davalliaceae *Nephrolepis* fern (Roucoux et al., 2013; Amariei, 2018). Furthermore, as discussed above, trees can act as CH_4 and CO_2 conduits. The internal CO_2 may be preferred in some tree species to that occurring externally of the tree bark and, under the closed canopy, CO_2 mixing with the atmosphere can be reduced. Diploptene was in high enough concentrations for CSIA at this depth, and had a value of -48.04‰, slightly more depleted than the surface values. Previous biomarker analysis indicated an increase in the concentrations of iso-GDGT-0, associated with methanogens (Schouten *et al.*, 2013), and it was expected that the peatland acted as a CH_4-source. It is possible that either, given the anoxic and waterlogged conditions of QT, the aerobic methanotroph community was not well developed or it was limited to oxic microsites around root systems. Within the top 15 cm of QT, Finn et al. (2020) did not find evidence of (NC10) anaerobic methanotrophs, and it is likely that anaerobic methanotrophy was limited in this zone as well, a few cm below their sampling point.

Finally, in the surface samples, previously analysed data from this peatland (Amariei, 2018) indicated a strong odd-over-even predominance of n-alkanes. These isotopic values show

the highest depletion of *n*-alkanes from PMFB (n=18; samples above 5 cm depth included) and those reported in Inglis et al. (2019). In fact, the isotopic values of *n*-C_{29} from n=3 samples and of *n*-C_{31} (n=5) reported here are more depleted than the minimum values of *n*-C_{29} and *n*-C_{31} from the entire *n*-alkane T-GRES peatland database which spans a wide range of peatlands (n=199; Inglis et al., 2019), making the *n*-alkane isotopic values of *n*-C_{29} and *n*-C_{31} from the surface of QT (Table 3.2) the most negative isotopic values reported at the global peatland scale.

The present-day palm swamp vegetation, *M. flexuosa,* is believed to be an important source of *n*-alkanes to the peat's surface. Although no study confirming its C_3 photosynthetic pathway could be found, C_4 plants (including palm trees) are known to grow in arid and hot climates, which do not characterise PMFB. This palm species grows in waterlogged areas, and high mortality was reported during prolonged drier periods related to the El Niño Southern Oscillation (Phillips *et al.*, 2010). The depleted *n*-alkane isotopic values are also consistent with the C_3 photosynthetic pathway (Collister et al., 1994; Table 2.1). *n*-Alkanes from lacustrine and marine sediments produced by C_3 plants were averaged at -33.1 ± 2.3‰ (1σ) while those produced by C_4 plants, at -21.7 ±2.4‰ (1σ) (Tipple and Pagani, 2010 and reference therein). Table 3.2 values are also within the isotopic range of *n*-alkanes from a C_3 sphagnum-dominated peatland (Xie *et al.*, 2004), yet, as highlighted above, the isotopic values of long-chain *n*-alkanes at the surface QT, especially of *n*-C_{29} and *n*-C_{31}, are more depleted. At QT, in samples 2377, 2380 and 2381 (Table 3.2), *n*-C_{23} is the most enriched *n*-alkane, followed by *n*-C_{25} in sample 2379. Interestingly, the most enriched isotopic value is for *n*-C_{27}, followed closely by *n*-C_{33}, indicating that the *n*-alkane input may come from multiple C_3 plant sources (i.e., mix input). The palm swamp covers approximatively 78% of PMFB (Draper et al., 2014) and *M. flexuosa* is one of the most common palm trees in Amazonia (Urrego *et al.*, 2016). It is at this point expected that similar isotopic values of *n*-alkanes to occur at the surface of peatlands where *M. flexuosa* is the dominant species. This assumption can be correlated with similar isotopic values from sample QT-3a when *M. flexuosa* appeared for the first time in the pollen record (Table 3.2).

Diploptene isotopic values were extracted from all 5 samples. The average isotopic value was of -44.5‰, with a minimum of -45.5‰ and a maximum of -43.12‰, implying overall isotopic uniformity at the surface. These values are the most enriched when compared to previous depths from where isotopic values of diploptene are available (i.e., QT-2, QT-4b and QT-6). At the surface of the QT peatland, Finn et al. (2020) found evidence of the highest relative input of *Proteobacteria* of which methanotrophs are a part of, when compared to other PMFB and Norther peatlands. Planctomycetes occurred at the surface of all peatlands,

which are known producers of hopanoids (i.e., diploptene; Sinninghe Damsté *et al.*, 2004). The implications of these findings to paleoenvironmental assessments, coupled with the isotope records, are further discussed in Subsection 3.3.4. No Verrucomicrobial or NC10 anaerobic methanotrophs were identified in the first 30 cm of peat at QT (Finn et al., 2020), making it less likely that CH_4 is incorporated by anaerobic methanotrophs.

3.4.2. SJO lipid isotopic signatures in the wider context

From sample SJO-1 (230-238 cm), only two *n*-alkanes could have been isotopically measured in this sample, *n*-C_{29} and *n*-C_{31}. The values record the plant wax isotopic signatures of the first vegetation available for this site. The values are within the same isotopic range, -37.02‰ and -36.80‰, respectively, and within the range of present-day values for the same lipids (Table 3.3). Throughout the core, *n*-C_{29} is the only lipid available in all samples. It is likely that under anoxic conditions which lead to the initial peat accumulation, CH_4 was produced, yet diploptene could not be measured in this zone.

In the next zone, marked by sample SJO-2 (207-215 cm), isotopic measurements are available for odd chain *n*-alkanes *n*-C_{23} to *n*-C_{33}. Both *n*-C_{29} and *n*-C_{31} display relatively enriched values compared to the previous sample SJO-1, indicating enriched CO_2 incorporation and *n*-C_{25} has the most enriched value across all *n*-alkanes from this site, with a value of -30.83‰, followed by *n*-C_{23} with -31.72‰ from the same depth. *n*-C_{33} displays a relatively depleted value compared to the shorter-chain *n*-alkanes, at -34.96‰. Pollen and biomarker analysis indicate herbaceous vegetation (Kelly et al., 2017) and more labile organic matter (low CPI) with decreased input across all *n*-alkanes (Amariei, 2018), thus it is expected that *n*-C_{23} and *n*-C_{25} record carbon isotopic values of herbaceous plant wax with *n*-C_{29} to *n*-C_{33}, the relatively more depleted values, those of higher plants such as tree leaf waxes. A similar *n*-alkane enrichment was seen at QT-4b during a return to herbaceous taxa. Diploptene carbon isotopic value was measured at -28.76‰ which does not indicate (depleted) CH_4 incorporation, thus methanotrophs are unlikely to be the source. Indeed, and as seen at QT-4b, CH_4 production potential was probably low due to the low availability of substrate in the subsurface rhizosphere (also indicated by low isoGDGT-0 concentrations; Amariei, 2018).

Zone SJO-3, with a sample from 140-148 cm, has pollen and biomarker records (i.e., P_{aq} ~ 0.18) indicating an aquatic setting, with a further indication from specific taxa of the lake waters being open, well-oxygenated and nutrient rich (Kelly et al., 2017). All available *n*-alkanes have more depleted values compared to the herbaceous setting from SJO-2, with

both n-C$_{29}$ and n-C$_{31}$ presenting a Δ^{13}C depletion of 4.5‰ and 5.4‰, respectively. As no diploptene or FAs isotopic signatures are available for this depth, it is difficult to comment further on the microbial activity at the time.

Auxiliary sample SV24 (Table 3.3) has very similar n-alkane isotopic measurements to those analysed in SJO-4, yet SJO-5's n-C$_{31}$ has relatively more depleted values. The uniformity of isotopic measurements (also seen as the absence of various n-alkane measurements due to low concentrations, similar to this data) for lower carbon-number n-alkanes recorded in 2 different cores indicates the overall homogeny of carbon incorporation into vegetation, and similar environmental conditions that led to similar isotopic values, irrespective of peatland core location. Diploptene was measured in SV24, with an isotopic value more enriched compared to SJO-4 (below), yet within the same range of values, more enriched at SJO compared to QT and BVA.

Similarly to SJO-2, in the sample from 70-78 cm within <u>zone SJO-4</u>, all odd chain n-alkanes in the range of n-C$_{23}$ to n-C$_{33}$ were formed during a time when the site was subject to flooding regime, during which the palm swamp forest established (Kelly et al., 2017). Longer chain n-alkanes, n-C$_{31}$ and n-C$_{33}$ continued the trend of more depleted isotopic values until the surface while n-C$_{25}$, n-C$_{27}$ and n-C$_{29}$ have relatively more enriched values compared to the previous depth, indicating different bio-producers. Diploptene has an isotopic value of -37.6‰, the most depleted value recorded at SJO, indicating, compared to the value in SJO-2, more depleted carbon incorporation, potentially from CH$_4$, and thus a methanotroph contribution to the biomarker pool. This value is also more depleted when compared to n-alkanes from the same depth, which was not the case for SJO-2, highlighting the different substrates used by the diploptene-producers.

Finally, within the <u>surface samples from SJO</u>, isotopic values of n-alkanes reflect the present-day pole forest vegetation growing under ombrotrophic conditions. n-C$_{23}$ and n-C$_{25}$ could not be measured due to low concentration (Table 3.3). For the remaining n-alkanes, they represent higher plant wax isotopic values that are within the same isotopic range, implying surface homogeny which was also seen at depth, from the auxiliary SJO isotopic data from Inglis et al. (2019). n-C$_{31}$ and n-C$_{33}$ have the most depleted values at the surface, following the depletion trend previously observed. One diploptene value is available from the surface, slightly more enriched than the value recorded in SJO-4. Previous biomarker analysis of FAs indicated the presence of C$_{18:1\omega8}$, alongside C$_{18:1\omega9}$ and C$_{18:1\omega7}$ (Amariei, 2018). The double bond position between the 8th and 9th carbon was found in FAs produced by type II methanotrophs (but not characteristic; Nichols *et al.*, 1985; Bull et al., 2000)

capable of consuming both CO_2 and CH_4, (Hanson and Hanson, 1996) which could explain the less depleted signature of diploptene from SJO, when compared, for example, to the surface of QT. Furthermore, active CH_4 consumption was previously detected in a SJO core between 30-40 cm depth (Buessecker et al., 2021) with more enriched CH_4 values occurring at that depth, yet CH_4 values recovered towards the surface (i.e., more depleted), indicating that CH_4 production also takes place in the top parts of the peatland irrespectively of active consumption, with the most depleted CH_4 recorded for this peatland. Furthermore, within the same study, α- and β-*Proteobacteria* appear to be the most active at the 20-60 cm depth and representants from the order Methanomicrobiales (i.e., methanogens) account for 72% of the archaeal 165 rRNA gene read in the top 100 cm, indicating that methanogenesis is distributed at least at SJO well beneath the surface (Buessecker et al., 2021). Given these lines of evidence, diploptene's isotopic values are relatively enriched, indicating other bio-producers and CO_2 incorporation, without discounting methanotroph input.

3.4.3. BVA isotopic signatures in the wider context

In the silty-clay sample of BVA-1 (332-340 cm), although *n*-alkanes were likely not produced *in-situ* but deposited by Amazon waters, they had high enough concentrations to be isotopically measured. *n*-C_{23} has a highly enriched value of -19.40‰, and upon further chromatogram inspection, although the peak height of the compound is relatively low, there is no co-elution with the neighbouring peak (most likely an alkene). Furthermore, similarly depleted values are seen at the surface for the same compounds. This is a highly enriched value for PMFB and overall the peatland database (Inglis et al., 2019), in which the most enriched *n*-alkane value for recent peat samples was -27.3‰. There are several possibilities for this depleted value, given that it occurs again at the surface for the same lipid: i) highly degraded organic material by local microbes (and subsequent isotopic enrichment of remaining reactant) is unlikely given that *n*-alkanes are recalcitrant in nature and that *n*-C_{25} or short-chain FAs, do not display the same enrichment; ii) allochthonous input from near-by plants or bacteria, which would make the source difficult to identify and comment or, iii) input from a C_4 plant (Brüggemann *et al.*, 2011; Table 2.1) which would be observed for the first time via CSIA in PMFB. There may be potential input from allochthonous plants such as the Polygonaceae Family (Soreng *et al.*, 2015), as explained further for the surface plants. Pollen interpretation may allow a better constraint of the nature of *n*-C_{23}.

The same can be argued about the isotopic values of *n*-C_{25} and *n*-C_{27} which also present relatively enriched values however, they become more depleted towards the surface of BVA

(Table 3.4) and return to the same isotopic values in 2 of the 4 samples for n-C_{27} at the surface, indicating mixed sources. Isotopic values for n-C_{29}, n-C_{31} and n-C_{33} are more depleted, possibly from a C_3 higher plant wax source.

Diploptene has a value of -56‰, which is more depleted than present-day surface values at BVA, QT and SJO, where active CH_4 emissions have been confirmed by field measurements. Upon further chromatogram inspection, diploptene in this sample does not co-elute with a different compound, the peak is well defined and the background noise is low enough to provide an accurate measurement. The sample is low in organic matter given the pale colour and, isoGDGTs showed previously very low concentrations, with a low CH_4 production potential identified at the time (Amariei, 2018). However, the diploptene isotopic value indicates a light carbon source incorporation, typical for methanotrophy. If produced by the local microbial community, this value indicates atmospheric CH_4 level consumption and, if not produced *in-situ*, it suggests occurring methanotrophy in the surrounding area.

The start of peat accumulation in zone BVA-2, with a sample from 266-270 cm, with a strong odd-over-even carbon preference and an increase in the CPI index suggests that higher plants were established at the site (Amariei, 2018). n-C_{27} has a similar isotopic value as the previous inorganic BVA-1, however there is a stronger depletion in the plant wax n-C_{29}, n-C_{31} and n-C_{33} lipids. From previous lipid concentration analysis, isoGDGT-0, linked to methanogens, is the dominant isoGDGT followed by isoGDGTs 1-4, linked to anaerobic methane oxidizers (Elvert *et al.*, 2000; Schouten et al., 2013). As further seen for diploptene, which peaks in and has an isotopic value comparable to the previous depth, -54.4‰, both methanogens and methanotrophs were present and active at this point in time.

The following core samples (BVA-3, 212-204 cm; BVA-4, 132-124 cm; BVA-5, 68-60 cm; and BVA-6, 8-0 cm) are similar from a carbon stable isotope point of view and can be discussed together. n-Alkanes n-C_{25}, n-C_{27}, n-C_{29} and n-C_{31} show a depletion trend towards the surface while n-C_{33} has only minor isotopic fluctuations. Vegetation does not appear to have overall shifted in the main assemblage, being dominated by vascular higher plants (i.e., woody species, trees) however, the canopy may have closed towards the surface and, as CH_4 production and consumption continued, CO_2 values provided to the atmosphere via CH_4 oxidation by aerobic methanotrophs could have led to more depleted plant wax n-alkanes.

Flooding events are likely to have continued as isotopic values of n-alkanes are similar to those recorded during the present-day, with the microbial community benefiting from higher nutrient input and oscillating water tables. BVA-3 is the last core sample from which a diploptene isotopic value was extracted at -59.2‰ marking the most depleted values for this

core, indicating active CH_4 consumption and conditions. It should be noted here that it is likely that this value is somewhat diluted by heterotrophic producers and that methanotroph-produced diploptene would have had even more depleted values. Given the high nutrient content and oscillating water tables (and likely not all-year anoxic status), it would be of interest to run PSIA on diploptene from this depth.

In sample BVA-4, biomarker evidence of type I methanotrophs have been previously recorded (Amariei, 2018), indicators of obligate methanotrophy (i.e., preferred incorporation of CH_4 carbon source; Hanson and Hanson, 1996) yet none of the associated n-alkanes and FAs appear to have been isotopically influenced. A spike in hopanoid concentrations and a decrease in the archaeal community was seen in the previous biomarker analysis at BVA-5, however this is not recorded in n-alkane or FAs isotopic values and no hopanoid isotopes could have been extracted from this depth. A diploptene isotopic value is available from sample BVA-6, taken just before the surface of the peatland. The -50.87‰ value is slightly more enriched compared to previous diploptene values occurring in deeper parts of BVA, yet marking again biomarker input from aerobic methanotrophy. Within the larger context of PMFB, carbon isotopic measurements are still scarce, yet similar highly depleted diploptene values were also found in other (palaeo)environments. For example, diploptene analysed from Amazonian lake sediments was measured at -53.3‰ (Pereira *et al.*, 2022), a value within the range of diploptene measured at BVA, and was related to methanotrophic processes.

Finally, lipid concentrations were high enough in the surface samples for most n-alkanes, yet diploptene CSIA was only possible for one sample (Table 3.4). n-C_{23}, n-C_{25} and n-C_{27} have overall enriched values when compared to longer n-alkanes, indicating two types of bio-producers.

As discussed above, the isotopic signature of n-C_{23} is highly enriched at PMFB and compared to global values (Inglis et al., 2019). The isotopic trend of analysed $\delta^{13}C_{CH4}$ produced between 15 – 75 cm depth at BVA (and QT) is smooth, becoming slightly more enriched towards the top (Buessecker et al., 2021). This trend indicates that there are unlikely methanotrophs (aerobic or anaerobic) active (in a large community) between these depths at BVA, as some fluctuations would have been noticed in the CH_4's isotopic signatures (Buessecker et al., 2021). However, these gas samples were collected at the start of the rain seasons, with the water table very closed or at the surface of BVA (Buessecker et al., 2021), which would have limited the aerobic community to very shallow layers within the peatland and oxic microsites. The samples within the current study were collected during the dry season, when the water table was approximately 13 cm below the surface (Teh et al., 2017).

n-Alkanes' isotopic values of the 4 surface samples can be grouped into two classes: a class in which the odd *n*-alkanes present more enriched values (i.e., samples 2399, 2400) and a class in which the values are comparable to core isotopic measurements (i.e., samples 2401, 2403) (Table 3.4). Upon IRMS chromatogram inspection, for example, 2399 and 2401 do not differ by a great amount in terms of peak heights (concentrations), thus it is unlikely that the more enriched values are due to insufficient carbon amount available for combustion. Similar isotopic values have been recorded in the silty-clay sample BVA-1, indicating that the signal seen in 2399 and 2400 is an accurate isotopic signal. Furthermore, FAs isotopic values do not display the isotopic grouping seen above for the 4 samples, confirming that the sample extraction procedure did not influence the isotopic signatures. The isotopic signal seen in these *n*-alkanes reflects the input plant wax of a species which utilised carbon differently for their production. n-C_{23} present at the surface (-19.92‰, -19.44‰) cannot be explained by allochthonous input as in the case of BVA-1, even with reoccurring flooding events. One scenario is the possibility of C_4 plants, known to have more enriched isotopic values compared to their C_3 counterparts (Collister et al., 1994; Table 2.1). Kelly et al. (2014) provide a present-day vegetation survey, and amoung the top 10 most abundant species from BVA there are a few Families with C_4 representants such as Polygonaceae (with *Triplaris weigeltiana* species; Soreng et al., 2015). While pollen investigation may not be able to find evidence of C_4 species in the organic-poor BVA-1, a pollen survey, Bulk Stable Isotope Analysis (BSIA) of the present-day plants or CSIA done on lipids extracted solely from present-day growing vegetation may provide more evidence for the cause of the above seen enrichment.

3.4.4. Diploptene sources and implications for the sedimentary record at PMFB

Within the three peatlands investigated from PMFB, isotopic measurements of diploptene are limited due to the low concentration of this compound. Both QT and BVA have similar diploptene isotopic values at the surface (i.e. -42‰ to -45.5‰) indicating the similar processes of CH_4 production and consumption across the two peatlands. However, it should be noted that for BVA, Finn et al. (2020) found evidence of both type I and II methanotrophs (i.e., *Methylococcaceae* and *Methylocystaceae* Families, respectively) whereas at QT, the only evidence of type II methanotrophs, which was previously inferred from the occurrence of methanotroph-type specific FAs (Amariei, 2018). The obligate nature of type I methanotrophs should have produced more depleted signatures of diploptene at BVA

(although only one value available), thus source mixing can be inferred as an important process, as discussed below. Diploptene could be measured in all 5 samples from the surface of QT, with values within 1.5‰ from each other. The uniformity in isotopic values indicates the uniform distribution of the microbial community. SJO displays more enriched diploptene values however, $\delta^{13}C_{CH4}$ measured in the top 60 cm of the peatland has the most depleted signatures of the three peatlands (Buessecker et al., 2021) yet with a very low efflux (approaching 0 mg/L CH_4, Buessecker et al., 2021) and the lowest efflux rate amoung all 3 peatlands during the dry season (Teh et al., 2017). All three lines of evidence indicate limited CH_4 production and consumption at SJO compared to QT and BVA, at least at the time of sample collection (i.e., dry season, 2010). This can be due to the oscillating nature of the water table and domed morphology of SJO, which may restrict methanogenesis to already substrate-depleted depths during the dry season.

Although enough evidence exists from these sites to support methanotrophs as contributors to the diploptene pool (i.e., DNA, rRNA from referenced studies; CSIA, methanotroph-specific biomarkers from these studies), source mixing from other non-CH_4 consuming producers cannot be ruled out, especially when recent data on phyla relative abundance of both archaea and bacteria is available (Finn et al., 2020). Data however indicates that *Proteobacteria*, which incorporates aerobic methanotrophs, is the most dominant in surface samples with almost similar abundances between BVA and QT, and relatively lower at SJO (Finn et al., 2020). Source mixing becomes more likely when compound-specific isotope values of other hopanoids are taken into consideration, as seen in Appendix A.3.7 and the T-GRES Peat database (Inglis et al., 2019). The relatively enriched hop-17(21)-ene and αβ C_{29}-hopane from BVA indicate input from other non-methanotrophic microbes. Furthermore, although QT-2 records the most depleted diploptene value from PMFB at -65.6‰, the most depleted value of diploptene from the T-GRES peatland database and the 2nd most depleted value across all hopanoid biomarkers from the same database (Inglis et al., 2019), indicating a strong methanotroph signal, QT-6 and QT-4b samples are 17.6‰ more enriched, with likely input from other diploptene producers or higher input of CO_2-consuming type II and X methanotrophs.

Hopanoids are pentacyclic triterpenoid compounds with wide spread sources in nature (i.e., Rohmer *et al.*, 1984; Rohmer *et al.*, 1992). Within the sedimentary record, they are attributed to bacteria, with the first wide assessment finding them in half of the 100 strains studied, being produced by cyanobacteria, obligate methylotrophs, purple non-sulphur bacteria, several chemoheterotrophs of Gram-negative and -positive (Rohmer et al., 1984).

Diploptene and diplopterol, C_{30}-hopanoids, were produced by most hopane-producing prokaryotes (Rohmer et al., 1984).

The list of diploptene-producing organisms has widely expanded since the study of Rohmer et al. (1984), with the addition of strictly anaerobic bacteria such as Planctomycetes (Sinninghe-Damsté *et al.*, 2004), Geobacter species (Härtner *et al.*, 2005) and sulfate reducing bacteria (i.e., genus *Desulfovibrio*; Blumenberg et al., 2006) yet in most (palaeo)environments, it is attributed to aerobic bacteria (see below). When coupled with carbon stable isotope analysis, diploptene can be attributed to CH_4-consuming bacteria (methanotrophs; see Appendix A.3.1.). However, questions such as *"Are C_{30} hopanoids reliable biomarkers for aerobic methanotrophy?"* (Birgel and Peckmann, 2008) have been asked and assessed again and again throughout literature, mostly with the same conclusions. Irrespective of their source, authors (e.g., Birgel and Peckmann, 2008; Jahnke et al., 1999) have warned about the risk regarding assigning hopanoids (diploptene, diplopterol) to bio-sources, especially to methanotrophs without further evidence of strong isotopic depletion in hopanoids and in other methanotroph-related biomarkers. Even when isotopic evidence is available for hopanoids, the (palaeo)environmental conditions, such as limited CH_4 or copper availability, may lead to methanotroph-produced lipids whose isotopic signatures are indistinguishable from those produced by heterotrophic- or cyano-bacteria (Jahnke et al., 1999). A literature review of diploptene CSIA values and proposed sources can be found in Appendix A.3.1. while current known bio-producers are summarised below, indicating other possible sources and highlighting again the need for better constraints when assigning bio-sources.

I) *Trees and Ferns*

Maybe the most unexpected, diploptene is a compound produced by a limited number of plants. Even the name of hopanoids has a non-prokaryote origin, originating from trees of the *Hopea* genus, from where it was first isolated by John Hope in 1955 (Ourisson and Rohmer, 1992, Ourisson and Albrecht, 1992; Kannenberg and Poralla, 1999). Ageta *et al.* (1963) reported isolated diploptene from ferns (as well as Ageta *et al.*, 1964; Ageta and Arai, 1983; Li *et al.*, 2022b) and Gelpi *et al.* (1970) have found evidence of a compound with a similar mass spectrum as diploptene in 3 fern species, alongside squalene. Bottari *et al.* (1972) found diploptene as the exclusive hopanoid in 3 of the 21 studied ferns, and present in another 10. Only as late as the 1970s, crude oil studies started identifying hopanoids in organic sedimentary deposits, and their correlation to past living microbes has been implied (Ensminger *et al.*, 1972; Kimble *et al.*, 1974).

II) Cyanobacteria

Diploptene and diplopterol have been widely associated with cyanobacteria in aquatic environments. In a lab-growth experiment by Sakata *et al.* (1997), both lipids were more depleted relative to the biomass of cyanobacterium *Synechosystis*. Schouten *et al.* (2001) assigned $\delta^{13}C_{diploptene}$ values of -27‰ to -35.7‰ to cyanobacteria and heterotrophic or chemoautotrophic bacteria in lake sediment core and, similarly in the study of Zhang *et al.* (2007), diploptene extracted from a microbial mat was associated with cyanobacteria.

III) Facultative and strictly anaerobic bacteria

Hopanoids (diploptene, diplopterol) have been further identified in facultative anaerobes (Blumenberg *et al.*, 2006) and most importantly, Sinninghe-Damsté et al. (2004) identified diploptene in **Planctomycete** (*Pirellula marina*), with further evidence of the squalene-hopane cyclase gene present, and in 3 bacteria species of *Candidatus* which can anaerobically oxidize ammonium (anammox). As hopanes (diploptene) do not require O_2 for their biosynthesis, their presence in anoxic parts of the peatlands, oceanic floors, may lead to increased input of diploptene that can falsely indicate a more active aerobic community and oxic conditions, isotopic palaeosignal masking and source mixing. In fact, DNA evidence of Planctomycetes was found across all 7 sites from PMFB investigated by Finn et al. (2020), with a higher relative abundance in SJO compared to BVA and QT investigated here, where diploptene displayed the most enriched overall values.

Two anaerobically grown ***Geobacter*** species (*G. metallireducens* and *G. sulfurreducens* - with the latter can sustain temporary exposure to oxic conditions) were investigated to determine the potential of hopanoid production in strictly anaerobic bacteria (Härtner et al., 2005). Diploptene was among the produced hopanoids, together with hop-21-ene and bishomohopan-32-ol acetate. Squalene and the squalene-hopene cyclase gene were also identified in both strains.

Three strains of the **sulfate-reducing bacteria** genus *Desulfovibrio* later joined the list (Blumenberg et al., 2006). They were isolated from marine microbial mats and can have a wide spread in aquatic anoxic and Sulphur-containing environments. All three strains produce small amounts of both diploptene and diplopterol as well as a few BHPs which account for most of the produced hopanoids. A strong depletion was seen in the C16:1Δ9 fatty acids compared to the growth substrates, yet diploptene and diplopterol were isotopically enriched compared to the substrate, and only slightly depleted compared to the biomass, indicating two carbon sources used for the FAs and hopanoids, with a MEP-derived hopanoid synthesis pathway (Blumenberg et al., 2006).

3.4.5. Environmental limitations of hopanoid CSIA – lessons for PSIA

Given the complex nature of (palaeo)environmental samples, limitations such as low compound concentration and co-elution, restricted CSIA analysis in this work. These limitations are expected when performing pyrolysis of targeted compounds for PSIA and thus they are discussed here in relationship with PMFB samples and will be taken into consideration when developing the instrumental methodologies for diploptene pyrolysis, and in future PSIA investigations.

From QT, diploptene isotopic values were extracted from only 8 samples of the 13 samples, 5 of which were from the surface of the peatland. Previous biomarker concentration assessments (Amariei, 2018) calculated this compound to be between 0.0481 to 6.6504 µg/g of dried sediment, peaking in surface samples (Appendix A.3.8.). Similarly, at SJO, CSIA values for diploptene are reported in only 3 samples and diploptene concentrations were measured between 1.9982 and 40.7825 µg/g (Appendix A.3.8.) at the surface (although the other 3 surface samples had lower concentrations). At BVA, diploptene's isotopic value was measured only from 5 samples and previous lipid concentrations were between 1.2781 to 23.7439 µg/g, peaking again at the surface of the peatland (Amariei, 2018). Although new aliquots from the freeze-dried samples have been extracted, the peat was initially homogenised and 0.5 g were added to ASE cells for extraction, following the same protocol previously used for lipid concentration measurement during the MSc project. It is thus expected that lipid concentrations are within the same ranges for isotopic analysis and display the same concentration trends. This is confirmed for most samples when comparing, for example, diploptene concentrations (Appendix A.3.8.) and the samples from which an isotopic value could have been extracted due to relatively higher amounts.

Continuous flow (CF) GC-IRMS allows a lower amount of sample to be analysed than a Dual-Inlet system, in the range of 100s nmol and possibility of lower amounts (10s nmols) with system and method optimization (Dunn and Carter, 2018). The obtained isotopic values are also independent of the amount of compound introduced, if full combustion is achieved and if the column's capacity is not exceeded, an assumption dictated by the principle of isotopic linearity (Carter and Barwick, 2011). New instrumentation capabilities (i.e., axial secondary electron multipliers) can further decrease the sample amount required and provide high sensibility for molecular fragment and site-specific isotopic measurements (i.e., Thermo Ultra Resolution IRMS).

However, for the GC-IRMS used in this chapter, and by making the assumption that the previously measured sample concentrations are true for the current isotopic analysis, for 1 µL splitless injection of an N1 fraction dissolved in 50 µL hexane from which a diploptene value could not be calculated due to low concentrations, the amount injected ranged between 0.037-0.193 nmol (Appendix A.3.8.). For these samples, extracting a higher amount of sample or injecting a higher volume would have cause compounds that have already good concentrations for CSIA (i.e., n-alkanes) to exceed the CO_2 pulse intensity and FAs external standard calibration peaks range, may cause peaks to co-elute further and produce incorrect values, requiring two different runs with varying analytical and injection methodologies.

Put in the context of future PSIA, for diploptene analysis in these samples, and as the peak has to be heart-cut from its complex matrix, it would be ideal that only this compound (and others of interest) would be preferentially concentrated (i.e., concentration here refers to compound quantity increase via multiple injections and targeted trapping). Moiety analysis for future PSIA will also require a higher amount of sample, compared to the parent-molecule, for reliable isotope analysis.

One important further chromatography issue, which also impacts IRMS measurements, is that of co-elution. While co-elution is best avoided in all types of chromatography analysis, certain scan methods (i.e., selected ion mode; SIM), data extraction procedures (i.e., spectrum deconvolution) and instrumentation (e.g., 2D-GC, heart-cut) allow baseline separation of compounds and more refined compound identification. Urea adduction can also be used (Ourisson *et al.*, 1979; Inglis et al., 2019) to separate the straight compounds
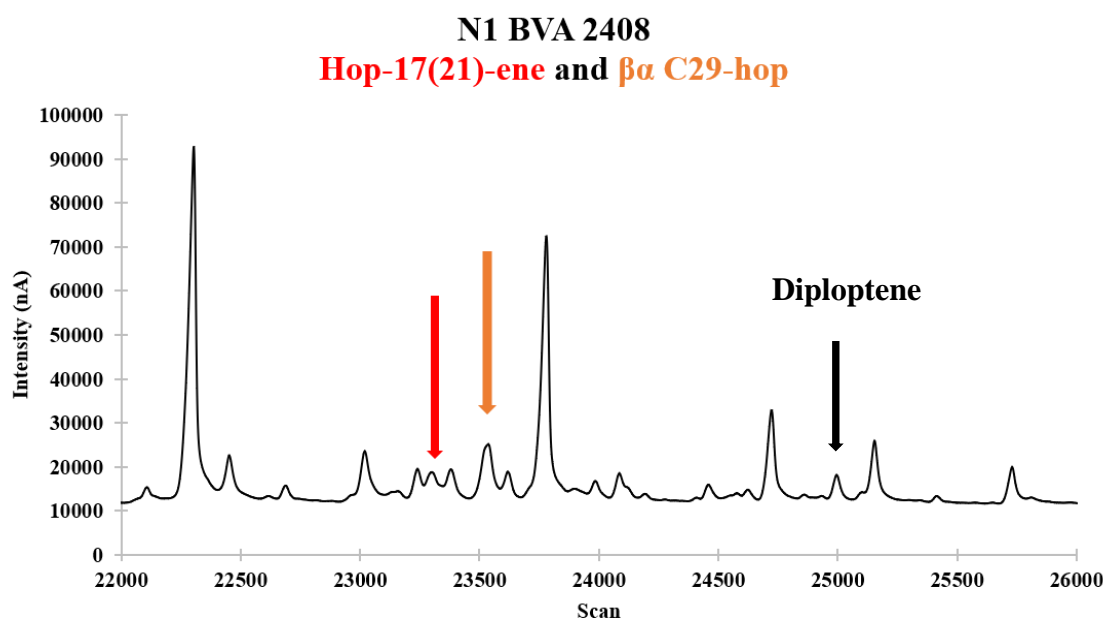
Figure 3.6 Co-elution of two compounds, potential hop-17(21)-ene and βα C29-hop based on elution order and compared against the GC-MS run, on a GC-IRMS chromatogram from BVA.

from cyclic hopanoids, providing a cleaner chromatogram. In this instance, a higher volume of the hopanoid fraction can be injected. This technique however cannot guarantee complete separation (Winkler *et al.*, 2001) and may result in low recovery, requiring several repetitions (Inglis et al., 2019). Heart-cutting of targeted compounds, and their subsequent trapping for compound enrichment has been a frequently employed technique (De Alencastro *et al.*, 2003), and, given the issue of co-elution encountered for other hopanoids from the same samples (i.e., hop-17(21)-ene; Figure 3.7. and Appendix A.3.7.), it can also provide a means to fully separate co-eluting compounds prior the IRMS analysis. One option that can benefit both issues (i.e., low concentrations and co-elution) is the heart-cutting and trapping of a number of compounds of interest from higher injection volumes (i.e., 2 µL → 5 µL) or over several 1 µL injection runs and their subsequent release on a second column, with a different polarity or by employing a different oven ramp, for their full separation prior to combustion. Focus will be put on these two techniques in the following chapters as they will be optimized on the prep-GC system for diploptene PSIA at environmental concentrations.

3.5. Conclusions

Vegetation- and microbial-specific lipids from three peatlands in PMFB were subjected to compound specific isotope analysis (CSIA), providing the first isotopic record from this area that can be used in correlation with lipid concentrations and previous palaeo-records to aid palaeoenvironmental reconstructions. As such, *n*-alkanes and hopanes were analysed from all three peatlands, and FAs only from QT and BVA. CSIA complements well existing datasets and interpretations.

n-Alkanes, apart from *n*-C_{23} and *n*-C_{25} in BVA and QT, display values within the isotopic range -25.65‰ and -43.7‰, specific to C_3 plants recorded in other peatlands across the globe (Inglis et al., 2019). They appear to have however relatively more depleted values when the canopy is closed, with one possible explanation being the incorporation of methanotrophy-dissimilated CO_2 into plants and plant wax. Given its enriched isotopic signatures seen for BVA (i.e., -19.5‰ to -20‰) and QT, *n*-C_{23} is likely a biomarker produced by a C_4 plant.

Only a few hopanoids were in high enough concentrations for CSIA, were not co-eluting and occurred across multiple samples for isotopic analysis and comparisons. Diploptene could be measured in only 16 of the 32 available samples and it displayed overall depleted values, ranging between -65.6‰ and -28.7‰, with the most enriched values recorded in SJO. CH_4 consumption and incorporation by methanotrophs is confirmed via isotopic means QT and BVA, with the domed morphology of SJO inferred to affect the local methanotrophic community, providing increased input of diploptene from non-methanotroph producers in this peatland. When compared to the peatland global database (Inglis et al., 2019), the value recorded in the QT-2 sample, was the most depleted across present and ancient peatlands, at -65.6‰. At SJO, aerobic methanotrophs are not the sole producers of diploptene and, diploptene cannot be used with high confidence to determine aerobic time intervals when CH_4 was consumed by these microbes. There is thus of further interest to access the *intra*molecular information available within this biomarker, and perform part- or position-specific isotope analysis (PSIA) on hopanoids, with an aim to reach the isotopic signature of the initial ("ancient") incorporated C-CH_4.

Two further chromatography-related issues are highlighted in this chapter for this class of compounds. Diploptene (as well as other hopanoids) did not have high enough concentrations for CSIA in all samples. Diploptene occurred as a well-defined peak given the slow oven ramp (i.e., 5°C/min to 310°C and hold time of 33 min) and the fact that samples were already separated into fractions, with aliphatic compounds analysed separately on a

50m long column. However, co-elution for hop-17(21)-ene and αβ C_{29}-hopane, expected to occur in samples from the same peatlands, make further hopanoid measurements less reliable. Before studying the pyrolytic breakdown of diploptene for future PSIA assessments of environmental samples, these chromatographic issues should be considered and incorporated within the methodology. Given the complex (palaeo)environment of PMFB and unknown past CH_4 isotopic signature, fractionation factors and further investigations within diploptene's ability to reflect CH_4 concentrations and availability could not have been investigated. In order to understand better these relationships, a simplified system is required in which the conditions which led to isotopic values of diploptene are known. The following chapter will thus investigate the isotopic signature of diploptene in two controlled lab cultures of aerobic methanotrophs: *M. methanica* and *M. trichosporium* OB3b.

4. CSIA of lab grown methanotroph cultures

4.1. Introduction

Several environmental and chromatographic issues were highlighted in the previous chapter, which have the potential to impact the accuracy of CSIA and, consequently, PSIA. This chapter aims to investigate the isotopic relationship and fractionation factors between diploptene and the available CH_4 source within a simplified system, in pure methanotrophs cultures. Three different methanotroph strains were grown under defined lab conditions. *M. methanica* (type I), *M. trichosporium* OB3b (type II) and *M. capsulatus* (type X) were selected due to the extensive research already conducted on these strains. These are aerobic methanotrophs which employ distinct pathways of CH_4-C incorporation into membrane lipids, further detailed in Subsection 7.3.1. This will provide uniform growth conditions and a single-source hopanoid sample, against which diploptene's isotopic signature at the compound-specific level can be correlated to the signature of provided CH_4 and the differences between type I and II methanotrophs bio-producers compared, based on their fractionation factors. As pool contamination suspected in natural samples (i.e., as discussed in Chapter 3) is eliminated, the culture experiments tracked the fractionation of headspace CH_4 with a known isotopic composition into membrane lipids such as hopanoids, aiming to distinguish between the different pathways of hopanoid formation in methanotrophs.

This chapter thus provides a link between Chapter 3 which dealt with diploptene CSIA from complex (palaeo)environmental samples and investigates further chromatographic issues arising in pure cultures (e.g., low sample concentration leading to whole lipid fraction analysis, co-elution) which will be carried forward in the design of the prep-GC in Chapters 5 and 6. It also provides examples of types I, II and X methanotroph strains that will be further discussed in Chapter 7, which assesses the breakdown pattern of diploptene during pyrolysis and the potential of diploptene PSIA as a proxy for CH_4 incorporation.

4.2. Materials and methods

4.1. Methanotrophs strains and materials

Three strains were ordered from NCIMB. *M. methanica* (type I; NCIMB 11130) arrived as a live culture while *M. trichosporium* OB3b (type II; NCIMB 11131) and *M. capsulatus* (type X, NCIMB 11922) arrived lyophilized.

An analytical diploptene (hop-29(22)-ene) standard (Sigma-Aldrich), with a concentration of 0.1mg/mL in isooctane (04626-1mL) and an *n*-alkane standard (68281; *n*-C_{10} to *n*-C_{40}, all even), 50 mg/l each) was purchased from Merck. An Indiana B5 Mix isotopic standard (*n*-C_{16} to *n*-C_{30}) was purchased from Indiana University Bloomington (Schimmelmann, 2024). The in-lab (BECS) analytical standard (Appendix A.3.2., for composition and concentration) was used as an external standard and injected on the GC-FID and GC-MS.

CH_4 was provided at 100% concentrations, CO_2 gas was provided at 20% (in N_2), and Zero Air for O_2. The gases were analytical grade and were purchased from BOC, UK.

4.2. Growth medium, preparation and conditions

For cultivation, nitrate mineral salts (NMS) medium developed by Whittenbury *et al.* (1970) was used. The receipt (NMS 131) and growth conditions were provided by NCIMB company, upon strain delivery (Appendix A.4.1.).

All glassware was cleaned prior to medium preparation in a dishwasher and was thoroughly washed with Milli-Q water prior to autoclaving and before each medium batch was prepared. Iron EDTA, sodium molybdate, trace elements solution and the phosphate buffer (Appendix A.4.1.) were prepared only when exhausted or if they were considered no longer fit for purpose (i.e., improper storing, precipitation). The trace elements and iron EDTA were stored under dark conditions at 4ºC. The initial solution containing KNO_3, $MgSO_4.6H_2O$ and $CaCl_2$ was dissolved in Milli-Q water and autoclaved. In order to avoid further contamination, the addition of iron EDTA, trace elements, sodium molybdate and the phosphate buffer solutions was done via syringes fitted with 0.22 µm filters (Fisher Scientific). The pH of each medium batch was tested by aseptically removing a small amount of solution in a centrifuge tube that was then probed with an Orion 8156BNUWP Ross Ultra Combination pH meter. Either a small amount of concentrated HCl or NaOH was added by

filtration, as required, and the pH was again assessed through the same method until the overall pH was 6.8.

Experimental layout: *M. methanica* (type I) growth experiment was run for 8 days with triplicate measurements for the first 7 days and 15 replicate measurements on the 8th day of the experiment (total 36 vials) and *M. trichosporium* OB3b (type II) growth experiment was conducted for 12 days, with daily triplicate vials (total 36 vials). All vials were 250 mL in volume. Each experiment contained 3 vials that represented day 0 of inoculation, 3 abiotic blanks containing the same gas concentration as experimental vials and 2 biotic controls that contained the bacteria inoculum growing under atmospheric concentration headspace (i.e., no gases removed or added). One flask containing *M. methanica* culture was grown for the initial identification of lipids. Only these lipids were derivatised using TMS (Section 4.4.).

Growth setup: For each experiment, one inoculum vial was incubated 5-6 days prior to the experiment, contamination was assessed using LB media (Appendix A.4.1) and the cells were studied under the microscope to test if they exhibited motility, indicating thus an active culture. *M. methanica* cultures were grown in 100 mL of NMS medium to which 1 mL of inoculum was added. *M. trichosporium* cultures were grown in 80 mL of NMS medium to which 0.5 mL of inoculum was added. Medium and inoculum addition to each 250 mL vial was done under sterile conditions (UV pre-treated Cat-2 fume hood). The bottles were sealed using autoclaved black rubber buns and metal seals (Figure 4.1; Yang *et al.*, 2013b). After inoculation, glycerol and DMSO stocks from the inoculum vial were prepared for future experiments.

Figure 4.1 Lab photos of growth experiments. Figure left shows one batch of sealed and inoculated vials on the first day of the experiment while the 3 tubes on the right represent the collected cell mass after centrifugation on day 6.

Contamination assessment: The LB medium (Appendix A.4.1.) proved to be a good contamination indicator for methanotroph cultures. *M. methanica* cells have also a distinctive pink colouration, while *M. trichosporium* OB3b presents a white-grey colouration, which was a qualitative measure to assess contamination over the entire

cultures. The abiotic and biotic controls' optical density were also measured to assess if any growth took place.

Gases provided: Each air-tight vial was flushed with N_2 for 45 seconds via an input syringe needle connected to the N_2 gas line to which a 0.22 μm filter was attached. An output needle connected to another filter was also inserted for pressure release. For each culture vial, 80 mL for *M. methanica* and 85 mL for *M. trichosporium* OB3b of headspace gas was removed using a 60 mL luer-end syringe to which a 0.22 μm filter and a lock-valve were added. The lock-valve allowed the headspace gas to be kept in the syringe and then evacuated even when the pressure in the vial was below atmospheric pressure (i.e., suction would appear).

The 80 mL and 85 mL of initially removed headspace gas were added back in a proportion of 6:4 CH_4:Air for *M. methanica* and 40 mL CH_4 (100%), 40 mL Air and 5 mL CO_2 (20% in N_2) for *M. trichosporium Ob3b*, respectively. The syringe used to add back the gases was again fitted with a 0.22 μm filter and lock-valve to avoid contamination. Once gases were added back, vials were labelled, left overnight and inoculated the next day, marking day 0 of the experiment.

Growth conditions: Following inoculation, vials were incubated at 30ºC and 150 RPM under dark conditions.

Analysis: Each day, 3 vials were analysed (i.e., triplicates/day). Measurements included: 1 mL of each culture was measured for optical density for the wavelength of 600 (i.e., OD_{600}; JENWAY 6320D Spectrophotometer), Picarro headspace gas isotopic analysis (mainly for CH_4). After isotopic headspace gas analysis, the vials were opened, the media and bacteria centrifugated (Figure 4.1.) and the collected biomass was frozen prior to freeze-drying. The centrifuge tubes were weighed empty and after freeze-drying to get the dried mass of methanotrophs collected. Figure 4.2 summarises the experimental steps until total lipid extraction (TLE).

Vial preparation → Headspace flushing with N2 → Headspace gas removal → Headspace gas replacement → Inoculation → Incubation

Optical Density → PICARRO $\delta^{13}C$ for CH_4 → Centrifuge → Frozen biomass → Freeze-drying → Homogenization
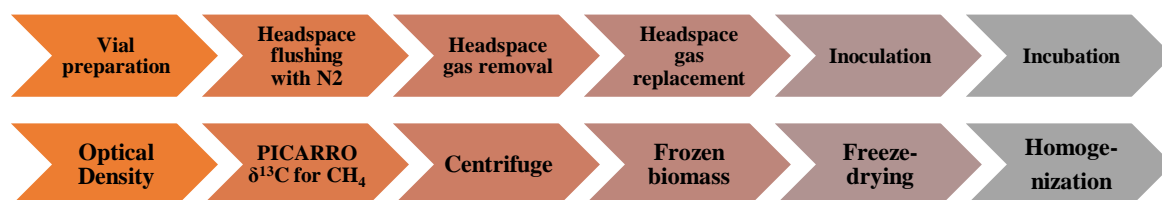
Figure 4.2 Visual representation of methodology steps for methanotroph cultures.

M. capsulatus growth: This type X strain, was only grown for lipid assessment in several vials as it required 45°C incubation temperature (an uncommon temperature to accommodate other lab users). Similarly to the above experiments, inoculum was added to 250 mL vials to which NMS medium was aseptically added. The headspace was flushed using N_2 and CH_4,

CO_2 and Air were added. No headspace measurements or optical density were taken for this strain; the biomass was centrifuged and the lipid analysed on a GC-MS after freeze-drying and extraction.

4.3. Headspace isotopic gas analysis

The PICARRO system and cavity ring-down spectroscopy technique were used to measure the isotopic values of headspace CH_4 gas for the two growth experiments. The system's working principle is presented in Appendix A.4.2.

For high-precision measurements, the CH_4 within the sample introduced in the cavity needs to be between 1.8 ppm and 12 ppm whereas for CO_2, between 100 ppm and 4000 ppm (PICARRO, 2016). Given the nature of the headspace and the initial added concentrations, the samples were diluted and isotopically analysed only for CH_4. 5 mL were removed from the headspace of each sample in a 60 mL syringe equipped with a luer lock-valve. 45 mL of Zero-Air (BOC, analytical grade; CH_4 concentration at 0.01 ppm) were used to dilute 3 times the initial amount, by flushing out of the syringe 45 mL. The sample was again diluted to 50 mL, and provided to a 1 L gas bag which was previously flushed twice with Zero-Air gas and evacuated using a suction pump. The sample was further diluted with 450-480 mL, which gave CH_4 concentrations within the range of 2-7 ppm and the gas bag was connected to the Picarro instrument until the measurement stabilized (5-8 min). A Zero-Air (blank) gas bag was provided between the measurements to flush the system. For reported values, 2 minutes of stable CH_4 isotopic values were averaged in the output report of each sample.

4.4. Lipid extraction and derivatization

Total lipid extraction (TLE) protocol: The freeze-dried biomass was crushed using a mortar and pestle. Combusted sand was added to the mortar to remove the remaining biomass. Due to the low amount of freeze-dried material, days 1,2,4, 5 and 6 were combined prior to ASE extraction. Similarly, for days 7, 8 and 9, two of the three replicates were combined to aid recovery. The TLE was extracted using an ASE 350 (Thermo) using DCM:MeOH (9:1, vol:vol) heated 6°C/min to 120°C (5 min) over 2 cycles, and a purge time of 100 sec (Figure 4.3). Once extracted, the TLE was dried under a gentle stream of N_2, weighted, and transferred into 150 µL inserts in 2 mL GC vials. Due to the low mass of the TLE, no further separations were done into specific lipid classes. Only the TLE of the *M. methanica* flask culture was derivatised using TMS, following the procedure: 15µL of BSTFA and 20µL pyridine were added to the TLE content, heated for 2h at 80°C, dried under a stream of N_2 and transferred to GC vial inserts. To preserve the integrity of the compounds of interest, such as aliphatic compounds, hopanoids, and squalene, lipids from the sacrificial cultures were not derivatised.
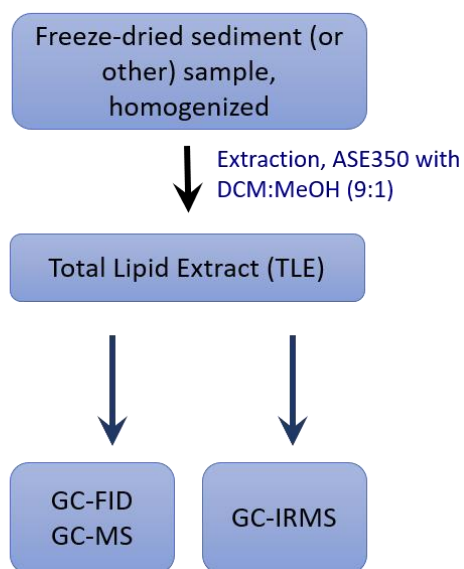
Figure 4.3 Left: Modified BECS laboratory protocol to take into account the low freeze-dried sample amount. The TLE was directly injected onto the GC-FID, GC-MS and GC-IRMS. Right: Biomass homogenisation prior to ASE extraction.

4.5. Lipid identification and relative quantification

4.5.1. GC instrumentation for lipid analysis

TLE fractions of *M. methanica* and *M. trichosporium* OB3b cultures were analysed on a GC-FID Agilent 9870A for quantification and Agilent 7890B coupled with a 5977A MSD for identification in the BECS laboratories, University of Glasgow.

The GC-FID was equipped with a 60 m x 0.250 mm x 0.25 µm RTX-1 Restek column. The oven program was 60°C (2 min), 30°C/min to 120°C (0 min), 5°C/min to 330°C (hold time 15 min). The inlet was set to 320°C in splitless mode, with a 1.2 mL/min helium flow (13.38 psi initial pressure).

The GC-MS was equipped with a HP-1-MS grade column, 60 m x 0.250 mm x 0.25 µm. The oven program was 60°C (2 min), 30°C/min to 120°C (0 min), 5°C/min to 310°C (33 min). The inlet was set at 320°C in splitless mode, with a 1.2 mL/min helium flow. The MSD scan range was between 40-650.

M. capsulatus (type X) was analysed on an Agilent 7890A coupled with an Agilent 5975C Mass Spectrometer, and equipped with a 30 m x 250 µm x 0.25 µm HP-5 MS column, in the Water and Environment department, hiRACE group, University of Glasgow.

4.5.2. Software for lipid analysis

The software used for GC-FID concentration calculations was OpenLAB CDS, Rev. C01.27 while the GC-MS used MassHunter GC/MS Acquisition, B.07.04.2260 software and a MassHunter Workstation Software for Qualitative Analysis Version B.07.00 coupled with NIST Version 2.0 g for compound identification.

4.5.3. Lipid concentration calibrations and relative quantification

The normalised lipid amount is reported in µg lipid/mg sample. The peak area of a certain lipid is calculated via integration within the analytical software. It is then divided to the response factor of a known lipid within in-lab standard which contains 10 *n*-alkanes and squalene (i.e., BECS standard, Appendix A.3.2.). The analytical standard lipid is selected to elute within a similar chromatographic time as the calibrated sample lipid. The BECS standard is injected at 100 µg/mL, 75 µg/mL, 50 µg/mL and 25 µg/mL and a calibration curve is made (see Appendix A.4.3. for an example). The number is then normalised against

the amount of solvent in which the sample was dissolved in (µL solvent), against the TLE and the mass of the sample extracted as shown in Eq. 10 below:

$$\text{Lipid amount} = \frac{\text{PA} \times \text{response factor std calibration} \times \text{amount solvent}}{\text{sample} \times \text{TLE} \times \text{sample mass in ASE cell}} \quad \text{Eq. 10}$$

No internal standard was used as the lipid samples were kept at the TLE level. Without further separation into lipid fractions, co-elution between an internal standard and sample peaks could have led to miscalculations. The calibrations are thus semi-quantitative and reported compound amounts relative to this experiment, to understand culture growth trends.

4.6. GC-IRMS

Compound-specific isotope analysis (CISA) was performed on the TLE fractions. TLE was reconstructed for GC-IRMS analysis, using between 60 and 75 µL of DCM (75µL was used for samples that had a slight colouration, particularly for those that were collected later in the growth experiment and were considered to have a higher concentration of lipids).

4.6.1. GC-IRMS system setup

CSIA was conducted on a Trace GC Ultra coupled with a GC Isolink, a Conflow IV and Delta V Advantage from Thermo Scientific, at Strathclyde University. The associated data acquisition and processing software was Isodat 3.0. The Carbon-Nitrogen (CN) system setup
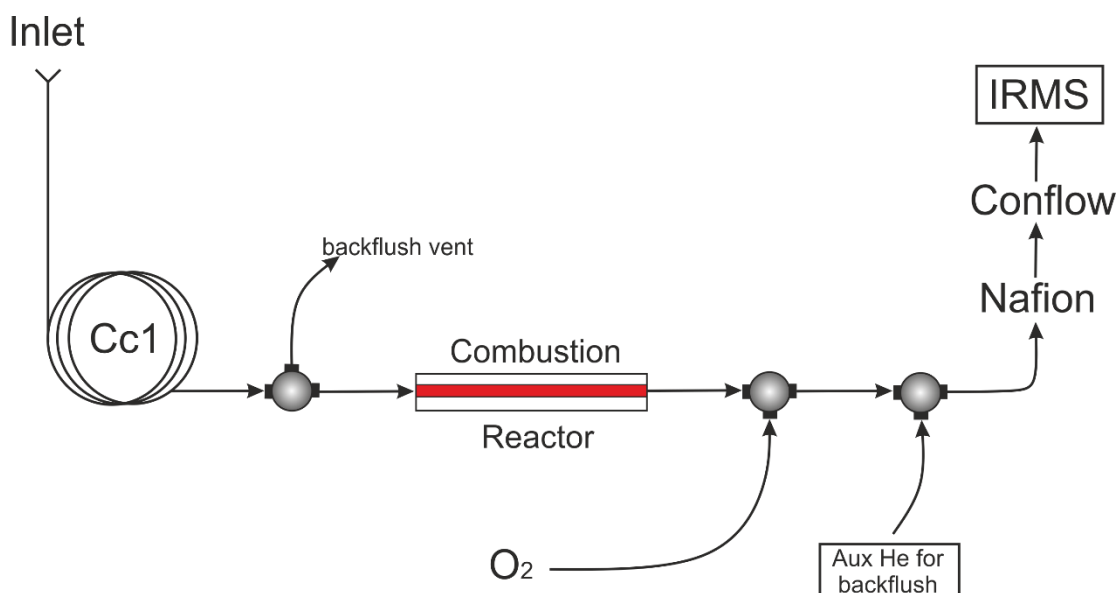
Figure 4.4 Schematic of the simplified GC-IRMS flow for isotopic measurements. Cc1 was a 60 m x 0.250 mm x 0.25 µm DB-5MS-UI Agilent column.

is presented in Figure 4.4. The combustion reactor (P/N 1255321; 0.5 mm internal diameter) was regenerated using O_2 prior to analysis.

4.6.2. GC-IRMS methods

Several methods have been used in this analysis, depending on the type of sample. CO_2 stability and linearity tests were analysed using the same method, provided below. For each type of sample analysis: calibration standard (Indiana) and TLE samples, a general method was used for the Triplus autosamples, GC and IRMS instruments. Several parameters were adjusted slightly, with the reasoning provided. Culture samples were randomly analysed to avoid instrumental bias.

4.6.2.1. CO_2 stability and linearity methods

For the CO_2 working reference gas stability and linearity, only the IRMS method was used. Within a sequence, for these measurements, the ASL and GC methods were disabled. The oven was however set at 60°C and the flow at 1.2 mL/min in a standby state. The backflush was turned on, with no column helium reaching the combustion furnace or the IRMS source. The CO_2 gas pulses were provided via the Conflow IV.

CO_2 pulses for instrument stability: To test the instrument's stability, CO_2 On/Off tests were performed at the start of the day, ensuring that the gas lines were flushed (as fractionation occurred within the line while the instrument was not in operation) and throughout the sequence, every 5-8 samples. 10 pulses were added at the start of each sample run to test the integrity of the instrument and measurement. In this case, the backflush was turned on (i.e., no compounds or He coming from the column entered the source) and CO_2 pulses were provided to the IRMS from the working cylinder. The CO_2 pulses lasted 20 seconds each, 30 seconds apart.

CO_2 linearity tests: For linearity tests, a series of 8 CO_2 pulses of different intensities (i.e., dilutions) were run throughout the analysis sequences, lasting 20 seconds each, 30 seconds apart. Their intensities (mV) ranged from 2000 to 14000 mV.

4.6.2.2. Sample GC-IRMS methods

Some general method parameters were kept the same for all sample methods. A 10 µL syringe with an 80 mm needle was used. 8 plunger strokes were set to eliminate any air bubbles from the syringe and the Air and Filling modes were set to Auto. The dwell time

pre- and post-injection was set at 2 seconds, the injection depth within the inlet was set at 70 mm and the injection speed was set at 20 µL/sec. The sampling depth (within the sample insert) was set at 75% given the small amount of solvent used to reconstruct the samples (between 60 and 75 µL) and the sample type was defined as non-viscous. The pre-injection wash solvent was DCM as this was also used to dilute the samples. 4 wash cycles of 8 µL DCM were used, while the post-injection solvent was MeOH, a highly polar solvent that would further clean the syringe using 3 cycles of 8 µL solvent.

A 60 m x 0.250 mm x 0.25 µm DB-5MS UI Agilent column was used for all isotopic analyses done on the Trace GC Ultra-Delta V Advantage IRMS. The column had a low polarity, similar to the HP-1-MS grade column used on the GC-MS, ensuring targeted aliphatic compounds (i.e., hopanoids) elution order was the same. The GC oven method followed the GC-FID and GC-MS methods that provided previously good resolution and separation on several methanotroph lipid selected samples: 60°C (4 min), 30°C/min to 120°C (0 min), 5°C/min to 320°C (20 min) with a final hold time of 20 min, following the BECS method The flow was 1.5 mL/min. One full run lasted 66 minutes.

The IRMS method had the backflush turned On between 0 and 10 min, while 10 CO_2 reference gas pulses eluted. The backflush was turned Off between 10 min and 66 min, allowing the sample peaks to reach the combustion furnace and reach the IRMS source. Another 3 CO_2 pulses were provided at the end of the run for inter-sample comparison.

<u>Calibration of the CO_2 cylinder – Indiana standard:</u> Prior to any sample analysis, the CO_2 reference gas cylinder (working gas cylinder) had to be calibrated against an external standard with known isotopic values for accurate sample measurements. Calibration was done with an Indiana Alkane B5 Mix sample, whose values are reported against the VPDB scale. The chromatogram and isotopic values of the Indiana B5 Mix are provided in Appendix A.4.4, containing reported mean values from the supplier and measured values on the GC-IRMS instrument after CO_2 calibration. Following CO_2 cylinder calibration, the samples were measured in a short time interval and calibrated against the CO_2 working gas, under the assumption that its isotopic signature remained constant during the analysis of these samples.

The GC and ASL Triplus methods were as follows: 1 µL of Indiana STD was injected in the 320°C heated inlet operating in 20:1 split mode. The split was chosen to allow the *n*-alkane Indiana peaks to be within the range of the CO_2 pulses for calibration.

<u>Sample analysis</u>: For samples, given their low concentration, 1.2 µL was injected in an attempt to increase the concentration of some late eluting peak of interest (hopanoids). The

injection was done in splitless mode. Diploptene identification was done by comparing its RT in analysed samples with the RT of an analytical standard (04626-1mL, Merck), following the same GC method.

Instrument parameters: During sample analysis, the emission was set at 1.50 mA, trap at 40.00 V, electron energy: 124.000 eV, with an extraction efficiency at 98.5%, symmetry: -21.03%, X-Focus: 39.32%, X-Focus Sym.:-7.25%, X-Deflection:33.92%, Y-Deflection: 56.36%, Y-Deflection Sym: -0.56% and nd SE-Suppression: 80.855%.

During analysis, the MS parameters were: the high voltage [KV]: at 2.997 KV, magnet [Steps] 11943 (CO_2 gas), HV:3.05 KV, box: 0.68 mA and trap: 0.82 mA, and the vacuum around 1.8-006 mBa.

Peak Detection@CO_2: For peak detection, the pre-defined software and manual parameters were used, also allowing for comparisons to other instruments using the same settings. The start slope [mV/s]=2 and the End slope [mV/s]=0.4. The peak min height [mV]=50 while the peak resolution was set at 50%. The Max Peak width (s)=180 (although this value was later considered too high, no peaks spanned over 3 minutes, as the solvent peak was backflushed). The background parameter type was selected as Individual BGD with a History of 5 seconds. The time shift was limited to 1 Data Point. While these parameters were kept throughout the analysis, they can be changed at later points by redefining a new IRMS method and re-evaluating the previously obtained data.

Data processing, analysis and compound identification: Once the chromatograms were acquired, .csv files of each sample were generated in Isodat Workspace. Mass *m/z* 44 was then plotted in Excel as a scatter plot (smooth lines), obtaining thus the chromatogram for each run. Similarly, the isotopic values were exported by using the Re-evaluate function in Isodat Workspace, following an Isodat Export template.

4.3. Results

4.3.1. Main findings

This chapter presents data regarding the isotopic fractionation between the provided CH_4 and methanotroph-produced hopanoids in pure methanotroph cultures grown under controlled lab parameters. *M. methanica*, *M. trichosporium* Ob3b and *M. capsulatus* (Aberdeen(IIA)), representatives of type I, II and X methanotrophs, respectively, are grown and the lipid content identified and measured, with results comparable to other publications. Overall, the isotopic values of all three *M. methanica* hopanoids that were identified, diploptene, hop-21-ene, and diplopterol, were more depleted than those of the diploptene produced by *M. trichosporium* OB3b. The fractionation factors between the CH_4 provided headspace and the hopanoids of *M. methanica* are larger than for *M. trichosporium* Ob3b, however the headspace fractionation of CH_4 between the experiment's beginning and ending values is larger for *M. trichosporium* OB3b, indicating that CH_4 is utilised for non-hopanoid lipids or intracellular components. The CH_4 values of the *M. methanica* experiment showed an isotopic difference ranging from 3.8‰ to 11.6‰, while the *M. trichosporium* cultures showed a difference of 20‰ for CH_4 between the start and end of the experiment. However, the former fractionation was not observed within diploptene, as it displayed relatively enriched values compared to *M. methanica* lipid.

Chromatographic considerations and challenges in analyzing stable isotope signatures at a compound-specific level compounds were highlighted, and are further taken forward in designing the prep-GC system for diploptene pyrolysis; furthermore, this chapter discusses, from a PSIA point of view, the expected unique challenges that type X poses due to its production of sterols and hopanoids from the same squalene pool.

4.3.2. GC-IRMS and CO₂ gas calibration

For isotopic calibration, 3 consecutive Indiana mix injections were analysed on the same day. The standard deviation (SD) of each triplicate peak was below 0.1‰, deemed acceptable. The isotopic values measured on GC-IRMS were subtracted from their corresponding values provided for the Indiana Alkane B5 Mix standard (Appendix A.4.4). The working gas (CO_2) isotopic value was calculated at -23.7‰, a correction that provided the highest R^2 value (Figure 4.5, top graph).
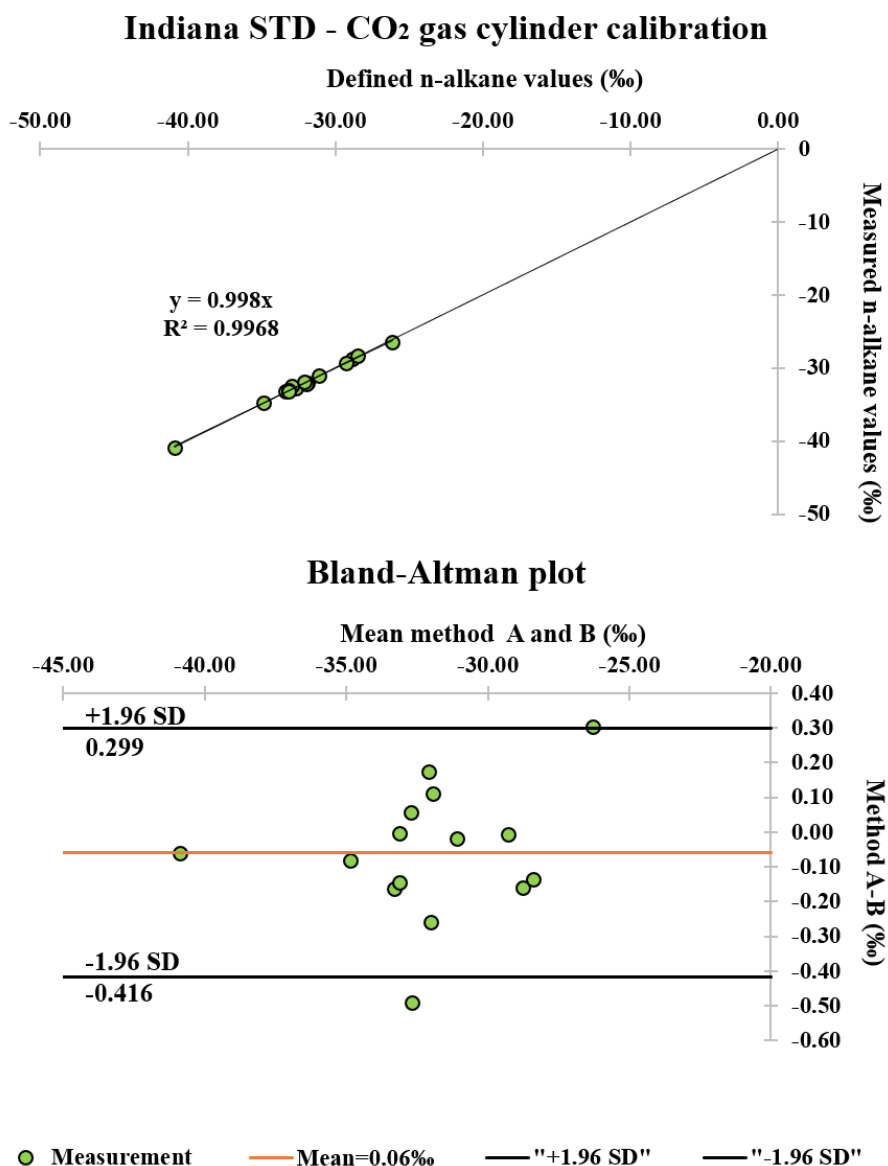
Figure 4.5 Top: Calibration of the CO_2 gas cylinder using the Indiana University isotopic standard calibration (Mix B5). Values represent B5 Mix n-alkanes measured after the calibration of the CO_2 cylinder, against their reported values, prior to lipid analysis. Bottom: Bland-Altman plot describing the agreement between two measurement methods by plotting the differences between their values against their averages, with 1.96s limits of agreement (95% confidence intervals). Method A=Indiana Mix values; Method B=n-alkanes values based on calibrated CO_2 cylinder value.

The corrected value was introduced to the software for accurate sample lipid measurements. Plotting the provided Indiana isotopic values vs. the measured isotopic values for each corresponding *n*-alkane after CO_2 cylinder calibration returned an $R^2=0.968$ indicating that the isotopic offset is constant. The Bland-Altman plot was also constructed to verify the fit of the calibration. The plot represents the agreement between the two measurement methods by plotting the differences between their values against their averages. The mean difference and limits of agreement provide insights into the bias and precision of the methods, helping assess their agreement and potential systematic errors (Giavarina, 2015). The plot indicated that CO_2 cylinder calibration utilizing the external Indiana standard was accurate.

The standard deviation (SD) was applied to isotopic values of CO_2 peaks. SD of On/Off tests was for almost all samples better than 0.1‰ (Dunn and Carter, 2018; with values between 0.12‰ and 0.01‰; Figure 4.6), which indicated that the instrument was stable. The standard deviation of every Linearity test was better than 0.1‰ (with values between 0.11‰ and 0.03‰).
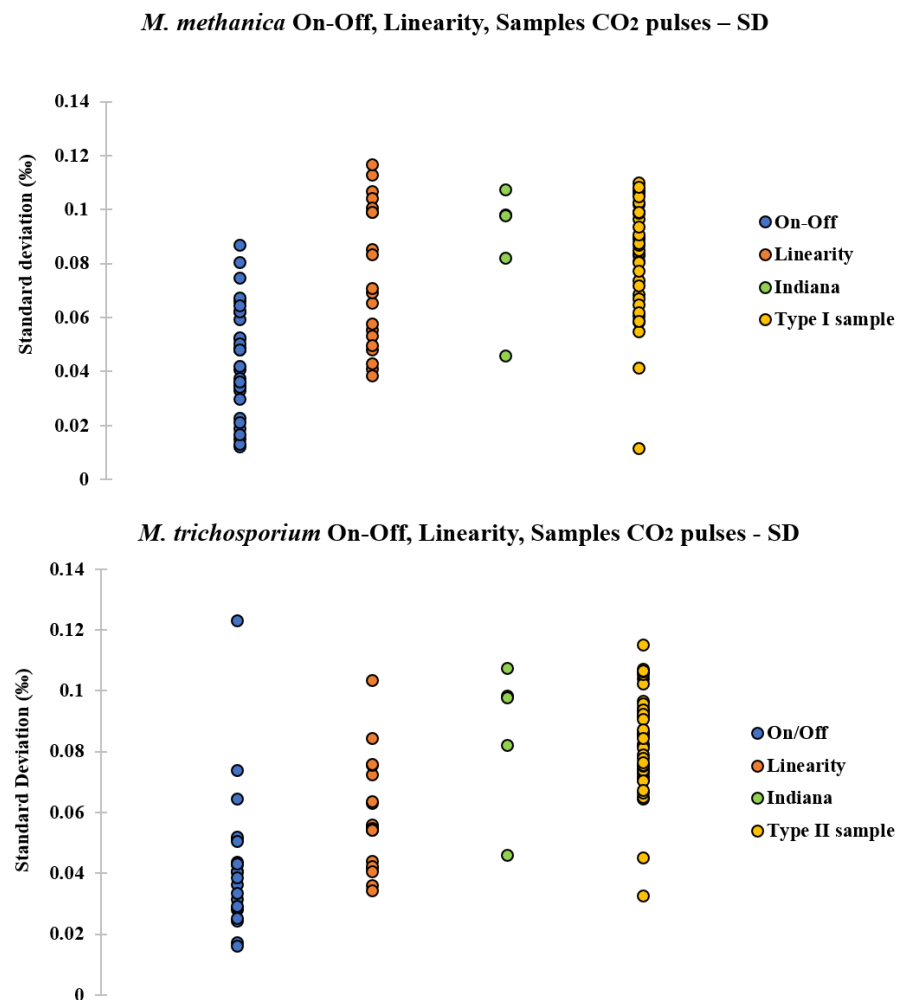
Figure 4.6 Standard deviation of (On-Off pulses) Repeatability and Linearity tests for each methanotroph type and instrument calibration.

4.3.3. Type I – *M. methanica*

4.3.3.1. M. methanica – sacrificial experiment measurements

M. methanica was grown for 8 consecutive days, with 15 replicates for the last day, in a sacrificial experiment under controlled laboratory conditions to assess the correlations between the growth that the culture exhibited, CH_4 headspace isotopic trends, produced lipids and their isotopic signatures.
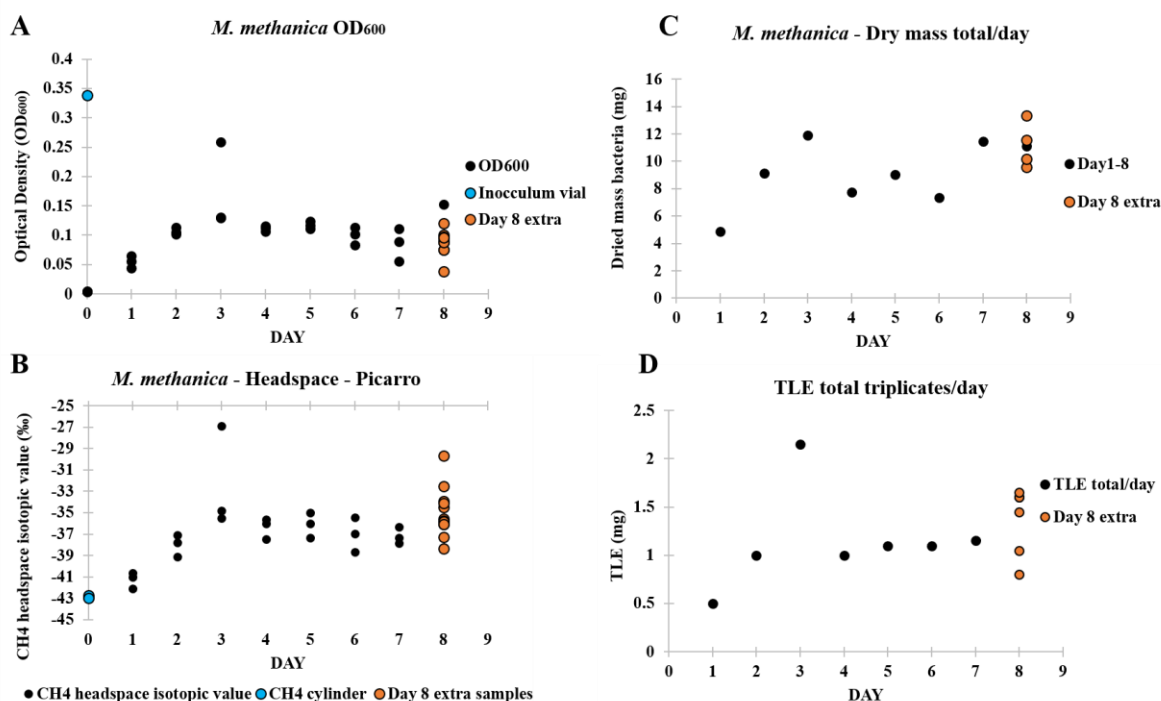
Figure 4.7 A: OD_{600} recorded from triplicates daily. Initial OD_{600} of vial used for inoculation is available. As experiment was stopped on day 8, data from 12 other samples are presented for day 8 showing variation in results. B: Isotopic headspace values of daily triplicates measured on PICARRO instrument. The isotopic signature of the CH_4 cylinder provided as carbon source in the headspace is provided as day 0. C: Summed dry mass of centrifugated cultures. After freeze-drying, the tubes containing the centrifugated mass were re-weighted. D: Amount of Total Lipid Extract (TLE) from ASE, summed for each day of the experiment.

Optical density (OD_{600}) shows an increasing trend in the first 3 days of the culture growth, reaching 0.130 on day 3, after which a plateau is reached (Figure 4.7.A). The 0.258 value for the same day is considered to be due to an outperforming type I culture, given the correlations with the isotopically enriched CH_4 headspace from the same vial. The inoculum vial's OD_{600} was measured prior to the experiment at 0.338.

The headspace of each triplicate culture vial was analysed by PICARRO, offering the isotopic signature of the headspace CH_4. The $\delta^{13}C_{vPDB}$ of CH_4 in the vials became enriched over the first 3 days, compared to the original gas signature measured at -42.8‰. The CH_4

headspace was measured at around -35.2‰ in 2 of the 3 vials on the 3rd day of the experiment, with the 3rd vial at -26.5‰. The most enriched CH_4 value for day 8 corresponded however to the highest OD_{600} seen in Figure 4.7.

The freeze-dried methanotroph mass were summed, measuring 4.86 mg on day 1 and 11.88 mg on the 3rd day. Day 8 range was between 9.6-13.35 mg. The TLE amount was measured post-lipid ASE extraction. For day 1, 0.5 mg of lipids were recovered, with the maximum amount measured on the 3rd day at 2.15 mg.

4.3.3.2. Lipid content

A flask-grown *M. methanica* culture was used for the initial identification, with compounds displaying functional groups derivatised, to gain a full picture of the lipids. The derivatised identified lipids of type I are presented in Appendix A.4.7.

The sacrificial experiment samples were not derivatised and they were used for identification, semi-quantification and CSIA. Figure 4.8 displays the main peaks of interest, with squalene, diploptene, hop-21-ene and diplopterol identified for type I based on Sessions et al., 2013. Chromatograms from samples of the sacrificial experiment were compared to GC-IRMS chromatograms to confirm lipid identity.
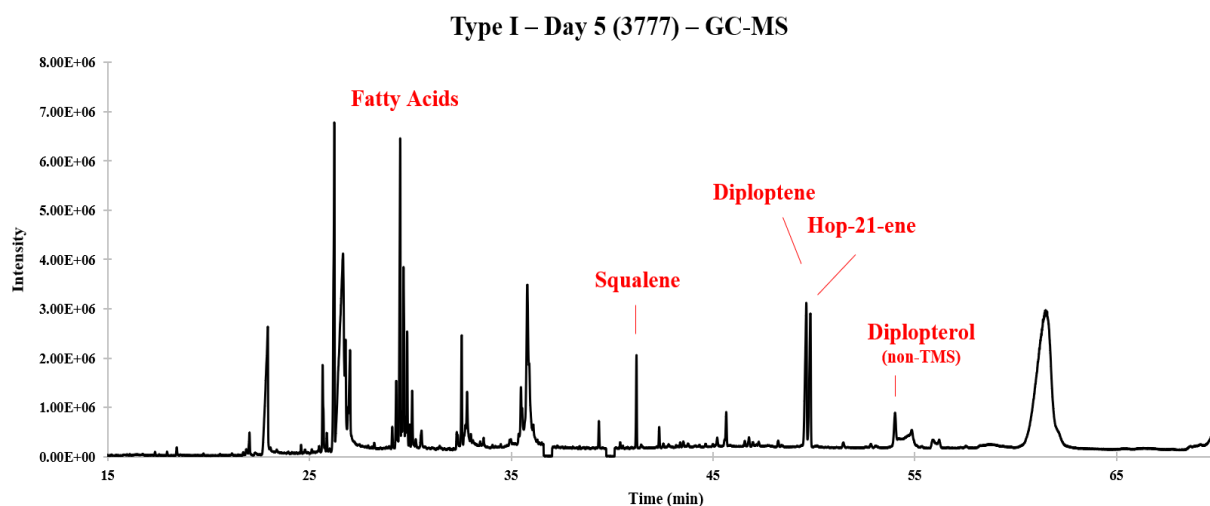
Figure 4.8 Total ion chromatogram (TIC) view of a M. methanica from day 5 of the growth experiment. Main lipids of interest were identified on this chromatogram.

The distribution of the lipids in type I methanotrophs, and in *M. methanica* specifically, has been well studied throughout the literature (Rohmer et al., 1984; Bowman *et al.*, 1991; Summons *et al.*, 1994; Bodelier *et al.*, 2009) and the lipid observed here (Figure 4.8) matched the literature. Importantly, diploptene was identified.

4.3.3.3. Lipid concentrations

The relative concentrations (semi-quantification) of diploptene and hop-21-ene biomarkers are presented in Figure 4.9. The trend seen after day 6 is due to the way the vials were extracted for lipid analysis. After day 6, as some of the TLE was higher, some triplicates were individually extracted and analysed on the GC-MS, yet results are presented as summed amounts for each day. Two replicates of intended days 8 and 9 were extracted and analysed together. Intended vials for days 10 to 12 were extracted and analysed as triplicates, all representing however day 8 replicates. Analysing individual dried-mass cultures likely caused a loss of biomass and lipids at the extraction stage, when the dried mass was crushed and loaded into ASE cells for extraction, and when the TLEs were dried and transferred into GC inserts. Even if concentrations are summed, the loss of compound took place most likely between the crushed dried mass loading into ASE and TLE transfer into vials for GC analysis. For diploptene, the peak concentration was reached on day 3, at 28.1 µg/mg, with
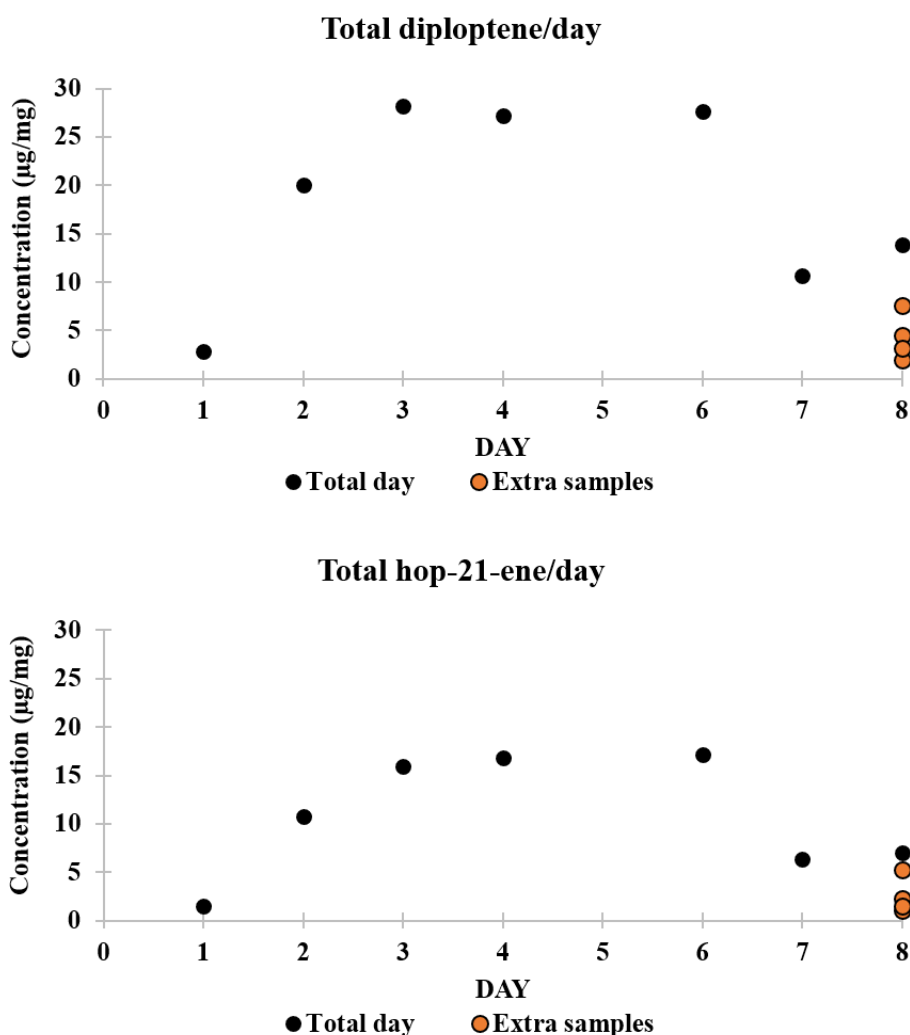
Figure 4.9. Total diploptene and hop-21-ene lipid amount for each day of experiment.

135

day 4 at 27.2 µg/mg and dropping in concentration towards the last days of the experiment. Hop-21-ene, peaks in concentration on day 6th at 17.18 µg/mg yet with very similar measurements recorded on days 3 and 4. Further lipid concentrations of *M. methanica* are available in Appendix A.4.5.

4.3.3.4. Compound-specific isotope analysis

CSIA was employed to study the isotopic signatures of *M. methanica* sacrificial experiment membrane lipids. GC-IRMS identification was done by comparing the elution time of a diploptene analytical standard to the sample's compounds, and the relative elution order of other lipids initially identified on the GC-MS chromatograms.
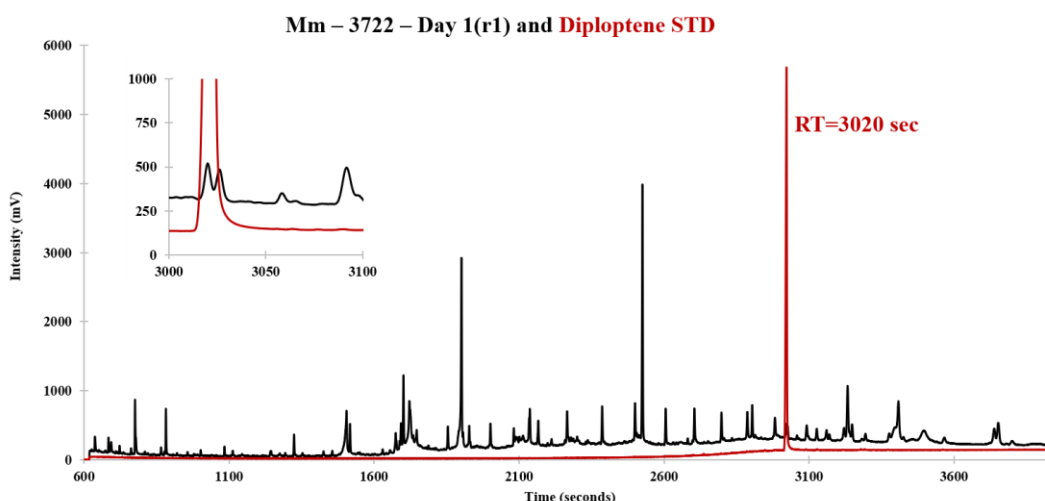
Figure 4.10. Identification of Diploptene in a M. methanica (Mm) sample from Day 1 of the experiment on a GC-IRMS chromatogram using an analytical external standard (red graph). For diploptene, retention time (RT) was measured at 3020 seconds.

There is considerable co-elution between diploptene and hop-21-ene (Figure 4.10, Zoom-in view) on the GC-IRMS chromatogram when compared to the GC-MS (Figure 4.10). Compound separation previously achieved on the 60 m column of the GC-IRMS, also seen in Figure 4.10, is partially lost as the compounds enter the larger internal diameter reactor (0.5 mm compared to 0.25 mm; Meier-Augenstein, 2004), where a pressure and flow difference is experienced. Duplicate analysis of each sample was performed to understand the reproducibility of the analysis, given also the fact that the two molecules have low concentrations, and background column noise at higher temperatures can impact their

isotopic signatures. As seen in Figure 4.11, only several diploptene duplicates have similar isotopic values due to a slight co-elution with hop-21-ene and low lipid amount.
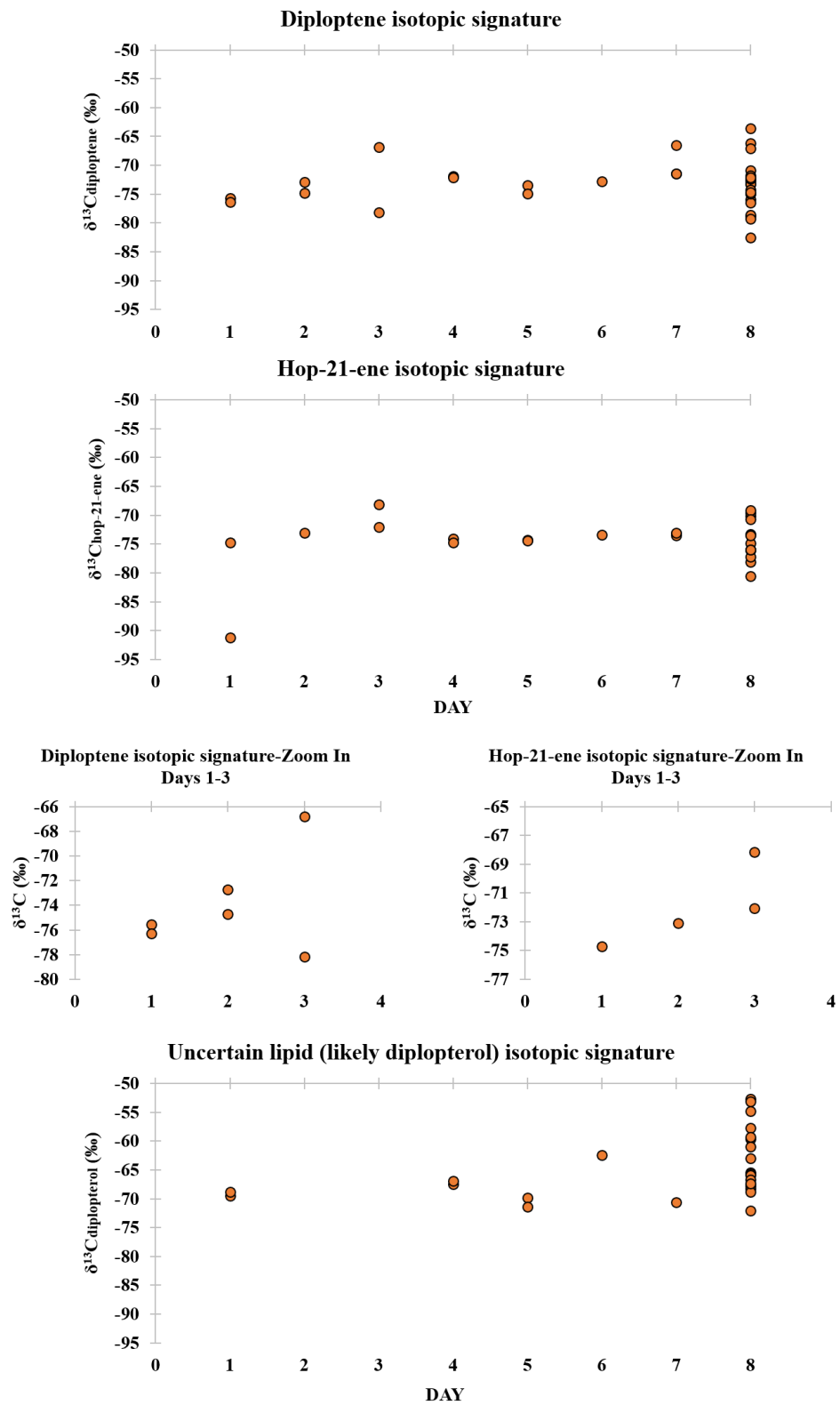
Figure 4.11. Duplicate measurement of compound-specific isotopic signatures of diploptene, hop-21-ene and likely diplopterol lipids.

No trend can be inferred from the isotopic distribution of diploptene and hop-21-ene (Figure 4.11), however, even if co-elution occurred, both lipids are produced through the same biosynthetic pathways, they are seen in day 1 samples and have the same number of carbons, with similar isotopic values. In the *M. methanica* culture, diploptene's isotopic values were between -80.6‰ to -66‰ while hop-21-ene's, between -82.9‰ to -69.1‰. Diplopterol's identification on the GC-IRMS was done with less confidence, hence the isotopic values cannot be correlated with high confidence to this lipid.

4.3.4. Type II – *M. trichosporium*

4.3.4.1. M. trichosporium – sacrificial experiment measurements

Measured OD_{600} is presented below as individual measurements from triplicates of each experimental day. The plateau is reached on day 3, after which the cultures display relatively the same OD_{600} values, measured between 0.12 and 0.07. The low OD_{600} on day 7 was due to the fact that the headspace did not initially contain CH_4, and it was added at a later stage, during inoculation. Again, as seen for *M. methanica*, the OD_{600} of *M. trichosporium* cultures
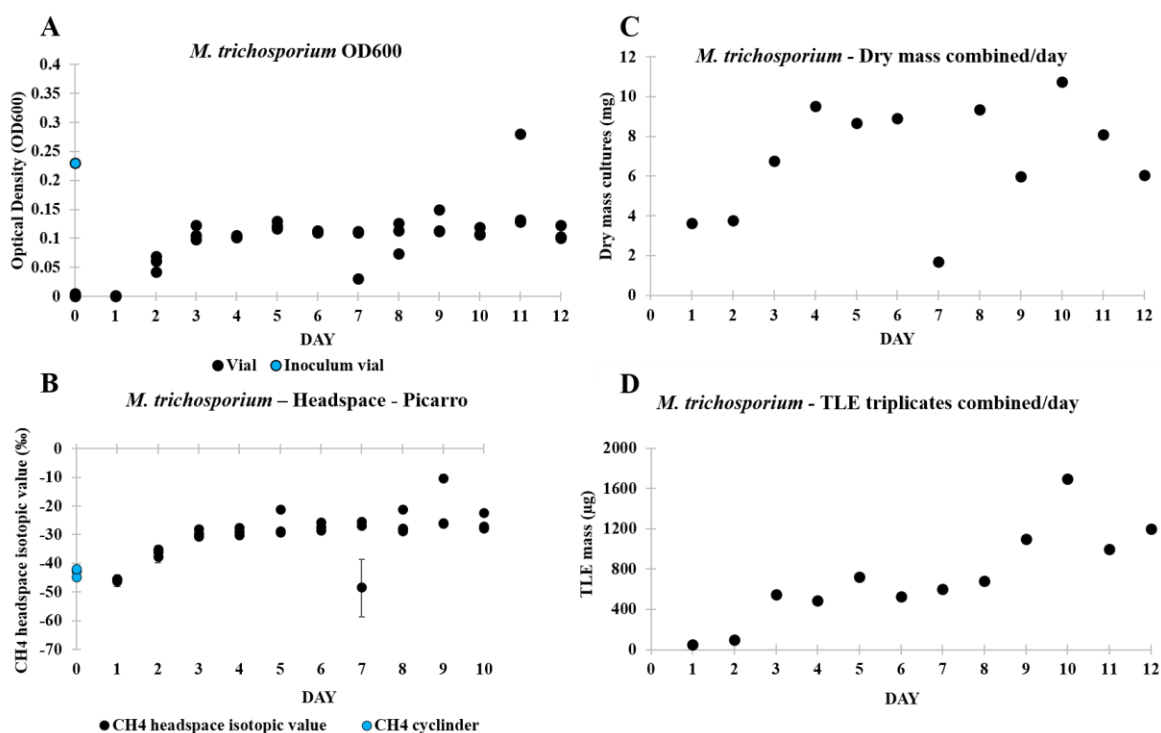
Figure 4.12 A: OD600 of type II, M. trichosporium growth experiment. Data presents triplicates/day. The OD600 of the inoculum vial is provided on day 0. B: Isotopic measurements of CH4 headspace from M. trichosporium growth experiments analysed with PICARRO. The isotopic signature of the CH4 cylinder is provided on day 0. C and D: Type II, M. trichosporium dry mass and extracted TLE which were summed for each day of the experiments (triplicates added together).

was well below that of the inoculum vial. Only a culture from day 11, suspected of contamination, reached similar values.

Isotopic values of the fractionated CH_4 in the headspace of each vial are presented in Figure 4.12.B. Errors bars on each measurement are small (i.e., provided yet not apparent), apart from day 7 highly depleted value caused by an experimental error. Only the first 10 days were measured as the PICARRO instrument was not available after.

The dried biomass of each day was combined, showing an increasing trend for days 1-4, following OD_{600} and headspace fractionation trends. Day 7 presents a dip in the amount of dry mass recovered, yet this is not translated into the TLE amount (Figure 4.12.D). The two measurements are independent (i.e., not normalised one against the other) yet the lower dry mass amount will have an effect on the normalised lipid concentration (see Eq. 10). In both cases, day 10 shows the highest mass when the triplicates were summed, with 10.75 mg of culture measured, with the TLE also displaying the highest amount on the same day, with 1700 µg of lipids recovered.

4.3.4.2. Lipid content

Day 5 contains the summed triplicates before the GC analysis stage and, overall was selected for lipid identification given its clean chromatogram. The lipids from Box A and B of Figure 4.13 have been individually identified in the following table and figures.

Table 4.1 Box A and B lipid identification of Figure 4.12 for M. trichosporium.

BOX A		BOX B	
PEAK NO	Compound	PEAK NO	Compound
3	FA C16:1ω5 (non-TMS)	2	FA C19:1ω7 (C21-TMS)
4	FA C16:1ω5 (non-TMS)	3	**Diploptene**
7	Phthalic	4	**Hop-21-ene**
8	FA C18:1ω9 (non-TMS)	5	**Diplopterol**
9	FA C18:1ω7 (non-TMS)		
10	FA C18:1ω7 (non-TMS)		
12	FA C18:1ω7 (non-TMS)		

Type II, *M. trichosporium*, presents again diploptene and hop-21-ene, which were identified based on their mass spectra (Sessions et al., 2013) and by comparison to *M. methanica* chromatograms. The lipid profile of *M. trichosporium* seen in present cultures matches that of existing literature (Jahnke et al., 1999; Scanlan *et al.*, 2022).
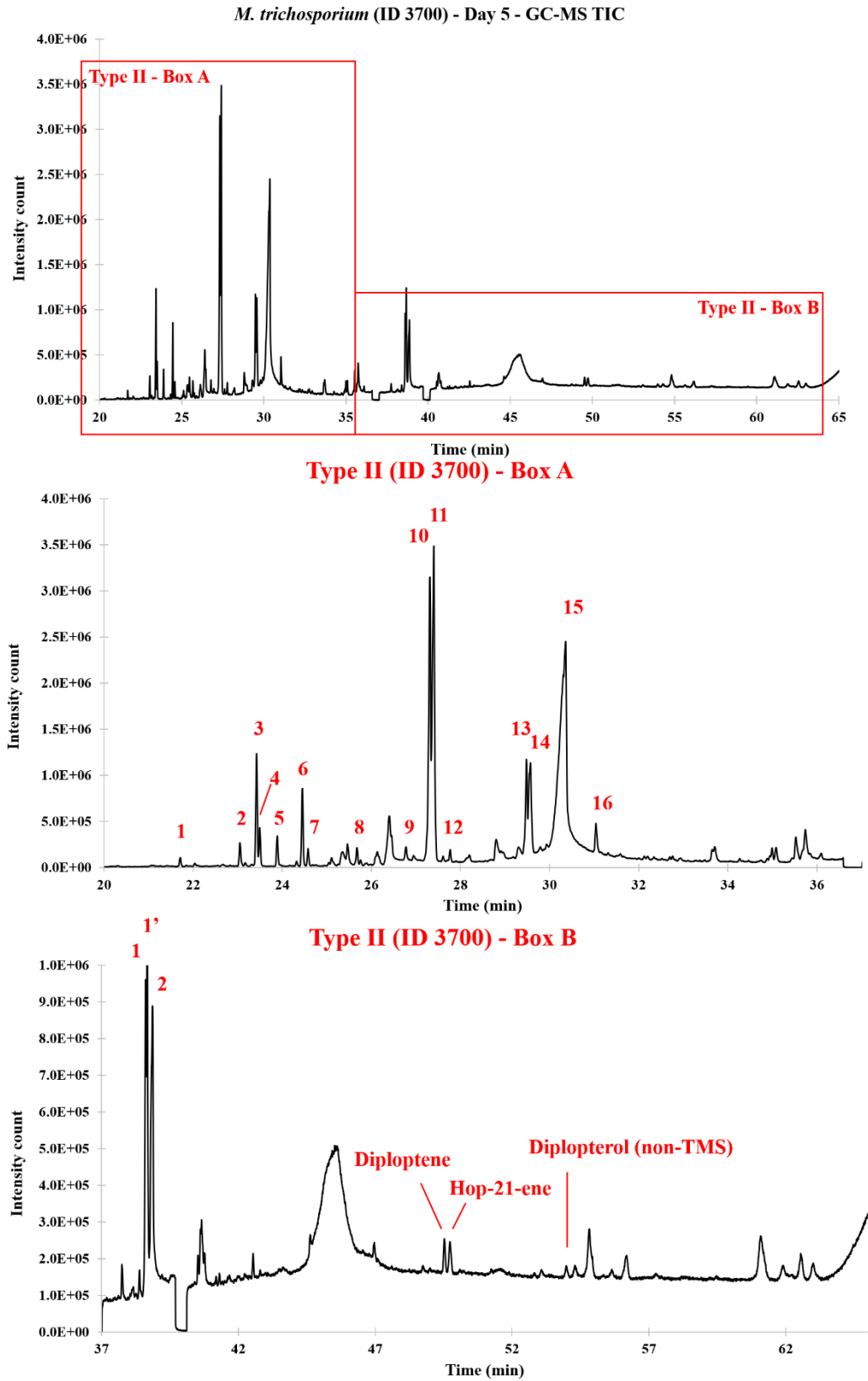
Figure 4.13. Zoomed-in view of Figure 4.19, box A. Numbered lipids corresponding to Table 3, zoomed-in view of Figure 4.19 to ease identification.

140

4.3.4.3. Lipid concentrations

Diploptene and hop-21-ene show increasing concentrations (semi-quantification) up to day 5, past which both decrease in concentrations. Diploptene peaks at 1.3 µg/mg while hop-21-ene at 0.67 µg/mg (Figure 4.14). Day 6 was extracted and analysed with the triplicates pulled in the same sample from the centrifugation step, indicating that loss of sample during further steps cannot be a reason for this decrease.
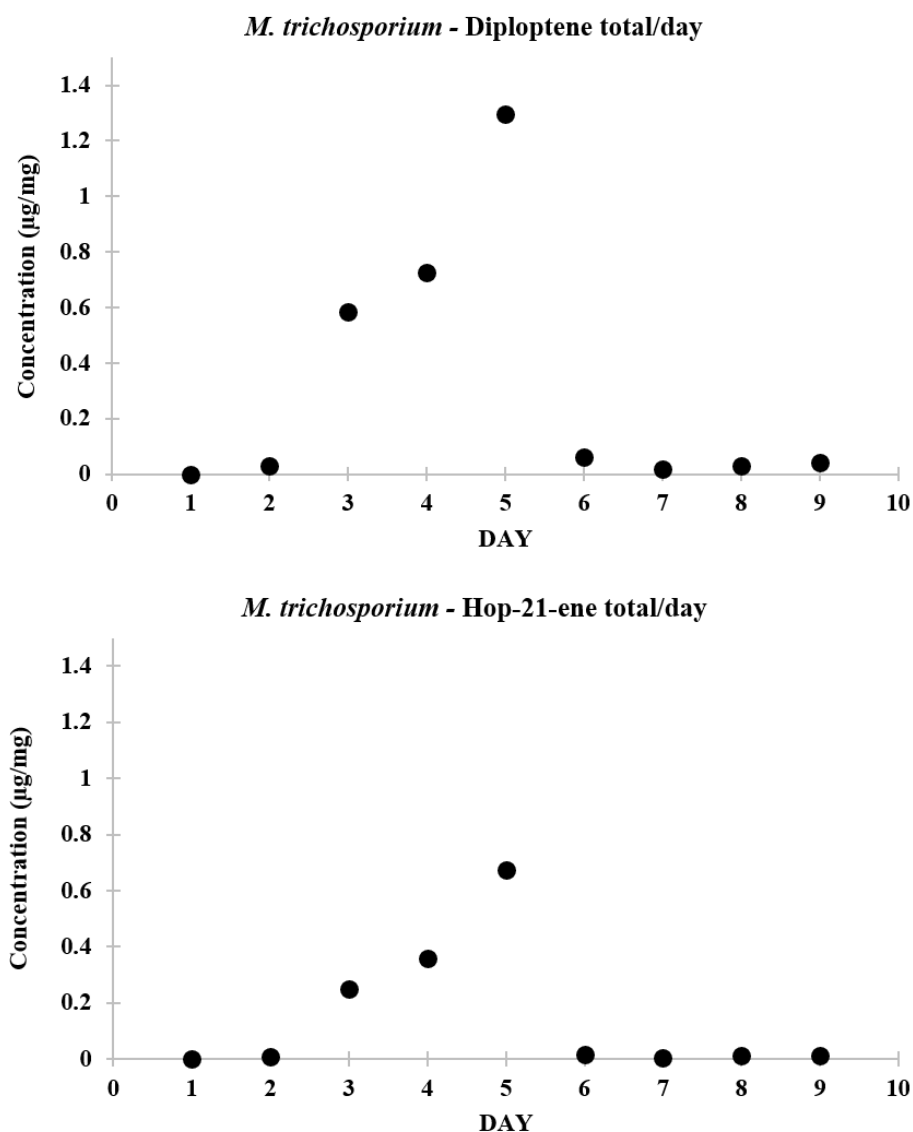
Figure 4.14. Diploptene and hop-21-ene concentrations in M. trichosporium growth experiment. Amounts were summed for each day.

4.4.4.4. Compound-specific isotopic data of M. trichosporium lipids

While CSIA was performed on all samples of *M. trichosporium* experiment, and diploptene was identified using an analytical standard (04626-1mL, Merck), co-elution of diploptene and hop-21-ene occurred as seen in *M. methanica*, and with a further unidentified compound, eluting before diploptene (Figure 4.15). Diploptene thus co-eluted with two compounds, and CSIA was not possible in most samples (Figure 4.16). In available samples, its values were measured between -53‰ and -27‰.
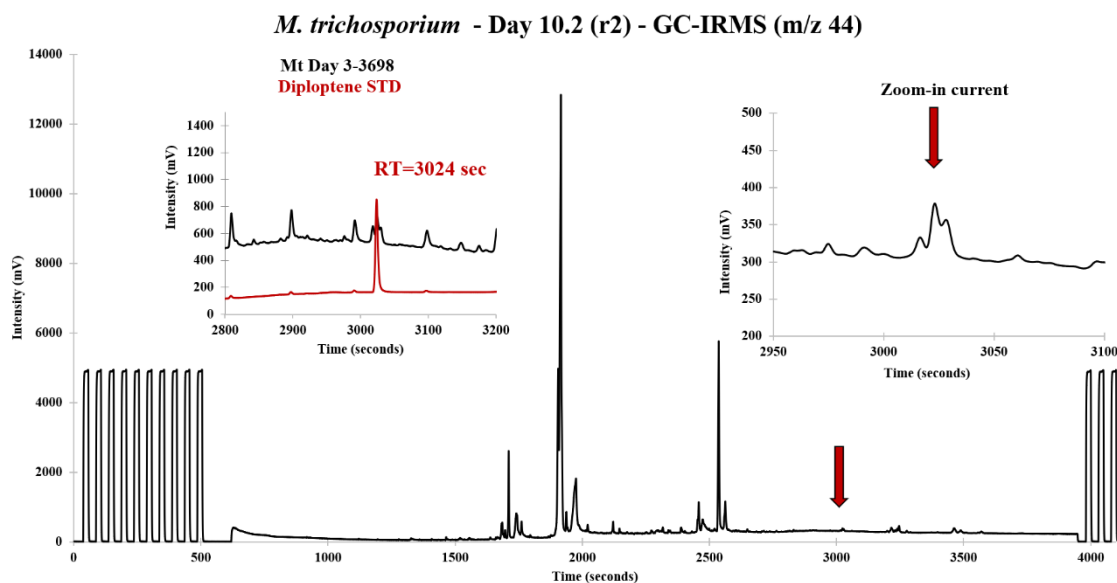
Figure 4.15 GC-IRMS chromatogram of plotted m/z 44 to show the retention time of diploptene, identified using an analytical standard, and the co-elution between diploptene, hop-21-ene to the right and an unknown compound to the left.
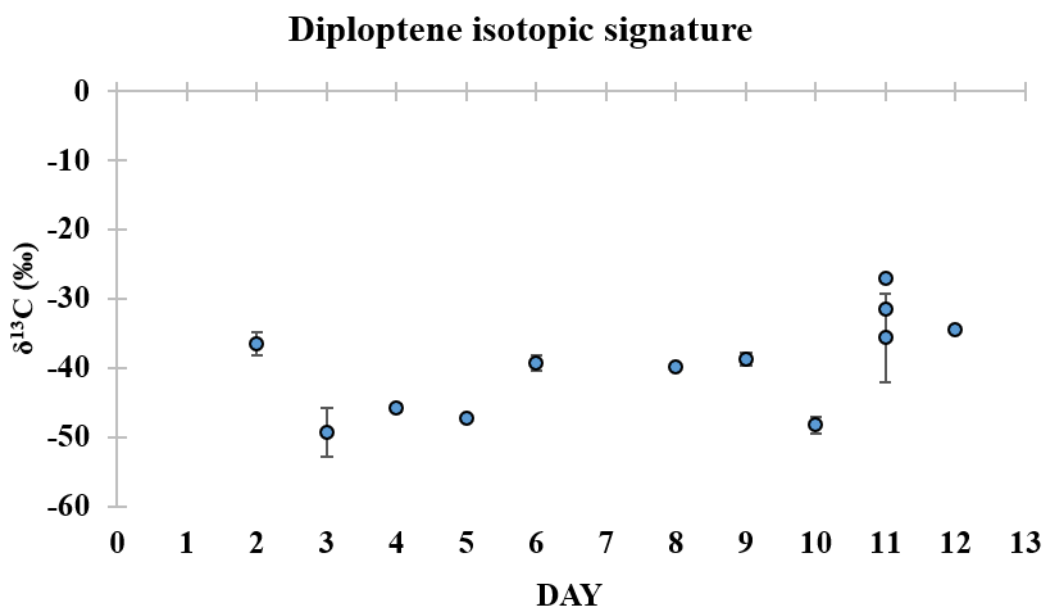
Figure 4.16. Diploptene isotopic signature in M. trichosporium OB3b.Error bars as SD.

4.3.5. Type X - *M. capsulatus*

M. capsulatus was grown under similar lab conditions yet in only a few vials for lipid identification. While fatty acids and both squalene and diploptene were identified, indicating that this strain can also be employed for PSIA investigations, cholesterol and associated compounds were also identified in this sample (Figure 4.17, Table 4.2).
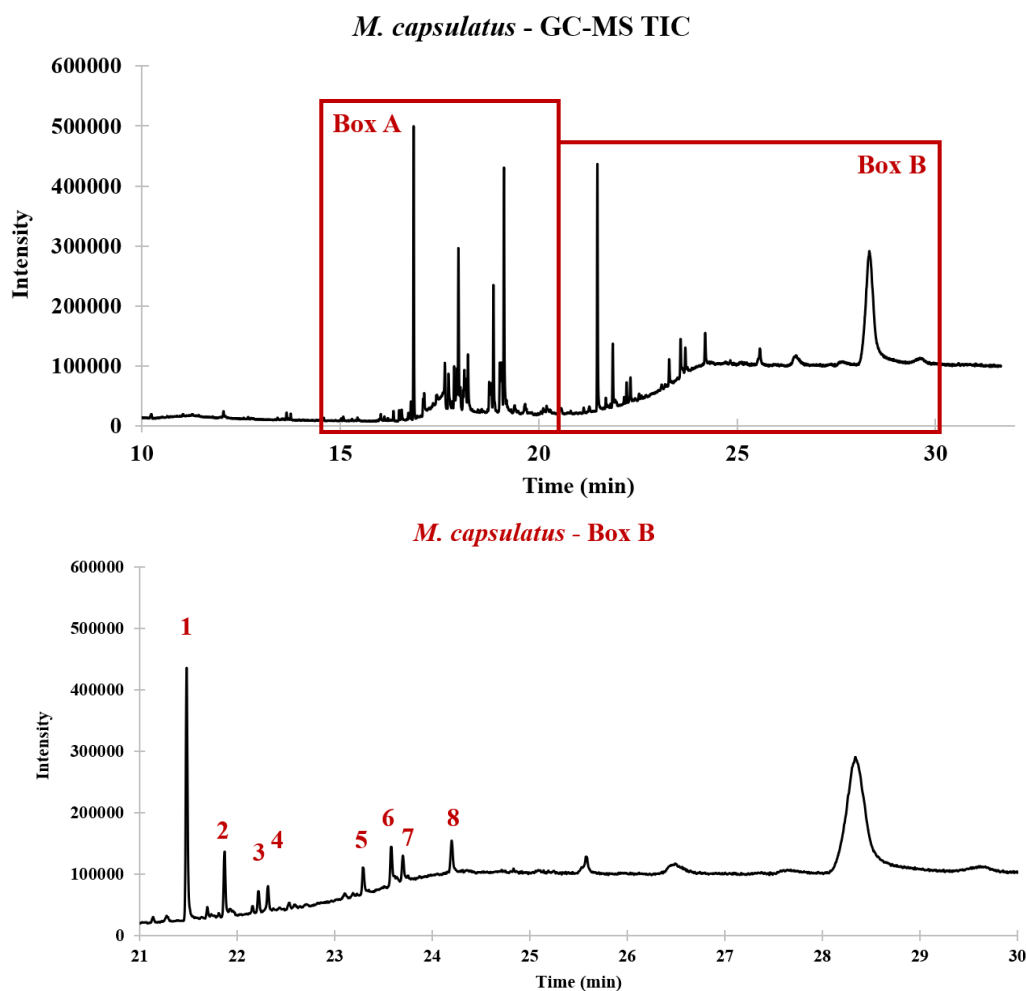
Figure 4.17. Total ion chromatogram (TIC) view of a type X methanotroph, M. capsulatus. Numbers correspond to lipids identified in Table 4.2.

Table 4.2 Box B compounds of M. capsulatus.

No	COMPOUND	No	COMPOUND
1	Phthalate	5	Cholesterol
2	Squalene	6	Cholest-7-en-3-ol, 4-methyl (3β, 4α, 5α)
3	Cholesta-4,6-dien-3-ol, (3β)-	7	Cholesta-3,5-dien7-one
4	Cholesterol, chloroformate	8	**Diploptene**

Cholesterol and the associated compounds are not generally known to be produced by bacteria, but by plants, fungi and animals (i.e., eukaryotes; Voet and Voet, 2021). While the culture did not appear to be contaminated (i.e., no visual growth of algae or fungi), and cross-sample contamination could have occurred at the lipid extraction phase, on the ASE, this methanotroph is known for its unusual production of sterols, barring an oxygen-dependent gene for squalene cyclization (Sessions *et al.*, 2002; Jahnke and Nichols, 1986), indicating that the compounds are produced *de novo*. Apart from diploptene and squalene, the study of Sessions et al. (2002) has also identified hopan-30-ol and 3β-methylhopan-30-ol, which were not seen in this culture.

4.4. Discussions

4.4.1. Type I – *M. methanica*

4.4.1.1. Culture growth, isotopic signature of CH_4 in the headspace of each vial and dried mass of cells/day

Type I sacrificial experiment was conducted over 8 days, with 15 replicate measurements on the final day of the experiment. Several measurements were taken during (i.e., OD_{600}, isotopic analysis of the CH_4 headspace gas) and after the growth of the bacteria (i.e., dry mass measurements, lipid identification and semi-quantification, lipid isotope analysis).

Optical density (OD) is correlated to the activity and density of the microbial culture. Thus, the initial increase in OD_{600} is explained by the increase in the biomass of the cultures (Figure 4.7.A). A relative decrease was observed after day 3, indicating that the culture reached a plateau or death phase after 3-4 days. The OD_{600} of the sacrificial vials did not match the inoculum vial's OD_{600}, indicating that less growth occurred. When *M. methanica* was grown for this experiment, the colonies showed biofilm growth, potentially leading to lower overall OD_{600} as the biofilms could not be analysed by the spectrometer. It is not clear why this different behaviour occurred, yet it is likely that several new media stressors (i.e., refreshed pH at 6.8, less O_2, lack of initial headspace CO_2) inhibited the growth of the already accommodated inoculum culture. However, looking at the dry mass total and Picarro headspace gas isotopic data (Figures 4.7.B and 4.7.C) there is a similar trend, indicating that overall, the culture ceased growing.

The headspace of each triplicate culture vial was analysed by PICARRO, offering the isotopic signature of the headspace CH_4. The $\delta^{13}C_{VPDB}$ of CH_4 in the vials became enriched over the first 3 days, compared to the original gas signature, indicating growth as it showed that CH_4 was being consumed. This corroborated with the results from the OD_{600}.

The enriched signature in one of the day 3 triplicates corresponded to an increased OD_{600} measurement for the same vial suggesting that a higher mass of methanotrophs utilised more CH_4. The following days show slightly less enriched values compared to the first 3 days; however, the headspace isotopic values are enriched compared to the CH_4 cylinder's isotopic signature, indicating overall incorporation of CH_4 within the bacteria biomass, probably on the first 3 days of growth. Further data scattering can be seen when the extra samples for day 8 were added (i.e., orange dots, Figures 4.7 and 4.9), representative of some vials which

performed better in terms of growth, than others. The most enriched CH_4 value for day 8 corresponded however to the highest OD_{600} seen in Figure 4.7.A, indicating a good correlation and lack of contamination, further investigated in Subsection 4.3.5.

4.4.1.2. Biomass of the dried M. methanica culture and Total Lipid Extract (TLE)

The freeze-dried methanotroph mass was summed. There is a similar distribution in terms of dry mass (Figure 4.7.C) as seen in the OD_{600} and headspace $\delta^{13}C_{vPDB}$ of CH_4, correlating days 1-3 to growth. The TLE amount was measured post lipid ASE extraction. For the pure *M. methanica* cultures, it is expected to be correlated to the OD_{600}, isotopic value of the headspace CH_4 and dry methanotroph mass extracted, displaying similar lipid profiles between samples. The amount extracted from day 3 is impacted by the higher growth exhibited by one of the three vials. In order for this not to lead to less accurate compound-specific isotopic values by adding the triplicates together prior to CSIA, the vial which displayed the higher growth was individually analysed on the IRMS, yet Figure 4.7.D. shows the summed TLEs for each day.

The OD_{600}, isotopic value of the headspace CH_4 and TLE displayed similar trends, indicating *M. methanica* growth in the first 3 days of the experiment, consuming CH_4 and producing membrane lipids as the culture grew in density. The replicate measurements for day 8 show a range of values. The initial addition of headspace CH_4 (Figure 4.7.B), was impacted by manual errors in extracting and replacing the gas, which may explain the variations on day 8.

4.4.1.3. Lipid concentrations

Analysing individual dried-mass cultures likely caused a loss of biomass and lipids at the extraction stage, when the dried mass was crushed and loaded into ASE cells for extraction, and when the TLEs were dried and transferred into GC inserts. Even if concentrations are summed, the loss of compound took place most likely between the crushed dried mass loading into ASE and TLE transfer into vials for GC analysis. Overall, diploptene has relatively higher concentrations than hop-21-ene. Further lipid concentrations of *M. methanica* are available in Appendix A.4.5.

4.4.1.4. Compound-specific isotope analysis

Compound separation previously achieved on the 60 m column of the GC-IRMS, also seen in Figure 4.8, is partially lost as the compounds enter the larger internal diameter reactor (0.5 mm compared to 0.25 mm; Meier-Augenstein, 2004), where a pressure and flow difference is experienced. Duplicate analysis of each sample was performed to understand the reproducibility of the analysis, given also the fact that the two molecules have low concentrations, and background column noise at higher temperatures can impact their isotopic signatures. As seen in Figure 4.11, only several diploptene duplicates have similar isotopic values due to a slight co-elution with hop-21-ene and low lipid amount.

Even if co-elution occurred between diploptene and hop-21-ene (Figure 4.10), both lipids are produced through the same biosynthetic pathways, they are seen in day 1 samples and have the same number of carbons, with similar isotopic values. In the *M. methanica* culture, diploptene's isotopic values were between -80.6‰ to -66‰ while hop-21-ene's, between -82.9‰ to -69.1‰. The inoculum vial corresponding lipids were not analysed on the GC-IRMS due to the low volume remaining after inoculation thus, the isotopic depletion cannot be accurately quantified. However, day 0 of the experiment measured an OD_{600} that was close to 0 (i.e. average value of 0.004, n=9), signifying that the concentration of *M. methanica* in the provided medium was very low, translating into low concentration of membrane lipids. If diploptene concentration on day 2 was measured at 19.9 µg/mg and corresponded to an average OD_{600} of 0.107 (n=0), on day 0, a likely 0.7 µg/mg diploptene would have been introduced from the inoculum vial, impacting only 3.5% the overall isotopic signature. The contribution to the overall diploptene signature is thus considered negligible, and the experiment can assume that all lipids were produced *de novo*. Furthermore, the previous inoculum culture was grown for 5 days prior to this experiment using the same CH_4 cylinder for headspace gas with similar concentrations of CH_4 and O_2, and that the OD_{600} of the inoculum vial had higher values (more than double) than those reached during this experiment. This indicates that the inoculum lipids experienced a higher fractionation of the headspace gas and had, potentially, less depleted lipids than those seen in this experiment. Increasing OD_{600} values of the sacrificial experiment represented that the cultures grew in size, producing *de novo* lipids, also supported by the enrichment in the provided CH_4 headspace, suggesting that both diploptene and hop-21-ene were formed from the provided CH_4 ($\delta^{13}C_{CH4}$= -43‰), with a potential level of fractionation as high as $\Delta^{13}C_{CH4}$=42.8‰.

4.4.2. Type II – *M. trichosporium*

4.4.2.1. Culture growth, isotopic signature of CH_4 in the headspace of each vial and dried mass of cells/day

Type II cultures were grown for 12 days, with triplicate vials for each day of the experiment. Similar to type I, OD_{600}, isotopic analysis of the CH_4 headspace gas, dry mass measurements, lipid identification and semi-quantification, and lipid isotope analysis were performed during and after the experiment.

Similarly to *M. methanica*, the type II culture increased in OD_{600} and size up to day 3, after which a plateau was reached, with only a few vials deviating from the average OD_{600} either due to experimental errors in providing the headspace gases or due to potential culture contamination (e.g. day 11). Apart from one day 11 vial, all cultures displayed values below the inoculum vial's OD_{600}. This is also seen in the consumption of depleted CH_4, which is highly visible up to day 3, after which the values stabilise, following the OD_{600} data (Figure 4.12.A).

Headspace depletion on CH_4 is also apparent up to day 3, indicating active CH_4 consumption and incorporation, as the culture grew in mass, also indicated through the dry mass amount recovered at the end of the experiment (Figures 4.12.B and 4.12.C).

4.4.2.2. Lipid identification and concentrations

Diploptene, hop-21-ene and potentially diplopterol were identified for *M. trichosporium*, yet squalene was not among the peaks present in the day 5 type II sample. Diploptene and hop-21-ene amounts peak on the 5th day of the experiment, followed by a dip in their concentration. Day 6 was extracted and analysed with the triplicates pulled in the same sample from the centrifugation step, indicating that loss of sample during further steps cannot be a reason for this decrease.

Type II has lower levels of diploptene, diplopterol, and hop-21-ene compared to Type I, despite having 20 mL more media in each vial. It was noticed (Kannenberg and Poralla, 1999) that hopanoid concentrations increase in order to increase the membrane's rigidity when stress is imposed. In this case, a lower oxygen content and more acidic pH can be inferred mid-way through the experiment, yet this is not observed in terms of hopanoid concentration increase in this culture. This caused issues in quantifying the isotopic signature

of the two compounds and, for *M. trichosporium*, this was previously observed by other studies (Rohmer et al., 1984).

4.4.2.3. Compound-specific isotopic data of M. trichosporium lipids

Diploptene thus co-eluted with two compounds, and CSIA was not possible in most samples (Meier-Augenstein, 2004). For type II methanotrophs, as further shown in Chapter 7, CO_2 is required in a higher percentage for lipid biosynthesis than for type I, thus CO_2 was added in the headspace of the cultures, leading to the mix of the two gases, and the incorporation with hopanoids of carbon with two distinct isotopic signatures (i.e. CH_4 = -42.8‰ and CO_2= -36‰). Is it thus expected that hopanoid lipids of type II would show less depleted signatures than type I, which used primary CH_4 for lipid synthesis (Jahnke et al., 1999).

4.4.3. *M. methanica* and *M. trichosporium* lipids – isotopic comparison

M. methanica CH_4 headspace isotopic values were averaged from the vials which were combined for TLE extraction while the diploptene values were averaged from the duplicate GC-IRMS runs (Figure 4.18). Working under the consideration that the isotopic contribution of inoculum diploptene was only 3.5% and negligible, the averaged isotopic difference between the provided CH_4 and CSIA of diploptene (i.e., $\Delta^{13}C$) is relatively constant for the first 7 days yet displays a larger spread of values, especially for diploptene, in the replicates available on the 8th day of the experiment. The averaged $\Delta^{13}C$ was equal to or less than 35.4‰ for the first 7 days, and equal to or less than 36.9‰ for the entire experiment, considering that the isotopic values of the lipids from the inoculum were not measured.
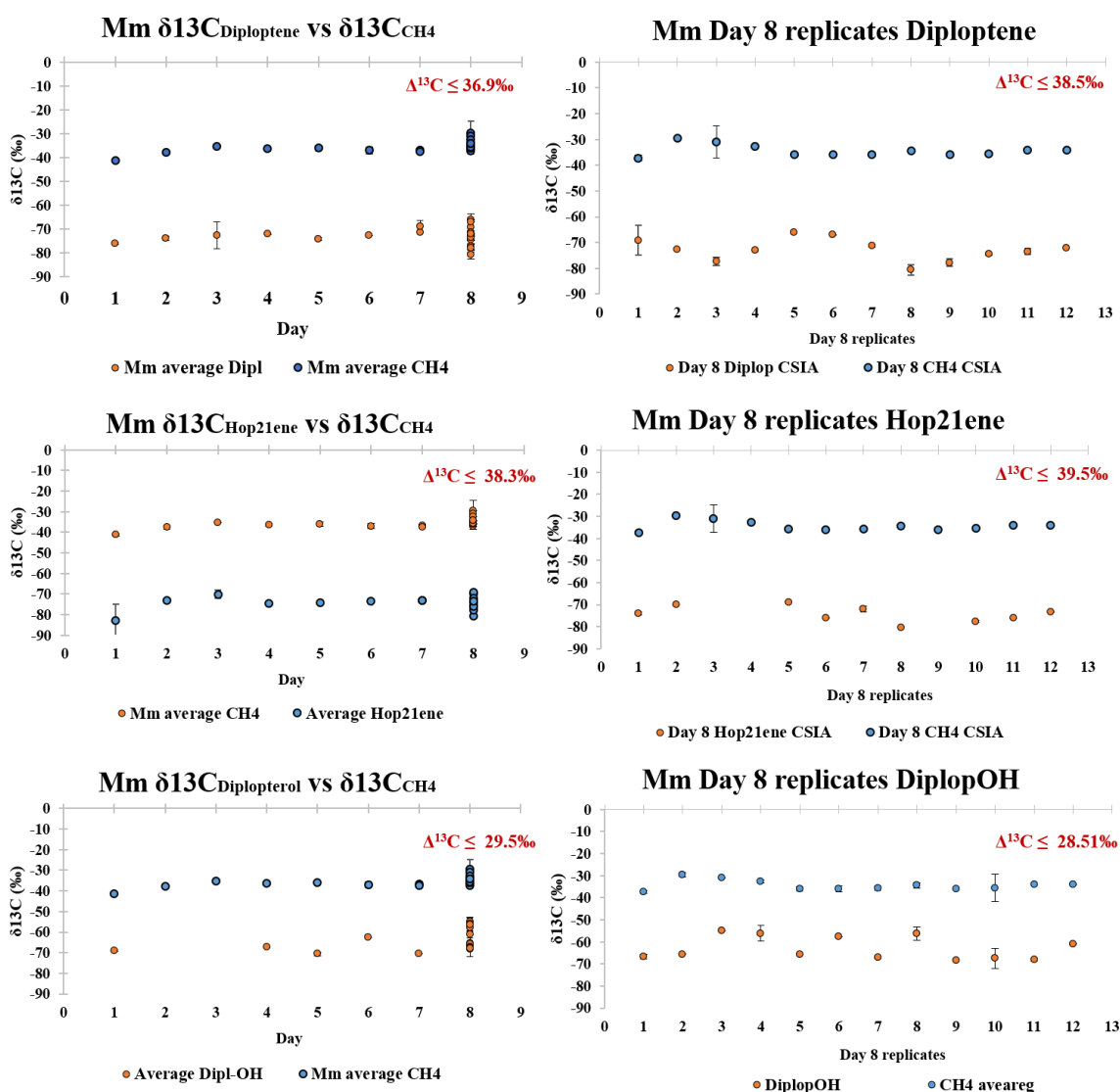
Figure 4.18 Isotopic differences (Δ13C) between provided headspace CH4 (blue) and CSIA of diploptene, hop-21-ene and diplopterol (orange). Error reported for combined standard deviation for headspace and CSIA measurements. Mm = M. methanica.

A similar depletion between the isotopic values of the provided headspace CH₄ was seen for hop-21-ene: with a maximum value of 37.1‰ for the first 7 days and a maximum value of 38.3‰ across the entire experiment, considering again that the initial isotopic signatures of day 0 lipids from the inoculum vial were not measured. Assuming that day 0 diploptene, hop-21-ene and diplopterol were thus, very low in concentration (i.e., approximated around 0.7 µg/mg for diploptene) and with isotopic values equal or more enriched than those measured on day 1, fractionation factors were simulated (Figure 4.19).

In this experiment, on average, hop-21-ene displayed relatively depleted values when compared to diploptene, with regards to the isotopic signature of the CH₄. However, diplopterol displayed less depleted values and the isotopic difference between diplopterol and CH₄ was less pronounced, averaging at 30‰ for the first 7 days and overall at 28.5‰ over the entire experiment. As the isotopic value of squalene could not be calculated, fractionation factors were simulated between the headspace CH₄ and these hopanoids, taking into account the above stated assumptions. For day 4, for example, fractionation factors (i.e.,
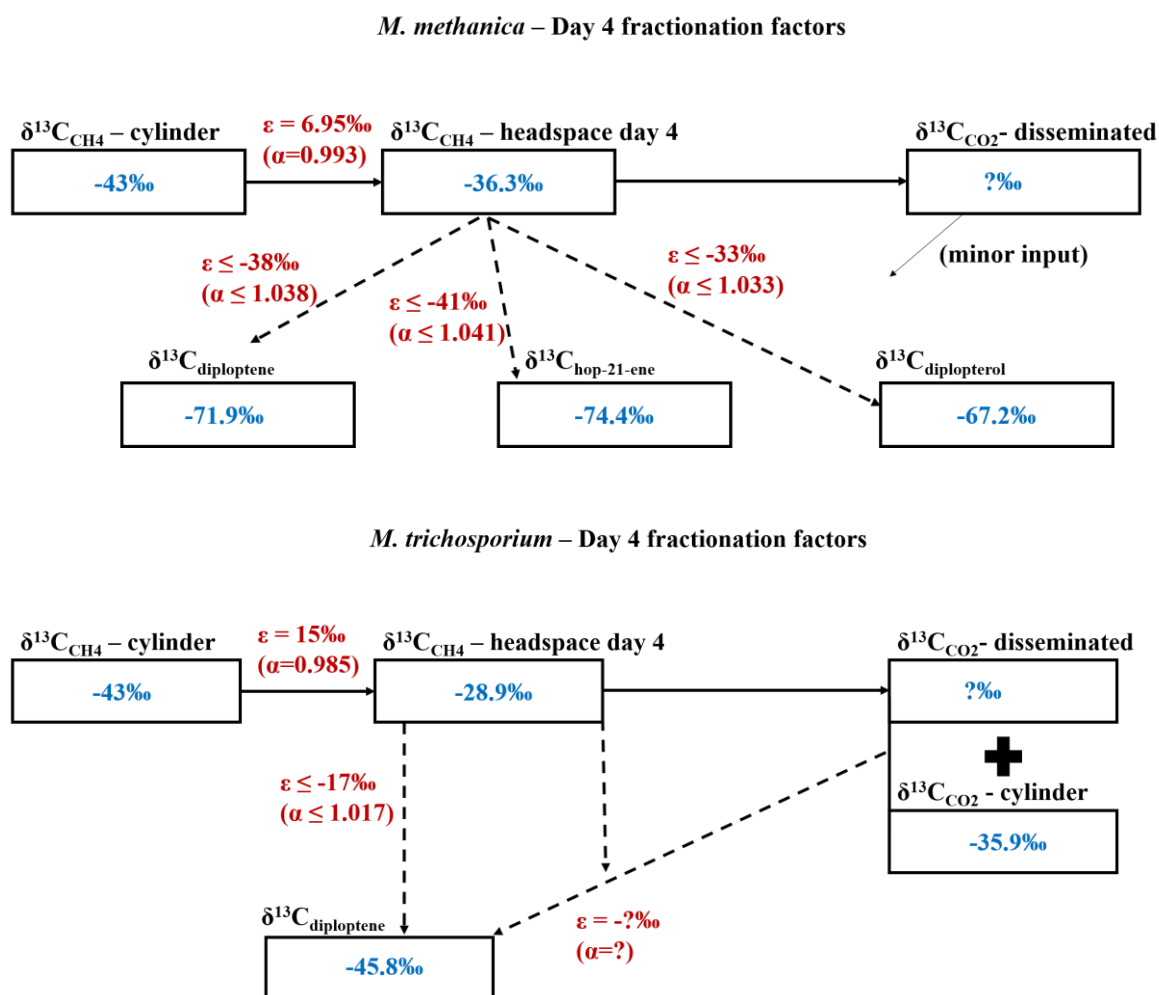
Figure 4.19 Fractionation factor (ε) simulated for day 4 of the experiment, when all 3 hopanoids could be measured at the CSIA level.

ε) between the isotopic value of the headspace CH_4 and the three lipids were larger for hop-21-ene (i.e., ε=-41‰), followed by diploptene (i.e., ε=-38‰) and diplopterol (i.e., ε=-33‰, Figure 4.27).

In the case of *M. trichosporium*, diploptene had overall enriched isotopic values when compared to *M. methanica* (Figures 4.18 and 4.20) and the CH_4 headspace was less fractionated (Figure 4.21) due to the initial incorporation of cylinder-provided CO_2 measured at -35.9‰. On average (Figure 4.20.B), the difference between the isotopic value of the CH_4 headspace gas and *M. trichosporium* OB3b diploptene, was 14.9‰ and, for example, on day
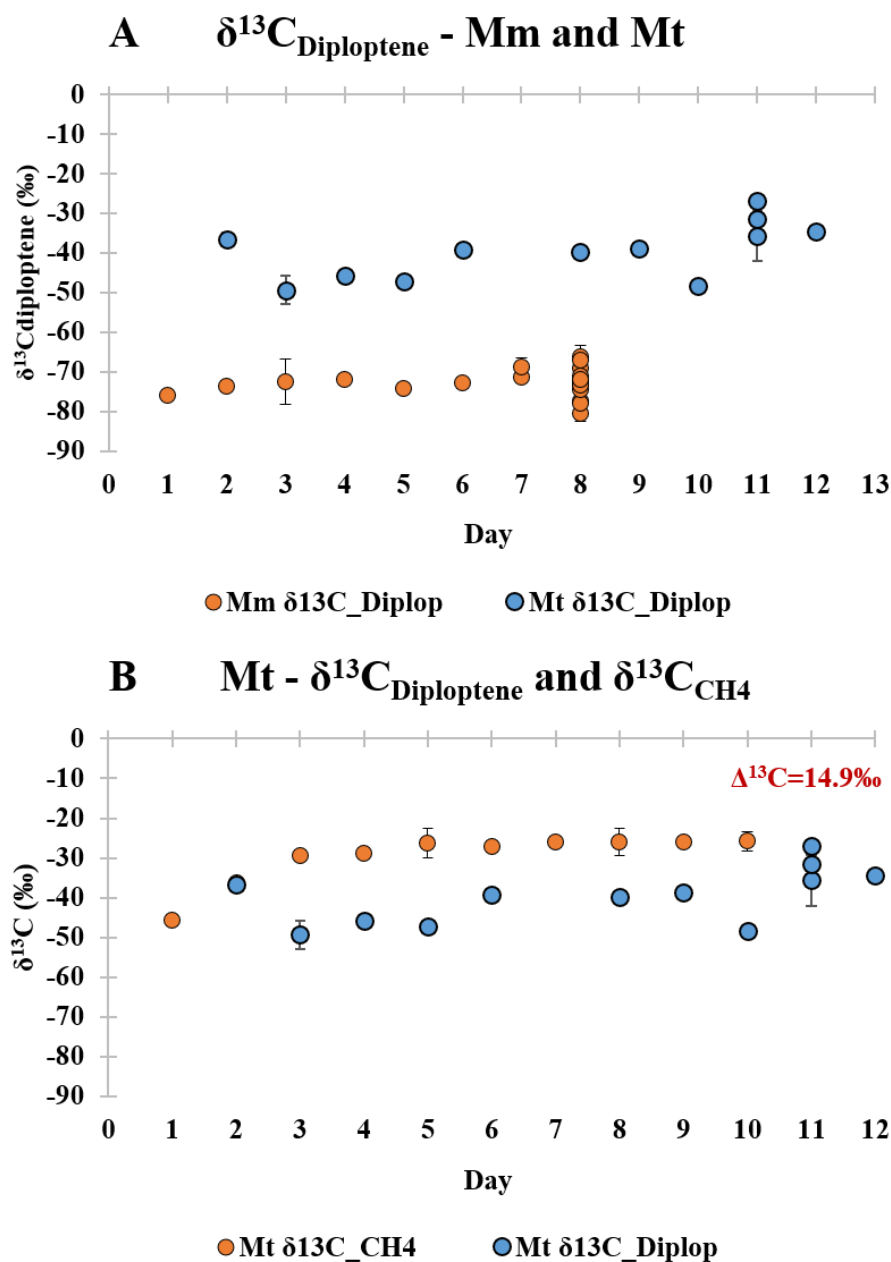
Figure 4.20 A: Different diploptene isotopic values as produced by M. methanica (orange) and M. trichosporium (blue). B: Averaged isotopic difference (Δ13C) between headspace CH4 and diploptene during the M. trichosporium experiment. Mm=M. methanica; Mt=M. trichosporium.

4, the fractionation factor between *M. trichosporium* produced diploptene and headspace CH_4 was only -17‰ (Figure 4.19), reflecting the contribution of CO_2 incorporation. This was expected as type II methanotrophs incorporate more CO_2 relative to type I. The CO_2 cylinder also had a more enriched isotopic signature relative to the CH_4, measured at -35‰, meaning that type II diploptene was expected to have relatively enriched values, and present a less enriched (fractionated) CH_4 headspace.

However, the CH_4 headspace gas is more fractionated in the case of *M. trichosporium*, showing an enrichment of 20‰ between day 1 and 10, while *M. methanica* headspace gas displays only a 3.8‰ to 11.6‰ enrichment between day 1 and the highest and lowest value of the replicates on day 8 (Figure 4.21). This indicates that, although CH_4 is not incorporated into the *M. trichosporium* diploptene at the same rate as in *M. methanica* due to the contribution of CO_2 for *M. trichosporium* biomass, that CH_4 is more readily incorporated into other lipids such as PLFA, or transformed CH_4 into CO_2 for energy, via the dissimilation pathway for this type II methanotroph. This is also observed as a comparison between Figure 4.19 as, on day 4, the fractionation factor for CH_4 headspace between the starting isotopic composition and the one recorded on day 4 was 8‰ for *M. methanica* and 15‰ for *M. trichosporium*.
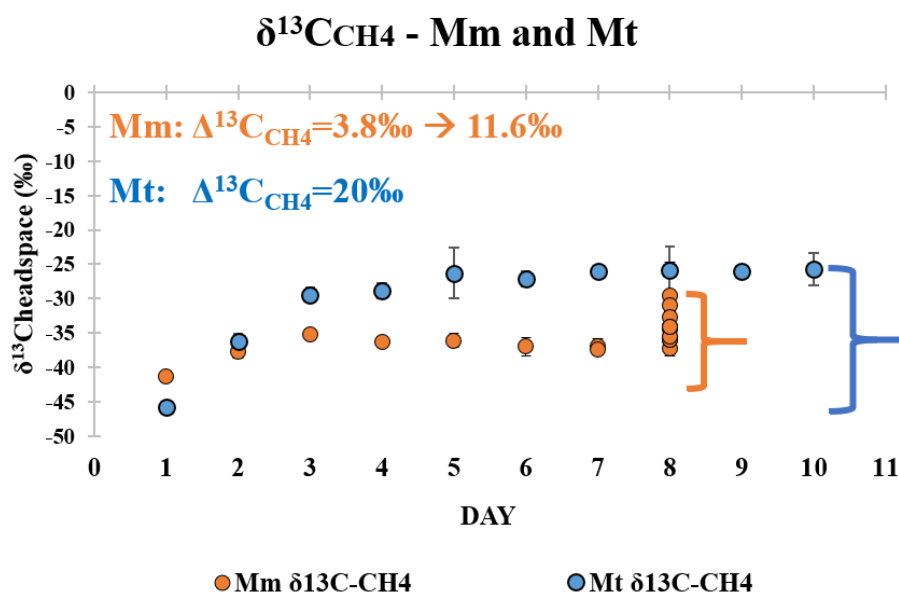
Figure 4.21 Headspace CH_4 difference between the start of the experiments and end. M. methanica value provided as range due to multiple measurements available for the final day of the experiment.

A mixing model was analysed, under three scenarios, taking into account the isotopic values of diploptene recorded on the 4th day of each of the growth experiments, with the first scenario representing the diploptene amounts and isotopic values measured in this work for the same day (Figure 4.22). Depending on the environmental conditions, one methanotroph type might prevail over another (i.e., scenario I and III). While scenario I diploptene isotopic values would indicate methanotroph contribution to the diploptene pool of an environmental sample ($\delta^{13}C_{diploptene}$=-71.2‰), scenario III, with a relatively enriched diploptene value of -46.5‰, could be seen as a mix of source, with possible input from other non-CH_4 consuming bacteria (depending also on the environmental $\delta^{13}C_{CH4}$). For example, this diploptene value is slightly more depleted when compared to the diploptene value recorded at the surface of BVA in Subsection 3.3.5 (-42‰) where evidence of both type I and II methanotrophs has been recorded, alongside a wider microbial community capable of producing membrane hopanoids (Finn et al., 2020). In an open-system setting, accessing the isotopic signatures of specific carbons within the diploptene pool would have the potential to indicate active CH_4 consumption and would reflect closely the isotopic signature of the CH_4 source. In the

Mixing model – Day 4
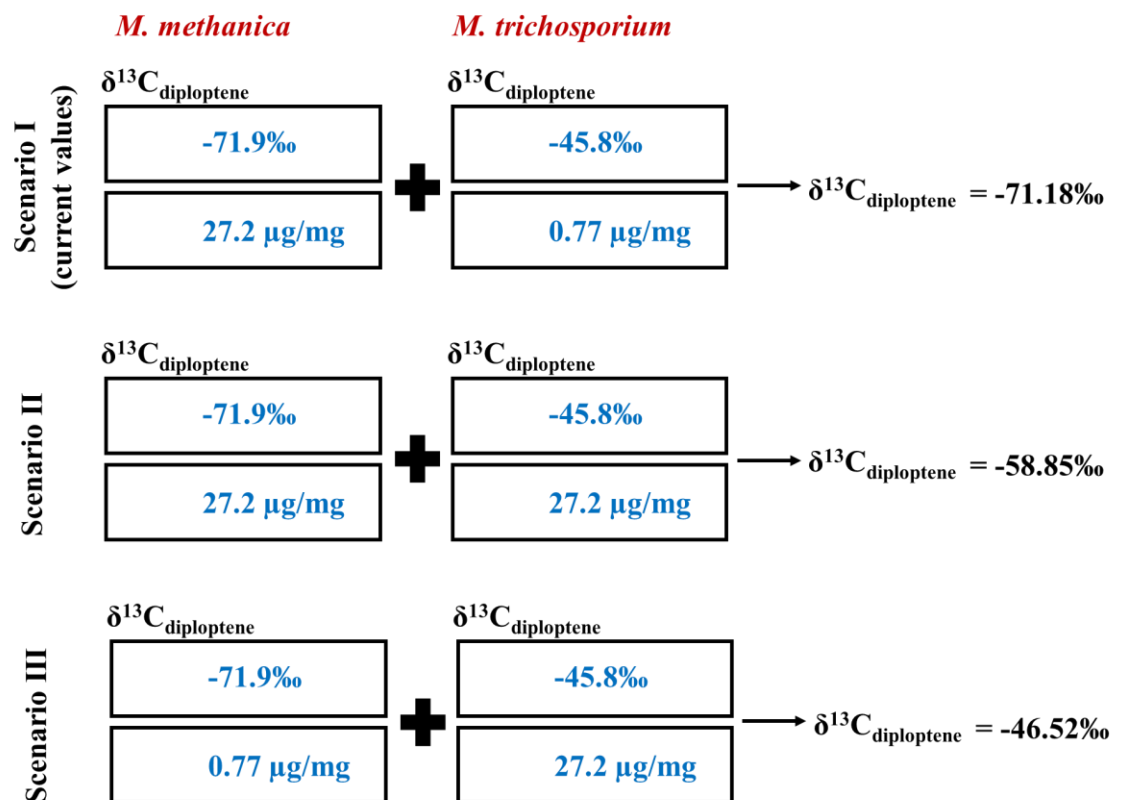
Figure 4.22 Three mixing scenarios of diploptene amounts and isotopic composition from a type I and II methanotroph bio-producers, highlighting the fast enrichment of diploptene and signal muting when the type II methanotroph becomes the main biomarker pool contributor.

current case, the isotopic contribution from CO_2 would be removed by investigating carbon positions that bear only the C-CH_4 isotopic signature.

Two overlooked aspects do not allow diploptene extracted from these samples to be the ideal candidates for studying further the CSIA vs PSIA framework. These should be improved by analysing the isotopic signature of diploptene within the inoculum culture, understanding thus its isotopic contributions within the lipid pool of types I and II methanotroph strains. Furthermore, in future similar experiments aimed at PSIA, since methanotrophs can disseminate CO_2, it is recommended that the headspace for both methanotroph types have the same composition, in order to accurately track the isotopic evolution of both gases and the differences in C-CH_4 and C-CO_2 assimilation.

4.4.4. Type X – *M. capsulatus*

Finally, *M. capsulatus* was grown only for lipid identification purposes, in a single batch. Apart from fatty acids, squalene and diploptene which were identified in this strain, cholesterol and other similar compounds presented in Table 4.2 were also found in this culture. Cholesterol and the associated compounds are not generally known to be produced by bacteria, but by plants, fungi and animals (i.e., eukaryotes; Voet and Voet, 2021). While the culture did not appear to be contaminated (i.e., no visual growth of algae or fungi), and cross-sample contamination could have occurred at the lipid extraction phase, on the ASE, this methanotroph is known for its unusual production of sterols, barring an oxygen-dependent gene for squalene cyclization (Sessions et al., 2002; Jahnke and Nichols, 1986), indicating that the compounds are produced *de-novo*. Apart from diploptene and squalene, the study of Sessions et al. (2002) has also identified hopan-30-ol and 3β-methylhopan-30-ol, which were not seen in this culture. It would be of PSIA interest to understand how the squalene pool is divided between hopanoids and sterols, and how the isotopic signatures at the compound levels for both diploptene and cholesterol are changing during the experiment. For this reason, cholesterol has been added to the pyrolytic simulations done in Subsection 7.3.6, to understand its breakdown pattern and potential for PSIA.

M. capsulatus thus poses another research challenge due to its production of both sterols and hopanoids from the same squalene pool, which would require a more detailed investigation into the isotopic fractionation processes at the CSIA level for understanding the origin of diploptene PSIA signatures after this branching point. While in terms of hydrogen, Sessions et al. (2002) reported that 31.4±1.7% is derived from CH_4, CH_4 is initially converted to H_2O and no direct transfer of H-CH_4 takes place, in terms of carbon isotopes, within this microbe,

squalene is expected to incorporate both C-CH$_4$ and C-CO$_2$ via its complex metabolism depicted in Figure 7.9. The two enzymes, hopene-squalene cyclase and squalene oxidocyclase that lead to the formation of hopanoids and sterols, respectively, will have different activity rates and fractionation factors of squalene, and the CSIA of hopanoids, diploptene including, may not reflect a direct relationship with the remaining squalene pool. From a chromatographic point of view, while squalene and hopanoids could be analysed for CSIA within the same fraction (see Figure 4.25), sterols CSIA will involve derivatization and an added chromatographic run for a compressive characterization.

It would be of PSIA interest to understand how the squalene pool is divided between hopanoids and sterols, and how the isotopic signatures at the compound levels for both diploptene and cholesterol are changing during the experiment. For this reason, cholesterol has been added to the pyrolytic simulations done in Subsection 7.3.6, to understand if, by having a common precursor, would mean that the two lipids breakdown in a similar fashion and if the incorporation of CH$_4$ into the two lipids can be studied at intramolecular levels.

4.5. Chapter 4 conclusions

In terms of growth and carbon incorporation, type I and II cultures performed similarly. In both cases, an active methanotroph culture is observed until day 3 based on OD$_{600}$, headspace isotopic composition and lipid isotopic measurements. All three methanotroph types cultures were centrifugated and the TLE was analysed on GC-FID and GC-MS showing defining lipids of each type, and most importantly, identifiable and measurable diploptene and hop-21-ene compounds.

All three analysed hopanoids of *M. methanica* (diploptene, hop-21-ene and diplopterol) displayed overall depleted isotopic values than the diploptene produced by *M. trichosporium* OB3b. Similarly, the fractionation factors between the provided CH$_4$ and hopanoids of *M. methanica* are greater when compared to those of *M. trichosporium* OB3b, yet the headspace fractionation of CH$_4$ between the starting and end value of the experiments is greater for *M. trichosporium*. There is an isotopic difference between 3.8‰ and 11.6‰ in the CH$_4$ values of the *M. methanica* experiment and a difference of 20‰ in the *M. trichosporium* cultures, although this former fractionation was not recorded within diploptene. It is thus expected that in *M. trichosporium* OB3b cultures, the provided CH$_4$ was either incorporated into other lipids or that the CH$_4$ was more readily oxidised to CO$_2$ for energy purposes.

A mixing model was produced for three scenarios in which the day 4 diploptene isotopic values of both *M. methanica* and *M. trichosporium* were combined at the measured lipid concentrations, highlighting the enrichment in diploptene as type II diploptene prevailed. In environmental samples, a diploptene value of -46.5‰ can be further muted by input from other non-CH_4 consumers, leading to uncertainty when assessing the active methanotroph community of past methanotrophy within an environment. In an open-system setting, accessing the isotopic signatures of specific carbons within the diploptene pool through PSIA would have the potential to indicate active CH_4 consumption and would reflect closely the isotopic signature of the CH_4 source, eliminating the CO_2 isotopic contribution, allowing more reliable investigation of palaeoenvironments.

The pure methanotroph culture experiments will also further guide the instrumental and analytical requirements to facilitate a compressive position-specific isotopic study in (palaeo)environmental samples. CSIA is a pre-requisite to PSIA in order to understand the isotopic context of a position/part-specific isotopic value. Issues in measuring the stable isotope signatures at a compound-specific level, previously addressed in Chapter 3 (peatland samples) due to the challenges posed by co-elution and low lipid concentrations, were encountered again in the context of pure cultures. The limitations in sample availability or the need to increase sample concentration or injection amounts to reach the detection limit for multiple compounds can result in instrument failure and unreliable results. To address these analytical constraints seen in both environmental and pure culture samples, the next chapters will focus on the methodology developed on a GC-FID system to handle such samples prior to pyrolysis and isotope analysis (prep-GC), with the goal to optimise the instrument for a wide range of analytical compounds and classes relevant for palaeoenvironmental reconstructions.

5. The prep-GC system: MTBE pyrolysis

5.1. Introduction

*Intra*molecular isotopic analysis is an emerging powerful tool to study the origin and fate of compounds. For offline PSIA systems (reviewed in Subsection 2.7.1), the process however requires an initial large amount of pure sample and a time-consuming procedure, even in the ideal cases when the right chemical reactions allow the study of moieties of interest. Online PSIA has developed taking into account the lessons of offline studies, incorporating the analytical robustness of GC systems with the high sensitivity and reproducibility of the associated detectors (Subsection 2.6). However, while most online systems for PSIA no longer require large amounts of pure samples due to the evolution of sensible detectors, there are several drawbacks that can limit the application range, which were detailed in Subsection 2.7.2. The hyphenation of GC instruments, pyrolysis units and GC-MS/FID/IRMS detectors decreases equipment availability and increases laboratory costs, which can be further impacted if a PSIA system was designed only for a particular application or molecule type. A narrow application range can also be imposed through the design of the PSIA systems that are prone to cold-spots occurrences, which can impact particularly higher molecular compounds. On the other hand, the ability to cool down a part of the system may be required for concentrating and releasing targeted compounds when they have low concentrations, particularly in (palaeo)environmental samples, yet the system would also require the ability the accurately heart-cut these compounds of interest from complex samples, and release them in a reproducible manner for further pyrolysis and isotope analysis. All these instrumental constraints were taken into consideration during the prep-GC system design in this chapter.

The aims of this chapter were to develop further and demonstrate for the first time the ability of a bespoke prep-GC instrument to achieve pyrolysis and the complete transfer and identification of pyrolysates, with an application on the MTBE compound. The experimental conditions were then adapted to the RMG code, and results compared, validating RMG as a fitted *in-silico* application for the developed prep-GC instrument and methodology. System development was done focusing on the final aim of this work, a prep-GC adapted to handle new and complex compounds that are key molecules in palaeoenvironmental studies and that were never subjected to pyrolysis (i.e., hopanoids). The setup was thus kept highly

adaptable to new compounds and able to be modified with ease. The current prep-GC system for PSIA follows closely the first-generation system and principles used in Gauchotte-Lindsay et al. (2009 and the work presented in this chapter took place with a series of goals in sight, leading to a continuous increase in the complexity of the system design and analytical methods.

5.2. Materials and methods

5.2.1. Materials

MTBE (tert-Butyl methyl ether, 99.8% purity) was purchased from SupraSolv® and methanol (HPLC grade, ≥99.8% purity) from Fisher Scientific. Toluene was available from Sigma-Aldrich, 99.8% purity. Two-way unions were purchased from VALCO (P/N 20147), with ferrules selected to fit the employed column(s) dimensions.

5.2.2. Prep-GC system overview

The main gas chromatography (GC) instrument used in this system is referred to as the prep-GC, a GC system used to prepare samples for pyrolysis (Figure 5.1). The prep-GC system is based on a gas chromatography (GC) instrument (Agilent 9870A), coupled with a Flame Ionizing Detector (FID). The system is a modified version of a simple GC-FID comprised
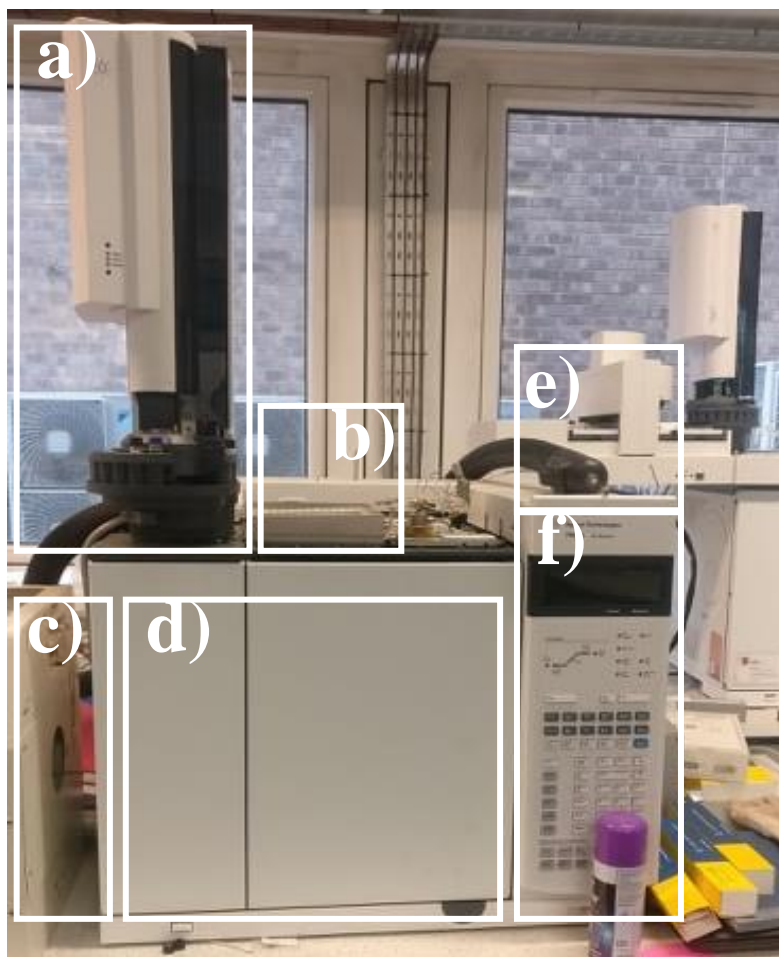
Figure 5.1 The prep-GC-FID system – simplified view showing main components. a) Autosampler tower covering inlet port; b) valve box; c) pyrolyser; d) oven; e) transfer line; f) system keyboard for manual control and display.

of an inlet port in which the first-dimension capillary column is installed, a user-controlled oven, a detector and an autosampler tower (Figure 5.1). The current prep-GC system was designed to handle environmentally complex samples and prepare them for PSIA by trapping and concentrating a compound of interest, delivering it to the pyrolysis unit and redirecting the pyrolysates to a different detector. It contains auxiliary components such as a valve box which is installed on top of the GC (Figure 5.1b) and is configured as a Thermal Auxiliary component, a Cool Cube system that is integrated into the GC-oven (Figure 5.1d, white arrow), a heated transfer line (Figure 5.1e) and, additionally, a pyrolysing unit connected to the GC (Figure 5.1c). These components are described in the following subsections. The system can be programmed via the side integrated keyboard or through software, Chemstation (Rev C.01.05). A schematic of a general prep-GC configuration is presented in Figure 5.2.
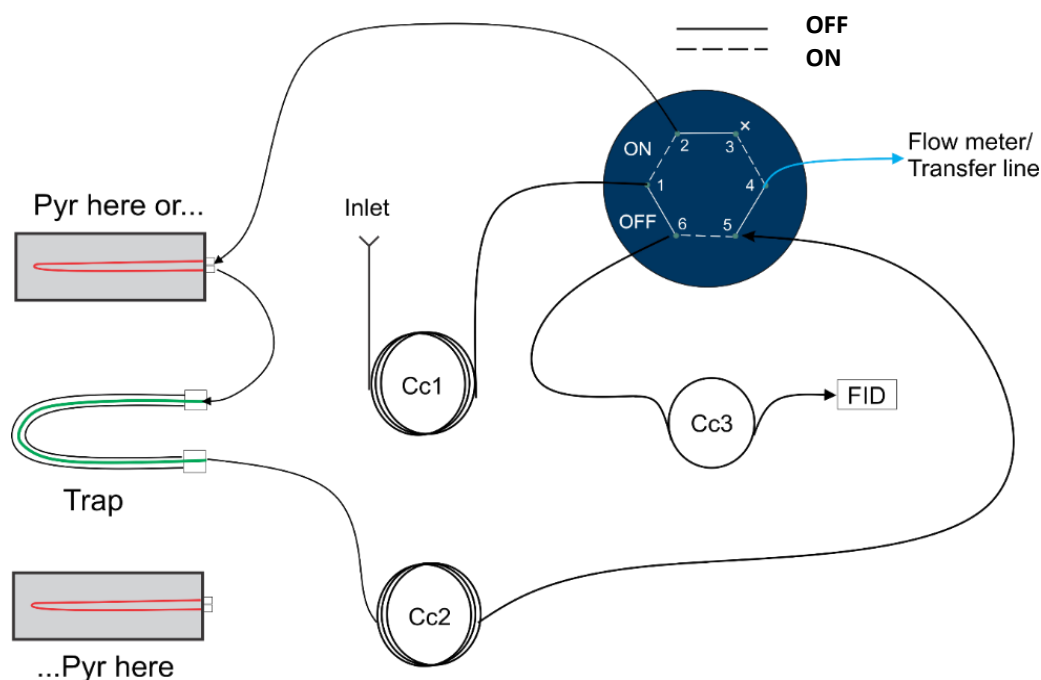
Figure 5.2 Overview of the prep-GC system. The sample is introduced via the Inlet and after Capillary column 1 (Cc1) can either be analysed by prep-GC's own FID (valve OFF) or be transferred to the pyrolyser and/or trap. The pyrolyser can be either connected prior or after the trapping device, depending on the application. Pyrolysates are then separated by Cc2 and diverted either to the same prep-GC FID (valve ON) or to a different detector via the transfer line.

5.2.3. Valve box

The prep-GC system is fitted with three diaphragm 6-port switching valves placed in a heated enclosure on top of the oven (Figure 5.1), with its switch time and temperature programmable from Chem Station. The valves are capable to withstand a maximum of 250°C working temperature (AFP, 2022). The heated and isolating enclosure maintains the selected temperature over multiple runs and, most importantly, it is not affected by the cooling-heating cycles that take place in the oven. However, the heating pace of the valve-box is slow (approx. 10-15°C/min) and, without a cooling fan, it cannot be considered an oven. The valves can operate in an ON or OFF position, connecting neighbouring auxiliary components and allowing the sample transfer. The operating principle is described in Appendix A.5.1.

The valves are programmable (temperature and ON/OFF switch time), a process automated from Chem Station. Each valve port contains a ferrule (P/N 20142, Restek) in which the column is inserted, and the connection is made air-tight using a 1/16" nut.
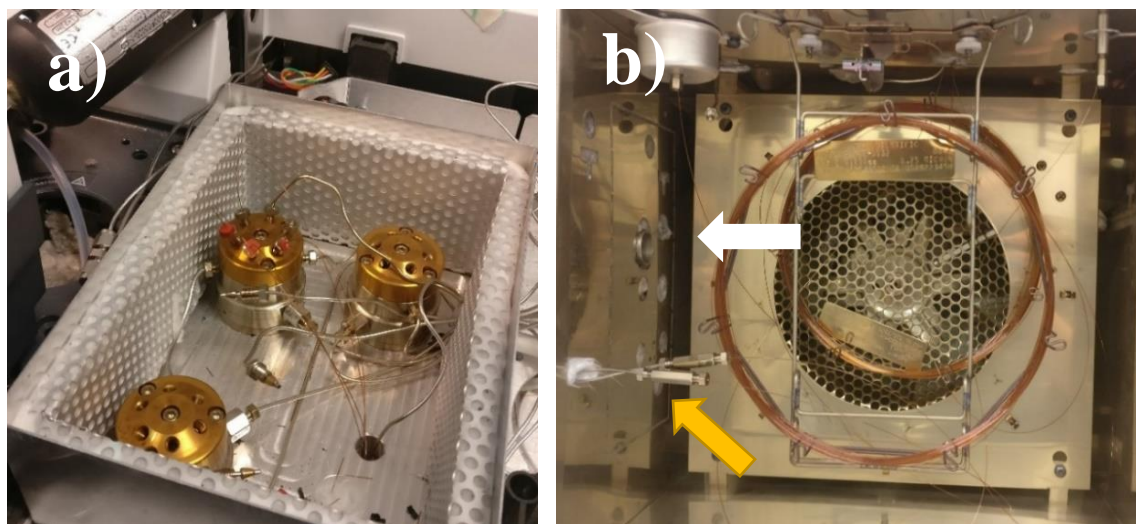
Figure 5.3 Inside view of Valve Box (a) and Oven (b). Notice the 3 valves isolated in a metallic case over which a lid is placed and the two columns placed in the oven. Yellow arrow points towards the connections between column and pyrolyser while the white arrow, towards the oven-integrated Cool-Cube.

5.2.4. Pyrolyser

The pyrolyser is a VG ISOCHROM-GC combustion furnace, a unit that was previously used in a GC-IRMS system to combust molecules to CO_2. It is located on the left of the GC oven and it is made of a resistively heated ceramic tube, with an internal diameter of 1 cm and a length of approx. 40 cm. The temperature is set by the user using the front dial. It was

experimentally observed that, when in function, the ceramic tube is not heated equally throughout, with only a middle section reaching the required temperatures.

Several pyrolysis tubes spanning different materials and placement options were tested using the same compound, MTBE. Due to the location of the pyrolyser (i.e., placed on the left-hand side of the prep-GC; Figure 5.1) and due to the very narrow ID of the heated ceramic interior (1 cm diameter), a U-bend of the pyrolysis tubes was required, allowing the pyrolysis tube of choice to return in the oven, avoiding thus cold-spot generation (Figure 5.3b). Placing only half of the pyrolysis tube within the pyrolyser and the other half on the exterior, would have created a cold spot where higher molecular weight compounds or fragments would have been trapped. The tested tubes were connected with the other capillaries or components of the prep-GC system via 2 two-way Valco unions (P/N 20147, Restek). This U-configuration meant however that the molecules pass the pyrolytic zone twice, where the maximum temperature is reached, and a potential cold spot developed between the oven and pyrolyser, and on the far left-side of the pyrolyser, which was again in contact with the atmosphere. Pyrolysis was tested using 5 different options, with results of deactivated fused silica (FS) capillary presented in this chapter.

5.2.5. Heated transfer line

The transfer line is connected to the prep-GC and has the role of transferring pyrolysates or compounds to another GC system (Figure 5.4). It is a heated line embedded within an isolating and flexible material through which a 1/16" stainless steel tubing is threaded. It is connected to an XMT7100 Series Intelligent PID Temperature Controller, with a maximum temperature of 250°C.

For transfer, the heated line was connected to the prep-GC valve via a 0.25 mm deactivated FS capillary. A zero dead-volume two-way Valco union (P/N 20147, Restek) connected the FS capillary to the stainless steel 1/16" tubing and the end of the line fitted with an autosampler syringe needle (P/N 7785-10, Hamilton, Figure 5.4).

The connection between the capillary from position Valve-4 and the transfer line takes place within the oven. To avoid leakage at the connection between the transfer line and column, a Vespel ferrule (P/N 0100-1329) was used. The end of the transfer line was then tested in terms of flow and leaks by submerging it in a solvent.

Once the peaks were ready to be transferred, the transfer line's needle was injected into the inlet of a second GC instrument. Based on the transferred compounds' nature and the selected pressures and flows in the prep-GC, the transfer lasted between 2 and 5 minutes. The analysis on the second GC is manually started once the transfer line is introduced. During the transfer, the second oven was kept isothermal at a low temperature (i.e., 30-50°C), with some transferred compounds condensing at the head of the column. Once the transfer line is removed, the type of column, head pressure and oven method of the second GC will act as a second-dimension separation.
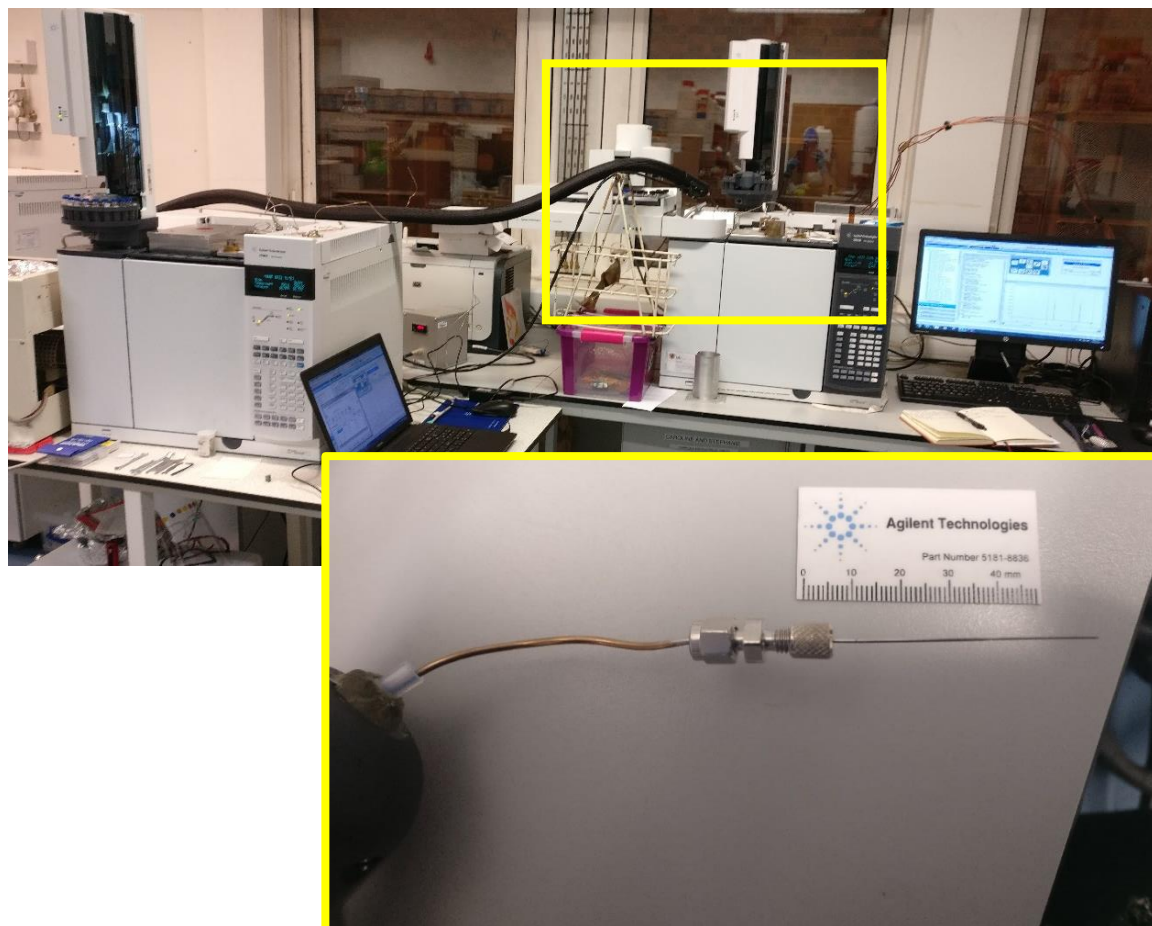
Figure 5.4 The end of transfer line showing the connection with the syringe needle (P/N 7785-01, Hamilton) that it is inserted into the second GC inlet.

5.2.6. Capillary columns

Several capillary columns were employed in this study to test the ability of the system to separate the pyrolysates. The initial prep-GC system seen in Figure 5.2 had two columns with the same characteristics and polarities, the Agilent DB-5 and HP-5. When transferred to the GC-FID, a ZB-Wax column was used. The higher polarity of this column ensured that

the compounds were well separated, allowing quantification. The columns used either in the prep-GC or the secondary GC system are presented in Table 5.1.

Table 5.1 Capillary columns used for the work conducted in Chapter 5.

Column name	Measurements	Work in which it was involved
HP-5 Agilent	30m × 0.25mm × 0.25µm	Exp 1
DB-5 Agilent	30m × 0.25mm × 0.25µm	Cc2 dimension
DB-5MS Agilent	30m × 0.25mm × 0.25µm	GC-MS column Exp 3
ZB-Wax	30m × 0.32mm × 0.50µm	Exp 2-second GC-FID column
FS deactivated capillary, Agilent	0.18mm or 0.25mm ID	Pyrolysis tubing

The initial FS deactivated capillary used in the first pyrolysis of MTBE was available in the lab. Fused silica capillaries were purchased from Restek, in either 15m or 30m of non-polar deactivated guard column (0.25 mm ID; P/N CP6575, Agilent).

5.2.7. Software

The prep-GC chromatographic data was acquired using Agilent's OpenLAB CDS ChemStation Edition software, the chromatograms were exported as .csv files. Similarly, GC-MS chromatograms were acquired on MSD ChemStation E.02.01.1177 software.

OpenChrom, Community Edition 1.2.0 (Alder) is an open-source software which was used to study GC-MS chromatograms. It was coupled with the NIST Mass Spectra Search Program, Version 2.0 g library to identify the mass spectra of selected compounds. CorelDRAW x5 was used to produce the diagrams and figures.

5.3. Methods and system configurations

5.3.2. Previous system configuration

The simplified version of the prep-GC system is presented in Figure 5.2 and can be compared to the pre-defined initial system (Figure 5.5), which was designed to employ all three valves. The simplified design has the same method complexity, being capable to heart-cut, pyrolyse, trap and concentrate a compound and, finally, transfer the pyrolysates to a second GC system, yet it utilises only one valve. This design was preferred as it limits the complexity of the method, focusing only on the ON or OFF position and timings of a single valve and has fewer connections and transfer capillaries, limiting thus the potential for leaks. In future experiments, as the prep-GC system will analyse more complex molecules, its complexity will increase, with the number of valves and connections kept to a minimum.
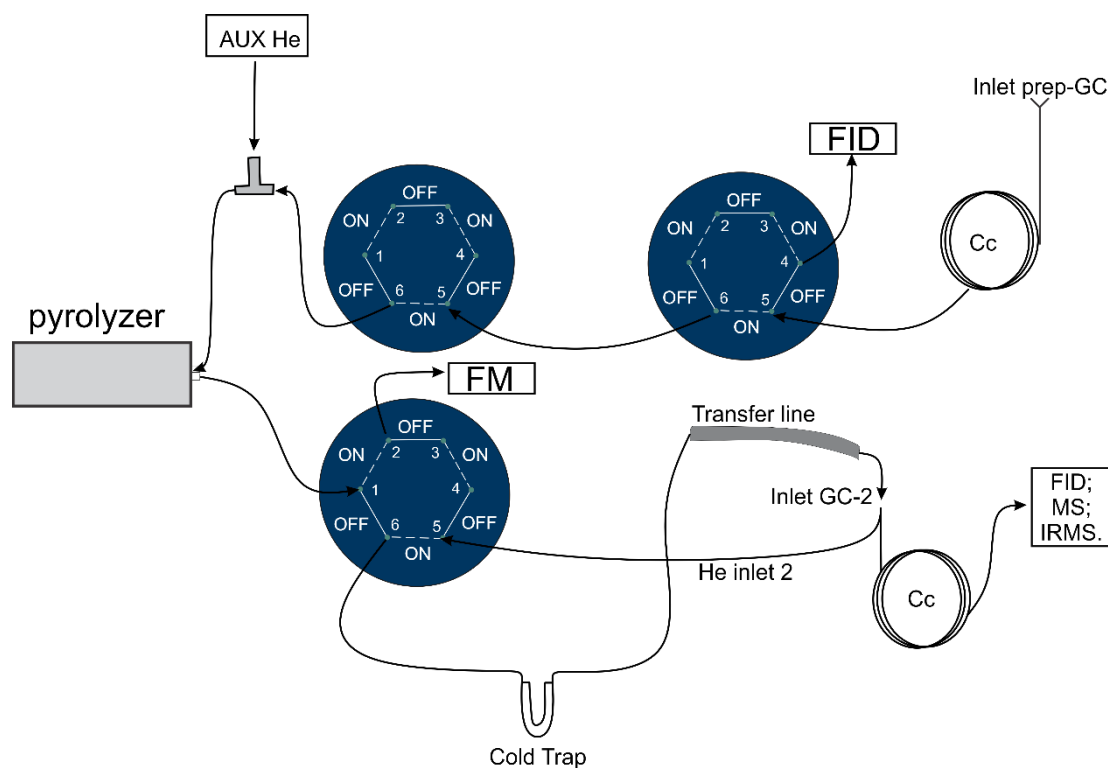
Figure 5.5 Initial valve design of the prep-GC. All three valves were in use, a T-union provided auxiliary He to the system before the pyrolyser, and the He from the second GC inlet was used to remobilise trapped compounds and push them through the transfer line into the second GC. FM=flow meter reading point.

5.3.3. MTBE pyrolysates analysed on the prep-GC FID

<u>Experiment 1</u>, refers to the first pyrolysis of MTBE on the prep-GC which confirmed the ability of the system and methodology to pyrolyse a compound over a range of temperatures in a reproducible fashion, using a FS deactivated column within the pyrolyser. The experiment was done using Cc1 (Table 5.1) and a 0.25 mm ID FS capillary within the pyrolyser (Figure 5.6). The valve set in the ON position redirected the compound towards the FID for quantification and retention time determination, while the OFF position directed the compound towards the pyrolyser. The pyrolysates thus obtained were separated within the second column in the prep-GC, Cc2 (Table 5.1). After separation on the second-dimension column Cc2, the pyrolysates and the remaining, unpyrolysed, parent molecule were sent to the FID connected indirectly via the valve to Cc2. Since pure MTBE was used, no heart-cut testing was done at this time.
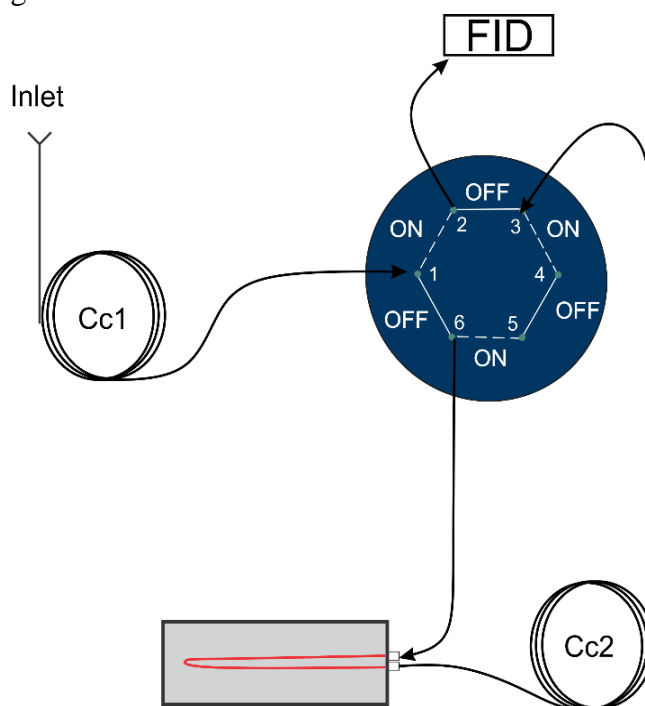
Figure 5.6 Prep-GC setup for the first successful MTBE pyrolysis using a FS capillary column within the pyrolyser. Cc1 was a 30 m Agilent HP-5 while Cc2 was a 30 m DB-5 column (Table 5.2). For the pyrolysis of pure MTBE, the system was operated with the Valve in the OFF position, transferring the pyrolysates from the pyrolyser to the FID.

The GC method consisted of a 1 μL of MTBE injection done using a 100:1 split, with a carrier gas flow rate of 2 mL/min and a head pressure of 19.39 psi. The two capillary columns were placed in the same oven and were subjected to the same temperature programme. The column length defined for both valve ON and OFF methods was 60 m, for retention time consistency. The oven was set isothermal at 100°C for 15 minutes to accommodate MTBE

(boiling point 55.2°C) as well as isobutylene and methanol (methanol boiling point 64.7 °C), and other secondary pyrolysis products.

With the valve in the OFF position, MTBE was exposed in triplicate runs to 250°C (to calculate pre-pyrolysis peak area), 500°C, 550°C, 600°C, 650°C, 700°C and 750°C. Pyrograms of Experiment 1 are presented in Figure 5.11 and the peak area of observed compounds are plotted in Figure 5.10, and reported in Table 5.4. Finally, in order to confirm the identity of one of the peaks, pure methanol (MeOH) was injected into the system with the pyrolyser at 650°C, following the same prep-GC method for retention time comparison (Figure 5.13).

5.3.4. MTBE pyrolysates transferred and analysed on a second GC-FID

Experiment 2 quantitatively tested the ability of the prep-GC system to transfer MTBE and pyrolysates to a different GC system. Triplicate analysis was performed for each pyrolytic temperature: 200°C, 450°C, 500°C, 550°C, 600°C, 650°C, 675°C, 700°C and 800°C. Given that the previous prep-GC configuration confirmed the successful pyrolysis and analysis on an FID detector, transfer was first tested to a second GC-FID (Agilent 7890B) adjacent to the prep-GC (Figure 5.4). This was preferred over an initial direct transfer to a GC-MS due to the fact that outlet pressure in a GC-FID is at atmospheric levels. The method used on the prep-GC to pyrolyse and transfer the pyrolysate as well as the second GC-FID method are described next.
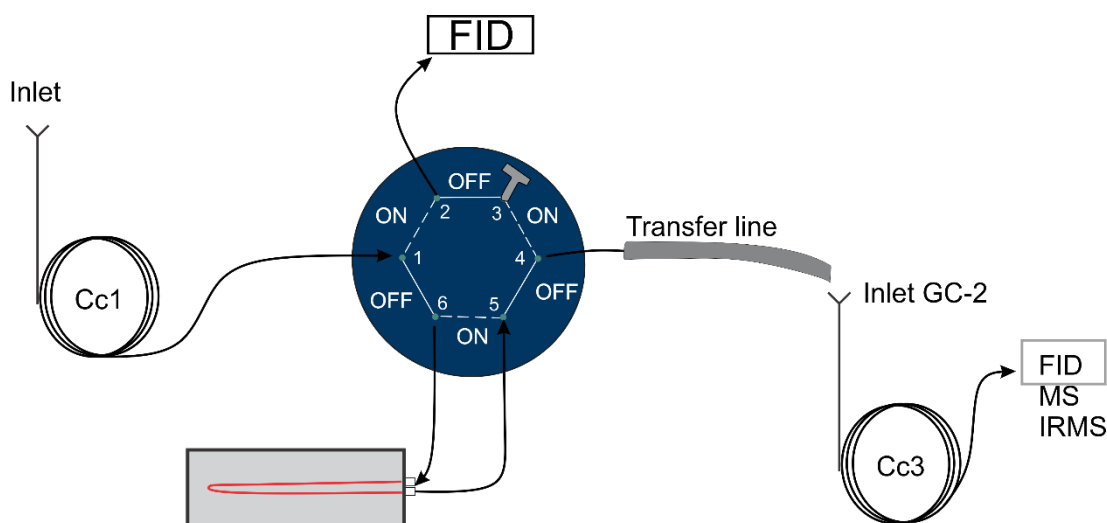
Figure 5.7 System flow for pyrolysis and transfer to a 2ⁿᵈ GC-system for further analysis. Valve in OFF position for transfer. The trap was not used during the experiment. Cc1-Agilent HP-5.

5.3.4.1. Prep-GC method

The previous second-dimension Cc2 column (Figure 5.6) was removed from the prep-GC as pyrolysate separation is done in the column installed in the second GC-FID (Figure 5.7). As 1µL pure MTBE was used, the prep-GC inlet was run in 30:1 split mode, with a carrier gas flow of 1.5 mL/min and a head pressure of 16.7 psi. Cc1 (Table 5.1) was left in the oven and during the entire prep-GC run (Table 5.2), the prep-GC's oven temperature was set as isothermal at 120°C to maintain a constant (and reproducible) system pressure and, high enough to cover the boiling points of MTBE and a wider range of pyrolysates, allowing them to remain volatile through the first system. The boiling point of MTBE is 55°C and, from previous studies (Gauchotte-Lindsay et al., 2009) the expected pyrolysates were isobutylene with a boiling point -7°C, and methanol with a boiling point 64.7°C, above that of its parent molecule.

MTBE was injected in the prep-GC initially with the valve turned ON (Figure 5.7), reaching the prep-GC-FID, in order for retention times to be calculated. A pre-eluting MTBE peak (pre-MTBE peak) was seen on all prep-GC chromatograms. The pre-MTBE peak had a retention time of 1.86 min – 1.94 min, while the main MTBE peak eluted between 2.05 - 2.12 min (Figure 5.14). This offered the possibility to test the system's heart-cutting ability and reproducibility, given the two closely eluting peaks.

In order to pyrolyse only MTBE (without the pre-eluting peak), a valve switch was introduced in the transfer method for the subsequent runs, sending thus the "pure" MTBE to the pyrolyser and second GC-FID, and confirming correct heart-cutting by observing in each run the peak area (PA) of the pre-MTBE peak (Figure 5.14). It was experimentally determined that the time window 1.99-5 minutes was enough to allow MTBE and its pyrolysates to reach the second GC-system inlet. For MTBE pyrolysis and transfer, the prep-GC method was run with the valve in the ON-OFF-ON sequence, as shown in Table 5.2.

Table 5.2 Time and method points for MTBE pyrolysis using the system from Figure 5.7.

Time (min)	Event	Method point
0 → 1.95	Valve ON	pre-MTBE peak reached prep-GC FID and confirmed injection
1.99 → 5	Valve OFF	MTBE to reach the pyrolyser, travel through the transfer line and reach the second GC-system inlet;
5 → end	Valve ON	Valve returning to the original ON position for the next injection

For transfer, as explained previously, the transfer line's needle was inserted into the inlet of the secondary GC-FID system and the valve was set in the OFF position (Figure 5.7). The transfer line was held constant at 200°C. The pressure of the transfer line is defined as the inlet pressure in the prep-GC, at 16.7 psi, with a flow of 1.5 mL/min. This prep-GC's inlet pressure was enough to allow pyrolysate to be transferred.

5.3.4.2. GC-FID 2 method for pyrolysates analysis

The second GC-FID system (Agilent 7890B; Figure 5.4) was equipped with the ZB-Wax column (Table 5.1). The inlet was at 250°C, operated in splitless mode to ensure that the compounds were fully transferred to the head of the ZB-Wax capillary column. The carrier gas flow rate was set to 1 mL/min for pyrolysate separation, and the head pressure was at 4.68 psi.

The method on the 2nd GC-FID was manually started once the transfer line was inserted in the inlet. The oven had a starting temperature of 40°C which was kept isothermal for 3 minutes while the transfer line was connected (i.e., until the prep-GC method finished; Table 5.2), and the compounds were transferred to the 2nd inlet. The oven method then followed a slow ramp of 5°C/min until 85°C. The ramp together with the ZB-Wax high polarity column and flow rate allowed the transferred compounds to be well-resolved.

Similarly to Experiment 1, methanol was transferred using the same prep-GC and second GC-FID methods for pyrolysate identification by retention time comparison (Figure 5.17).

5.3.5. MTBE pyrolysates transferred and analysed on a GC-MS

Experiment 3 was a qualitative transfer, following Experiment 2, to a GC-MS. As the transfer to a second GC system was successful and in order to be able to identify future pyrolysates, pyrolysis products obtained on the prep-GC system were redirected to an MSD. The transfer line was thus injected into a GC inlet coupled with a Mass Spectrometer with a Triple-Axis Detector used in the Electrical Ionizing mode (EI), following the same prep-GC system design used to transfer to the second GC-FID (Figure 5.7).

Similar to the transfer to the second GC-FID, the transfer to the GC-MS took place as a manual injection once the transfer line was connected to the second inlet. The ZB-Wax column (Table 5.1) was installed in the GC-MS oven, similar to Experiment 2.

The GC-MS inlet was set in splitless mode at 220°C. The oven program was set as follows: 30°C (2 min), 5°C/min to 85°C. Helium flow on the GC-MS was set at 1 mL/min. The scan

range for this method was between *m/z* 45 - 600. Identification of compounds was done using MSD Enhanced Chemstation software (E.02.02.1177, Agilent) linked to the NIST library.

An entire MTBE injection prep-GC run (i.e., no heart-cutting or valve switching) was transferred to the GC-MS with the pyrolyser set at a non-pyrolytic temperature (350°C) to confirm the successful transfer and identify the pre-MTBE peak (Figure 5.19). MTBE was pyrolysed at 600°C, 675°C and 725°C within the prep-GC and the peaks were transferred for pyrolysate identification.

5.3.6. Reaction Mechanism Generator – methodology for MTBE pyrolysis

The Python software Reaction Mechanism Generator (RMG), published by Dr Green's group from MIT (Gao et al., 2016), was implemented in this project. The software contains an extensive database of reactions and is fitted for studying gas phase pyrolysis in modelled reactors, ideal for this project. The input file contains the reacting molecules, temperatures and residence times of pyrolysis, system pressure, molecular starting concentrations and modelling constraints that can be edited by the user to match experimental conditions. The foundation RMG code (rmg.py), capable of providing data on the reactions that take place at various pyrolytic temperatures and resulting pyrolysates was used and tested against data previously published by Gauchotte-Lindsay et al. (2009) on MTBE pyrolysis and against results generated by the prep-GC current system, taking into account the dimensions of the capillary within the pyrolyser, specific oven temperatures, system's pressures and gas flow rates.

The RMG database was set similarly to the analysis of propane by Goldman et al. (2019) and as instructed by the "RMG Documentation Release 4.0.1" (Green and Team, 2013). The simulations used the "primaryThermoLibrary", and the "rate rules" for the kinetics estimator option. These settings were kept for other molecules simulated in this work (Chapters 6 and 7).

The chemical structure of MTBE was provided as SMILES notation, COC(C)(C)C, and the molecule was set as reactive, while helium, the carrier gas, was set as non-reactive. The simulated pyrolyser temperature was converted for each experimental temperature in degrees Kelvin and the pressure in the system was provided by the ChemStation software, at 19.39 psi and was converted to bar units for RMG input, at 1.33 bar. Finally, the concentration of MTBE in this experiment was calculated as a mole fraction at 2.2321E-09 (i.e., based on injection amount and split ratio).

The terminationTime parameter, which indicates the amount of time the molecules spent within the pyrolysis zone, is provided in Table 5.3. The volume of the reactor was calculated following Eq. 8 in Subsection 2.9, taking into account the ID of the capillary used, in this case, an ID of 180 µm, giving a radius of 90 µm and length over which pyrolysis occurred. The approximate length of the pyrolytic zone was 20 cm for each side of the U-bend, giving a total length of 40 cm. This gave a volume of pyrolysis of 101787 μm^3 or 0.0101787 cm^3, required by RMG. The flow rate of helium was 2 mL/min (or 2 cm^3/min). The absolute and relative tolerance of the system (i.e., atol and rtol) were kept at 1e-16 and 1e-8, respectively and the model had a toleranceKeepInEdge = 0.0, toleranceMoveToCore = 0.1 and toleranceInterruptSimulation = 0.1 to allow, in the case of MTBE, most moieties to be included within the core of the simulation. The maximumEdgeSpecies was set at 8000, and other constraints were kept above the required MTBE carbon number, with maximumCarbonAtoms = 30, and maximumRadicalElectrons = 8, to allow the study of combination reaction (if occurring).

Table 5.3 MTBE residence time within the pyrolyser for each pyrolytic temperature.

Temp pyrolysis (ºC)	Residence time (seconds)
250	0.217
450	0.157
500	0.147
550	0.138
600	0.130
650	0.123
675	0.120
700	0.117
750	0.111

MTBE pyrolysis was modelled using RMG for the following pyrolytic temperatures, also investigated through the prep-GC system: 250°C, 450°C, 500°C, 550°C, 600°C, 650°C, 675°C, 700°C and 750°C. Due to the small size of this molecule (i.e., 5 carbons), the execution time for this model was short (i.e., less than one hour on the Orion Cluster of Dr Umer Ijaz from the University of Glasgow, Civil Engineering).

5.4. Results and discussions

5.4.1. Main findings

In this chapter, the pyrolysis of MTBE on the improved prep-GC was achieved and accompanied by 4 lines of evidence, i) the pyrolysis and identification of MTBE and its pyrolysates within the prep-GC system, ii) transferred to a second GC-FID and iii) to a GC-MS. The highlighted aspect of this work is the transfer to a GC-MS via the heated line which confirms the ability to inject in a GC-IRMS, with the available lab instruments also capable of individual sample analysis, expanding the types of analysis and lowering the PSIA system costs. These previously discussed instrumental and methodology limitations were thus overcome. The fourth line of evidence is introduced by results generated through pyrolysis simulations done in RMG software; these evidence replicate the experimental results and are discussed in relationship with the previous work of Gauchotte-Lindsay et al. (2009), confirming that RMG can be used in the following chapters as an *in-silico* assessment to understand the breakdown of other targeted compounds.

5.4.2. Pyrolysis tubing

In order to achieve pyrolysis of high molecular weight (HMW) compounds such as hopanoids within the available pyrolytic unit, 5 different types of tubing were tested. Given the narrow ID of the pyrolyser (1 cm) and the aimed flexibility of the prep-GC system, the tested tubing had to be flexible or designed in a U-shaped, returning into the pyrolyser and GC oven to avoid cold spot formation for later HMW compound pyrolysis. Testing was done with variable injection amounts of MTBE (1-0.5 µL), different injection splits (splitless →
80:1), with a carrier gas flow between 0.5 → 2 mL/min. For each tubing option, this tested whether a smaller amount of compound or a longer residence time within the pyrolyser led to pyrolysis or to different pyrolytic behaviours. The pyroliser's temperature was also varied between 200-865°C. The tubes tested for pyrolysis were:

- Quartz tube: a custom-made quartz tube, ID 4 mm (Figure 5.8.d)
- Steel tubing: a stainless-steel tubing, ID 1/16" (Figure 5.8.c)
- Ultimetal: an Agilent UltiMetal column, ID 250 µm (P/N CP6575, Agilent)
- DB-5: a piece of DB-5 column, ID 250 µm

- Fused-silica (FS) capillary: fused silica deactivated capillary columns, ID 180 µm or 250 µm (Figure 5.8.a and b, P/N 137296-1, Restek)
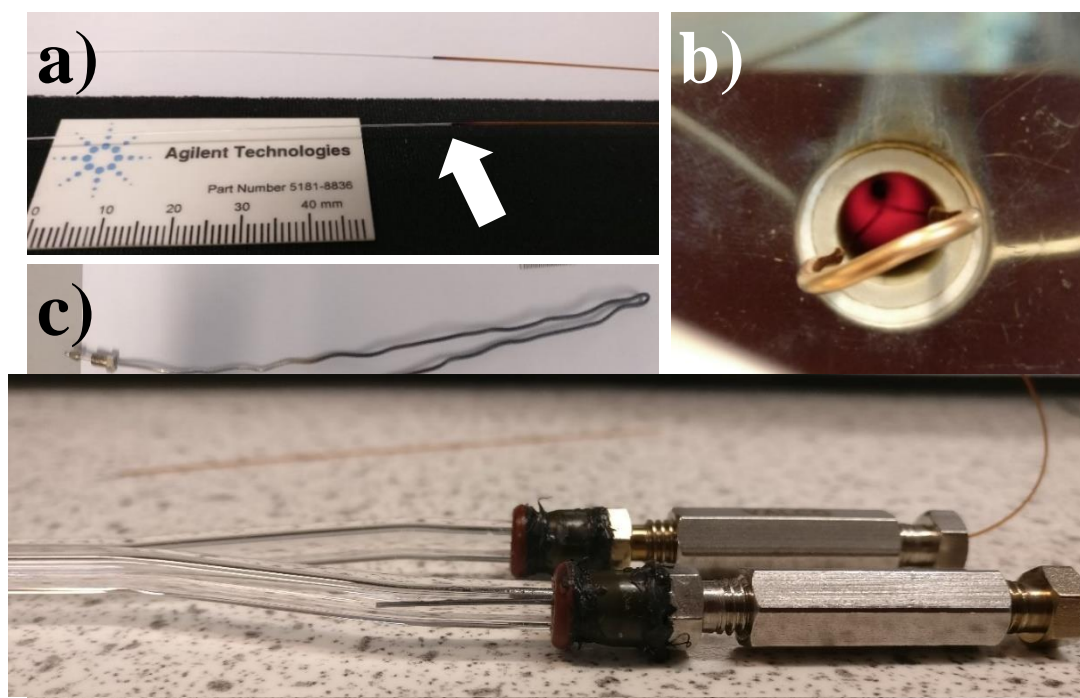
Figure 5.9 Valco connections made to accommodate custom made quartz tube. Ferrules (P/N 5080-8774) and O-rings (P/N 5181-3344) were connected to Valco nuts and made air tight using silicone (Visbella HT RTV Silicone Gasket Maker). Two Ultimetal 3.5 cm column pieces were extended within the quartz tube and connected to the union using P/N 20142 Restek ferrules.

The **quartz tube** was custom-made, with an ID of 4 mm, designed in a similar fashion to the glass U-tube of the Cool-Cube holder and to reproduce Gauchotte-Lindsay et al. (2009) work in which a straight quartz tube was used. The tube was produced by the Glass Blowing facilities, School of Chemistry, University of Glasgow. The quartz material that was used was selected to withstand pyrolytic temperatures up to 950°C-1000°C. Two in-house connections were made to accommodate the pyrolytic tube and the system's capillaries. Leak testing was conducted by submerging its end and unions in solvent and passing carrier gas through the tubing, indicating that the quartz tube was air-tight. MTBE was tested at various pyrolytic temperatures at which the compound should have broken down (500°C-800°C). No pyrolysis took place and a wide MTBE peak eluted given the wider ID of the quartz tube, indicating that this option was unsuitable for pyrolysis and assessing any produced pyrolysates. It is possible that the wider ID of the tube, together with its thicker walls and low thermal conductivity of the quartz material (i.e., 3 W/(m·K), Material-Properties, 2024) lead to conditions unsuitable for pyrolysis, and would have led in the end to a less reliable pyrolytic reaction given the longer time the compounds would have spent in the pyrolytic zone.

The **steel tubing** (ID 1/16") was tested due to its resistant and bendable nature, its narrower ID compared to the quartz tube and higher thermal conductivity (~45 W/(mK), Thermtest, 2021). At temperatures above 550°C, this stainless-steel tube displayed incandescence, indicating the area with the highest temperatures for pyrolysis (also seen in Figure 5.8.b). When removed from the pyrolyser, the 1/16" stainless-steel tube had a degraded and porous exterior. The interior of the tube was assumed to have the same aspect. While this change in outer appearance allowed for more exact measurements of the length through which pyrolysis could have taken place that is required for RMG modelling (Subsection 5.3.6.), it also raised questions about the possibility of active sites within the tube and internal tube damage. No compound, apart from MTBE, reached the FID when the pyrolyser was between 200-865°C and, overall, given the lack of results and decayed aspect of the tubing, it was considered unsuitable for pyrolysis.

One **Ultimetal column** from Agilent (P/N CP6575) was tested as it presented again a robust alternative that can be easily bent within the pyrolyser. Compared to the previous two options, this tube had the advantage of having a similar ID as that of the capillary columns within the prep-GC oven (ID 0.25 µm), maintaining the carrier gas pressure constant as it entered the pyrolyser and allowing the residence time within the pyrolyser to be easily calculated and modified. No pyrolysis took place, assessed through the production of new compounds and a decrease in MTBE peak area, making this tubing unsuitable.

Finally, **capillary columns** were fitted in the pyrolyser and tested as used by Corso and Brenna (1997). However, their design, as shown in Figure 2.10, had the advantage of connecting the capillary to a transfer line, in a straight fashion, as it exited the pyrolytic chamber. The **DB-5% Agilent column** could not be fitted without breaking once the U-bend was created yet the **deactivated Fused Silica (FS) capillary** was flexible enough to withstand the initial bend. For MTBE, the FS capillary was placed outside the pyrolyser and was fitted through a short (5 cm) copper 1/16" tube for reinforcement as seen in Figure 5.8.b. Overall, the length of the FS capillary was measured at 95 cm before being placed within the pyrolyser. It was seen that above 500°C the coating is degraded, leaving behind clear capillary (Figure 5.8.a). This can be used to measure the exact length over which pyrolysis takes place (i.e., where temperatures are higher than 500°C) for RMG modelling, once the column is removed from the pyrolyser. The FS capillary proved to be a good setup for low molecular weight compounds as, although in contact with the atmosphere and thus defined as a "cold-spot", the temperatures were not low enough to condense the compounds in gas phase. MTBE was pyrolysed using deactivated FS capillaries, with the results presented in the following subsections.

5.4.3. Experiment 1: Pyrolysates analysis within the prep-GC-FID

Experiment 1 consisted of the first pyrolysis and identification of MTBE and its pyrolysates within the prep-GC system. The objectives of this experiment were to i) test the pyrolysis capability and reproducibility of the FS capillary and prep-GC system and ii) test if the pyrolysates can be separated, identified and comparable to previous experiments (Gauchotte-Lindsay et al., 2009).
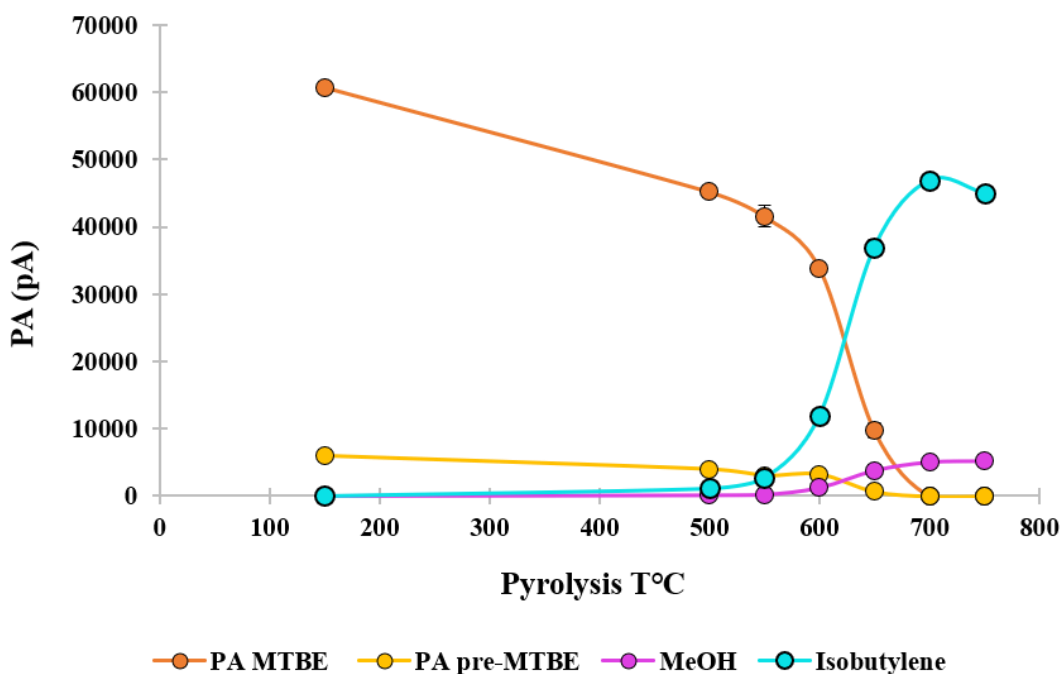
Figure 5.10 Peak area of MTBE and pyrolysates as analysed on the FID of the prep-GC. Triplicate measurements for temperatures between 500°C and 750°C. Chromatograms and identification of peaks done in Figure 5.17. Error bars as SD (standard deviation) from triplicate measurements.

Table 5.4 Average PA and SD for compounds plotted in Figure 5.10 for n=3 for temperatures between 150°C-700°C and n=1 for 750°C.

Temperature pyrolyser (°C)	Average PA (n=3)				SD (n=3)			
	MeOH	pre-MTBE	Isobutylene	MTBE	MeOH	pre-MTBE	Isobutylene	MTBE
150	0	5929	0	60739	0	0	0	0
500	119	3984	1120	45202	10	327	54	603
550	204	3052	2682	41558	4	123	92	1570
600	1233	3240	11975	33870	136	275	255	694
650	3815	683	36970	9724	776	126	1130	1074
700	5073	0	46876	0	155	0	492	0
750*	5233	0	44941	0	0	0	0	0

176

Pyrolysis was assessed as a decrease in the peak area (PA) of the parent MTBE (calculated at a non-pyrolytic temperature) at the expense of new peaks forming within the system with increasing pyrolytic temperatures. Initial identification of compounds (Figures 5.10 and 5.11) was based on PA, previous results (Figure 5.12) of Gauchotte-Lindsay et al. (2009) and the expected interactions between MTBE, its pyrolysates and the second capillary column (i.e., Cc2, Table 5.1). The two main pyrolysates expected for this study were methanol (MeOH) and isobutylene.

When integrated, PA results are highly reproducible, with triplicate measurements for each pyrolytic temperature. The PA of MTBE measured 60739 pA at 150°C, decreased to an average of 33870 pA at 600°C and the compound was completely pyrolysed at 700°C. The provided standard deviation (SD) values were between 1.8-20‰ for methanol, 1-4.8% for isobutylene, 4-18% for pre-MTBE, and 1-11% for MTBE (standard deviation error bars provided in Figure 5.10) indicating that FS capillary is a suitable pyrolysis tubing and that the overall prep-GC system is apt for pyrolysis.

Figure 5.11 shows the pyrograms for each temperature. The RT of the MTBE and pre-MTBE peaks, and that of the produced pyrolysates, shifted from 150°C to 500°C and with increasing pyrolytic temperatures. This was also observed in the case of toluene analysed during the same experiment (Appendix A.5.2.) and it is due to the increased temperature in one part of the system caused by the pyrolyser. The oven was set isothermal at 100°C, a temperature at which MTBE and its pyrolysates are unretained on the column. As the temperature within the pyrolyser is increased, the viscosity of the carrier gas also increased (Ettre, 1984) in that part of the system, until the carrier gas cooled down to the oven's temperature. The increase in viscosity leads to a decrease in flow rate and to an increase in the hold-up time (McCann et al., 2020), increasing the RT of MTBE and pyrolysates and the times they reach the FID. This was not observed in Gauchotte-Lindsay et al. (2009) as seen in Figure 5.12, yet the presence of the split vent after the pyrolytic unit in System 4 (Figure 2.14) could have prevented the formation of a high-pressure point.

In the 150°C pyrogram, a minor peak eluted (arrow; yellow peak) before the main MTBE peak (orange peak; MTBE). The 1µL injection done in splitless mode was reduced through the incorporation of a high split (100:0) to not overload the pyrolyser (i.e., MTBE had an elution time over 1 min when splitless) and to provide a well-defined peak for pyrolysis, with a short retention time. When a split was applied, a minor fronting peak appeared, well resolved from the main MTBE peak of interest (Figures 5.11 and 5.14). During this experiment, this compound was not removed by means of valve switching. This was done

however for Experiments 2 and 3. As 150°C was not considered a pyrolytic temperature, the pre-MTBE peak was not considered a pyrolysate. Nonetheless, their different elution times, led to the two peaks entering the pyrolyser as two separated compounds. As seen in Figure 5.11, the presence of the pre-MTBE peak co-elutes with MTBE pyrolysates, making identification and quantification difficult in the absence of an MS detector. Furthermore, although this was not obvious in Experiment 1, it can also lead to undesired secondary reactions, as pyrolysis of the pre-MTBE peak takes place before the main MTBE pyrolysis and, given the different residence time of pyrolysates, recombination reactions between pyrolysates of prep-MTBE and MTBE may occur. For this reason, the pre-MTBE was heart-cut in the following experiments, when the main MTBE peak was pyrolysed and transferred to a second GC system.

A first well-defined pyrolysate is seen at 500°C (blue compound in Figure 5.11) which continued to increase in PA with increasing pyrolytic temperatures. At 550°C a second pyrolysate is more pronounced at this intensity resolution (purple peak) which again, increased in PA and height in the following pyrograms (Figure 5.10). As MTBE breakdown was promoted by higher temperatures, its peak area started to decrease and MTBE completely disappeared when subjected to 700°C, indicating quantitative pyrolysis, with two main pyrolysates appearing. Although not apparent on the 700°C pyrogram, two new yet minor pyrolysates also started forming (Appendix A.5.3). At 750°C, the two main pyrolysate peaks are still present, as well as several other minor secondary pyrolysates (red and green arrows in Figure 5.11). These compounds were thought to have formed from the pyrolysis of the two primary pyrolysates seen until this temperature. Figure 5.10 shows that at 750°C the peak area of the blue compound starts decreasing, indicating secondary pyrolytic breakdown.
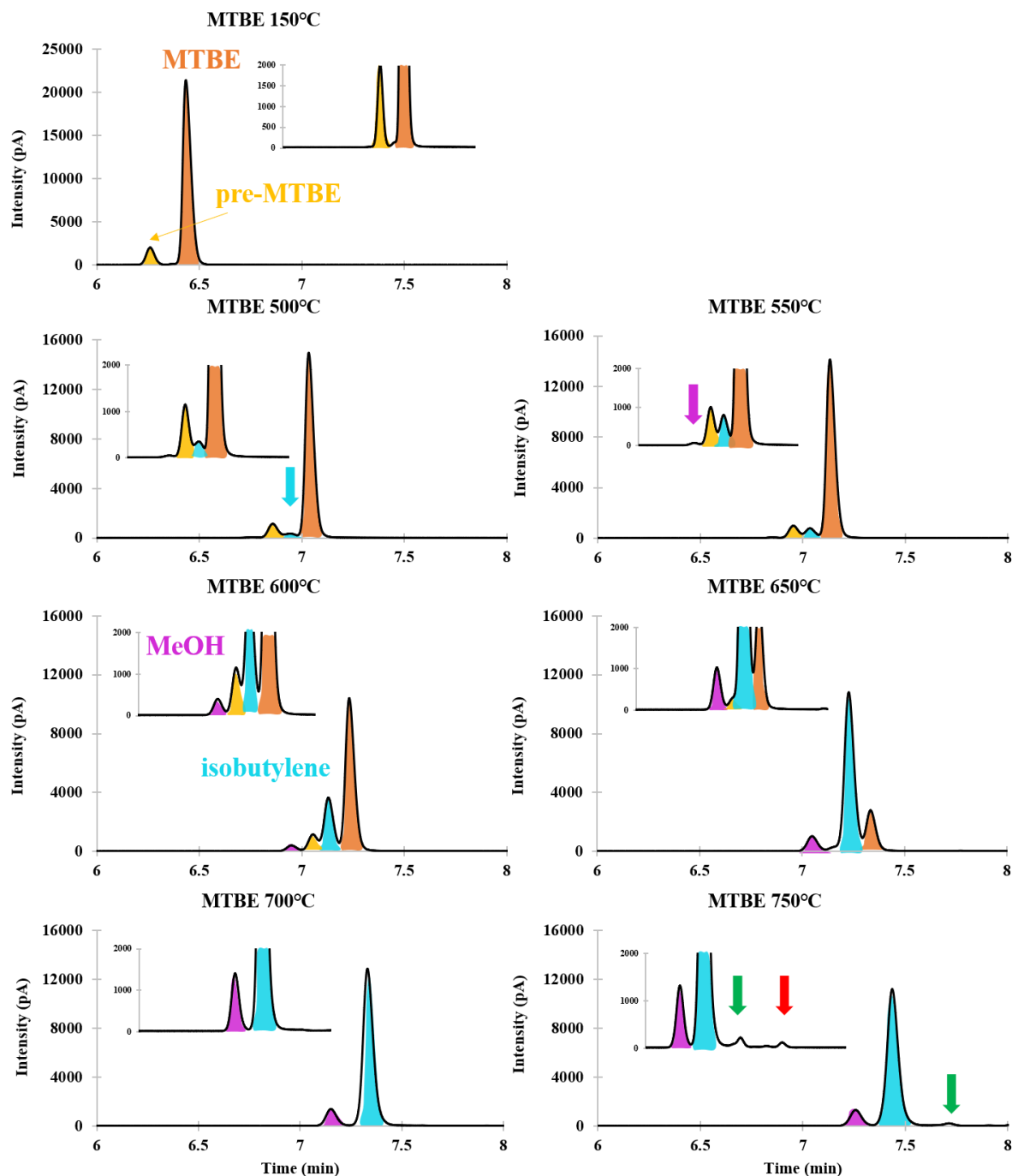
Figure 5.11 Chromatograms of MTBE pyrolysis and transfer to the prep-GC-FID. Colour coding: Orange=MTBE; Yellow=pre-MTBE; Blue=Isobutylene; Purple=MeOH. Notice the occurrence of both pre-MTBE and MTBE from 250°C to 650°C, both peaks disappear at higher temperatures. At 700°C only MeOH and Isobutylene are seen, and at 750°C secondary reactions take place, with pyrolysates being produce at the expense of MeOH and isobutylene.

By comparing the current results with those of Gauchotte-Lindsay et al. (2009) acquired on the previous version of the prep-GC for the pyrolytic temperature of 650°C (Figure 5.12), the prep-MTBE peak is the only extra compound that appears in the current pyrograms (making abstraction of the benzene that was used in the previous work as an internal standard). MTBE and two main pyrolysates were hypothesised in Experiment 1 to be isobutylene and methanol. As the second-dimension column (i.e., Cc2) had a low polarity, mainly selecting the molecules based on their molecular size within a system set isothermal at 100°C, the first peak (purple) was assessed based on its RT, PA and peak height as methanol (i.e., 1-carbon compound), the pre-MTBE peak and MTBE were matched with their previous relative RTs seen at the non-pyrolytic temperature of 150°C and finally, the blue peak, seen as a major pyrolysate after the temperature of 650°C was identified as isobutylene, a 4-carbon compound eluting before its higher molecular weight parent.
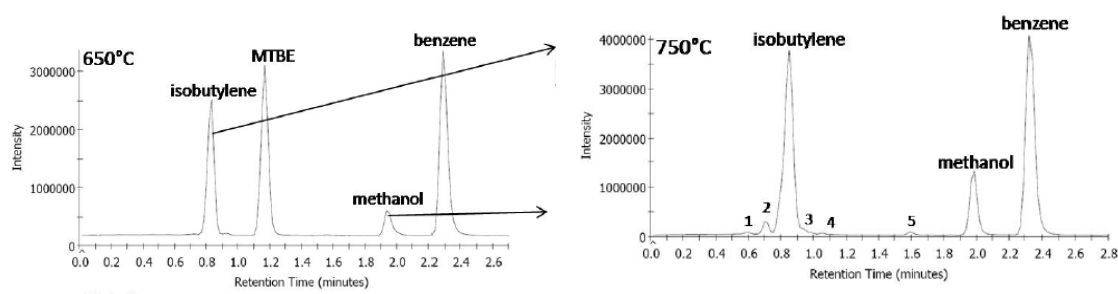
Figure 5.12 Data generated by Dr Gauchotte-Lindsay, C., PhD thesis (2009). MTBE pyrolysis at 650°C and 750°C, with benzene used as an internal standard. Notice at 650°C that isobutylene and MeOH are present along unpyrolysed MTBE while at 750°C, MTBE completely pyrolyses, and secondary compounds (peaks) start to form.

In order to confirm the above peak assignment, a pure methanol sample was injected on the prep-GC method with the pyrolyser set at the temperature of 650°C to compare RT with the assumed methanol peak resulted through pyrolysis. A fronting peak is also seen for this run and methanol (red chromatogram in Figure 5.13) eluted slightly sooner than the inferred methanol peak. The retention time difference is possibly due to the slightly later time at which methanol was produced within the pyrolyser (i.e., several cm within the furnace) while pure methanol entered and exited the pyrolyser unaffected at this temperature. Based on the relative retention time comparison, pyrolysate production and comparison with previous results (Gauchotte-Lindsay et al., 2009), this peak was identified at this stage as methanol, leading the remaining peak to be identified as isobutylene.
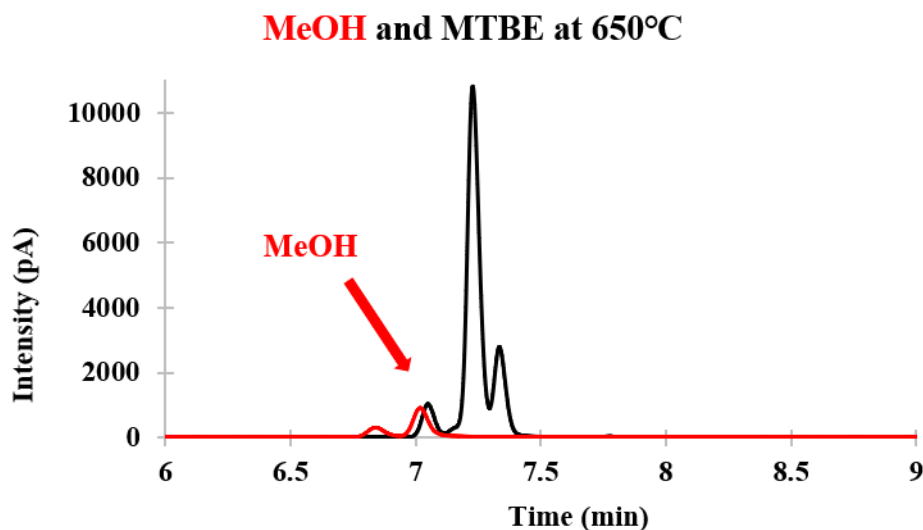
Figure 5.13 Overlap of MTBE (black graph) and MeOH (red graph) analysed on the prep-GC-FID done for the identification of MeOH.

5.4.4. Experiment 2: Pyrolysate transfer to second GC-FID

Experiment 2 involved the transfer of pyrolysates to a second GC-FID system by employing a heated transfer line ending in an analytical micro-syringe needle (Figure 5.4). The transfer to a GC equipped with an FID was done in order to utilise an oven ramp for pyrolysate separation, which was not possible on the prep-GC system due to the low boiling points of MTBE and pyrolysates. This also allowed to safely assess the ability of the prep-GC to transfer pyrolysates via the heated transfer line to a similar system with a detector operating at atmospheric pressure. At this stage, it was not certain that the transfer line could be connected to a GC-MS and if the MSD could be safely used without contaminating the ion source or disturbing the vacuum required for analysis. With the valve ON (Figure 5.7), the RT of MTBE on Cc1 was measured, enabling to determine the timing for heart-cutting of MTBE. The pre-eluting minor MTBE peak was taken as a confirmation of correct injection on the prep-GC-FID (Figure 5.14; Appendix A.5.4.). Once the valve had switched OFF, the transfer line was manually injected into the inlet of the second GC-FID system, available to the left of the prep-GC.

MTBE: Retention Time for Valve Switch

pre-MTBE post heartcut at 600°C
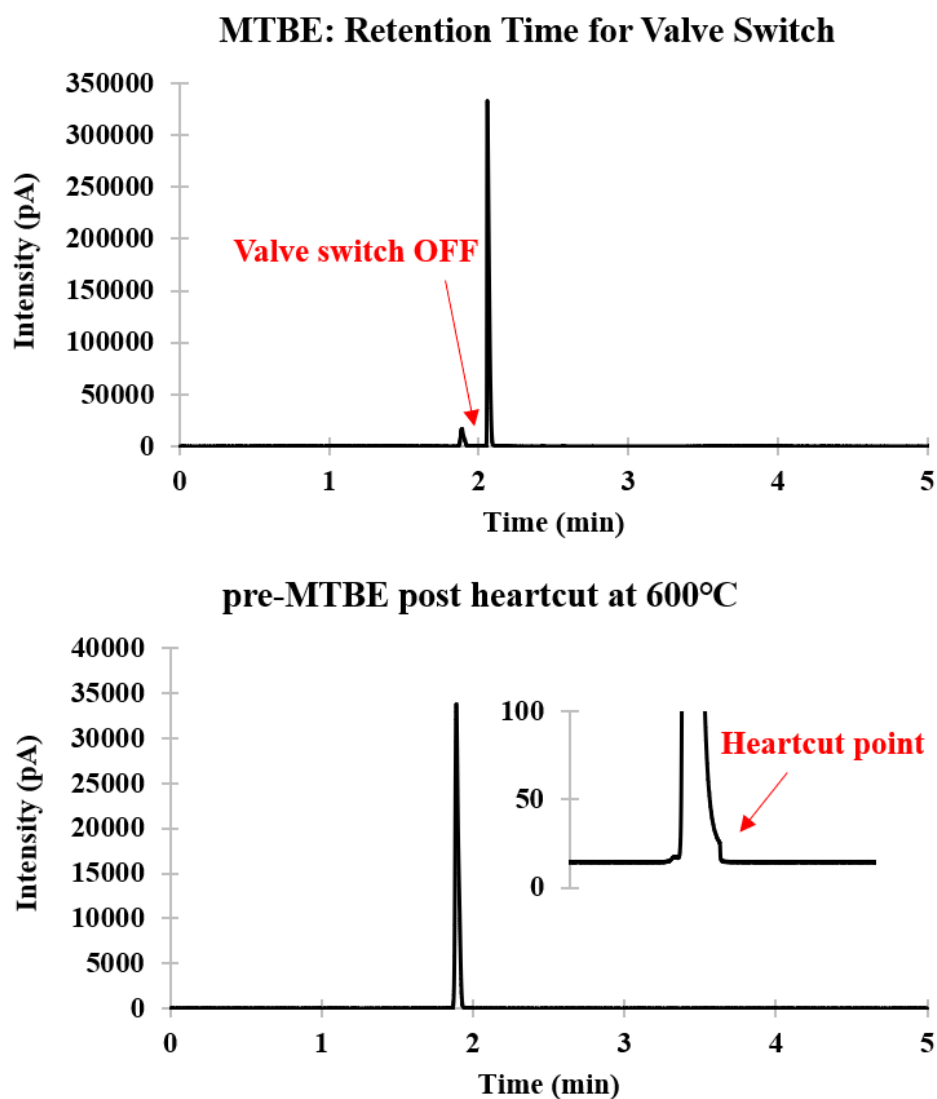
Figure 5.14 Top: MTBE seen on the prep-GC. First peak represents a pre-MTBE eluting peak. Bottom: Pre-MTBE peak eluting on prep-GC-FID with heart-cutting of main MTBE for transfer to a second GC-FID system. Notice

MTBE heart-cut, pyrolysis and transfer to a second GC-FID were successful and highly reproducible (Figure 5.15). The reported SD from all 3 transferred compounds was between 1-13% for the isobutylene PA, 0.3-16% for MTBE PA and 2.2-36% for methanol PA. These values are available in Table 5.5. When comparing with Experiment 1, the PA of compounds in the current experiment is considerably lower. This was attributed to the drop in the pressure experienced by the employment of the 2 m transfer line and its wider internal diameter (ID of 1/16") as no leaks were identified at this point to explain the loss of compound and to the lower flow in the second GC-FID.

The pyrolysates' behaviour is similar to what was seen in Experiment 1 (Figure 5.10). The PA of MTBE started decreasing after 450°C which was not observed in the previous experiment as this temperature was not investigated.

MTBE and pyrolysate PA on GC-FID2
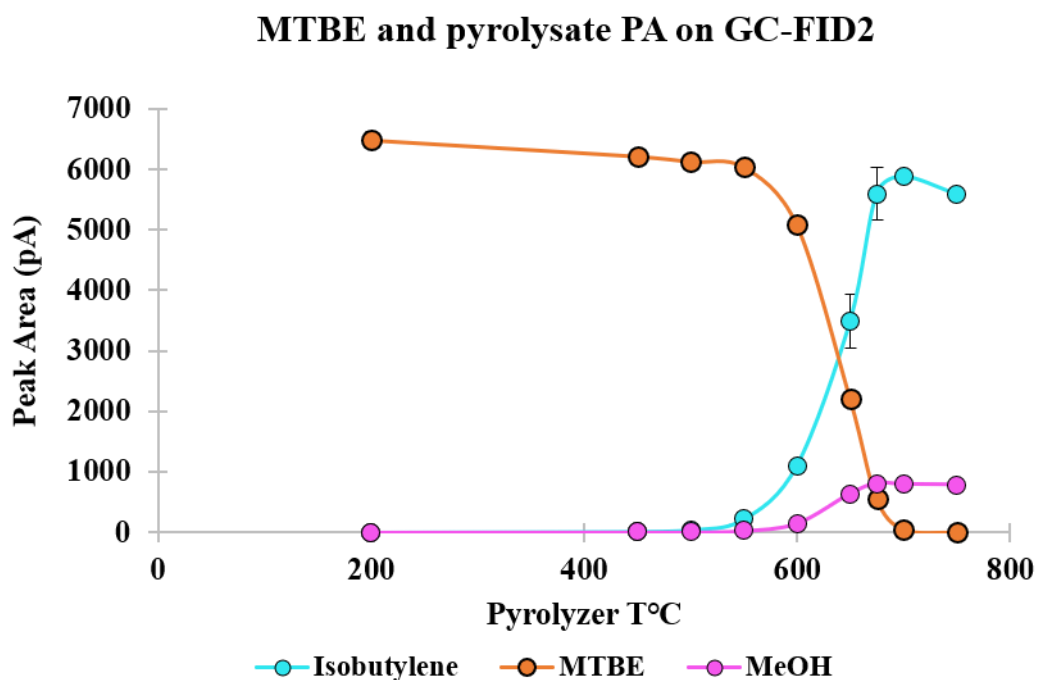
Figure 5.15 Pyrolytic decay graph of MTBE and formation of methanol (purple) and isobutylene (blue) pyrolysates, as recorded on the second GC-FID.

Table 5.5 Average PA and SD for compounds plotted in Figure 5.15 for n=3 for temperatures between 200°C-700°C and n=1 for 750°C.

Temperature pyrolyser (°C)	Average PA (n=3)			SD (n=3)		
	Isobutylene	MTBE	MeOH	Isobutylene	MTBE	MeOH
200	0	6485	0	0	141	0
450	14	6217	2	1	20	0
500	40	6130	4	4	47	1
550	214	6044	26	9	63	2
600	1102	5087	146	12	70	4
650	3485	2217	635	451	116	14
675	5593	560	805	430	7	32
700	5881	52	793	72	8	92
750	5591	0	784	0	0	0
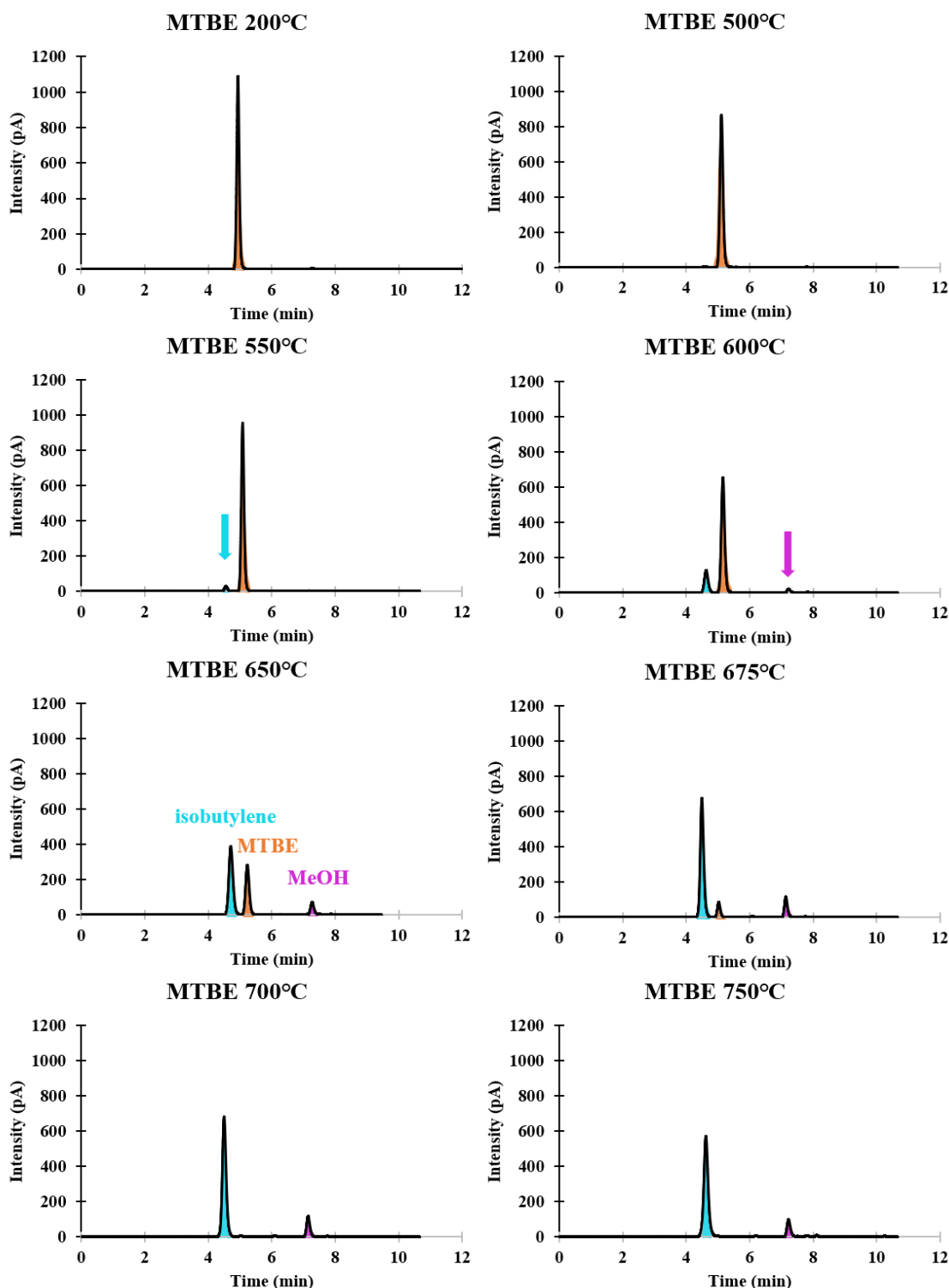
Figure 5.16 MTBE and pyrolysates transferred to a second GC-FID where separation took place. Column employed: 30 m ZB-Wax. Notice due to the high polarity of this column and low initial oven temperature at 30°C, MeOH eluting after isobutylene and MTBE.

As in Experiment 1, methanol (MeOH) was injected in the prep-GC system, sent to the pyrolyser set at 675°C and transferred via the heated line to the second GC-FID to identify the pyrolysates. The elution time of pure MeOH overprinted the late eluting peak in Figure 5.24, confirming its identity and that of isobutylene. During Experiment 2, a ZB-Wax

column was installed in the second GC-FID, which gave a different pyrogram than that seen in Experiment 1, with MeOH eluting last due to its higher polarity
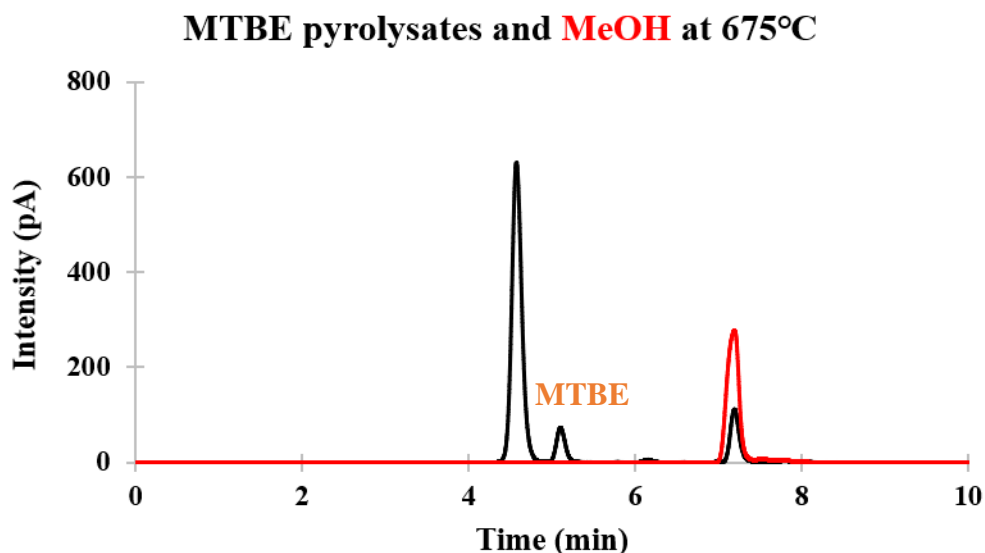
Figure 5.17 Overlap of MTBE pyrolysed at 650°C (black graph) and MeOH (red graph) analysed following the same method. Both chromatograms acquired on the second GC-FID after transfer from the prep-GC.

With increasing pyrolyser temperatures, the MTBE amount reaching the second GC-FID decreases due to pyrolytic breakdown, while methanol and isobutylene increase in PA, and thus in concentration. MTBE is still present within the system at 700°C (Figure 5.18), with methanol and isobutylene reaching peak concentrations. The occurrence of a small MTBE peak at this temperature was not observed in Experiment 1 due to co-elution. At 750°C, both pyrolysates decreased in concentrations, as secondary reactions took place. Figure 5.18 depicts zoomed-in chromatograms seen on the second GC for the temperatures of 650°C, 700°C and 750°C, highlighting secondary pyrolysate formation.

MTBE 650°C - zoom-in

MTBE 700°C - zoom-in

MTBE 750°C - zoom-in
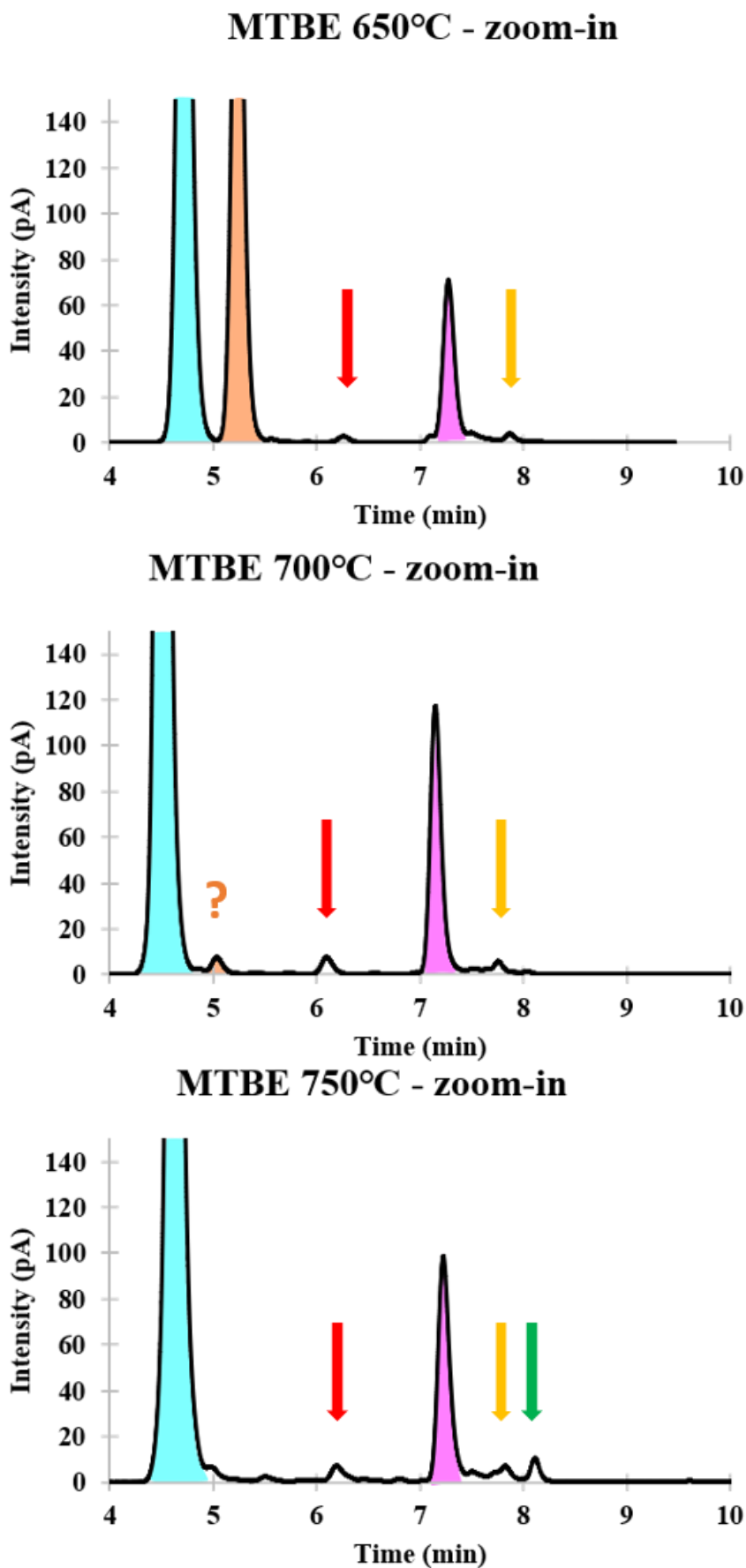
Figure 5.18 Zoom-in view on chromatograms showing the progressive breakdown of MTBE and occurrence of secondary pyrolysates. Minor secondary pyrolysates indicated by arrows.

5.4.5. Experiment 3: Pyrolysate transfer and identification on GC-MS

Experiment 3 confirmed by means of an MSD the identity of the pyrolysates, proving that the prep-GC system can be linked to a GC-MS without further system adaptations. This ultimately demonstrates that the pyrolysates can be safely sent to a GC-IRMS for isotopic analysis, which has a similar system configuration and requirements as a GC-MS.

The first transfer confirmed the identity of the pre-eluting MTBE peak at a pyrolytic temperature of 350°C. The ZB-Wax column was installed in the GC-MS, similarly to Experiment 2. The pre-MTBE has the same mass spectrum as the main MTBE peak (Figure 5.19). The scan range was lowered to *m/z* 30 after the initial full transfer to allow identification of low molecular weight compounds and MTBE was pyrolysed and transferred to the GC-MS.
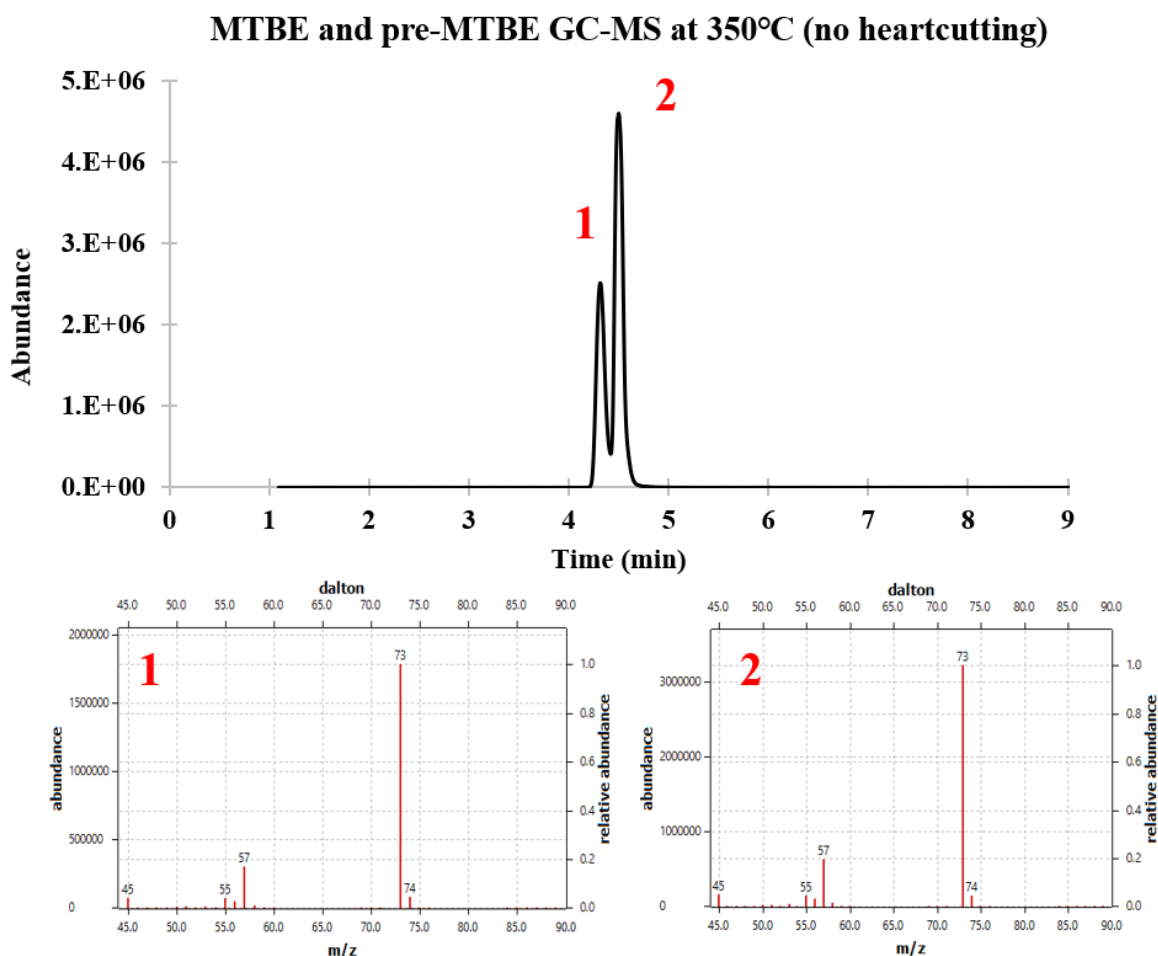
Figure 5.19 GC-MS identification of the two peaks when pure MTBE was injected. Peak 1 is named "pre-MTBE" given their similar mass spectra and was 'heart-cut' during MTBE (peak 2), pyrolysis experiment. Right graphs display abundance of a scanned mass-to-charge ratio (m/z) on the X-axis while on the Y-axis, the particular m/z fragment.

At 650°C, a temperature at which the parent molecule and the two main pyrolysates were previously seen, peaks 1 and 2 (Figure 5.20; Table 5.6) were both identified as O_2, the first peak considered the residual O_2 within the GC-MS column and source, while the second peak, eluting closely to isobutylene has most likely been introduced in the system via the transfer line and from the prep-GC system. Peaks 3, 5 and 8 were identified as isobutylene, unpyrolysed MTBE and methanol, respectively. Peak 9 is DCM, a contaminant introduced from the transfer line's needle as it was routinely used as a solvent to check the flow at the end of the transfer line. The remaining peaks are minor secondary pyrolysates, identified in Table 5.6. The pyrogram for 675°C presents the same peaks, with secondary pyrolysates having slightly higher concentrations. Peak number 4 is not seen at 675°C and the above temperatures however, given that at 650°C it co-elutes with isobutylene, it is expected to be fully overprinted by isobutylene in pyrograms at higher temperatures.

Table 5.6. Compounds from MTBE pyrolysis at 650°C from Figure 5.27.

Peak	Compound	Peak	Compound
1	Oxygen (O_2) MS source	5	**MTBE**
2	Oxygen (O_2) transfer line	6	Acetone
3	**Isobutylene**	7	2,5-dimethyl 1,5-Hexadiene
4?	1,1-dimethyl-Cyclopropene (or)	8	**Methanol**
4?	Isopentene (most likely compound)	9	DCM

Apart from confirming the mass spectrum of the pyrolysates, this provided an opportunity to verify secondary pyrolysates of MTBE obtained through the prep-GC pyrolysis and those obtained by Gauchotte-Lindsay et al. (2009) and available within the associated PhD Thesis annexe (Gauchotte, 2009).

In Experiment 2, a small amount of MTBE was still seen at 700°C (see Figure 5.18 – question mark indicating the presence of minor MTBE), with isobutylene and MeOH reaching peak concentrations at 700°C (Figures 5.15 and 5.16) yet several secondary peaks are seen forming lower temperatures, starting from 650°C on the GC-MS pyrogram, a temperature at which MTBE is still not fully pyrolysed. Secondary pyrolysates were not seen in the work of Gauchotte-Lindsay et al. (2009) for the temperature of 650°C yet this can be due to the different pyrolyser tube material (i.e., unpacked quartz tube vs FS capillary), inner diameter (i.e., 700 µm vs 250 µm) and overall, system.

MTBE transfer GC-MS at 650°C
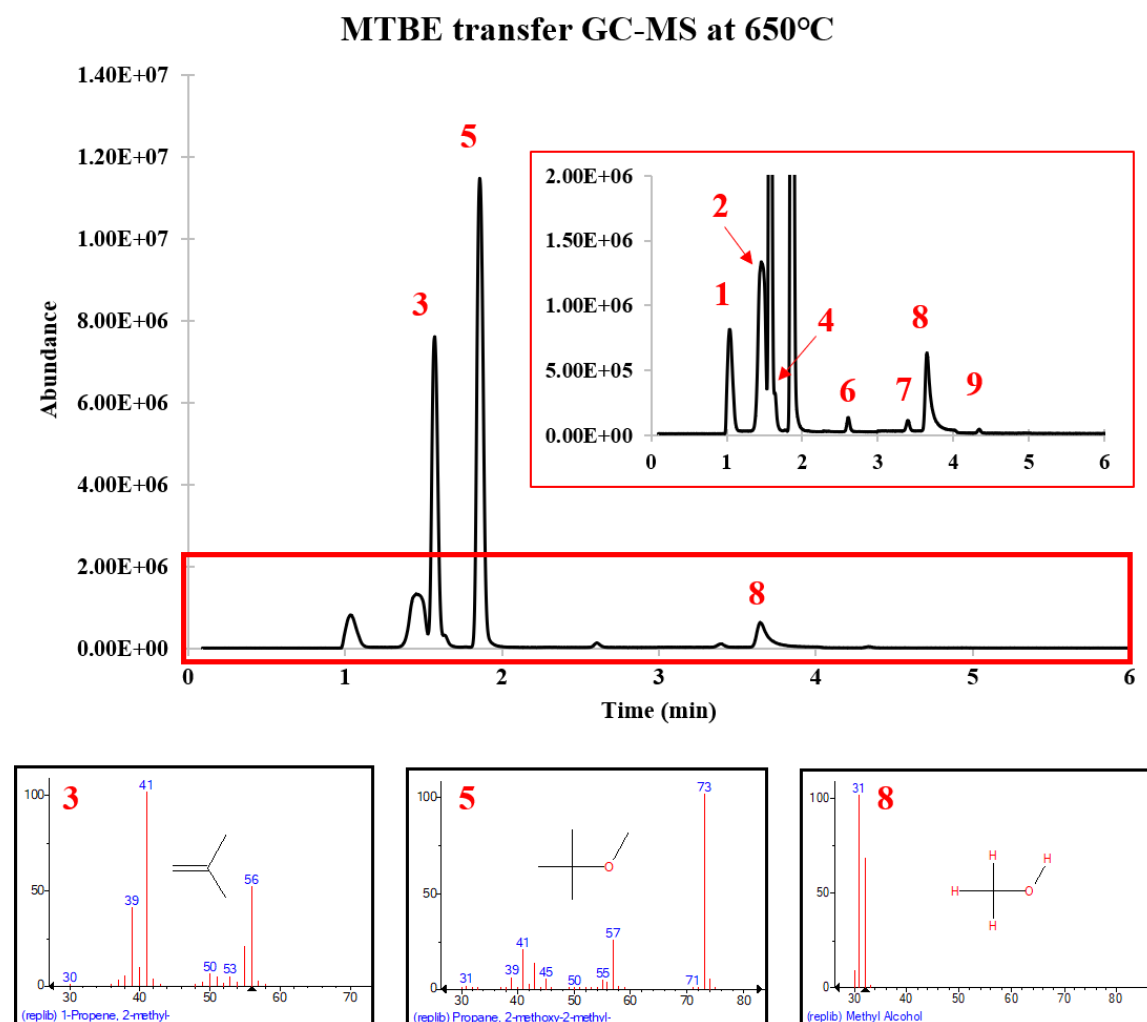
Figure 5.20 Pyrolysate identification on GC-MS equipped with a 30m WAX column after pyrolysis at 650°C. Peak 3 is isobutylene, peak 5 is the remaining unpyrolysed MTBE and peak 8 is MeOH. The remining compounds are identified in Table 5.6.

The comparison of secondary pyrolysates obtained during Experiment 3 and the data from Gauchotte-Lindsay et al. (2009) is done for the temperatures of 650°C and 750°C. The identification of compounds in Table 5.7 is done based on the best match and taking into account the molecular ion (M^+) and mass of the compound as seen on the mass spectrum. The mass spectra included column and septa bleed ions (i.e., *m/z* 73, 207, 208 etc.) which lowered the identification confidence of the software. The mass spectra of these compounds are provided in Appendix A.5.5.

Several compounds were similar between the two different experiments and pyrolytic systems. Isopentene, a secondary pyrolysate previously reported in Gauchotte (2009)'s PhD thesis was seen in the current 650°C pyrogram and it is believed that this compound still occurred at 750°C yet it was co-eluting with isoprene. 1,3-Pentadiene was also a potential compound (i.e., two potential compounds with a similar mass spectrum) identified by

189

Gauchotte-Lindsay et al. (2009) as well as acetone. In this experiment, however, several cyclic compounds were identified, which were not seen in the previous work. Apart from oxygen atoms of MeOH and acetone, oxygen atoms are not involved in any further secondary pyrolysates, which is also later confirmed by RMG results.

MTBE transfer GC-MS at 750°C
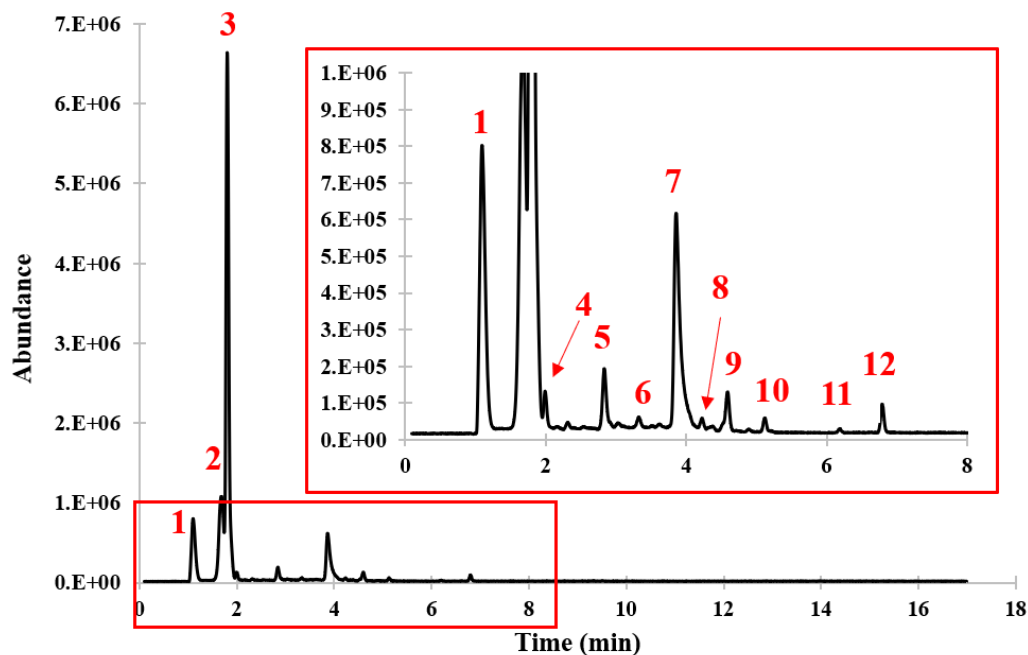
Figure 5.21 Peaks seen after MTBE was pyrolysed at 725°C and transferred to a GC-MS. Zoom-in view of minor peaks identified in Table 3.4. Similarly, as in Figure 3.42, peak 1 have a later eluting "shoulder".

Table 5.6 Compounds and molecular structures of 750°C MTBE pyrogram from Figure 5.21.

Peak	Compound	Peak	Compound
1	Oxygen (O_2) MS source	**7**	**Methanol**
2	Oxygen (O_2) transfer line	**8**	1-methyl-1,4-Cyclohexadiene
3	**Isobutylene**	9	Benzene
4	1,3-Pentadiene	10	1-Methylcyclohexa-2,4-diene
5	Acetone	11	Toluene (most likely)
6	Unidentified	**12**	1,3,5-Cycloheptatriene

5.4.6. RMG calibration for MTBE

MTBE pyrolysis was modelled using the rate-based software RMG and results were compared to data obtained by Gauchotte (2009) and from the current prep-GC system setup in Experiments 1, 2 and 3. Previously presented data indicated that after pyrolysis at 650℃, MTBE was still present alongside its two main pyrolysates, isobutylene and methanol while at 750℃, MTBE was completely pyrolysed, and minor secondary pyrolysates were present alongside isobutylene and methanol. RMG simulations display the same pyrolytic behaviours for these two temperatures (Figure 5.22), indicating that the RMG-adapted code
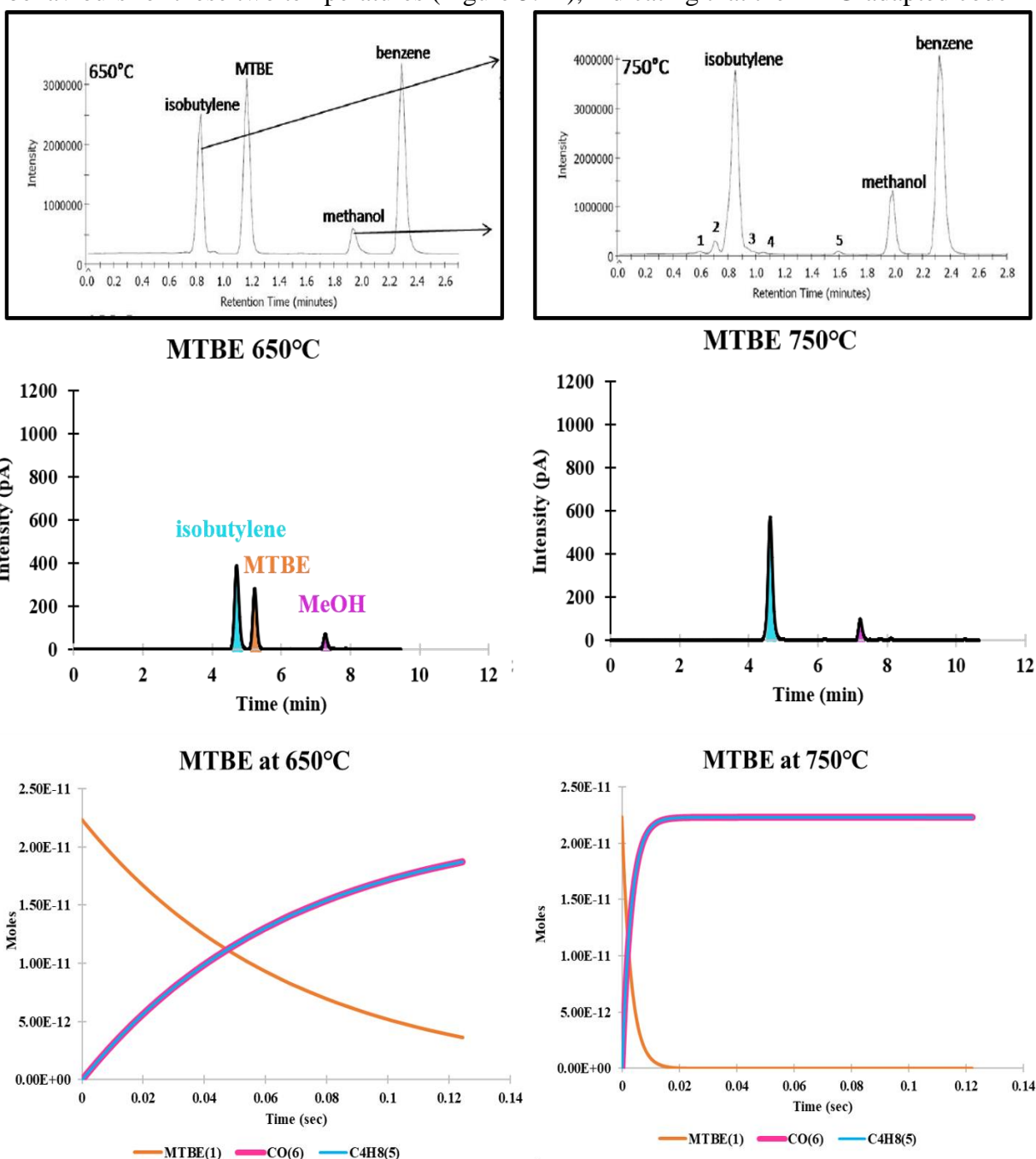
Figure 5.22 Comparison between MTBE pyrolysis results obtained by Gauchotte-Lindsay et al. (2009) and Gauchotte, 2009 (top), recorded on the second GC-FID after transfer from the prep-GC in Experiment 2 (middle) and RMG simulations.

191

for MTBE pyrolysis is compatible with the prep-GC system setup and experimental results. RMG can be thus used to provide further information on the processes and reaction rates that are taking place during pyrolysis and to inform on the pyrolysis of further molecules investigated in this thesis.

The simulated pyrolysis results in Figure 5.24 indicate that minor breakdown of MTBE occurs at 500°C, and increases with increasing pyrolytic temperatures. Molecular breakdown is represented by RMG as a decrease in the number of moles of the parent molecular and an increase in that of the pyrolysate(s). Until 675°C, only MTBE, isobutylene and methanol are present in the simulated system, the latter two primary pyrolysates occurring in equal amounts. Until this temperature, the core RMG simulation contains only the MTBE breakdown reaction into isobutylene and methanol (Figure 5.23). RMG also provides H_{298} (standard enthalpy of formation) values required for the formation of the two species (pyrolysates), to form MTBE (Figure 5.23). The bond dissociation energy (BDE) has the opposed value of H_{298}, calculated by RMG at 14.73 kcal/mol, attributed to the 1,3_Insertion_ROR reaction. At 750°C, apart from the main dissociation of the C-O bond that leads to the formation of methanol and isobutylene, RMG predicts the formation of several secondary pyrolytic products from primary pyrolysates, whose BDEs are displayed in Figure 5.23.
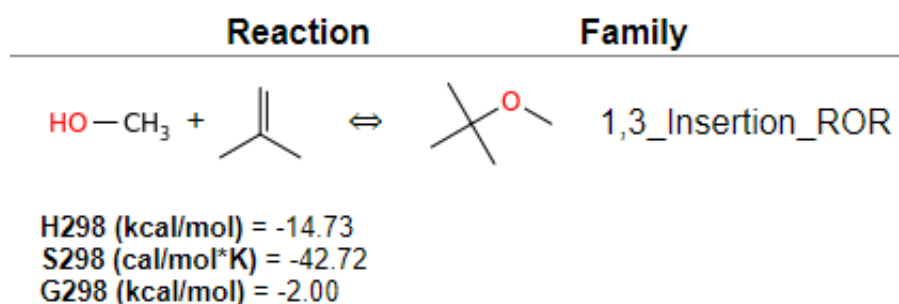
Figure 5.23 Thermodynamic data and mechanisms of MTBE pyrolysis as provided by RMG.

It was of interest to understand at this point how well the three different lines of data comply with each other, and if RMG was able to predict within its core simulation the experimentally obtained secondary pyrolysates. For the temperatures of 700°C and 750°C in RMG, the secondary pyrolysates within the core of the simulation are plotted separately from the main pyrolysates given their reduced concentration (Figure 5.24). Table 5.8 compiles the secondary pyrolysis products seen in the core results of RMG simulations for 700°C and 750°C, to allow comparisons between RMG results, pyrolysis on the prep-GC and data of Gauchotte (2009).
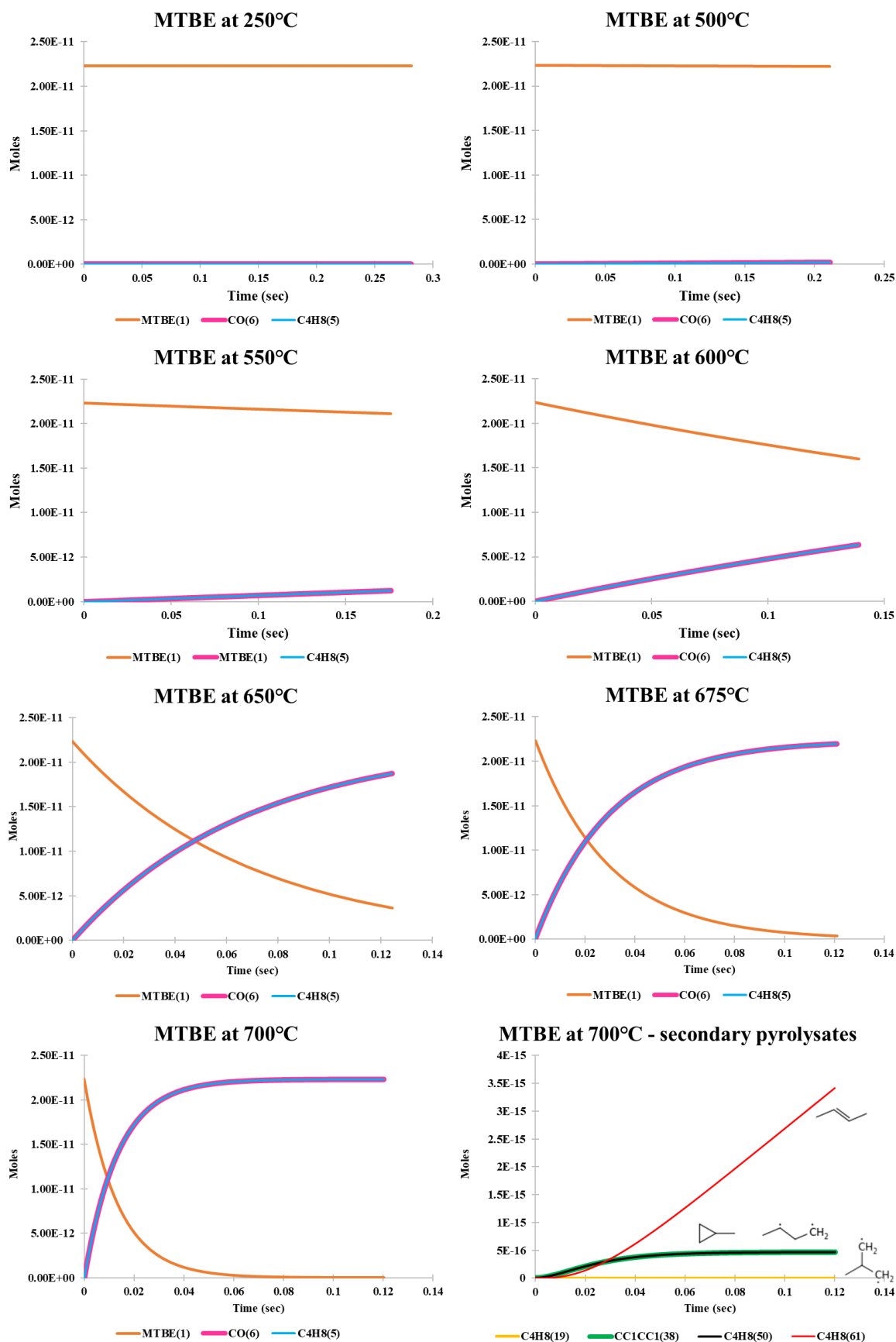
Figure 5.24 RMG predicted behaviour of MTBE pyrolysis between 250°C and 750°C (continued following page). For the pyrolysis temperatures of 700°C and 750°C, secondary pyrolysates are also plotted.

193
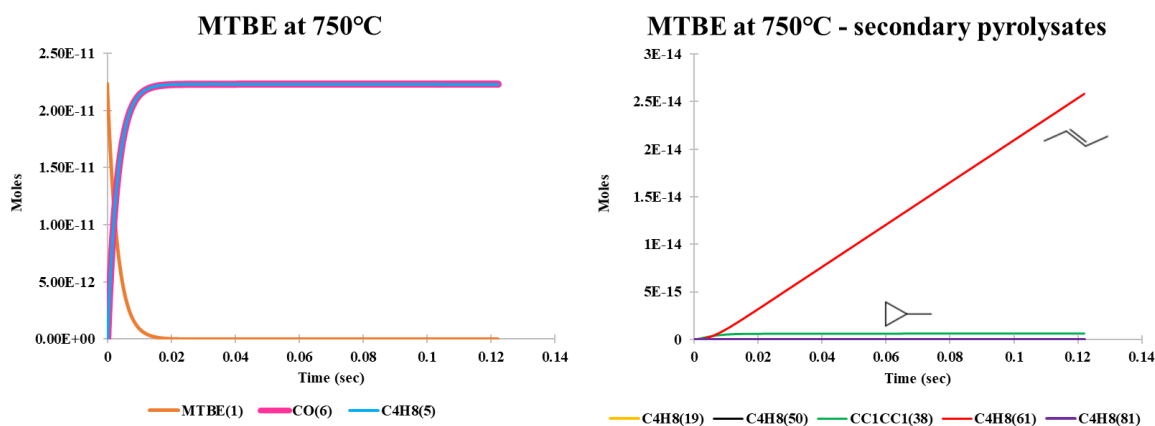
Figure 5.24 Continued.

Table 5.7 Chemical structure of secondary pyrolysates predicted by RMG as provided by the software when simulated at pyrolytic temperatures of 700℃ and 750℃.

700℃	750℃
(19) ĊH₂ / CH₂ structure	(19) ĊH₂ / CH₂ structure
(38) △ 1-Methylcyclopropane	(38) △ 1-Methylcyclopropane
(50) CH₂ radical structure	(50) CH₂ radical structure
(61) 2-butene	(61) 2-butene
	(81) butane

RMG data compared to GC-MS results

The occurrence of the RMG compounds from Table 5.8 in MTBE experimental pyrograms is discussed further. To avoid damaging the GC-MS source, the scan range selected was above *m/z* 30. **The** RMG edge results and the 750℃ pyrolysates thus cannot be entirely compared. This eliminates RMG species that contain 2 or 1 carbons, however, none of Table 5.8 compounds were identified in GC-MS results.

RMG core results: Compared to the results obtained from Experiment 3, in RMG simulations (Figure 5.24), methanol is not involved in further pyrolytic reactions within the core of the simulation as no oxygen atoms are seen in the secondary pyrolysates (i.e., no acetone formation); only isobutylene is further pyrolytically altered to different species. The software is designed to simulate reaction mechanisms for species that include carbon,

194

hydrogen and oxygen, thus secondary pyrolysates containing oxygen should have been taken into account if they would have formed in high enough amounts to be included within the core results of the simulation.

From Experiments 1 and 2 (Figures 5.10 and 5.15), it is seen that both methanol and isobutylene breakdown at 750°C, indicating that methanol is also used in the formation of secondary pyrolysates, yet this was not the case for the RMG simulation at the same temperature. The current GC-MS pyrograms also indicate the formation of **acetone**, and this compound is not found within the core or edge of the RMG simulations, yet was observed in Gauchotte (2009).
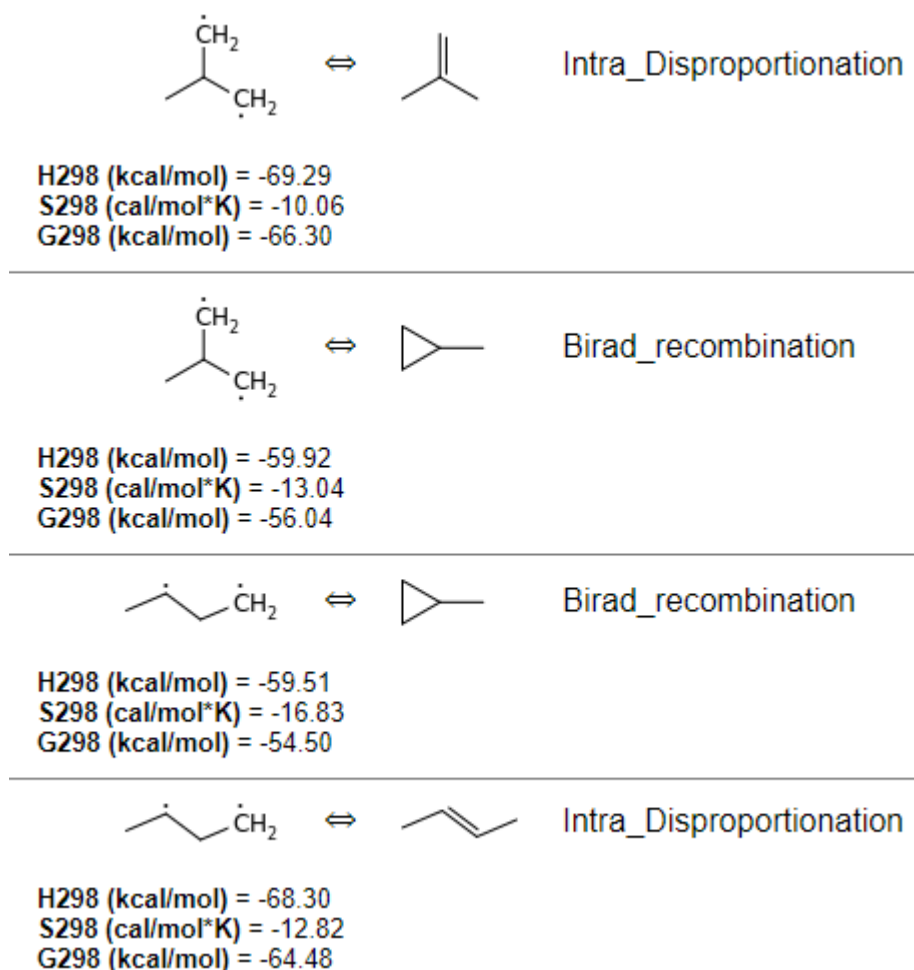
Figure 5.25 RMG predicted pyrolysis mechanisms for the formation of pyrolysates.

Secondary pyrolysates that occur within the **core** of the simulation are plotted in Figure 5.24 for the temperatures of 700°C and 750°C. One particular compound, **2-butene** (C_4H_8-specie number 61 in RMG core simulation) is seen to increase in concentration between the three RMG temperatures. This compound has a mass of 56.106 g/mol and its mass spectrum is presented in Figure 5.27. This species has the same mass spectrum as isobutylene and could have co-eluted with the main isobutylene peak during Experiment 3, similarly to isopentane.

This compound was not identified in the pyrolysis experiments done by Gauchotte (2009) or within the pyrograms of Experiment 3. Furthermore, none of the other secondary
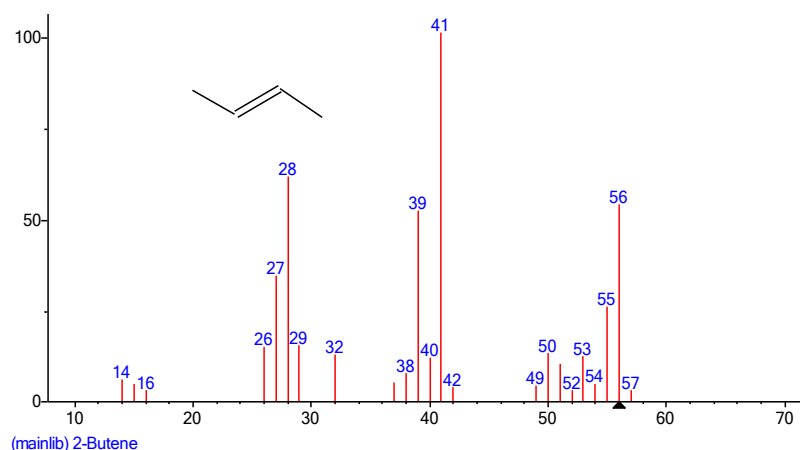
Figure 5.27 Mass spectrum of 2-butene as provided by NIST library.

pyrolysates identified during Experiment 3 (Tables 5.6 and 5.7) could be matched with the core species provided by RMG.

RMG edge results: The **edge** of the RMG simulations for 675°C and 750°C were further compared to the secondary pyrolysates seen on the GC-MS at 675°C and 750°C. As the edge contains compounds that had reaction rates that were not high enough to be included in the core of the simulation, it contains a higher number of pyrolysates. For the remaining species, none of the proposed RMG compounds matched the molecular structure or weight of the compounds identified by the MSD. The same was found for the comparison at 675°C and 725°C. Furthermore, the cyclic compounds identified on GC-MS in Experiment 3 (Tables 5.6 and 5.7) were not seen in either the core or edge simulations of RMG at any temperature between 250°C and 750°C.

RMG compared to Gauchotte (2009) results Comparing the data obtained by Gauchotte (2009) from the pyrolysis of MTBE using a 0.7 mm ID straight quartz tube and the RMG results, one observation would be the similar mass spectrum of 2-butene to that of isobutylene. One compound, identified as propene appears in the edge simulation of MTBE pyrolysis at 750°C, yet it is not being identified as a major secondary pyrolysate (Figure 5.24). No other compounds experimentally obtained by Gauchotte (2009) were found within the edge simulations of RMG.

RMG code variations Four different simulations were run to try to understand if changes in: i) pressure, ii) initial parent molecule concentration, iii) residence time or iv) reactivity of primary pyrolysates have an effect on RMG-predicted secondary pyrolysates. No new

species were formed, indicating that the prep-GC method can be altered, without an impact on RMG results.

The 4 parameters were changed independently following the same initial script, and the results were compared to compounds experimentally obtained by Gauchotte (2009). The increase in simulated pressure from 1.33 bars to 2 bars provided the same species, similarly did a 4.47E+7-fold increase in the initial concentration of MTBE, from an initial 2.23E-09 moles number to 0.1 moles. The residence time was doubled, from 0.114 seconds to 0.228 seconds, providing no new species. This was also true when methanol and isobutylene were provided as "reactive" molecules within the initial script to test whether their interaction was different when they enter the reactor at the same time (and not as products of MTBE decomposition).

Figure D.5: Mass spectrum of pyrolysate 2 - Best NIST library match was propene
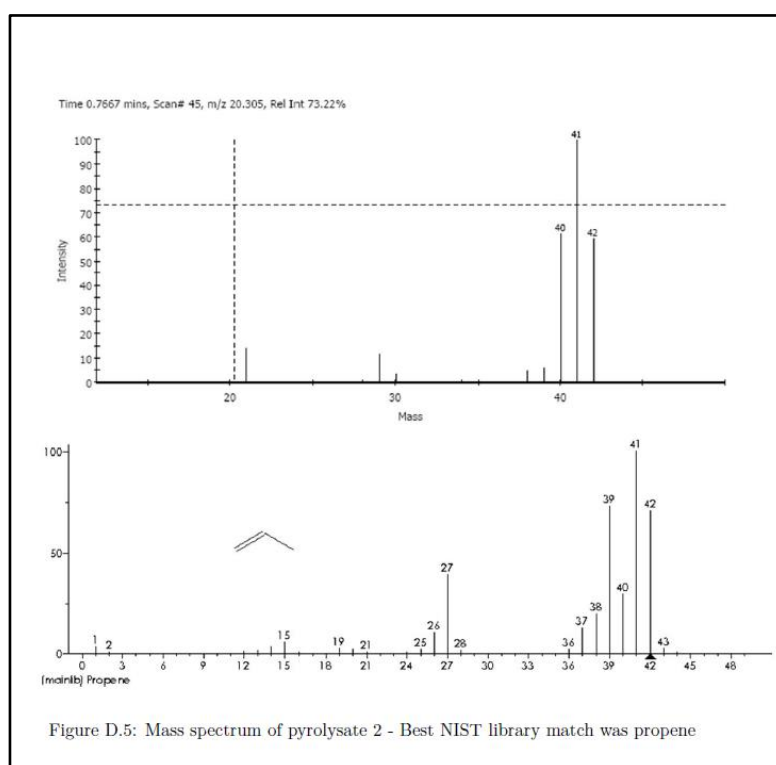
H298	S298	Cp300	Cp500	Cp1000	Cp1500		C3H6(18)	C=CC	42.08
4.65	63.81	15.45	22.64	34.38	40.37				

Figure 5.28 Top: Mass spectrum of pyrolysate 2 identified by Gauchotte (2009) (PhD Thesis Appendix). Bottom: propene predicted within the edge of RMG simulation at 750°C as a pyrolysate of MTBE.

5.5. Conclusions

The work presented in this chapter demonstrated the ability of the prep-GC system to pyrolyse low molecular weight compounds and transfer them to a secondary GC system. MTBE was used for method and system development. The system was adapted to pyrolyse and transfer the pyrolysates to a secondary GC-FID and a GC-MS for identification of pyrolytic products, proving at the same time its compatibility for hyphenation to a GC-IRMS.

During system calibration, 5 pyrolysis tubes were tested. More robust options were tested first, given the narrow ID of the pyrolytic furnace. As the tube had to return to the prep-GC oven to limit the formation of cold spots, a U-bend of the tube had to be formed. No pyrolysis was achieved using stainless steel, a custom-made quartz tube and an Agilent UltiMetal column. A small amount of Capillary column, DB-5 was also placed in the pyrolyser yet it could not be bent in a U-shape and tested. Finally, deactivated fused silica (FS) was successfully tested, and pyrolysis of MTBE took place. Although this is not a robust option, the FS capillary can be bent to fit the pyrolyser's dimensions (1 cm ID), and can be replaced with ease. For this setup, approximatively 1 m of FS capillary was used, reaching into the GC oven, connected to the rest of the system via unions. FS capillaries were also used in PSIA systems reviewed in Subsection 2.7.2., thus apart from their capacity for pyrolysis, they are flexible enough to accommodate a wider variety of pyrolyser designs.

For the pyrolysis of MTBE, the prep-GC system was simplified to use only one valve, limiting the possibility of leaks and making the testing process easier. It was demonstrated that pyrolysis of MTBE followed predicted reactions (Gauchotte-Lindsay et al., 2009), leading to the formation of isobutylene and methanol as primary pyrolysates after the temperature of 450°C. The reaction is quantitative (i.e., MTBE fully pyrolyses) within this system between 700°C and 750°C as seen in Experiments 2 and 3. Several secondary pyrolysates are seen once the pyrolysis products are sent to a second GC-FID system, with MTBE still present after pyrolysis at 700°C (Figure 5.18). These compounds were not observed in Experiment 1 due to co-elution with the prep-GC. Having the ability to transfer the pyrolysates to a secondary GC-FID or GC-MS led to improved separation of the compounds. The use of a heated transfer line fitted with a micro-syringe needle also allowed the temporary hyphenation of the prep-GC with a secondary GC-FID and GC-MS, proving that PSIA can be achieved with reduced laboratory equipment costs. While secondary pyrolysis can lead to isotopic fractionation (and scrambling), a Rayleigh plot can be constructed for previous pyrolytic temperatures where no secondary reactions occur, and the

enrichment factor calculated (Gauchotte-Lindsay et al., 2009). MTBE is recommended as a good option to test the capacity of new systems for pyrolysis, pyrolysate separation and transfer as it is a low molecular weight compound that is not affected by potential cold spots and as its pyrolytic reaction is straightforward, leading to easily identifiable pyrolysates.

Finally, the input file for the RMG software was adapted for MTBE, testing its capacity to provide reliable data for the prep-GC system. The prep-GC method and the required parameters for system pressure and residence time within the pyrolyser were calculated and provided to RMG. Within its core results of simulations done between 200°C and 750°C, RMG correctly predicted the formation of the two pyrolysates, methanol and isobutylene, providing quantitative data on the reaction rates and processes. Discrepancies occurred when secondary pyrolysates identified in Experiment 3 were compared to previously published results (Gauchotte-Lindsay et al., 2009) and RMG species stored both in the core and edge simulations. Secondary pyrolysates could not be matched across all three lines of data (Experiments 2 and 3, data from Gauchotte-Lindsay et al. (2009) and RMG). It may be that their generation is system-specific given the differences in the pyrolyser tubes used in these experiments and that of Gauchotte-Lindsay et al. (2009). However, given the good correlations between core simulation of primary pyrolysates on RMG and Experiments 1, 2 and 3 (Figure 5.22), RMG will be further used to understand the pyrolytic behaviour of more complex molecules and formation of pyrolysates.

Given the low molecular weight of MTBE, cold spot formation could not be tested in the current chapter. These would impact the ability of the prep-GC to pyrolyse and transfer high molecular weight compounds (or fragments) such as hopanoids. Furthermore, MTBE required a high split to not overload the pyrolyser, yet within environmental samples, low concentrations of targeted compounds are expected. Coupled with pyrolysis which leads to an even lower amount of carbon reaching the detector, PSIA may not be achievable within detection limits without concentrating the compounds or fragments prior to or post pyrolysis, respectively. The following chapter will thus test the ability of the prep-GC system to handle higher molecular weight compounds (dimethyl naphthalenes) to eliminate system cold spots, and their online concentration, release, pyrolysis and transfer to a second GC system.

6. The prep-GC system: DMNs pyrolysis

6.1. Introduction

Studying diploptene from natural and lab-grown methanotroph samples highlighted this compound as a fit candidate for PSIA, with pyrolysis as a viable technique to provide access to moieties of isotopic interest. However, building the methodology for this higher molecular weight compound (HMW) took place through several iterative modifications of the prep-GC system design and methodology. DMNs were used in this study as they have comparable backbone skeletons and attached methyl radicals to diploptene, and different physical and chemical proprieties when compared to MTBE used to calibrate the prep-GC, allowing further testing of the prep-GC system using HMW compounds, prior to hopanoid pyrolysis work. Due to its low boiling point, MTBE could not be trapped within the two available traps. Furthermore, cold spots, if occurring, could not be assessed using this molecule and, the pyrolysis and transfer experiments used high amounts of MTBE, which are not representative of environmental concentrations. Thus, the prep-GC's ability to perform heart-cutting, concentration and pyrolysis of molecules available at low concentrations could not be tested in Chapter 5. Compound concentration refers here to the process of trapping and retaining compounds from more than one injection into a trap (i.e., not to be mistaken with isotopic enrichment), with the ability of subsequent release. The increased physical and chemical complexity of DMNs enabled the development of a comprehensive prep-GC methodology prior to diploptene work. **2,3 DMN** and **2,6 DMN** (Figure 6.1) were specifically selected as they were also identified in extra-terrestrial samples, being investigated under the emerging astrobiology field (Pering and Ponnamperuma, 1971; Naraoka *et al.*, 1988; Zenobi *et al.*, 1989), a fitted application example in which PSIA can be applied as a tool for accessing valuable new information. The boiling points of these two compounds (i.e., 269.2°C and, respectively, 262.0°C, Kim, 2019) are between those of MTBE and diploptene (and other hopanoids), allowing to test the abilities of the prep-GC for compound concentration within the trap, release and transfer. This chapter therefore contains experiments aimed to:

1. Test the full workflow for online pyrolysis on the prep-GC for a new compound class (DMNs).

2. Heart-cut, trap and concentrate the compound of interest prepared at natural concentrations.

3. Assess the efficiency of two different trapping systems, referred to as the SIM and ICE traps.

4. Release trapped compounds and transfer them first to the prep-GC-FID to verify the accuracy of release and then to the GC-MS at a non-pyrolytic temperature (375°C).

5. Study the pyrolytic behaviour of 2,3 DMN and transfer pyrolysates to the GC-MS for identification, preparing thus the full methodology for hopanoid pyrolysis presented in Chapter 7.

6.2. Material and methods

6.2.1. Materials

One stock solution was prepared to contain 10 mg of 2,6 DMN (Sigma-Aldrich, 97%) and 18 mg of 2,3 DMN (Sigma-Aldrich, 99%) dissolved in 40 mL Hexane (Sigma-Aldrich 296090-2L; 95%), giving concentrations of 0.25 mg/mL (0.25 µg/µL) and 0.45 mg/mL (0.45 µg/µL), respectively. The solution was transferred in 200 µL inserts in 2 mL GC vials which were capped and sealed using paraffin film before storage at -20°C for further analysis. One *n*-alkane analytical standard (04070-1ML; C_8-C_{20}; 40mg/L) was purchased from Sigma-Aldrich)

6.2.2. Prep-GC system components

6.2.2.1.   System setup

The prep-GC system setup for DMNs experiments is illustrated in Figure 6.1, incorporating the trapping auxiliary which was not previously used in Chapter 5. The system and flow designs could contain two types of traps, defined here as the ICE and SIM traps, which are defined and further discussed in Subsection 6.2.2.3. When employed, they were placed in the same position within the prep-GC system. The connecting capillaries between valve position 6 and between the pyrolyser and valve position 5 were deactivated fused silica (FS) glass.

Table 6.1 Summary of capillary columns used in Chapter 6 work.

Capillary column	Measurements (length x ID x film thickness)	Name	Work in which it was involved
Cc1 - ZB-1HT Inferno	30m x 0.25mm x 0.25µm	HT-1	Cc1 dimension
Cc2 - DB-5 J&W	30m x 0.25mm x 0.25µm	DB-5	Cc2 dimension
ZB-WAX	30m x 0.32mm x 0.50µm	WAX	GC-MS column
Restek fused silica capillary	various x 0.25mm x 0.25µm	FS	Pyrolysis, compound trapping, connections

The prep-GC system employed in this work used the same valve as in Chapter 5. Compound quantification and retention time determination were done with the valve in the ON position, delivering the compounds to the FID. The trap was connected between the first- and second-dimension capillary columns (i.e., Cc1 and Cc2, Table 6.1). When the valve was operated in the OFF position, the trap could be regarded as a second inlet if its heating ramp was high enough to vaporise and focus the trapped compounds at the head of the second-dimension column. Following this, the compounds could be further separated prior to pyrolysis and transferred to a different GC and detector (Figure 6.1).

6.2.2.2. Cold spots assessments

Cold spot testing was conducted by analysing the DMN solution on the prep-GC system in Figure 6.1, with the capillary exiting the pyrolyser connected to position 3, transferring the peaks to the prep-GC's own FID. The assessment was done with the valve in the ON and OFF positions, investigating the elution time, peak area and peak shape on the prep-GC-FID. The FS pyrolysis capillary had to be placed further inside the pyrolyser than in Chapter 5 (Figure 5.8.b). This, however, led to tears developing at the U-bend point of the FS capillary caused by the bending tension, high temperature differences (room temperature – up to 750°C) and high pressure experienced when the valve switched from the ON to the OFF
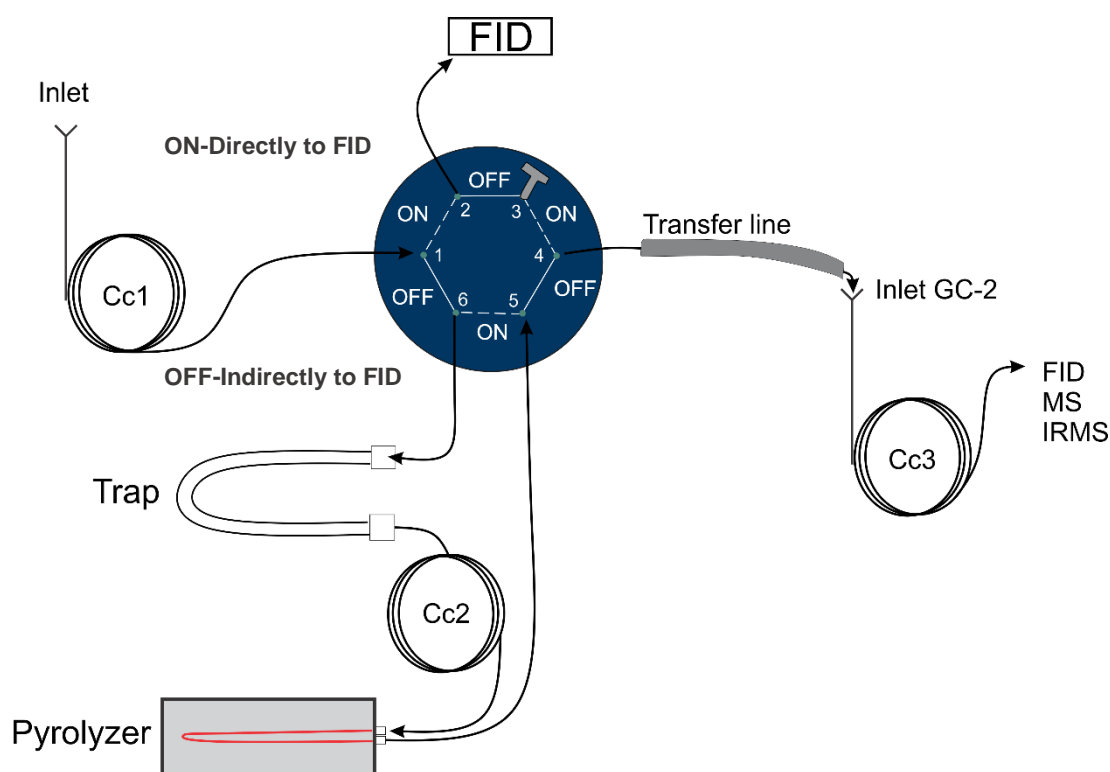
Figure 6.1 The flow diagram of the prep-GC system employed for DMNs work presented in this chapter.

position. The best option was to not use any reinforcement structures at the U-bend yet to position the column within the pyrolyser, where the polyimide coating would not be (completely) burnt.

6.2.2.3.   *Trapping devices: ICE and SIM traps*

Trapping and concentrating compounds may be required when working with environmental samples that contain compounds of interest in low concentrations (De Alencastro et al., 2003). The role of the cold traps in the current prep-GC, apart from concentrating the compound was to provide a secondary "injection" point at a different oven temperature, acting thus as an inlet port for larger compounds and (cryo)focusing them at the head of the second column. During the time that the compounds are maintained within the trap, the over temperature decreased and the compounds were re-vaporised by applying a high temperature to the trap, and focused at the head of Cc2. A new oven ramp could have been then employed.

Two different trapping devices were available for the prep-GC, an oven-integrated SIM Multi Cooling Device referred to as the SIM trap, and an oven-adjacent low-cost device referred to as the ICE trap. Two different aliquots of the DMNs stock solution were used when trapping in the ICE (Figure 6.2) and SIM traps (Figure 6.3).

a) The ICE trap for trapping and compound concentration

Trapping was first tested using a lab-made setup that involved one plastic 50 mL Falcon tube with the lid cut, in which approximatively 25 mL of ice was topped with liquid water (Figure 6.2). A deactivated FS column connected to the rest of the system was removed from the oven via an opening and was introduced in the tube during trapping. The column is cooled down to approx. 2°C. Subsequent release of the enriched compounds was done by placing the capillary previously submerged in cold water within the oven. The side oven opening was then covered with glass wool and isolated from the atmosphere for uniform heating. Once the compounds were ready to be released, the oven was cooled down to lower temperatures, usually below 50°C. The inlet's helium flow was initially redirected toward the FID detector (i.e., Figure 6.1 valve in ON position) before the start of the method such as no gas flew through this part of the system to remobilise the trapped compounds. This setup was initially tested with the n-alkane analytical standard (n-C_8 to n-C_{20}; 40 mg/L, Appendix A.6.1.).
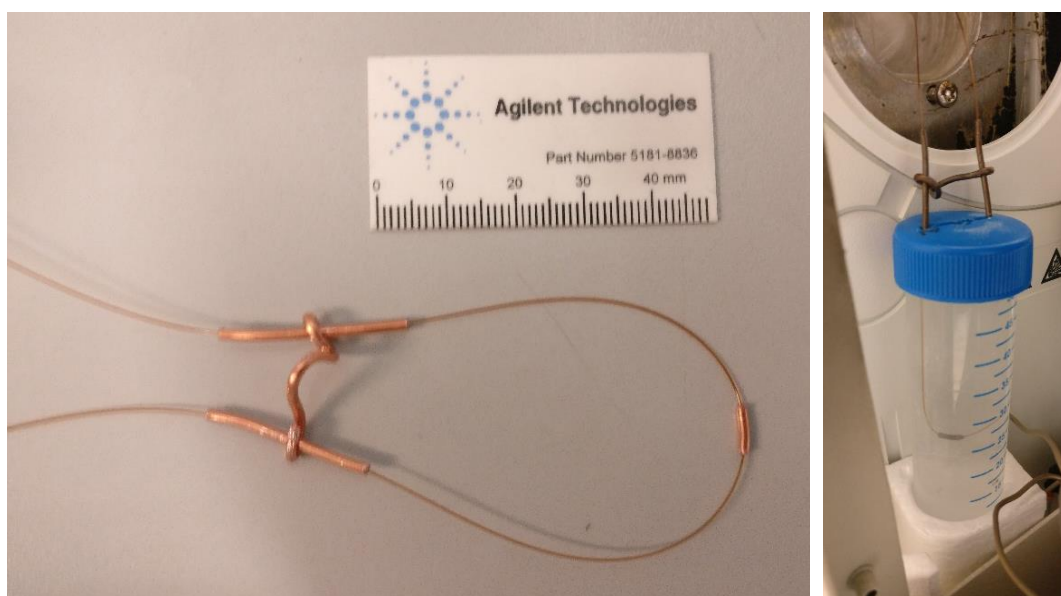
Figure 6.2 The cold tube setup, placed between the pyrolyser and GC (Trap location in Figure 6.1.). The capillary exits the hot oven and the He flow carrying compounds passes through the tube, where a cold spot is formed. The copper H-structure provides stability and can be placed on a nut inside the oven, with the capillary thus not in direct contact with the oven walls.

b) SIM Multi Cooling Device and compound trapping

The SIM Multi Cooling Device coupled with a SIM CRYO-TRAP (SIM and GmbH, 2024) is a SIM GmbH product, B 0800 04 50. It is an oven-integrated closed-circuit GC-auxiliary component used to cool down, over a short period of time, a part of the system and it is controlled via ChemStation. The system is made up of a Multi Cooling Device, a relatively small closed-box maintenance-free system that can be placed near the GC-system and a cryo-trap body that contains a metal round jacket. The metal jacket is connected to the Multi Cooling Device and it is integrated on the side of the GC system oven (Figure 5.3.b, white arrow). The metal jacket contains an enclosure with threaded walls in which a holder is inserted (Figure 6.3). The holder can contain an empty glass U-tube that can be packed with molecular sorbent materials or through which a piece of capillary column can be threaded. Similarly to the ICE trap, compound concentration took place over multiple injections, with the valve programmed to send towards the trap only the compounds of interest (Figure 6.1, valve in ON position). The experiments employing the two trap types are described below.

Figure 6.3 Metal holder and glass tube device that were placed into jacked to coolcube integrated with the prep-GC's oven (Trap location in Figure 6.1.). Two applications presented: left figure showing glass device packed with TANAX TA, a molecular sorbent, right figure showing a capillary threaded through the glass U-tube.

6.2.3. Methods and parameters

a) General prep-GC method

For all methods used, the main parameters were kept identical to allow comparisons between peak areas, retention times and system behaviour. Both trapping device testing methods had the same Cc1 and Cc2 columns installed in the prep-GC (Table 6.1), as shown in Figure 6.1. The column length was defined at 70 m within the Chem Station software to account for the 60 m of Cc1 and Cc2 column lengths, the fused silica capillary connections within the prep-GC system and the transfer line. The oven started isothermal at 100°C (2 min), followed by a 10°C/min ramp to 150°C (variable hold time). The final temperature was kept isothermal for different lengths of time, which did not influence the retention times or peak areas as the peaks eluted prior to 150°C (see RTs in Tables 6.7 and 6.8). Chromatography was improved by increasing the injection amount to 2 µL of DMN solution and the split ratio to 10:1. The inlet was heated at 250°C while the FID was heated to 300°C.

The SIM trap heater was set at 220°C when no trapping took place and the valve box was set at 220°C to allow an unhindered flow of the compounds. The pyrolyser was set at 375°C, a non-pyrolytic temperature, higher than the other temperatures in the system to avoid the formation of cold spots along the copper transfer lines. The flow was kept constant at 1.5 mL/min.

b) Direct and indirect path to FID methods (Valve ON or OFF)

The peak area of DMNs in both experiments was initially assessed without trapping, by sending the compounds to the FID with the valve in the ON and then, OFF position.

The methods for sending the compounds directly to the FID and via Cc1→Trap→Cc2→Pyrolyser→FID (indirectly, long way to FID) were identical between the two versions of the ICE and SIM traps. The difference between the direct and indirect methods was the position in which the valve operated from the start of the method: the valve was operated solely in the ON position for the direct transfer to the FID, and in the OFF position in order to pass through the heated trap, Cc2 and pyrolyser set at 375°C, and reach indirectly the FID.

c) ICE trap: Trapping, concentration and release methodology

Several methods had to be optimised for heart-cutting, multiple trapping and release of compounds. They are described below, following a process that should be employed for each new compound.

ICE trap - Retention times (RT) calculation methods:

The valve was operated in the ON position for retention time (RT) calculation (i.e., Inlet→Cc1→FID), as the compounds were separated in the first dimension Cc1 and reached the FID. This method was named "straight to FID". Although Cc1 was a 30 m column, it was defined as a 70 m within the software when the compounds were sent directly to the FID (i.e., valve ON). This was done to calculate the RTs of the two compounds through the Cc1→FID (RT_1, RT_2). These RTs were then defined as the timing of the valve switch, as they represented the time when compounds reached the valve (the short FS capillary, 40 cm, between valve position 2 and FID, did not add to RTs). This also ensured that the flow rate is optimised for the valve OFF method (Inlet→Cc1→Valve→Trap+Pyr→Cc2→FID), after the valve switch. The peak area of the two compounds, together with their RT, were calculated at this stage (Table 6.2).
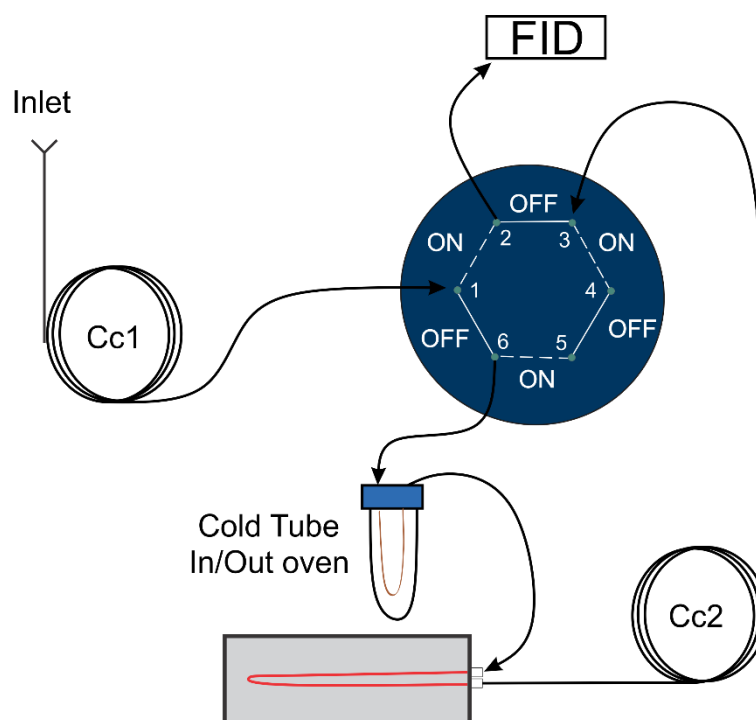
Figure 6.4 The flow diagram of the prep-GC system for assessing directly and indirectly, via the FID, the PA of the two DMNs, with the Cold Tube attached. Cc1 refers to the first-dimension capillary column while Cc2, to the second capillary column (Table 6.1).

It is important to note here that, although the head pressure and carrier gas flow rate is optimal in the prep-GC software for the valve OFF (i.e., 70 m column length), it is not within optimal flow parameters for the path taken when the valve is ON (i.e., 30 m of column defined as 70 m). This had an effect on the sensitivity of the FID and reported peak areas of compounds in Subsection 6.3. This is reported as an effecting factor by specialised literature (e.g., Chromatography-Today, 2024; Grob Jr, 1980) and at the time of the experiments, the detector's make-up gas and fuel flow were not optimised through the software option to account for a higher head pressure and carrier gas flow rate.

ICE trapping:

In order for the compounds to be trapped in the ice-cooled water, the trapping capillary was removed from the oven via the side opening (Figure 6.2) and inserted in the ICE trap. For trapping, the valve operated in the ON-OFF-ON sequence (Table 6.2). Between 1 and 5 consecutive runs were analysed to concentrate a compound (i.e., up to 5x compound concentration) prior to compound release. Trapping took place over 2.1 minutes and the method lasted in total 8.8 minutes. At the end of the method, ice was still present in the tube, and the temperature of the water was measured between 2-5°C.

Table 6.2 Time and method points for the ICE trapping method. The symbol → represents the time interval.

Time (min)	Event	Method point
0 → 5.8	Valve ON	Solvent peak and 1st part of chromatogram to FID
5.8 → 7.9	Valve OFF	Targeted trapping takes place
7.9 → end	Valve ON	2nd part of chromatogram to FID + confirmation of retained compounds within trap

ICE trap release:

A release method was run after compound trapping (Table 6.3). No sample injection took place at this point, and thus, a manual start was required. The oven was cooled down to 70°C and the capillary used for trapping was removed from the ICE trap and placed in the oven. The oven was kept isothermal at 70°C for 1 minute while the valve was in the ON position. The valve was then switched OFF, with He flowing through the trap as the oven heating ramp was set to 25°C/min until 200°C and kept isothermal for 1 minute, allowing the trapped compounds to elute.

Table 6.3 Time and method points for the ICE trap release method. The symbol
→ *represents the time interval.*

Time (min)	Event	Method point
0 → 1	Valve ON	Helium flows directly to FID
0 → 1	Oven 70°C	Low temperature to retain the compounds
1 → end	Valve OFF	Helium flows through trap
1 → end	GC oven: 70°C (1 min hold);	Trap heating same rate as oven, remobilizing compounds;
	25°C/min→200°C (1 min hold)	Compounds reaching the prep-GC-FID

ICE trap – assessment of compound retention:

A trap-retention test was performed, with the compounds kept in the ICE trap outside of the oven. The oven ramp was the same as above, with the valve kept in the OFF position, allowing carrier gas to flow through the trap and reach the FID, thus indicating if the compounds were remobilised from the trap.

d) SIM Cool Cube: Trapping, concentrating and release methodology

SIM trap - Retention time (RT) calculation methods:

RTs were calculated in the same way as described for the ICE trap methodology, by operating the valve solely in the ON position (Table 6.4) and then, solely in the OFF position. Cc1 was again defined as 70 m to calculate the RTs for the valve switch.

The valve was operated solely in the OFF position (70 m actual column length) to calculate the compounds' peak area. As the compounds passed through both Cc1 and Cc2 (compared to the valve ON where they passed only through Cc1 with the same head pressure and software-defined helium flow rate), the peak area appears to have decreased (Table 6.7 and 6.8) yet, due to optimal flow conditions, it reflects the FID signal under "optimal" parameters. The SIM trap was set at 220°C during these runs, 20°C over the oven's temperature. Peak areas and RT are reported in Table 6.7.

SIM trapping method:

The valve was operated in the ON-OFF-ON sequence during compound trapping and concentration (Table 6.4). The run was started when the SIM trap stabilised at 0°C. The first part of the run allowed the solvent peak to elute from the first Cc1 and reach the FID. The valve was then switched to the OFF position based on the measured RTs of the two DMNs peaks, sending them to the cold trap (6.2 min – 7.8 min). A slightly longer trap window than the elution time interval of the two RTs had to be implemented as the chromatography was affected by a flow rate decrease as the valve switches from ON to OFF, affecting compound elution times from Cc1. Once the trapping window was confirmed, this method was selected for a number of consecutive GC runs (i.e., between 1 and 5), leading to compound concentration in the trap prior to release.

Table 6.4 Time and method points for the SIM trap method. The symbol → represents the time interval.

Time (min)	Event	Method point
0 → 6.2	Valve ON	Solvent peak and 1st part of chromatogram to FID
6.2 → 7.8	Valve OFF	Targeted trapping takes place
7.8 → end	Valve ON	2nd part of chromatogram to FID + confirmation of retained compounds within trap

SIM trap - Release method:

The first minute of this method had the valve in the ON position with no helium flowing through the trap to remobilise the trapped compounds. In the first minute, the trap's temperature varied between 0°C-20°C as its cryo-cooling software option was switched off at the start of the run to allow the trap to heat faster during compound release.

The GC oven had a program that started isothermal at 70°C (1 min hold), followed by a 10°C/min ramp until 100°C, and by 15°C/min ramp until 180°C (1 min hold). After the first minute, the valve was turned OFF allowing He to flow through the trap, Cc2 and pyrolyser and the trap started to heat to 200°C. It was observed that the trap reached its final temperature within 30 to 35 seconds.

Table 6.5 Time and method points for the SIM release method. The symbol → represents the time interval.

Time (min)	Event	Method point
0 → 1	Valve 2 ON	Solvent reaches the FID; no flow through the trap
0 → 1	Trap 0°C - 20°C	Trap on standby, slowly warming from oven temperature
1 → 13	Valve 2 OFF	Helium flows through the trap
1 → 13	Trap heating to 200°C	Trap heating us, transferring compounds to the head of Cc2 (second inlet behaviour)
0 → 13	GC oven: 70°C (1 min hold); 10°C/min→100°C, 15°C/min→180°C (1 min hold)	Compounds get separated on Cc2, and reach the FID via the long pathway

SIM trap – assessment of compound retention:

As done for the ICE trap, several tests were also conducted to confirm that compounds are retained within the trap (i.e., not eluting after trapping). Trapped compounds were kept within the SIM trap at 0°C while the valve was switched OFF, the oven followed the above-described ramp, heating to 180°C while the FID response was monitored in order to indicate if the compounds were remobilised from the trap.

e) GC-MS transfer method of 2,3 DMN and pyrolysates

To test the ability of the system to heart-cut and transfer higher molecular weight compounds to a different detector, 2,3 DMN was heart-cut on the prep-GC, pyrolysed between 300°C-850°C and sent to the GC-MS for pyrolysate identification. The oven program was isothermal for 2 min at 120°C, after it increased with 10°C/min to 170°C (3 min hold). As the GC-MS's column will provide the second-dimension separation, post pyrolysis, Cc2 from Figure 6.1 was taken out of the prep-GC oven. The defined column length on the prep-GC Chem Station was kept at 70 m to match previous trap experiments RTs and added volume of the transfer line. For each pyrolysis temperature and transfer, and in order to not overload the MSD, 0.2 µL was injected in the prep-GC using a split ratio of 5:1.

After method optimization, the transfer of 2,3 DMN to the pyrolyser and GC-MS was done over 4 minutes. A GC-MS method for the separation of the pyrolysis fragments was created. A 30 m × 0.32 mm ID ×0.50 µm film thickness ZB-Wax column was installed within the

GC-MS. The GC-MS inlet was set in splitless mode and was heated to 260°C, above the temperature of the transfer line (approx. 210°C) for any transferred compounds to be quickly mobilised and transferred to the head of the column. The GC-MS oven program was isothermal at 100°C for 4 min, the pre-determined time required for the transfer of compounds from the prep-GC. A ramp of 10°C/min up to 200°C was set, with a final hold time of 2 min (total run time=16 min). Flow in the GC-MS was set at 1.5mL/min. The solvent delay was set to 0 min, as the solvent peak was redirected to the prep-GC-FID and only high boiling compounds were sent via the transfer line. The MSD scan range was set between *m/z* 45-500.

6.2.4. DMN - RMG parameters

Similarly to MTBE work, RMG was employed to study the pyrolytic reactions of 2,3 DMN for temperatures between 800-900°C (Table 6.6). The oven's temperature for compound elution was set as 160°C (433.15 K), with a pre-calculated reactor volume of 0.0245 cm^3, and flow rate of 1.5 mL/min (cm^3/min). The residence time of the molecule within the reactor was thus calculated for the above parameters, leading to the different residence times for pyrolysis (Eq. 8).

Table 6.6 RMG residence time of 2,3 DMN within the pyrolyser using Eq.8.

Temp pyrolysis (°C)	Temp pyrolysis (K)	Time for RMG, seconds
800	1073.15	3.963E-01
825	1098.15	3.872E-01
850	1123.15	3.786E-01
875	1148.15	3.704E-01
900	1173.15	3.625E-01

6.3. Results

6.3.1. Main findings

In this chapter, the capabilities of the prep-GC system were successfully extended to higher molecular compounds. DMNs (MW=156 g/mol) were used as intermediary compounds between MTBE (MW=88 g/mol) and diploptene (MW=410 g/mol) and 2,3 DMN was specifically heart-cut, trapped, released, pyrolysed and transferred via the heated transfer line to the GC-MS, with pyrolysates identified. Between 800-850°C, methyl naphthalene was seen, indicating the production of methyl radicals through pyrolysis, making DMNs suitable for PSIA. Two different types of cold traps were tested, one consisting of a low-cost tube with ice (ICE trap) and one of a method-controlled and oven integrated trap (SIM trap). It was found that the SIM trap performed overall better, yet both traps successfully retained the heart-cut compound, making the ICE trap a viable option in reducing the costs associated with compound concertation prior to pyrolysis and PSIA. The prep-GC system was confirmed to be apt for hopanoid pyrolysis.

6.3.2. Assessment of peak area of compounds

The peak areas (PA) of the two DMNs are reported in triplicate for the two GC methods that sent them directly to the FID (valve ON) and indirectly, via the longer path (valve OFF). This was carried out primarily to understand the FID's response, as the experiments were conducted two months apart, and to assess the different performances of the ICE and SIM traps (Tables 6.7 and 6.8).

Firstly, the PAs are compared between the two experiments (i.e., trap devices) when the valve was in the ON position (Table 6.8). For the ICE trap, the PAs were slightly lower, averaging 284 pA, than for the SIM Cold Cube, with an average of 299 pA for the 2,6 DMN and 536 pA compared to 569 pA for 2,3 DMN. The same is noticed for results collected when the valve was OFF (Table 6.9). The average PA of 2,6 DMN on the ICE trap was 99.6 pA, compared to 121.6 pA. while for 2,3 DMN, the averaged PAs were at 199 pA and 238 pA, respectively.

*Table 6.7 PA of compounds when sent directly to the FID (valve in **ON** position). RTs reported as elution times, to understand variation. The symbol → represents the time interval.*

ICE Trap assessment (14-01-2022)		SIM Trap assessment (27-03-2022)	
PA 2,6 DMN	**PA 2,3 DMN**	**PA 2,6 DMN**	**PA 2,3 DMN**
RT = 6.2→6.3min	RT= 6.6→6.71min	RT=6.2→6.35 min	RT=6.6→6.68 min
283	533	300	570
287	541	299	569
284	535	300	569

*Table 6.8 PA of compounds when sent indirectly to the FID (valve in **OFF** position). The symbol → represents the time interval.*

ICE Trap assessment (14-01-2022)		SIM Trap assessment (27-03-2022)	
PA 2,6 DMN	**PA 2,3 DMN**	**PA 2,6 DMN**	**PA 2,3 DMN**
RT=11.9→12.2min	RT=12.86→13.25min	RT=11.9→12.15min	RT=12.9→13.2min
101	204	121	239
101	199	122	237
97	196	122	238

Secondly, there appears to be a large difference between compounds' PAs for runs when the valve was operated only in the ON and only in the OFF positions during the same trap-type experiment (Table 6.9). This is observed for both compounds and both the ICE and SIM traps. For 2,6 DMN, the PA % gain is between 64-65% between the valve operating in the ON and OFF positions for the ICE trap and around 59% for the SIM trap experiment. Similarly, for the 2,3 DMN, a PA % gain between 61-63% was recorded between the valve operating in the ON and OFF positions for the ICE trap experiment and around 58% for the SIM trap experiment. Chromatograms of the two trap experiments with peaks eluting through the ON and OFF valve are shown in Figure 6.5. A small solvent peak elutes prior to the main solvent peak (red arrows) only when the samples are sent indirectly to the FID (valve OFF). The reduction in PA for the indirect (valve OFF) transfer to the FID is apparent for both experiments.

In terms of RTs differences between the valve operating in the ON and OFF positions, there is a 5.7 min difference for 2,6 DMN which increases slightly to 6.26 min for 2,3 DMN for the ICE trap experiment. The same RTs differences are seen for the experiments performed at a later date on the SIM trap. This confirms that the prep-GC system setup was the same for the two experiments.

215

Table 6.9 PA % gain of compounds sent straight to the FID, compared to PA of compounds that reached the FID via the long pathway (Figure 6.1)

ICE Trap			SIM Trap		
2,6 DMN ICE			**2,6 DMN SIM**		
V ON	V OFF	PA % gain (%)	V ON	V OFF	PA % gain (%)
283	101	64.31	300	121	59.67
287	101	64.81	299	122	59.20
284	97	65.85	300	122	59.33
2,3 DMN ICE			**2,3 DMN SIM**		
V ON	V OFF	PA % gain (%)	V ON	V OFF	PA % gain (%)
533	204	61.73	570	239	58.07
541	199	63.22	569	237	58.35
535	196	63.36	569	238	58.17
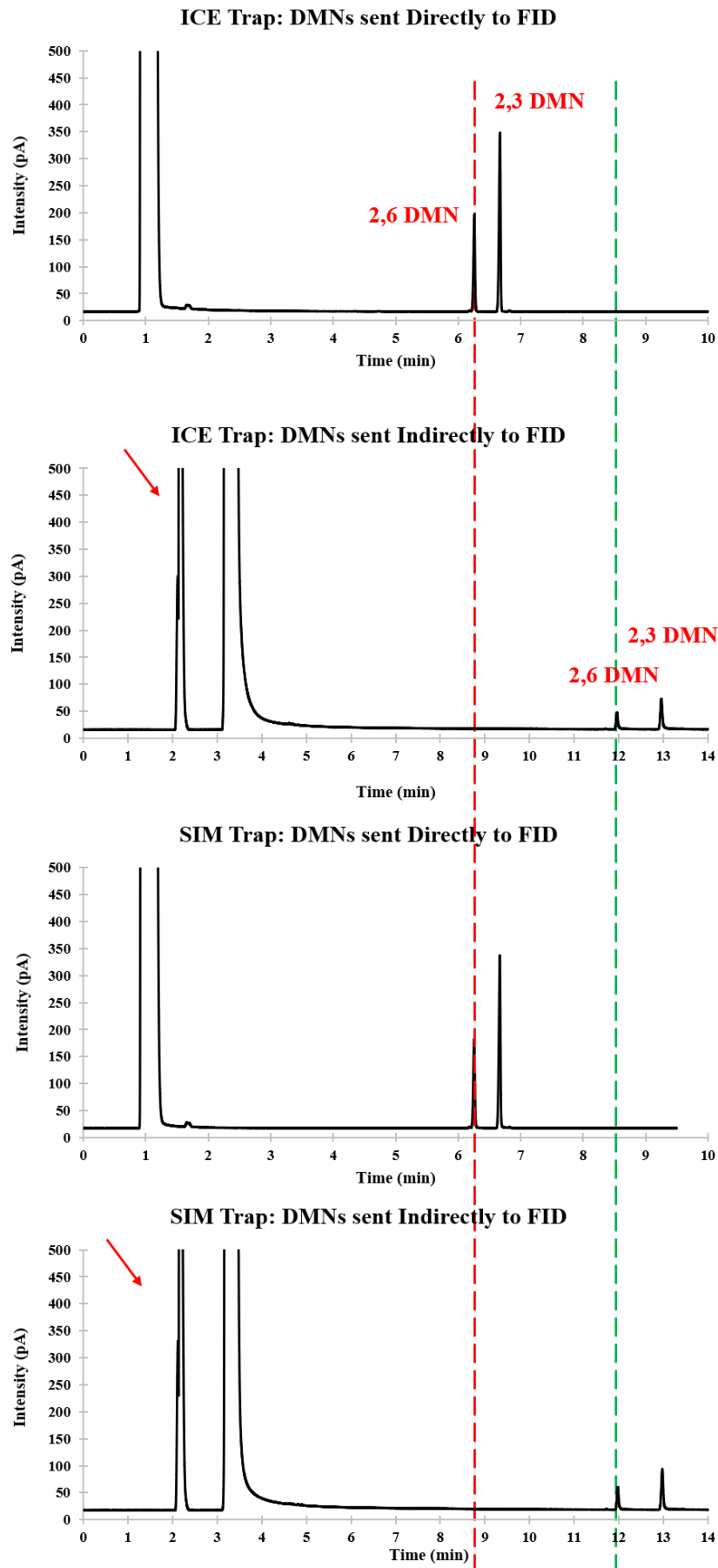
Figure 6.5 SIM and ICE trap experiments chromatograms when the 2 DMNs were sent to the FID directly, or indirectly. The retention time delay is associated with the two peaks eluting through both the first and second capillary column, yet it is the same between the two trap types (red and green dotted lines). A pre-fronting solvent peak is seen in the indirect runs (valve OFF; red arrow).

6.3.3. DMNs – ICE trap and release experiments

Compounds analysed with the ICE trap installed in prep-GC were heart-cut and retained. The ICE trap has successfully retained compounds above $n\text{-}C_{12}$ from the n-alkane standard ($n\text{-}C_8$ to $n\text{-}C_{20}$; Appendix A.6.1), indicating that it would also be able to trap DMNs. The top chromatogram of Figure 6.6 represents the trapping window, with the valve operating in the ON-OFF-ON sequence. In both ICE and SIM experiments, no peaks eluted after the valve was switched back ON, indicating complete trapping of the two compounds.
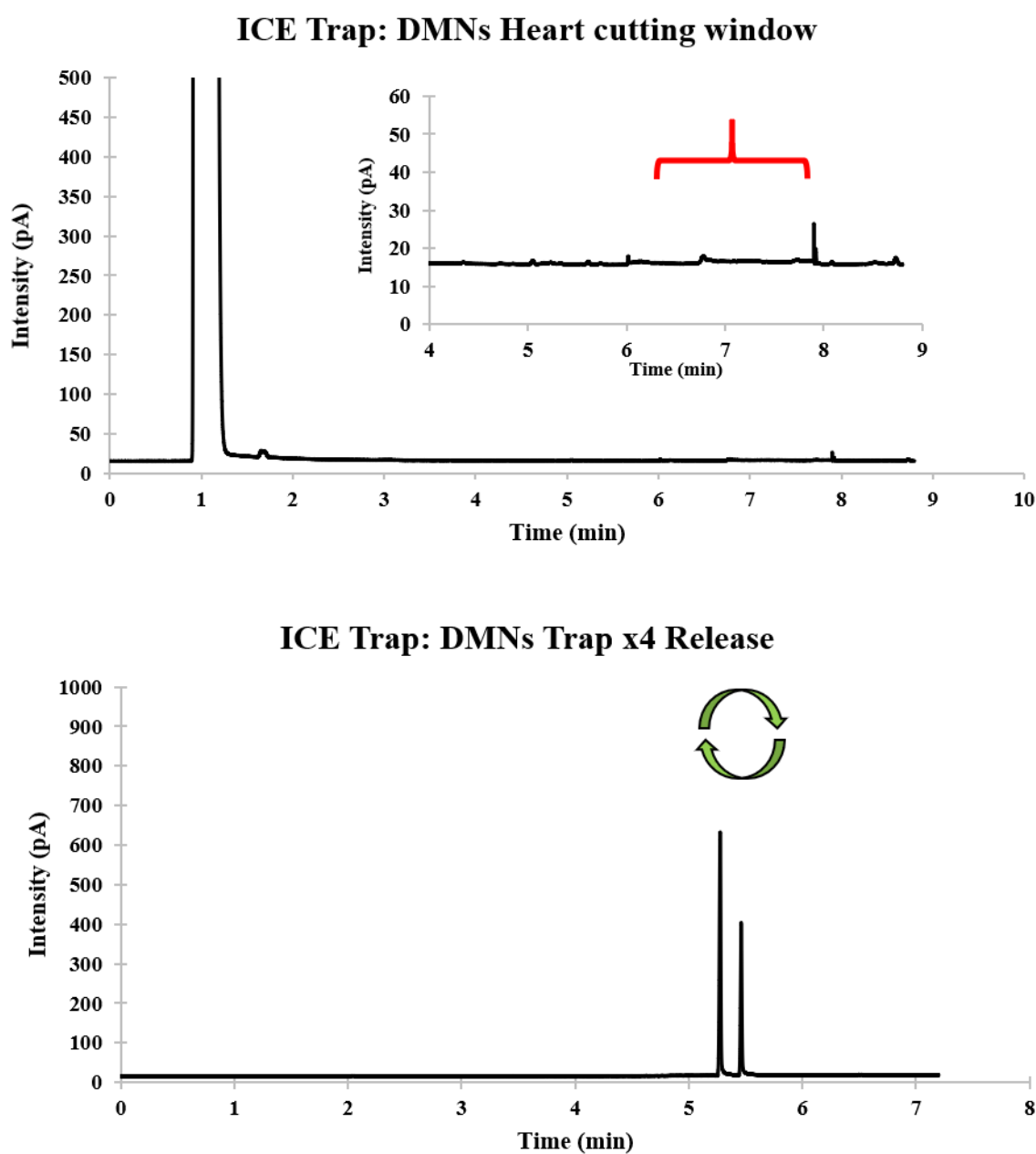
Figure 6.6 Top: The previously seen DMNs peaks in Figure 6.6 are heart-cut and trapped within the ICE trap over the indicated time frame (red bracket). Bottom: The release of the two DMNs from the ICE trap takes place, with peak RT swap indicated by the arrows.

During release from the ICE trap (Figure 6.6, bottom), the two DMNs appear to have swapped their elution times, with 2,3 DMN, the more concentrated compound, eluting before the 2,6 DMN. Their peak areas were plotted against their concentration ratio (Figure 6.7), testing the assumption of retention order swapping. The PA ratio of the two swapped compounds (2,6 DMN/ 2,3 DMN) plotted closer to their concentration ratio, and the PA ratio when the compounds were sent straight to the FID (valve ON) or via the long pathway (valve OFF), confirming this assumption. This was an effect of a fast oven ramp (25°C/min) heating of the capillary trap and the similar boiling points of the two compounds. An explanation for this behaviour is provided in Subsection 6.4.2.
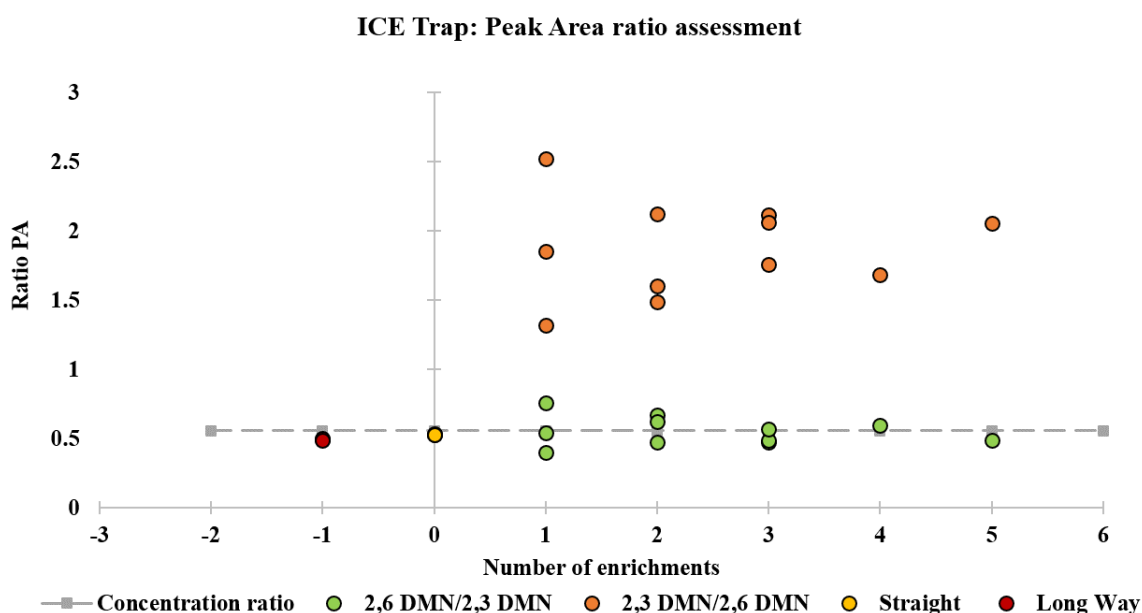
Figure 6.7 PA of the two DMNs plotted as ratio (2,3 DMN/2,6 DMN) by considering swapped elution order (green dots) and normal elution order with affected PAs (orange dots). The gray line represents the solution mix DMNs ratios. The swapped elution order PAs ratios (green dots) plot closely to expected PAs.

The PAs of the released compounds from the ICE trap are plotted in Figure 6.8. On the *oX* axis, the PA of the two compounds sent to the FID via the ON valve is plotted on -1, the PA of compounds when sent to the FID via the OFF valve is plotted above the graph origin point. The axis follows the number of runs over which the compounds were trapped and concentrated (i.e., 2 representing the release after 2 consecutive trapping methods). For the ICE trap experiment, triplicate measurements were conducted for the trap and release of 1, 2 and 3 concentration runs, and single measurements for 4 and 5 trappings of the compounds. Upon release, 2,3 DMN had an overall R^2 of 0.97, with most of the compound being recovered from the trap, whereas 2,6 DMN, had an R^2 of 0.85. Compared to the PAs of the compounds measured via the long pathway (valve OFF, graph origin measurements in

Figure 6.8), the PAs of the two DMNs after 3 trap runs increased approximatively twice (i.e., $PA_{2,3DMN\_0}$=200 pA, and $PA_{2,3DMN\_3}$=439pA), and after 5 trap runs, approximatively 3 times.
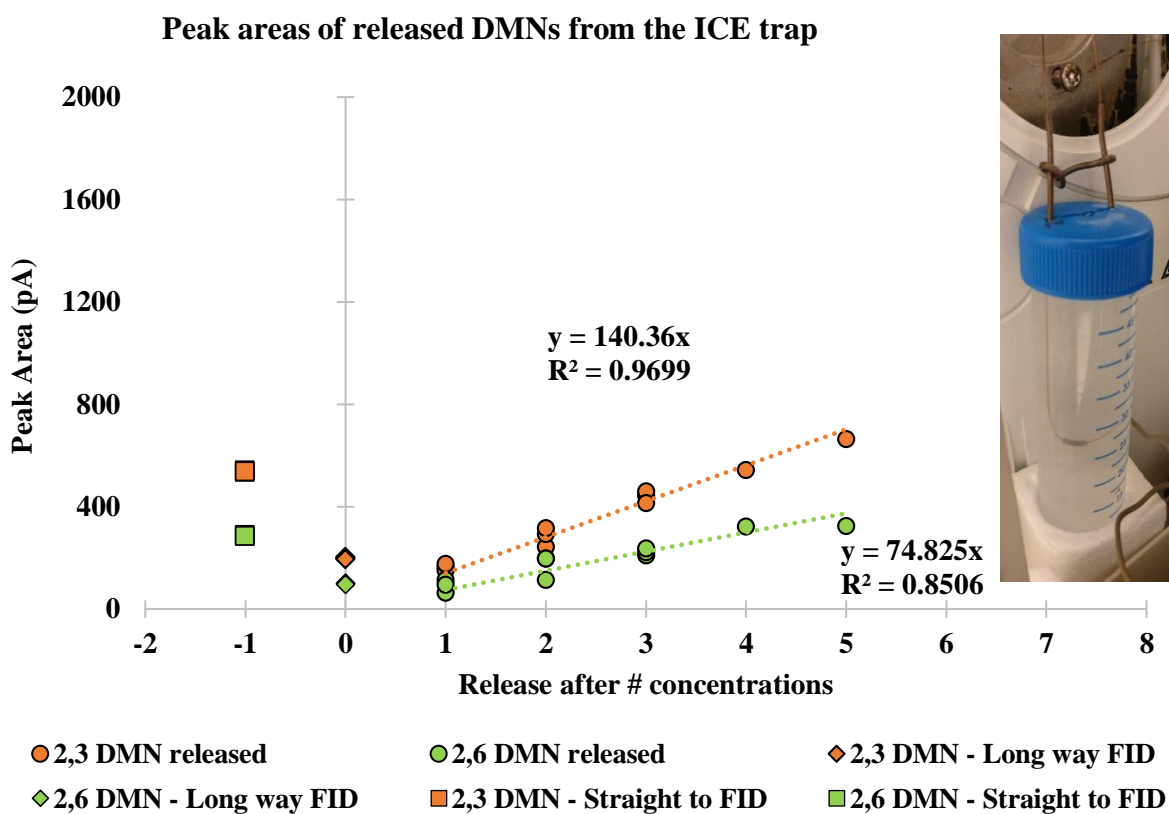
Figure 6.8 PAs of DMNs upon release from the ICE trap, compared to the PA showed by compounds when send straight to the FID (plotted on the -1 Ox coordinate; square symbols) and via the long way to FID (plotted on the 0 Ox coordinate; diamond symbols).

6.3.4. DMNs – SIM trap and release experiments

Similarly to the above section, compounds analysed with the SIM trap installed were heart-cut and retained. The top chromatogram of Figure 6.9 represents the trapping window, with the valve operating in the ON-OFF-ON sequence, showing that no peaks eluted after the valve was switched back ON. The following chromatogram shows the two peaks released from the trap, with well-defined peak shapes.
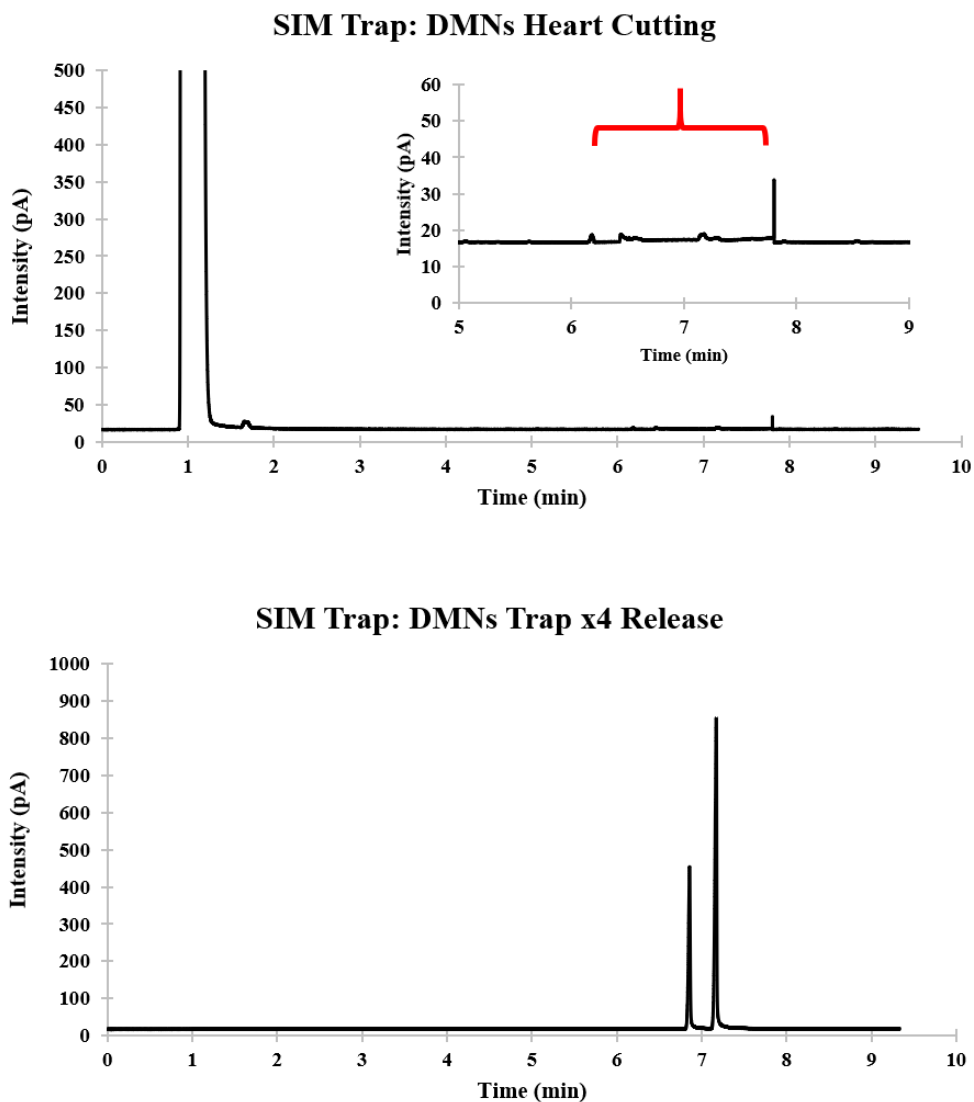
Figure 6.9 Top: The previously seen DMNs peaks in Figure 6.6 are heart-cut and trapped within the SIM trap over the indicated time frame (red bracket). Bottom: Release of the two DMNs from the SIM trap takes place, with the peaks eluting in the expected order and concentrations.

Compared to the ICE trap experiment, the performance of the concentration and release is improved for the SIM device, with both R^2 above 0.99. Interestingly, although linearity is good in both experiments, and the same amount was injected with a similar FID response (Tables 6.7 and 6.8), the SIM concentrated the compounds within the trap with a higher efficiency than the ICE trap. For example, after 3 consecutive concentration runs, the released PA of both compounds has tripled.

Peak areas of released DMNs from the SIM trap

$y = 319.89x$
$R^2 = 0.9975$

$y = 159.2x$
$R^2 = 0.9961$

Peak Area (pA)

Release after # concentrations

● 2,6 DMN released   ● 2,3 DMN released   ◆ 2,6 DMN - Long way FID
◆ 2,3 DMN - Long way FID   ■ 2,6 DMN - Straight to FID   ■ 2,3 DMN - Straight to FID
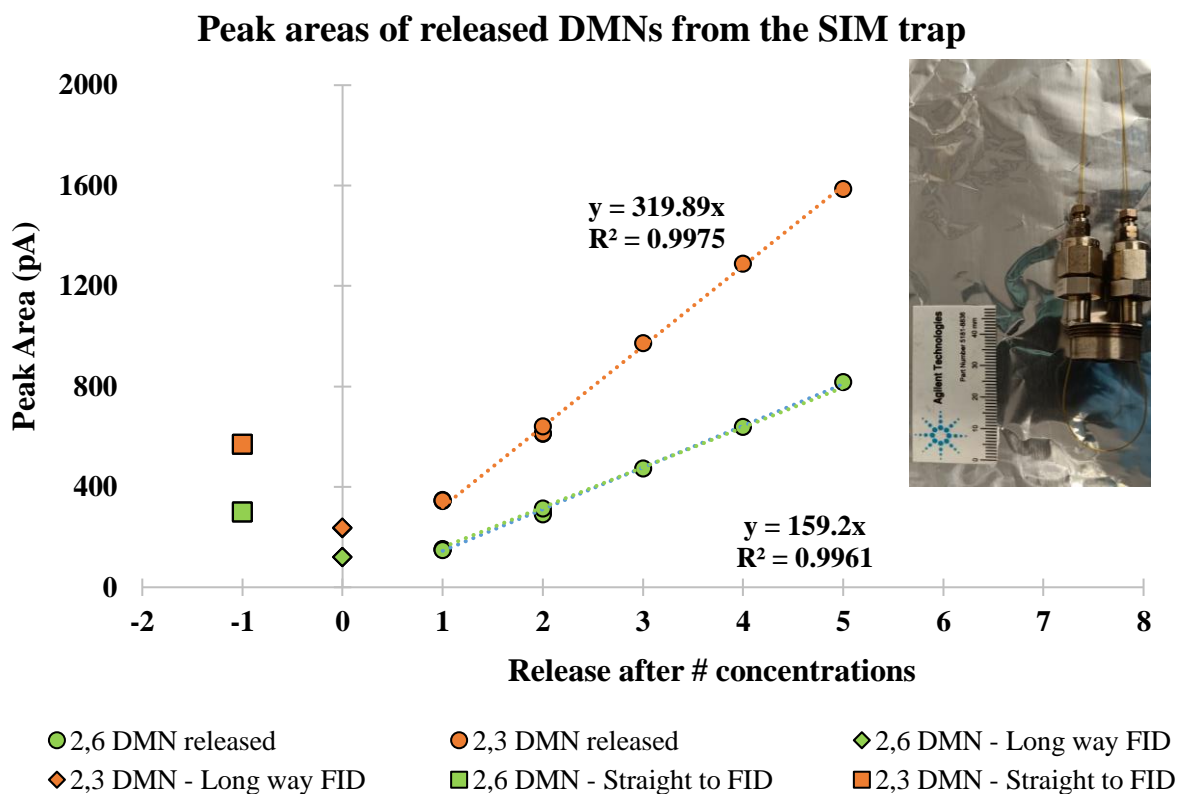
Figure 6.10 PAs of DMNs upon release from the SIM trap, compared to the PA showed by compounds when send straight to the FID (-1 Ox coordinate; squares) and via the long way to FID (0 Ox coordinate; diamonds).

Finally, the sample concentration ratios between the two compounds (grey line), and their PA ratios between the different runs were calculated and plotted in Figure 6.11. While the ratio between the 2,6 DMN to 2,3 DMN amounts mixed in Hexane is 0.5556, the PA ratios of the SIM trap experiment (orange diamonds) are closer to this value than for the ICE experiment (green dots), indicating that the SIM trap has a better efficiency at concentrating targeted compounds.
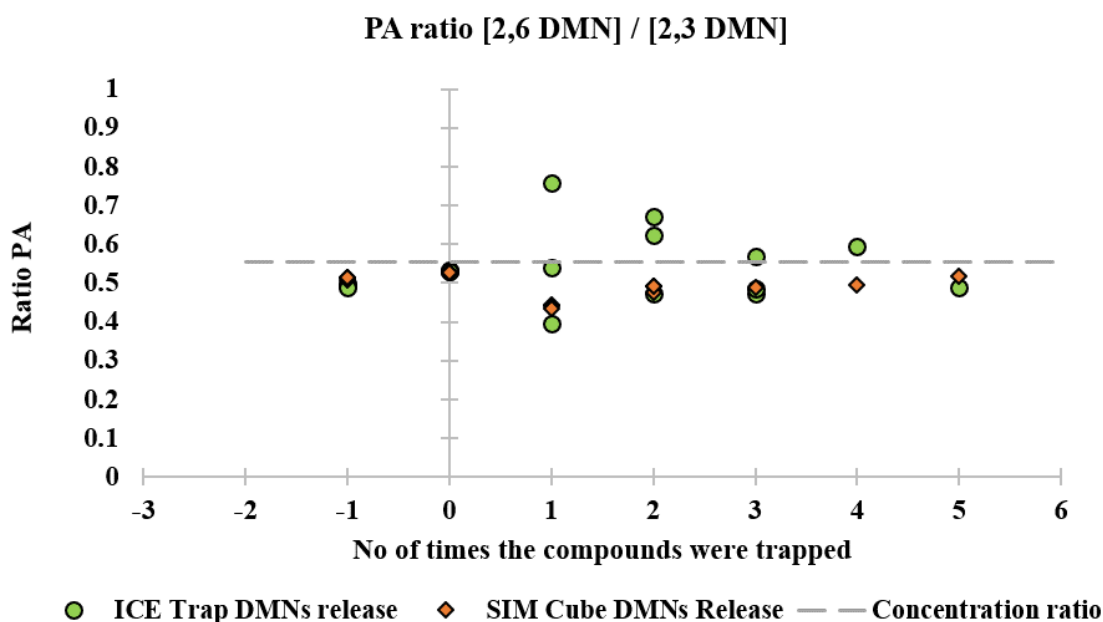
Figure 6.11 Comparison between PAs ratios (2,6 DMN/ 2,3 DMN) of the two DMNs released from the ICE (green) and SIM (orange) traps and original compound concentration ratio of the two DMNs (grey line).

6.3.5. DMNs pyrolysis, transfer and pyrograms

In order to understand the pyrolytic behaviour of DMNs and the capacity of the prep-GC system to handle molecules with higher boiling points, an aliquot from the same solution used for trapping and concentrating the compounds was used to pyrolyse 2,3 DMN.

Figure 6.13 shows both DMNs transferred from the prep-GC to the GC-MS for analysis at a non-pyrolytic temperature (350°C) to confirm the correct transfer, identification of the parent molecules and pre-existing contamination peaks. The two compounds are well separated and the chromatogram displays only a few contaminant peaks, with peaks #1, #4 and #5 identified as siloxanes (see Appendix A.6.2.).

The 2,3 DMN was heart-cut from prep-GC injections, exposed to temperatures between 350°C and 850°C within the pyrolyser, and transferred to the GC-MS inlet via the heated transfer line. Pyrograms of 2,3 DMN are plotted in Figure 6.14. From the pyrolyser's temperatures of 350°C and 500°C, only one peak appeared on the GC-MS, the transferred 2,3 DMN (red arrow). A vertical line for correlating the elution times is drawn from these two chromatograms as the peak appears to split in programs obtained at higher temperatures (see however pyrogram for 800°C). The mass spectra of the two peaks are provided in Figure 6.14 for the 650°C pyrogram, where they are only slightly co-eluting. When 2,3 DMN appears split, the peak areas of both peaks are calculated, and provided in Figure 6.14, next

Pyr T°C vs PA of 2,6 DMN in prep-GC
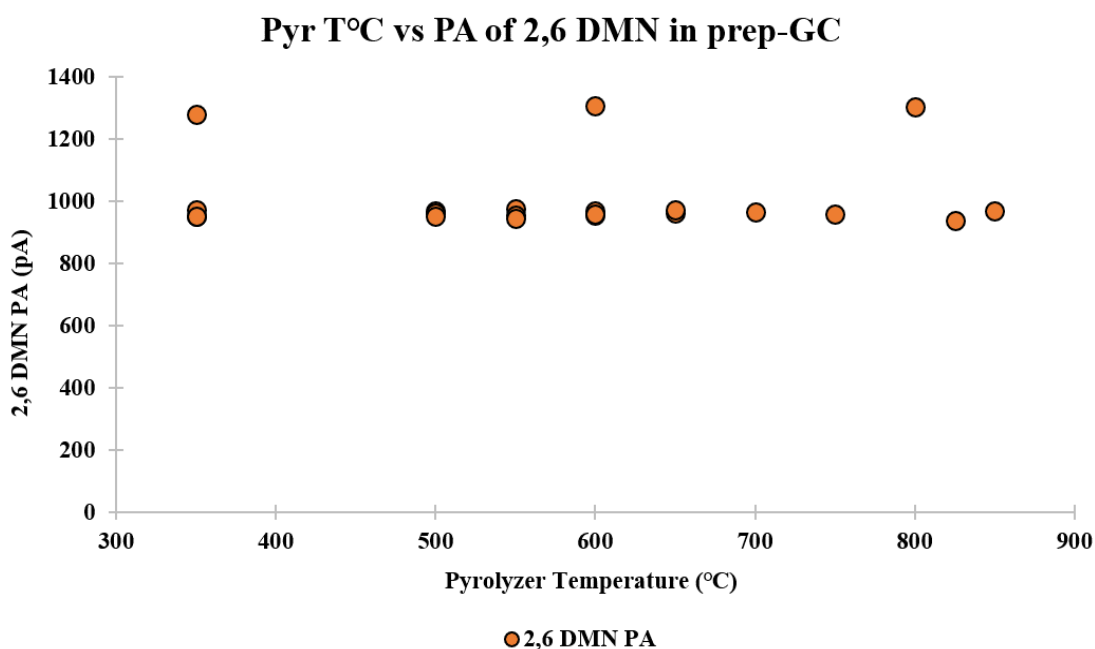
Figure 6.12 PA of 2,6 DMN that confirmed injection as recorded on the prep-GC-FID, correct heart-cut of 2,3 DMN. The relatively stable PA values indicate overall correct prep-GC injection apart from 3 samples recorded at the start of the sequence, assumed to be caused by prep-GC or pyrolyser unequilibrated temperatures.

to each peak. There is no decrease in peak area with increasing pyrolytic temperature for the main 2,3 DMN peak. At 825°C, in which the peak is split, the PA of the main peak was 19% above the PA of the same compound at 700°C. To understand the transfer of 2,3 DMN to the GC-MS, the PA of 2,6 DMN is plotted in Figure 6.12, highlighting overall a reproducible injection. The 3 higher PA values of 2,6 DMN were observed for the first runs of each of the three days over which this experiment was run.
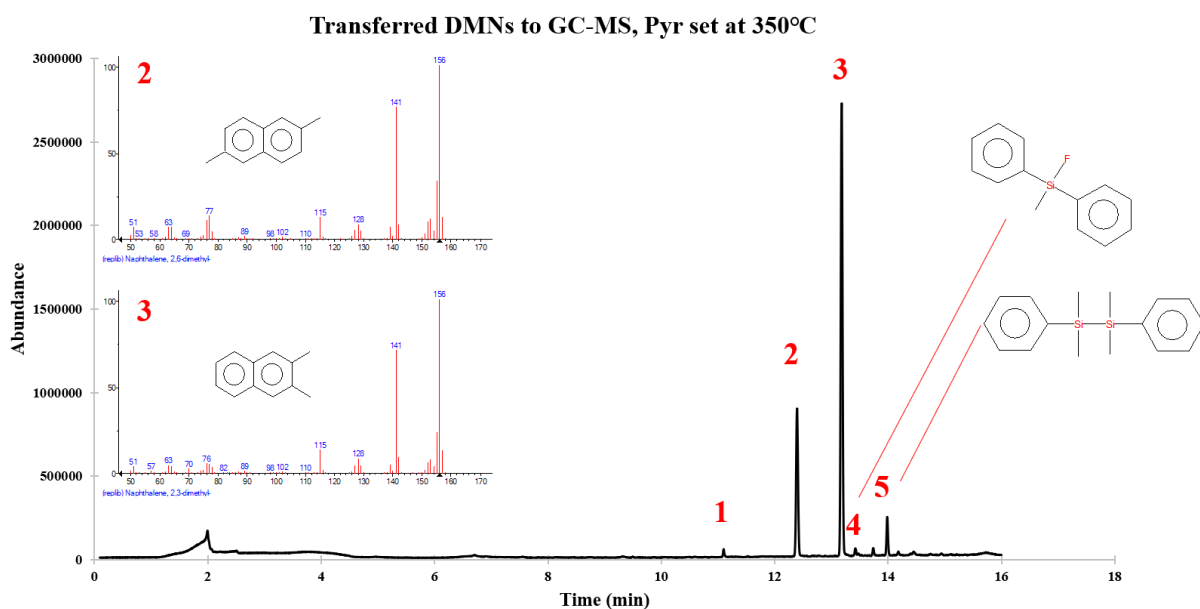
Figure 6.13 Direct transfer of DMNs from the prep-GC to the GC-MS with the pyolyser at 350°C.

224
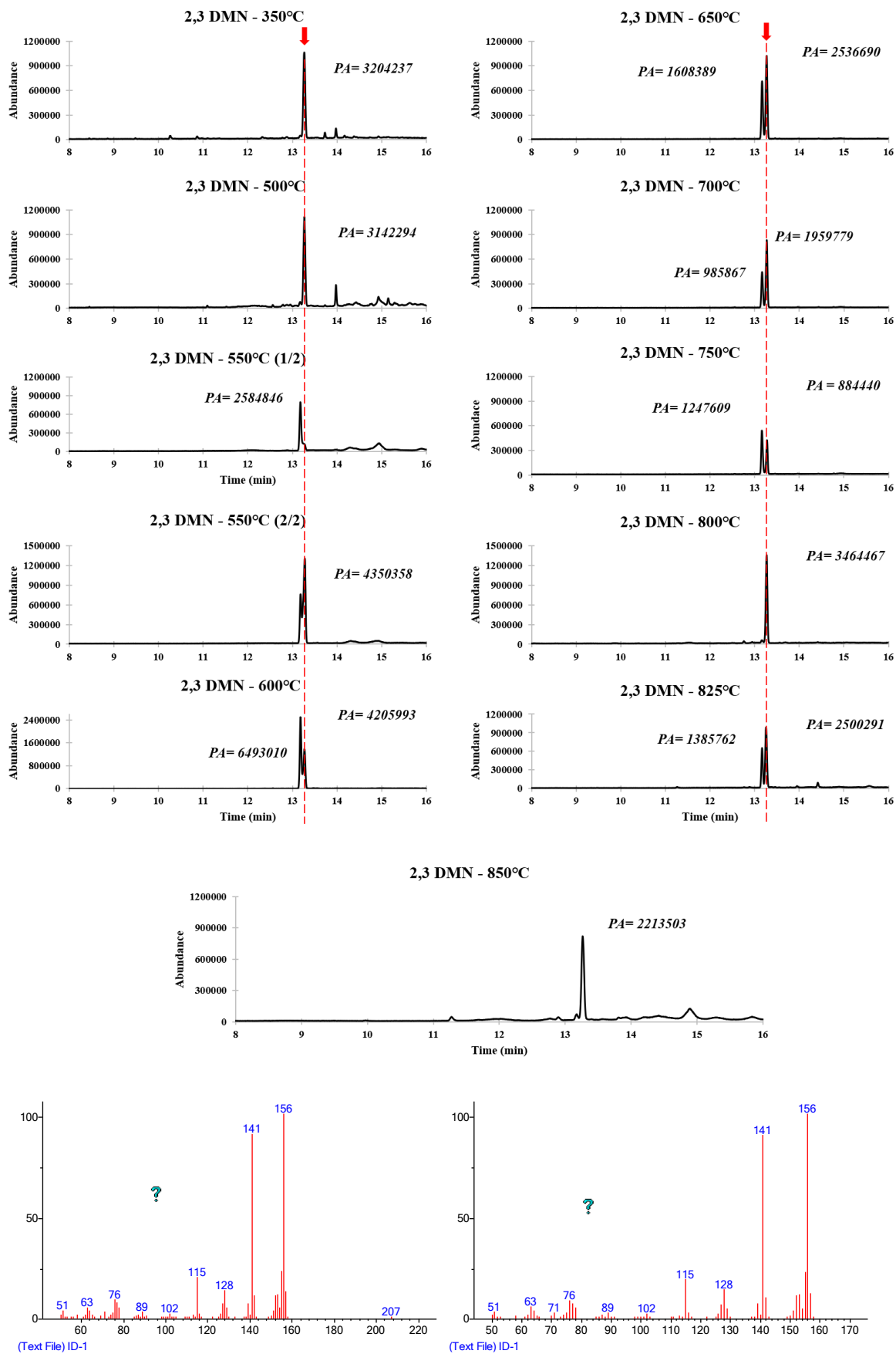
Figure 6.14 Top: Pyrograms of 2,3 DMN as transferred and analysed on the GC-MS, between 350°C-850°C. The peak area (PA) is provided next to each peak. The red line and arrow highlight the RT of 2,3 DMN at a non-pyrolytic temperature, to aid with the visual assessment of the split peak's RTs. Bottom: The mass spectra of the two split peaks for the 650C pyrolyser temperature is the same, with m/z 207 occurring due to the column bleed.

Above 800°C, pyrolysis was suspected to have taken place and the pyrograms were further analysed (Figure 6.15). 2,3 DMN was only pyrolysed until 850°C, a temperature at which the fused silica capillary placed in the pyrolyser broke. Apart from the main 2,3 DMN, two peaks, #2 and #4 (potentially #3 as well) appear in the three pyrograms. Peak #2, a methyl naphthalene, also appears to increase in peak area. The secondary compounds are labelled in Figure 6.15 and the mass spectrum with the highest match and probability is provided in Figure 6.16.
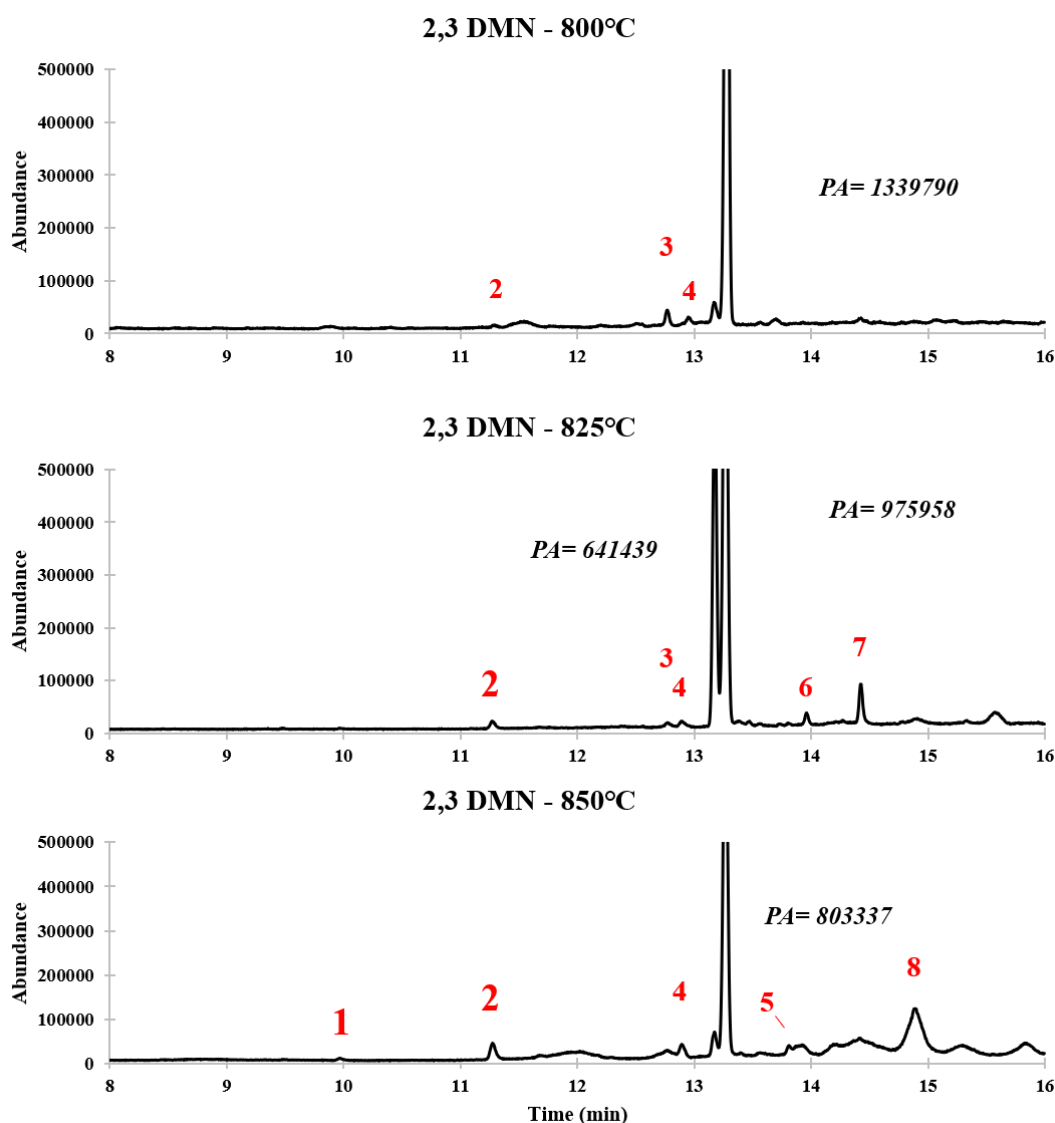
Figure 6.15 High temperature GC-MS pyrograms, for pyrolysate identification. Peak names, chemical structure and mass spectra are presented in Figure 6.16.
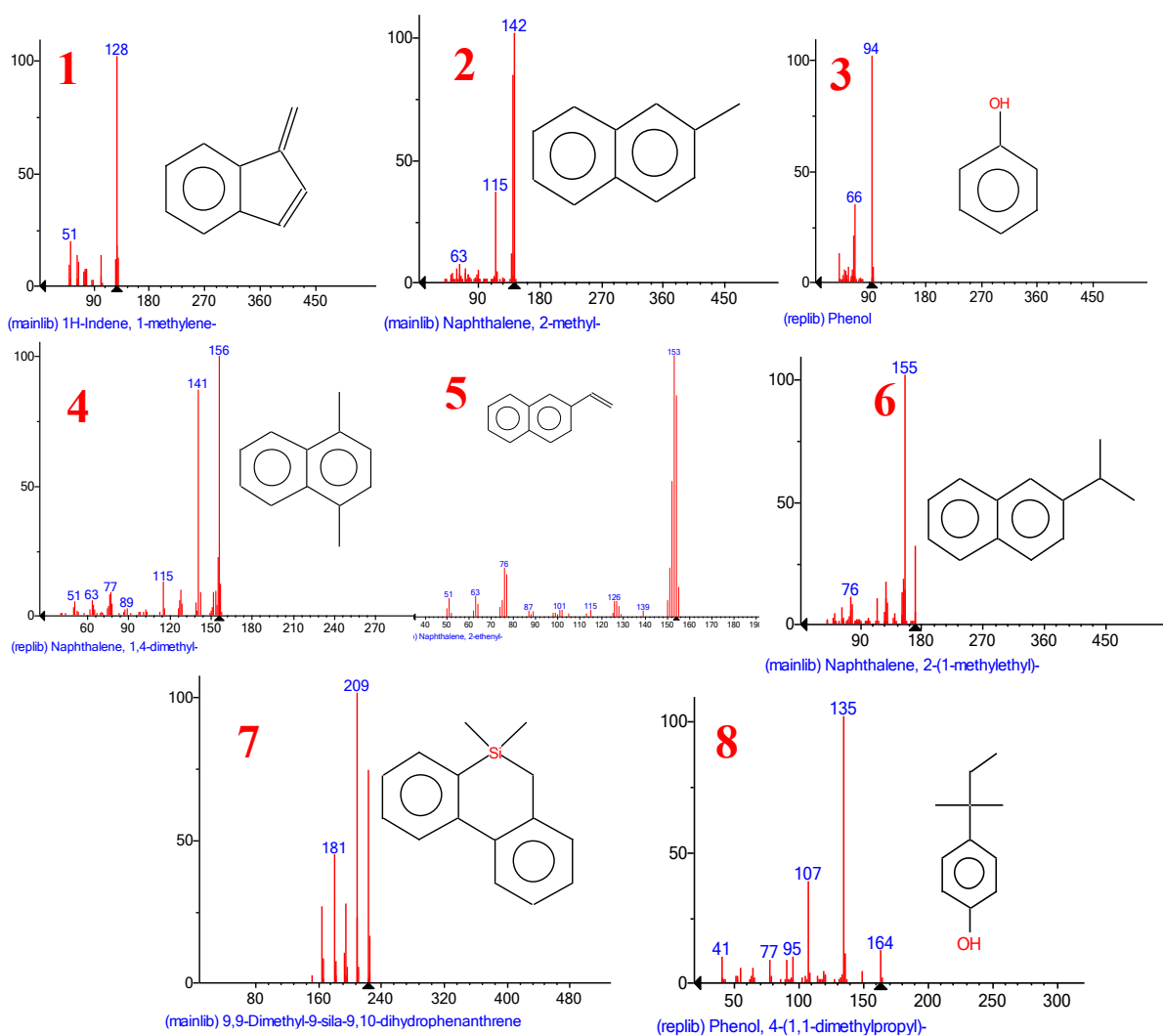
Figure 6.16 Best compound match for peaks labelled in Figure 6.16. Compound mass spectra is provided in Appendix A.6.3.

6.3.6. RMG results of 2,3 DMN pyrolysis simulations

Due to the fact that the pyrolysis capillary could not withstand temperatures above 850°C in this experiment, RMG was employed to study the pyrolytic breakdown of 2,3 DMN for higher temperatures and is used to investigate, as in the case of MTBE, the corresponding reactions and predicted Bond Dissociation Energies (BDEs) for DMN pyrolysis. Given that 2,3 DMN has a higher molecular weight when compared to MTBE, the reactions did not run to completion, yet a series of observations can be drawn from the generated data.

In the three plots of Figure 6.18, only the primary pyrolysates are plotted. 2,3 DMN presented only a minor decrease in concentration, and for the simulated short time these reactions ran, 2,3 DMN plotted as a straight line, obscuring the pyrolysates' trends. For comparison reasons, 2,3 DMN was not plotted together with its pyrolysates. In Figure 6.18 the main pyrolysates are plotted on a skewed scale to show trends (i.e., see zoom-out insert). There is one compound, a methylnaphthalene (MNA) which is present in all three RMG simulations, between 850°C-900°C. A similar compound was seen in the experimental pyrograms and is further discussed in Subsection 6.4.3. The BDEs for this compound and the reactions that lead to its formation are investigated further (Figure 6.17). The reactions are grouped based on the type of energy required with respect to the reactant (i.e., negative or positive BDE), as provided by RMG. It should be noted that the reactions are bidirectional, and the BDE value is provided only for the reaction leading to the formation of 2-Methyl-2,3-dihydronaphthalene, a precursor of the methylnaphthalene seen on experimental pyrograms (and not for the reactions that lead to the formation of its precursors).
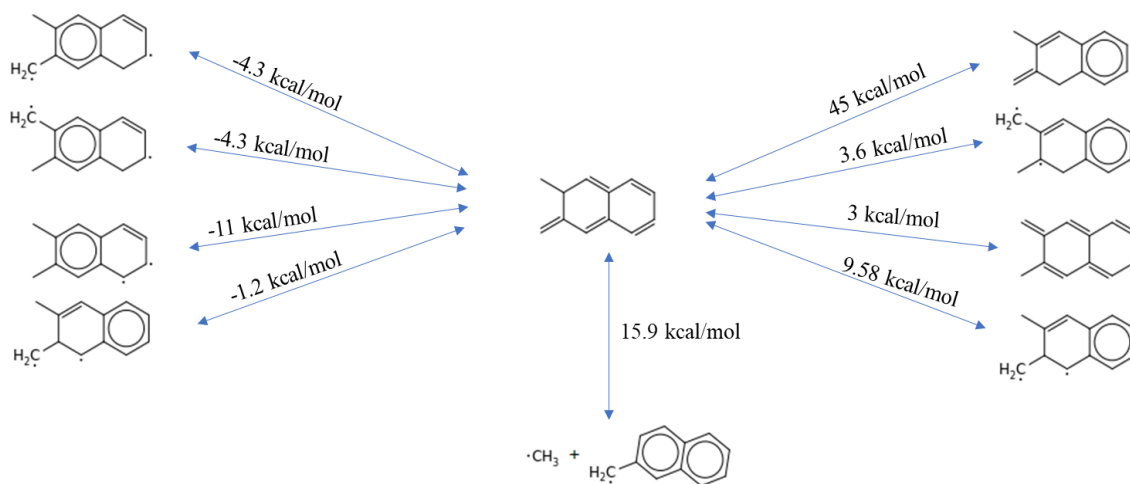
Figure 6.17 RMG predicted BDEs and relationship of MNA to 2,3 DMN. To lead to the formation of the pyrolysates on the left, the dissociation energy is negative (exothermic reaction), while to form the bottom and right pyrolysates, the energy require is positive (endothermic reaction).

A

RMG 2,3 DMN pyrolysates at 850°C

RMG_2,3 DMN pyr_850°C

Legend: S(1015), S(1016), CH3(42), S(50724)

B

RMG 2,3 DMN pyrolysates at 875°C

Legend: CH3(42), S(1016), S(54907), S(116047), S(1015)

C

RMG 2,3 DMN pyrolysates at 900°C

Legend: CH3(42), S(1015), S(1016), S(54907), S(116047), S(71654)
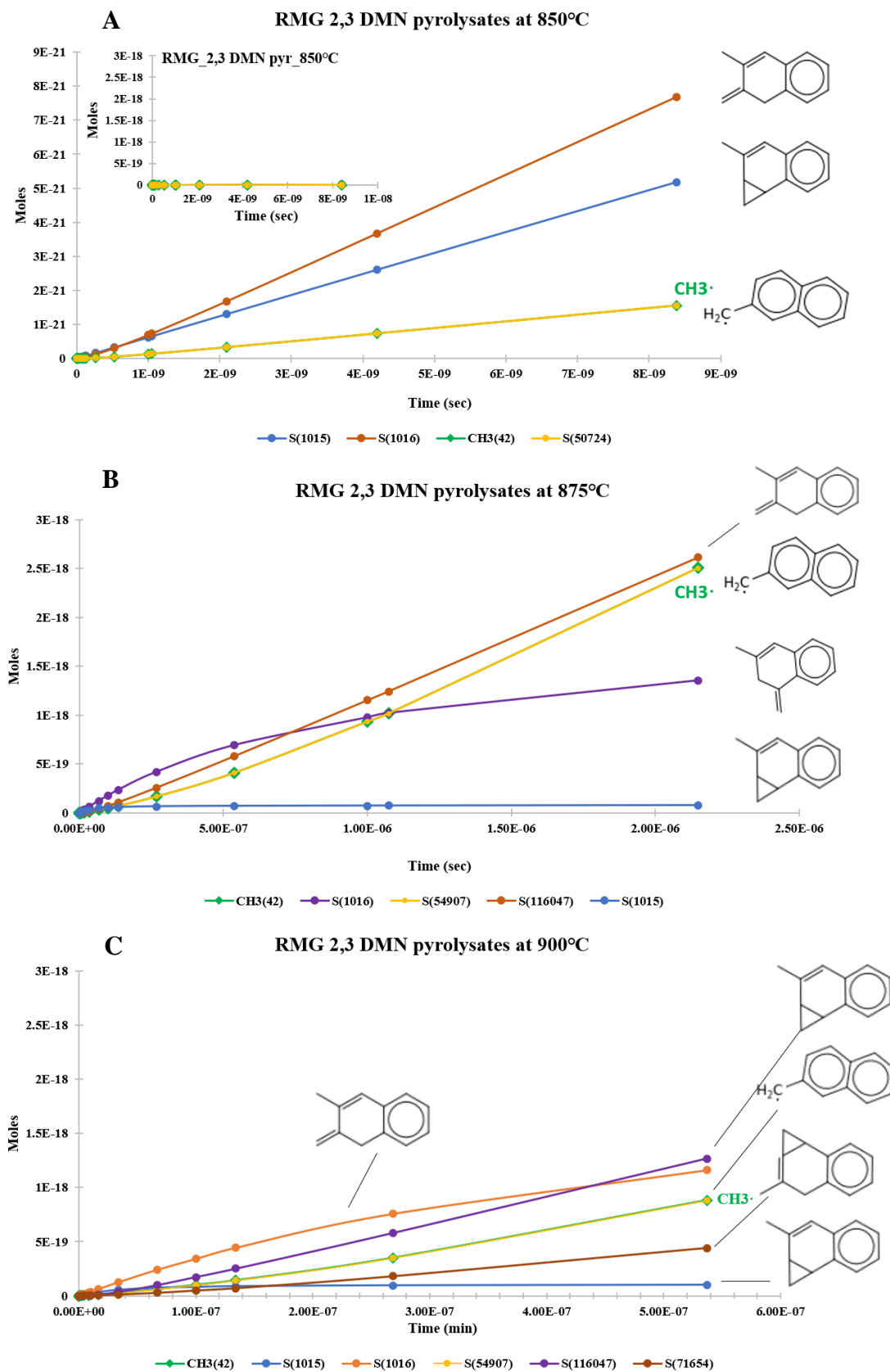
Figure 6.18 RMG zoomed-in pyrolysates of 2,3 DMN exposed to 850°C, 875°C and 900°C. 2,3 DMN is only plotted in the zoomed-out plot (Figure 6.18 A) as only minor breakdown took place.

Due to the different *Ox* axis for the following three plots, Figure 6.18.C has an apparent decrease in concentration compared to Figure 6.18.B, however, the 900°C RMG simulation stopped after a relatively shorter time, and it is expected that the mole concentrations of the plotted pyrolysates to be above the concentrations plotted in Figure 6.18.B if ran for the same amount of reaction time.

6.4. Discussion

6.4.1. High molecular weight compounds, cold spots and prep-GC upgrades

Cold spots: The prep-GC system coped with the analysis of DMNs, compounds that have higher boiling points than MTBE (i.e., 262°C and 269°C vs 55°C), used for overall system testing. Thus, work done on DMNs allowed improvements to the system, which could have not been assessed during MTBE work due to its high volatility and concentration. These mainly regarded the occurrence of cold spots. These are defined as system capillaries in contact with atmospheric air or zones where the temperature does not reach that of the oven and where higher molecular weight compounds, such as the parent molecules of investigated pyrolysates, can condensate and get trapped. Cold spots were thus detected by operating the valve in the OFF position (Figure 6.1), and monitoring the FID response: missing peaks, wider peak shapes or poor reproducibility of the retention times were considered artefacts of occurring cold spots. Furthermore, as expected from literature results (e.g., Madison and Roberts, 1958), DMNs do not break down easily during pyrolysis, preserving their polycyclic aromatic structure. It was not expected to obtain smaller molecular fragments through low temperature pyrolysis thus, delivering the two compounds to the GC-MS via the transfer line could not have been done with the system setup used for MTBE. Using DMNs allowed testing for cold spots of the full flow path.

Two cold spots were inferred between the pyrolyser and the prep-GC oven, where the FS capillary was in contact with the atmosphere. These were eliminated by fitting two long (approx. 20 cm) copper tubes, ID 1/16", extending between the oven and pyrolyser, conveying the heat across. Copper tubing was selected as it is a flexible material which offers good heat conductivity (371 W/mK for a temperature of 527°C, EngineeringToolBox, 2014). The FS capillary was brought further within the pyrolyser than was needed for the MTBE (Figure 5.8), also eliminating a cold spot at the end of the U-bend point within the pyrolyser.

The transfer line's prep-GC end was introduced further into the oven and the tubing was replaced with a similar stainless-steel tubing with a reduced ID (i.e., ID from 1/16" (1.5875 mm) to 0.25 mm (P/N CP4003, Agilent). This allowed a faster transfer of the parent molecules and pyrolysates to the GC-MS inlet, and reduced the temperature decrease the carrier gas experienced during transfer.

One important cold spot may be still inferred within the system: the connection of the transfer line with the transfer needle; while reducing the internal diameter of the transfer line aided in this regard, data presented in Figure 6.14 shows that, for most pyrolytic temperatures, the transferred 2,3 DMN arrives as a split peak to the MSD. However, the occurrence of a split 2,3 DMN peak did not correlate to the pyrolyser's temperature as a single peak eluted at 800°C, with the same RT as for 350°C and 500°C (Figure 6.14). No relationship was found between the PAs of the two peaks and those of the peaks in the immediate pyrograms, indicating that 2,3 DMN was not retained within the prep-GC, and was subsequently released in the succeeding run. The PA of the 2,3 DMN for pyrograms at 350°C and 500°C also cannot be linked to that at 800°C, with the latter having a higher peak area. This also does not correlate with 2,3 DMN (even minor) pyrolytic breakdown as seen in Figure 6.14, as a lower PA would have been expected at higher pyrolytic temperatures. Furthermore, the two peaks display the same mass spectrum, no secondary pyrolysates are seen at 550°C - the first temperature for which the 2,3 DMN appears as a split peak and, the same amount of sample was injected in the prep-GC, as confirmed by the stable PA of 2,6 DMN (Figure 6.12), the peak which was used to quantify compound injection on the prep-GC-FID, with the valve operating in the ON position (i.e., straight to FID).

The most likely possibility for this behaviour would be the GC-MS's inlet method and the oven program. The inlet was set at 260°C start temperature of the GC-MS oven method, set isothermal at 100°C during transfer. It was observed from the prep-GC-FID runs, that the two DMNs reach the FID when the oven's maximum temperature was between 140-150°C. The introduction of the 2,3 DMN in the GC-MS inlet is done at a temperature at which the compound is kept in gas-phase and is transferred to the MSD after it elutes from the transfer line. The split may thus be caused by the difference in the flows and pressures experienced by the GC-MS as the transfer line is removed after 4 minutes. This can be tested by adjusting the GC-MS oven start temperature to a lower one (i.e., 50°C) for the duration of the transfer, allowing the peak to be retained at the head of the column during transfer and moved through the system only by the head-pressure and flow rate of the GC-MS system after the transfer line is removed.

It was not believed that cold spots occurred in the system after both peaks were successfully transferred from the prep-GC to the GC-MS and identified. This confirms the ability of the prep-GC system to pyrolyse further high weight molecular weight compounds, such as squalene and hopanoids, and transfer higher weight pyrolysates to the GC-MS via the transfer line. The molecular weight of the 2,3 DMN is 156 amu, indicating that compounds with a mass at least as high as 156 amu can be successfully transferred to a GC-MS (or GC-IRMS). Furthermore, although the 2,3 DMN occurs in most chromatograms as a split peak, its identification was aided by the MSD, ensuring that this is a chromatographic issue and that pyrolysis did not take place, skewing interpretation. DMNs, in general, are stable compounds which do not pyrolyse easily, however, as seen in the case of MTBE, compound breakdown improves chromatography.

Valve ON/OFF FID response: The PAs differed between the valve operating in the ON and OFF position for the transfer to the FID (i.e., no trap or release; Tables 6.7 and 6.8). This was due to the way the system was configured within the software: the column length was set to 70 m for the valve OFF to account for both Cc1 and Cc2 column lengths, FS capillary connections and eventually that of the transfer line. Within the software, for the constant flow of 1.5 mL/min, the start head pressure of the carrier gas was at 34.7 psi, and increased to 39.7 psi with the oven's program. In order to avoid an experimental RTs determination for the valve's switch timing for trapping, the same column length (70 m), and head pressure (34. 7psi) were defined for the valve operating in the ON position, although Cc1 which connected the inlet to valve and FID, was only 30 m in length. This meant that the carrier gas flow rate (volumetric flow) was higher when the valve operated in the ON position than in the OFF position, and this was the only different variable between the two valve positions. This had an impact on the way the FID operated. On the software, the carrier flow was selected to not affect the makeup gas (N_2) and fuel flow (H_2 and air) within the FID. Within the literature (Grob Jr, 1980), the response of the FID was seen to be influenced by the temperature, combustion gas flow rates and carrier gas flow rates (Henshaw, 2005). Up to a point, higher flow rates can increase the sensitivity and response of the detector (Grob Jr, 1980). This is due to the dilution a flow experiences when eluting from a 0.25 mm column ID to the wider board of the FID body and tip, and the role of the makeup gas in ensuring the flow is optimal, delivering peaks quickly to the detector. During the DMNs experiments, an optimised response to the FID was seen when the carrier gas flow rate was higher, enhancing the combustion process within the FID. The gain in PA for both trap type experiments was over 50% however, the results between valve ON or OFF are highly

reproducible as seen from triplicate measurements (Table 6.9). No further flow rate optimization was done for subsequent analyses.

6.4.2. Trapping, concentration and release

The role of the cold trap in the prep-GC, apart from concentrating the compound, was to provide a secondary "injection" point, at a different oven temperature, acting thus as a sample inlet for high molecular weight compounds and (cryo)focusing them at the head of the second column. During the time that the compounds are maintained within the trap, the over temperature decreased and the compounds were re-vaporised by applying a high temperature to the trap.

The current tests were done to assess the ability of the traps to retain and concentrate DMNs (and HMW compounds) present at environmental concentrations within the sample, as the diploptene analytical standard used in Chapter 7 had a low concentration of 0.1 mg/mL (0.1 µg/µL) and as diploptene environmental concentrations prior calculated for the PMFB samples were between 0.0015 mg/mL and 0.08 mg/mL (see Appendix A.3.8). Given the mixture concentrations of the two DMN and the applied 10:1 split, the injected amount of 2,6 DMN was 0.041 mg/mL and that of 2,3 DMN was 0.022 mg/mL. Trapping and concentration of the compounds was successful in both trap devices, yet with different performances (Table 6.10).

ICE trap: Trapping and releasing of compounds within the ICE trap had overall lower performances than the SIM trap. First, the assignment of compound names should be addressed, with the two peaks swapping elution order after trap and release when compared to measurements that did not involve a trapping stage. As seen in Figure 6.6, the higher concentrated 2,3 DMN elutes before 2,6 DMN. When comparing a different trap and release analysis done with the same setup but with a different prep-GC oven method, the two peaks eluted in the expected order (Appendix A.6.4.). The difference between the two methods which would have impacted the results was the oven ramp. The oven ramp in the current ICE experiment was set at 25°C/min to quickly heat the trap inside the oven, released and focused the compounds whereas the Appendix A.6.4. method had a slower ramp at 10°C/min. At this high heating ramp, both compounds vaporised from the trap at the same time given the small differences in their boiling points and it is likely that due to the geometry of the trap and the location of trapping, they have switched elution order. This issue can lead to erroneous identifications when multiple concentrated compounds are sent to an IRMS yet

it was observed later that a 10°C/min ramp has the ability to evaporate trapped compounds and separate them without leading to different RTs.

In terms of trapping performance, as seen from Figure 6.8 regression equation, the PA of the two trapped compounds is below the PA of the compounds reaching the FID via Cc1 and Cc2 (i.e., "long way to FID") in the absence of a trap indicating a loss within the system or unsuitable trap and release methodology. While no compounds eluted during the trap-retention tests and the background level did not increase above expected values due to the column heating, the PA of the compounds, once released as described above, was considerably lower, potentially indicating that the compounds were escaping the trap below or close to the detection limit (Figure 6.8). The lower R^2 for 2,6 DMN might indicate that is either less well retained and eluted from the ICE trap compared to the 2,3 DMN. As an efficiency summary, concentrating 5 times the compounds, only increased their PA 3 times. This may make the ICE trapping option undesirable given the instrument's running costs. However, the ICE trap was previously tested with 2 highly concentrated Dimethyl Naphthalenes (i.e., 2,7 DMN and 2,3 DMN) as shown in Appendix A.6.5, with similar results, indicating that this device can handle a wide range of concentrations.

Table 6.10 Percentage % of released DMNs from the SIM and ICE traps, compared to the PA of compounds when sent indirectly to the FID. The concentration column and values represent the number of runs (and times) over which the compounds were trapped and concentrated.

	SIM PA increase %		ICE PA increase %	
Concentration	2,6 DMN	2,3 DMN	2,6 DMN	2,3 DMN
x1	124.9	145.7	92.9	82.1
x2	248.8	261.6	172.0	142.4
x3	390.4	409.2	225.7	220.0
x4	525.2	542.0	327.4	272.0
x5	673.2	666.8	328.4	333.1

SIM trap: The SIM trap performed overall better than the ICE trap when comparing the amount of compound concentrated and linear regressions for both compounds (Figure 6.10 and Table 6.10). For the SIM trap, when the DMNs were trapped 4 times and released, the PA for 2,6 DMN was ×5.2 higher than the PA of the initial peak when it reached the FID indirectly, via Cc1 and Cc2 combined, making this option more effective.

There are several reasons for the difference in the amount each trap managed to concentrate, even if the trapping temperatures were similar. First, the method-automated behaviour of the SIM trap allowed the user to limit the time between trapping and release, as the trap capillary is not brought back into the oven as in the case of the ICE device. Upon oven introduction,

although the oven was cooled down to 70°C, a temperature at which the two compounds would not elute, the higher temperatures can mobilise a part of the trapped compound and release it as part of background noise. Furthermore, the amount trapped and released for the triplicates in the case of ×1, ×2 and ×3 enrichments is not as constant in the case of the ICE trap as it is in the case of the SIM trap, making it less reliable for stable isotopes analysis. A lower trapping temperature in the ICE trap, given, for example, by a mix of dry ice and acetone or liquid N_2 may improve the trapping capacity of this device yet this was not tested further in this work.

6.4.3. 2,3 DMN pyrolysis

2,3 DMN was heart-cut from the DMNs solution, and subjected to pyrolysis for 0.39-0.36 seconds, over a wide range of temperatures: 350°C – 850°C, and under 32.9 – 35.8 psi (2.2 -2.5 bars), with the flow directed to a GC-MS for pyrolysate identification.

Methylnaphtahelenes (MNAs) and dimethylnaphthalenes (DMNs) have been previously subjected to pyrolysis or have occurred as pyrolysates, yet under different conditions than those investigated in this work. Previous pyrolysis experiments such as the work of Madison and Roberts (1958) which exposed a series of aromatics, 2,3 DMN and 2,6 DMN including, to both liquid and vapour phase pyrolysis between 300-430°C, indicated that hydrogen and CH_4 were generated in their setup, indicating that this expected reaction is of PSIA interest. Other pyrolytic studies done under atmospheric pressures (Gräber and Hüttinger, 1982; Yang and Lu, 2005) exposed MNAs to temperatures between 600°C – 1100°C for 1 and 50 seconds and have also reported the formation of methane, naphthalene, ethylnaphthalene and dimethylnaphthalenes.

In the current work, the experimental pyrograms for 2,3 DMN above 800°C are presented in Figure 6.14, with the compounds identified in Figure 6.16. For the same temperature and the pyrolysis of 1-MNA, Yang and Lu (2005) reported that 20% of the parent molecule was pyrolysed, with a complete breakdown at 1000°C. In the current experiment of 2,3 DMN pyrolysis, minor pyrolysate peaks occur between 800°C and 850°C yet do not indicate a major parent molecule breakdown. It should be however noted the difference in residence time of the different molecules in the reactor (i.e., 1 second and 0.4 seconds). In the study of Yang and Lu (2005), several DMN isomers are formed from the breakdown of 1-MNA starting with the temperature of 800°C, are stable between 800°C and 850°C, after which they start decreasing in concentration, indicating that after the temperature of 850°C, multiple pyrolysates will be formed. However, in the current experiment, the pyrolysis FS

capillary did not withstand temperatures above 850°C, leading to only minor pyrolysate formation under the short residence time in the pyrolyser.

The pyrolysates of 2,3 DMN are depicted in Figure 6.19, based on their occurrence at different temperatures. The two methyl radicals of 2,3 DMN are bonded to two naphthalene β-carbons, meaning they are weaker bonds, and easier to break during pyrolysis (Madison and Roberts, 1958). It should be noted that the mass spectra of the identified pyrolysates led to low "highest probability scores" provided by the NIST library and identification is uncertain as no analytical standards were used to confirm the exact isomer or compound (Figure 6.16). The compound names are used to refer to occurring peaks and to define their potential structures. Based on this, there are however a number of several compounds that appear to be structurally related.
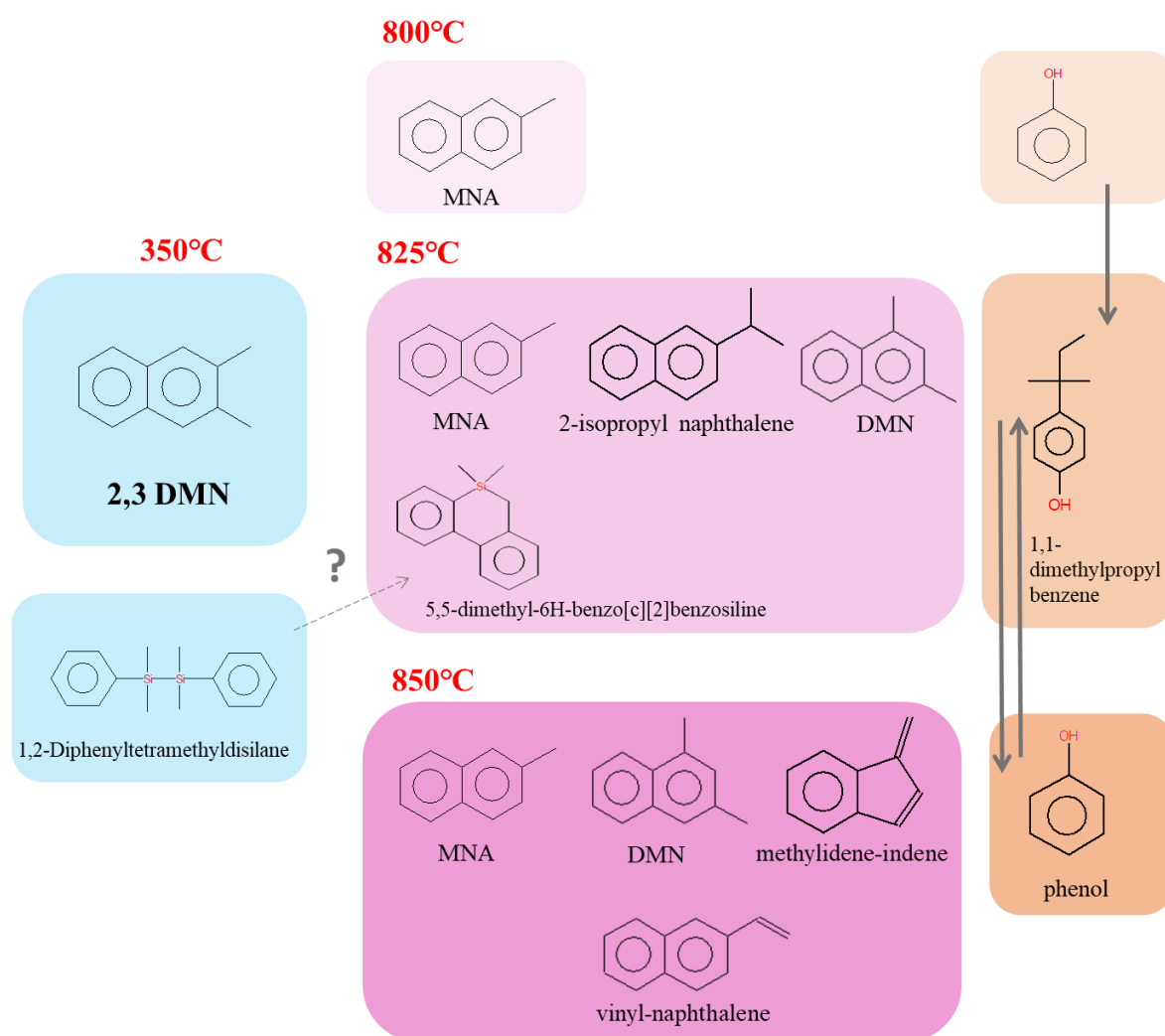
Figure 6.19 Graphic representation of the formed pyrolysates when the heart-cut 2,3 DMN (and 1,2-Diphenyltetramethyldisilane contaminant seen in Figure 6.1) was exposed to 800°C, 825°C and 850°C on the prep-GC, and transferred on the GC-MS.

One MNA compound appears in the three pyrograms (compound #2) between 800°C and 850°C. Although only a small fraction (unquantified) of 2,3 DMN is pyrolysed, the loss of a methyl radical from this compound can have wide applications if the pyrolysis time is increased for the reaction to run close to or to completion, thus it is important to understand the further reactions in which the methyl radical is involved. It should be also noted that the occurring pyrolysates are stable.

2,3 DMN pyrolyses in a similar fashion to MNAs (Yang and Lu, 2005; Gräber and Hüttinger, 1982), losing a methyl radical and, as naphthalene was not seen in the presented pyrograms, it appears that only one C-C bond is broken. Due to the symmetry of the position 2 and 3 methyls on the naphthalene backbone, it is unlikely that one is preferred over the other, both methyls being attached to β carbons (Madison and Roberts, 1958) on the naphthalene backbone. The methyl radical or radicals detached from the backbone of 2,3 DMN appear to lead to the formation of a different 2,3 DMN isomer and 2-isopropylnaphthalene at 825°C. They are potentially involved in the radical addition reactions to the contaminant molecule phenol, whose parent molecule is unknown. 2-isopropylnaphtahelene is only seen at 825°C and 2 new molecules are seen at 850°C: vinyl-naphthalene and methylidene-indene.

1,2-Diphenyltetramethyldisilane enters the pyrolyser as a contaminant that was not heart-cut from the injected DMNs sample (Figure 6.13). This can lead to isotopic scrambling, where both methyl radicals from 2,3 DMN and 1,2-Diphenyltetramethyldisilane can be used to form secondary pyrolysates which should be avoided in PSIA studies. If compound identification is accurate, peak #7 can be a result of 1,2-Diphenyltetramethyldisilane pyrolysis.

Unlike the 1,2-Diphenyltetramethyldisilane contaminant seen in Figure 6.19, it is not clear how phenol and 1,1-dimethylpropylbenzene formed in the system, and from which parent molecule. Phenol has a lower boiling point than DMNs, meaning it would have appeared only in one pyrogram and then it would have been eliminated from the prep-GC if it occurred as a contaminant. Furthermore, it is unlikely to be introduced in the same heart-cut window as the 2,3 DMN due to their different boiling points. The presence of phenol and 1,1-dimethylpropylbenzene indicates oxidative reactions and the presence of oxygen or oxygen-containing species in the system, yet in the oxidative experiment of Yang and Lu (2005) done on 1-MNA, the parent compound did not breakdown to pyrolysates containing one aromatic ring, indicating that, in this case, an oxygen-containing mono-aromatic contaminant molecule is more likely the case.

6.4.4. Comparison between the RMG and prep-GC results

Both experimental results and RMG simulation outputs indicate one common compound, formed through the cleavage between a methyl radical and the backbone of naphthalene, methylnaphthalene. RMG simulations at and above 850℃ indicate minor pyrolysate production relative to further increase in temperatures (zoom-out insert in Figure 6.18), which is also expected in experimental pyrolysis.

2,3 DMN pyrolysis leads, in both lines of evidence, to one methyl radical loss, as naphthalene was not seen in the presented prep-GC pyrograms and, as the 2- and 3- radical positions are both attached to β carbons, it is unlikely that one is preferred over the other. Several other pyrolysates from Figures 6.15 and 6.16, seem however to have formed via radical recombination reactions, where the methyl radical attaches to a different pyrolysate. Even if the identification of pyrolysate is not accurate, their number indicate that both the methyl radical, the MNA and potentially 2,3 DMN are involved in a series of reactions due to pyrolysis. This has the potential to lead to isotopic scrambling, defying the purpose of PSIA.

6.5. Conclusions

The current version of the prep-GC system (Figure 6.1) was used in the study for natural concentration DMNs heart-cutting, trapping, concentration and pyrolysis, testing all auxiliaries available for the prep-GC system that are further involved in the pyrolysis of diploptene in the following chapter. Testing of the system with high boiling molecules indicated the formation of cold spots in several areas within the prep-GC which were remediated. It was confirmed that the prep-GC system can successfully trap, concentrate and release compounds of interest in a reproducible and repeatable manner and it is able to pyrolyse and transfer the pyrolysates to a second GC instrument, methodologies which will be used, in the analytical pyrolysis of diploptene. Analysis of DMNs on the prep-GC also confirmed the ability of the system to cope with high molecular weight compounds present at natural concentrations, expected in the case of most natural samples.

Furthermore, two different compound trapping devices have been assessed. The SIM oven-integrated trap performed overall better than the ICE trap, yet both trap systems managed to concentrate the desired compound. 2,3 DMN was heart-cut, pyrolysed and transferred to a GC-MS for pyrolysate identification. RMG simulations and experimental results indicate at least one common pyrolysate, MNA. All 5 set aims of this chapter were thus met, indicating that the prep-GC system is fit for analysing compounds with molecular weights at least in the range of 88-156 g/mol. In the final Chapter, diploptene, with a molecular weight significantly higher than DMNS, at 410 g/mol, will be analysed, with final modifications brought to the prep-GC system.

7. Diploptene pyrolysis

7.1. Introduction

The work conducted in Chapter 3 (PMFB peatland samples) demonstrated the challenges in attributing the source of diploptene in (palaeo)environmental samples due to the wide range of potential bio-producers (Subsection 3.4.4). Even in pure methanotroph cultures, type II-produced diploptene had a muted methanotrophic signature given the incorporation of C-CO_2 (Chapter 4). It is thus necessary to have better constraints and methodologies when working with lipids which have multiple sources. Position-specific isotope analysis (PSIA) can provide an increased level of information, allowing to assess isotopic signatures at the *intra*molecular level and ideally, the carbon that comes from the original CH_4 molecule (CH_4-C) at the time of lipid production, having thus the potential to confirm, with a higher confidence, a methanotroph bio-producer. Hopanoids, however, have never been subjected to direct pyrolysis, and their potential for PSIA is not known.

There has long been evidence of hopanoid occlusion in kerogen and asphaltene (Rubinstein *et al.*, 1979; Mycke and Michaelis, 1986), and many studies have looked at the pyrolytic temperatures necessary for their release in order to characterise the complex hydrocarbon structures yet did not increase the temperatures further to look at the degradation products of the released compounds (i.e., common temperatures of 350-450°C; Rubinstein et al., 1979, Klesment, 1980; Eglinton and Douglas, 1988). The mechanisms of hopanoid breakdown during pyrolysis are thus unknown. In a kerogen hydropyrolysis study, Farrimond *et al.* (2003) increased the temperature **up to 500°C**, with no hopanoid breakdown data or evidence being reported. Seifert (1978) described the changes in the sterane/terpane ratio during a ramped **370-550°C** pyrolysis, noting the decrease in this ratio as a function of pyrolysis temperature and the generation of new terpanes from primary C_{30} ones, the formation of 17β(H),21α(H)-hopane from 17β(H),21β(H)-hopane due to the input of pyrolytic energy, and the presence of hopanes of various molecular sizes. This potentially indicates that hopanoids may start breaking down into pyrolysates above 550°C. Van Graas (1986) compared solvent extracted (dried lipids) with asphaltenes subjected to a **600°C pyroprobe**, with the products analysed via GC-MS. Triterpenes characterised by *m/z* 191 were seen in good abundance at this temperature, however several peaks of non-regular hopanes (of which only a C_{30}-triterpene) were seen in the extracted, yet not in the pyrolysed

fraction. This was attributed to a shift that hopanes experienced, degrading from C_{30} and higher compounds into C_{27} and C_{29} hopanes, potentially indicating that at temperatures higher than 550°C, a small degradation of the hopanoid skeleton may take place. Lastly, isotope fractionation effects were highlighted for C-C bond breaking, noting the isotopically lighter nature of pyrolysates, seen especially for smaller molecular weight compounds. The study exposed kerogens for 20 sec to **800°C**, where activation energies would have been high enough for breaking the ^{12}C-^{12}C and ^{12}C-^{13}C bonds, and avoiding isotopic effects. Interestingly, hopanoids with C_{27}-C_{33} structures were still present in a few of the pyrolysed samples of different kerogen origins upon exposure to 800°C, indicating that hopanoid breakdown did not occur (at least quantitative; Eglinton, 1994).
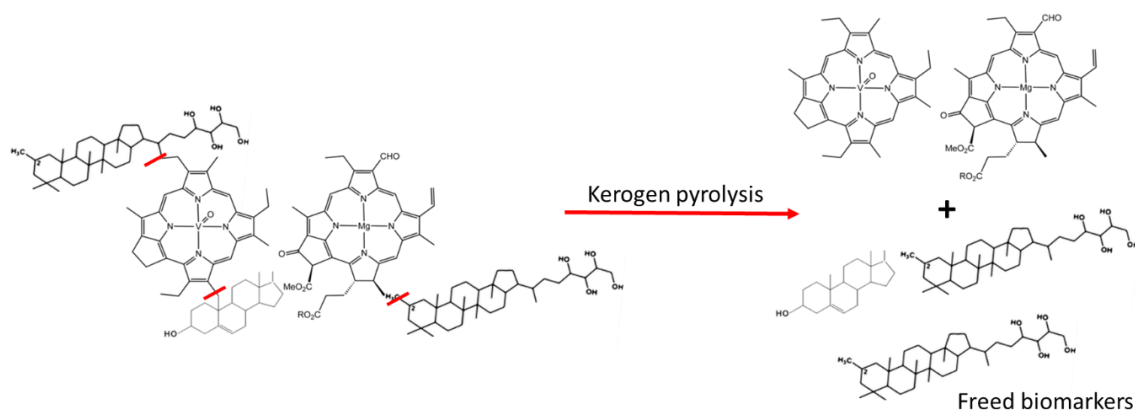
Figure 7.1 Kerogen pyrolysis leading to bond breaking and free biomarker. Figures edited from Wikiwand (2024), Schaechter (2014) and Stillwell (2016) .

The studies reviewed above highlight the standing gap in knowledge, that there is a lack of understanding of how diploptene, and hopanoid in general, would pyrolyse, and if PSIA can be achieved via pyrolysis-achieved moieties of diploptene. The development of the prep-GC system (Chapters 5 and 6) was based on previous online PSIA instruments and provides the analytical instrument to study this complex and HMW compound and understand its pyrolytic breakdown. This chapter thus aims to investigate the pyrolysis patterns of diploptene, assessing its potential for PSIA. This is done first by studying, based on current literature, the pathways of CH_4 incorporation into diploptene produced by the three types of methanotrophs (type I, II and X), highlighting molecular moieties of PSIA interest, followed by an *in-silico* and experimental approach to understand its breakdown patterns, investigating if moieties with a close link to the CH_4-C can be obtained for future PSIA studies.

7.2. Methods and methods

7.2.1 Reactants and chemicals

An analytical diploptene (Hop-29(22)-ene) standard was purchased from Merck (Sigma Aldrich), with a concentration of 0.1mg/mL in isooctane (04626-1ML). Squalene (≥98.0% GC; 8210680100) and isoprene (99% with <1000 ppm p-tert-butylcatechol as inhibitor; I19551-100ML) were also used from the same distributor.

A 1% squalene in GC-grade hexane (anhydrous, 95%, Sigma Aldrich) solution was prepared and divided into 2 mL GC vials that were stored in a fridge for further analysis. Due to its low boiling point, isoprene was injected as a pure chemical in the GC, with a high split.

7.2.2. RMG *in-silico* pyrolysis methods

RMG simulations were originally performed using a modified code used for MTBE in Chapter 5, to inform on the pyrolytic behaviour of diploptene, squalene and isoprene, followed by an analysis of laboratory-performed pyrolytic experiments. However, once the experiments were conducted, several parameters were tuned to match the lab setup and the optimised GC methods. The RMG data presented here for squalene and isoprene were subsequently adjusted to the GC methods, to inform on the pyrolytic reaction and pathways that led to species formation during the following experiments within the prep-GC.

7.2.2.1. Diploptene – RMG parameters

Diploptene was modelled within RMG using the following parameters. The standard's concentration, the amount injected, molar mass and molarity were used to calculate N, the number of mols subjected to RMG pyrolysis, and mol fraction with regards to helium. The system's pressure for the selected flow (1.2 mL/min) was set for the temperature at which diplotene arrived in the pyrolyser, determined by its retention time in the prep-GC method presented below (Table 7.1).

Concentration diploptene standard in isooctane = 0.1 mg/mL (µg/µL)

Diploptene molar mass = 410 g/mol

Molarity = 0.0002439 mmol/mL

Injection volume = 1 µL

Amount diploptene injected = 0.1 µg

N= 0.1 µL x 0.0002439 mol/L = 2.439 E – 11 mols

Mole fraction for RMG

Diploptene + Helium = 1

Diploptene = 0.00000000002439 (number required by RMG) = 2.439 E-11

Helium = 0.99999999997561 (number required by RMG) = 9.9999999997561 E-1

RMG programme and Retention Times in the pyrolyser

Temperature of oven at elution $\approx$ 290°C $\rightarrow$ 563.15K

Volume reactor $\approx$ 0.245 cm^3

Flow rate GC method = 1.2 mL/min = 1.2 cm^3/min

Pressure psi system $\approx$ 30 psi $\rightarrow$ 2.068 bars

Table 7.1 Diploptene residence time with the pyrolyser calculated based on Eq 8.

Temp pyrolysis (°C)	Temp pyrolysis (K)	Time for RMG (seconds)
350	623.15	11.07
500	773.15	8.92
550	823.15	8.38
600	873.15	7.90
650	923.15	7.47
700	973.15	7.09
750	1023.15	6.74
800	1073.15	6.43
850	1123.15	6.14

7.2.2.2. Squalene – RMG parameters

Similarly, the injection method and dilution of squalene were used to calculate its mole fraction relative to helium. The prep-GC method was translated to fit RMG required parameters, and for calculating the residence time within the pyrolyser (Table 7.2).

Squalene pure standard (Sigma Aldrich, 1615-91-4, 04626-1mL)

Concentration standard = 100%; Dilution = 1%

Injection volume = 1 µL

Split = 20:1

Moles with split applied = 0.00000000111607 = 1.11607 E-9

Mole fraction for RMG

Squalene + Helium = 1

Squalene = 0.00000000111607 = 1.11607 E-9

Helium = 0.99999999888393 = 9.9999999888393 E-1

RMG programme and Retention Times in pyrolyser

Temperature of oven at elution ≈ 70°C → 343.15K

Volume reactor ≈ 0.245 cm^3

Flow rate GC method=1.2 mL/min=1.2 cm^3/min

Pressure psi system ≈ 27.3 → 1.88 bars

Table 7.2 Squalene residence time with the pyrolyser calculated based on Eq. 8.

Temp pyrolysis (°C)	Temp pyrolyser (K)	Time for RMG (seconds)
350	623.15	8.86
450	723.15	7.63
500	773.15	7.14
550	823.15	6.70
600	873.15	6.32
650	923.15	5.98
700	973.15	5.67
750	1023.15	5.39

7.2.2.3. Isoprene – RMG parameters

Finally, isoprene's concentration relative to helium and residence time within the pyroliser were calculated.

Isoprene pure standard (Sigma Aldrich, 1615-91-4, 04626-1mL)

Concentration standard = 100%

Injection volume = 0.5 µL

Split = 35:1

Moles with split applied = 0.00000000063776 = 6.3776×E−10

Mole fraction for RMG

Isoprene + Helium = 1

Isoprene = 0.00000000063776 = 6.3776×E−10

Helium = 0.99999999936224 = 9.9999999936224×E-1

RMG programme and Retention Times in pyrolyser

Temperature of oven at elution ≈ 70°C → 343.15K

Volume reactor ≈ 0.245 cm^3

Flow rate GC method=1.2 mL/min = 1.2 cm^3/min

Pressure psi system ≈ 27.3 → 1.88 bars

Table 7.3 Isoprene residence time with the pyrolyser calculated based on Eq. 8.

Temp pyrolysis (°C)	Temp pyrolysis (K)	Time for RMG (seconds)
300	573.15	7.33
500	773.15	5.44
550	823.15	5.11
600	873.15	4.81
650	923.15	4.55
675	948.15	4.43
700	973.15	4.32
750	1023.15	4.11
800	1073.15	3.92
850	1123.15	3.74
900	1173.15	3.58

7.2.3. Capillary columns

Table 7.4 contains the capillary columns used in the various GC analyses in this chapter and highlights the instrument and experiments in which they were involved, as well as their abbreviation notations used in further system figures.

Table 7.4 Capillary columns used in Chapter 7 experiments.

Column	Measurements (length x ID x film thickness)	Abbreviation	Work in which it was involved
ZB-1HT Inferno	30m x 0.25mm x 0.25µm	HT-1	Main column for the first dimension
DB-5 J&W	30m x 0.25mm x 0.25µm	DB-5	GC-MS main column
ZB-WAX	30m x 0.32mm x 0.50µm	WAX	GC-MS diplopt 2.6.2.
DB-5	5m x 0.25mm x 0.25µm	DB-5	Diploptene method secondary dimension column
ZB-624 plus	70cm x 0.25mm x 1.40µm	ZB-642 piece	Diplopte pyrolysates trapping and separation
Restek	various x 0.25mm x 0.25µm	FS capillary	Pyrolysis, compound trapping, connections

During method development, some columns were defined within ChemStation as longer than their actual length, as done for DMN and MTBE work. This was done either to incorporate a short secondary column in the prep-GC (see for example Figure 7.3, diploptene 5m DB-5) or to keep RTs consistent between head pressure experienced by the compounds when they travelled a 30 m column with the valve in the ON position or a 60 m column, when the valve was in the OFF position (see Subsection 7.2.5.).

7.2.4. Squalene - experimental pyrolysis methods

7.2.4.1. Squalene prep-GC method

1µL of squalene at 1% concentration (in Hexane) was injected in the prep-GC with a 20:1 split. The prep-GC was connected as seen in Figure 7.2 and was equipped with the HT-1 column, defined as 30 m in length. The GC oven temperature program was 200°C (2.5 min hold), 20°C/min to 325°C (2 min hold) for a total run time of 10.75 min. The flow was set at 1.5 mL/min with an inlet pressure of 40.4 psi (2.8 bars). Squalene's RT was assessed in the prep-GC, with the valve in the ON position (Figure 7.2), reaching the FID between 7.4 – 7.7 min. For pyrolysis and transfer to the GC-MS, the valve position was defined as ON between 0-7.3 min and then switched to the OFF position past 7.3 min. Squalene pyrolysis was assessed with the pyrolyse set at 300°C, 450°C, 500°C, 550°C, 600°C, 650°C, 675°C and 700°C, allowing for equilibration time between different temperatures.
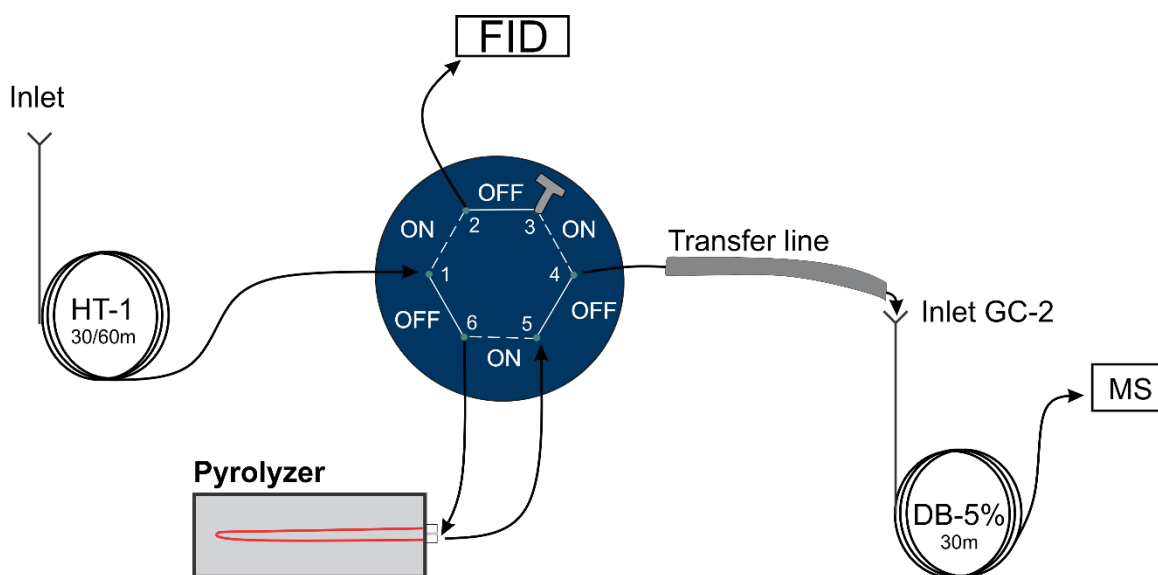
Figure 7.2 Prep-GC analytical setup used for the pyrolysis of Squalene and Isoprene.

Table 7.5 Method and time points for squalene heart-cutting, pyrolysis and GC-MS transfer.

Time (min)	Event	Method point
0 → 7.3	Valve ON	Solvent peak and 1st part of chromatogram to FID
7.3 → 10.75	Valve OFF	Squalene heart-cut, sent to the pyrolyser and to the GC-MS

7.2.4.2. Squalene GC-MS method

The transfer line was set at 200°C and, for the pyrolytic experiments, the transfer line needle was inserted into the GC-MS inlet when the valve was switched to the OFF position, marking the start of the GC-MS run. The GC-MS inlet was set in a 20:1 split.

The GC-MS was equipped with the DB-5 column defined as 30 m in length within the software. The oven program was 100°C (10 min), 15°C/min to 200°C (2 min). The transfer line was connected for 4 min at the start of the method. The flow was set at 1 mL/min. The MS scan range was between 30 – 500 amu.

7.2.5. Isoprene - experimental pyrolysis methods

7.2.5.1. Isoprene prep-GC method

0.5µL of pure isoprene was injected in the prep-GC with a 35:1 split. The prep-GC was connected as seen in Figure 7.2 and equipped with the HT-1 column, defined as 60 m in length. The oven was set isothermal at 70°C (5 min). The flow was set at 1.2 mL/min and the inlet pressure was 27.3 psi (1.88 bars). Isoprene's RT was assessed in the prep-GC, with the valve in the ON position (Figure 7.2), reaching the FID between 1.26 – 1.33 min. For pyrolysis and transfer to the GC-MS, the valve was in the OFF between 1.26 – 4.2 min. Isoprene pyrolysis was assessed with the pyrolyse set at 350°C, 500°C, 600°C, 650°C, 700°C, 750°C and 800°C, allowing for equilibration time between different temperatures.

Table 7.6 Method and time points for isoprene heart-cutting, pyrolysis and GC-MS transfer.

Time (min)	Event	Method point
0 → 1.26	Valve ON	1st part of chromatogram to FID
1.26 → 4.2	Valve OFF	Isoprene heart-cut, sent to the pyrolyser and to the GC-MS

7.2.5.2. Isoprene GC-MS method

The transfer line was set at 200°C and, for the pyrolytic experiments, the transfer line needle was inserted into the GC-MS inlet when the valve switched to the OFF position, marking the start of the GC-MS run (Figure 7.2). The GC-MS inlet was set in a 20:1 split.

The GC-MS was equipped with the DB-5 column defined as 30 m in length. The oven was set at 30°C (2 min), 10°C/min to 150°C (1 min). The transfer line was connected for 1.5 min

at the start of the method. The flow was set at 1 mL/min. The scan range was between 30 – 500 amu.

7.2.6. Diploptene - experimental pyrolysis methods

Due to the fact that diploptene is a HMW compound, with low concentration in the used analytical standard (0.1 mg/mL) and due to the temperature limitations on the prep-GC components, method development was done in several steps throughout the work in Chapter, with tests done to a) move the compound through the system (Subsection 7.2.6.1.), eliminating any cold spots and b) to confirm pyrolysis of diploptene prior to pyrolysate identification.

The methodology below was based on a pilot experiment (Appendix A.7.1.). No valves were involved during the main experiment (Figure 7.3) due to temperature limitations and the slightly colder thermal zone that the valve area represented for diploptene when compared to the GC oven (i.e., valve box maximum temperature of 250℃). The valve box had a widening effect on the peak shape of diploptene as seen in Appendix A.7.1. Only the SIM trap was employed in these experiments.

7.2.6.1. Prep-GC pyrolysis of Diploptene

Two methods were applied for the pyrolysis of 1 µL of the Diploptene standard (0.1 mg/mL) in isooctane. The first method was called the "**Solvent flush**" **method**, ran in splitless mode, in which the oven was programmed isothermal for 4 min at 230℃. The flow was set at 1.7 mL/min. During this method the isooctane peak eluted (Figure 7.3) and diploptene compound was retained onto the column for further analysis.

The initial solvent flush method was followed by a "**Diploptene pyrolysis**" **method,** which was selected and manually started when the pyrolyser reached and stabilised at the set temperature. The HT-1 column used was defined as 35 m to incorporate the length of the 2nd capillary column (approximated at 5 m). The oven program was: 230℃ (1min), 5℃/min to 310℃ (4 min). The flow was set at 1.2 mL/min. The SIM trap was set at 350℃ for both the unpyrolysed diploptene and any pyrolysates to reach the FID.
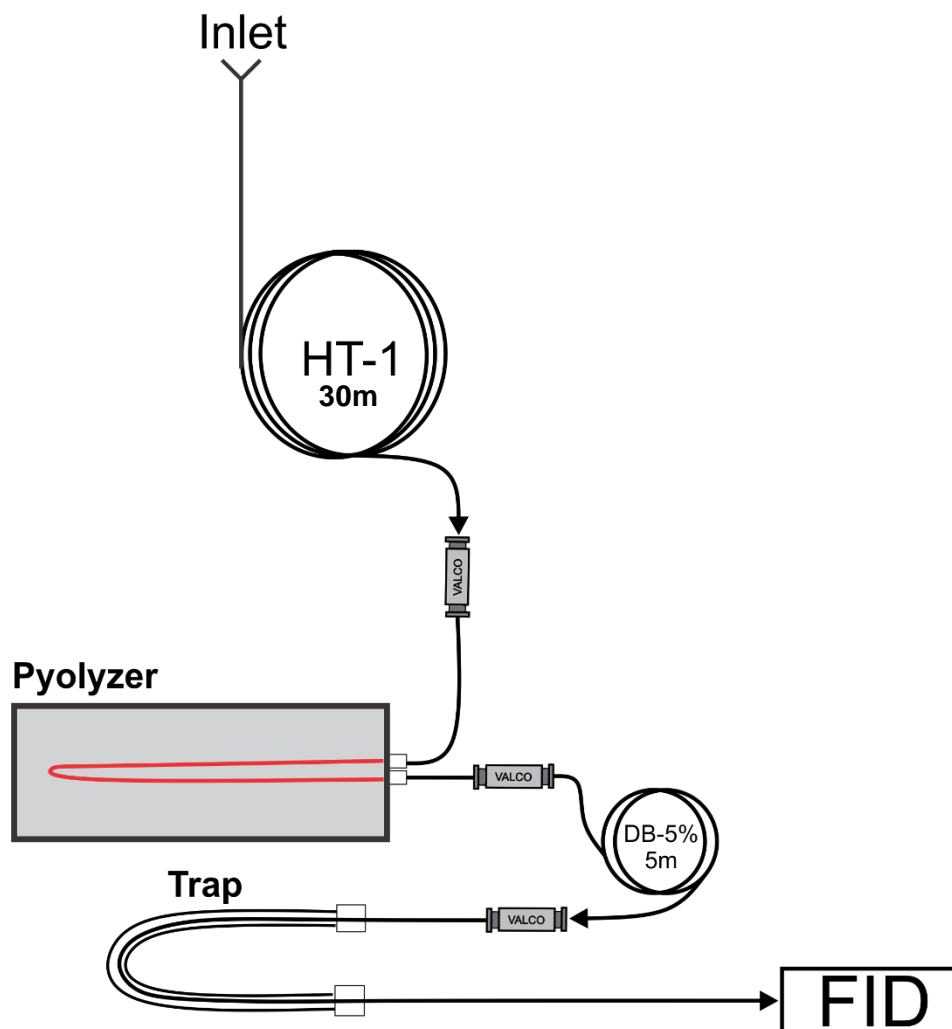
Figure 7.3 Prep-GC setup for diploptene pyrolysis. Only the SIM trap was employed with this system setup.

Trapping of the pyrolysed compounds was tested on 2 types of columns: a FS capillary and a piece of ZB-624plus column (Table 7.4), as well as on a U-shaped stainless-steel piece, placed within the SIM trap to test the retention of diploptene (and pyrolysates) on different surfaces. This method was called "**trap and flush**" and was conducted by adjusting the SIM trap temperature between -25°C and -27°C. Trapping of high boiling diploptene was done on both the FS capillary and on the U-shaped stainless-steel and the release of the compounds was done by flushing out the traps with solvent, concentrating and re-injecting the collected trapped fraction onto the GC-MS. For the flushing of the FS capillary, a modified analytical syringe was used (Figure 7.4; results in Subsection 7.3.6.3).

The manual injection was done on the GC-MS with the collected trapped fraction which started at 60°C (6 min hold), followed by an oven ramp of 10°C/min to 320°C (6 min hold), a flow of 1.2 mL/min and scan range between 50-600 amu. The analytical standard was

injected following the same method to confirm the correct MS library identification of diploptene (Figure 7.34).

FS capillary

Figure 7.4 Modified 100 µL Hamilton syringe with a FS capillary attached to the syringe body with 2 ferrules for compound flushing post trapping.

Previously, when a direct transfer to the GC-MS was conducted, only siloxane peaks were transferred from the prep-GC to the GC-MS (Appendix A.7.2.).

7.2.7. Software

The prep-GC chromatographic data was acquired using Agilent's OpenLAB CDS ChemStation Edition software, the chromatograms were exported as .csv data files aided by the Chemstation Offline software. Similarly, GC-MS chromatograms were acquired on MSD Chemstation E.02.01.1177 software and were plotted using Excel software.

OpenChrom, Community Edition 1.2.0 (Alder) is an open-source software which was used to process GC-MS chromatograms. It was coupled with thes NIST Mass Spectra Search Program, Version 2.0 g to identify mass spectra of selected compounds. CorelDRAW x5 was used to produce the diagrams and figures.

7.3. Results and discussion

7.3.1. Main findings

In this chapter, theoretical tracking of C-CH$_4$ revealed 12 key positions of PSIA interest in type II and X methanotroph-produced diploptene and 6 within type I diploptene. *In-silico* pyrolysis of this compound led to the formation of **isoprene** as the main pyrolysate, with experimental results indicating the formation of a major, low-molecular weight compound, assumed at this point to be isoprene based on further indirect evidence. In current experiments, diploptene starts breaking down at 575°C and RMG simulations indicate that during pyrolysis, the action of the cyclase enzyme which lead to the folding of squalene into diploptene is undone, squalene occurs as an unstable intermediate, and breaks down into isoprene units. It was also shown through RMG pyrolytic simulations that this breakdown mechanism may be unique to diploptene, as the pyrolysis of hop-21-ene and C$_{31}$-hopene do not lead to the formation of isoprene. Through theoretical research, isoprene is shown to not contain any new isotopic information compared to diploptene, and to lead to polymerization through pyrolysis, which defies the purpose of PSIA. A new mechanism, ozonolysis, is thus proposed for future investigations, if isoprene is reached through diploptene pyrolysis.

7.3.2. Theoretical research – Linking CH$_4$-carbon to hopanoids bio-synthetic pathways

The molecular carbon assimilation was compared for type I, II and X methanotrophs as they use distinctive bio-synthetic pathways to produce membrane-located hopanoid lipids (Anthony, 1982; Rohmer, 1999; Trotsenko and Murrell, 2008), focusing on the bio-synthesis of diploptene. In this subsection, the C-CH$_4$ is tracked within the molecular structure of the diploptene's predecessors of the three different types of methanotrophs (Figure 7.5, the red carbon, called also a labelled carbon within this thesis), highlighting the positions of interest for PSIA. The main outcome of this literature review is the location of labelled C-CH$_4$ of PSIA interest, which can be found summarised in Figure 7.12.

Methanotrophs consume and oxidise C_1 compounds (see for example reviews by Anthony, 1982; Hanson and Hanson, 1996; Knief, 2015). Based on their type, methanotrophs can employ two main pathways of carbon assimilation, RuMP and serine for type I and type II, respectively, and a combination of the two that also includes the Calvin-Benson-Bassham cycle (CBB), for type X. These cycles are summarised in Figures 7.7, 7.8 and 7.9 with respect to the two main metabolite formation (GA-3-P and pyruvate) that can further lead to the formation of squalene, which later gets folded and transformed into diploptene. The summary of the process presented in Figure 7.5 is further discussed as 5 different phases for simplicity.
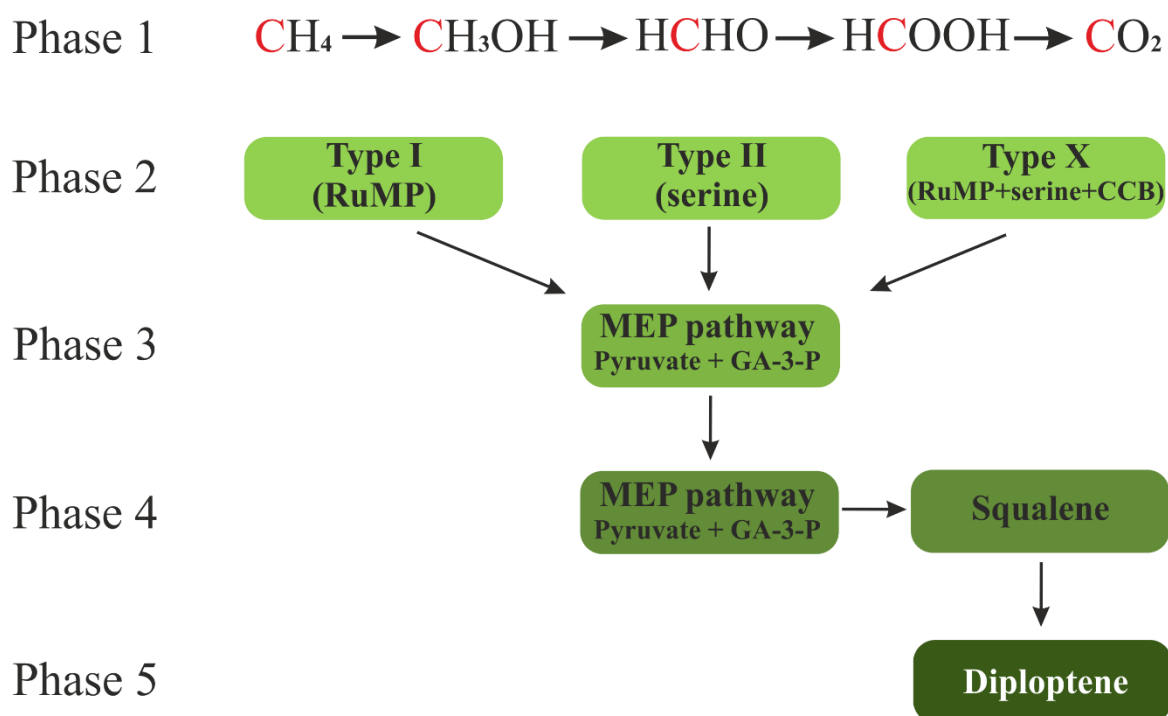
Figure 7.5 *The main phases of hopanoid production. Phase 1: oxidation of CH_4 that can branch into an assimilation process during which the red highlighted carbon is taken into the cell for metabolism, or dissimilation, when CO_2 is released. Phase two is further detailed in Figure 7 and refers to the different pathways for carbon incorporation into metabolites. Phase 3 consists of isoprenoid formation via the MEP pathway characteristic to a wide variety of Bacteria while Phase 4 follows the processes pyruvate and GA-3-P combination processes that lead to the formation of squalene, and further, in Phase 5, to diploptene, the studied hopanoid.*

7.3.2.1. Phase 1: Carbon assimilation and dissimilation

The first isotopic fractionation step takes place when a CH_4 atmospheric molecule is preferentially oxidised into methanol (CH_3OH) by the methane monooxygenase enzyme (MMO), a key enzyme characteristic of methanotrophs (Hanson and Hanson, 1996).

CH₃OH is further oxidised into formaldehyde (HCHO) by methanol dehydrogenase (MDH) and, for type I and X methanotrophs, formaldehyde is then assimilated as cell carbon and goes into the bio-synthetic cycles and the required compounds (Hanson and Hanson, 1996; Jahnke et al., 1999). This was also thought to be true for type II, yet there is now new evidence of a different assimilation point (Jahnke et al., 1999; Yang et al., 2013a). As seen in Figures 7.6 and 7.8, for the type II Serine pathway (i.e., *M. trichosporium* OB3b studied organism), there is a further oxidation step upstream from formaldehyde, and the branching point between C assimilation and dissimilation is at the formate level (CH_2O_2, Figure 7.6). Formate can be further transformed into CO_2 through formate dehydrogenase (FDH) via the dissimilatory pathway as a final product of CH_4 oxidation (Hanson and Hanson, 1996; Jahnke et al., 1999; Knief, 2015).
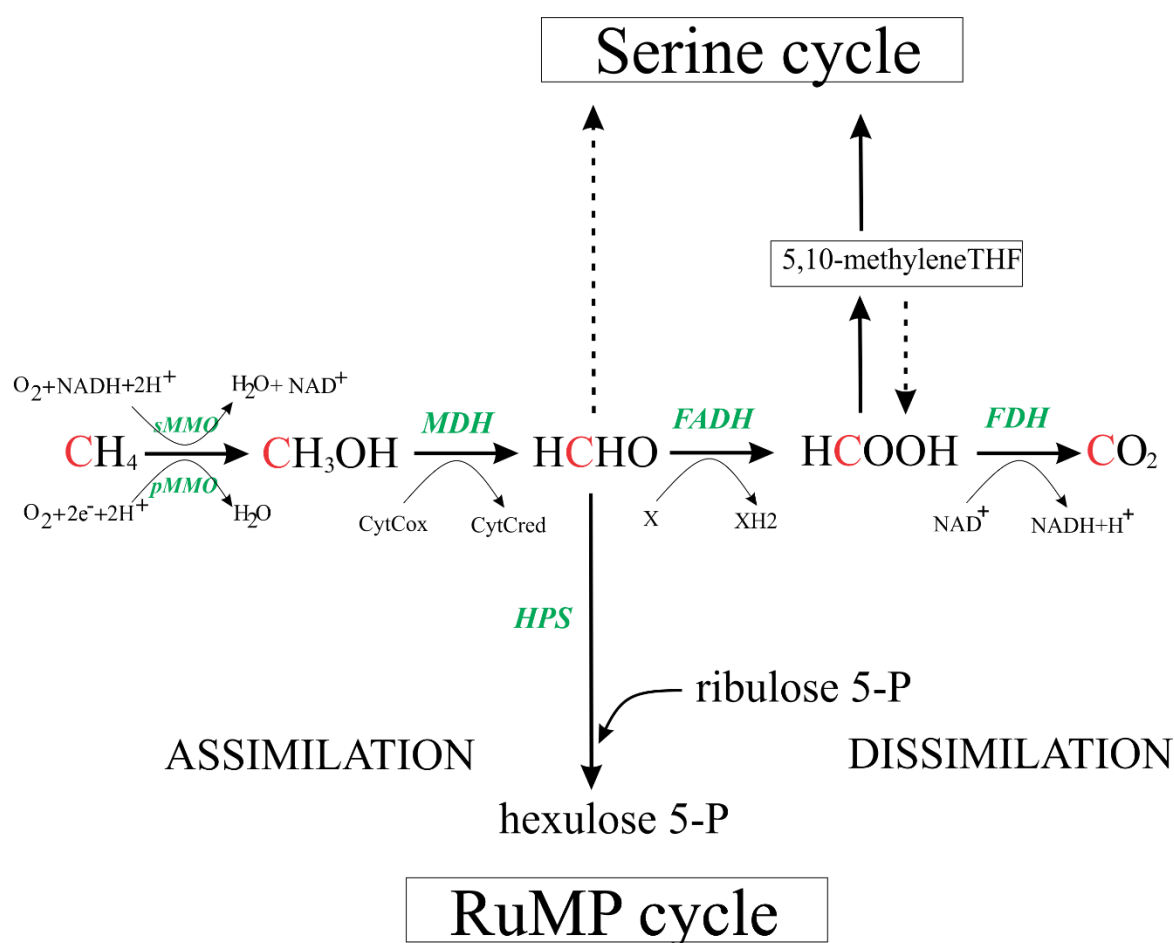
Figure 7.6 CH₄ enzymatic oxidation and incorporation into the RuMP or Serine cycles. Dissimilation takes place as CO₂. Notice the red C-CH₄ (edited from Jahnke et al., 1999).

In the following sections, the focus will be on the chemical reactions that follow the incorporation of C-CH₄ via formaldehyde (type I) or formate (type II and X) and the production of **pyruvate** and glyceraldehyde-3-phosphate (**GA-3-P**), the two precursors of isoprene, and eventually of squalene and hopanoids in bacteria that can employ the MEP pathway (Rohmer et al., 1993). The C-CH₄ of PSIA interest is highlighted in red and the

following diagrams of pyruvate and GA-3-P bio-synthesis, highlighting the position of isotopic interest.

7.3.2.2. Phase 2.1: Carbon assimilation into Type I through RuMP pathway

For type I methanotrophs, only a small fraction of CO_2 is incorporated into the biomass (5-15%; Dedysh and Dunfield, 2011), however the entry point of CO_2 is downstream from the diagram below (Figure 7.7), thus it does not influence the highlighted C-CH_4 positions from an isotopic point of view.

Formaldehyde (HCHO) incorporation is described in Figure 7.7, branching into two pathways (yellow boxes). In the EDD pathway (or KDPG variant), F-6-P is transformed into Glucose-6-Phosphate, which is oxidised into 6-phosphogluconate (not shown on graph) and, through the removal of a water molecule, is transformed into 2-keto, 3-deoxy, 6-phosphogluconate (KDPG). The presence of KDPG aldolase leads to the formation of glyceraldehyde 3-phosphate (GA-3-P) and of pyruvate (Anthony, 1982). In the EMP variant,
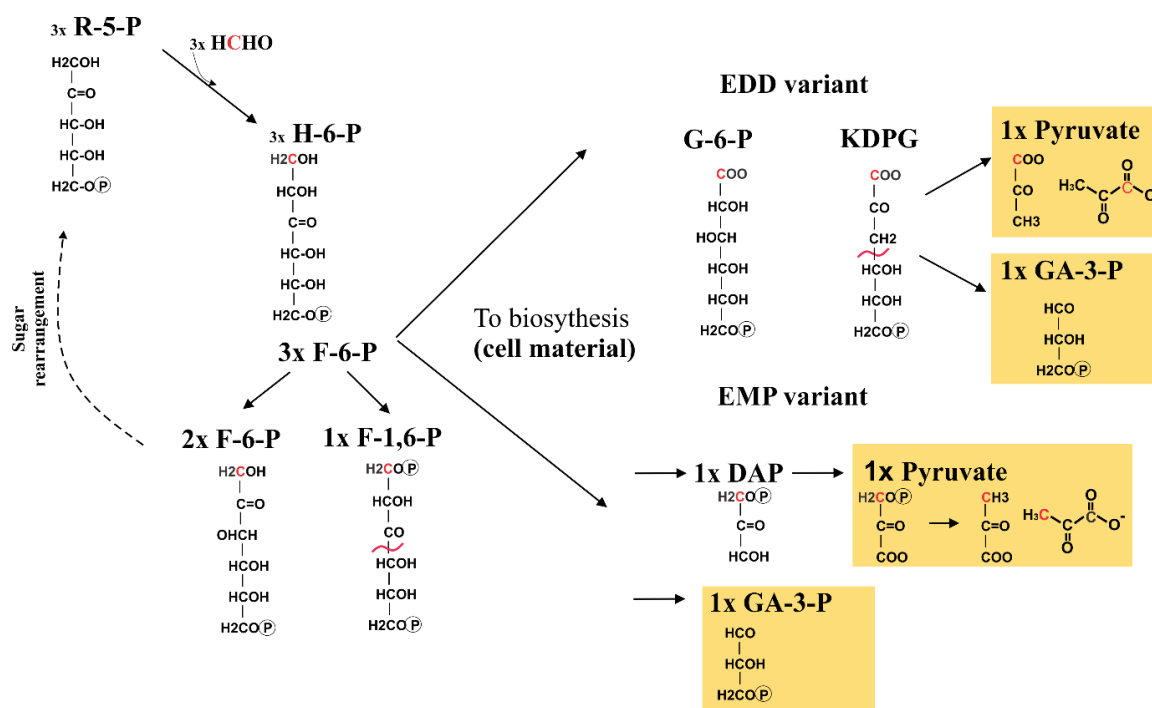
Figure 7.7 Both EDD and EMP pathways are available in M. methanica. Adapted from Anthony, 1982;Hanson and Hanson, 1996; Kalyuzhnaya et al., 2013. Formaldehyde (HCHO) bearing the carbon isotopic signature from the initial CH_4 molecule (red carbon) combines with Ribulose-5-Phosphate (R-5-P) through a key RuMP cycle enzyme (D-arabino-3-hexulose 6-phosphate formaldehyde lyase), leading to the formation of Hexulose-6-Phosphate, which is then isomerised into Fructose-6-Phosphate (F-6-P) or Fructose 1,6 -biphosphate (F-1,6-P) (Anthony, 1982). Here, two pathways can take place: the Entner-Doudoroff (EDD) pathway and Embden-Meyerhof-Parnas (EMP) pathway (e.g. Anthony, 1982; Kalyuzhnaya et al., 2013).

F-1,6-P is cleaved into dihydroxyacetone phosphate (DAP) and glyceraldehyde-3-phosphate (GA-3-P) (Anthony, 1982; Trotsenko and Murrell, 2008). Through a series of reactions (DAP→GAP→PEP), DAP can be transformed into pyruvate, thus the pathway providing again GA-3-P and pyruvate as products for isoprene synthesis (Phase 3).

In the sugar rearrangement phase, R-5-P is formed, which can combine with formaldehyde, closing thus the RuMP cycle (Anthony, 1982; Hanson and Hanson, 1996). A complete cycle is provided in the review of Trotsenko and Murrell (2008).

7.3.2.3. Phase 2.2: Carbon assimilation into Type II through Serine pathway

In Chapter 4, *Methylosinus trichosporium* OB3b, a type II representative, was grown to calculate the fractionation factor between provided headspace gases and diploptene and it is further studied in this section to better understand the assimilation pathway of the CH_4-C within hopanoids as this methanotroph type utilises both CH_4 and CO_2. *M. trichosporium*
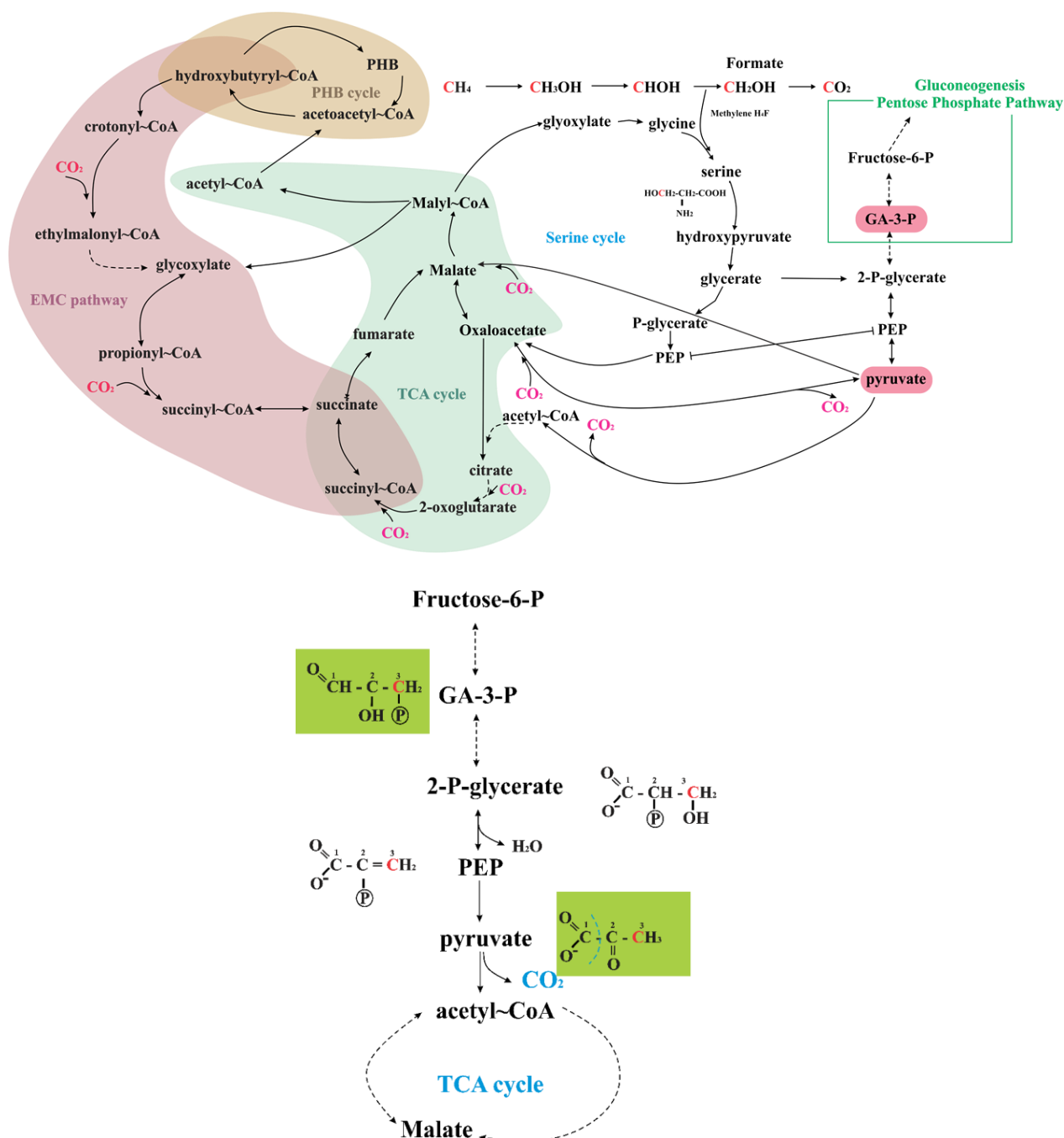
Figure 7.8 Briefly, formate is incorporated into glyoxylate, leading to the formation of serine, hydroxypyruvate and eventually phosphoglycerate (PG). PG can then be converted into phosphoenolpyruvate (PEP) that lead to the formation of pyruvate, while PG, through a series of reactions, to GA-3-P (Matsen et al., 2013; Yang et al., 2013a). The red highlighting of C of pyruvate and GA-3-P track the initial C-CH_4 assimilated at the formate point.

OB3b contains three known metabolic cycles that are connected: the serine, citric acid and ethylmalonyl-CoA (EMC) cycles (Yang et al., 2013a). Hanson and Hanson (1996) indicated that between 50-70% of C comes from CH_4 (i.e., formaldehyde assimilation) in type II, yet Yang et al. (2013a) found evidence of a higher percentage, of up to 62% of assimilated C comes from CO_2 (i.e., 6 molecules) and the remaining 38%, from CH_4 (i.e., for every 4 molecules), with potential carboxylation reactions that were so far unaccounted for. Furthermore, Yang et al. (2013a) and Matsen et al. (2013) report that, at least in *M. trichosporium* OB3b, CH_4 assimilation does not take place at formaldehyde branch point as previously thought (Hanson and Hanson, 1996), but at formate intermediate (Figures 7.6 and 7.8; methylene-tetrahydrofolate-MeH_4F).

Based on the current knowledge (Anthony, 1982; Hanson and Hanson, 1996; Trotsenko and Murrell, 2008; Yang et al., 2013a; Matsen et al., 2013), the pathway of C assimilation into type II-serine pathway methanotrophs is presented in Figure 7.8, with the C-CH_4 highlighted in GA-3-P and pyruvate.

7.3.2.4. Phase 2.3: Carbon assimilation into Type X through a combined pathway

A complete predicted pathway for cell biosynthesis intermediates within *M. capsulatus*, a type X representative, is provided in Ward *et al.* (2004). This type combines the RuMP, serine and Calvin (RuBisCo) pathways in a complicated metabolism however, in Figure 7.9, the focus is again only on the production of GA-3-P and pyruvate.

As in the EDD variant for the RuMP cycle, the formation of G-6-P can take place: G-6-P→gluconolactone-6P→6P-gluconate→KDPG → **GA-6-P** and **pyruvate** as one route of GA-3-P and pyruvate formation. However, this route records the C-CH_4 at the position in pyruvate that is cleaved during the formation of DOXP/MEP, meaning it will not be contained in the final hopanoid (see Figure 7.10). 6P-gluconate can also lead to the formation of R-5-P.

R-5-P can acquire another PO_4 (phosphate) unit, and transform into R-1,5-P which via the RuBisCO pathway, is carboxylated into 3-phosphoglycerate (3-PG). Via a series of chemical reactions, 3-PG leads to the formation of **pyruvate** which can be further transformed into **GA-3-P** given that all necessary enzymes are available (Ward et al., 2004).

To summarise, GA-3-P can either be formed from F-6-P in the RuMP pathway, from KDPG via the EDD variant or from a backward reaction from pyruvate. Pyruvate can be formed via the KDPG variant or from R-1,5-P via the RuBisCo pathway, in a series of downstream

reactions from 3-PG. The carboxylation reaction introduces a molecule CO_2 into the system, which can lead to shifts in the expected isotopic composition of lipids produced by *M. capsulatus*. There is also the possibility of an operational serine cycle in type X methanotrophs (Figure 7.9). The GA-3-P and pyruvate will bear the formate-C at the same positions as in type II. A complete type X pathway is presented in Ward et al. (2004) and in Trotsenko and Murrell (2008).
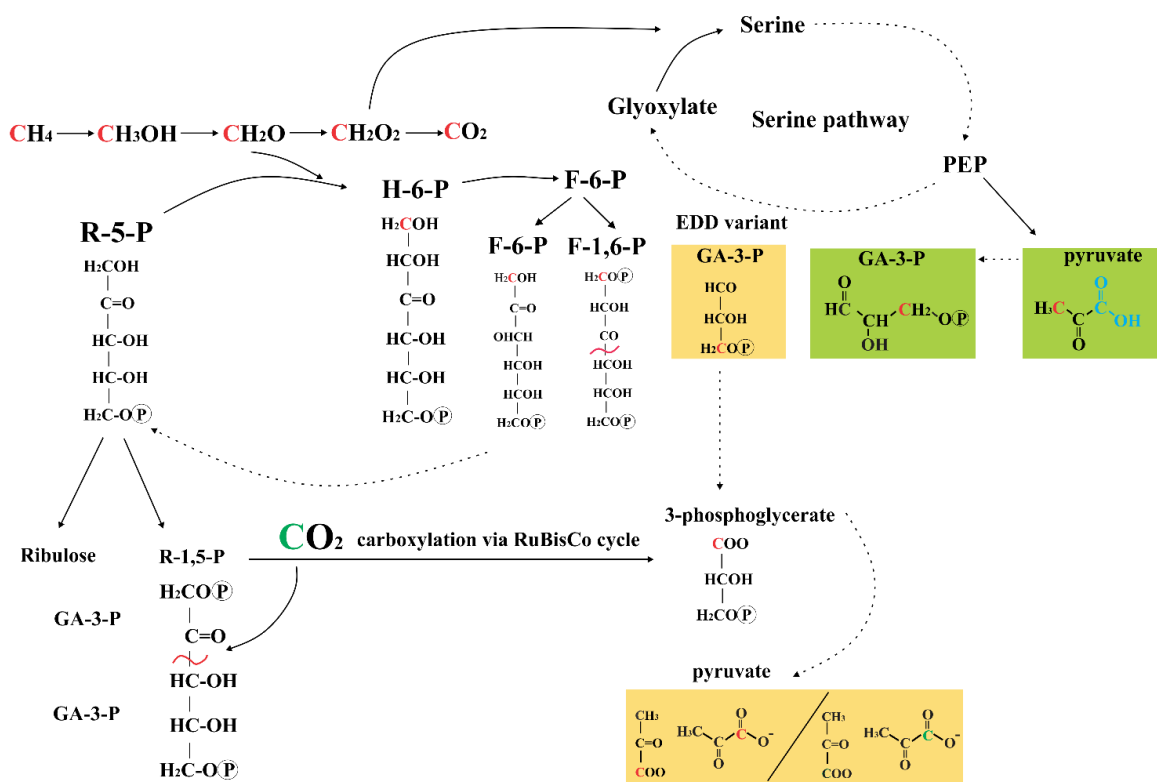
Figure 7.9 Type X assimilation pathway. Notice initial RuMP cycle and the presence of RuBisCo cycle that can lead to the carboxylation of Ribulose-1,5-P and to the formation of pyruvate that carries a carbon from CO_2. Briefly, formaldehyde follows the RuMP pathway in the first part, being condensed with R-5-P into H-6-P, which is further isomerised into fructose. F-6-P can then cleave into erythrose-4P and GA-3-P, that combined with a pyruvate molecule lead to the formation of xylulose-5-P, that then leads to a R-5-P for a complete RuMP cycle (not shown; see Ward et al., 2004). F-1,6-P can give a molecule of GA-3-P that contains the isotopic signature of the carbon from a CH_4 molecule (formaldehyde). Although this could have great implications on the isotopic signature of hopanoids, the 3rd carbon in pyruvate is not carries into the isoprenoid molecule as it combines with GA-3-P to give a C_5 compound (decarboxylation reaction). There are also enzymes that indicate the occurrence of serine cycle. If formate gets incorporated through the serine pathway, the GA-3-P and pyruvate will carry the formate-C at the same position as in Figure 7.8 (adapted from Ward et al., 2004).

7.3.2.5. Phase 3: MEP pathway of isoprene formation

The synthesis of IPP and DMAPP was initially thought to be via the mevalonate pathway (MVA), yet the pathway of isoprenoid formation via DOXP/MEP (1-deoxy-D-xylulose-5-phosphate/ 2C-methyl-D-erythritol-4-phosphate) is characteristic to a wide diversity of Bacteria (Rohmer et al., 1993; Rohmer, 1999; Rohmer, 2008) and it is further discussed in Hunter (2007) and Price *et al.* (2016). The MEP was recognised with the discovery of hopanoids and in the search for their ubiquitous bio-producers (Rohmer et al., 1993). Notice the position of the labelled carbons that represent the location of CH_4-derived carbon (CH_4-C) during one cycle of GA-3-P and pyruvate formation.
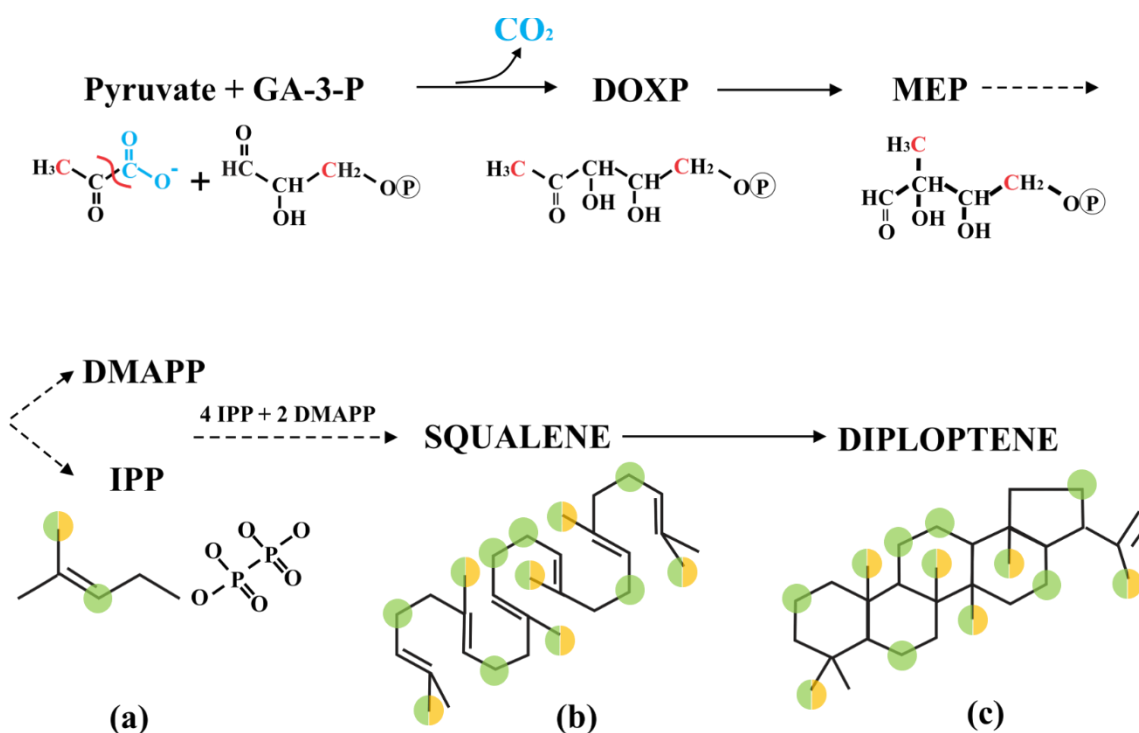
Figure 7.10 Pyruvate combines with GA-3-P leading to the formation of DOXP, and then, MEP. Notice the position of the carbons that come from either the RuMP (yellow half circles) or serine (green half or full circles) pathway. The 3rd carbon of pyruvate is not included in the DOXP and MEP molecules as CO_2, marked in blue, is released during the reaction (cleavage indicated with red line). MEP can either transform into one IPP (a) or a DMAPP molecule. The combination of 4 IPP and two DMAPP leads to the formation of one molecule of squalene (b), and then diploptene (c). Some reactions are omitted, as indicated by the dotted line.

7.3.2.6. Phases 4 and 5: From squalene to hopanoid formation

Squalene gets cyclised into a hopane via the squalene-hopane cyclase enzyme (SHC), known as the most complex one-step reaction in this field (Corey *et al.*, 1993; Feil *et al.*, 1996). During this process, 9 stereocenters and 5 cycles are created, and 13 covalent bonds are altered (Pale-Grosdemange *et al.*, 1998; Kannenberg and Poralla, 1999; Gao *et al.*, 2006). However, this reaction is considered to be less complex than the oxidosqualene cyclase (OSC) enzyme, responsible for sterol formation in eukaryotes (Abe et al., 1993). The folding of squalene in a minimum strained "all prechair configuration" (Abe et al., 1993) in the aqueous cell space takes place with minimum "enzymatic assistance" and it does not require only squalene substrate as it can also cyclise oxidosqualene enantiomers and polyprenols (Abe et al., 1993 and references therein).

SHC leads to the formation of several hydrocarbons, diploptene and diplopterol included (Abe et al., 1993). Squalene cyclisation starts from a proton attack on a terminal double bond (yellow label-Figure 7.11; Abe et al., 1993). The **hopanyl C-22 carbocation** is formed with a 5-membered E-ring (i.e., cyclopentane ring-red label Figure 7.11; only 5 carbons in the E ring, compared to cyclohexane rings A, B, C and D). To form diploptene (structure 10 in Figure 7.11), the H-29 proton is removed and, in order to form diplopterol (structure 11 in Figure 7.11), H_2O is added at the cationic centre (at **C-22 carbocation**) (Abe et al., 1993).
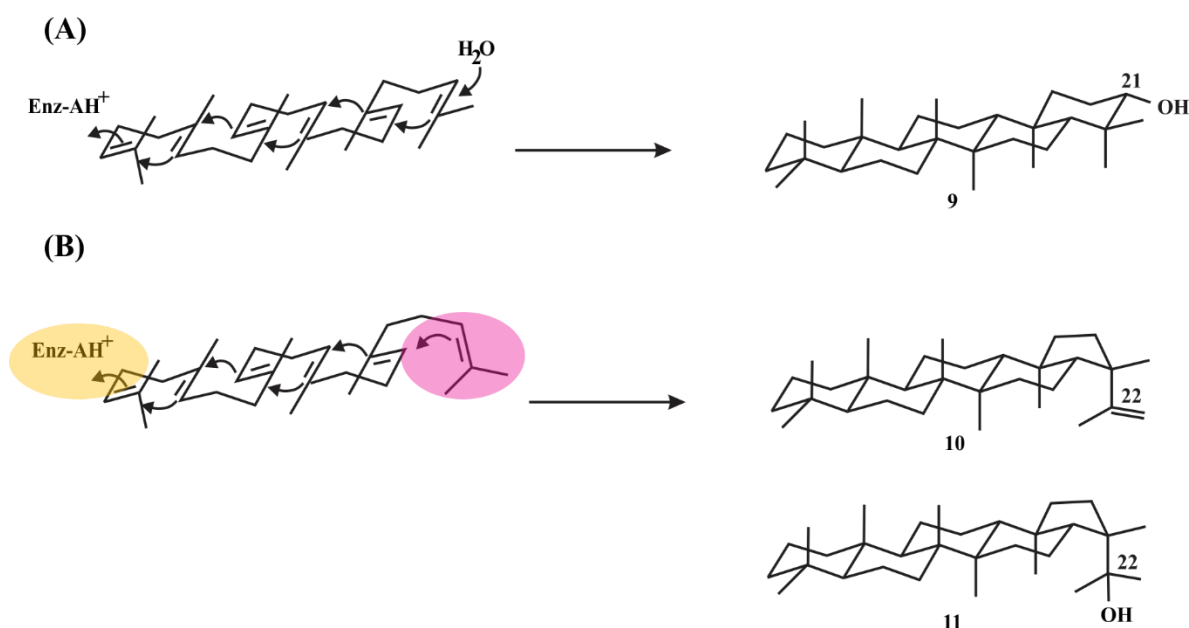
Figure 7.11 Hopanoid and sterol formation. (A) Sterol formation by OSC enzyme action and formation of sterols (compound 9). (B) Hopanoid formation by SHC enzyme: formation of diploptene (compound 10) and diplopterol (compound 11) (edited from Abe et al., 1993). The yellow label highlights the point of the proton attack on the terminal double bond, while the red label highlights the formation of the cyclopentane ring).

Squalene cyclization reaction takes place in bacteria, hence in primary aerobic organisms, yet, in the absence of oxygen, thus it can also take place in anoxic settings, linking its roots to the anaerobic stages of evolution (Abe et al., 1993). The OSC reaction that requires oxygen thus postdates SHC, and it is linked to the evolution of photosynthetic processes (Abe et al., 1993). A summary of the labelled squalene for type I, II and X methanotrophs is presented in Figure 7.10 and a summary of the labelled CH$_4$-C of PSIA interest for diploptene is presented in Figure 7.12.

Type I   **Type II and X**
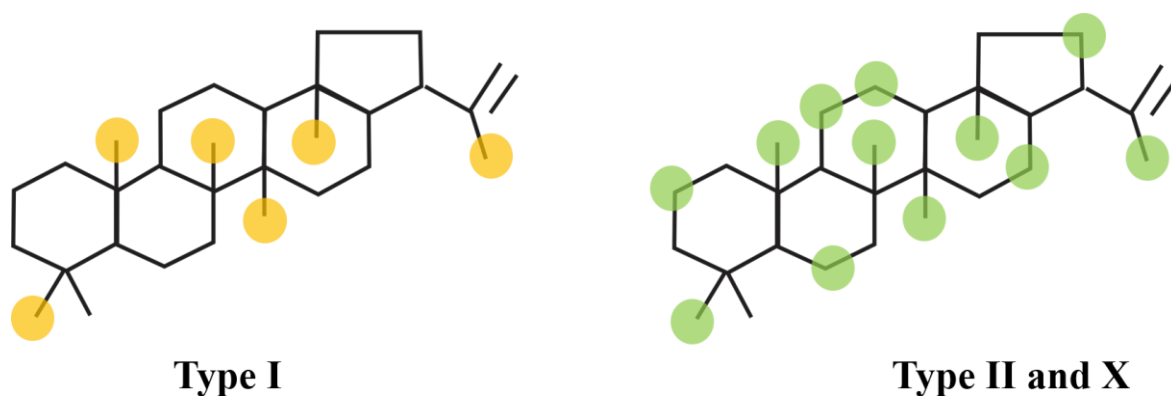
Figure 7.12 Summary of CH$_4$-C of PSIA interest in diploptene for types I, II and X methanotrophs. Yellow circles denote the location of C-CH$_4$ carbons after one RuMP cycle while the green circles the C-CH$_4$ carbons after one cycle characteristic of type II and X methanotrophs as detailed by Phase 2 (Subsections 7.3.1.2-7.3.1.4).

Having defined the carbons of PSIA interest (Figure 7.12), the aim is now to understand whether, through pyrolysis, these moieties can be accessed and isotopically analysed. Since the pyrolytic breakdown pattern of diploptene is unknown, this is done first via an *in-silico* experiment, to understand the feasibility of diploptene pyrolysis and the main formed fragment/s and then, experimentally, by employing the prep-GC instrument developed in Chapter 5.

7.3.3. RMG diploptene pyrolysis and hypothesis

RMG was employed to understand the breakdown mechanism of diploptene, prior to its experimental pyrolytic study. Diploptene is a HMW compound (i.e., mass 410 amu) with an elution temperature within the prep-GC experimentally observed at approximatively 290°C. Due to the compound's high boiling point (460.7±12.0°C at 760 mmHg) which is above the maximum temperature of the valve box and transfer line, RMG data provided the initial breakdown mechanism and main pyrolysates. Multiple simulations were performed, taking into account different pyrolytic temperatures, residence times and initial diploptene concentrations. Due to the size of the molecule, complicated reaction pathways for the produced intermediary pyrolysates, computational power and time required to finish one analysis, none of the employed simulations for diploptene ran to completion. Preliminary results indicate however that **isoprene** is the main produced fragment of diploptene pyrolysis.

Pyrolysis of diploptene was initially simulated at 750°C, based on the literature review of kerogen pyrolytic studies in this chapter. The limited RMG data only offered a restricted view of the start of this pyrolytic reaction which crashed after 24 days of simulation. The simulation results are only for 0.00018 seconds of reaction time, a fraction of the 6-11
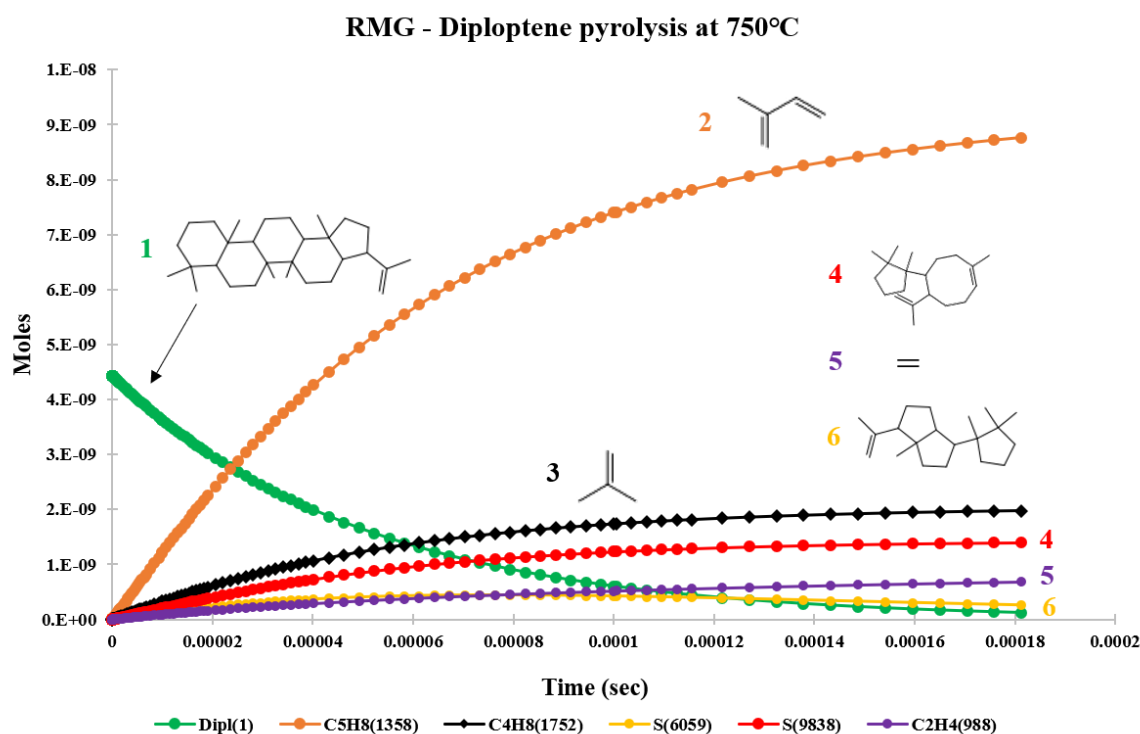
Figure 7.13 Simulation of diploptene pyrolysis at 750°C using RMG software. The molecular structures of species are provided within the plot, with the number colour-coordinated with the graph line. Isoprene (compound 2; orange) is the main pyrolysate. The key denotes the colour of the graph lines, together with the notations of species (S), as provided by RMG.

263

seconds calculated diploptene residence time within the reactor (Table 7.1). Variations of the initial code did not produce different reactions or main pyrolysates from the initial output. The initial simulation is used here for hypothesis generation and, although not complete, it provides an important view of the reaction's onset and expected mechanism. Valuable information was extracted and tested independently, confirming the RMG simulation.

The data plotted in Figure 7.13 shows diploptene breaking down and several pyrolysates increasing in concentration. The main produced pyrolysate is **isoprene** (i.e., orange plotted specie 1358). This is the main simulation based on which the work in this chapter developed. Although this is not a 1-carbon molecule, which would be PSIA preferable, the possibility of breaking down diploptene into smaller fragments is highlighted for the first time in this thesis, with the further intention to study the potential for diploptene PSIA via a fragment. The mechanism through which isoprene, the most abundant pyrolysate, formed is also investigated in Subsection 7.3.4., through the pyrolysis of squalene. A less prominent compound indicated by the simulation was **isobutylene,** produced in lower concentrations, followed by **ethene** and compounds #1 and #3 seen in Figure 7.13. The RMG-provided concentration values after 0.00018 sec for diploptene is 1.184E-10 moles and for isoprene is 8.760E-9 moles. The ratio between isoprene:diploptene (mol:mol) is 74 and only 17 between diploptene and isobutylene (mol:mol). Ethene had concentrations that were too reduced to be studied further.

RMG provides for each simulation an output file where reactions are depicted with their associated BDEs. The reactions have been plotted in Figures 7.14 and 7.15, providing a summary of the mechanism that led to the formation of isoprene. Appendix A.7.2 presents simulation reactions that show the formation of isobutylene for further investigation.

It is observed that there are 3 molecules first formed during diploptene pyrolysis, yet only one reacted further (Figure 7.15). It is important to note that the associated BDEs are the largest recorded in this simulation. The molecule that is broken down further is the one which requires the smallest amount of energy for its formation (i.e., 69.19 kcal/mol). Following the breakup of this bond, the BDEs required are quantitatively smaller and the reaction is expected to proceed with ease. It should be noted that there are several pathways to reach some molecules and that the process presented by RMG is not entirely linear. For example, molecules numbered 1 and 2 within the green rectangle of Figure 7.14 are reached through various breakdown and re-arrangement reactions. Together with a third molecule, they can lead to the formation of an unfolded diploptene backbone, known as **squalene**. This is the first time that this hypothesis is put forward: through pyrolysis, diploptene backbone unfolds

RMG-provided breakdown reaction tree for diploptene pyrolysis at 750°C - Part 1/2
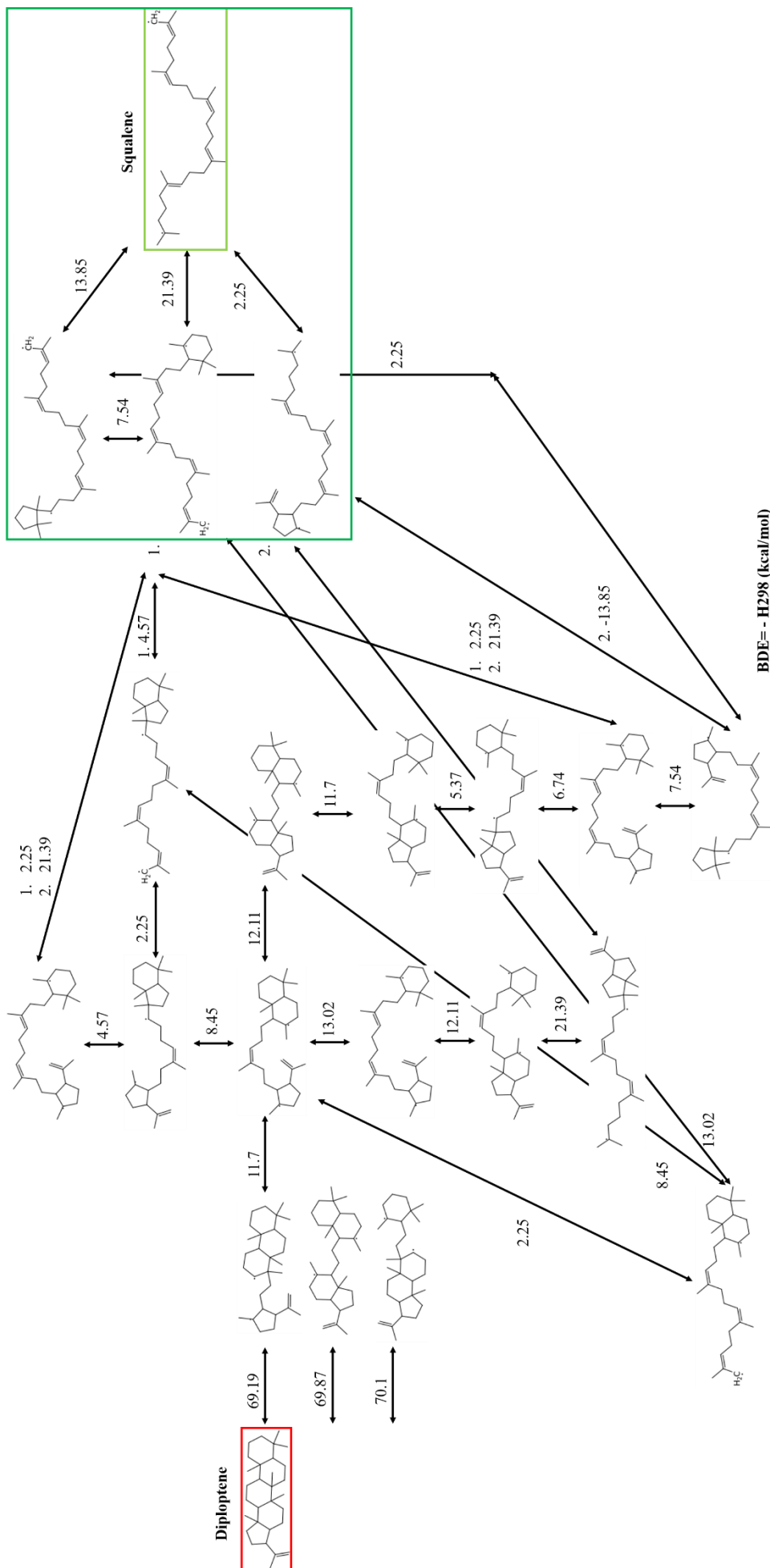
Figure 7.14 Initial reaction pathway of diploptene pyrolysis as depicted in Figure 7.13, and as provided by RMG. This is the first time the breakdown mechanism is presented, leading to the formation of a main isoprene pyrolysate. The numerical values represent BDEs expressed in kcal/mol.

RMG-provided breakdown reaction tree for diploptene pyrolysis at 750°C - Part 2/2

a
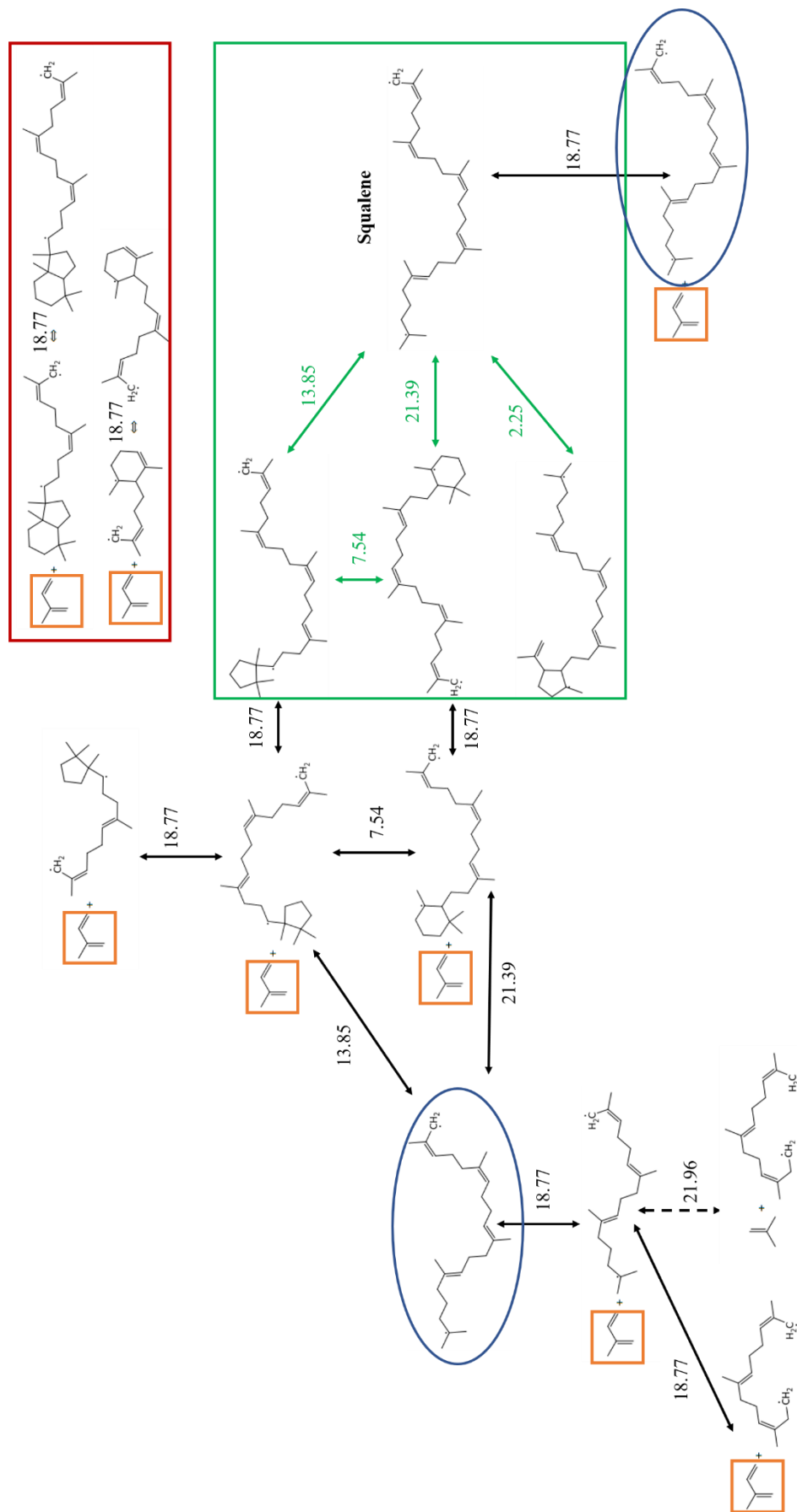
Figure 7.15 Continued RMG simulation of diploptene breakdown, starting from the previous green square reactions, displaying the breakdown of squalene intermediate, leading to the formation of isoprene units. The numerical values represent BDEs expressed in kcal/mol.

leading to the formation of squalene. Squalene is however not seen within the suggested main pyrolysates of diploptene in Figure 7.13 and, as seen in Figure 7.15, it further breaks down. Squalene is thus considered here an unstable intermediate, yet one of significant isotopic fractionation importance when referring to the formation of diploptene (Subsection 7.3.2, Phases 4 and 5). The un-doing of the cyclase action appears to be specific solely to diploptene as other compounds formed via a cyclase enzyme, such as trichodiene, lanosterol, cholesterol, hop-21-ene and that of C_{31}-hopane, did not display the same behaviour when pyrolysed *in-silico*, using RMG. This is further discussed in Subsection 7.3.7.

Figure 7.15 presents the following reactions predicted by RMG to take place once squalene is reached, highlighting the mechanisms through which isoprene is produced as a stable pyrolysate. Two out of the three squalene intermediates (i.e., green rectangle species) are reacted further, following again the reaction which requires the least energy. This weakest bond is located at the "tail" of the intermediate pyrolysates and 18.77 kcal/mol are required to cleave isoprene from a parent molecule across all reactions. The transformation of one molecule into a different species requires additional energy. Within the red rectangle of Figure 7.15, two reactions are displayed which contain parent molecules reached through various reactions. While the RMG simulation was not run to completion, this provides a quantitative view of the reactions that lead to the breakdown of diploptene. Taking into account what was observed in the first step of diploptene breakdown (i.e., that only the branch of reactions from the bond with the least BDEs required were further simulated), it is likely that the reaction tree is not missing a further branch of reactions due to the unfinished simulation, but that other reaction pathways were not taken due to higher BDEs required.

Based on the above simulations, diploptene is plotted in Figure 7.16 with several BDEs of interest, highlighting the first point of bond breaking (i.e., 69.19 kcal/mol, red arrows and values), summarizing the main findings. One further simulation, which stopped at a reaction time prior to the one presented in Figure 7.13, was also investigated. It provided further BDEs, showing reactions that were not kept in the core of Figure 7.13, and which could have not been investigated otherwise. It provided the BDEs required for the breaking of the bond between the methyl moieties and main backbone of diploptene (i.e., 87.1 kcal/mol, yellow arrows and values), which are of particular interest as they would have provided direct access to the CH_4-C for PSIA (more detail in Appendix A.7.3). The release of these methyl radicals requires larger BDEs, indicating that they are unlikely to be formed during diploptene pyrolysis, and that the breakdown to squalene and other intermediates, which lead to the formation of isoprene, is the preferred pathway from an energetic point of view. This data

helped further confirm the reaction mechanisms of diploptene pyrolysis presented in this chapter.
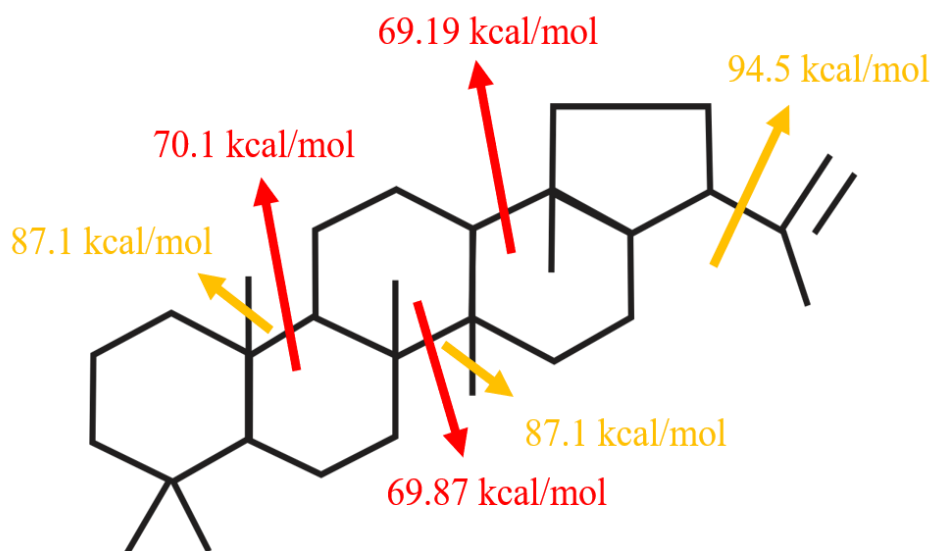
Figure 7.16 RMG provided BDEs for diploptene. The arrows represent the breaking of a bond between 2 carbons, with the yellow arrows denoting the breaking of a bond between the backbone and a "sticking-out" carbon or moiety, while the red arrows the breaking of a bond within the backbone of diploptene. Notice how the red BDEs have lower values, indicating that the bonds will break first within the backbone of diploptene.

Based on the presented preliminary RMG data of diploptene pyrolysis, this chapter will test whether, via pyrolysis, diploptene breaks down into isoprene as its main pyrolysate (Figure 7.17). Diploptene is presented in Figure 7.17 with the highlighted carbon atoms of interest for PSIA, and their expected location in isoprene for the three types of methanotrophs.
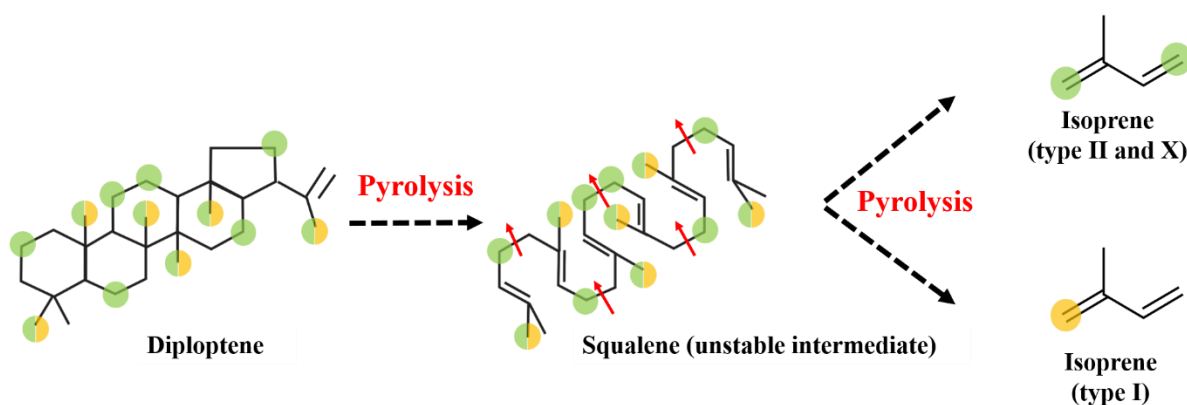
Figure 7.17 Main hypothesis based on preliminary RMG results and further tested in this chapter to understand and confirm diploptene's pyrolytic behavior. The red arrows represent the breaking of bonds breaking within unstable squalene intermediate, and the production of isoprene units with labeled carbons of type I, II and X methanotrophs as described in Phase 2 of subsection 7.3.1.

268

Regardless of the type of methanotroph bio-producer, as seen in Subsection 7.3.2., isoprene is expected to have the same highlighted carbon atoms obtained from CH_4-C.

To test this, the pyrolysis of squalene, which was seen as an unstable intermediate during the *in-silico* breakdown (Figures 7.14 and 7.15) was first simulated using RMG, to understand whether isoprene is a main pyrolysate of this reaction. Due to squalene's chemical proprieties, this compound was prep-GC amiable and was also pyrolysed in the lab to confirm the RMG results. Isoprene was then subjected to both *in-silico* RMG and analytical pyrolysis on the prep-GC, in order to understand whether position-specific levels can be achieved through the pyrolysis of this compound. These two lines of experiments provided the evidence to pursue the analytical pyrolysis of diploptene. Diploptene was successfully pyrolysed on the prep-GC, the results are further discussed in this chapter, and are corroborated with *in-silico* and experimental results of squalene and isoprene pyrolysis.

7.3.4. Squalene RMG and experimental pyrolysis

7.3.4.1. RMG pyrolysis of Squalene

The pyrolysis of squalene was initially simulated using RMG following parameters from Subsection 7.2.2.2. The provided results containing the most abundant molecules are plotted
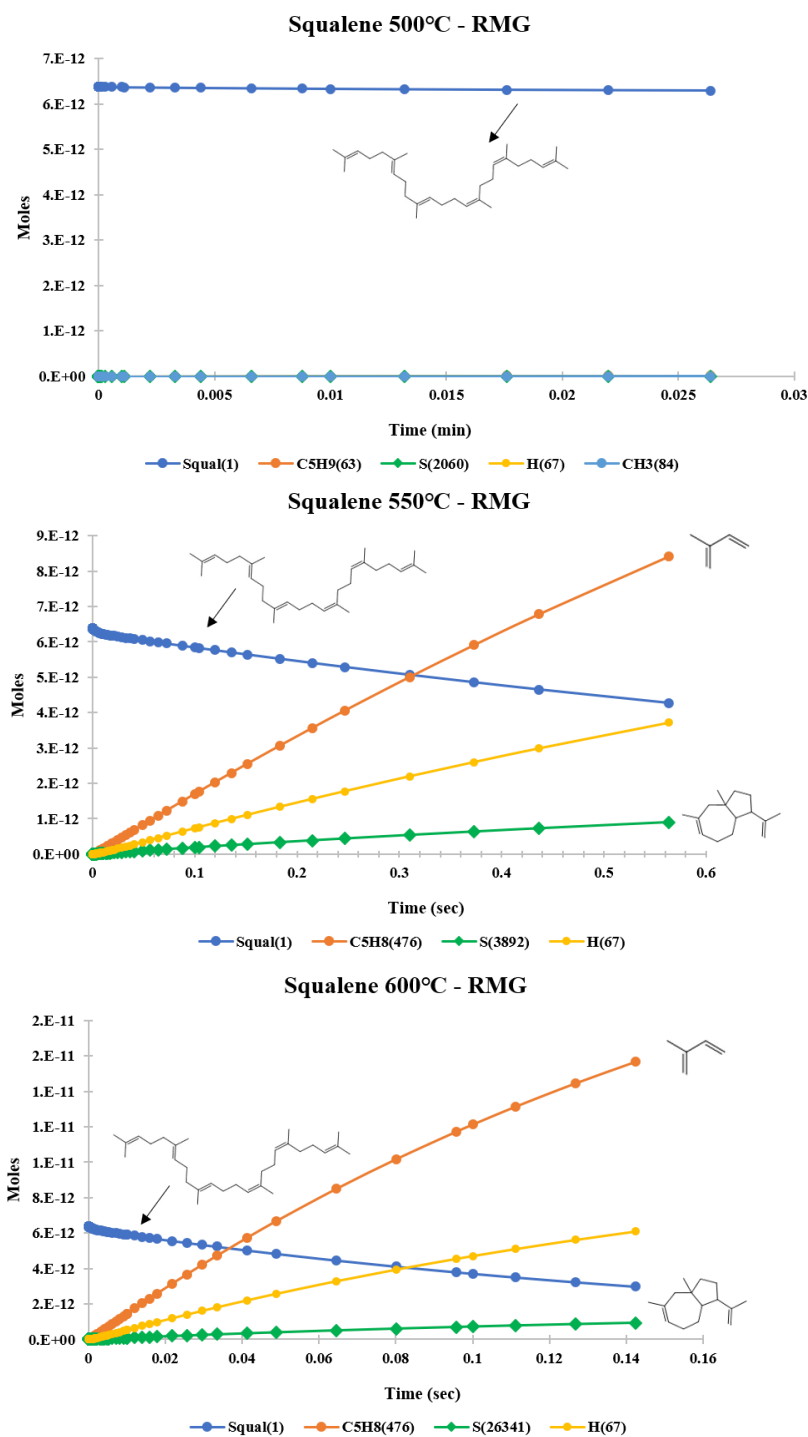
Figure 7.18 RMG simulations of squalene pyrolysis, with formation of a main isoprene pyrolysate as predicted by the first simulation of RMG diploptene pyrolysis. H refers to molecular hydrogen, while S(number) to a species associated with the RMG output file.

in Figures 7.18 and 7.19. Similarly to the diploptene, not all pyrolytic reactions of squalene run to completion, and the reaction times are different for Figure 7.18 simulations, yet **isoprene** was seen as the main pyrolysate in all squalene simulations, confirming previous data.

Breakdown of squalene starts taking place on RMG at 500°C, since during the 0.025 sec analysis, the molecule's concentrations slightly decreased, indicating that this temperature was high enough for bonds to start breaking. For 550°C and 600°C, the formation of three abundant pyrolysates is observed, with **isoprene** being the most abundant compound, followed by atomic hydrogen and a cyclic molecule. When exposed to 700°C, RMG predicts that squalene fully reacted and, at this temperature isoprene, the main pyrolysate also starts breaking down (Figure 7.19). The isoprene fragments produced during the pyrolysis of squalene will be tested against isoprene pyrolysis simulations discussed in the next section.
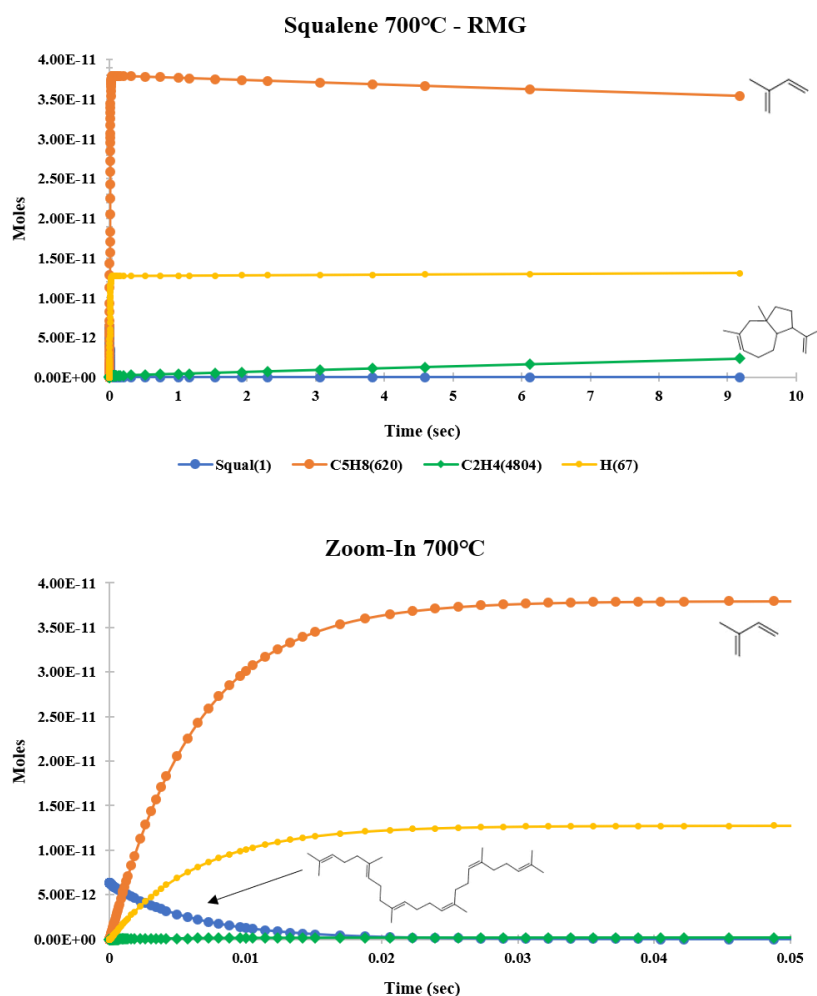
Figure 7.19 RMG simulation of squalene pyrolysed at 700°C and a zoom-in view that shows the steep breakdown of squalene at this temperature, and production of isoprene units. H refers to molecular hydrogen, while S(number) to a species associated with RMG output file.

271

The reaction mechanism is provided in Figure 7.21, containing the corresponding BDEs as provided by RMG. It is worth noting that the pathway of squalene breakdown does not follow the reaction path seen in Figure 7.15 of diploptene pyrolysis. In the diploptene reaction tree, once squalene was reached, the breakdown proceeds with the formation of one isoprene unit, which requires a BDE of 18.77 kcal/mol and its corresponding isoprenoid with a mass of 341 amu. In comparison, squalene breakdown from Figure 7.21 undergoes several different pathways: the ones which require lower BDEs eventually lead to specie break down and formation of isoprene units, while the reaction which produced one isoprene unit and an associated 340 amu fragment, requires a higher BDE (i.e., 61.15 kcal/mol). Two branches of the reaction tree lead to bonds breaking within the interior of the molecule, requiring higher BDEs, yet once the bond is broken, less energy is needed to reach isoprene units via several routes through which squalene is quantitatively transformed into isoprene. The larger initial BDEs were investigated and it was observed, within RMG, that the elimination of an atomic hydrogen requires the bulk part of the required energy as seen in the examples from Figure 7.20. The below reactions, displaying isoprene breakdown, exemplify the higher BDE required for the loss of one or two hydrogen atoms.
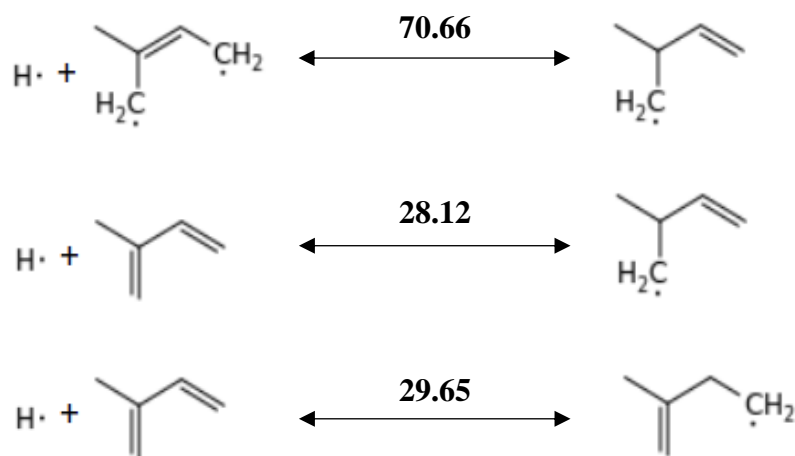
Figure 7.20 RMG-provided BDEs for the loss of one atomic hydrogen. The numerical values are in expressed in kcal/mol.

RMG-provided breakdown reaction tree for squalene pyrolysis at 700°C
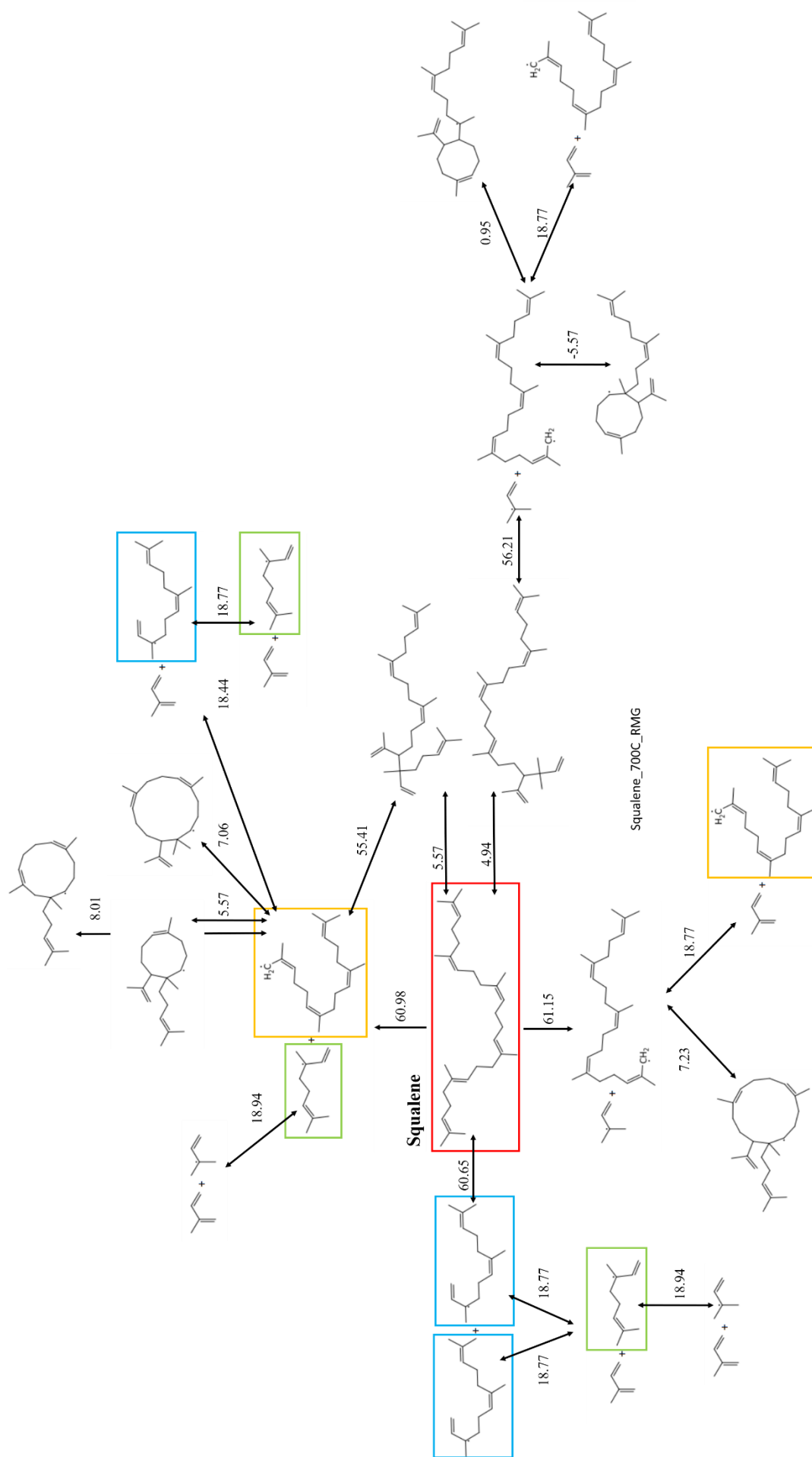
Figure 7.21 RMG-provided pathway of squalene (red rectangle) breakdown during pyrolysis, related to the Figure 7.18 and the reaction mechanism of squalene. The numerical values represent BDEs expressed in kcal/mol.

7.3.4.2. Experimental pyrolysis of squalene

The experimental pyrolysis of squalene was conducted on the prep-GC between 300°C and 700°C without further system modifications due to its lower boiling point (429.3°C at 760 mmHg) when compared to diploptene. The pyrolysates were transferred to the GC-MS for identification. The GC-MS chromatogram of squalene exposed to 300°C in the pyrolyser (i.e., oxygen and a contaminant) and late eluting peaks, confirming that they are not products of pyrolysis as, at this temperature, squalene was expected to be a stable compound (Figure 7.22). No relationship between the pyrolytic temperatures and the peak area of contaminants was observed, indicating that they probably originated downflow of the pyrolyser within the prep-GC (i.e., within the transfer line, needle, GC-MS).

The red arrow in Figure 7.22 marks the location where a new peak identified as **isoprene** appeared in the chromatogram with its mass spectrum presented in Figure 7.23 (Appendix A.7.4. provides the mass spectrum of the 2-7 peaks). Isoprene is thus confirmed as a pyrolysate of squalene, confirming RMG results. While isoprene is not clearly seen on the
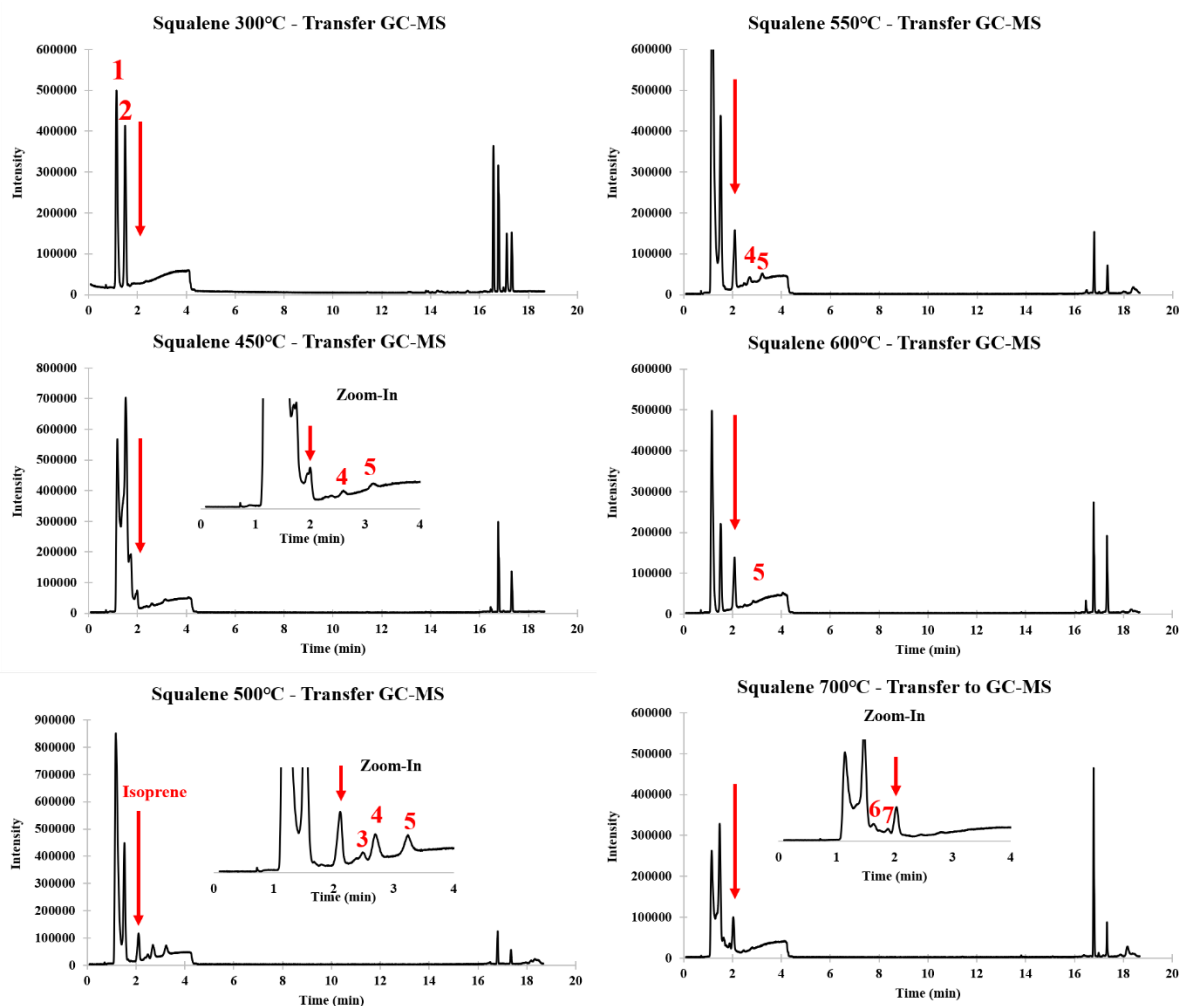
Figure 7.22 GC-MS pyrograms of squalene between 300°C and 700°C. Only pyrolysates of this reaction are seen as squalene could not be transferred via the heated transfer line.

450°C pyrogram (co-elution with DCM contaminant), the presence of peak #4, a C_{10}-isoprenoid indicates that pyrolysis of squalene already took place at this temperature as this intermediate compound was seen in RMG simulations of squalene yet that the pyrolytic reaction did not run to completion. Peak #5 is identified as D-Limonene, a cyclic 10-carbon compound, which could have been formed by the cyclisation of two isoprene units. This compound also appears in RMG simulations above 600°C, as well as 2,6-dimethyl-2,6-octadiene, yet in low concentrations relative to isoprene. Isoprene is seen in the 500°C as a well-defined peak, while compounds 4 and 5 also increase in concentration, together with the elution of peak #3, a C_{10}-isoprenoid (see Appendix A.7.4).
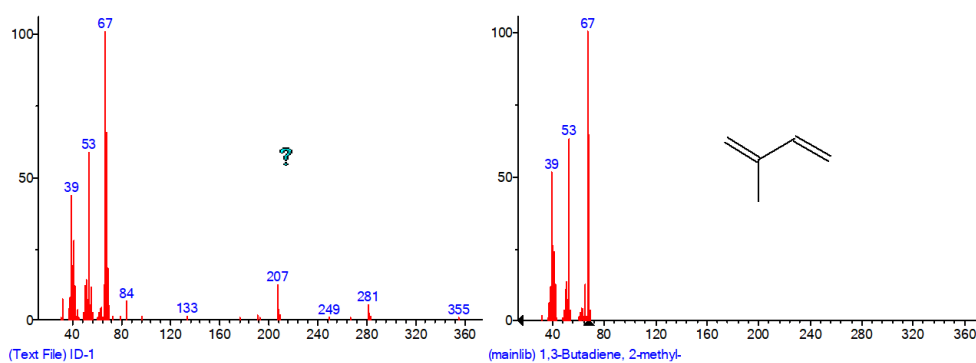
Figure 7.23 Mass spectrum and matched compound of isoprene pyrolysate. Peak is marked by the red arrow on pyrograms on Figure 7.22. The background noise was not subtracted for the unknown compound, with common system contamination ions such as m/z 207, 281, 355 appearing in its mass spectrum.

A smaller isoprene peak is present in the 700°C pyrogram. Peak #7 was identified as toluene while peak #6's mass spectrum was a co-elution of a monocyclic compound (potentially benzene) with DCM. At this temperature, the presence of secondary pyrolysates (i.e., peak 7-toluene) indicated isoprene complete breakdown at this temperature. This compound, toluene, was not seen in RMG results.

The pyrograms conducted between 450°C-700°C confirm the breakdown of squalene into a main isoprene pyrolysate. The peak area of pyrolysates cannot be used to study the reaction curve of squalene given the current pyrolysis experiment was not done in triplicate for each pyrolytic temperature, and as squalene could not be transferred to the GC-MS via the transfer line due to temperature limitations. However, and most importantly, isoprene was identified in all 5 pyrograms, between 450°C and 700°C and, squalene was previously pyrolysed within literature, confirming the above results. A parallel study (Kimura et al., 2020) to this work noted the increase in the pyrolysate production from squalene from 8% to 98% between 713 K and 723 K, the equivalent of 439.85°C to 449.85°C. Isoprene was confirmed to be the

main compound of squalene pyrolysis, with its production percentage dependent on the residence time, followed by peak 4- 2,6-Dimethyl-2,6 octadiene, which was seen in the 450°C, 500°C and 550°C pyrograms of this study, and peak 3, its isomer. As postulated in this hypothesis, that diploptene bonds will break undoing the action of the squalene-hopene cyclase enzyme, Kimura et al. (2020) also tied the fragmentation pattern of squalene to its biosynthetic pathway, as the 30-carbon terpene is produced through the condensation of 6 5-carbon isoprenoid molecules. Interestingly, their squalene cracking experiment predicted the formation of C_1 moieties through the addition of acidic catalysis such as SiO_2-Al_2O_3 and ZSM5 within the reactor. Based on the proposed mechanism, the C_1 obtained has been highlighted here as a site of PSIA interest (Kimura et al., 2020; Figure 7.24), and this is thus proposed as a viable mechanism for future experiments.
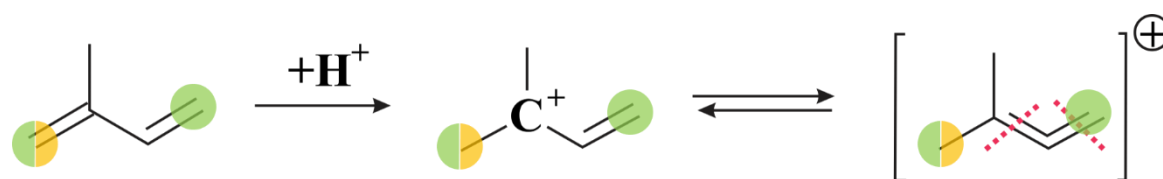
Figure 7.24 Proposed isoprene pyrolysis mechanism with the addition of acidic catalysis (edited from Kimura et al., 2020), with the highlighted carbon atoms of PSIA importance.

In a different study, during the pyrolysis of squalene at 900°C, Moldoveanu (2010) observed the formation of a large number of pyrolysates, with dominating 2-methyl-2-butene, 1,3-pentadiene and 2,7-dimethyl-1,6-octadiene produced by a β-scission cleavages of squalene. At this temperature, multiple monocyclic molecules elute, yet isoprene is not directly identified; however, a compound with the same mass as isoprene, 68 amu, was seen, and identified as 1,3-Pentadiene. Limonene also appeared in the 900°C pyrogram. Given the high temperature of 900°C and the following results of isoprene pyrolysis (Subsection 7.3.4.), the pyrolysates reported in Moldoveanu (2010) are caused by a further breakdown of squalene pyrolysates (i.e., high temperature pyrolysis leading to secondary pyrolysates).

7.3.5. Isoprene RMG and experimental pyrolysis

7.3.5.1. RMG pyrolysis of isoprene

Finally, to understand whether PSIA of diploptene could be achieved via isoprene pyrolysis, through a diploptene pyrolysis-isoprene trap-isoprene pyrolyse sequence, RMG simulations were conducted for isoprene between 500°C-850°C. This smaller 5-carbon molecule was readily modelled by RMG over the entire reaction time and the results are presented below.

RMG predicts minor isoprene breakdown between 500°C and 700°C, as more apparent in Figure 7.25 than seen in Figure 7.26. The breakdown is noticeable starting with 750°C, with the 850°C graph provided to show the complete breakdown of isoprene and its stable pyrolysates. If at 750°C, there are equal parts of ethene and 1,2-propadiene (mol:mol), at 850°C it can be observed that 1,2-propadiene is also undergoing pyrolysis, losing one atomic hydrogen and leading to the formation of C_3H3 (species 926).

When comparing the breakdown at 700°C of squalene pyrolysate, isoprene, from Figure 7.21 to the pyrolysates of pure isoprene pyrolysis at 850°C below, the same fragments are seen. Thus, RMG species numbers 592, 179, 926 and 1247 of isoprene pyrolysis from Figure 7.26 are also produced during squalene pyrolysis (data for squalene in output file not shown). Only species 179 and 1247 are seen as major compounds plotted on the 700°C isoprene RMG graph, yet the remaining ones are seen in the RMG isoprene output file.
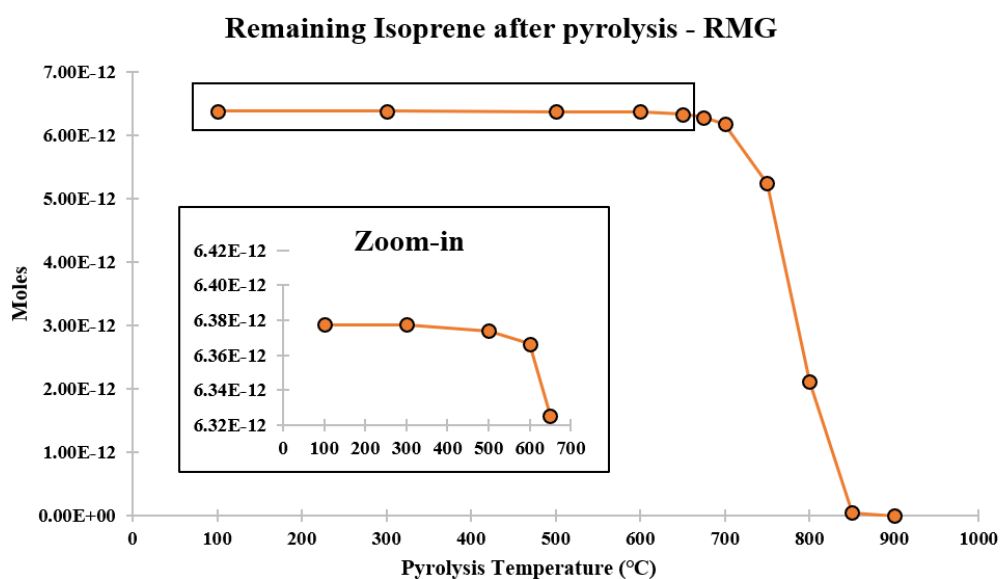
Figure 7.25 RMG-predicted isoprene breakdown with increasing temperatures.
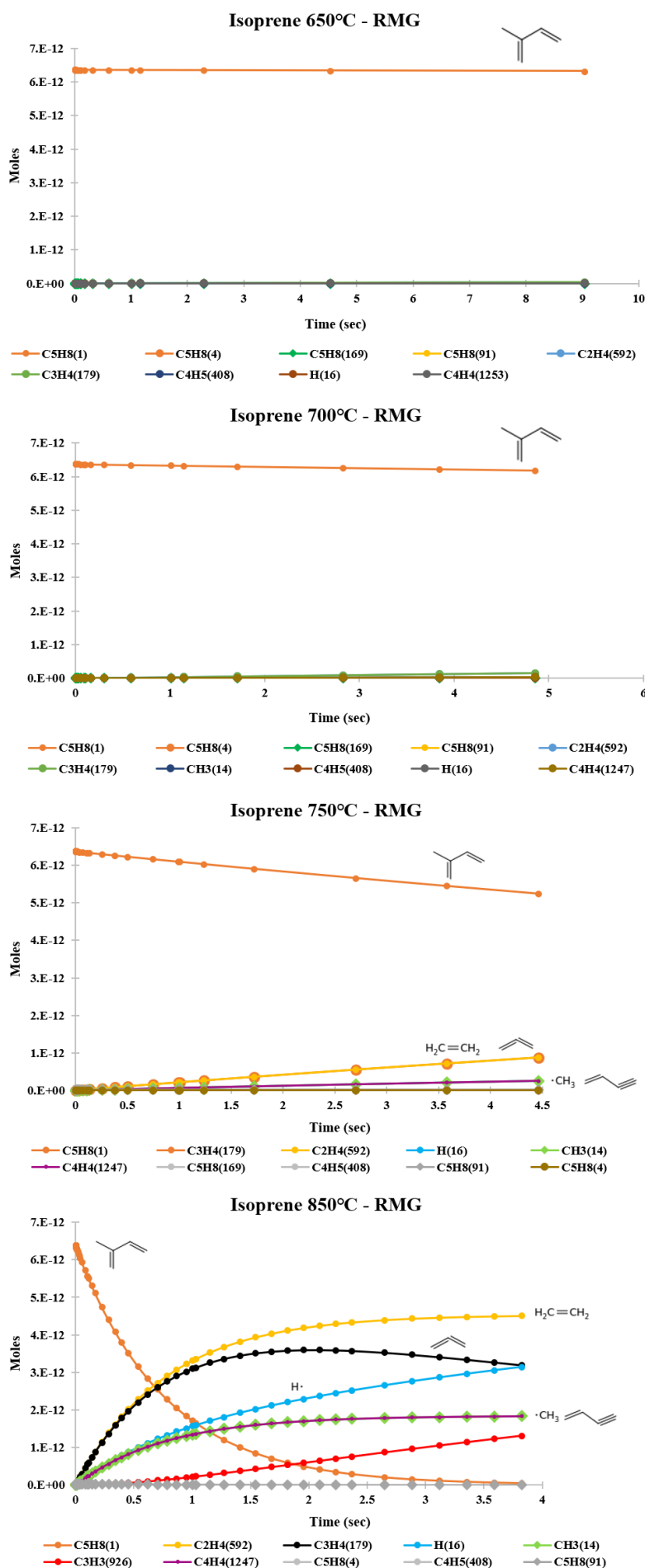
Figure 7.26 RMG predicted breakdown of isoprene (moles) at different temperatures, and production of several lower molecular mass compounds.

The reaction mechanism of isoprene pyrolysis is plotted in Figure 7.27. The two products which require 42.54 kcal/mol are expected to be formed first. This reaction mechanism also highlights the addition of BDEs required to reach a certain species, either directly or via another reaction (i.e., 58.55 kcal or 42.54+16.01 kcal/mol). Although an initial higher BDE is needed (i.e., 58.55 kcal/mol+17.29 kcal/mol) to reach the parent of ethene and 1,2-propadiene, this path is also predicted by RMG and the two end products are stable. On the other branch, $CH_3\cdot$ and vinylacetylene (C_4H_4) require further energy to be reached and further break down into more stable compounds. This is also illustrated through the provided BDEs in the chemical reactions below the reaction mechanisms of Figure 7.27.

The carbon positions of PSIA interest have been highlighted in Figure 7.27 for the main pyrolysates. While reaction 1 shows the formation of ethene and 1,2-propadiene, it does not provide access to a carbon of interest for further PSIA. Reaction 2 requires more energy to proceed, and it is not clear from RMG simulation which $CH_3\cdot$ is accessed via this reaction, yet this is here highlighted as a pathway that can provide isotopic information at the *intra*molecular level for isoprene. Further isotopic labelling can aid in determining the provenience of the end products. It is important to highlight that, through RMG work solely, diploptene was simulated to lead to the formation of isoprene as a main pyrolysate, and this work provided evidence that isoprene can further breakdown into a methyl radical, which can contain a carbon of interest initially highlighted in Figure 7.27.

RMG-provided breakdown reaction tree for isoprene pyrolysis at 850°C

Figure 7.27 RMG provided reaction mechanisms of isoprene pyrolysis, followed by two distinct pathways through which RMG indicates the formation of smaller fragments, with the methyl radicals of potential PSIA interest (reaction 2). The green labeling of the C moiety is representative of C-CH₄ for type II and X methanotrophs, and the yellow labeling of type I methanotrophs.

7.3.5.2. Experimental pyrolysis of isoprene

Isoprene was pyrolysed in the prep-GC between 300°C-750°C and the pyrolysates of isoprene were transferred to the GC-MS via the transfer line for identification. Isoprene pyrolysis leads to polymerisation, as HMW compounds were identified, defying the purpose of PSIA.

Isoprene was exposed to **300°C** and the identified peaks within this chromatogram are pre-eluting oxygen and two D-Limonene compounds at 8.6 min. While 300°C was believed to be a non-pyrolytic temperature for squalene, RMG indicates minor breakdown between 100°C-300°C, with the two late-eluting peaks of 10 carbons each suggesting a combination reaction of two isoprene units occurring at 300°C. D-Limonene is a terpene, which was also seen in the experimental pyrolysis of squalene in Subsection 7.3.4., and was found in other pyrolytic studies in which squalene was present (Morales *et al.*, 2014). However, the production of both isoprene and limonene can be achieved via waste tyre pyrolysis (Mkhize
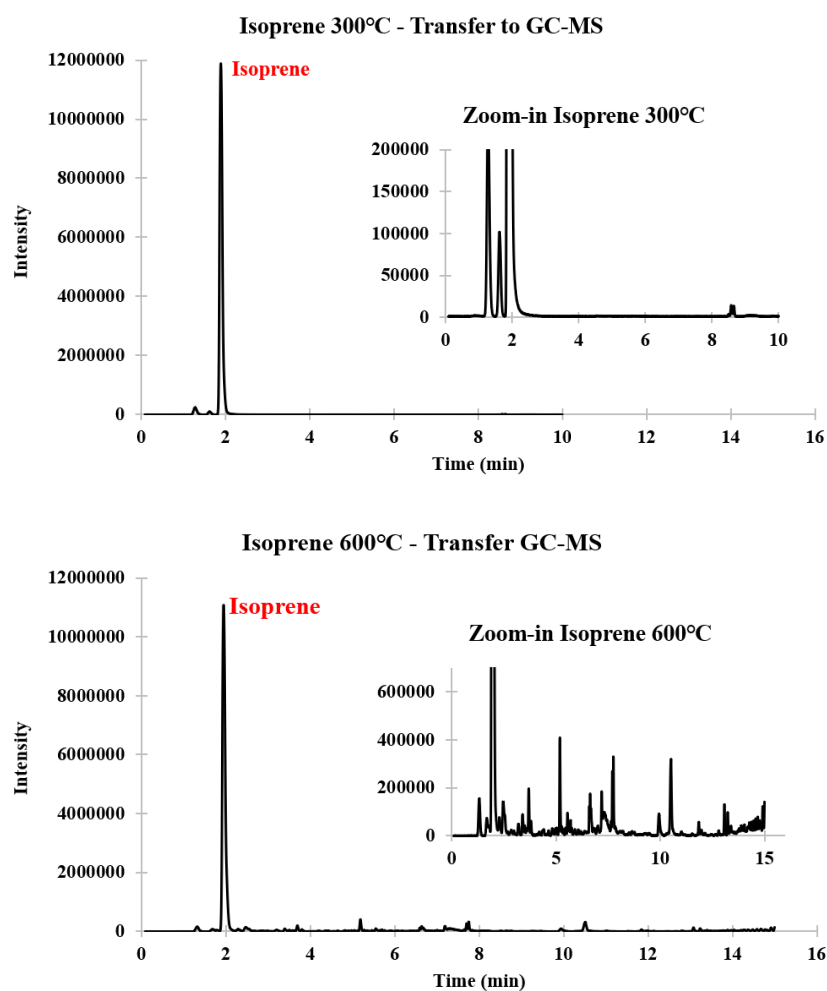
Figure 7.28 Experimental pyrolysis and transfer of isoprene and its pyrolysates to a GC-MS, at 300°C and 600°C, with zoomed-in views of the baseline.

et al., 2019), as such, depending on the mechanism through which the isoprene chemical was produced, small amounts of contaminants may also be present (Isoprene, 99% purity). Their mass spectra are provided in Appendix A.7.5. No other pyrolysates are seen in the zoom-in view, with isoprene in Figure 7.28 having the highest peak height (intensity) and concentration when compared to the other pyrograms.

Confirming RMG results in which isoprene starts breaking down at 600°C, the **600°C** pyrogram displays minor yet numerous secondary pyrolysate formation and a decrease in the peak height and concentration of isoprene. The two late-eluting D-Limonene peaks are again seen, this time eluting between 7.6-7.7 min, with slightly higher intensities. They are seen again in the 650°C with slightly higher peak intensities and concentrations, suggesting that they are produced as pyrolysates.

Pyrograms for **675°C**, **700°C** and **750°C** are plotted together in Figure 7.29, highlighting the main pyrolysates which appear across all three temperatures. Overall, these pyrolysates have a higher mass than isoprene, indicating polymerization. They are identified with their chemical structure in Table 7.7, and their associated mass spectra in Appendix A.7.6. Several isoprene pyrolytic studies confirm the formation of higher molecular weight aromatics together with that of smaller isoprene fragments, with an extensive list of compounds provided in Oro *et al.* (1967) and the reaction mechanism detailed in Grajales-González *et al.* (2022). Both references confirm the occurrence of cyclic and polycyclic molecules and isotopic scrambling. This was also observed in studies investigating the impact of high-pressure hydrogen pyrolysis, which limits the amount of formed aromatics, with molecular hydrogen hindering radical recombination reactions (Burnham and Happe, 1984).

The range of the MS scan for isoprene was *m/z* 30-500, the methyl radical of PSIA interest, if occurring, could not have been scanned and confirmed via experimental means. The only compound clearly seen on the pyrograms with a mass lower than isoprene is compound 0 in Figure 7.29, identified by NIST as methylenecyclopropane. However, the mass of the compound is approximated at 54 amu and within RMG there are several compounds with a 53 amu mass, which display one missing H atom. This indicates that the breakdown of isoprene potentially takes place through the mechanism generated by RMG, and that the $CH_3 \cdot$ or CH_4 can be reached and measured on an IRMS for squalene and isoprene PSIA. Unlike RMG however, the analytical pyrograms display a large number of peaks with retention times (and masses) higher than isoprene. Table 7.7 displays their most likely chemical structure. With increasing temperatures, polymers or larger secondary pyrolysates start forming from the pyrolysis of isoprene. From a PSIA point of view, this reaction,

although it can potentially lead to a measurable $CH_3\cdot$ radical or CH_4 compound, and provide thus access to sites of diploptene-PSIA interest, it also leads to a process known as "isotopic scrambling" (Gauchotte-Lindsay and Turnbull, 2016). The initially targeted carbons can no
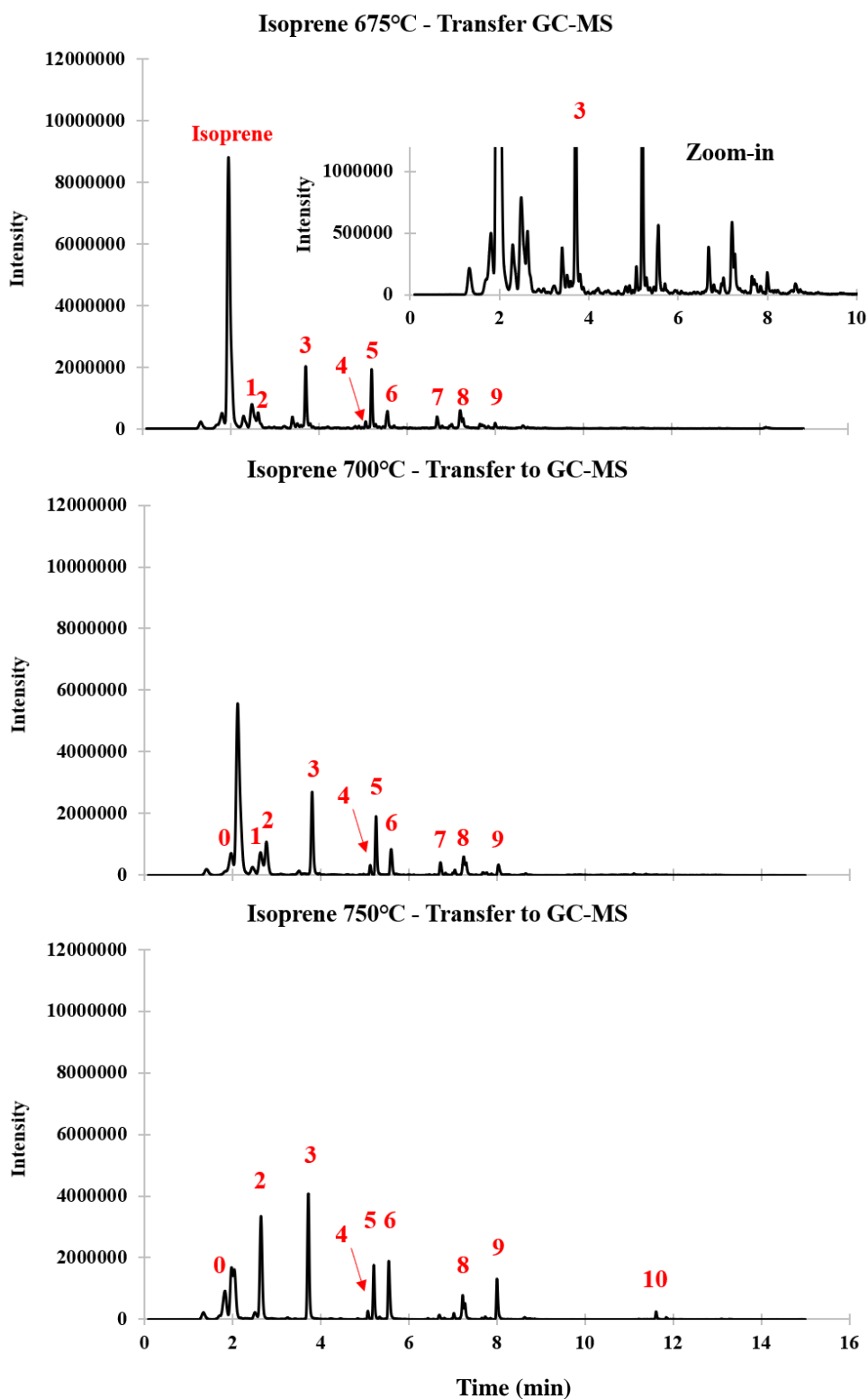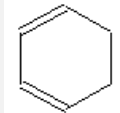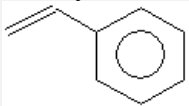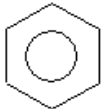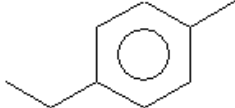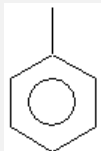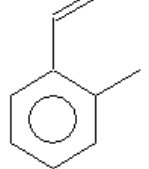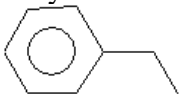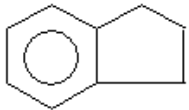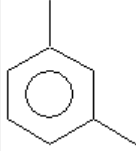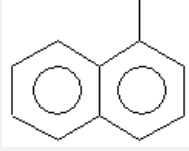
Figure 7.29 Isoprene pyrolysis across 3 temperatures and transfer of pyrolysates to a GC-MS for identification. Mass spectra in Appendix A.7.9.

longer be accessed or tracked within polymers, and there is no useful information extracted from comparing the isotopic signature of a fragment against its parent molecule (i.e., a Rayleigh plot cannot be constructed). However, PSIA of isoprene is still possible via a different process if the compound can be trapped and accumulated either in a cold trap or sorbent, and later released. As this was already shown to be possible, the potential of ozonolysis in achieving isoprene PSIA is discussed in Subsection 7.3.6.5., highlighting the production of formaldehyde which contains the carbons for PSIA.

Table 7.7 Pyrolysates of isoprene pyrolysis, following peak numbering from Figure 7.29.

Peak	Compound	Peak	Compound
1	1,3-Cyclohexadiene	6	Styrene
2	Benzene	7	Benzene, 1-ethyl-4-methyl-
3	Toluene	8	Benzene, 1-ethenyl-2-methyl-
4	Ethylbenzene	9	Indene
5	Benzene, 1,3-dimethyl-	10	Naphthalene, 1-methyl-
0	Methylenecyclopropane		

284

When comparing the compounds from Table 7.7 to RMG results, methylenecyclopropane and structures similar to Benzene, 1-ethyl-4-methyl-, Benzene, 1-ethenyl-2-methyl- and Ethylbenzene were seen, yet only within the edge of isoprene RMG pyrolysis output, indicating very low concentrations, unlike in the experimental results. No naphthalene-type structures were seen within the core or edge results, indicating that for isoprene, experimental and RMG results diverged.

Although the pyrolysis of isoprene has been widely investigated, no isotopic study looked at the signatures of the produced compounds from a PSIA point of view. Within literature, Weber and Zhang (2007) applied the technique of supersonic expansion to isolate the fragments produced post isoprene flash pyrolysis at 1400 K (1126.85°C), limiting reactive species from combining and forming larger pyrolysates. Analysis was then conducted using a vacuum UV single photon ionization time-of-flight mass spectrometer. This technique yielded fragments such as: CH_3, C_2H_4, C_3H_3, C_3H_4, C_4H_4, C_4H_5, C_5H_6, C_5H_7, C_6H_6. The methyl radical is formed above 1200 K (926.85°C) via the reaction presented below (Weber and Zhang, 2007, Moldoveanu, 2010; Figure 7.30), on which the carbons of PSIA interest have been labelled. The resulting methyl radical via this technique does not contain the carbon of PSIA interest, making ozonolysis a viable PSIA alternative.
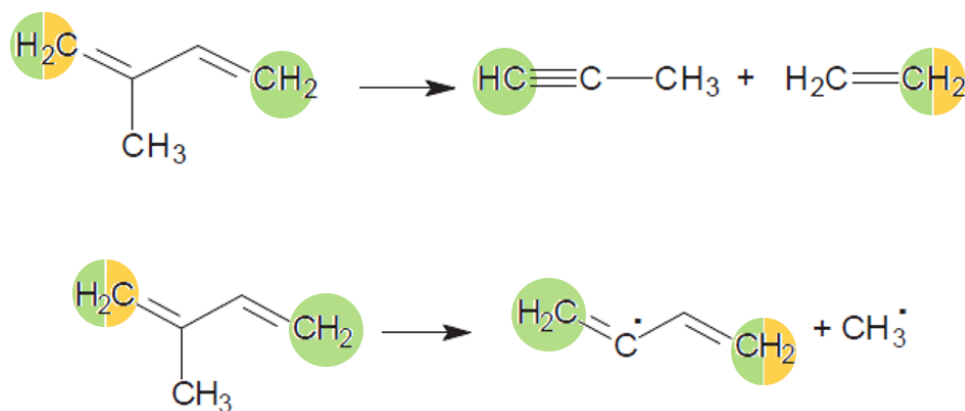
Figure 7.30 Figure edited from Moldoveanu (2010) based on experimental results produced by Weber and Zhang (2007). Green (semi)circles mark the location of C-CH_4 moiety within isoprene for type II and X methanotrophs, while yellow semicircles, for type I methanotrophs.

7.3.6. Diploptene experimental pyrolysis

Diploptene was pyrolysed within the prep-GC as the final experiment within this study. In order to provide an unrestricted flow path, only for this experimental set, the switching valve was removed, eliminating thus an important "cold" spot that slowed down diploptene and widened its peak shape prior to pyrolysis (system in Figure 7.3). Since the switching valve was not involved in this experiment, retention times were not deemed important. A series of experiments were conducted to understand the behaviour of diploptene and of its main pyrolysate. The following experiments thus test 1) reproducibility, 2) a wider range of pyrolysis temperature investigation to study the main pyrolysate's behaviour, 3) diploptene compound accumulation within the trap and investigation of pyrolysate trapping and reinjection into the GC-MS, 4) the possibility of pyrolysate separation for IRMS investigation.

7.3.6.1. Diploptene pyrolysis reproducibility

Within the prep-GC pyrograms, the pyrolysis of diploptene (0.1 mg/mL in isooctane) led to the formation of one main pyrolysate (see pyrograms in Figure 7.32). The injection of the same amount of sample was subjected in duplicate or triplicate to the same pyrolytic temperature with the results plotted in Figure 7.31. Overall, there are smaller error bars for the diploptene peak area than on the produced main fragment. This data however confirms the production of one main pyrolysate, with the same retention time across all pyrograms.

Figure 7.31 thus maps the breakdown of diploptene at 4 pyrolytic temperatures, between 575°C and 650°C, a final temperature at which the compound is completely broken down into a main pyrolysate. The pyrolysate is most abundant at 625°C, a temperature at which minor diploptene amounts are still seen eluting from the pyrolyser. Diploptene quantitative pyrolysis is expected thus to take place between 625°C-650°C. The further breakdown of the main pyrolysate at 650°C indicates also that the temperature range of 625-650°C is an optimal window for a PSIA study. A previous experiment, which involved the valve box connected to the system showed the same results, with diploptene completely breaking down at 650°C. The results and pyrograms are presented in Appendix A.7.7, illustrating that similar results are expected upon modifying the system and flow path as well as the amount of injected diploptene.

Diploptene STD - Pyrolysis GC-VAL reproducibility
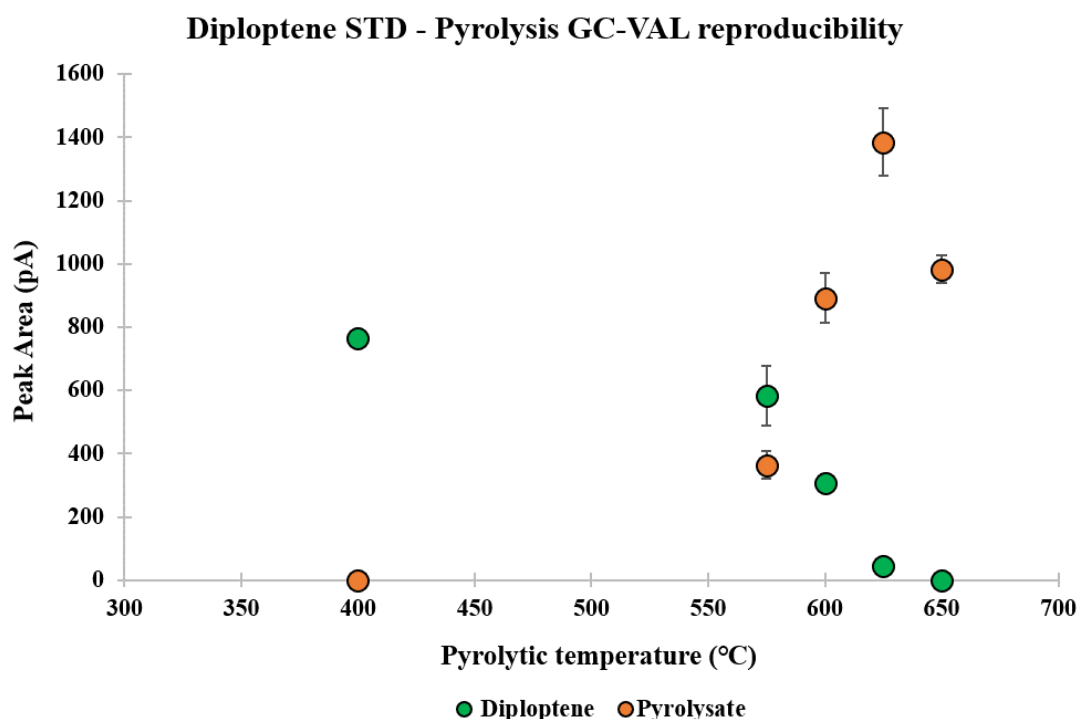
Figure 7.31 Breakdown of diploptene across a range of pyrolytic temperatures, as measured on the prep-GC-FID.

7.3.6.2. Diploptene pyrolysis and pyrolysate investigation

To understand the behaviour of the main pyrolysate, a higher concentration of diploptene (0.2 mg/mL in hexane) was pyrolysed over a wider range of temperatures. The results are shown in Figure 7.33 across the range 400°C-750°C, a temperature above which the FS capillary within the pyrolyser snapped.

The peak area of the main pyrolysate, diploptene started breaking down around 550°C. Diploptene was completely broken down at 650°C, confirming previous results. However, in this experiment, the main pyrolysate reaches peak concentrations at 650°C and starts breaking down after this temperature (Figure 7.33). The difference between the two sets of results, which conflict for the 650°C pyrolytic temperature can be explained by the higher starting concentration of diploptene as a lower amount of compound will quantitatively pyrolyse faster.
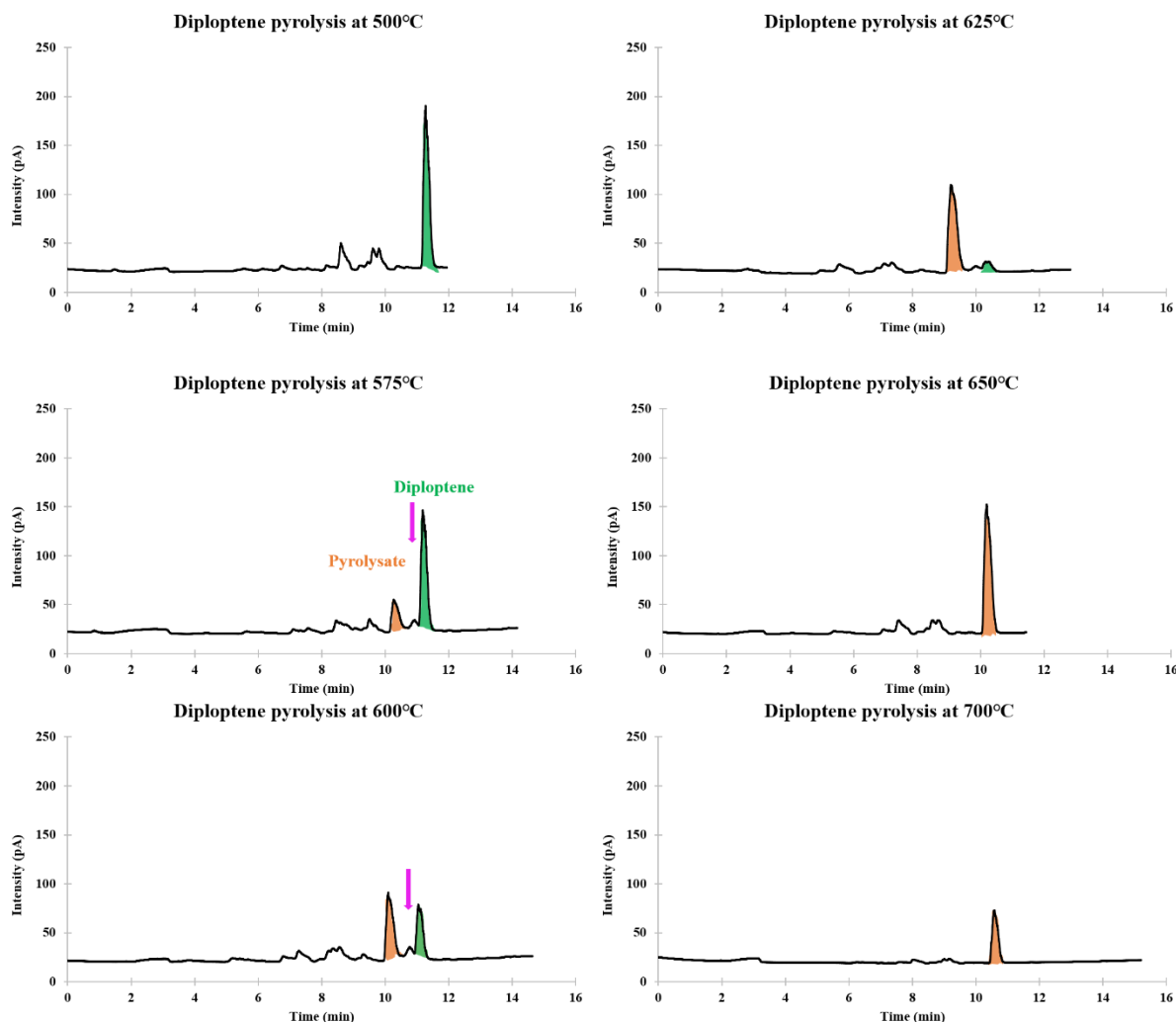
Figure 7.32 Pyrograms of diploptene as seen on the prep-GC-FID. Diploptene is highlighted as the green peak, its main pyrolysate-orange, and the pink arrow indicates the potential occurrence of a different, lower concentration, pyrolysate.

The pyrograms, as seen on the prep-GC and recorded on the FID, are provided in Figure 7.32. In this experiment, diploptene is still clearly seen at 625℃ and completely disappears from the system at 650℃. The peaks which elute prior to diploptene are system or sample contaminants as they were also present in the 400℃ pyrogram. Both 700℃ and 750℃ pyrograms were kept at 310℃ for several minutes to confirm that no late eluting compounds were observed (i.e., short isothermal time due to the already short length between the pyrolyser and FID, Figure 7.3). A second pyrolysate is potentially seen (i.e., pink arrow) forming between the main orange pyrolysate and diploptene in Figure 7.32 between 575℃ and 625℃.

Diploptene STD - Pyrolysis GC-VAL
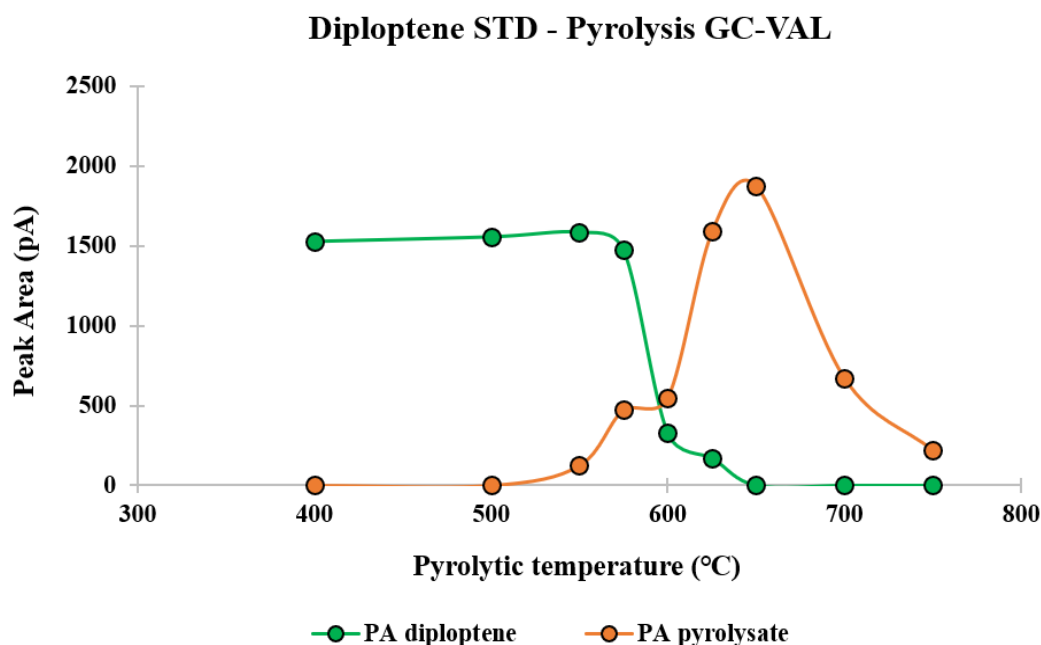
Figure 7.33 Pyrolytic investigation of the main pyrolysate fate with increasing temperatures.

This is the first time targeted diploptene pyrolysis has been conducted. Within the literature context, the studies reviewed in the chapter investigated macromolecular cracking that released hopanoids via pyrolysis, followed by their rapid removal from the pyrolytic zone. Hopanoids were still present for example in pyrograms when kerogen was exposed to 310-560°C (Li *et al.*, 2023) or 800°C (Eglinton, 1994) yet this is interpreted as macromolecular cracking, which through bond breaking allowed occluded molecules to be released, and thus the different results cannot be compared due to different experimental setups, conditions and sample types.

7.3.6.3. Post-pyrolysis trapping and GC-MS investigation

In order to understand and identify the produced pyrolysate, the prep-GC system was set as seen in Figure 7.3. Post-pyrolysis direct transfer from the prep-GC to the GC-MS via the transfer line was not possible at the time of diploptene pyrolysis. The trap was set at the lowest possible temperature (i.e., -27°C) with a fused silica capillary (or stainless-steel tubing, results in Appendix A.7.8.) connected via unions to the rest of the system.

Figure 7.35 presents diploptene going through the system at a non-pyrolytic temperature of 400°C (top), diploptene pyrolysis at 600°C with the trap heated at 320°C, behaving as part of the oven system, showing both diploptene and its main pyrolysate as in Figure 7.32 (middle); and a third run, with the pyrolyser set at 600°C and the trap at -27°C (bottom).

An unpyrolysed diploptene peak was observed at 400°C, and both diploptene and its main pyrolysate at 600°C with the trap set at 320°C (Figure 7.35). When the trap was set to -27°C, only one peak eluted from the trap. The mass spectrum of the trapped peak was confirmed by means of GC-MS.
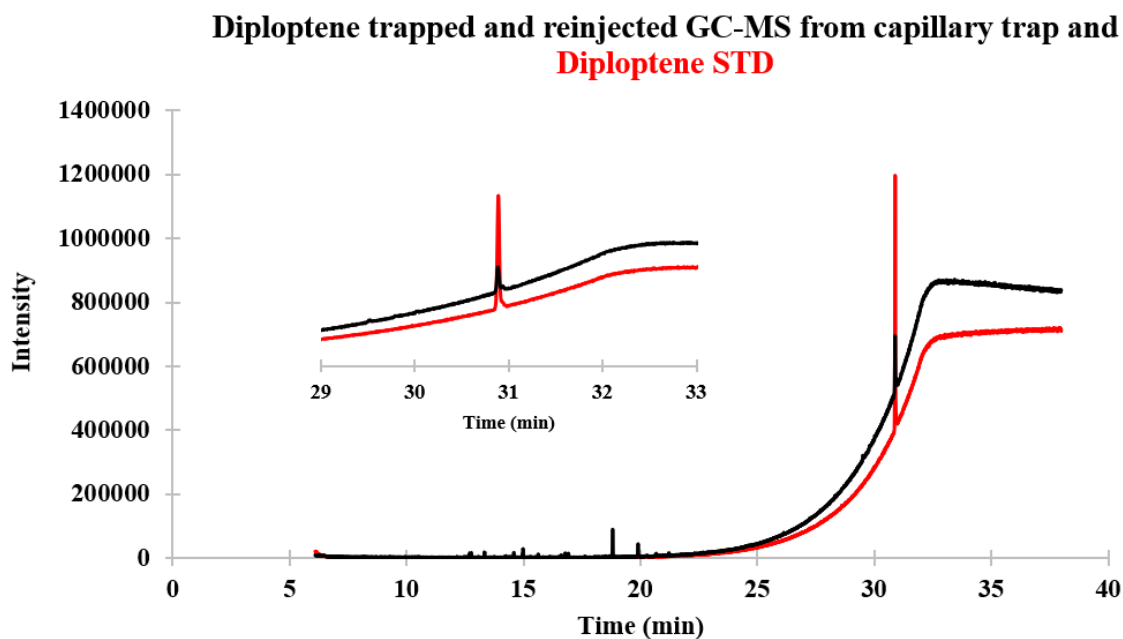
Figure 7.34 Reinjection of trapped diploptene on the GC-MS overlaid on a chromatogram of the pure diploptene standard.

The capillary (or stainless-steel tubing) placed within the trap was flushed with hexane using a modified syringe (Figure 7.4) and the elutant was collected in a GC vial insert. Figure 7.34 shows the manual injection of a 1 µL trapped and flushed compound (i.e., black graph;) and the overlaid chromatogram of the diploptene analytical standard analysis, confirming that diploptene was retained within the trap and its pyrolysate was in the gaseous phase at -27°C. This indicates that diploptene's main pyrolysate is a small fragment that could not have been retained at -27°C on either the fused silica capillary, or the stainless-steel tubing.
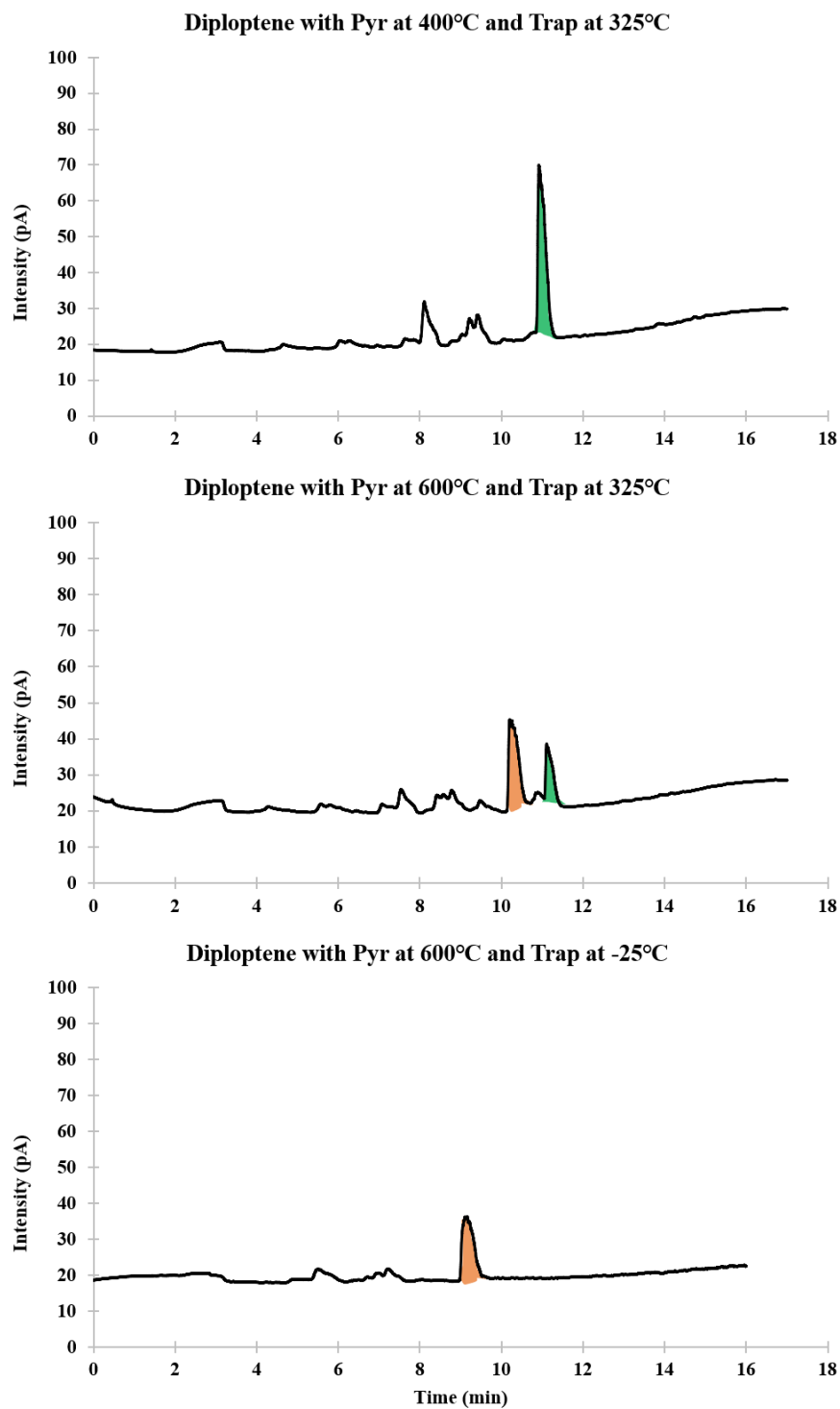
Figure 7.35 Trapping of diploptene at -27°C, leaving its main pyrolysate still eluting on the chromatogram.

291

7.3.6.4. Separation of compounds for IRMS detection

To test the applicability of the prep-GC system for a direct IRMS detector connection, the chromatography was improved by replacing the fused silica capillary column between the pyrolyser and FID (Figure 7.3) with a 70 cm ZB-624 column (Table 7.4). Diploptene was pyrolysed at 600°C, and the trap was set at 320°C, behaving as part of the oven system. Figure 7.36 shows the pyrogram with baseline separation between the main pyrolysate, diploptene and potentially one or two extra eluting peaks, produced either by the pyrolytic process or contaminants of the system or sample. This indicates that baseline separation is possible, allowing the compounds to combust as separate peaks, and that separation can be further improved by providing a longer piece of capillary between the pyrolyser and the FID.
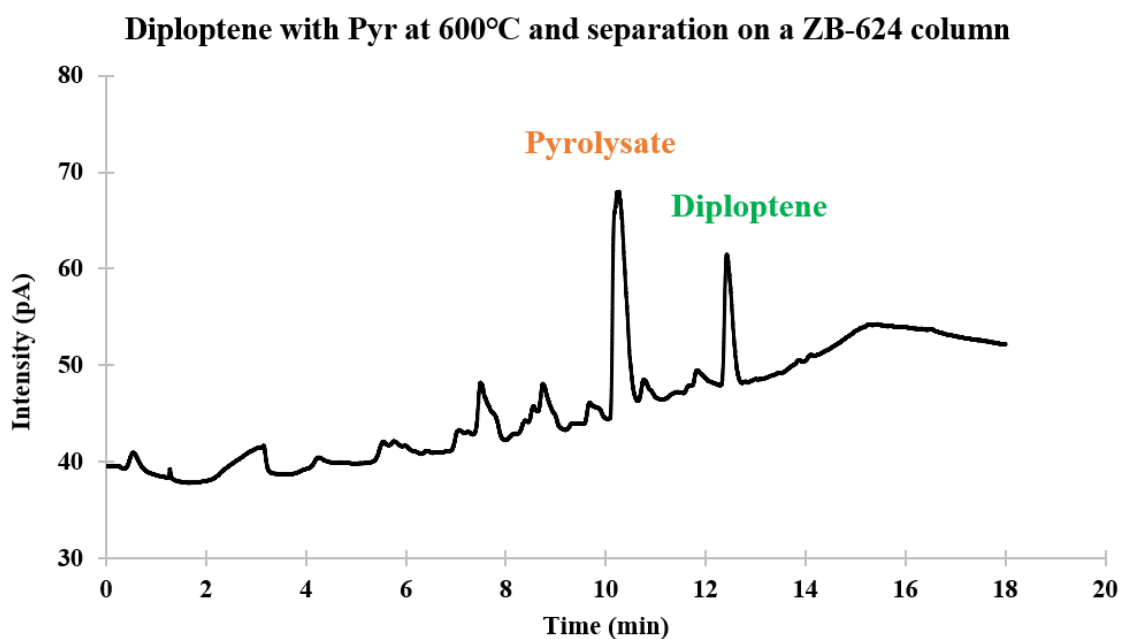
Figure 7.36 Baseline separation of diploptene and its main pyrolysate by using a high polarity 70 cm column.

7.3.6.5. Diploptene pyrolysis and PSIA significance

This chapter showed for the first time the possibility of pyrolysing diploptene and the formation of one major pyrolytic fragment, assumed to be isoprene based on the following evidence. The main pyrolysate cannot be trapped at -27°C, indicating that it is a highly volatile, low molecular weight compound. However, due to the highly distinct physical properties between diploptene and its pyrolysate, the prep-GC cannot be configured in a way to identify via means of an external standard whether the pyrolysate is isoprene, as RMG pyrolysis simulation of diploptene predicted (Figure 7.13; see Appendix A.7.11 for limitations and requirements of isoprene pyrolysate confirmation).

RMG has correctly predicted the produced fragments of MTBE and squalene pyrolysis that were experimentally tested in this thesis. Taking a 2-step hypothesis approach, RMG and experimental testing in this chapter increased the confidence that the produced main fragment is isoprene, which is also supported by the fact that it does not trap at -27°C, hence it is a low molecular weight compound. Another line of evidence is the further breakdown of the main diploptene pyrolysate after 600°C, which was also seen in the individual pyrolysis of isoprene (Figure 7.29). If it is later confirmed that indeed, diploptene pyrolyses to a main fragment isoprene, this compound would bear, for example, 2 carbons of interest for Type II methanotrophs-produced diploptene. Figure 7.37 shows the highlighted carbons for this diploptene, and the positions of the highlighted carbons on a suspected isoprene fragment. It is important to note here the C-CH₄ dilution factor between diploptene and isoprene; while diploptene has for type I, 6 highlighted C-CH₄, the dilution factor would be 1:5, similar to an isoprene fragment produced via pyrolysis; for types II and X methanotrophs, 12 highlighted C-CH₄ (i.e., 12:30), isoprene would have 2 out of 5, maintaining the same ratio (Figure 7.37).
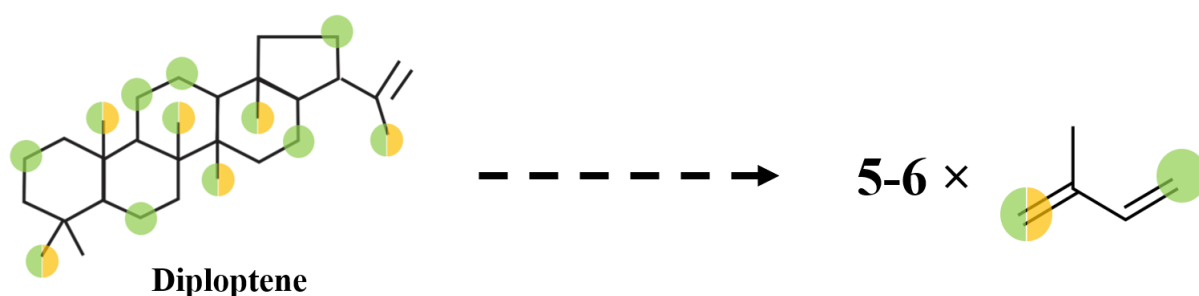
Figure 7.37 Proposed hypothesis of diploptene pyrolysis, with the labelled positions of environmentally incorporated CH₄ and their location in its suspected main pyrolysate, for type I (yellow label), and II and X methanotrophs (green label).

During the experimental pyrolysis of isoprene, various cyclic polymers were seen through means of GC-MS transfer, indicating that a second-stage pyrolysis of isoprene fragments would not produce valuable position-specific isotopic information. However, it is known that the breakdown of isoprene into smaller fragments is possible in the presence of ozone, a reaction known as ozonolysis (Criegee, 1975; Barber *et al.*, 2018). Figure 7.38 represents a simplified mechanism of this reaction, as literature (Nguyen *et al.*, 2016) indicates that this is a multi-step and multi-compound reaction, currently still debated (Riva *et al.*, 2016). However, the production of methyl vinyl ketone (MVK), methacrolein (MACR) and formaldehyde was confirmed by multiple studies (e.g., Paulson *et al.*, 1992; Barber et al., 2018). During the ozonolytic cleavage of isoprene, both carbons of interest would be accessible via formaldehyde, indicating that PSIA of diploptene is possible, however, through both pyrolysis and ozonolysis (if the main diploptene pyrolysate is confirmed to be isoprene).
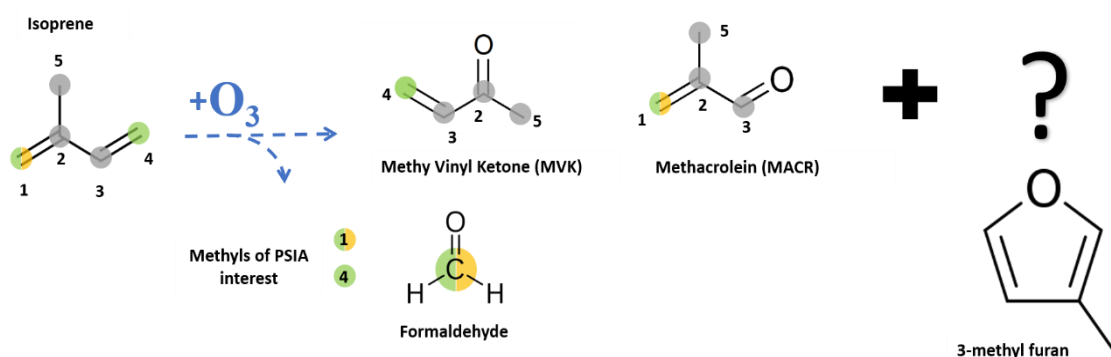
Figure 7.38 Ozonolysis reaction of isoprene, with labelled carbons in green of PSIA interest for type II and X methanotrophs, and in yellow for type I methanotrophs.

This is the first time an indirect link between diploptene, isoprene pyrolysate and C-CH$_4$ is highlighted, via pyrolysis and then, ozonolysis of the produced isoprene. An experimental setup for achieving this new information is proposed in Future work, Subsection 8.2.3.

Comparing CSIA to PSIA of pre-selected moieties would provide the ultimate advantage of the PSIA technique, especially for biomarkers expected to have multiple bio-producers and/or *intra*molecular isotopic dilution. Figure 7.39 displays a potential distribution of CSIA and PSIA values based on the type of organism, carbon source and employed pathway for diploptene formation in methanotrophs, yet this graph is provided to highlight the concept described here, and is subjective to further research and field advances. Similar graphs have been used to separate, for example, methanotrophs from photoautotrophs, albeit only at CSIA levels (e.g., Ménot and Bard, 2010). As an example of the potential of plotting CSIA against PSIA values in natural samples, the diploptene isotopic value of -60.7‰ (Uemura

and Ishiwatari, 1995) which was linked to a mix of cyanobacteria and methanotroph bio-producers in Lake Suigetsu sediments, plots across type I, II and X methanotrophs in Figure 7.39. At the diploptene PSIA level, the $C-CH_4$ moieties would also be diluted by carbons of heterotroph origin, yet the CH_4 isotopic signal would be greater at the position level than at the compound level, indicating methanotroph input via a highly depleted value. A $C-CH_4$ moiety as depleted as -160‰ would plot within type II methanotrophs. A mass balance equation, would determine that if at least 12 of the 30 carbons have together a -160‰ isotopic values (Figure 7.39. intersection with A value on oX axis), the remaining 18 carbons would account for 99‰, or 5.2‰, indicating heterotrophic input and a high degree of enrichment. Similarly, a PSIA value of -70‰, would provide the remaining of 18 carbons with an individual value of -54.5‰ (assuming uniformity), to account for the -60.7‰ diploptene isotopic value (intersection with C value on oX axis). However, with enough data to constrain the isotopic values from both CSIA and PSIA from lab cultures exposed to various starting CH_4 and CO_2 isotopic values, trends will be formed and the confidence in the main bio-producer, improved.
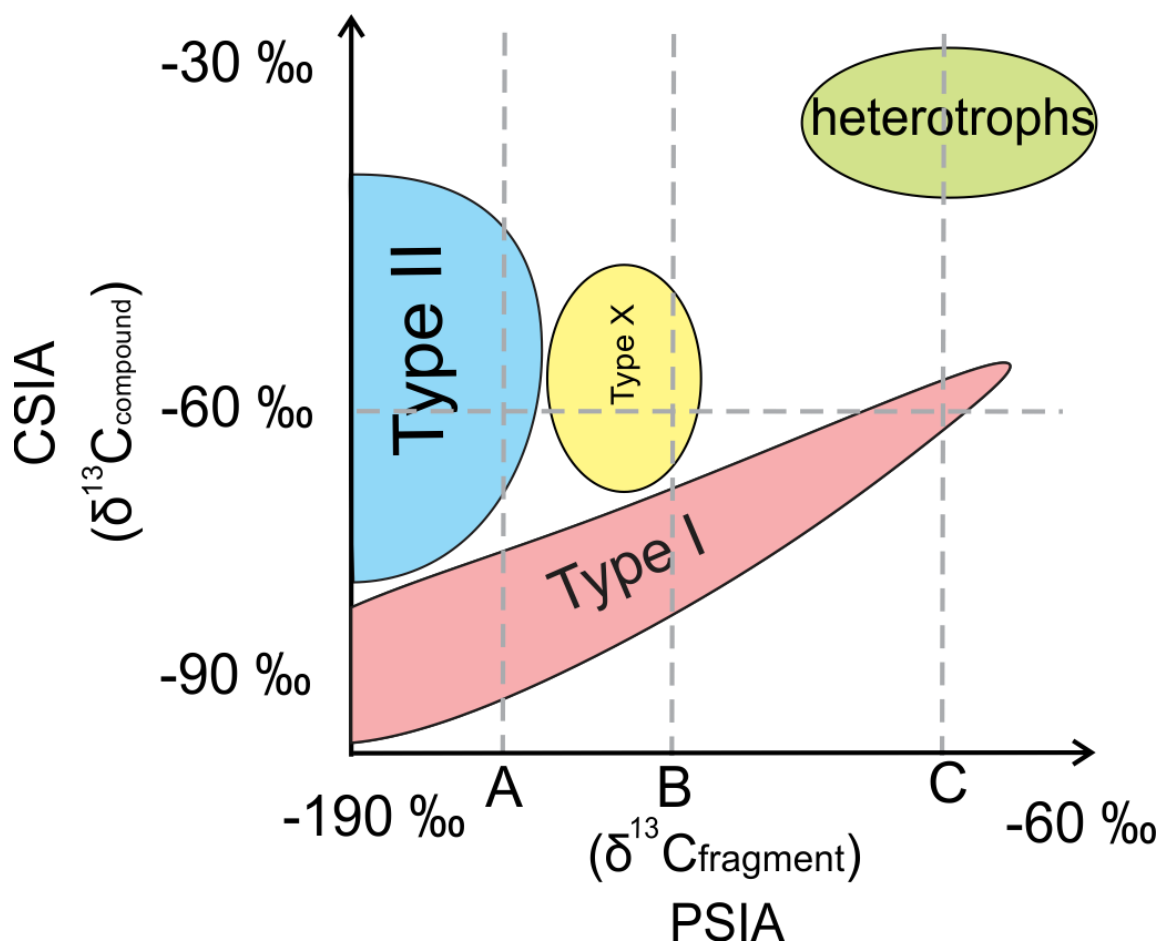
Figure 7.39 Plot displaying a potential isotopic distribution at the compound and position-specific levels for an improved framework of determining the main bio-producer of lipids in environmental samples. Isotopic values are provided for highlighting the concept, and may not reflect real PSIA and CSIA measurements.

Nonetheless, even if isoprene is not confirmed as the main pyrolytic fragment of diploptene, a pyrolysate was also seen to break down between 650°C-750°C, indicating that PSIA should still be investigated for the secondary pyrolysates (i.e., further breakdown on main pyrolysate, yet no further compounds were seen on the prep-GC-FID during its decay). The analytical and *in-silico* confirmation of the squalene→isoprene pyrolytic link, coupled with the ozonolytic breakdown of isoprene into formaldehyde and further compounds, can still be studied from a PSIA point of view. In chapter 4, Figures 4.8 and 4.17, showed that methanotrophs of type I and X produce squalene, in measurable amounts, as a hopanoid intermediate while Figure 7.10 presents the folding of squalene into diploptene (or other hopanoids) via the enzymatic activity of the squalene-hopane cyclase (shc). Although less recalcitrant in nature compared to hopanoids, and with multiple important bio-producer pools relative to the bacteria pool, squalene lipid can be subject to pyrolysis and its produced isoprene main pyrolysate can be further subjected to ozonolysis to access position-specific carbons of interest. To the author's best knowledge, PSIA was never targeted in isoprene ozonolytic studies although isotopic studies of its produced fragments exist (Iannone *et al.*, 2008; Iannone *et al.*, 2009; Iannone *et al.*, 2010). Furthermore, only two studies (Moldoveanu, 2010; Kimura et al., 2020) have previously pyrolysed squalene to understand its pyrolytic breakdown, without further isotopic investigation.

7.3.7. RMG pyrolysis of similar compounds for PSIA investigation

During the initial RMG diploptene 750°C pyrolysis simulation, which led to the main hypothesis, the backbone of diploptene opened, leading to the formation of an unstable pyrolysate, squalene, undoing the squalene-hopane cyclase biological action, and further leading to the formation of isoprene units. Hopanoid pyrolysates have never been the subject to direct pyrolysis investigation, thus this subsection investigates: i) if during pyrolysis of compounds formed through the action of cyclase enzymes, the bond that breaks first is expected to occur at the point of cycle-formation (closure) and ii) if similar hopanoids are expected to pyrolyse in a similar fashion. For i), trichodiene, lanosterol and cholesterol have been investigated using RMG, while for ii) Hop-21-ene and C_{31}-hopane have been selected.

7.3.7.1. Trichodiene

Trichodiene is formed through the cyclisation of farnesyl diphosphate by a terpenoid cyclase (Figure 7.40; Gao et al., 2006). The compound was subjected to 600°C in RMG and it was observed that, in this example, the pyrolytic reaction did not undo the cyclase action, the reaction leading to the separation of the two cyclic molecules as seen in Figure 7.40, with the highlighted bond breaking first.
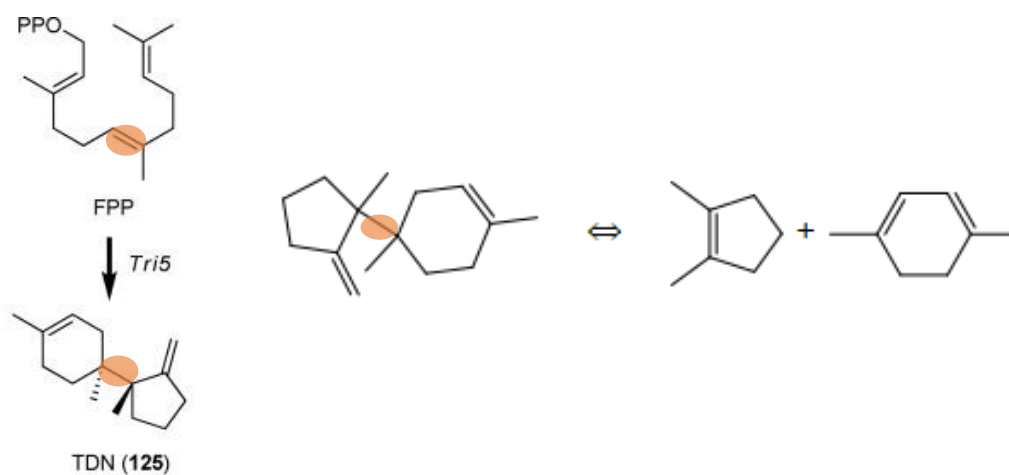
Figure 7.40 Formation of trichodiene via an enzymatic activity-Left, as edited from Shukla et al. (2009) and the pyrolytic breakdown of trichodiene at 600°C as predicted by RMG-Right.

7.3.7.2. Lanosterol

Lanosterol is formed via the mevalonic pathway, through the condensation of acetyl-CoA molecules and further cyclisation activity by oxidosqualene enzyme (Wendt *et al.*, 2000; Huff and Telford, 2005), similar to the activity of squalene-hopene cyclase. Being the precursor of cholesterol, and produced via a similar cyclisation process, it was of interest to introduce this molecule in the current study. RMG simulation of lanosterol pyrolysis at 700°C did not run to completion, yet, similarly to the diploptene molecule, the start of the reaction provides an informative view of how the reaction is most likely to proceed. Lanosterol is broken down into two main C-15 fragments provided in Figure 7.41. The reaction proceeds initially similarly to diploptene pyrolysis, with the opening of bonds within
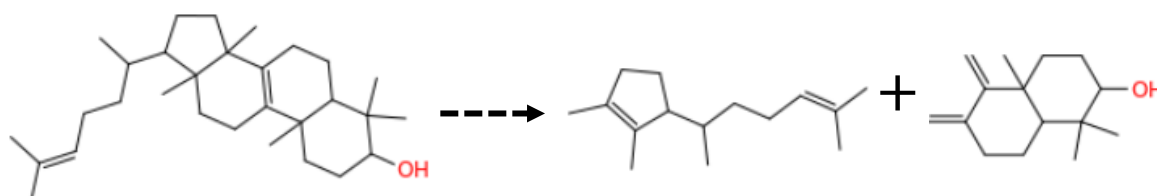
Figure 7.41 Lanosterol breakdown via multiple steps into the 2 main fragments.

the backbone, yet the main molecule breaks apart into large pyrolysates, that are not predicted to further breakdown into acetyl-CoA equivalents, and in the case of diploptene.

7.3.7.3. Cholesterol

Cholesterol is an indirect compound of lanosterol, formed via oxidosqualene cyclase of squalene, similar to the action of squalene-hopane cyclase (Figure 7.42). Both compounds were thus studied via RMG. At 550°C, cholesterol broke into two main fragments, the hydroxy-containing ring breaking from the main molecule, without the opening of the backbone as seen in the case of diploptene. At 650°C, the larger fragment continues to breakdown, with 2-butene breaking apart. As it was clear from this one reaction that squalene and isoprene would not be reached via cholesterol pyrolysis, cholesterol's breakdown mechanism was not studied further.
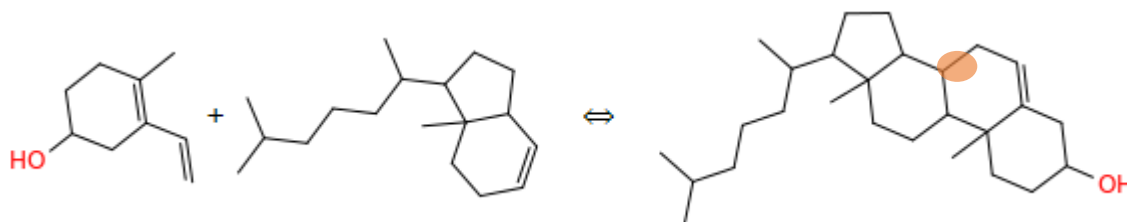
Figure 7.42 Cholesterol breakdown at 550°C as predicted by RMG.

7.3.7.4. Hop-21-ene

Hop-21-ene is a compound similar to diploptene, composed from the cyclisation of a squalene molecule and composed of 6 isoprene units, with the only distinction being the position of the double bond. The first three to four steps of hop-21-ene pyrolysis at 700°C follow the steps of diploptene breakdown, with the similar species highlighted in blue in 7.45, differing only in the location of the double bond. Figure 7.44 shows the comparison of the breakdown mechanisms between diploptene and hop-21-ene, indicating that, although the two hopanoids only differ in the location of the double bond, they pyrolyse differently due to different BDEs, leading to different products. However, isoprene is no longer formed during this process, and a different pyrolysate, a 9C-compound appears to be the main pyrolysate of hop-21-ene breakdown (C_9H_{14} – species 280, compound #2, Figure 7.43).
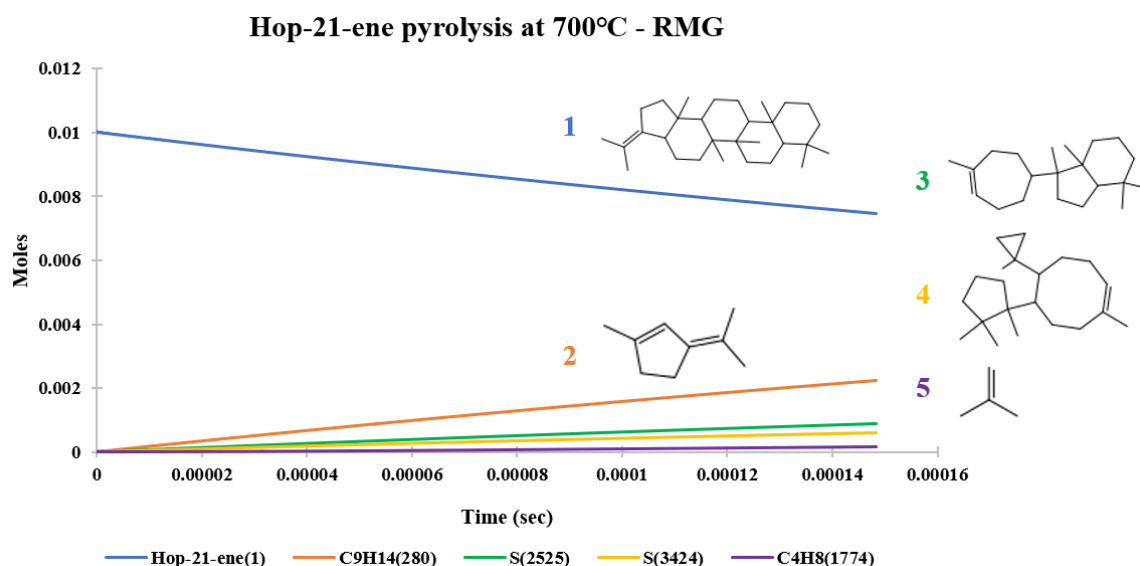
Figure 7.43 Pyrolytic breakdown of hop-21-ene at 700°C and main pyrolysates as predicted by RMG. Number colour coding link the molecular structure to the graph lines.

The position of the double bond increases the required BDEs, thus hop-21-ene does not lead to the formation of intermediate squalene. Instead, the 9C-compound (#2 in Figure 7.43) is cleaved from the hop-21-ene intermediate and the remaining does not further breakdown into isoprene units, although the tail structure allowed for this in diploptene (Figure 7.44) as the required BDEs for the next steps are lower (i.e., 6.45 kcal/mol and 4.8 kcal/mol compared to 18.77 kcal/mol, Figure 7.45). Although similarly formed, diploptene and hop-21-ene pyrolyse differently, indicating the need to study individually the pyrolysis mechanisms of other hopanoids.

Summarized comparison between reaction pathways and pyrolysates of diploptene and hop-21-ene
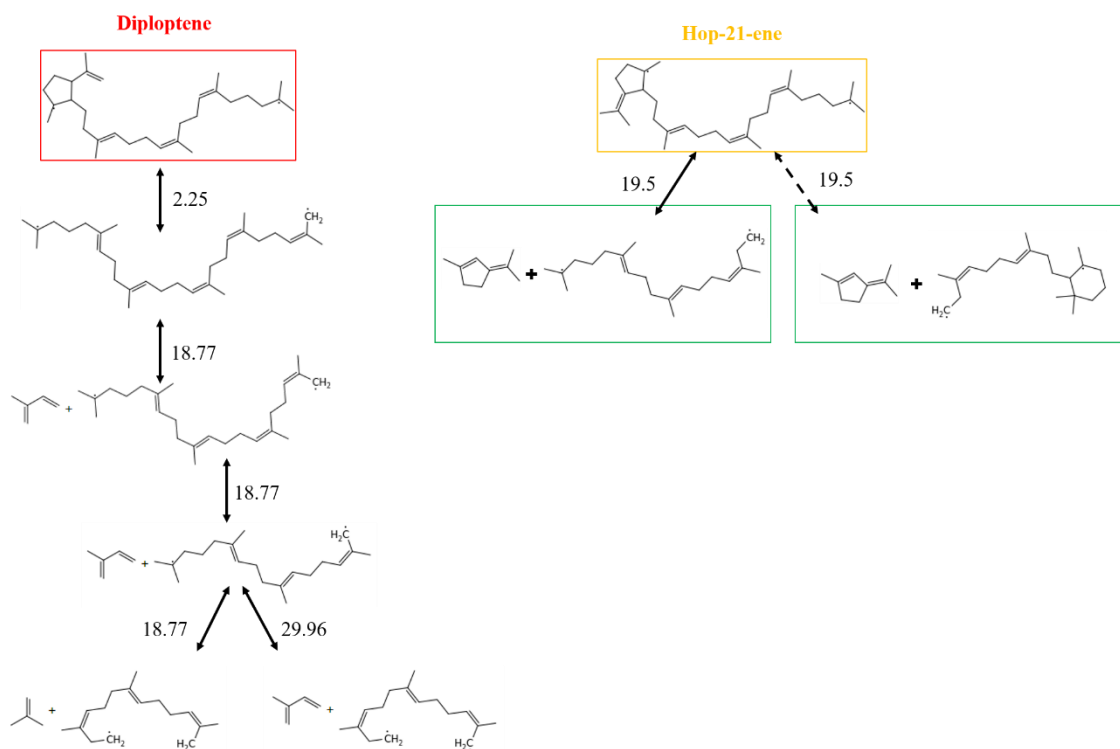
Figure 7.44 Summary of diploptene and hop-21-ene breakdown as proposed by RMG, indicating the formation of similar unstable pyrolysates (top molecules highlighted in red and yellow rectangles) and their different breakdown patterns and pyrolysates caused by the location of the double bond which altered the required BDEs. Numerical values represent BDEs expressed in kcal/mol.

7.3.7.5. C_{31}-hopanoid

Similarly, RMG predicts a different fragment from isoprene forming through the pyrolysis of a **C_{31}-hopanoid**, although a C31-squalene equivalent is produced as an intermediate (Figure 7.46). Although part of this data is missing due to extensive RMG simulation times, it is likely that 3-methyl-1-pentene has the highest concentration, as isobutene is seen both for diploptene and hop-21-ene to form in lower amounts. However, the distribution of carbon atoms, from a PSIA point of view, would be different to the two hopanoids, and again, an individual study is required.

As demonstrated through the 5 RMG simulations of molecules similar in proprieties to diploptene, the expected breakdown mechanisms are not predictable based on biological cycles and cyclase enzyme actions. Even within the same class of compounds, hopanoids were seen through RMG simulations to lead to different pyrolysates. The link diploptene-isoprene and isoprene ozonolysis for PSIA appears to be unique to diploptene, and thus these reactions are of immediate attention in the field of PSIA.

RMG-provided breakdown reaction tree for hop-21-ene pyrolysis at 750°C
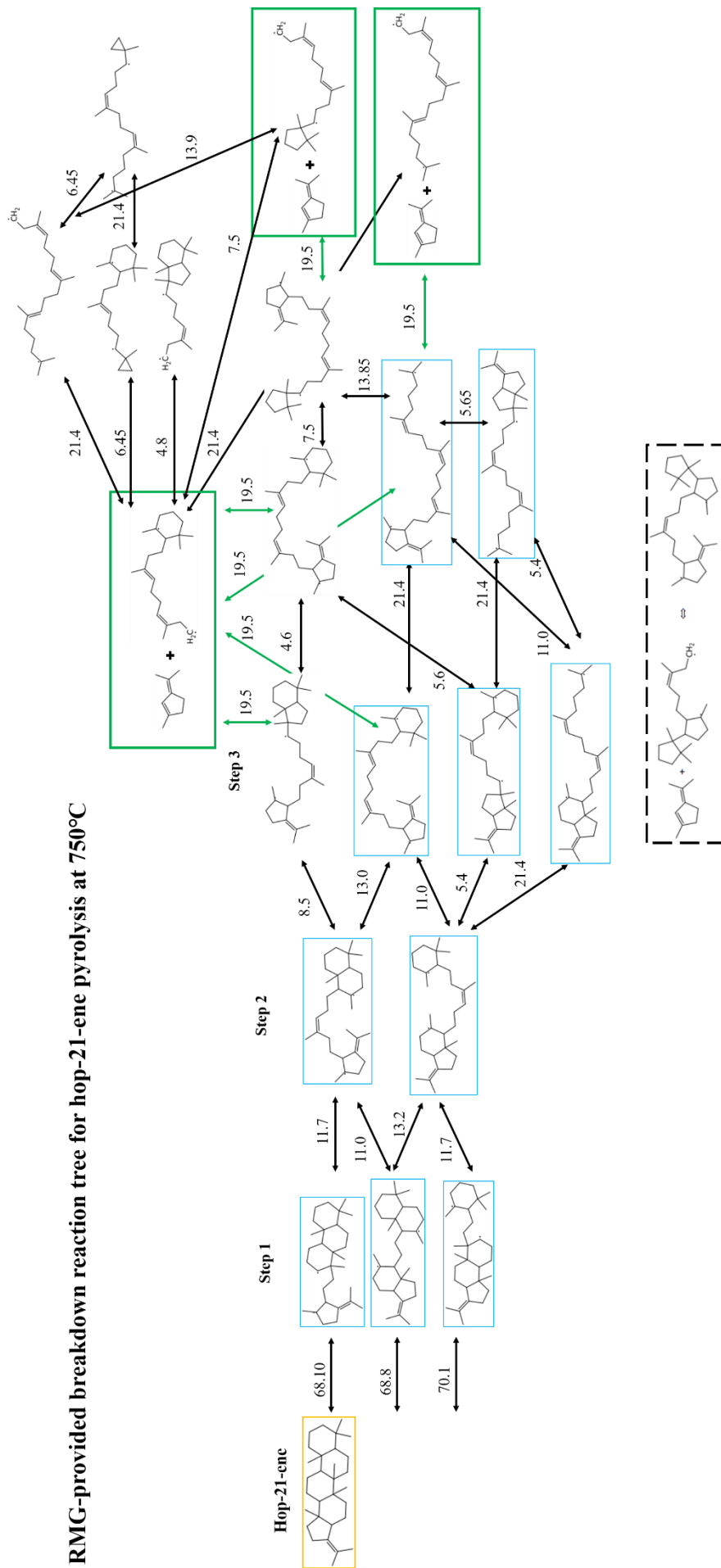
Figure 7.45 Reaction pathway of hop-21-ene pyrolysis as provided by RMG. The numerical values represent BDEs expressed in kcal/mol.

RMG-provided breakdown reaction tree for C₃₁-hopene pyrolysis
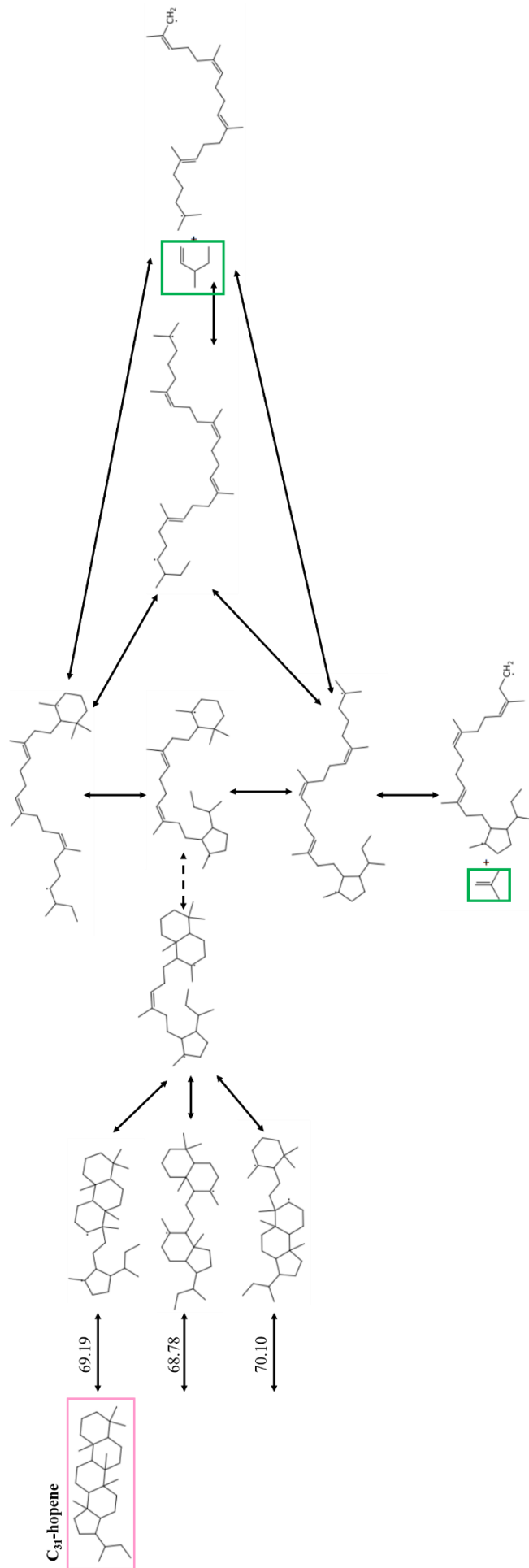
Figure 7.46 Reaction pathway of C₃₁-hop as provided by RMG. Numerical values are BDEs expressed in kcal/mol.

7.4. Conclusions

This chapter investigated for the first time the pyrolytic breakdown of diploptene, a highly recalcitrant biomarker, commonly used at the CSIA levels to inform on the presence (or absence) of aerobic methanotrophs in a wide range of environments (Appendix A.3.1.).

As diploptene pyrolysis was attempted for the first time, RMG was used to initially study *in-silico* the pyrolytic behaviour. The simulation conducted at 750°C indicates the breakdown of diploptene into isoprene as the main fragment, with the formation of squalene as an unstable intermediate. This is the first time this process is observed (and a novelty for the field) with further interesting implications, such as the reversing, via pyrolysis, the enzymatic *squalene-hopane cyclase* action. The "sticking-out" methyl-moieties of PSIA interest (carbon positions 23, 24, 25, 26, 27 and 28 in Figure 2.3) are not accessible via pyrolysis, as it was shown that breaking the chemical bonds between them and diploptene backbone has a higher BDE than the BDE required to break the bonds within diploptene's backbone (Figure 7.16). However, RMG simulations confirmed the feasibility of PSIA for diploptene, as a high number of fragments and recombination reactions would have caused isotope fractionation and scrambling issues which would have led to less accurate *intra*molecular values. RMG also provided BDEs indicating the bonds which require less energy to break and the reaction pathways that led to isoprene formation were further investigated. The initial diploptene pyrolysis simulation led to the main chapter's hypothesis that tested whether, via pyrolysis, squalene, the unstable intermediate, leads to the formation of isoprene. Isoprene was confirmed to be the major pyrolysate of squalene through both RMG and experimental means and a similar approach was applied to isoprene.

Isoprene RMG pyrolysis only indicated the formation of lower molecular weight pyrolysates within the core of the simulation, while the analytical experiment showed the formation of multiple HMW cyclic molecules. This will, in turn, lead to "isotopic scrambling", and unreliable fragment values, making PSIA of hopanoids via the isoprene pyrolysis route undesirable and futile.

Finally, the analytical pyrolysis of diploptene on the prep-GC showed the formation of one major pyrolysate between 550°C-650°C temperatures, which starts breaking down after 650°C. Subsection 7.3.6.3. also proved that this is a low molecular weight compound, with a low boiling point as it cannot be trapped at -27°C and, based on RMG simulation and provided reaction mechanisms, this may prove to be isoprene upon transfer to a GC-MS. If isoprene is confirmed in future experiments to be the main pyrolysate of diploptene,

ozonolysis is suggested as a breakdown mechanism for this pyrolysate, which could provide access to *intra*molecular moieties of interest for diploptene.

Further RMG simulations indicated that the cyclase enzyme is not necessarily an indicator of the pyrolytic breakdown of a molecule as the overall molecular structure, occurrence of methylation and of double bonds have a great effect on the BDEs and consequently, on the main formed pyrolysates. This was seen through the examples of hop-21-ene and C_{31}-hopane. It is recommended that further hopanoids are individually studied via RMG together with the reaction mechanisms that lead to their breakdown.

8. Conclusions and further work

8.1. Restatement of the thesis aim and objectives

This thesis aimed to develop the analytical methodology for diploptene pyrolysis, assessing thus the potential of its pyrolysates as proxies for aerobic methanotrophy for future PSIA studies. The pyrolytic breakdown pattern on diploptene, and of other hopanoids, were never investigated. It was also previously unknown the relationship between the pyrolysates of methanotroph-produced diploptene and the CH_4 cycle, and if the key $C-CH_4$ moieties can be accessed through pyrolysis, as a future application for PSIA. Furthermore, PSIA is an emerging field, with widely promising applications and high potential to offer new avenues for research and a better understanding of past climates and environments, yet it is still limited by instrumental capabilities, analytical limitations and high costs. To achieve the set aim, better understand these challenges and tackle the identified gaps in knowledge, 5 primary objectives were set, provided below:

- The isotopic investigation of hopanoids (and *n*-alkane) biomarkers extracted from 3 recently discovered peatlands from Pastaza-Marañón Foreland Basin (PMFB), Peru to evaluate the advantages and limitations of diploptene as a proxy for methanotrophy assessment, achieved in Chapter 3;

- To calculate the CSIA fractionation factors between diploptene and CH_4 source in pure cultures of type I and type II aerobic methanotrophs, achieved in Chapter 4;

- To develop the instrumental methodology for online pyrolysis by employing a modified GC-FID, a GC-MS and *in-silico* validation, achieved in Chapter 5;

- To further extend the application range of the developed analytical instrument for low concentration and high molecular weight compounds, demonstrated in Chapter 6 via the heart-cut, compound concentration, pyrolysis and pyrolysate identification of a DMN compound;

- To pyrolyse diploptene, assess its breakdown mechanisms and potential for PSIA through *in-silico* and experimental pyrolysis coupled with GC-MS and GC-FID analysis of the produced fragments, achieved in Chapter 7.

8.2.   Summary of met objectives and key findings

Objective 1

Objective 1 was set with the intention to study first diploptene, from an isotopic point of view, in a natural environment, where it can be associated with methanotroph producers. This objective was met in Chapter 3 by isotopically studying lipids from 32 samples from 3 Amazonian peatlands. Arising CSIA limitations for this compound, such as low concentrations and co-elution meant that diploptene's isotopic signature could not be analysed in all samples.

The three peatlands from PMFB provided however the ideal study site for Objective 1, due to their high palaeoenvironmental complexity. Thus Chapter 3, also presented the first multi-biomarker yet low-resolution isotope record, investigating *n*-alkanes, hopanoids and fatty acids in surface and core samples from Quistococha (QT), Buena Vista (BVA) and San Jorge (SJO) peatlands of PMFB. Diploptene displayed a wide range of isotopic values, fluctuating with changes in the (palaeo)environment, CH_4 producing potential of each depth zone and microbial community, and was identified as a fit compound for PSIA. The analytical limitations highlighted in this chapter are also expected to occur in PSIA studies, and once overcome, PSIA may be able to increase the confidence in assigning a diploptene main bio-producer.

Objective 2

The second objective was set to investigate the limitations of CSIA within less complex samples and assess the isotopic relationship and fractionation factors between methanotroph-produced diploptene and an isotopically known CH_4 source. This was conducted to understand and highlight the isotopic differences of diploptene when produced by different methanotroph types when the same CH_4 is provided, which was not possible for PMFB. This objective was achieved in Chapter 4 by isotopically analysing diploptene from pure *M. methanica* and *M. trichosporium* OB3b, representatives of type I and II methanotrophs. Diploptene and hop-21-ene were identified in all three cultures, with type X methanotroph, *M. capsulatus*, grown only for lipid assessment.

Diploptene fractionation factors between *M. methanica* and *M. trichosporium* OB3b and the provided CH_4 headspace gas were calculated and compared. Diploptene produced by *M. methanica* was relatively depleted when compared to *M. trichosporium* OB3b, showing on average a -29.3‰ difference, highlighting their different incorporation pathways and

percentage of C-CH$_4$ and C-CO$_2$ within this lipid, that are averaged at the compound-specific level. Even in pure cultures, performing PSIA can provide a wide amount of new information and can deepen the understanding of employed metabolic pathways.

Objective 3

Objective 3 was set to develop the instrumental methodology for experimental pyrolysis and future PSIA investigations, for the main aim of this thesis. This was successfully achieved in Chapter 5, through the pyrolysis and pyrolysate identification of MTBE via 4 individual lines of evidence.

The challenges of this objective were multiple, and were resolved in a step-like fashion, improving at each stage the capabilities of the prep-GC system and delivering in the end solutions that will lower the costs of PSIA. In order to achieve pyrolysis, 5 different types of pyrolytic reactors were tested, with fused silica capillary column proving to be the only successful option. It was demonstrated in this work that only 1 valve is needed to successfully heart-cut compounds of interest, trap, concentrate, release, pyrolyse and identify the targeted compounds and pyrolysates.

One major success of this chapter stands in the ability to transfer the molecule of interest and its pyrolysates to a second GC and detector via a transfer line. This was done in this work by fitting an analytical syringe needle to the end of the transfer line, making thus this connection cheap, reliable, and temporal, meaning that the secondary GC and detectors can also be employed for other work, highly decreasing the costs of PSIA and increasing instrument availability. Transferring MTBE and its pyrolysates to a GC-MS for identification, demonstrated that the prep-GC is also capable to transfer pyrolysates to a GC-IRMS, since the two instruments work on the same principles, making thus PSIA highly achievable.

Finally, this chapter tested RMG software with the MTBE molecule adapted to conditions used for its experimental pyrolysis. The *in-silico* RMG results matched the main pyrolysates as identified by transfer to the GC-MS. RMG is recommended as the first step for studying breakdown patterns of compounds of interest, understanding beforehand the expected pyrolysate, analytical requirements and conditions and feasibility for PSIA. MTBE is also recommended as a fitted candidate for system development and RMG-system calibration.

Objective 4

Objective 4 was set to further extend the application range to high molecular weight compounds of the prep-GC system developed for Objective 3. Since analytical challenges

expected for diploptene could not be assessed and solved through MTBE given its low molecular weight and high tested concentrations, 2,3-DMN was successfully employed in Chapter 6 to enhance the capacity of the prep-GC to heart-cut, trap, concentrate, pyrolyse and transfer the parent compounds and its pyrolysates to a second GC and detector. This compound was selected as it has a molecular mass above MTBE yet below diploptene, a similar backbone to hopanoids, with methyl moieties that may be of PSIA interest.

Cold spots were thus assessed and fixed using 2,3-DMN and 2,6-DMN, confirming that the prep-GC is capable of pyrolyzing high molecular weight compounds such as hopanes (diploptene). Two different traps were successfully tested and compared for their ability to trap, concentrate compounds, release and analyse these molecules at low concentrations. The SIM oven-integrated trap performed overall better than the ICE trap, yet both trap systems managed to concentrate the desired compounds, with the ICE trap representing a low-cost and readily available alternative. Finally, the main achievement of this chapter was the successful 2,3-DMN pyrolysis, with both the parent and produced pyrolysates transferred to the GC-MS for identification, indicating that all cold spots have been successfully eliminated, without added costs. 2,3-DMN was experimentally pyrolysed until 850°C with RMG confirming several observed reactions and extending the analysis to 900°C.

Objective 5

Finally, objective 5 was meant to answer the thesis's aim: to pyrolyse diploptene, assess the breakdown fragments and their relationship with the CH_4 cycle. Since diploptene's potential for PSIA and the new information its pyrolysates can provide in palaeoenvironmental assessments were never studied, work in Chapter 7 first targeted the identification of key moieties of PSIA interest that bear the $C-CH_4$ signal within diploptene. The $C-CH_4$ signal was thus theoretically tracked from CH_4 into diploptene for type I, II and X methanotrophs. Within types II and X, 12 key $C-CH_4$ were found while for type I, only 6 positions were confirmed to have with high certainty a $C-CH_4$ provenience. *In-silico* and experimental assessments were conducted to understand the potential of diploptene pyrolysis to provide access to these individual positions for isotope analysis.

RMG was first employed to understand, prior to experimental pyrolysis, the breakdown mechanism of diploptene. RMG predicted isoprene as the main pyrolysate, formed through the undoing of the hopanoid skeleton into an intermediary and unstable squalene, and the breakdown of squalene into isoprene units. It is the first time this mechanism has been reported and studied. This finding was the main challenge of this chapter and overall work which led to the study of isoprene pyrolytic breakdown, in an attempt to understand if

diploptene PSIA can be achieved through a 2-step pyrolytic experiment: diploptene pyrolysis, isoprene pyrolysate trapping, release and further pyrolysis. To test the RMG results, squalene was pyrolysed on the prep-GC, with isoprene being the main pyrolysate.

While RMG results indicated that diploptene PSIA can be conducted via isoprene, experimental pyrolysis of the later compound led to larger molecular compounds (i.e., isotopic scrambling), with positions of interest losing their isotopic fidelity. This was also the first time in this work where the main produced fragments diverged between experimental and core RMG pyrolysates, thus caution is recommended when assessing PSIA feasibility and results solely on *in-silico* results.

Finally, diploptene was experimentally pyrolysed, with one main pyrolysate formed. Given instrumental malfunction due to their relocation and reinstallation, the transfer to the GC-MS was no longer possible to identify diploptene's main pyrolysate. It was experimentally determined however that it was a low molecular compound which could not be trapped at -25°C, thus likely to be isoprene as RMG results predicted and as seen from the experimental pyrolysis of squalene. This result however needs to be experimentally confirmed and, if proven true, a new avenue than pyrolysis is required to access key moieties of PSIA interest. This is due to the fact that while isoprene is a stable pyrolysate that can be further isotopically analysed, CSIA of isoprene does not provide new information regarding diploptene's isotopic background (or squalene's), since it contained the same intramolecular isotopic information as the parent molecule as the ratios of C-CH4 label carbons to unlabelled carbons are the same for diploptene and isoprene: 2:5 for type II and X and 1:5 for type I methanotrophs. Isoprene ozonolysis is proposed in this chapter for the first time in relationship with PSIA. The chapter demonstrates, based on already existing studies, the feasibility of accessing key diploptene methyl moieties that contain the ancient incorporated C-CH$_4$ isotopic signal, via diploptene pyrolysis and isoprene ozonolysis (if isoprene is confirmed to be the main pyrolysate). The challenges of this experimental approach can be however numerous, and an experimental setup is presented in the Future Work, Subsection 8.2.3, as a suggestion of how the isoprene PSIA can be easily accessed using common laboratory equipment.

8.3. Future work

8.2.1. Hopanoids pyrolysis recommendations

The **identification of the main pyrolysate(s) of diploptene** via MSD means is of immediate interest. This work presents experimental and *in-silico* evidence of diploptene pyrolysis, and assumes isoprene to be the main fragment of diploptene breakdown. Previous experiments (i.e., MTBE, squalene, isoprene) showed that a direct transfer to the GC-MS is possible, via the transfer line. The methodologies were provided for the previous experimental setting, and low molecular weight pyrolysate could travel to the GC-MS without interference from the solvent front, proving that this analysis is possible. It was not clear for the prep-GC-produced chromatograms if a secondary pyrolysate of diploptene also occurs (Figure 7.32) and transfer to a GC-MS would concomitantly answer this question. If isoprene is confirmed as the main pyrolysate, achieving diploptene PSIA can be done thus indirectly, via pyrolysis, and ozonolysis, discussed in Subsection 8.2.3 below.

8.2.2. Prep-GC hyphenation to GC-IRMS and the study of isotopic errors

In the current setup, the transfer line can be heated up to 250°C, making diploptene transfer from the prep-GC to a different GC system challenging, given diploptene's high molecular weight (and boiling point). The transfer was however successful with DMNs in Chapter 6. It would be of interest to understand if the transfer is a source of isotopic error or if isotopic fractionation occurs within the first GC setup. A simple, one-compound standard with a boiling point lower than 250°C, should be isotopically analysed via direct analysis onto a GC-IRMS and via the transfer from a prep-GC, with the pyrolyser set at non-pyrolytic temperatures (i.e., matching the oven's highest temperature). Isotopic fractionation prior to pyrolysis can occur due to cold spots or improper transfer techniques, and can be eliminated before compound pyrolysis for PSIA. For PSIA investigations, the parent molecule should be always analysed via both methods regardless if it can be transferred from a prep-GC via the transfer line, leading to the next suggestion.

8.2.3. Ozonolysis

Isoprene is a highly reactive compound in the atmosphere due to its double bonds, which allows it to be easily oxidised by different molecules such as OH, NO_3 and O_3. Its atmospheric lifetime is short, only minutes to hours, in contrast to CH_4 which can last for years to a decade (Guenther *et al.*, 2006). Research has shown that the first-generation products of isoprene include a list of compounds such as C5-carbonyl, methyl vinyl ketone and hydroxy methyl vinyl ketone and methacrolein, which were confirmed experimentally by Galloway *et al.* (2011) and theoretically by (Dibble, 2004a;b).

Of interest is the reaction between isoprene and O_3 based on early studies of isoprene atmospheric reactivity (Pandis *et al.*, 1991; Paulson et al., 1992) and more recent publications (i.e., Bernhammer *et al.*, 2017). The three products of PSIA interest: MVK, MACR and formaldehyde are produced through the action of O_3 on isoprene (i.e., ozonolysis), summarised in Figures 7.38 and 8.1. The production of the two products is of interest from a PSIA point of view due to the elimination of the two terminal carbons on the double bonds of isoprene, in the form of formaldehyde. As discussed in Chapter 7, these two carbons contain the ancient incorporated environmental methane-derived carbon, and are hypothesised in this study to have isotopically depleted carbons, corresponding to incorporation by methanotrophs. Methyl vinyl ketone (MVK) contains C-4 of isoprene, while methacrolein (MACR) contains C-1 of parent isoprene (see Figure 7.38 for numbering). This pathway implies that PSIA of the two methyls of interest, C-1 and C-4, is possible either via direct IRMS analysis of formaldehyde, which will bear the two compounds that incorporated the CH_3-radical of PSIA interest, or via the indirect isotopic analysis of MVK and MACR and mass balance equations, that can output the position-specific isotopic values of the formaldehyde carbons. An experimental setup for ozonolysis is presented in Figure 8.1.b, highlighting the position of 2-way Valco connections at the FS capillary or a U-shape glass tube, similar to the one seen in Figure 6.3, that allows an easy connection to a GC instrument and the analysis of the trapped products of the ozonolysis reaction.
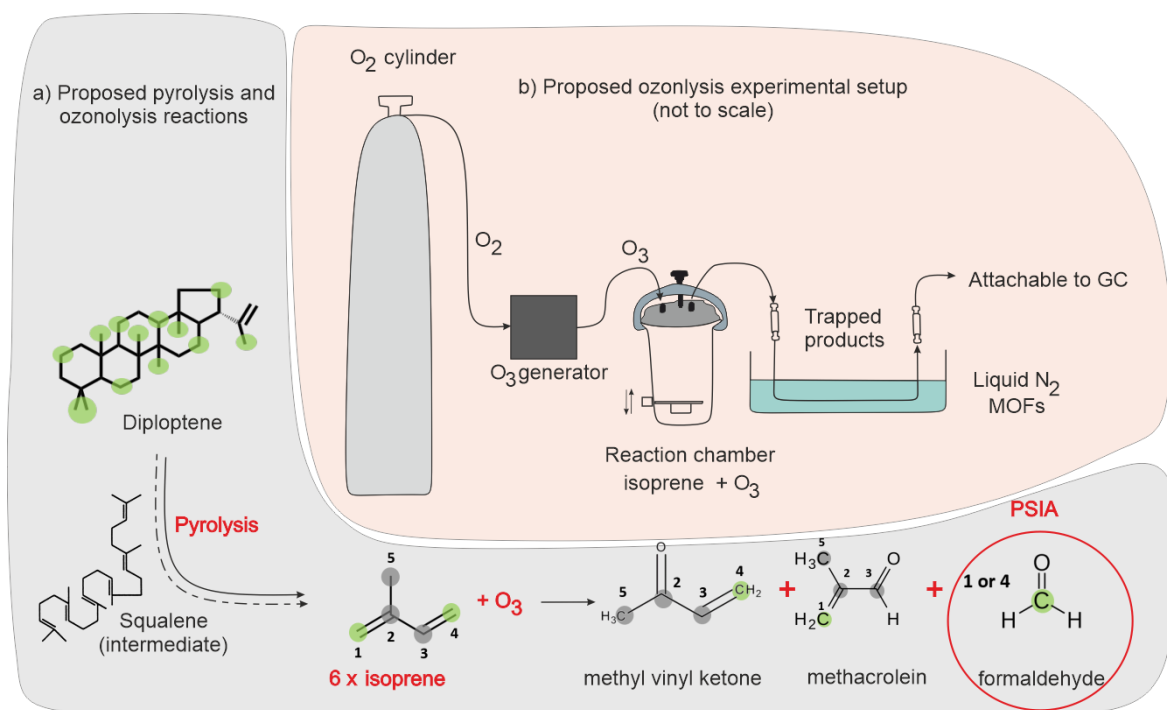
Figure 8.1 Proposed ozonolysis reaction and experiment for identifying produced moieties with an example from a Type II methanotroph.

8.2.5. Converting a Thermo Delta GC-IRMS system for one-oven pyrolysis and pyrolysate combustion for isotopic measurements

Isotopic measurements in Chapter 4 were conducted using a Thermo Delta GC-IRMS that has the flexibility of two individually heated furnaces. While one furnace is necessary for combustion, the other can be easily adapted for pyrolysis use (and, is actually intended for H_2 isotopic measurements via high-temperature pyrolysis), as shown in Figure 8.2, for low-complexity samples. This setup does not require a switching valve, yet PSIA is limited to low molecular weight pyrolysates given the existing cold spot between the two T-unions and the second-dimension capillary column. However, comparable GC-IRMS systems may offer the same conversion option, thus reducing the costs of this type of analysis and making it more available in labs that already conduct CSIA. The remaining requirement would be the breakdown mechanism of the parent molecule and produced fragments, which are now accessible via *in-silico* analysis on software such as RMG.
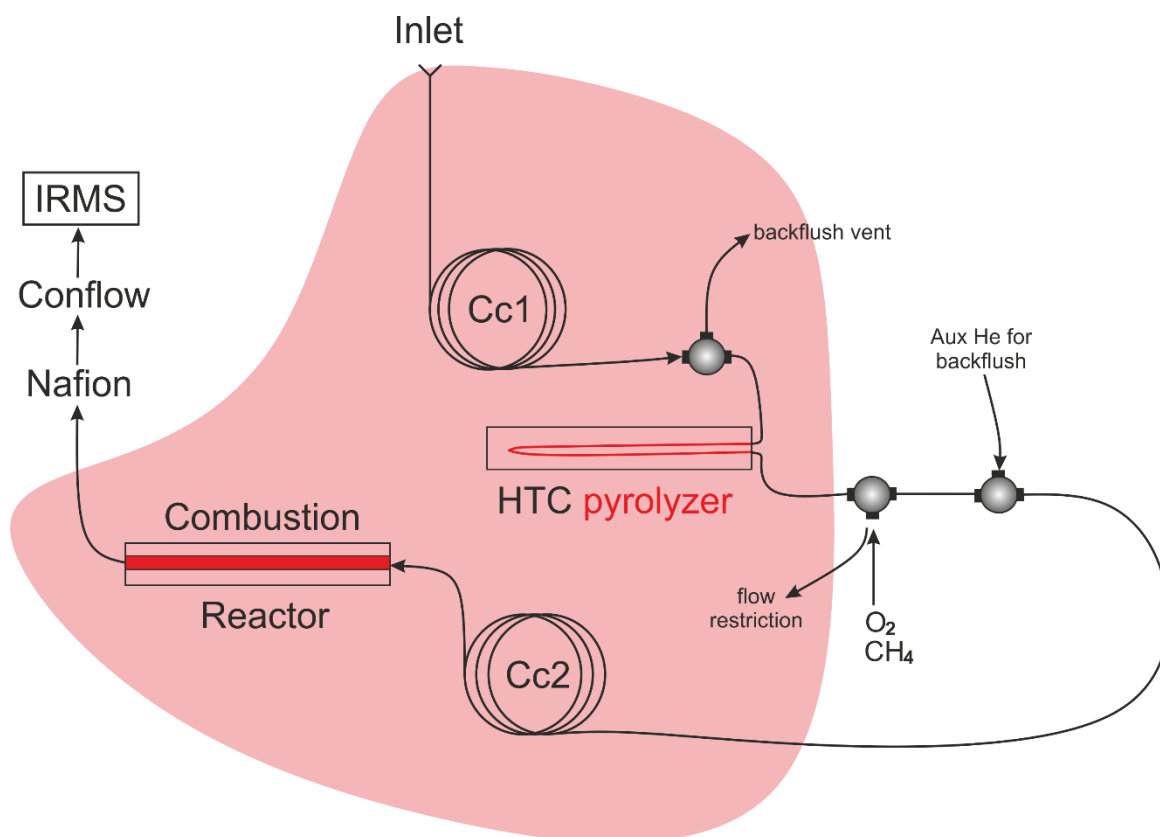
Figure 8.2 Proposed modifications for a Thermo Delta GC-IRMS for online PSIA measurements. The red shaded area represents the area heated by the instrument, highlighting configuration cold spots.

8.2.6. Environmental samples and further prep-GC improvements

1. **Investigation of the isotopic fractionation during compound trapping, concentration and release.**

   As it was noticed in Subsection 6.3, the amount of compound released during both trapping experiments, but especially during the ICE trap experiment, does not reflect the PA concentration of the molecules when analysed in the absence of a trap on the prep-GC-FID. This is believed to be due to the different carrier gas flow rates experienced by the two setups with the same head pressure (i.e., 30 m and 60 m columns) and the FID response. Trapping and concentrating the compounds over several runs should be conducted to assess the fractionation factor (if any) associated with this process as in the case of the ICE trap, the PA was below the expected values for the ICE trap, and above for the SIM trap. The tested compounds should be injected directly into the GC-IRMS and then via the transfer line post compound concentration. Based on this work, naphthalenes, mono or di-methylated naphthalenes are recommended as suitable compounds for this assessment, including the next recommendation to test (and potentially avoid) the split-peak behaviour.

2. **Testing of transfer of DMNs with the GC-MS oven set at a lower temperature.**

   When 2,3 DMN was transferred to the GC-MS oven, it was set isothermal at 150°C, the same temperature as in the prep-GC oven. The compound was already in gas phase when it reached the GC-MS and continued to travel through the GC-MS Wax column during the transfer. It is likely that the split peaks seen in Figure 6.15 are due to the pressure and flow differences, caused when the transfer line was removed from the GC-MS inlet after 4 minutes. To test this, the GC-MS oven can be set at a lower temperature (i.e., 50°C-70°C) at which the DMNs would be retained by the column and the oven temperature increased after the transfer line is removed. This is recommended also for the transfer to a GC-IRMS.

3. **Isotopic labelling of methyl radicals**

   It would be of PSIA interest to understand whether pyrolysis reactions do not discriminate against the two methyl radicals of 2,3 DMN. One [14]C- or ^{13}C-labeled methyl on the 2,3 DMN can be studied through the pyrolysis process and the mass spectrum of the MNA investigated.

4. **Testing of transfer of DMNs with the GC-MS oven set at a lower temperature.**

When 2,3 DMN was transferred to the GC-MS oven, it was set isothermal at 150°C, the same temperature as in the prep-GC oven. The compound was already in gas phase when it reached the GC-MS and continued to travel through the GC-MS Wax column during the transfer. It is likely that the split peaks seen in Figure 6.14 are due to the pressure and flow differences, caused when the transfer line was removed from the GC-MS inlet after 4 minutes. To test this, the GC-MS oven can be set at a lower temperature (50°C-70°C) at which the DMNs would be retained by the column and the oven temperature increased after the transfer line is removed. This is recommended also for the transfer to a GC-IRMS.

5. **Testing of the Cold Tube with dry ice and acetone.**

The ICE Cold Tube offers an inexpensive and easily sourceable alternative to the oven-integrated SIM Cool Cube trap or other similar devices. It is worth testing whether colder trap temperatures would improve the trapping capacity of the Cold Tube and would allow users to only employ one switching valve to trap and concentrate compounds of interest. The trap can be filled with dry ice in a bath of acetone, and a similar experiment conducted in order to be compared with the options used in this work.

8.4. Biomarker PSIA in the wider context and final conclusions

In the wider field context, PSIA can be applied in all fields in which CSIA is routinely employed. PSIA of diploptene is recommended for high-complexity environments, where multiple bio-producers and bio-synthetic pathways can contribute to a biomarker's environmental pool. The ubiquitous nature of diploptene (and by extension, squalene) which makes its source assignment difficult, may make PSIA (and ozonolysis) of these two lipids universal bio-source-assessments tools, not only for distinguishing aerobic methanotroph input or prevalence of a main methanotroph type. It was already shown through RMG simulations that isoprene is the main pyrolysate of diploptene and squalene, and that other hopanoids such as hop-21-ene and C_{31}-hopene are not expected to produce the same main fragment, thus targeted research is required for each hopanoid. Squalene was proven to be a new compound of PSIA interest, and the pyrolytic link between squalene and isoprene was experimentally proven, indicating that isoprene ozonolysis can be further studied within this context. Given the multiple bio-producers of squalene (e.g., microbes, plants) and its role as both sterol and hopanoid precursor, PSIA of squalene is expected to deepen the discussions regarding *intra*cellular processes, lipid pool consumption and fractionation for hopanoids (and sterol) formation and recorded (palaeo)environmental isotopic signals for this biomarker. Finally, as seen from RMG simulations of lanosterol and cholesterol, PSIA appears to be equally challenging for sterol compounds, with no one-carbon moieties formation predicted that can facilitate *intra*molecular isotopic analysis. These compounds and similar others that are routinely used in palaeoenvironmental reconstructions (such as bacteriohopanepolyols, BHPs, sterols, alcohols, methylated and demethylated naphthalenes etc.), should be first investigated *in-silico* and bond-breaking chemical reactions studied on produced pyrolysates, understanding thus their potential for PSIA.

Analytical development has been moved forward by discoveries or limitations that stood in the way of answering gaps in knowledge and research questions. In this regard, CSIA of diploptene (or of other hopanoids) may not always be a fit tool to detect methanotrophy given *intra*molecular $C-CO_2$ and biomarker pool dilution from non-methanotroph producers. PSIA presents itself as a tool that can elucidate subtle variations and discern minute differences at the *intra*molecular levels, yet as any analytical tool that is still being developed, imposes different challenges, some of which have been overcome in this thesis. Accessing *intra*molecular moieties of diploptene via pyrolysis for further isotopic investigation led to the development of a universal analytical instrument, capable of investigating compounds within the mass range of 32 - 410 g/mol, with a reduced complexity

and capabilities that do not limit other instrument use, proving that PSIA can be performed with decreased costs. The importance of accessing for the first time information regarding ancient carbon cycles locked at the *intra*molecular levels justifies the need for continuous development, further adaptation of analytical systems and future studies on similar biomarkers.

9. Bibliography

Bibliography

(Ec), C. R. 2000. No 2729/2000 of 14 December 2000 Laying Down Detailed Implementing Rules on Controls in the Wine Sector. *Off. J. Eur. Commun*.

Abe, I., Rohmer, M. & Prestwich, G. D. 1993. Enzymatic cyclization of squalene and oxidosqualene to sterols and triterpenes. *Chemical reviews,* 93**,** 2189-2206.

Abelson, P. H. & Hoering, T. 1961a. Carbon isotope fractionation in formation of amino acids by photosynthetic organisms. *Proceedings of the National Academy of Sciences of the United States of America,* 47**,** 623.

Abelson, P. H. & Hoering, T. 1961b. Carbon isotope fractionation in formation of amino acids by photosynthetic organisms. *Proceedings of the National Academy of Sciences,* 47**,** 623-632.

Afp 2022. Gas Chromatography Diaphragm Valves ELDV-MDVG Series. Accessible at: https://www.afproducts.ca/eldv-mdvg/ (Last accessed: 10/01/2024).

Ageta, H. & Arai, Y. 1983. Fern constituents: pentacyclic triterpenoids isolated from Polypodium niponicum and P. formosanum. *Phytochemistry,* 22**,** 1801-1808.

Ageta, H., Iwata, K. & Natori, S. 1964. Fern constituents: Adianene, filicene, 7-fernene, isofernene and diploptene. Triterpenoid hydrocarbons isolated from Adiantum monochlamys. *Tetrahedron letters,* 5**,** 3413-3418.

Ageta, H., Iwata, K. & Yonezawa, K. 1963. Fern constituents: fernene and diploptene, triterpenoid hydrocarbons isolated from Dryopteris crassirhizoma Nakai. *Chemical and Pharmaceutical Bulletin,* 11**,** 408-409.

Aichner, B., Wilkes, H., Herzschuh, U., Mischke, S. & Zhang, C. 2010. Biomarker and compound-specific δ 13 C evidence for changing environmental conditions and carbon limitation at Lake Koucha, eastern Tibetan Plateau. *Journal of Paleolimnology,* 43**,** 873-899.

Akalın, M. K. & Karagöz, S. 2014. Analytical pyrolysis of biomass using gas chromatography coupled to mass spectrometry. *TrAC Trends in Analytical Chemistry,* 61**,** 11-16.

Amariei, A. E. 2018. The potential of biomarkers for reconstructing long-term ecohydrological and microbial community changes in newly discovered Amazonian peatlands. *MSc Thesis* University of Glasgow, Accessible at: https://theses.gla.ac.uk/40970/

Aniceto, K., Moreira-Turcq, P., Cordeiro, R. C., Fraizy, P., Quintana, I. & Turcq, B. 2014. Holocene paleohydrology of Quistococha Lake (Peru) in the upper Amazon Basin: Influence on carbon accumulation. *Palaeogeography, Palaeoclimatology, Palaeoecology,* 415**,** 165-174.

Anthony, C. 1982. The biochemistry of methylotrophs.

Atahan, P., Grice, K. & Dodson, J. 2007. Agriculture and environmental change at Qingpu, Yangtze delta region, China: a biomarker, stable isotope and palynological approach. *The Holocene,* 17**,** 507-515.

Baker, A., Routh, J. & Roychoudhury, A. N. 2016. Biomarker records of palaeoenvironmental variations in subtropical Southern Africa since the late Pleistocene: Evidences from a coastal peatland. *Palaeogeography, Palaeoclimatology, Palaeoecology,* 451**,** 1-12.

Barber, V. P., Pandit, S., Green, A. M., Trongsiriwat, N., Walsh, P. J., Klippenstein, S. J. & Lester, M. I. 2018. Four-carbon Criegee intermediate from isoprene ozonolysis: Methyl vinyl ketone oxide synthesis, infrared spectrum, and OH production. *Journal of the American Chemical Society,* 140**,** 10866-10880.

Barrie, A. & Prosser, S. 1996. Automated analysis of light-element stable isotopes by isotope ratio mass spectrometry. *Mass spectrometry of soils. New York, Marcel Dekker***,** 1-46.

Bartle, K. D. & Myers, P. 2002. History of gas chromatography. *TrAC Trends in Analytical Chemistry,* 21**,** 547-557.

Bender, M. & Conrad, R. 1992. Kinetics of CH4 oxidation in oxic soils exposed to ambient air or high CH4 mixing ratios. *FEMS Microbiology Letters,* 101**,** 261-270.

Bender, M. & Conrad, R. 1993. Kinetics of methane oxidation in oxic soils. *Chemosphere,* 26**,** 687-696.

Benson, S. W. & Buss, J. H. 1958. Additivity rules for the estimation of molecular properties. Thermodynamic properties. *The Journal of Chemical Physics,* 29**,** 546-572.

Bernhammer, A.-K., Breitenlechner, M., Keutsch, F. N. & Hansel, A. 2017. Conversion of isoprene hydroxy hydroperoxides (ISOPOOHs) on metal environmental simulation chamber walls. *Atmospheric Chemistry and Physics,* 17**,** 4053-4062.

Beveridge, T. J. 1999. Structures of gram-negative cell walls and their derived membrane vesicles. *Journal of bacteriology,* 181**,** 4725-4733.

Bhomia, R. K., Van Lent, J., Rios, J. M. G., Hergoualc'h, K., Coronado, E. N. H. & Murdiyarso, D. 2019. Impacts of Mauritia flexuosa degradation on the carbon stocks of freshwater peatlands in the Pastaza-Marañón river basin of the Peruvian Amazon. *Mitigation and Adaptation Strategies for Global Change,* 24**,** 645-668.

Bird, M. I., Summons, R. E., Gagan, M. K., Roksandic, Z., Dowling, L., Head, J., Fifield, L. K., Cresswell, R. G. & Johnson, D. P. 1995. Terrestrial vegetation change inferred from n-alkane σ13C analysis in the marine environment. *Geochimica et Cosmochimica Acta,* 59**,** 2853-2857.

Birgel, D. & Peckmann, J. 2008. Aerobic methanotrophy at ancient marine methane seeps: A synthesis. *Organic Geochemistry,* 39**,** 1659-1667.

Blaser, M. & Conrad, R. 2016. Stable carbon isotope fractionation as tracer of carbon cycling in anoxic soil ecosystems. *Current opinion in biotechnology,* 41**,** 122-129.

Blaut, M. 1994. Metabolism of methanogens. *Antonie Van Leeuwenhoek,* 66**,** 187-208.

Blondal, K., Jelic, J., Mazeau, E., Studt, F., West, R. H. & Goldsmith, C. F. 2019. Computer-generated kinetics for coupled heterogeneous/homogeneous systems: A case study in catalytic combustion of methane on platinum. *Industrial & Engineering Chemistry Research,* 58**,** 17682-17691.

Blumenberg, M., Krüger, M., Nauhaus, K., Talbot, H. M., Oppermann, B. I., Seifert, R., Pape, T. & Michaelis, W. 2006. Biosynthesis of hopanoids by sulfate-reducing bacteria (genus Desulfovibrio). *Environmental Microbiology,* 8**,** 1220-1227.

Bodelier, P. L., Bär Gillisen, M.-J., Hordijk, K., Sinninghe Damsté, J. S., Rijpstra, W. I. C., Geenevasen, J. A. & Dunfield, P. F. 2009. A reanalysis of phospholipid fatty acids as ecological biomarkers for methanotrophic bacteria. *The ISME journal,* 3**,** 606-617.

Boschker, H. & Middelburg, J. 2002. Stable isotopes and biomarkers in microbial ecology. *FEMS Microbiology Ecology,* 40**,** 85-95.

Bottari, F., Marsili, A., Morelli, I. & Pacchiani, M. 1972. Aliphatic and triterpenoid hydrocarbons from ferns. *Phytochemistry,* 11**,** 2519-2523.

Botz, R., Pokojski, H.-D., Schmitt, M. & Thomm, M. 1996. Carbon isotope fractionation during bacterial methanogenesis by CO2 reduction. *Organic Geochemistry,* 25**,** 255-262.

Bouloubassi, I., Nabais, E., Pancost, R. D., Lorre, A. & Taphanel, M.-H. 2009. First biomarker evidence for methane oxidation at cold seeps in the Southeast Atlantic (REGAB pockmark). *Deep Sea Research Part II: Topical Studies in Oceanography,* 56**,** 2239-2247.

Bourgeau-Chavez, L. L., Grelik, S. L., Battaglia, M. J., Leisman, D. J., Chimner, R. A., Hribljan, J. A., Lilleskov, E. A., Draper, F. C., Zutta, B. R. & Hergoualc'h, K. 2022. Advances in amazonian peatland discrimination with multi-temporal PALSAR Refines estimates of Peatland distribution, C stocks and deforestation. *Observing, Modeling and Understanding Processes in Natural and Managed Peatlands*.

Bowman, J. P., Skerratt, J. H., Nichols, P. D. & Sly, L. I. 1991. Phospholipid fatty acid and lipopolysaccharide fatty acid signature lipids in methane-utilizing bacteria. *FEMS Microbiology Letters,* 85**,** 15-21.

Brenna, J. T., Corso, T. N., Tobias, H. J. & Caimi, R. J. 1997. <Brenna_et_al-1997.pdf>.

Brewer, P. & Cadillo-Quiroz, H. Magnitudes and Controls of Stem Methane Emissions in Amazonian Peatland Forests. AGU Fall Meeting Abstracts, 2020. B065-0008.

Bridgham, S. D., Cadillo-Quiroz, H., Keller, J. K. & Zhuang, Q. 2013. Methane emissions from wetlands: biogeochemical, microbial, and modeling perspectives from local to global scales. *Global change biology,* 19**,** 1325-1346.

Briggs, D. E. & Summons, R. E. 2014. Ancient biomolecules: their origins, fossilization, and role in revealing the history of life. *BioEssays,* 36**,** 482-490.

Brocks, J. & Summons, R. 2005. Sedimentary Hydrocarbons. *Biogeochemistry,* 8**,** 63.

Brocks, J. J., Buick, R., Summons, R. E. & Logan, G. A. 2003. A reconstruction of Archean biological diversity based on molecular fossils from the 2.78 to 2.45 billion-year-old Mount Bruce Supergroup, Hamersley Basin, Western Australia. *Geochimica et Cosmochimica Acta,* 67**,** 4321-4335.

Brocks, J. J., Logan, G. A., Buick, R. & Summons, R. E. 1999. Archean molecular fossils and the early rise of eukaryotes. *science,* 285**,** 1033-1036.

Brocks, J. J. & Pearson, A. 2005. Building the biomarker tree of life. *Reviews in Mineralogy and Geochemistry,* 59**,** 233-258.

Brownlow, R., Lowry, D., Fisher, R., France, J., Lanoisellé, M., White, B., Wooster, M., Zhang, T. & Nisbet, E. 2017. Isotopic ratios of tropical methane emissions by atmospheric measurement. *Global Biogeochemical Cycles,* 31**,** 1408-1419.

Brüggemann, N., Gessler, A., Kayler, Z., Keel, S., Badeck, F., Barthel, M., Boeckx, P., Buchmann, N., Brugnoli, E. & Esperschütz, J. 2011. Carbon allocation and carbon

isotope fluxes in the plant-soil-atmosphere continuum: a review. *Biogeosciences,* 8**,** 3457-3489.

Buessecker, S., Zamora, Z., Sarno, A. F., Finn, D. R., Hoyt, A. M., Van Haren, J., Muñoz, J. D. U. & Cadillo-Quiroz, H. 2021. Microbial communities and interactions of nitrogen oxides with methanogenesis in diverse peatlands of the Amazon basin. *Frontiers in Microbiology,* 12.

Bull, I. D., Parekh, N. R., Hall, G. H., Ineson, P. & Evershed, R. P. 2000. Detection and classification of atmospheric methane oxidizing bacteria in soil. *Nature,* 405**,** 175-178.

Burnham, A. K. & Happe, J. A. 1984. On the mechanism of kerogen pyrolysis. *Fuel,* 63**,** 1353-1356.

Carter, J. & Barwick, V. 2011. Good practice guide for isotope ratio mass spectrometry. *FIRMS Network,* 48.

Chanton, J. P. 2005. The effect of gas transport on the isotope signature of methane in wetlands. *Organic Geochemistry,* 36**,** 753-768.

Chanton, J. P., Chaser, L., Glasser, P. & Siegel, D. 2005. Carbon and hydrogen isotopic effects in microbial methane from terrestrial environments. *Stable isotopes and biosphere-atmosphere interactions***,** 85-105.

Chen, Y., Dumont, M. G., Mcnamara, N. P., Chamberlain, P. M., Bodrossy, L., Stralis-Pavese, N. & Murrell, J. C. 2008. Diversity of the active methanotrophic community in acidic peatlands as assessed by mRNA and SIP-PLFA analyses. *Environmental Microbiology,* 10**,** 446-459.

Chistoserdova, L. V. & Lidstrom, M. E. 1994. Genetics of the serine cycle in Methylobacterium extorquens AM1: identification of sgaA and mtdA and sequences of sgaA, hprA, and mtdA. *Journal of bacteriology,* 176**,** 1957-1968.

Chromatography-Today 2024. 8 Common Gas Chromatography Mistakes, Accessible at: https://www.chromatographytoday.com/news/gc-mdgc/32/breaking-news/8-common-gas-chromatography-mistakes/31345 (Last accessed: 10/01/2024).

Cicerone, R. J. & Oremland, R. S. 1988. Biogeochemical aspects of atmospheric methane. *Global biogeochemical cycles,* 2**,** 299-327.

Collister, J. W., Rieley, G., Stern, B., Eglinton, G. & Fry, B. 1994. Compound-specific δ 13C analyses of leaf lipids from plants with differing carbon dioxide metabolisms. *Organic Geochemistry,* 21**,** 619-627.

Collister, J. W., Summons, R. E., Lichtfouse, E. & Hayes, J. M. 1992. An isotopic biogeochemical study of the Green River oil shale. *Organic Geochemistry,* 19**,** 265-276.

Conrad, R. 2005. Quantification of methanogenic pathways using stable carbon isotopic signatures: a review and a proposal. *Organic geochemistry,* 36**,** 739-752.

Conrad, R. 2007. Microbial ecology of methanogens and methanotrophs. *Advances in agronomy,* 96**,** 1-63.

Conrad, R., Noll, M., Claus, P., Klose, M., Bastos, W. R. & Enrich-Prast, A. 2011. Stable carbon isotope discrimination and microbiology of methane formation in tropical anoxic lake sediments. *Biogeosciences,* 8**,** 795-814.

Cordova-Gonzalez, A., Birgel, D., Wisshak, M., Urich, T., Brinkmann, F., Marcon, Y., Bohrmann, G. & Peckmann, J. 2023. A carbonate corrosion experiment at a marine methane seep: The role of aerobic methanotrophic bacteria. *Geobiology*.

Corey, E., Matsuda, S. & Bartel, B. 1993. Isolation of an Arabidopsis thaliana gene encoding cycloartenol synthase by functional expression in a yeast mutant lacking lanosterol synthase by the use of a chromatographic screen. *Proceedings of the National Academy of Sciences,* 90**,** 11628-11632.

Coronado, E. N. H., Hastie, A., Reyna, J., Flores, G., Grández, J., Lähteenoja, O., Draper, F. C., Åkesson, C. M., Baker, T. R. & Bhomia, R. K. 2021. Intensive field sampling increases the known extent of carbon-rich Amazonian peatland pole forests. *Environmental Research Letters,* 16**,** 074048.

Corso, T. & Brenna, J. 1997. High precision position specific isotope analysis. *Proceedings of the National Academy of Sciences of the United States of America*.

Corso, T. N. & Brenna, J. T. 1999. On-line pyrolysis of hydrocarbons coupled to high-precision carbon isotope ratio analysis. *Analytica chimica acta,* 397**,** 217-224.

Corso, T. N., Lewis, B. A. & Brenna, J. T. 1998. Reduction of fatty acid methyl esters to fatty alcohols to improve volatility for isotopic analysis without extraneous carbon. *Analytical chemistry,* 70**,** 3752-3756.

Coskun, O. 2016. Separation techniques: chromatography. *Northern clinics of Istanbul,* 3**,** 156.

Cranwell, P., Eglinton, G. & Robinson, N. 1987. Lipids of aquatic organisms as potential contributors to lacustrine sediments—II. *Organic Geochemistry,* 11**,** 513-527.

Criegee, R. 1975. Mechanism of ozonolysis. *Angewandte chemie international edition in english,* 14**,** 745-752.

Davies, K. L., Pancost, R. D., Edwards, M. E., Walter Anthony, K. M., Langdon, P. G. & Chaves Torres, L. 2016. Diploptene δ 13 C values from contemporary thermokarst lake sediments show complex spatial variation. *Biogeosciences,* 13**,** 2611-2621.

De Alencastro, L. F., Grandjean, D. & Tarradellas, J. 2003. Application of multidimensional (heart-cut) gas chromatography to the analysis of complex mixtures of organic pollutants in environmental samples. *CHIMIA International Journal for Chemistry,* 57**,** 499-504.

De Coning, P. & Swinley, J. 2019. Chapter 1 - Overview and theory. *In:* DE CONING, P. & SWINLEY, J. (eds.) *A Practical Guide to Gas Analysis by Gas Chromatography.* Elsevier.

De Hoffmann, E. & Stroobant, V. 2007. *Mass spectrometry: principles and applications*, John Wiley & Sons.

Dedysh, S. 2002. Methanotrophic bacteria of acidic Sphagnum peat bogs. *Microbiology,* 71**,** 638-650.

Dedysh, S. 2009. Exploring methanotroph diversity in acidic northern wetlands: molecular and cultivation-based studies. *Microbiology,* 78**,** 655-669.

Dedysh, S. N. & Dunfield, P. F. 2011. Facultative and obligate methanotrophs how to identify and differentiate them. *Methods Enzymol,* 495**,** 31-44.

Dedysh, S. N., Knief, C. & Dunfield, P. F. 2005. Methylocella species are facultatively methanotrophic. *Journal of bacteriology,* 187**,** 4665-4670.

Derwent, R. G. 2020. Global warming potential (GWP) for methane: Monte Carlo analysis of the uncertainties in global tropospheric model predictions. *Atmosphere,* 11**,** 486.

Dettmer-Wilde, K. & Engewald, W. 2014. Practical gas chromatography. *A Comprehensive Reference.* Springer.

Dias, R. F., Freeman, K. H. & Franks, S. G. 2002. Gas chromatography–pyrolysis–isotope ratio mass spectrometry: a new method for investigating intramolecular isotopic variation in low molecular weight organic acids. *Organic Geochemistry,* 33**,** 161-168.

Dibble, T. S. 2004a. Intramolecular hydrogen bonding and double H-atom transfer in peroxy and alkoxy radicals from isoprene. *The Journal of Physical Chemistry A,* 108**,** 2199-2207.

Dibble, T. S. 2004b. Prompt chemistry of alkenoxy radical products of the double H-atom transfer of alkoxy radicals from isoprene. *The Journal of Physical Chemistry A,* 108**,** 2208-2215.

Dommain, R., Cobb, A. R., Joosten, H., Glaser, P. H., Chua, A. F., Gandois, L., Kai, F. M., Noren, A., Salim, K. A. & Su'ut, N. S. H. 2015. Forest dynamics and tip-up pools drive pulses of high carbon accumulation rates in a tropical peat dome in Borneo (Southeast Asia). *Journal of Geophysical Research: Biogeosciences,* 120**,** 617-640.

Dong, X., Ninnemann, E., Ranasinghe, D. S., Laich, A., Greene, R., Vasu, S. S. & Green, W. H. 2020. Revealing the critical role of radical-involved pathways in high temperature cyclopentanone pyrolysis. *Combustion and Flame,* 216**,** 280-292.

Draper, F. C., Honorio Coronado, E. N., Roucoux, K. H., Lawson, I. T., A. Pitman, N. C., A. Fine, P. V., Phillips, O. L., Torres Montenegro, L. A., Valderrama Sandoval, E. & Mesones, I. 2018. Peatland forests are the least diverse tree communities documented in Amazonia, but contribute to high regional beta-diversity. *Ecography,* 41**,** 1256-1269.

Draper, F. C., Roucoux, K. H., Lawson, I. T., Mitchard, E. T., Coronado, E. N. H., Lähteenoja, O., Montenegro, L. T., Sandoval, E. V., Zaráte, R. & Baker, T. R. 2014. The distribution and amount of carbon in the largest peatland complex in Amazonia. *Environmental Research Letters,* 9**,** 124017.

Dunfield, P. F., Yuryev, A., Senin, P., Smirnova, A. V., Stott, M. B., Hou, S., Ly, B., Saw, J. H., Zhou, Z. & Ren, Y. 2007. Methane oxidation by an extremely acidophilic bacterium of the phylum Verrucomicrobia. *Nature,* 450**,** 879-882.

Dunn, P. J. & Carter, J. F. 2018. Publication of the second edition of the FIRMS good practice guide for isotope ratio mass spectrometry. *Sci ence & Jus tice,* 58**,** 467-468.

Eakin, P., Fallick, A. & Gerc, J. 1992. Some instrumental effects in the determination of stable carbon isotope ratios by gas chromatography-isotope ratio mass spectrometry. *Chemical Geology: Isotope Geoscience section,* 101**,** 71-79.

Eckmeier, E. & Wiesenberg, G. L. 2009. Short-chain n-alkanes (C16–20) in ancient soil are useful molecular markers for prehistoric biomass burning. *Journal of Archaeological Science,* 36**,** 1590-1596.

Eglinton, G. & Calvin, M. 1967. Chemical fossils. *Sci AM,* 216**,** 32-43.

Eglinton, G. & Hamilton, R. J. 1967. Leaf Epicuticular Waxes: The waxy outer surfaces of most plants display a wide diversity of fine structure and chemical constituents. *Science,* 156**,** 1322-1335.

Eglinton, T. & Douglas, A. 1988. Quantitative study of biomarker hydrocarbons released from kerogens during hydrous pyrolysis. *Energy & fuels,* 2**,** 81-88.

Eglinton, T. I. 1994. Carbon isotopic evidence for the origin of macromolecular aliphatic structures in kerogen. *Organic Geochemistry,* 21**,** 721-735.

Elling, F. J., Evans, T. W., Nathan, V., Hemingway, J. D., Kharbush, J. J., Bayer, B., Spieck, E., Husain, F., Summons, R. E. & Pearson, A. 2022. Marine and terrestrial nitrifying bacteria are sources of diverse bacteriohopanepolyols. *Geobiology,* 20**,** 399-420.

Elvert, M., Greinert, J., Suess, E. & Whiticar, M. J. 2001a. Carbon isotopes of biomarkers derived from methane-oxidizing microbes at Hydrate Ridge, Cascadia convergent margin. *GEOPHYSICAL MONOGRAPH-AMERICAN GEOPHYSICAL UNION,* 124**,** 115-130.

Elvert, M. & Niemann, H. 2008. Occurrence of unusual steroids and hopanoids derived from aerobic methanotrophs at an active marine mud volcano. *Organic Geochemistry,* 39**,** 167-177.

Elvert, M., Pohlman, J. W., Becker, K. W., Gaglioti, B., Hinrichs, K.-U. & Wooller, M. J. 2016. Methane turnover and environmental change from Holocene lipid biomarker records in a thermokarst lake in Arctic Alaska. *The Holocene,* 26**,** 1766-1777.

Elvert, M., Suess, E., Greinert, J. & Whiticar, M. J. 2000. Archaea mediating anaerobic methane oxidation in deep-sea sediments at cold seeps of the eastern Aleutian subduction zone. *Organic Geochemistry,* 31**,** 1175-1187.

Elvert, M., Whiticar, M. J. & Suess, E. 2001b. Diploptene in varved sediments of Saanich Inlet: indicator of increasing bacterial activity under anaerobic conditions during the Holocene. *Marine Geology,* 174**,** 371-383.

Engineeringtoolbox 2014. Metals, Metallic Elements and Alloys - Thermal Conductivities. Thermal conductivities of common metals, metallic elements aand alloys. Accessible at: https://www.engineeringtoolbox.com/thermal-conductivity-metals-d_858.html (Last accessed: 10/01/2024).

Ensminger, A., Albrecht P., Ourisson G., Kimble B. J., R., M. J. & G., E. 1972. Homohopane in the Messeloil shale: first identification of a C31 pentacyclic triterpane in nature. *Tetrahedron Lett. 36, 3861-3864.*

Enzmann, F., Mayer, F., Rother, M. & Holtmann, D. 2018. Methanogens: biochemical background and biotechnological applications. *Amb Express,* 8**,** 1-22.

Etiope, G. & Sherwood Lollar, B. 2013. Abiotic methane on Earth. *Reviews of Geophysics,* 51**,** 276-299.

Ettre, L. 1984. Viscosity of gases used as the mobile phase in gas chromatography. *Chromatographia,* 18**,** 243-248.

Ettre, L. S. 1990. Professor Erika Cremer ninety years old. *Chromatographia,* 29**,** 413-414.

Ettre, L. S. 1993. Nomenclature for chromatography (IUPAC Recommendations 1993). *pure and applied chemistry,* 65**,** 819-872.

Ettwig, K. F., Butler, M. K., Le Paslier, D., Pelletier, E., Mangenot, S., Kuypers, M. M., Schreiber, F., Dutilh, B. E., Zedelius, J. & De Beer, D. 2010. Nitrite-driven anaerobic methane oxidation by oxygenic bacteria. *Nature,* 464**,** 543-548.

Ettwig, K. F., Shima, S., Van De Pas-Schoonen, K. T., Kahnt, J., Medema, M. H., Op Den Camp, H. J., Jetten, M. S. & Strous, M. 2008. Denitrifying bacteria anaerobically

oxidize methane in the absence of Archaea. *Environmental microbiology,* 10**,** 3164-3173.

Eusufzai, M. K., Tokida, T., Okada, M., Sugiyama, S.-I., Liu, G. C., Nakajima, M. & Sameshima, R. 2010. Methane emission from rice fields as affected by land use change. *Agriculture, ecosystems & environment,* 139**,** 742-748.

Farrimond, P., Love, G. D., Bishop, A. N., Innes, H. E., Watson, D. F. & Snape, C. E. 2003. Evidence for the rapid incorporation of hopanoids into kerogen. *Geochimica et Cosmochimica Acta,* 67**,** 1383-1394.

Feakins, S. J., Eglinton, T. I. & Demenocal, P. B. 2007. A comparison of biomarker records of northeast African vegetation from lacustrine and marine sediments (ca. 3.40 Ma). *Organic Geochemistry,* 38**,** 1607-1624.

Feakins, S. J., Wu, M. S., Ponton, C., Galy, V. & West, A. J. 2018. Dual isotope evidence for sedimentary integration of plant wax biomarkers across an Andes-Amazon elevation transect. *Geochimica et Cosmochimica Acta,* 242**,** 64-81.

Feil, C., Süssmuth, R., Jung, G. & Poralla, K. 1996. Site-directed mutagenesis of putative active-site residues in squalene-hopene cyclase. *European journal of biochemistry,* 242**,** 51-55.

Fermoso, F. G., Van Hullebusch, E., Collins, G., Roussel, J., Mucha, A. P. & Esposito, G. 2019. *Trace elements in anaerobic biotechnologies*, IWA publishing.

Ficken, K. J., Li, B., Swain, D. & Eglinton, G. 2000. An n-alkane proxy for the sedimentary input of submerged/floating freshwater aquatic macrophytes. *Organic geochemistry,* 31**,** 745-749.

Finn, D. R., Ziv-El, M., Haren, J. V., Park, J. G., Del Águila Pasquel, J., Urquiza Muñoz, J. & Cadillo Quiroz, H. 2020. Methanogens and methanotrophs show nutrient-dependent community assemblage patterns across peatlands of the Pastaza-Marañón Basin, Peruvian Amazonia.

Fischer, A., Gehre, M., Breitfeld, J., Richnow, H. H. & Vogt, C. 2009. Carbon and hydrogen isotope fractionation of benzene during biodegradation under sulfate-reducing conditions: a laboratory to field site approach. *Rapid Communications in Mass Spectrometry: An International Journal Devoted to the Rapid Dissemination of Up-to-the-Minute Research in Mass Spectrometry,* 23**,** 2439-2447.

Fritz, C., Pancotto, V. A., Elzenga, J. T., Visser, E. J., Grootjans, A. P., Pol, A., Iturraspe, R., Roelofs, J. G. & Smolders, A. J. 2011. Zero methane emission bogs: extreme rhizosphere oxygenation by cushion plants in Patagonia. *New Phytologist,* 190**,** 398-408.

Galloway, M., Huisman, A., Yee, L., Chan, A., Loza, C., Seinfeld, J. & Keutsch, F. 2011. Yields of oxidized volatile organic compounds during the OH radical initiated oxidation of isoprene, methyl vinyl ketone, and methacrolein under high-NO x conditions. *Atmospheric Chemistry and Physics,* 11**,** 10779-10790.

Games, L. M., Hayesrobert, J. & Gunsalus, P. 1978. Methane-producing bacteria: natural fractionations of the stable carbon isotopes. *Geochimica et Cosmochimica Acta,* 42**,** 1295-1297.

Gao, C. W., Allen, J. W., Green, W. H. & West, R. H. 2016. Reaction Mechanism Generator: Automatic construction of chemical kinetic mechanisms. *Computer Physics Communications,* 203**,** 212-225.

Gao, J., Ma, S., Major, D. T., Nam, K., Pu, J. & Truhlar, D. G. 2006. Mechanisms and free energies of enzymatic reactions. *Chemical reviews,* 106**,** 3188-3209.

Gauchotte-Lindsay, C., O'sullivan, G., Davis, S. & Kalin, R. M. 2009. Development of an advanced on-line position-specific stable carbon isotope system and application to methyl tert-butyl ether. *Rapid Communications in Mass Spectrometry: An International Journal Devoted to the Rapid Dissemination of Up-to-the-Minute Research in Mass Spectrometry,* 23**,** 3183-3193.

Gauchotte-Lindsay, C. & Turnbull, S. M. 2016. On-line high-precision carbon position-specific stable isotope analysis: A review. *TrAC Trends in Analytical Chemistry,* 76**,** 115-125.

Gauchotte, C. P. C. 2009. Development of an On-line Position Specific Carbon Isotope Analysis System with Application to Environmental Forensics. *PhD Thesis,* Queen's University of Belfast.

Gelpi, E., Schneider, H., Mann, J. & Oro, J. 1970. Hydrocarbons of geochemical significance in microscopic algae. *Phytochemistry,* 9**,** 603-612.

Gelwicks, J. T., Risatti, J. B. & Hayes, J. 1994. Carbon isotope effects associated with aceticlastic methanogenesis. *Applied and Environmental Microbiology,* 60**,** 467-472.

Giavarina, D. 2015. Understanding bland altman analysis. *Biochemia medica,* 25**,** 141-151.

Gilbert, A., Yamada, K., Suda, K., Ueno, Y. & Yoshida, N. 2016. Measurement of position-specific 13C isotopic composition of propane at the nanomole level. *Geochimica et Cosmochimica Acta,* 177**,** 205-216.

Girkin, N., Turner, B., Ostle, N., Craigon, J. & Sjögersten, S. 2018. Root exudate analogues accelerate CO2 and CH4 production in tropical peat. *Soil Biology and Biochemistry,* 117**,** 48-55.

Goevert, D. & Conrad, R. 2009. Effect of substrate concentration on carbon isotope fractionation during acetoclastic methanogenesis by Methanosarcina barkeri and M. acetivorans and in rice field soil. *Applied and Environmental Microbiology,* 75**,** 2605-2612.

Gohlke, R. S. 1959. Time-of-flight mass spectrometry and gas-liquid partition chromatography. *Analytical Chemistry,* 31**,** 535-541.

Gold, V. 2019. The IUPAC Compendium of Chemical Terminology; International Union of Pure and Applied Chemistry (IUPAC). Research Triangle Park, NC.

Goldman, M. J., Vandewiele, N. M., Ono, S. & Green, W. H. 2019. Computer-generated isotope model achieves experimental accuracy of filiation for position-specific isotope analysis. *Chemical Geology,* 514**,** 1-9.

Gräber, W.-D. & Hüttinger, K. J. 1982. Chemistry of methane formation in hydrogasification of aromatics. 2. Aromatics with aliphatic groups. *Fuel,* 61**,** 505-509.

Graham, D. W., Chaudhary, J. A., Hanson, R. S. & Arnold, R. G. 1993. Factors affecting competition between type I and type II methanotrophs in two-organism, continuous-flow reactors. *Microbial ecology,* 25**,** 1-17.

Grajales-González, E., Kukkadapu, G., Nagaraja, S. S., Shao, C., Monge-Palacios, M., Chavarrio, J. E., Wagnon, S. W., Curran, H. J., Pitz, W. J. & Sarathy, S. M. 2022. An experimental and kinetic modeling study of the pyrolysis of isoprene, a significant biogenic hydrocarbon in naturally occurring vegetation fires. *Combustion and Flame,* 242**,** 112206.

Gram, C. 1884. Ueber die isolirte Farbung der Schizomyceten in Schnitt-und Trockenpraparaten. *Fortschritte der Medicin,* 2**,** 185-189.

Green, W., Barton, P., Bhattacharjee, B., Matheu, D., Schwer, D., Song, J., Sumathi, R., Carstensen, H.-H., Dean, A. & Grenda, J. 2001. Computer construction of detailed chemical kinetic models for gas-phase reactors. *Industrial & engineering chemistry research,* 40**,** 5362-5370.

Green, W. H. & Team, A. T. R. 2013. RMG Documentation-Release 4.0.1; Accessible at: https://rmg.sourceforge.net/RMG-manual.pdf (Last accessed: 10/01/2024).

Green, W. H. & West, R. H. E. A. 2023. RMG molecule serach. Availabe at: https://rmg.mit.edu/molecule_search. (Last accessed: 10/01/2024).

Grob Jr, K. 1980. Stability of the FID sensitivity during an analysis in capillary GC. *Journal of High Resolution Chromatography,* 3**,** 286-290.

Guenther, A., Karl, T., Harley, P., Wiedinmyer, C., Palmer, P. I. & Geron, C. 2006. Estimates of global terrestrial isoprene emissions using MEGAN (Model of Emissions of Gases and Aerosols from Nature). *Atmospheric Chemistry and Physics,* 6**,** 3181-3210.

Hakobyan, A. & Liesack, W. 2020. Unexpected metabolic versatility among type II methanotrophs in the Alphaproteobacteria. *Biological Chemistry,* 401**,** 1469-1477.

Hanson, R. S. & Hanson, T. E. 1996. Methanotrophic bacteria. *Microbiological reviews,* 60**,** 439-471.

Harper, M. R., Van Geem, K. M., Pyl, S. P., Marin, G. B. & Green, W. H. 2011. Comprehensive reaction mechanism for n-butanol pyrolysis and combustion. *Combustion and Flame,* 158**,** 16-41.

Härtner, T., Straub, K. L. & Kannenberg, E. 2005. Occurrence of hopanoid lipids in anaerobic Geobacter species. *FEMS Microbiology Letters,* 243**,** 59-64.

Hastie, A., Honorio Coronado, E. N., Reyna, J., Mitchard, E. T., Åkesson, C. M., Baker, T. R., Cole, L. E., Oroche, C., Córdova, J. & Dargie, G. 2022. Risks to carbon storage from land-use change revealed by peat thickness maps of Peru. *Nature Geoscience,* 15**,** 369-374.

Hattori, R., Yamada, K., Kikuchi, M., Hirano, S. & Yoshida, N. 2011. Intramolecular carbon isotope distribution of acetic acid in vinegar. *J Agric Food Chem,* 59**,** 9049-53.

Hayes, J. 2001. Fractionation of the isotopes of carbon and hydrogen in biosynthetic processes, pp. 225Ð277. *Stable isotope geochemistry,* 43.

Henshaw, J. V. 2005. The flame ionization detector. *LCGC North America,* 23**,** 1262–1272-1262–1272.

Hidalgo Pizango, C. G., Honorio Coronado, E. N., Del Águila-Pasquel, J., Flores Llampazo, G., De Jong, J., Córdova Oroche, C. J., Reyna Huaymacari, J. M., Carver, S. J., Del Castillo Torres, D. & Draper, F. C. 2022. Sustainable palm fruit harvesting as a pathway to conserve Amazon peatland forests. *Nature Sustainability***,** 1-9.

Hinrichs, K.-U., Hmelo, L. R. & Sylva, S. P. 2003. Molecular fossil record of elevated methane levels in late Pleistocene coastal waters. *Science,* 299**,** 1214-1217.

Hinrichs, K. U. 2001. A molecular recorder of methane hydrate destabilization. *Geochemistry, Geophysics, Geosystems,* 2.

Hobbie, E., A & Werner, R. A. 2004. Intramolecular, compound-specific, and bulk carbon isotope patterns in C3 and C4 plants: a review and synthesis. *New Phytologist,* 161**,** 371-385.

Hoefs, J. 2015. *Stable Isotope Geochemistry*, Springer.

Hoffman, D. W. & Rasmussen, C. 2019. Position-specific carbon stable isotope ratios by proton NMR spectroscopy. *Analytical chemistry,* 91**,** 15661-15669.

Hoffmann, C. & Roksandic, Z. 1989. Stable isotopes—correction and normalization of delta values obtained on a mass spectrometer. *Computers & Geosciences,* 15**,** 1183-1192.

Holm, T. 1997. Mechanism of the flame ionization detector II. Isotope effects and heteroatom effects. *Journal of Chromatography A,* 782**,** 81-86.

Holm, T. 1999. Aspects of the mechanism of the flame ionization detector. *Journal of Chromatography A,* 842**,** 221-227.

Hoyos-Santillan, J., Lomax, B. H., Large, D., Turner, B. L., Lopez, O. R., Boom, A., Sepulveda-Jauregui, A. & Sjögersten, S. 2019. Evaluation of vegetation communities, water table, and peat composition as drivers of greenhouse gas emissions in lowland tropical peatlands. *Science of the Total Environment,* 688**,** 1193-1204.

Huff, M. W. & Telford, D. E. 2005. Lord of the rings–the mechanism for oxidosqualene: lanosterol cyclase becomes crystal clear. *Trends in pharmacological sciences,* 26**,** 335-340.

Hunter, W. N. 2007. The non-mevalonate pathway of isoprenoid precursor biosynthesis. *Journal of Biological Chemistry,* 282**,** 21573-21577.

Hyun, S., Bahk, J.-J., Yim, U. H., Uchida, M., Nam, S. & Woo, K. 2014. Carbon isotope variations in diploptene for methane hydrate dissociation during the last glacial episode in the Japan Sea/East Sea. *Geochemical Journal,* 48**,** 287-297.

Iannone, R., Koppmann, R. & Rudolph, J. 2008. The stable-carbon kinetic isotope effects of the reactions of isoprene, methacrolein, and methyl vinyl ketone with ozone in the gas phase. *Atmospheric Environment,* 42**,** 8728-8737.

Iannone, R., Koppmann, R. & Rudolph, J. 2009. 12C/13C kinetic isotope effects of the gas-phase reactions of isoprene, methacrolein, and methyl vinyl ketone with OH radicals. *Atmospheric Environment,* 43**,** 3103-3110.

Iannone, R., Koppmann, R. & Rudolph, J. 2010. Stable carbon kinetic isotope effects for the production of methacrolein and methyl vinyl ketone from the gas-phase reactions of isoprene with ozone and hydroxyl radicals. *Atmospheric Environment,* 44**,** 4135-4141.

Inglis, G. N., Naafs, B. D. A., Zheng, Y., Schellekens, J. & Pancost, R. D. 2019. δ13C values of bacterial hopanoids and leaf waxes as tracers for methanotrophy in peatlands. *Geochimica et Cosmochimica Acta,* 260**,** 244-256.

Ipcc 2021. Climate Change 2021: The Physical Science Basis. Contribution of Working Group I to the Sixth Assessment Report of the Intergovernmental Panel on

Climate Change. Masson-Delmotte, V., P. Zhai, A. Pirani, S.L. Connors, C. Péan, S. Berger, N. Caud, Y. Chen, L. Goldfarb, M.I. Gomis, M. Huang, K. Leitzell, E. Lonnoy, J.B.R.

Matthews, T.K. Maycock, T. Waterfield, O. Yelekçi, R. Yu, and B. Zhou (eds.).

Ipcc 2022. 6th Assesment Report, Climate Change 2022: Impacts, Adaptation and Vulnerability.

Ishiwatari, R., Hirakawa, Y., Uzaki, M., Yamada, K. & Yada, T. 1994. Organic geochemistry of the Japan Sea sediments-1: Bulk organic matter and hydrocarbon analyses of Core KH-79-3, C-3 from the Oki Ridge for paleoenvironment assessments. *Journal of Oceanography,* 50**,** 179-195.

Jahnke, L. L. & Nichols, P. 1986. Methyl sterol and cyclopropane fatty acid composition of Methylococcus capsulatus grown at low oxygen tensions. *Journal of Bacteriology,* 167**,** 238-242.

Jahnke, L. L., Summons, R. E., Hope, J. M. & Des Marais, D. J. 1999. Carbon isotopic fractionation in lipids from methanotrophic bacteria II: The effects of physiology and environmental parameters on the biosynthesis and isotopic signatures of biomarkers. *Geochimica et Cosmochimica Acta,* 63**,** 79-93.

Jansen, B. & Wiesenberg, G. L. 2017. Opportunities and limitations related to the application of plant-derived lipid molecular proxies in soil science. *Soil,* 3**,** 211-234.

Jézéquel, T., Joubert, V., Giraudeau, P., Remaud, G. S. & Akoka, S. 2017. The new face of isotopic NMR at natural abundance. *Magnetic Resonance in Chemistry,* 55**,** 77-90.

Julien, M., Goldman, M. J., Liu, C., Horita, J., Boreham, C. J., Yamada, K., Green, W. H., Yoshida, N. & Gilbert, A. 2020. Intramolecular 13C isotope distributions of butane from natural gases. *Chemical Geology,* 541**,** 119571.

Kallweit, T. 2020. Mauritia flexuosa as an Opportunity to Curb Tropical Peat Swamp Forest Degradation?

Kalyuzhnaya, M., Yang, S., Rozova, O., Smalley, N., Clubb, J., Lamb, A., Gowda, G., Raftery, D., Fu, Y. & Bringel, F. 2013. Highly efficient methane biocatalysis revealed in a methanotrophic bacterium. *Nature communications,* 4**,** 1-7.

Kang, C. S., Dunfield, P. F. & Semrau, J. D. 2019. The origin of aerobic methanotrophy within the Proteobacteria. *FEMS microbiology letters,* 366**,** fnz096.

Kannenberg, E. L. & Poralla, K. 1999. Hopanoid biosynthesis and function in bacteria. *Naturwissenschaften,* 86**,** 168-176.

Kaserer, H. 1905. Über die Oxidation des Wasserstoffes und des Methans durch Mikroorganismen. *Z. landw. Versuchsw. in Österreich,* 8**,** 789-792.

Kelly, T. J., Baird, A. J., Roucoux, K. H., Baker, T. R., Honorio Coronado, E. N., Ríos, M. & Lawson, I. T. 2014. The high hydraulic conductivity of three wooded tropical peat swamps in northeast Peru: measurements and implications for hydrological function. *Hydrological processes,* 28**,** 3373-3387.

Kelly, T. J., Lawson, I. T., Roucoux, K. H., Baker, T. R., Honorio-Coronado, E. N., Jones, T. D. & Rivas Panduro, S. 2018. Continuous human presence without extensive reductions in forest cover over the past 2500 years in an aseasonal Amazonian rainforest. *Journal of Quaternary Science,* 33**,** 369-379.

Kelly, T. J., Lawson, I. T., Roucoux, K. H., Baker, T. R., Jones, T. D. & Sanderson, N. K. 2017. The vegetation history of an Amazonian domed peatland. *Palaeogeography, Palaeoclimatology, Palaeoecology,* 468**,** 129-141.

Khanshan, F. S. & West, R. H. 2016. Developing detailed kinetic models of syngas production from bio-oil gasification using Reaction Mechanism Generator (RMG). *Fuel,* 163**,** 25-33.

Kim, S. J. 2019. Purification of 2, 6-dimethylnaphthalene containing in light cycle oil by distillation-solvent extraction-solute crystallization combination. *Journal of Industrial and Engineering Chemistry,* 79**,** 146-153.

Kimble, B., Maxwell, J., Philp, R., Eglinton, G., Albrecht, P., Ensminger, A., Arpino, P. & Ourisson, G. 1974. Tri-and tetraterpenoid hydrocarbons in the Messel oil shale. *Geochimica et Cosmochimica Acta,* 38**,** 1165-1181.

Kimura, K., Shiraishi, K., Kondo, T., Nakamura, J. & Fujitani, T. 2020. Cracking of squalene into isoprene as chemical utilization of algae oil. *Green Chemistry,* 22**,** 3083-3087.

Kip, N., Fritz, C., Langelaan, E., Pan, Y., Bodrossy, L., Pancotto, V., Jetten, M., Smolders, A. & Op Den Camp, H. 2012. Methanotrophic activity and diversity in different Sphagnum magellanicum dominated habitats in the southernmost peat bogs of Patagonia. *Biogeosciences,* 9**,** 47-55.

Kip, N., Van Winden, J. F., Pan, Y., Bodrossy, L., Reichart, G.-J., Smolders, A. J. P., Jetten, M. S. M., Damsté, J. S. S. & Op Den Camp, H. J. M. 2010. Global prevalence of methane oxidation by symbiotic bacteria in peat-moss ecosystems. *Nature Geoscience,* 3**,** 617-621.

Kirschke, S., Bousquet, P., Ciais, P., Saunois, M., Canadell, J. G., Dlugokencky, E. J., Bergamaschi, P., Bergmann, D., Blake, D. R. & Bruhwiler, L. 2013. Three decades of global methane sources and sinks. *Nature geoscience,* 6**,** 813-823.

Klesment, I. 1980. Investigation of aliphatic structures of oil shales by pyrolysis and chromatographic methods. *Journal of Analytical and Applied Pyrolysis,* 2**,** 63-77.

Knief, C. 2015. Diversity and habitat preferences of cultivated and uncultivated aerobic methanotrophic bacteria evaluated based on pmoA as molecular marker. *Frontiers in microbiology,* 6**,** 1346.

Knief, C., Lipski, A. & Dunfield, P. F. 2003. Diversity and activity of methanotrophic bacteria in different upland soils. *Applied and Environmental Microbiology,* 69**,** 6703-6714.

Kortschak, H. P., Hartt, C. E. & Burr, G. O. 1965. Carbon dioxide fixation in sugarcane leaves. *Plant physiology,* 40**,** 209.

Köster, J., Rospondek, M., Schouten, S., Kotarba, M., Zubrzycki, A. & Damsté, J. S. 1998. Biomarker geochemistry of a foreland basin: the Oligocene Menilite Formation in the Flysch Carpathians of Southeast Poland. *Organic Geochemistry,* 29**,** 649-669.

Krull, E., Bray, S., Harms, B., Baxter, N., Bol, R. & Farquhar, G. 2007. Development of a stable isotope index to assess decadal-scale vegetation change and application to woodlands of the Burdekin catchment, Australia. *Global Change Biology,* 13**,** 1455-1468.

Kunst, L. & Samuels, A. L. 2003. Biosynthesis and secretion of plant cuticular wax. *Progress in lipid research,* 42**,** 51-80.

Lab, T. S. 2024. Available at: https://summons.mit.edu/biomarkers/biomarker-classification/lipids/isoprenoids/polycyclic-isoprenoids-with-concatenated-ring-system/hopanoids/ (Last accessed: 10/01/2024).

Lähteenoja, O., Reátegui, Y. R., Räsänen, M., Torres, D. D. C., Oinonen, M. & Page, S. 2012. The large A mazonian peatland carbon sink in the subsiding P astaza-M arañón foreland basin, P eru. *Global Change Biology,* 18**,** 164-178.

Lähteenoja, O., Ruokolainen, K., Schulman, L. & Alvarez, J. 2009a. Amazonian floodplains harbour minerotrophic and ombrotrophic peatlands. *Catena,* 79**,** 140-145.

Lähteenoja, O., Ruokolainen, K., Schulman, L. & Oinonen, M. 2009b. Amazonian peatlands: an ignored C sink and potential source. *Global Change Biology,* 15**,** 2311-2320.

Lan, X., Thoning, K. & Dlugokencky, E. 2022. Trends in globally-averaged CH4, N2O, and SF6 determined from NOAA Global Monitoring Laboratory measurements. Version.

Lan, X., Thoning, K. W. & Dlugokencky, E. J. 2024. Trends in globally-averaged CH4, N2O, and SF6 determined from NOAA Global Monitoring Laboratory measurements; Available at: https://gml.noaa.gov/ccgg/trends_ch4/ (Last accessed: 10/01/2024).

Lattaud, J., De Jonge, C., Pearson, A., Elling, F. J. & Eglinton, T. I. 2021. Microbial lipid signatures in Arctic deltaic sediments–Insights into methane cycling and climate variability. *Organic Geochemistry,* 157**,** 104242.

Lawson, I. T., Jones, T. D., Kelly, T. J., Coronado, E. N. H. & Roucoux, K. H. 2014. The geochemistry of Amazonian peats. *Wetlands,* 34**,** 905-915.

Lawson, I. T., Kelly, T., Aplin, P., Boom, A., Dargie, G., Draper, F., Hassan, P., Hoyos-Santillan, J., Kaduk, J. & Large, D. 2015. Improving estimates of tropical peatland area, carbon storage, and greenhouse gas fluxes. *Wetlands ecology and management,* 23**,** 327-346.

Lawton, T. J. & Rosenzweig, A. C. 2016. Methane—make it or break it. *Science,* 352**,** 892-893.

Lee, T.-C. 2021. *Application of Reaction Mechanism Generator (RMG) for Modeling Heterogeneous Ammonia Oxidation.* Northeastern University.

Lelieveld, J., Crutzen, P. & Brühl, C. 1993. Climate effects of atmospheric methane. *Chemosphere,* 26**,** 739-768.

Lelieveld, J., Crutzen, P. J. & Dentener, F. J. 1998. Changing concentration, lifetime and climate forcing of atmospheric methane. *Tellus B,* 50**,** 128-150.

Li, J., Xue, J., Naafs, B. D. A., Yang, Y., Yang, H. & Liu, D. 2022a. Distribution and carbon isotopic composition of diploptene from epiphytic bryophytes in Wuhan, central China. *Organic Geochemistry,* 173**,** 104506.

Li, L., Zhang, Z., Greenwood, P. F. & Liu, Y. 2023. Biodegradation of occluded hydrocarbons and kerogen macromolecules of the Permian Lucaogou shales, Junggar Basin, NW China. *Energy Geoscience,* 4**,** 179-184.

Li, Y., Wang, J., Li, L., Song, W., Li, M., Hua, X., Wang, Y., Yuan, J. & Xue, Z. 2022b. Natural products of pentacyclic triterpenoids: from discovery to heterologous biosynthesis. *Natural Product Reports*.

Li, Y., Zhang, L., Xiong, Y., Gao, S., Yu, Z. & Peng, P. A. 2018. Determination of position-specific carbon isotope ratios of propane from natural gas. *Organic Geochemistry,* 119**,** 11-21.

Lichtfouse, E. 2000. Compound-specific isotope analysis. Application to archaelogy, biomedical sciences, biosynthesis, environment, extraterrestrial chemistry, food science, forensic science, humic substances, microbiology, organic geochemistry, soil science and sport. *Rapid Communications in Mass Spectrometry,* 14**,** 1337-1344.

Liu, M., Grinberg Dana, A., Johnson, M. S., Goldman, M. J., Jocher, A., Payne, A. M., Grambow, C. A., Han, K., Yee, N. W. & Mazeau, E. J. 2021. Reaction mechanism generator v3. 0: advances in automatic mechanism generation. *Journal of Chemical Information and Modeling,* 61**,** 2686-2696.

Lopes, A. A., Pereira, V. B., Amora-Nogueira, L., Marotta, H., Moreira, L. S., Cordeiro, R. C., Vanini, G. & Azevedo, D. A. 2021. Hydrocarbon sedimentary organic matter composition from different water-type floodplain lakes in the Brazilian Amazon. *Organic Geochemistry,* 159**,** 104287.

Madison, J. & Roberts, R. 1958. Pyrolysis of aromatics and related heterocyclics. *Industrial & Engineering Chemistry,* 50**,** 237-250.

Magoon, G., Green, W., Oluwole, O., Wong, H.-W., Albo, S. & Lewis, D. Updating Our Understanding of JP-10 Decomposition Chemistry: A Detailed JP-10 Combustion Mechanism Constructed Using RMG, an Automatic Reaction Mechanism Generator. 46th AIAA/ASME/SAE/ASEE Joint Propulsion Conference & Exhibit, 2010. 6825.

Marengo, J. 1998. Climatología de la zona de Iquitos, Perú. *Geoecologia y desarrollo Amazonico: estudio integrado en la zona de Iquitos, Peru,* 35**,** 57.

Martin, A. & Synge, R. 1941a. Separation of the higher monoamino-acids by counter-current liquid-liquid extraction: the amino-acid composition of wool. *Biochemical Journal,* 35**,** 91-121.

Martin, A. J. & Synge, R. L. 1941b. A new form of chromatogram employing two liquid phases: A theory of chromatography. 2. Application to the micro-determination of the higher monoamino-acids in proteins. *Biochemical Journal,* 35**,** 1358-1368.

Martin, G., Benbernou, M. & Lantier, F. 1985. APPLICATION OF SITE-SPECIFIC NATURAL ISOTOPE FRACTIONATION (SNIF-NMR) OF HYDROGEN TO THE CHARACTERIZATION OF EUROPEAN BEERS. *Journal of the Institute of Brewing,* 91**,** 242-249.

Martin, M., Zhang, B. & Martin, G. J. 2008. SNIF-NMR—Part 2: Isotope Ratios as Tracers of Chemical and Biochemical Mechanistic Pathways. *Modern Magnetic Resonance.* Springer.

Material-Properties 2024. Quartz – Density – Heat Capacity – Thermal Conductivity, Accessible at: https://material-properties.org/quartz-density-heat-capacity-thermal-conductivity/ (Last accessed: 10/01/2024).

Matsen, J. B., Yang, S., Stein, L. Y., Beck, D. & Kalyuzhnaya, M. G. 2013. Global molecular analyses of methane metabolism in methanotrophic alphaproteobacterium, Methylosinus trichosporium OB3b. Part I: transcriptomic study. *Frontiers in microbiology,* 4**,** 40.

Matthews, D. & Hayes, J. 1978. Isotope-ratio-monitoring gas chromatography-mass spectrometry. *Analytical Chemistry,* 50**,** 1465-1473.

Mccann, S., Rana, H., Handzo, B. & Snow, N. 2020. Go With the Flow: Thinking About Carrier Gas Flow in GC. *LCGC North America,* 38.

Meier-Augenstein, W. 2004. GC and IRMS technology for 13C and 15N analysis on organic compounds and related gases. *Handbook of stable isotope analytical techniques.* Elsevier.

Meinschein, W., Rinaldi, G., Hayes, J. & Schoeller, D. 1974. Intramolecular isotopic order in biologically produced acetic acid. *Biomedical Mass Spectrometry,* 1**,** 172-174.

Melander, L., Melander, L. G. & Saunders, W. H. 1980. *Reaction rates of isotopic molecules*, John Wiley & Sons.

Melton, J., Wania, R., Hodson, E., Poulter, B., Ringeval, B., Spahni, R., Bohn, T., Avis, C., Beerling, D. & Chen, G. 2013. Present state of global wetland extent and wetland

methane modelling: conclusions from a model inter-comparison project (WETCHIMP). *Biogeosciences,* 10**,** 753-788.

Melton, J. R., Chan, E., Millard, K., Fortier, M., Winton, R. S., Martín-López, J. M., Cadillo-Quiroz, H., Kidd, D. & Verchot, L. V. 2022. A map of global peatland extent created using machine learning (Peat-ML). *Geoscientific Model Development,* 15**,** 4709-4738.

Ménot, G. & Bard, E. 2010. Geochemical evidence for a large methane release during the last deglaciation from Marmara Sea sediments. *Geochimica et cosmochimica acta,* 74**,** 1537-1550.

Mitsch, W. J. & Gosselink, J. G. 2015. *Wetlands*, John Wiley & Sons.

Mkhize, N., Danon, B., Van Der Gryp, P. & Görgens, J. 2019. Kinetic study of the effect of the heating rate on the waste tyre pyrolysis to maximise limonene production. *Chemical Engineering Research and Design,* 152**,** 363-371.

Moldoveanu, S. 2010. Pyrolysis of hydrocarbons. *Techniques and Instrumentation in Analytical Chemistry,* 28**,** 131-229.

Moldoveanu, S. C. 2019a. General Information About Pyrolysis. *Pyrolysis of Organic Molecules.*

Moldoveanu, S. C. 2019b. Pyrolysis of Hydrocarbons. *Pyrolysis of Organic Molecules.*

Monson, K. & Hayes, J. 1982. Biosynthetic control of the natural abundance of carbon 13 at specific positions within fatty acids in Saccharomyces cerevisiae. Isotopic fractionation in lipid synthesis as evidence for peroxisomal regulation. *Journal of Biological Chemistry,* 257**,** 5568-5575.

Monson, K. D. & Hayes, J. 1980. Biosynthetic control of the natural abundance of carbon 13 at specific positions within fatty acids in Escherichia coli. Evidence regarding the coupling of fatty acid and phospholipid synthesis. *Journal of Biological Chemistry,* 255**,** 11435-11441.

Morales, S., Miranda, R., Bustos, D., Cazares, T. & Tran, H. 2014. Solar biomass pyrolysis for the production of bio-fuels and chemical commodities. *Journal of Analytical and Applied Pyrolysis,* 109**,** 65-78.

Murphy, W. A. 2020. *Methane fluxes from Amazonian tropical peatlands.* University of Leicester.

Murrell, J. 2010. The aerobic methane oxidizing bacteria (methanotrophs). *Handbook of hydrocarbon and lipid microbiology.*

Murrell, J. C., Gilbert, B. & Mcdonald, I. R. 2000. Molecular biology and regulation of methane monooxygenase. *Archives of microbiology,* 173**,** 325-332.

Murrell, J. C. & Smith, T. J. 2010. Biochemistry and Molecular Biology of Methane Monooxygenase. *Handbook of Hydrocarbon and Lipid Microbiology***,** 1045-1055.

Mycke, B. & Michaelis, W. 1986. Molecular fossils from chemical degradation of macromolecular organic matter. *Organic Geochemistry,* 10**,** 847-858.

Naeher, S., Niemann, H., Peterse, F., Smittenberg, R. H., Zigah, P. K. & Schubert, C. J. 2014. Tracing the methane cycle with lipid biomarkers in Lake Rotsee (Switzerland). *Organic geochemistry,* 66**,** 174-181.

Naloka, K. 2024. Available at: https://www.shutterstock.com/image-vector/cell-wall-structure-gramnegative-bacteria-1164058252?consentChanged=true (Last accessed: 10/01/2024)

Naraoka, H., Shimoyama, A., Komiya, M., Yamamoto, H. & Harada, K. 1988. Hydrocarbons in the Yamato-791198 carbonaceous chondrite from Antarctica. *Chemistry Letters,* 17**,** 831-834.

Naraoka, H., Yamada, K. & Ishiwatari, R. 2000. Recent sedimentary hopanoids in the northwestern Pacific alongside the Japanese Islands—their concentrations and carbon isotopic compositions. *Organic geochemistry,* 31**,** 1023-1029.

Nazaries, L., Murrell, J. C., Millard, P., Baggs, L. & Singh, B. K. 2013. Methane, microbes and models: fundamental understanding of the soil methane cycle for future predictions. *Environmental microbiology,* 15**,** 2395-2417.

Nguyen, T. B., Tyndall, G. S., Crounse, J. D., Teng, A. P., Bates, K. H., Schwantes, R. H., Coggon, M. M., Zhang, L., Feiner, P. & Milller, D. O. 2016. Atmospheric fates of Criegee intermediates in the ozonolysis of isoprene. *Physical Chemistry Chemical Physics,* 18**,** 10241-10254.

Nichols, J. E., Booth, R. K., Jackson, S. T., Pendall, E. G. & Huang, Y. 2006. Paleohydrologic reconstruction based on n-alkane distributions in ombrotrophic peat. *Organic Geochemistry,* 37**,** 1505-1513.

Nichols, P. D., Glen A, S., Antworth, C. P., Hanson, R. S. & White, D. C. 1985. Phospholipid and lipopolysaccharide normal and hydroxy fatty acids as potential signatures for methane-oxidizing bacteria. *FEMS Microbiology Ecology,* 1**,** 327-335.

Nier, A. O. 1947. A mass spectrometer for isotope and gas analysis. *Review of Scientific Instruments,* 18**,** 398-411.

Nimmanwudipong, T., Gilbert, A., Yamada, K. & Yoshida, N. 2015. Analytical method for simultaneous determination of bulk and intramolecular (13) C-isotope compositions of acetic acid. *Rapid Commun Mass Spectrom,* 29**,** 2337-40.

Nisbet, E. G., Dlugokencky, E. J. & Bousquet, P. 2014. Methane on the rise—again. *Science,* 343**,** 493-495.

Noaa 2024. The Data: What 13C Tells Us, Accessible at: https://gml.noaa.gov/ccgg/isotopes/c13tellsus.html (Last accessed: 10/01/2024).

Norris, C. E., Dungait, J. A., Joynes, A. & Quideau, S. A. 2013. Biomarkers of novel ecosystem development in boreal forest soils. *Organic geochemistry,* 64**,** 9-18.

O'leary, M. H. 1981. Carbon isotope fractionation in plants. *Phytochemistry,* 20**,** 553-567.

Oba, Y. & Naraoka, H. 2006. Site-specific carbon isotope analysis of aromatic carboxylic acids by elemental analysis/pyrolysis/isotope ratio mass spectrometry. *Rapid Communications in Mass Spectrometry: An International Journal Devoted to the Rapid Dissemination of Up-to-the-Minute Research in Mass Spectrometry,* 20**,** 3649-3653.

Op Den Camp, H. J., Islam, T., Stott, M. B., Harhangi, H. R., Hynes, A., Schouten, S., Jetten, M. S., Birkeland, N. K., Pol, A. & Dunfield, P. F. 2009. Environmental, genomic and taxonomic perspectives on methanotrophic Verrucomicrobia. *Environmental Microbiology Reports,* 1**,** 293-306.

Oro, J., Han, J. & Zlatkis, A. 1967. Application of high-resolution gas chromatography-mass spectrometry to the analysis of the pyrolysis products of isoprene. *Analytical Chemistry,* 39**,** 27-32.

Ourisson, G. & Albrecht, P. 1992. Hopanoids. 1. Geohopanoids: the most abundant natural products on Earth? *Accounts of Chemical Research,* 25**,** 398-402.

Ourisson, G., Albrecht, P. & Rohmer, M. 1979. The hopanoids: palaeochemistry and biochemistry of a group of natural products. *Pure and Applied Chemistry,* 51**,** 709-729.

Ourisson, G. & Rohmer, M. 1992. Hopanoids. 2. Biohopanoids: a novel class of bacterial lipids. *Accounts of Chemical Research,* 25**,** 403-408.

Page, S., Rieley, J. & Wüst, R. 2006. Lowland tropical peatlands of Southeast Asia. *Developments in earth surface processes,* 9**,** 145-172.

Pale-Grosdemange, C., Feil, C., Rohmer, M. & Poralla, K. 1998. Occurrence of cationic intermediates and deficient control during the enzymatic cyclization of squalene to hopanoids. *Angewandte Chemie International Edition,* 37**,** 2237-2240.

Pancost, R. D. & Damsté, J. S. S. 2003. Carbon isotopic compositions of prokaryotic lipids as tracers of carbon cycling in diverse settings. *Chemical Geology,* 195**,** 29-58.

Pancost, R. D., Sinninghe Damsté, J. S., De Lint, S., Van Der Maarel, M. J., Gottschal, J. C. & Party‡, M. S. S. 2000. Biomarker evidence for widespread anaerobic methane oxidation in Mediterranean sediments by a consortium of methanogenic archaea and bacteria. *Applied and Environmental Microbiology,* 66**,** 1126-1132.

Pandey, V. C., Singh, J., Singh, D. & Singh, R. P. 2014a. Methanotrophs: promising bacteria for environmental remediation. *International Journal of Environmental Science and Technology,* 11**,** 241-250.

Pandey, V. C., Singh, J., Singh, D. & Singh, R. P. 2014b. Methanotrophs: promising bacteria for environmental remediation. *International Journal of Environmental Science and Technology,* 11**,** 241-250.

Pandis, S. N., Paulson, S. E., Seinfeld, J. H. & Flagan, R. C. 1991. Aerosol formation in the photooxidation of isoprene and β-pinene. *Atmospheric Environment. Part A. General Topics,* 25**,** 997-1008.

Park, R. & Epstein, S. 1960. Carbon isotope fractionation during photosynthesis. *Geochim. et cosmochim. acta,* 21.

Park, R. & Epstein, S. 1961. Metabolic fractionation of C13 & C12 in plants. *Plant physiology,* 36**,** 133.

Party, T. M. S. S., Pancost, R., Hopmans, E. & Damsté, J. S. 2001. Archaeal lipids in Mediterranean cold seeps: molecular proxies for anaerobic methane oxidation. *Geochimica et Cosmochimica Acta,* 65**,** 1611-1627.

Paulson, S. E., Flagan, R. C. & Seinfeld, J. H. 1992. Atmospheric photooxidation of isoprene part II: The ozone-isoprene reaction. *International Journal of Chemical Kinetics,* 24**,** 103-125.

Pereira, V. B., Lopes, A. A., Dal Sasso, M. A., Amora-Nogueira, L., Fonseca, T., Marotta, H., Cordeiro, R. C. & Azevedo, D. A. 2022. Geochemistry of organic matter by multi-proxy analyses and temperature sensitivity of methanogenesis in clearwater Amazonian lake sediments. *Applied Geochemistry,* 146**,** 105467.

Pering, K. L. & Ponnamperuma, C. 1971. Aromatic hydrocarbons in the Murchison meteorite. *Science,* 173**,** 237-239.

Peters, K. E., Peters, K. E., Walters, C. C. & Moldowan, J. 2005. *The biomarker guide*, Cambridge university press.

Petit, J. R., Jouzel, J., Raynaud, D., Barkov, N. I., Barnola, J. M., Basile, I., Bender, M., Chappellaz, J., Davis, M., Delaygue, G., Delmotte, M., Kotlyakov, V. M., Legrand,

M., Lipenkov, V. Y., Lorius, C., Pépin, L., Ritz, C., Saltzman, E. & Stievenard, M. 1999. Climate and atmospheric history of the past 420,000 years from the Vostok ice core, Antarctica. *Nature,* 399**,** 429-436.

Petrišič, M. G., Heath, E. & Ogrinc, N. 2017. Lipid biomarkers and their stable carbon isotopes in oxic and anoxic sediments of lake bled (NW Slovenia). *Geomicrobiology Journal,* 34**,** 606-617.

Phillips, O. L., Van Der Heijden, G., Lewis, S. L., López-González, G., Aragão, L. E. O. C., Lloyd, J., Malhi, Y., Monteagudo, A., Almeida, S., Dávila, E. A., Amaral, I., Andelman, S., Andrade, A., Arroyo, L., Aymard, G., Baker, T. R., Blanc, L., Bonal, D., De Oliveira, Á. C. A., Chao, K.-J., Cardozo, N. D., Da Costa, L., Feldpausch, T. R., Fisher, J. B., Fyllas, N. M., Freitas, M. A., Galbraith, D., Gloor, E., Higuchi, N., Honorio, E., Jiménez, E., Keeling, H., Killeen, T. J., Lovett, J. C., Meir, P., Mendoza, C., Morel, A., Vargas, P. N., Patiño, S., Peh, K. S. H., Cruz, A. P., Prieto, A., Quesada, C. A., Ramírez, F., Ramírez, H., Rudas, A., Salamão, R., Schwarz, M., Silva, J., Silveira, M., Ferry Slik, J. W., Sonké, B., Thomas, A. S., Stropp, J., Taplin, J. R. D., Vásquez, R. & Vilanova, E. 2010. Drought–mortality relationships for tropical forests. *New Phytologist,* 187**,** 631-646.

Picarro, I. 2016. d13C in CH4 and CO2 Gas Analyzer. Accessible at: https://www.picarro.com/sites/default/files/product_documents/Picarro_%20G2201-i%20Analyzer%20Datasheet_053017.pdf (Last accessed: 10/01/2024).

Picarro, I. 2024. Cavity Ring-Down Spectroscopy (CRDS). Accessible at: https://www.picarro.com/company/technology/crds (Last accessed: 10/01/2024).

Preston, T. & Owens, N. J. 1983. Interfacing an automatic elemental analyser with an isotope ratio mass sepectrometer: the potential for fully automated total nitrogen and nitrogen-15 analysis. *Analyst,* 108**,** 971-977.

Price, K. E., Armstrong, C. M., Imlay, L. S., Hodge, D. M., Pidathala, C., Roberts, N. J., Park, J., Mikati, M., Sharma, R. & Lawrenson, A. S. 2016. Molecular mechanism of action of antimalarial benzoisothiazolones: species-selective inhibitors of the Plasmodium spp. MEP pathway enzyme, IspD. *Scientific reports,* 6**,** 1-12.

Quintana-Cobo, I., Moreira-Turcq, P., Cordeiro, R. C., Aniceto, K., Crave, A., Fraizy, P., Moreira, L. S., Contrera, J. M. D. a. D. & Turcq, B. 2018. Dynamics of floodplain lakes in the Upper Amazon Basin during the late Holocene. *Comptes Rendus Geoscience,* 350**,** 55-64.

Raghoebarsing, A. A., Smolders, A. J., Schmid, M. C., Rijpstra, W. I. C., Wolters-Arts, M., Derksen, J., Jetten, M. S., Schouten, S., Sinninghe Damsté, J. S. & Lamers, L. P. 2005. Methanotrophic symbionts provide carbon for photosynthesis in peat bogs. *Nature,* 436**,** 1153-1156.

Reid, L. M., O'donnell, C. P. & Downey, G. 2006. Recent technological advances for the determination of food authenticity. *Trends in Food Science & Technology,* 17**,** 344-353.

Rieley, G. 1994. Derivatization of organic compounds prior to gas chromatographic–combustion–isotope ratio mass spectrometric analysis: identification of isotope fractionation processes. *Analyst,* 119**,** 915-919.

Rieley, G., Collier, R. J., Jones, D. M., Eglinton, G., Eakin, P. A. & Fallick, A. E. 1991. Sources of sedimentary lipids deduced from stable carbon-isotope analyses of individual compounds. *Nature,* 352**,** 425-427.

Rinaldi, G., Meinschein, W. & Hayes, J. 1974a. Carbon isotopic fractionations associated with acetic acid production by Acetobacter suboxydans. *Biomedical mass spectrometry,* 1**,** 412-414.

Rinaldi, G., Meinschein, W. & Hayes, J. 1974b. Intramolecular carbon isotopic distribution in biologically produced acetoin. *Biomedical mass spectrometry,* 1**,** 415-417.

Riva, M., Budisulistiorini, S. H., Zhang, Z., Gold, A. & Surratt, J. D. 2016. Chemical characterization of secondary organic aerosol constituents from isoprene ozonolysis in the presence of acidic aerosol. *Atmospheric Environment,* 130**,** 5-13.

Roeske, C. & O'leary, M. H. 1984. Carbon isotope effects on enzyme-catalyzed carboxylation of ribulose bisphosphate. *Biochemistry,* 23**,** 6275-6284.

Rohmer, M. 1999. A mevalonate-independent route to isopentenyl diphosphate. *Comprehensive natural product chemistry,* 2**,** 45-67.

Rohmer, M. 2008. From molecular fossils of bacterial hopanoids to the formation of isoprene units: discovery and elucidation of the methylerythritol phosphate pathway. *Lipids,* 43**,** 1095-1107.

Rohmer, M., Bisseret, P. & Neunlist, S. 1992. The hopanoids, prokaryotic triterpenoids and precursors of ubiquitous molecular fossils. *Biological markers in sediments and petroleum,* 54**,** 1-17.

Rohmer, M., Bouvier-Nave, P. & Ourisson, G. 1984. Distribution of hopanoid triterpenes in prokaryotes. *Microbiology,* 130**,** 1137-1150.

Rohmer, M., Knani, M., Simonin, P., Sutter, B. & Sahm, H. 1993. Isoprenoid biosynthesis in bacteria: a novel pathway for the early steps leading to isopentenyl diphosphate. *Biochemical Journal,* 295**,** 517-524.

Rosenfeld, W. D. & Silverman, S. R. 1959. Carbon isotope fractionation in bacterial production of methane. *Science,* 130**,** 1658-1659.

Rossmann, A., Butzenlechner, M. & Schmidt, H.-L. 1991. Evidence for a nonstatistical carbon isotope distribution in natural glucose. *Plant Physiology,* 96**,** 609-614.

Roucoux, K. H., Lawson, I. T., Jones, T. D., Baker, T. R., Coronado, E. H., Gosling, W. D. & Lähteenoja, O. 2013. Vegetation development in an Amazonian peatland. *Palaeogeography, Palaeoclimatology, Palaeoecology,* 374**,** 242-255.

Rubinstein, I., Spyckerelle, C. & Strausz, O. 1979. Pyrolysis of asphaltenes: a source of geochemical information. *Geochimica et Cosmochimica Acta,* 43**,** 1-6.

Ruddiman, W. F. & Thomson, J. S. 2001. The case for human causes of increased atmospheric CH4 over the last 5000 years. *Quaternary Science Reviews,* 20**,** 1769-1777.

Ruiz, N., Kahne, D. & Silhavy, T. J. 2006. Advances in understanding bacterial outer-membrane biogenesis. *Nature Reviews Microbiology,* 4**,** 57-66.

Sacks, G. L. & Brenna, J. T. 2003. High-Precision Position-Specific Isotope Analysis of 13C/12C in Leucine and Methionine Analogues. *Analytical Chemistry,* 75**,** 5495-5503.

Saini, J., Günther, F., Aichner, B., Mischke, S., Herzschuh, U., Zhang, C., Mäusbacher, R. & Gleixner, G. 2017. Climate variability in the past~ 19,000 yr in NE Tibetan Plateau inferred from biomarker and stable isotope records of Lake Donggi Cona. *Quaternary Science Reviews,* 157**,** 129-140.

Sakata, S., Hayes, J. M., Mctaggart, A. R., Evans, R. A., Leckrone, K. J. & Togasaki, R. K. 1997. Carbon isotopic fractionation associated with lipid biosynthesis by a cyanobacterium: relevance for interpretation of biomarker records. *Geochimica et Cosmochimica Acta,* 61**,** 5379-5389.

Sanderson, R. 1975. Interrelation of bond dissociation energies and contributing bond energies. *Journal of the American Chemical Society,* 97**,** 1367-1372.

Sanez, J. P., Waterbury, J. B., Eglinton, T. I. & Summons, R. E. 2012. Hopanoids in marine cyanobacteria: probing their phylogenetic distribution and biological role. *Geobiology,* 10**,** 311-319.

Scanlan, J., Guillonneau, R., Cunningham, M. R., Najmin, S., Mausz, M. A., Murphy, A., Murray, L. L., Zhang, L., Kumaresan, D. & Chen, Y. 2022. The Proteobacterial Methanotroph Methylosinus trichosporium OB3b Remodels Membrane Lipids in Response to Phosphate Limitation. *mBio,* 13**,** e00247-22.

Schaechter 2014. Small Things Considered, Accessible at: https://schaechter.asmblog.org/schaechter/2014/09/bacterial-hopanoids-the-lipids-that-last-forever.html (Last accessed: 18/01/2024).

Schimmelmann, A. 2024. Schimmelmann Laboratory, Indiana University Bloomington. Accessible at: https://hcnisotopes.earth.indiana.edu/index.html (Last accessed: 10/01/2024).

Schouten, S., Hopmans, E. C. & Damsté, J. S. S. 2013. The organic geochemistry of glycerol dialkyl glycerol tetraether lipids: A review. *Organic geochemistry,* 54**,** 19-61.

Schouten, S., Rijpstra, W., Kok, M., Hopmans, E., Summons, R., Volkman, J. & Damsté, J. S. 2001. Molecular organic tracers of biogeochemical processes in a saline meromictic lake (Ace Lake). *Geochimica et Cosmochimica Acta,* 65**,** 1629-1640.

Schroll, M., Keppler, F., Greule, M., Eckhardt, C., Zorn, H. & Lenhart, K. 2020. The stable carbon isotope signature of methane produced by saprotrophic fungi. *Biogeosciences,* 17**,** 3891-3901.

Schwietzke, S., Sherwood, O. A., Bruhwiler, L. M., Miller, J. B., Etiope, G., Dlugokencky, E. J., Michel, S. E., Arling, V. A., Vaughn, B. H. & White, J. W. 2016. Upward revision of global fossil fuel methane emissions based on isotope database. *Nature,* 538**,** 88-91.

Segers, R. 1998. Methane production and methane consumption: a review of processes underlying wetland methane fluxes. *Biogeochemistry,* 41**,** 23-51.

Seifert, W. 1978. Steranes and terpanes in kerogen pyrolysis for correlation of oils and source rocks. *Geochimica et Cosmochimica Acta,* 42**,** 473-484.

Semrau, J. D., Dispirito, A. A. & Murrell, J. C. 2008. Life in the extreme: thermoacidophilic methanotrophy. *Trends in microbiology,* 16**,** 190-193.

Sessions, A. L., Jahnke, L. L., Schimmelmann, A. & Hayes, J. M. 2002. Hydrogen isotope fractionation in lipids of the methane-oxidizing bacterium Methylococcus capsulatus. *Geochimica et Cosmochimica Acta,* 66**,** 3955-3969.

Sessions, A. L., Zhang, L., Welander, P. V., Doughty, D., Summons, R. E. & Newman, D. K. 2013. Identification and quantification of polyfunctionalized hopanoids by high temperature gas chromatography–mass spectrometry. *Organic Geochemistry,* 56**,** 120-130.

Shukla, A. K., Vishwakarma, P., Upadhyay, S., Tripathi, A. K., Prasana, H. & Dubey, S. K. 2009. Biodegradation of trichloroethylene (TCE) by methanotrophic community. *Bioresource technology,* 100**,** 2469-2474.

Silverman, M. P. & Oyama, V. I. 1968. Automatic apparatus for sampling and preparing gases for mass spectral analysis in studies of carbon isotope fractionation during methane metabolism. *Analytical Chemistry,* 40**,** 1833-1837.

Sim & Gmbh, S. I. M. 2024. COOL-CUBE – Multi Cooling Device, Accessible at: https://sim-gmbh.de/images/PDF_Dokumente_neu/SIM_COOL-CUBE_ICE-DOOR_an16_e.pdf (Last accessed: 10/01/2024).

Sinninghe-Damsté, J. S., Rijpstra, W. I. C., Schouten, S., Fuerst, J. A., Jetten, M. S. & Strous, M. 2004. The occurrence of hopanoids in planctomycetes: implications for the sedimentary biomarker record. *Organic Geochemistry,* 35**,** 561-566.

Sinninghe Damsté, J. S., Rijpstra, W. I. C., Schouten, S., Fuerst, J. A., Jetten, M. S. M. & Strous, M. 2004. The occurrence of hopanoids in planctomycetes: implications for the sedimentary biomarker record. *Organic Geochemistry,* 35**,** 561-566.

Smemo, K. & Yavitt, J. 2011. Anaerobic oxidation of methane: an underappreciated aspect of methane cycling in peatland ecosystems? *Biogeosciences,* 8**,** 779-793.

Smith, T. & Dalton, H. 2004. Biocatalysis by methane monooxygenase and its implications for the petroleum industry. *Studies in surface science and catalysis,* 151**,** 177-192.

Smolková-Keulemansová, E. 2000. A few milestones on the journey of chromatography. *Journal of High Resolution Chromatography,* 23**,** 497-501.

Soosaar, K., Schindler, T., Machacova, K., Pärn, J., Fachín Malaverri, L., Rengifo Marín, J., Alegría Muñoz, W., Jibaja Aspajo, J. L., Negron-Juarez, R. & Zárate Gómez, R. 2022. High methane emission from palm stems and nitrous oxide emission from the soil in a peruvian Amazon peat swamp forest.

Soreng, R. J., Peterson, P. M., Romaschenko, K., Davidse, G., Zuloaga, F. O., Judziewicz, E. J., Filgueiras, T. S., Davis, J. I. & Morrone, O. 2015. A worldwide phylogenetic classification of the Poaceae (Gramineae). *Journal of Systematics and Evolution,* 53**,** 117-137.

Stillwell, W. 2016. *An introduction to biological membranes: composition, structure and function*, Elsevier.

Suda, K., Gilbert, A., Yamada, K., Yoshida, N. & Ueno, Y. 2017. Compound– and position–specific carbon isotopic signatures of abiogenic hydrocarbons from on–land serpentinite–hosted Hakuba Happo hot spring in Japan. *Geochimica et Cosmochimica Acta,* 206**,** 201-215.

Summons, R. E., Jahnke, L. L., Hope, J. M. & Logan, G. A. 1999. 2-Methylhopanoids as biomarkers for cyanobacterial oxygenic photosynthesis. *Nature,* 400**,** 554-557.

Summons, R. E., Jahnke, L. L. & Roksandic, Z. 1994. Carbon isotopic fractionation in lipids from methanotrophic bacteria: relevance for interpretation of the geochemical record of biomarkers. *Geochimica et Cosmochimica Acta,* 58**,** 2853-2863.

Swindles, G. T. 2018. The plight of Amazonia's oldest peatland. *Geology Today,* 34**,** 59-61.

Szwarc, M. 1950. The determination of bond dissociation energies by pyrolytic methods. *Chemical Reviews,* 47**,** 75-173.

Söhngen, N. L. 1906. Über Bacteria welche Methan als Kohlenstorfnahrung und Energie-quelle gebrauchen (On the bacteria which use methane as a carbon and energy source). *Zentr. Bact. Parazitenk.,,* 15**,** 513-517.

Tcherkez, G., Mahé, A. & Hodges, M. 2011. 12C/13C fractionations in plant primary metabolism. *Trends in plant science,* 16**,** 499-506.

Teh, Y. A., Murphy, W. A., Berrio, J.-C., Boom, A. & Page, S. E. 2017. Seasonal variability in methane and nitrous oxide fluxes from tropical peatlands in the western Amazon basin. *Biogeosciences,* 14**,** 3669-3683.

Thermtest 2021. Thermal Conductivity of Steel. Accessible at: https://thermtest.com/thermal-conductivity-of-steel#:~:text=The%20thermal%20conductivity%20of%20steel,235%20W%2F(mK)%20respectively. (Last accessed: 10/01/2024).

Thiel, V., Peckmann, J., Richnow, H. H., Luth, U., Reitner, J. & Michaelis, W. 2001. Molecular signals for anaerobic methane oxidation in Black Sea seep carbonates and a microbial mat. *Marine Chemistry,* 73**,** 97-112.

Thomas, C. L., Jansen, B., Van Loon, E. E. & Wiesenberg, G. L. 2021. Transformation of n-alkanes from plant to soil: a review. *Soil,* 7**,** 785-809.

Tipple, B. J. & Pagani, M. 2010. A 35Myr North American leaf-wax compound-specific carbon and hydrogen isotope record: Implications for C4 grasslands and hydrologic cycle dynamics. *Earth and Planetary Science Letters,* 299**,** 250-262.

Tiwari, M., Singh, A. K. & Sinha, D. K. 2015. Stable isotopes: Tools for understanding past climatic conditions and their applications in chemostratigraphy. *Chemostratigraphy.* Elsevier.

Treat, C. C., Jones, M. C., Brosius, L. S., Grosse, G., Walter Anthony, K. & Frolking, S. 2021. Methane emissions from high-latitude peatlands during the Holocene from a synthesis of peatland records. *EGU General Assembly 2021.*

Treibs, A. 1934. Chlorophyll-und Häminderivate in bituminösen Gesteinen, Erdölen, Erdwachsen und Asphalten. Ein Beitrag zur Entstehung des Erdöls. *Justus Liebigs Annalen der Chemie,* 510**,** 42-62.

Treibs, A. 1936. Chlorophyll-und Häminderivate in organischen Mineralstoffen. *Angewandte Chemie,* 49**,** 682-686.

Trotsenko, Y. A. & Murrell, J. C. 2008. Metabolic aspects of aerobic obligate methanotrophy⋆. *Advances in applied microbiology,* 63**,** 183-229.

Uemura, H. & Ishiwatari, R. 1995. Identification of unusual 17β (H)-moret-22 (29)-ene in lake sediments. *Organic Geochemistry,* 23**,** 675-680.

Urey, H. C. 1947. The thermodynamic properties of isotopic substances. *Journal of the Chemical Society (Resumed)***,** 562-581.

Urrego, L. E., Galeano, A., Pe, Xf, Uela, C., Xe, Nchez, M., Toro, E. & Xfa 2016. Climate-related phenology of Mauritia flexuosa in the Colombian Amazon. *Plant Ecology,* 217**,** 1207-1218.

Ushida, M., Shibata, Y., Ohkushi, K., Ahagon, N. & Hoshiba, M. 2004. Global climate change linkage with episodic methane release even in the western north Pacific in the last glacial period.

Valderrama, E. 2013. Floristics and above-ground biomass (AGB) in Peatlands in Peruvian Lowland Amazonia, Loreto–Peru.

Valley, J. W. & Cole, D. R. 2018. Stable isotope geochemistry.

Van Der Merwe, N. J. & Medina, E. 1991. The canopy effect, carbon isotope ratios and foodwebs in Amazonia. *Journal of archaeological science,* 18**,** 249-259.

Van Geem, K. M., Reyniers, M. F., Marin, G. B., Song, J., Green, W. H. & Matheu, D. M. 2006. Automatic reaction network generation using RMG for steam cracking of n-hexane. *AIChE Journal,* 52**,** 718-730.

Van Graas, G. 1986. Biomarker distributions in asphaltenes and kerogens analysed by flash pyrolysis-gas chromatography-mass spectrometry. *Organic Geochemistry,* 10**,** 1127-1135.

Van Haren, J., Brewer, P. E., Kurtzberg, L., Wehr, R. N., Springer, V. L., Espinoza, R. T., Ruiz, J. S. & Cadillo-Quiroz, H. 2021. A versatile gas flux chamber reveals high tree stem CH4 emissions in Amazonian peatland. *Agricultural and Forest Meteorology,* 307**,** 108504.

Van Haren, J. L. & Cadillo-Quiroz, H. Controls on tree species stem transport and emission of methane from tropical peatlands. AGU Fall Meeting Abstracts, 2016. B33E-0656.

Van Lent, J., Hergoualc'h, K., Verchot, L., Oenema, O. & Van Groenigen, J. W. 2019. Greenhouse gas emissions along a peat swamp forest degradation gradient in the Peruvian Amazon: soil moisture and palm roots effects. *Mitigation and Adaptation Strategies for Global Change,* 24**,** 625-643.

Van Winden, J. F., Talbot, H. M., De Vleeschouwer, F., Reichart, G.-J. & Damsté, J. S. S. 2012. Variation in methanotroph-related proxies in peat deposits from Misten Bog, Hautes-Fagnes, Belgium. *Organic Geochemistry,* 53**,** 73-79.

Voet, D. & Voet, J. G. 2021. *Biochemistry*, John Wiley & Sons.

Vogler, E. A. 1979. *THE BIOGEOCHEMISTRY OF THE STABLE CARBON ISOTOPES IN CARBOXYLIC ACIDS*, Indiana University.

Vogler, E. A. & Hayes, J. 1979. Carbon isotopic fractionation in the Schmidt decarboxylation: evidence for two pathways to products. *The Journal of Organic Chemistry,* 44**,** 3682-3686.

Volkman, J. K. 2005. Sterols and other triterpenoids: source specificity and evolution of biosynthetic pathways. *Organic geochemistry,* 36**,** 139-159.

Wakeham, S. G., Amann, R., Freeman, K. H., Hopmans, E. C., Jørgensen, B. B., Putnam, I. F., Schouten, S., Damsté, J. S. S., Talbot, H. M. & Woebken, D. 2007. Microbial ecology of the stratified water column of the Black Sea as revealed by a comprehensive biomarker study. *Organic Geochemistry,* 38**,** 2070-2097.

Wang, S., Zhuang, Q., Lähteenoja, O., Draper, F. C. & Cadillo-Quiroz, H. 2018. Potential shift from a carbon sink to a source in Amazonian peatlands under a changing climate. *Proceedings of the National Academy of Sciences,* 115**,** 12407-12412.

Ward, N., Larsen, Ø., Sakwa, J., Bruseth, L., Khouri, H., Durkin, A. S., Dimitrov, G., Jiang, L., Scanlan, D. & Kang, K. H. 2004. Genomic insights into methanotrophy: the complete genome sequence of Methylococcus capsulatus (Bath). *PLoS biology,* 2**,** e303.

Webb, A. J., Bösch, H., Parker, R. J., Gatti, L. V., Gloor, E., Palmer, P. I., Basso, L. S., Chipperfield, M. P., Correia, C. S. & Domingues, L. G. 2016. CH4 concentrations over the Amazon from GOSAT consistent with in situ vertical profile data. *Journal of Geophysical Research: Atmospheres,* 121**,** 11,006-11,020.

Weber, K. H. & Zhang, J. 2007. Mechanistic study of thermal decomposition of isoprene (2-methyl-1, 3-butadiene) using flash pyrolysis supersonic jet VUV photoionization mass spectrometry. *The Journal of Physical Chemistry A,* 111**,** 11487-11492.

Weilacher, T., Gleixner, G. & Schmidt, H.-L. 1996. Carbon isotope pattern in purine alkaloids a key to isotope discriminations in C1 compounds. *Phytochemistry,* 41**,** 1073-1077.

Wendt, K. U., Schulz, G. E., Corey, E. J. & Liu, D. R. 2000. Enzyme mechanisms for polycyclic triterpene formation. *Angewandte Chemie International Edition,* 39**,** 2812-2833.

Werne, J. P., Baas, M. & Sinninghe Damsté, J. 2002. Molecular isotopic tracing of carbon flow and trophic relationships in a methane-supported benthic microbial community. *Limnology and Oceanography,* 47**,** 1694-1701.

Werner, R. A. & Cormier, M.-A. 2022. Isotopes—Terminology, Definitions and Properties. *Stable Isotopes in Tree Rings: Inferring Physiological, Climatic and Environmental Responses.* Springer International Publishing Cham.

West, R. H., Allen, J. W. & Green, W. H. 2012. Automatic reaction mechanism generation with group additive kinetics. *ChemInform,* 43**,** no.

Whiticar, M. J., Faber, E. & Schoell, M. 1986. Biogenic methane formation in marine and freshwater environments: CO2 reduction vs. acetate fermentation—isotope evidence. *Geochimica et Cosmochimica Acta,* 50**,** 693-709.

Whiting, G. J. & Chanton, J. P. 1993. Primary production control of methane emission from wetlands. *Nature,* 364**,** 794-795.

Whittenbury, R., Phillips, K. C. & Wilkinson, J. F. 1970. Enrichment, isolation and some properties of methane-utilizing bacteria. *Microbiology,* 61**,** 205-218.

Wikiwand 2024. Kerogen, Accessible at: https://www.wikiwand.com/en/Kerogen (Last accessed: 10/01/2024)

William, I. G. & Dewar, R. A. 1958.

Williams, C. J. & Yavitt, J. B. 2010. Temperate wetland methanogenesis: the importance of vegetation type and root ethanol production. *Soil Science Society of America Journal,* 74**,** 317-325.

Winkler, A., Haumaier, L. & Zech, W. 2001. Variation in hopanoid composition and abundance in forest soils during litter decomposition and humification. *Organic geochemistry,* 32**,** 1375-1385.

Winton, R. S., Flanagan, N. & Richardson, C. J. 2017. Neotropical peatland methane emissions along a vegetation and biogeochemical gradient. *PLoS One,* 12**,** e0187019.

Wolyniak, C. J., Sacks, G. L., Metzger, S. K. & Brenna, J. T. 2006. Determination of Intramolecular δ13C from Incomplete Pyrolysis Fragments. Evaluation of Pyrolysis-Induced Isotopic Fractionation in Fragments from the Lactic Acid Analogue Propylene Glycol. *Analytical Chemistry,* 78**,** 2752-2757.

Wolyniak, C. J., Sacks, G. L., Pan, B. S. & Brenna, J. T. 2005. <Wolyniak et al., 2005 - Carbon PSIA exhibiting Nonideal Pyrolytic Fragmentation.pdf>.

Xie, S., Nott, C. J., Avsejs, L. A., Maddy, D., Chambers, F. M. & Evershed, R. P. 2004. Molecular and isotopic stratigraphy in an ombrotrophic mire for paleoclimate

reconstruction2 2Associate editor: R. Summons. *Geochimica et Cosmochimica Acta,* 68**,** 2849-2862.

Xiong, Y., Geng, A., Pan, C., Liu, D. & Peng, P. 2005. Characterization of the hydrogen isotopic composition of individual n-alkanes in terrestrial source rocks. *Applied geochemistry,* 20**,** 455-464.

Yamada, K. & Ishiwatari, R. 1999. Carbon isotopic compositions of long-chain n-alkanes in the Japan Sea sediments: implications for paleoenvironmental changes over the past 85 kyr. *Organic Geochemistry,* 30**,** 367-377.

Yamada, K., Ishiwatari, R., Matsumoto, K. & Naraoka, H. 1997. δ13C records of diploptene in the Japan Sea sediments over the past 25 kyr. *Geochemical Journal,* 31**,** 315-321.

Yamada, K., Tanaka, M., Nakagawa, F. & Yoshida, N. 2002. On-line measurement of intramolecular carbon isotope distribution of acetic acid by continuous-flow isotope ratio mass spectrometry. *Rapid Commun Mass Spectrom,* 16**,** 1059-64.

Yang, J. & Lu, M. 2005. Thermal growth and decomposition of methylnaphthalenes. *Environmental science & technology,* 39**,** 3077-3082.

Yang, S., Matsen, J. B., Konopka, M., Green-Saxena, A., Clubb, J., Sadilek, M., Orphan, V. J., Beck, D. & Kalyuzhnaya, M. G. 2013a. Global molecular analyses of methane metabolism in methanotrophic Alphaproteobacterium, Methylosinus trichosporium OB3b. Part II. Metabolomics and 13C-labeling study. *Frontiers in microbiology,* 4**,** 70.

Yang, S., Matsen, J. B., Konopka, M., Green-Saxena, A., Clubb, J., Sadilek, M., Orphan, V. J., Beck, D. & Kalyuzhnaya, M. G. 2013b. Global molecular analyses of methane metabolism in methanotrophic alphaproteobacterium, methylosinus trichosporium OB3b. Part II. metabolomics and 13C-labeling study. *Frontiers in Microbiology,* 4**,** 1-13.

Yankwich, P. E. & Promislow, A. L. 1953. Carbon isotope constitution of some acetic acids. *Journal of the American Chemical Society,* 75**,** 4881-4882.

Zenobi, R., Philippoz, J.-M., Zare, R. N. & Buseck, P. R. 1989. Spatially resolved organic analysis of the Allende meteorite. *Science,* 246**,** 1026-1029.

Zhang, C. L., Huang, Z., Li, Y.-L., Romanek, C. S., Mills, G. L., Gibson, R. A., Talbot, H. M., Wiegel, J., Noakes, J. & Culp, R. 2007. Lipid biomarkers, carbon isotopes, and phylogenetic characterization of bacteria in California and Nevada hot springs. *Geomicrobiology Journal,* 24**,** 519-534.

Zhang, G., Meredith, T. C. & Kahne, D. 2013. On the essentiality of lipopolysaccharide to Gram-negative bacteria. *Current opinion in microbiology,* 16**,** 779-785.

Zhang, T. & Krooss, B. M. 2001. Experimental investigation on the carbon isotope fractionation of methane during gas migration by diffusion through sedimentary rocks at elevated temperature and pressure. *Geochimica et Cosmochimica Acta,* 65**,** 2723-2742.

Zhao, H., Wu, L., Patrick, C., Zhang, Z., Rezgui, Y., Yang, X., Wysocki, G. & Ju, Y. 2018. Studies of low temperature oxidation of n-pentane with nitric oxide addition in a jet stirred reactor. *Combustion and Flame,* 197**,** 78-87.

Zheng, Y., Singarayer, J. S., Cheng, P., Yu, X., Liu, Z., Valdes, P. J. & Pancost, R. D. 2014. Holocene variations in peatland methane cycling associated with the Asian summer monsoon system. *Nature communications,* 5**,** 1-7.

Zhuang, Q., Lähteenoja, O., Draper, F., Yu, Z., Bridgham, S., Keller, J. & Cadillo-Quiroz, H. Contrasting carbon sink and source activities in Amazonian and Arctic peatlands under a changing climate. Geophysical Research Abstracts, 2019.

10. Appendix

Chapter 3: Appendix

Appendix A.3.1 Diploptene isotopic values (vs PDB) reported in literature and proposed bio-producers

Table 10.1 Literature review of diploptene isotopic values.

No	Reference	$\delta^{13}C_{Diploptene}$ or associated hopanoids	Environmental setting/sample type	Proposed bio-producer
1	Prahl et al. 1992	-48‰ → -30.4‰	Costal sediments	Soil microorganisms
2	Spooner et al., 1994	-64‰ → -55‰	Lacustrine sediments	
3	Ishiwatari *et al.*, 1994	-66.3‰	Sediment core from Oki Ridge, Japan Sea	Methanotroph origin
4	Freeman et al., 1994	Water: -35.4‰ Sediment: -45.4‰→-41‰	Marine sediments, Cariaco Trench and Black Sea	Black Sea: chemo-autotrophs (nitrifying bacteria); Cariaco Trench: chemoautotrophs and aerobic methanotrophs
5	Uemura and Ishiwatari, 1995	-60.7‰	Lake Suigetsu sediments	Mix of cyanobacteria with methanotrophic bacteria
6	Yamada *et al.*, 1997	-23.9‰ → - 57.1‰	Japan Sea sediment core (36 samples)	-23.9‰→-26.1‰ cyanobacteria; -44.3‰ →-57.1‰ mainly methanotrophic bacteria

7	Sakata et al., 1997	Diploptene, diplopterol – depleted by 6.4 to 6.9‰ relative to average biomass	Cultures of cyanobacterium	
8	Köster *et al.*, 1998	n/a	Black shale oil source rock	
9	Yamada and Ishiwatari, 1999	-66 ‰	Marine sediments	
10	Ishiwatari et al., 1994	-66.3‰	Laminated marine sediment core	Methanotrophic bacteria
11	Naraoka *et al.*, 2000	-31.6‰ → -26.3‰ -29.4 → -24.9‰	Recent marine sediments Riverine, bay and coastal	Cyanobacteria (Collister *et al.*, 1992aerobic photosynthetic microbes)
12	Pancost *et al.*, 2000	Diploptene: ~ -62‰ → Diplopterol: ~ -60‰ →		→ uncertain → possible methanotroph association
13	Elvert et al., 2000	-74.4 → -72.7‰ Squalene: -60.5‰	Deep-sea sediments, at cold seeps, eastern Aleutian subduction zone	Bacteria (sulfate reducers) growing on CO_2 mediated by anaerobic methanotrophic archaea
14	Elvert *et al.*, 2001a	On the ridge:-61‰ → -87.7‰ Off ridge:-33.6‰→-36.3‰	Marine, Hydrate Ridge, Cascadia Convergent Margin	On the ridge: aerobic methanotrophs yet not-produced *in-situ*
15	Elvert *et al.*, 2001b	-39.6‰ → -26.3‰	varved sediments of Saanich Inlet	Diverse bacteria from marine and terrestrial input; nitrifying bacteria an/-oxic interface; and some part from aerobic methanotrophs for depleted values (mixing); cyanobacteria input for enriched values
16	Elvert et al., 2001b	-31.5‰ → -39.6‰	Varved sediments in Saanich Inlet fjord	
17	Hinrichs, 2001	Diplopterol: -61‰		From methanotrophic processes

18	Schouten et al., 2001	-27‰ → -35.7‰	Ace Lake	Cyanobacteria and heterotrophic or chemoautotrophic bacteria
19	Thiel *et al.*, 2001	-61.4 ‰	Black Sea seep carbonates and microbial mats	Methanotroph association
20	Werne *et al.*, 2002	Diploptene: -54.1, -59.7‰ Diplopterol: -55.5‰, -62.3‰	Cold-seep surface sediments, Kazan mud marine volcano, Mediterranean Sea	Aerobic methane oxidizers and potential source mixing or Rayleigh distillation effect
21	Hinrichs *et al.*, 2003	Diplopterol: -72‰ → -54‰	Marine sediments, Santa Barbara Basin	Methanotrophic origin
22	Thiel et al., 2003	-62‰ → -35‰	marine sediments	
23	Pancost and Sinninghe Damste, 2003	Diploptene -41‰ → -61‰ and are 20 to 50 times enriched in ^{13}C relative to archaeal biomarkers.	Mediterranean cold seeps Holocene peat deposit	
24	Pancost and Damsté, 2003	Variable depending on site -62‰ ; -42‰	Napoli Crust and Napoli Seep	No source constrained
25	Ushida *et al.*, 2004	-41‰ → -26.1‰	Marine sediments from eastern margin of the Japanese main island Honshu	Multiple bacteria sources
26	Schubert et al., 2006	Diploptene -42‰ → -39‰ Diplopterol -40‰ → -30‰	Water column	
27	Atahan *et al.*, 2007	-39.6‰ → -47.4‰	Yangtze delta, China, Holocene	Methanotroph origin
28	Wakeham *et al.*, 2007	-39.8‰ -42.3‰	Stratified water column, Black Sea	Multiple sources: methanotrophs and chemoautotrophs

29	Chen *et al.*, 2008		UK peatlands	
30	Elvert and Niemann, 2008	Diploptene -70‰ → -75 ‰ Diplopterol -68 ‰	Surface sediments	
31	Bouloubassi *et al.*, 2009	Diploptene: -73‰, -68‰	Cold seeps in Southeast Atlantic	Aerobic methanotrophic origin surface layers, sulphate-reducing sp. In deeper layers
32	Ménot and Bard, 2010	Diploptene and diplopterol -67‰ → – 46‰	Gas hydrates destabilization in Sea of Marmara	Methanotrophic activity
33	Aichner *et al.*, 2010	Diploptene -64.5‰ → -45.5‰	Lake Koucha, sediment core, eastern Tibetan Plateau	Methanotrophs primary producers (acetate fermentation CH_4 source)
34	van Winden et al., 2010	Strong incorporation of label into diploptene (unquantified) Hop-17(21)-ene 2-methylhop-17(21)-ene -31‰ → -38‰	Peat moss (*Sphagnum* spp.)	
35	Van Winden *et al.*, 2012	(approx.) -29‰ → -34‰	Peat, Misten Bog, Hautes-Fagnes, East Belgium	high methanotroph activity 20-40cm, type II methanotrophs or signal dilution
36	Hyun *et al.*, 2014	-22.3‰ → -61.3‰	Japan Sea/East Sea; hydrate methane dissociation	Depleted values-in part, methanotroph bacteria; Enriched values-mainly cyanobacteria
37	Zheng *et al.*, 2014	-32‰ to -42‰ to -50‰ around 6.4 to 4k years ago)	Holocene wetland deposits	Methanotroph activity
38	Naeher et al., 2014	-60‰ → -43‰	Lake Rotsee,Switzerland	
39	Kaiser and Arz, 2016	No isotopic measurements	Baltic Sea surface sediments	

40	Davis et al., 2016	-68.2‰ → -50.1‰ -56.8‰ → -38.8 ‰	Recent surface sediments in 2 thermokarst lakes	
41	Petrišič *et al.*, 2017	Diploptene: -71.9 → -53.1‰ Hop-17(21)-ene:-74‰→-63‰	Lake Bled,	Methanotrophic bacteria
42	Birgel and Peckmann, 2008			
43	Inglis et al., 2019	-45‰ → -29‰	wetlands, peat material	Global peatlands database, 'T-GRES; type II methanotrophs dominate and input from other microbes
44	Lopes *et al.*, 2021	-42‰ -26‰	Sediments Brazilian Amazon floodplain lakes	Association with methanogenic archaea at site
45	Lattaud *et al.*, 2021	~ -57‰ →-45‰	Arctic deltaic sediments	Aerobic bacteria oxidation (aerobic methanotrophs)
46	Li *et al.*, 2022a	-39.2‰ → -31.2‰	Bryophytes in Wuhan, China	Heterotrophic bacteria, with contribution from methanotrophs or methylotrophs
47	Elling *et al.*, 2022	Diploptene: -13.5± -0.1 ‰ → -44.5±0.3‰	4 lab grown chemolithoautotrophic nitrite-oxidising bacteria	Nitrite-oxidising bacteria
48	Pereira et al., 2022	-53.3‰	Amazonian lake sediments	Methane-oxidising bacteria
49	Cordova-Gonzalez *et al.*, 2023	Diploptene -79‰ Diplopterol -84‰	Marine methane seeps	Aerobic methanotrophic bacteria

Appendix A.3.2. BECS laboratory calibration standard
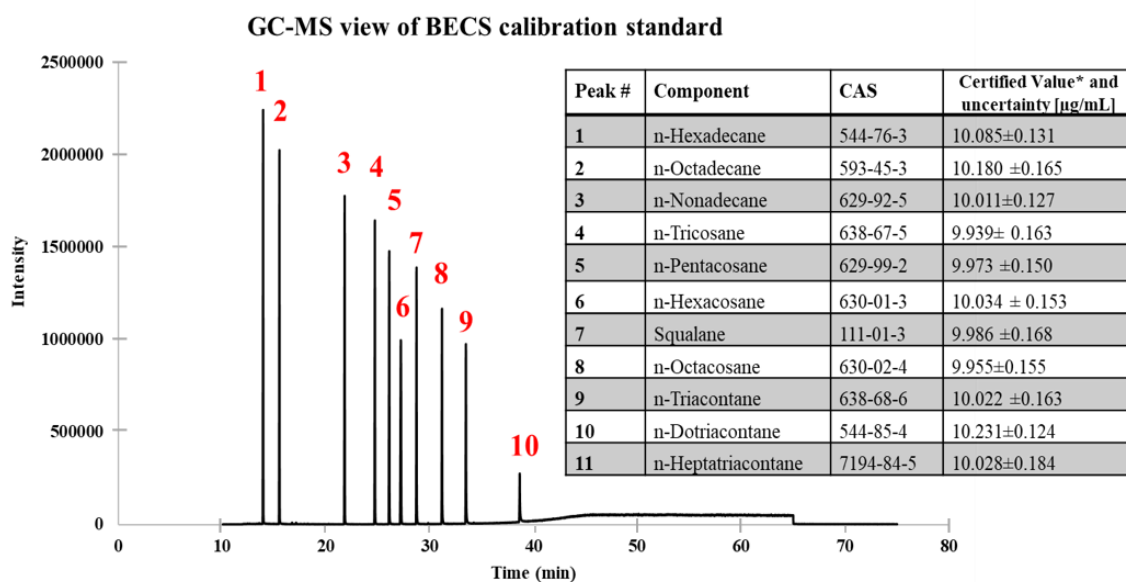
Figure 10.1 BECS calibration external standard and associated compounds.

Appendix A.3.3. GC-IRMS external standard calibration

The Fatty Acid (FA) analytical standard was previously calibrated by OGU, University of Bristol, and the isotopic values provided in the lab.

Table 10.2 OGU FAME calibration standard, with associated isotopic values.

External Standard Compound	Expected $\delta^{13}C$ value (‰)	Elution time interval (min)	SD measurements (n=18)
C11:0 FAME	-28.83	12.07→12.32	0.13
C13:0 FAME	-30.42	15.96→16.21	0.15
C16:0 FAME	-30.71	21.76→22.03	0.15
C18:0 FAME	-31.61	25.32→25.61	0.13
C21:0 FAME	-29.27	30.19→30.50	0.17
C23:0 FAME	-31.58	33.14→33.36	0.19

The measured FAMEs reported against their real isotopic values returned a $R^2=0.981$, indicating that the instrument was functioning within the required parameters during analysis.

Expected vs Measured with SD error
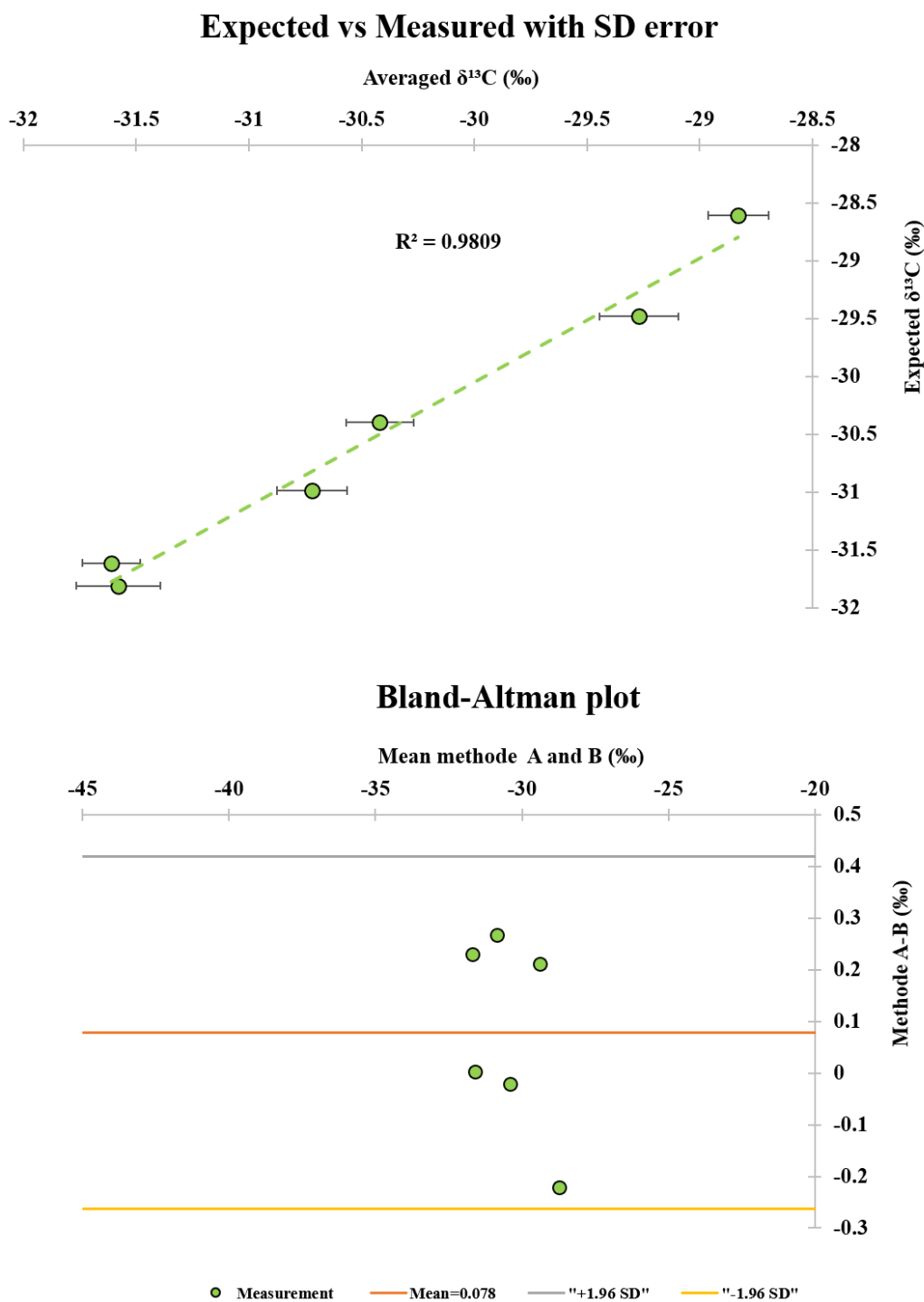
Bland-Altman plot

Figure 10.2 Top: Expected vs Measured FAMEs isotopic measurements (n=18). $R^2=0.98$ with provided Standard deviation error bars. Bottom: Bland-Altman plot.

351

Appendix A.3.4. QT fatty acids isotopic values and depth profiles
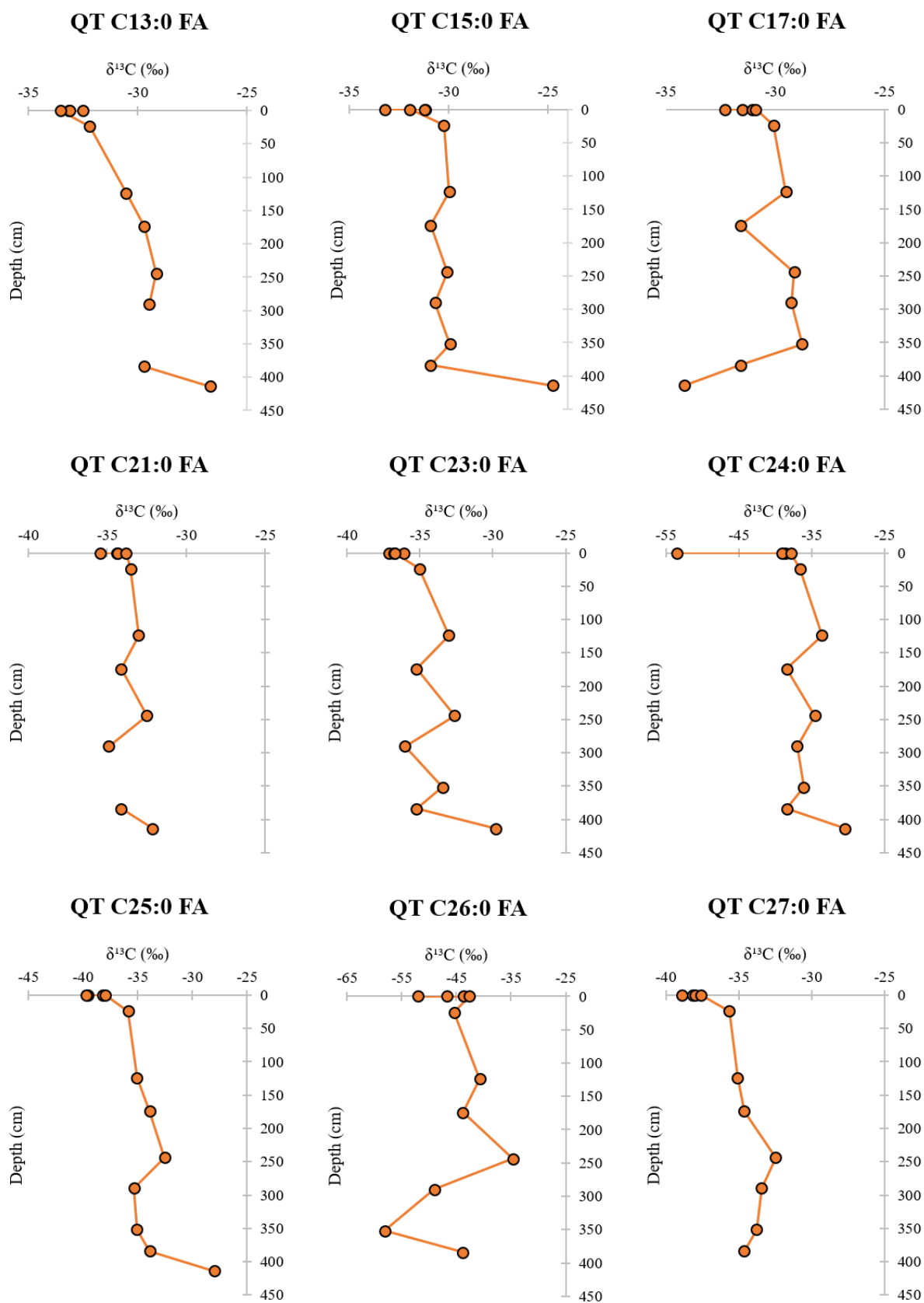
Figure 10.3 QT FA C13:0 to C27:0 isotopic values for surface and core samples.

QT C28:0 FA

QT C29:0 FA

QT C30:0 FA

QT C31:0 FA

QT C32:0 FA

QT C33:0 FA

QT C35:0 FA
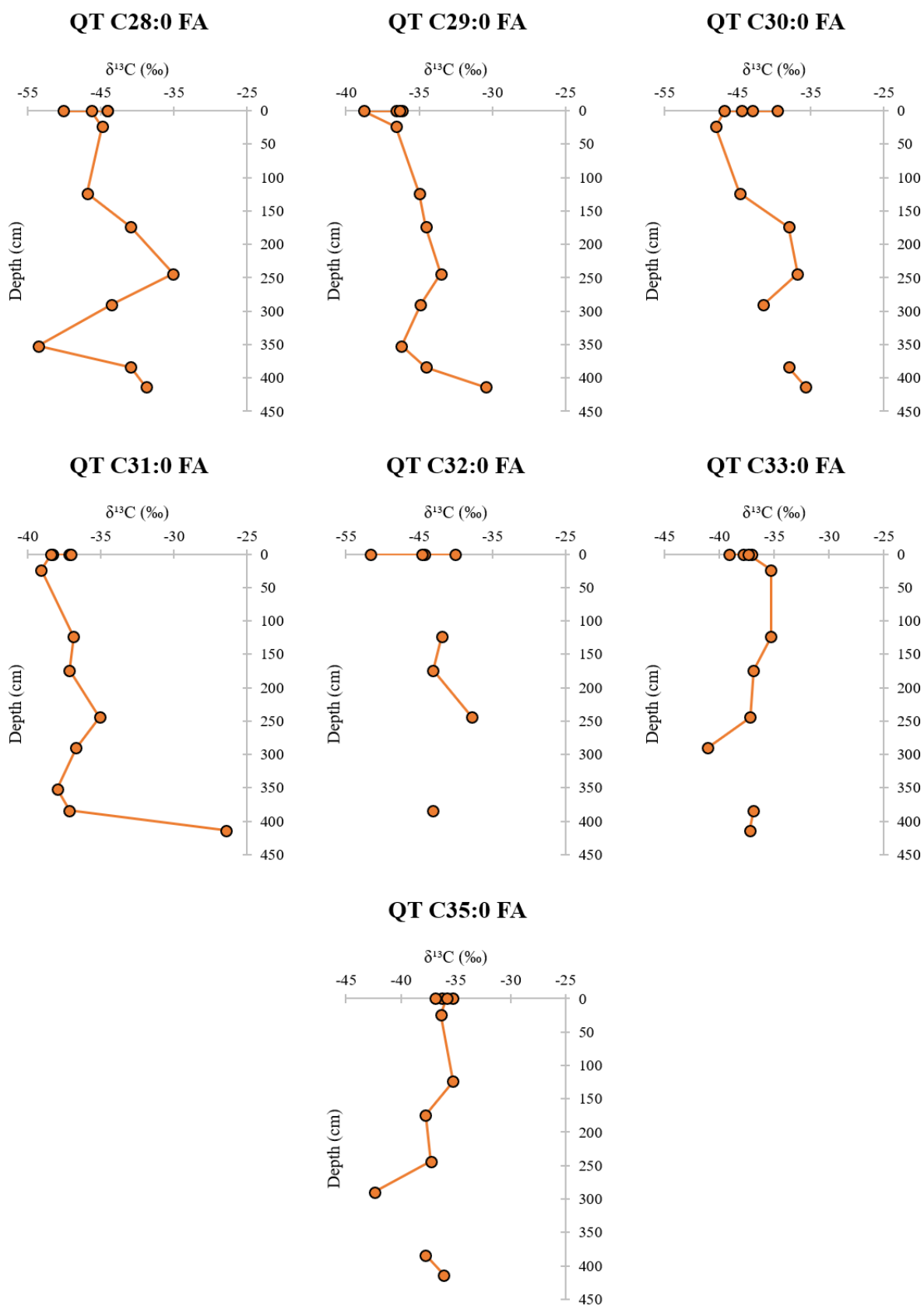
Figure 10.4 (Continued) QT FA C28:0 to C35:0 isotopic values for surface and core samples.

Appendix A.3.5. Auxiliary βα C$_{29}$-hopane isotopic values at QT peatland

N1 2388 QT βα C$_{29}$-hop
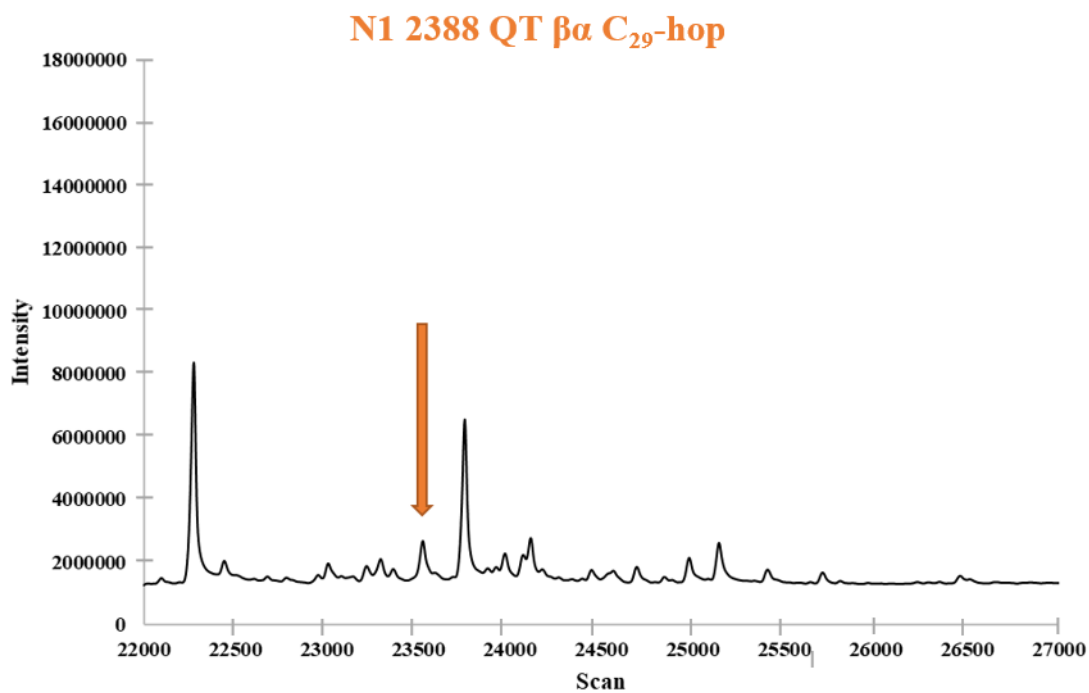
Figure 10.5 QT βα C$_{29}$-hopane peak and associated isotopic values in Table 10.2.

Table 10.3 QT βα C29-hopane isotopic value when above detection limit.

BECS ID	Averaged depth	βα C$_{29}$-hopane
2377	0	
2378	0	
2379	0	
2380	0	
2381	0	
2382	24	**-37.44**
2383	124	**-36.97**
2384	174	**-35.10**
2385	244	**-44.41**
2386	290	
2387	352	
2388	384	**-57.70**
2389	414	

Appendix A.3.6. BVA fatty acids isotopic values
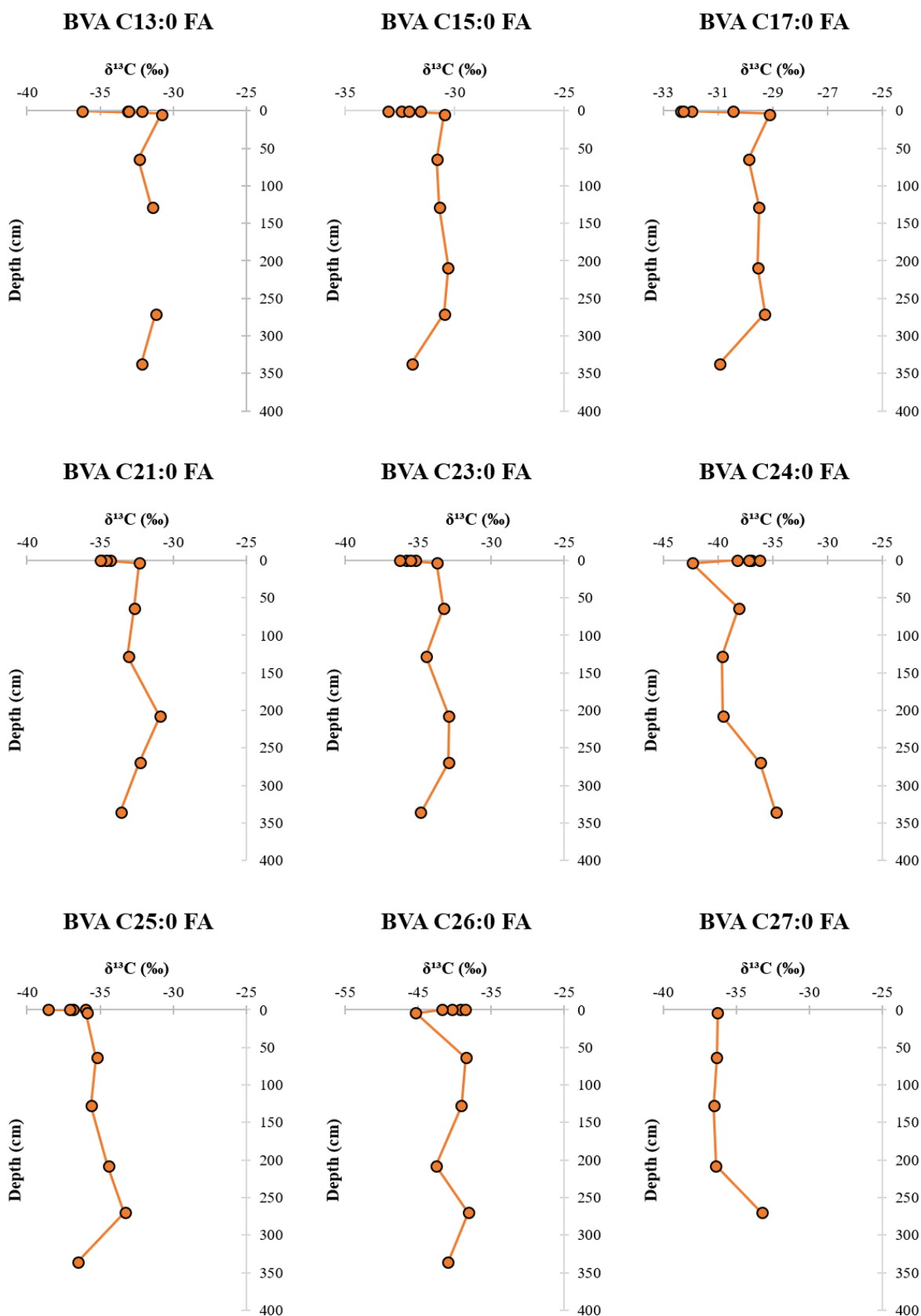
Figure 10.6 BVA FA C$_{13:0}$ to C$_{27:0}$ isotopic values for surface and core samples.

BVA C28:0 FA

BVA C29:0 FA

BVA C30:0 FA

BVA C31:0 FA

BVA C32:0 FA

BVA C33:0 FA

BVA C35:0 FA
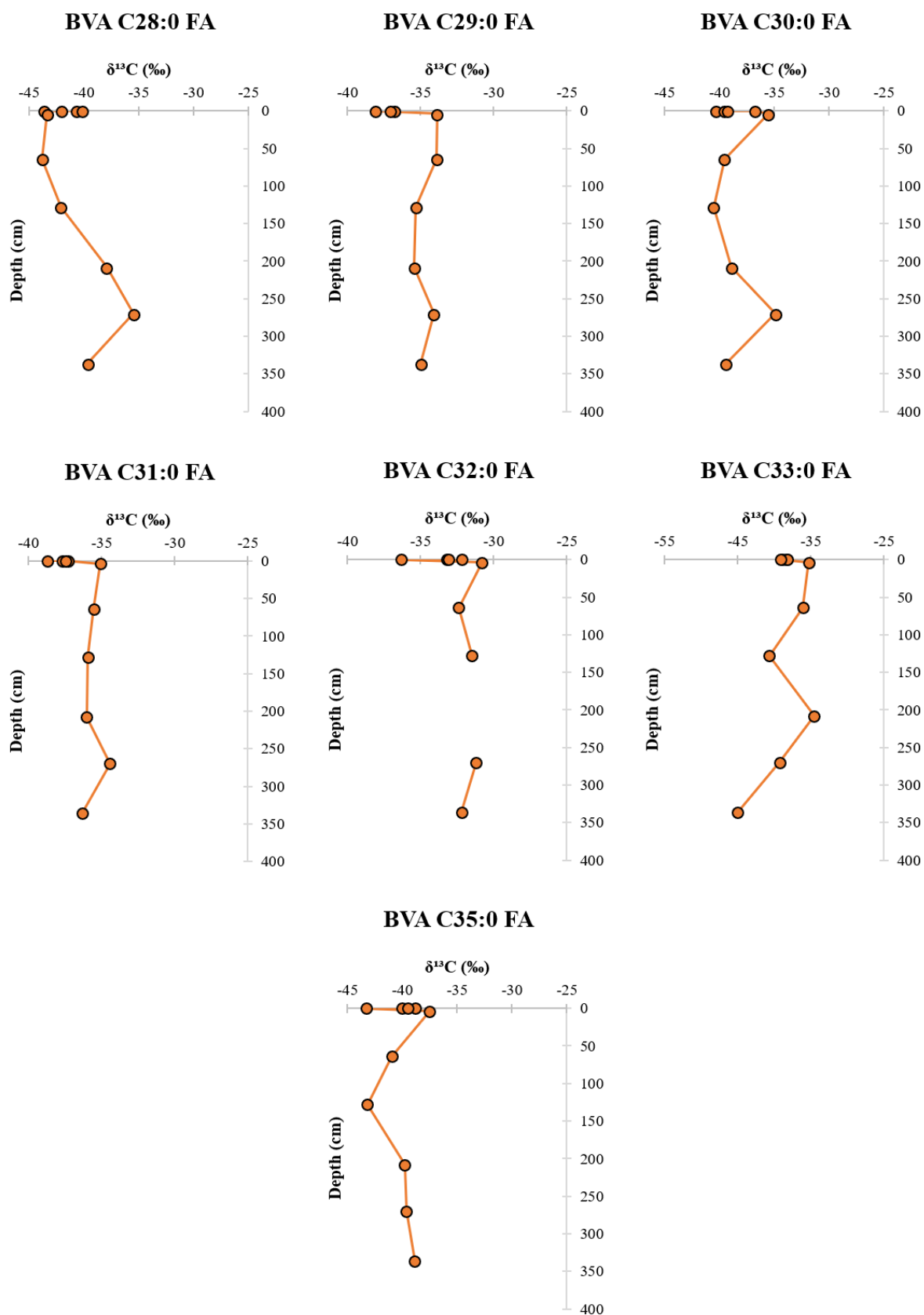
Figure 10.7(Continued) BVA FA $C_{28:0}$ to $C_{35:0}$ isotopic values for surface and core samples.

Appendix A.3.7. BVA hopanoids values extracted
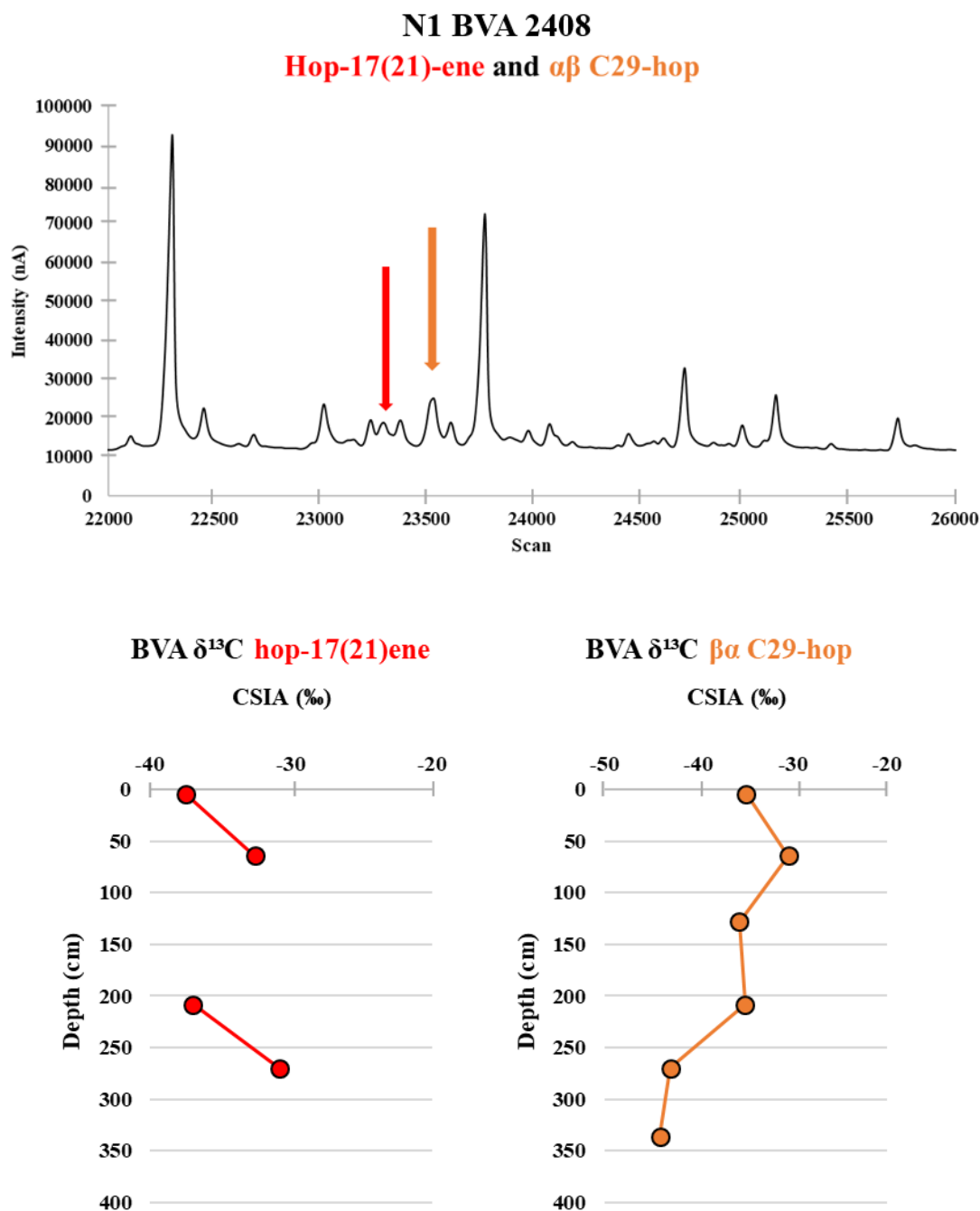
Figure 10.8 BVA hopanes. Top: Notice co-elution of Hop-17(21)-ene and well-defined peak of βα C₂₉-hopane. Bottom: Isotopic values of the two compounds, with depth.

Appendix A.3.8. Diploptene concentrations in the three peatlands
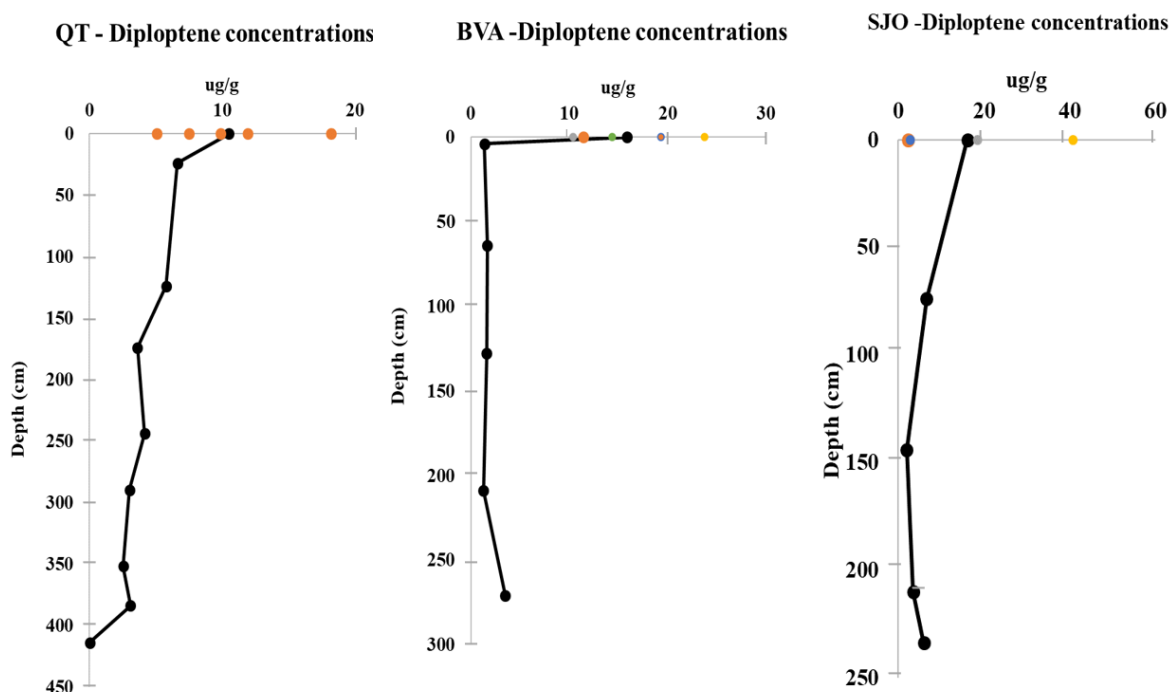
Figure 10.9 Diploptene concentration distribution (µg compound/g dried peat sediment) at the three peatlands as measured in Amariei, 2018

Diploptene concentrations in 1µL injection splitless

Working example: For sample 2377 from the surface of QT, diploptene had a peak area of 22.8 pA with a calculated response factor of 3.975 mg/L for the elution time of diploptene, calculated for the closest eluting compound in the BECS analytical standard injected at 100%, 50% and 25% concentrations. This gave a concentration of 5.735… µg/mL (i.e., 5.73 ng/µL).

Each 1µL injection into the IRMS thus introduced 5.73 ng of diploptene. For the mol conversion, this in grams would be equal to 5.73E-9 g. The molar mass of diploptene is rounded here to 410 g/mol. Thus, by dividing the diploptene mass of 5.73E-9 g to its molar mass, **1.3975E-11 moles** would be injected per 1µL into the GC-IRMS. This would be equivalent to a 1µL injection from sample 2377 containing **0.013975 nmols** of diploptene.

Table 10.4 QT, SJO and BVA calculated diploptene amounts for 1µL sample injection.

QT sample	Depth	mg/L*	mg/mL**	mols	nmols
2377	0	5.73556	0.005736	1.39892E-11	0.01399
2378	0	15.1942	0.015194	3.7059E-11	0.03706
2379	0	7.39585	0.007396	1.80387E-11	0.01804
2380	0	10.0624	0.010062	2.45424E-11	0.02454
2381	0	60.7013	0.060701	1.48052E-10	0.14805
2382	24	11.9741	0.0119741	2.92051E-11	0.02921
2383	124	4.98069	0.0049807	1.2148E-11	0.01215
2384	174	6.76103	0.0067610	1.64903E-11	0.01649
2385	244	20.9213	0.0209213	5.10276E-11	0.05103
2386	290	6.23138	0.0062314	1.51985E-11	0.0152
2387	352	4.56956	0.0045696	1.11453E-11	0.01115
2388	384	7.46954	0.0074695	1.82184E-11	0.01822
2389	414	2.20263	0.0022026	5.37227E-12	0.00537

SJO sample	Depth	mg/L*	mg/mL**	mols	nmols
2390	0	1.87246	0.00187	4.56696E-12	0.00457
2391	0	14.4276	0.01443	3.51892E-11	0.03519
2392	0	31.7398	0.03174	7.74143E-11	0.07741
2393	0	2.27966	0.00228	5.56015E-12	0.00556
2395	74	5.16404	0.00516	1.25952E-11	0.0126
2396	144	1.55516	0.00156	3.79307E-12	0.00379
2397	210	2.75323	0.00275	6.71519E-12	0.00672
2398	234	4.67542	0.00468	1.14035E-11	0.0114

BVA sample	Depth	mg/L*	mg/mL**	mols	nmols
2399	0	38.1626	0.03816	9.308E-11	0.09308
2400	0	34.6282	0.03463	8.4459E-11	0.08446
2401	0	79.1462	0.07915	1.9304E-10	0.19304
2402	0	64.513	0.06451	1.5735E-10	0.15735
2403	0	47.787	0.04779	1.1655E-10	0.11655
2404	4	2.28434	0.00228	5.5716E-12	0.00557
2405	64	1.6506	0.00165	4.0259E-12	0.00403
2406	128	5.39545	0.0054	1.316E-11	0.01316

2407	209	1.47792	0.00148	3.6047E-12	0.0036
2408	271	3.90581	0.00391	9.5264E-12	0.00953
2409	336	0	0	0	0

* - values calibrated using BECS external standards and calibration curves after injections at several concentrations

** - provided as reference for DMNs work and concentration of diploptene analytical standard = 0.1 mg/mL

Chapter 4: Appendix

Appendix A.4.1. NMS 131 and LB media for culture growth and contamination testing

Recipe for NMS medium is provided below. Quantities are in grams.

In 700mL distilled water, dissolved in the following order: 10.0g KNO3, 10.0g MgSO4.6H2O, 2.0g CaCl2 (anhydrous) and dilute to 1L. This creates the base solution, 10x concentration for the medium. The Iron EDTA is made by adding 3.8g in 100mL distilled water. Sodium molybdate is made by adding 0.26g Na2MoO4.2H2O to 1L of distilled water. The trace solution contains the following chemicals and amounts, diluted in 5L.

Table 10.5 Trace Element solution chemical amounts.

Chemical	Amount (g)
CuSO4.5H2O	1.00
FeSO4.7H2O	2.50
ZnSO4.7H2O	2.00
H3BO3	0.075
CoCl2.6H2O	0.25
EDTA di sodium salt	1.25
MnCl2.4H2O	0.10
NiCl2.6H2O	0.050

The phosphate buffer solution is made by adding 71.6g Na2HPO4.12H2O and 26.0g KH2PO4 to 800mL water, adjusting the pH to 6.8 and diluting to 1L.

The NMS combines the above solutions, following the recipe:

- Dilute 100mL of solution 1 (10x salts) to 1 litre.
- Add 1 mL of solution 3 (Na molybdate) and 1 ml of solution 4 (trace elements).
- Add 0.1 mL of solution 2 (Fe EDTA).
- Add 1.5% agar for plates.
- Autoclave at 15 psi for 15 minutes
- Autoclave separately 10 mL of solution 5 (phosphate buffer) for every litre of NMS.
- When the NMS is cool enough to hold in the hand, aseptically add the phosphate buffer. If this is done too early the phosphate will precipitate out.

The LB (Luria-Bertani) medium was prepared for each culture using by dissolving 10g tryptone, 10g sodium chloride and 5g of yeast extract in 1L of distilled water.

Appendix A.4.2. PICARRO instrument – working principle

The instrument's working principle and concentration calibrations are based on the strength of absorption of a laser beam by the small mass molecules introduced into the chamber. Each gas molecule has a known unique wavelength that is able to absorb the beam (PICARRO, 2024) leading to a decrease in the strength of the recorded output beam intensity that is then correlated to the concentration of the molecule, in this case CH_4. Once the beam is introduced, it bounces of a series of mirrors within the cavity; 3 mirrors are used in the case of PICARRO, with 99.999% reflectivity. Once a threshold is reached in a photodetector, the beam is turned off and no sample is further introduced. The beam intensity experiences an exponential decay (i.e., ring-down) until it reaches zero. Based on the decay time and wavelength-specific absorption of light, the concentration of a sample and its isotopic composition is calculated. When the sample is introduced into the cavity, the time it takes for the beam intensity to decay to 0 is shorter, as the light is absorbed into the molecules. The laser can be tuned for different wavelengths for different molecules, such that, measurements for multiple molecules can be taken during a run (i.e., CO_2 and CH_4).

Appendix A.4.3. Type II Diploptene and Hop-21-ene calibration curve
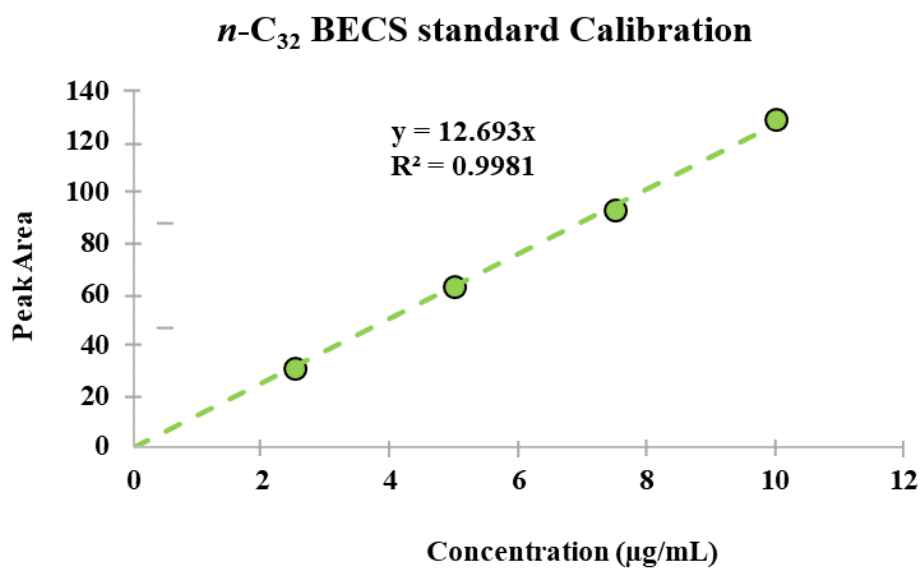
Figure 10.10 Calibration example of $n\text{-}C_{32}$ for 4 different concentrations.

Appendix A.4.4. Indiana B5 Mix - isotopic standard – values and calibration

Table 10.6 Indiana B5 Mix n-alkane composition and isotopic values.

n-Alkane	$\delta^{13}C$ (‰)	σ (‰)	Range (‰)	n
C16	-26.15	0.02	-26.13 to -26.17	5
C17	-31.87	0.02	-31.84 to -31.90	8
C18	-32.7	0.01	-32.69 to -32.72	5
C19	-31.99	0.01	-31.98 to -32.02	6
C20	-40.91	0.02	-40.89 to -40.94	7
C21	-28.83	0.02	-28.81 to -28.85	5
C22	-34.89	0.02	-34.87 to -34.92	6
C23	-33.37	0.03	-33.33 to -33.40	5
C24	-32.13	0.02	-32.11 to -32.16	6
C25	-28.46	0.02	-28.42 to -28.48	7
C26	-32.94	0.01	-32.92 to -32.95	8
C27	-31.11	0.01	-31.11 to -33.12	5
C28	-33.20	0.01	-33.20 to -33.20	5
C29	-29.30	0.02	-29.27 to -29.32	5
C30	-33.14	0.02	-33.12 to -33.16	6
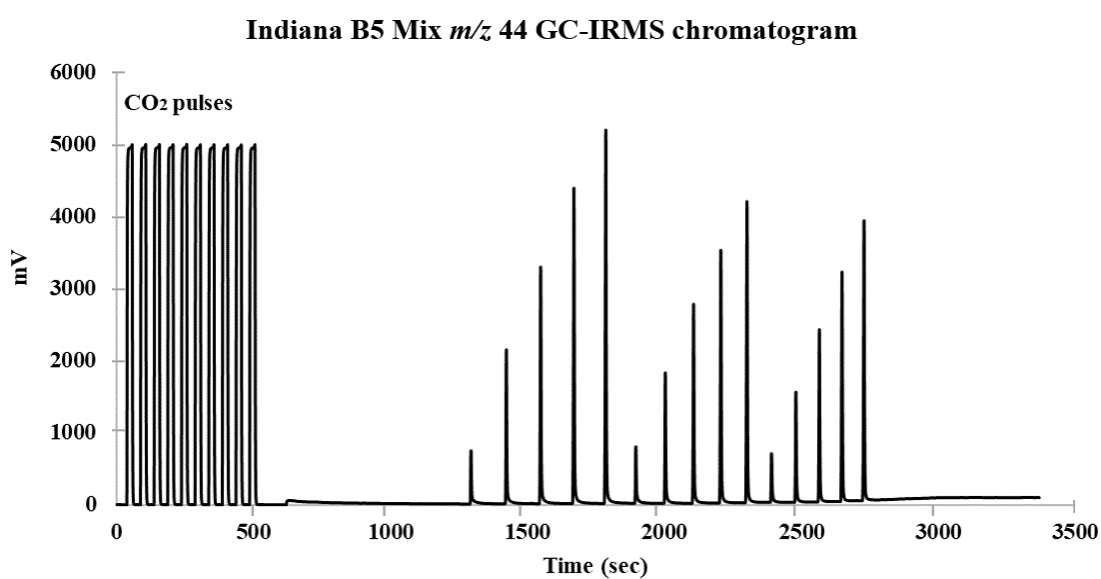
Figure 10.11 Indiana B5 GC-IRMS chromatogram.

Appendix A.4.5. Type I – Squalene, αβ-C31-hop/day and βα-C31-hop/day lipid concentrations

Total squalene/day

Total αβC$_{31}$-hop/day

Total βαC$_{31}$-hop/day
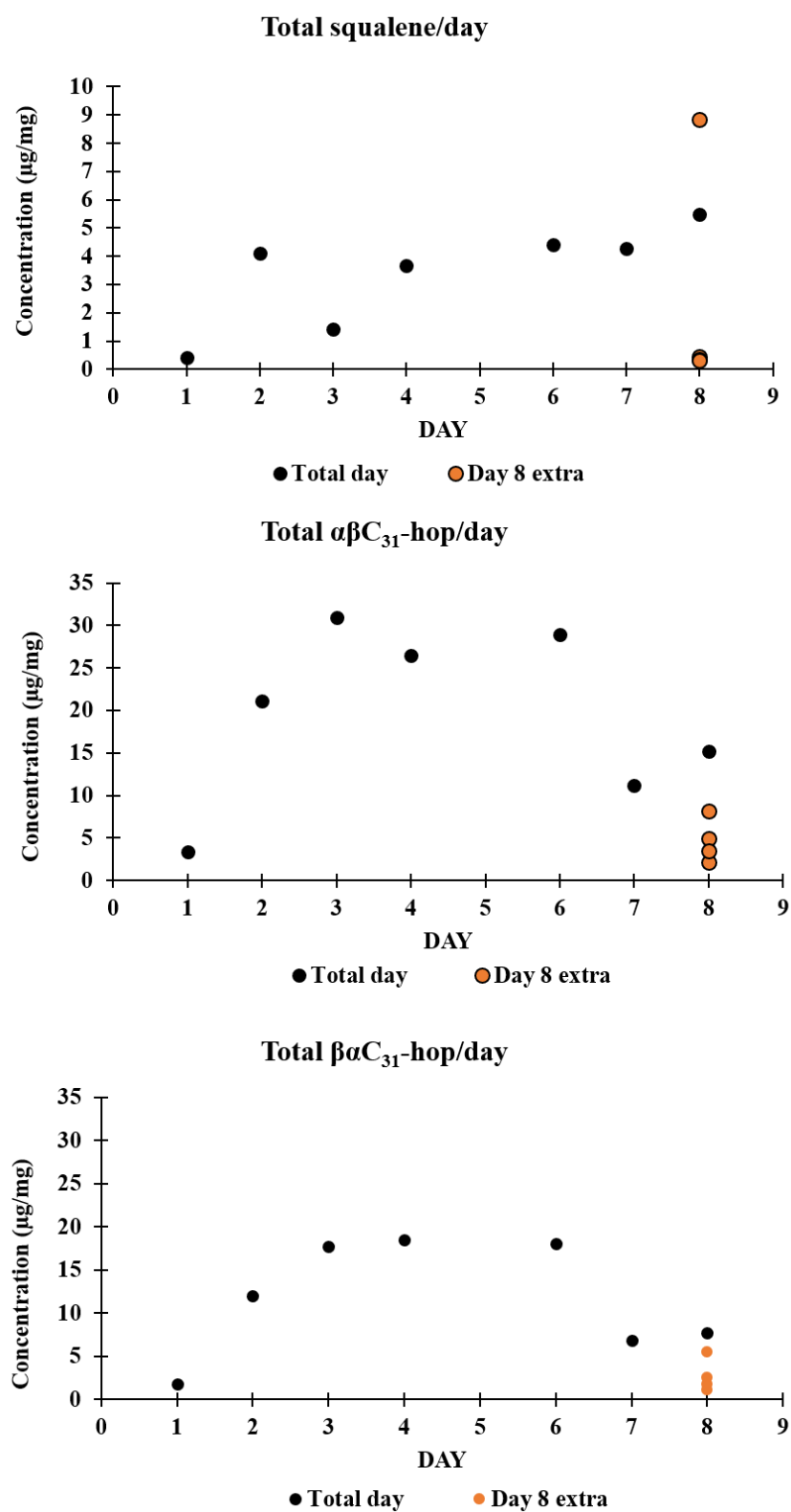
Figure 10.12 Type I, M. methanica, further lipid concentration.

Appendix A.4.6. Diploptene and hop-21-ene identification in type I and II
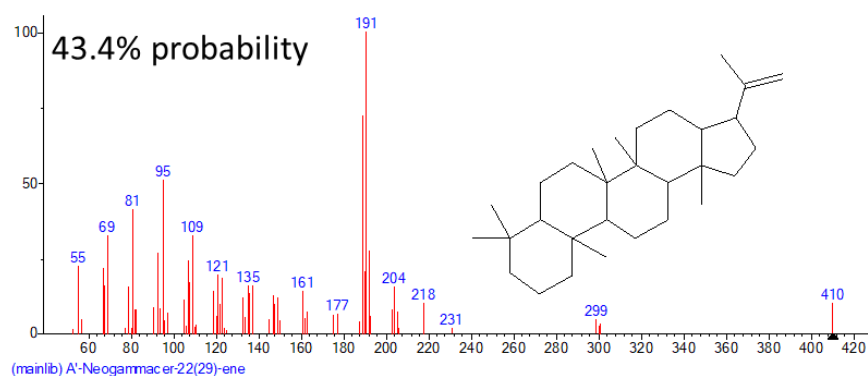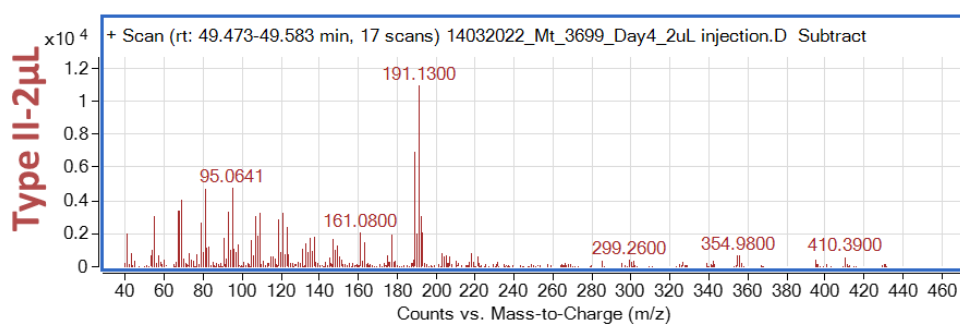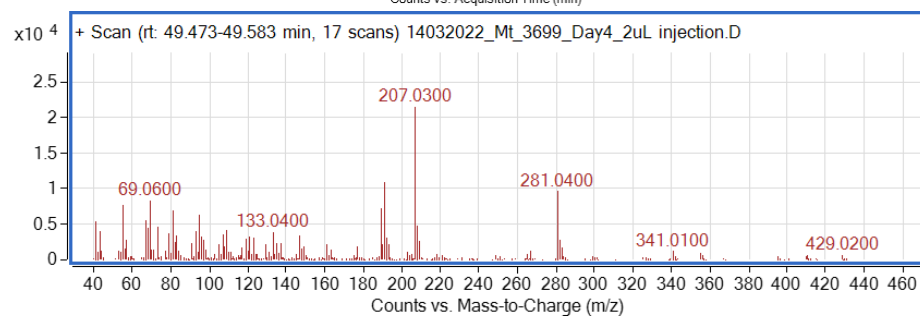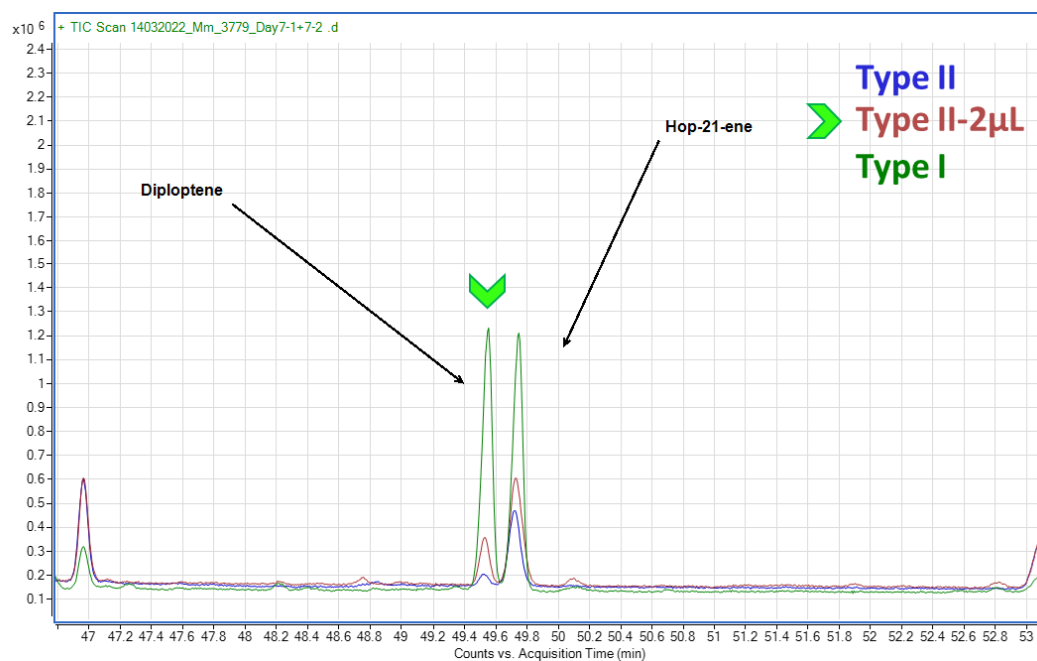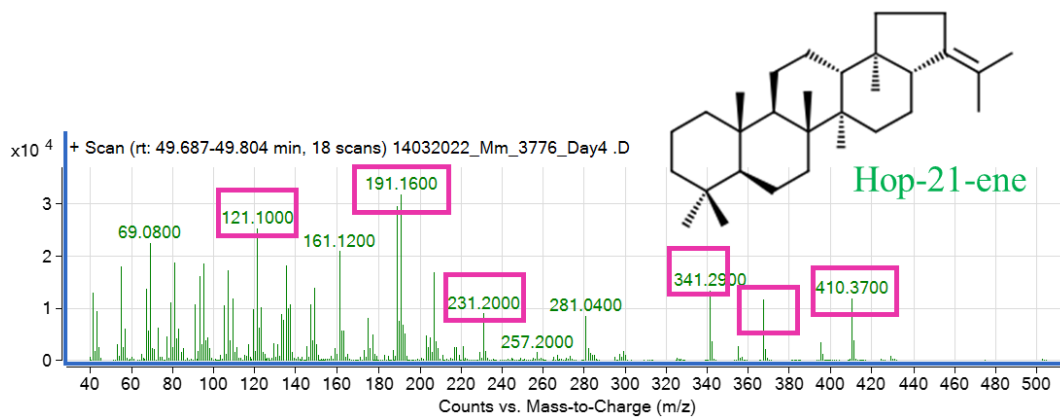
Figure 10.13 Major peaks based on Sessions et al., 2013 aided identification of compound as hop-21-ene.

Appendix A.4.7. Type I – Derivatised flash sample and lipid identification
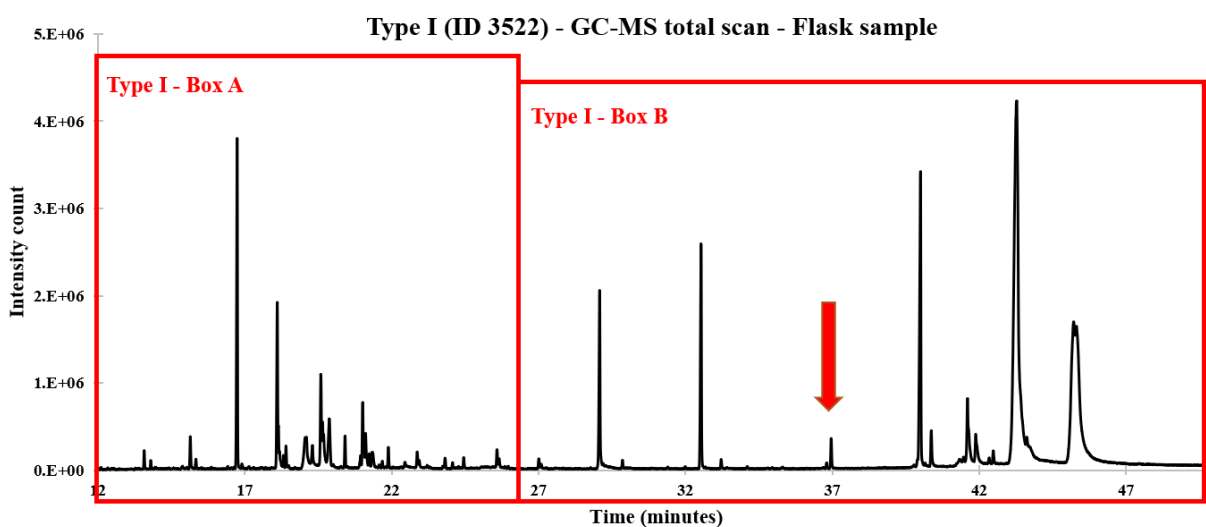
Figure 10.14 Total ion chromatogram (TIC) view of a M. methanica flask sample. Only this sample was TMS derivatised for lipid identification. Boxes A and B are further detailed below, with lipids identified in the corresponding tables. Arrow points to the position of diploptene and hop-21-ene.

FIGURE BOX A

NO	Compound	NO	Compound
1	FA C12:0 (C15:0-TMS)	12	FA C16:1ω7(C19:1-TMS)
2	C14-OH (C17:0-TMS)	13	FA C16:0 (C19:0-TMS)
3	FAME C15:0	14	Phthalate
4	C15-OH (C18:0-TMS)	16	FA C18:0 (C21:0-TMS)
5	FA C14:0 (C17:0-TMS)	18	FAME C17:1ω7
6	FAME C17:1ω7	20	Tris2-chloro-1-methylethyl-phosphate
7	FA C15:0 (C18:0-TMS)	21	Nonadecanenitrile
8	FAME C17:0	25	Palmidrol
9	non-TMS C16:1 (coelution)	26	FAME 16-Me C19:0
10	non-TMS C16:0	28	Phthalate
11	FA C16:1ω7(C19:1-TMS)		

FIGURE BOX B

NO	Compound	NO	Compound
1	Squalene	6	**Hop-21-ene**
2	Phthalate	7	Diplopterol + TMS
3	Phthalate	8	Diplopterol (Sessions et al., 2013)
4	Phthalate	11	αβC31-hopane
5	**Diploptene**	12	βαC31-hopane
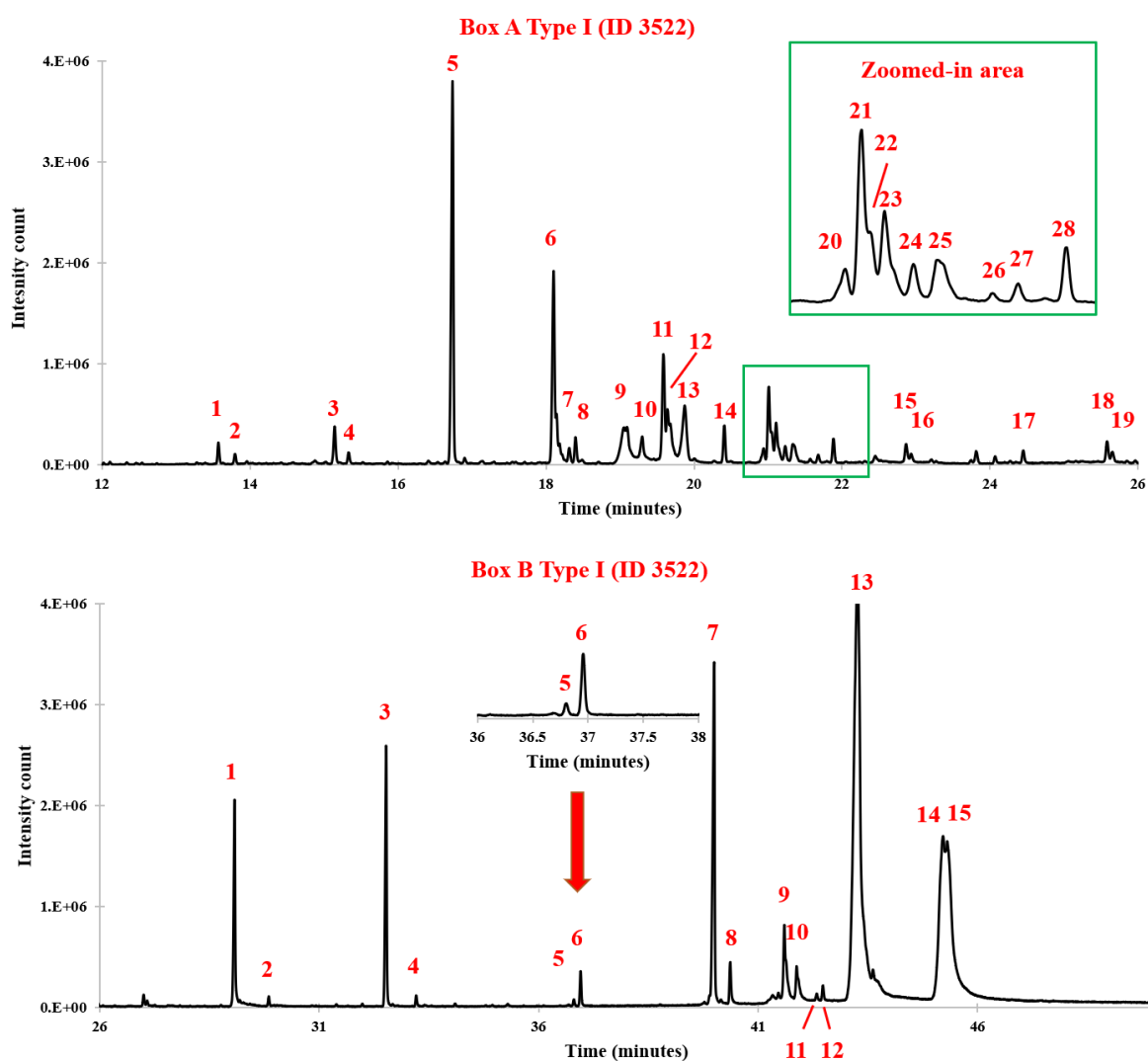
Figure 10.15 Zoomed-in views of Figure 4.11. Numbers above peaks denote compounds that are identified in Tables 1 and 2. Arrow and zoom-in view in Box B show chromatographically resolved diploptene and hop-21-ene peaks, indicating that the GC-IRMS analysis is possible for diploptene on a similar column and GC method.

Chapter 5: Appendix

Appendix A.5.1. Valve Box and unions

The valves were produced by Analytical Flow Products (AFP, Canada) and are part of the MDVG-6 Series, fitted with an AFPD-3 diaphragm. Both the body and valve head are made of Stainless Steel-316L. The port connections are 1/16" wide, with a port size of 0.030" and an internal dead volume of 0.14 µL.

The working principle is based on a pneumatic piston (with a spring for the return position) located at the base of each valve which is pressure activated. The activating pressure (i.e., up to 60-65 psig) is provided by compressed air from the GC-system, the same air used for the FID from an air compressor. For each actuation, 0.75 cm^3 of air are consumed. The piston contains plungers and when the piston moves up, normal open position (valve ON), positions 1-2, 3-4 and 5-6 are connected. When the piston moves down, positions 1-6, 2-3, 4-5 are connected (valve OFF).

Two-way valco unions (P/N 20147) were used to connect the two ends of the pyrolysis capillary with the On/Off valve and the second capillary column (i.e., Cc2 in Figure 3.26).
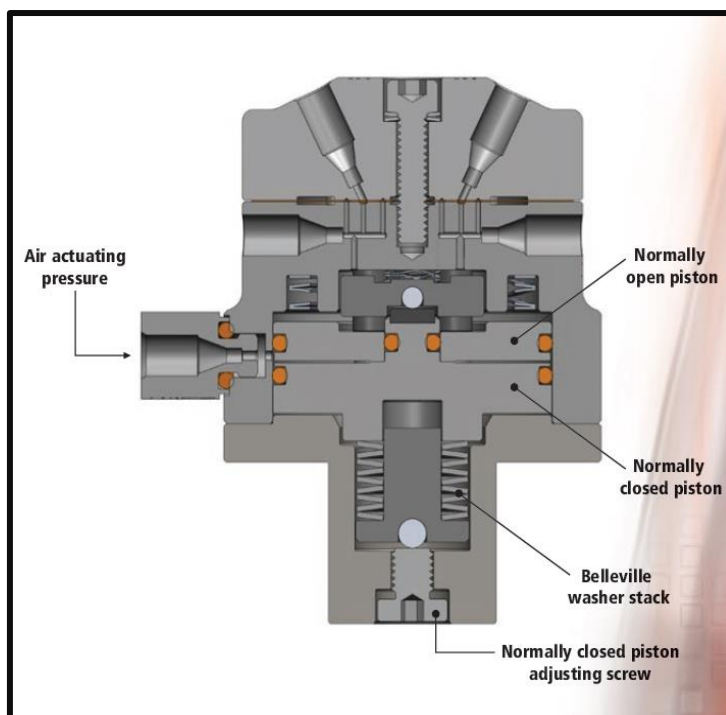
Figure 10.16 AFSolutions Diaphragm valve used in the prepGC (Website).

Every union or valve connection had a ferrule in place. The connections were checked for leaks using a Leak Detector (P/N 22839, 113030, Restek) and the Valco unions were also submerged in Ethanol to investigate leaks. Acetone was not used at this point due to the residue that it leaves on components. The unions were towel dried and the oven was set at 50°C with He flowing through the system and the Valve position 3 disconnected (i.e., venting into atmosphere).

Appendix A.5.2. Toluene retention time shift with Pyrolytic temperature
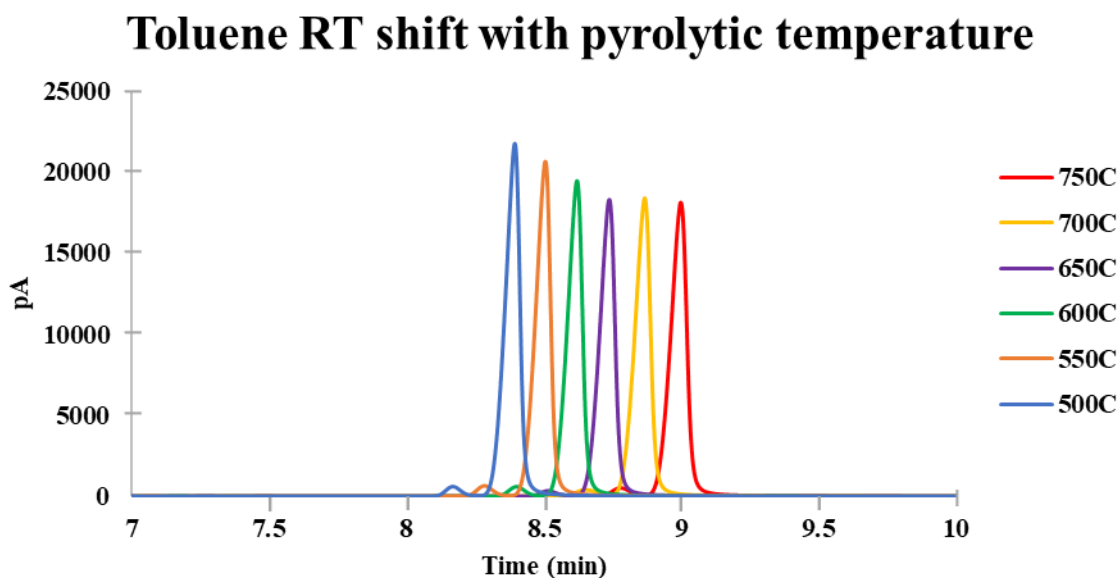
Figure 10.17 Toluene RT migration with increasing pyrolytic temperatures.

Appendix A.5.3. Experiment 1 – pyrogram zoomed-in view
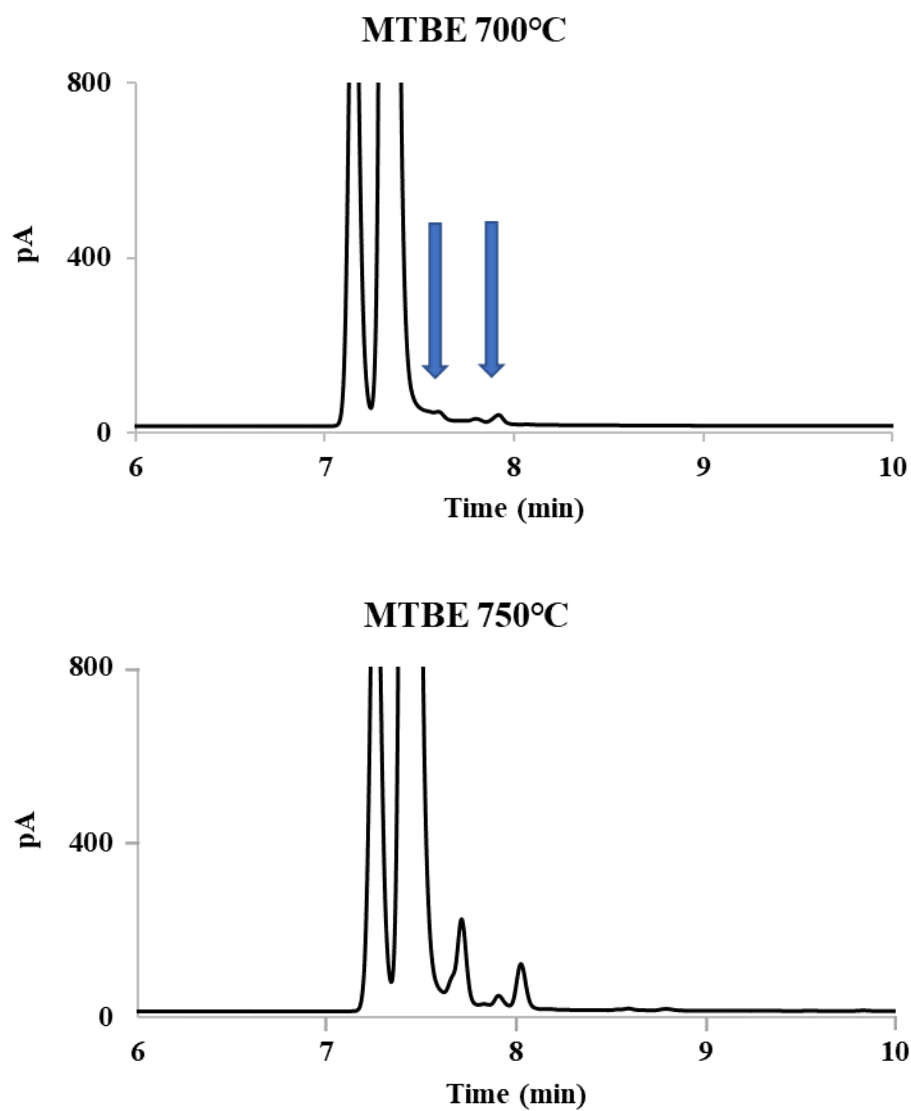
Figure 10.18 MTBE zoom in indicating secondary pyrolysate formation with the pyrolytic temperature of 700°C

Appendix A.5.4. Experiment 2 – pre-MTBE peak area variations as measured on the prep-GC-FID
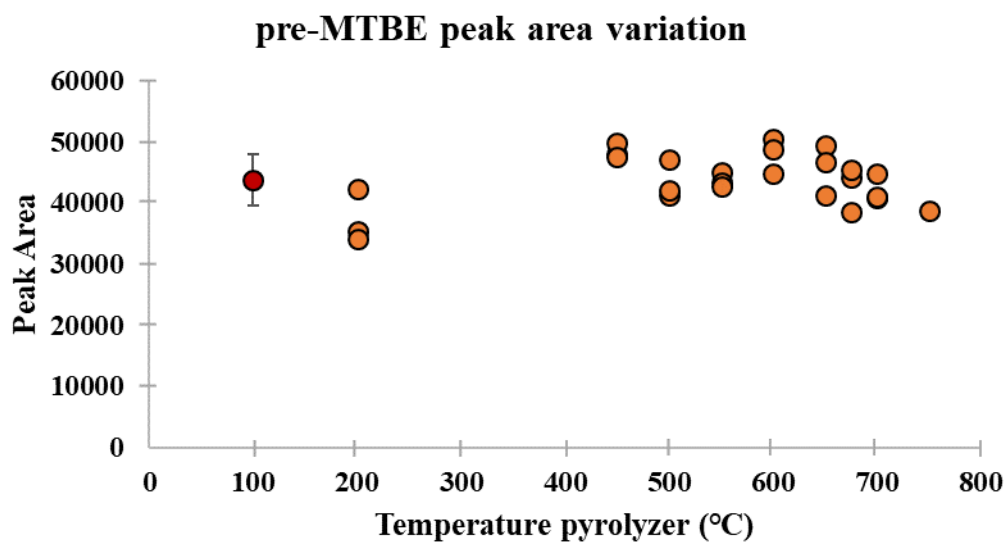
Figure 10.19 Pre-MTBE peak in experiment 2 was used as a confirmation of injection and correct heart-cut of main MTBE peak. The PA of this compound can also serve to study the variation in PA of pyrolysates and prep-GC injection. Red measurement represents the PA of pre-MTBE peak from Experiment 1.

Appendix A.5.5. Mass spectra of pyrolysates at 750°C GC-MS

750°C compound 6 Mass Spectrum
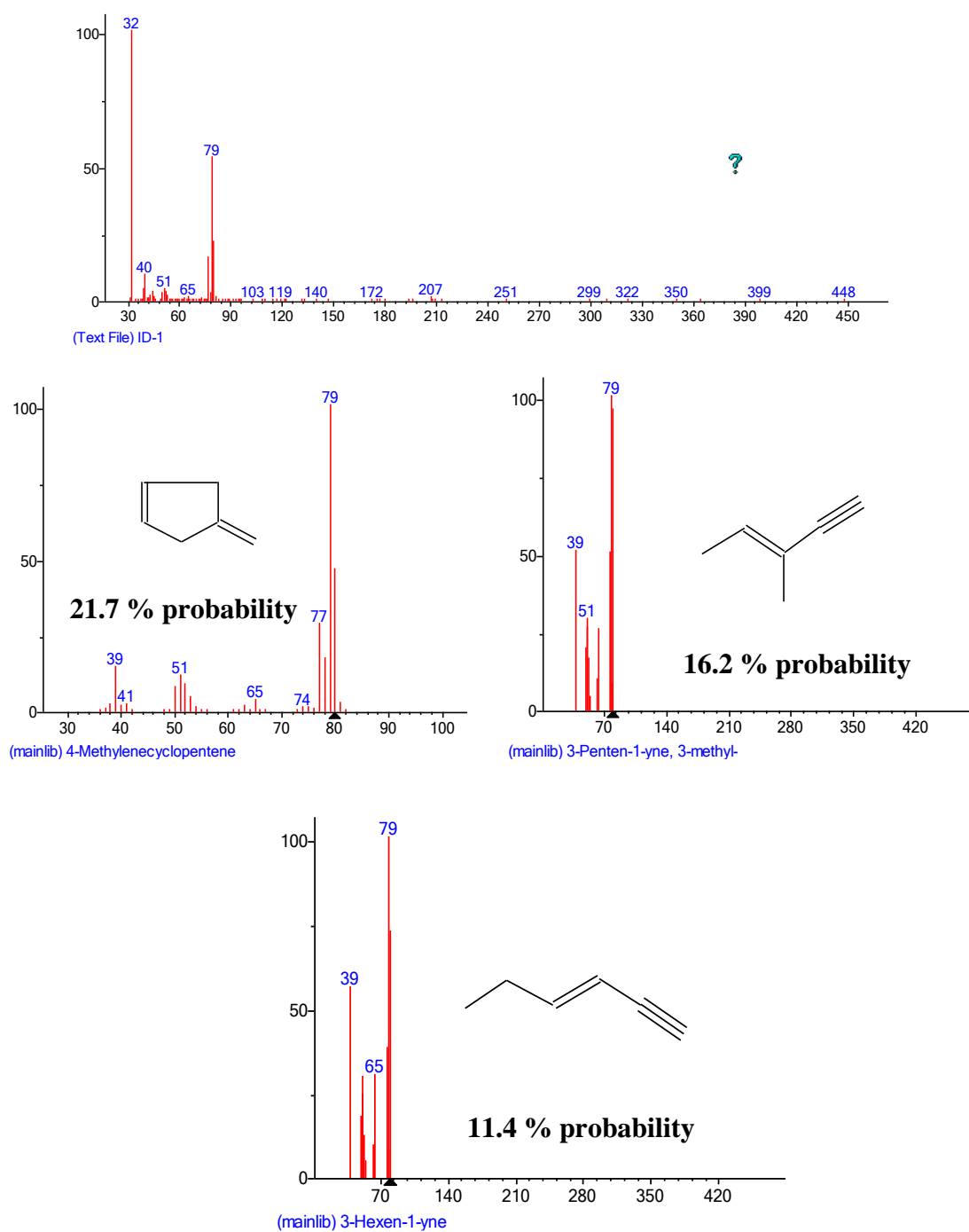
Figure 10.20 Possible compounds for the MS of compound 6.

Appendix A.5.6. 675°C - MTBE pyrolysis and transfer to the GC-MS. Mass spectra with best match

3

(Text File) Scan 384 (2.510 min): 210319_10_MTBE_675C_LONGER TL IN.D\data.ms

(replib) Furan, 2-ethyl-5-methyl-

4

(Text File) Scan 424 (2.762 min): 210319_10_MTBE_675C_LONGER TL IN.D\data.ms

(mainlib) 1-Heptyn-6-one

5

(Text File) Scan 518 (3.355 min): 210319_10_MTBE_675C_LONGER TL IN.D\data.ms

(replib) 1,5-Hexadiene, 2,5-dimethyl-

6

(Text File) Scan 545 (3.526 min): 210319_10_MTBE_675C_LONGER TL IN.D\data.ms

(replib) 1,4-Cyclohexadiene, 1-methyl-
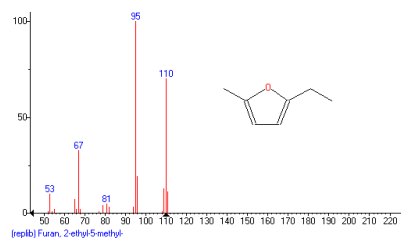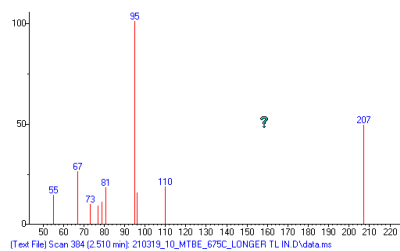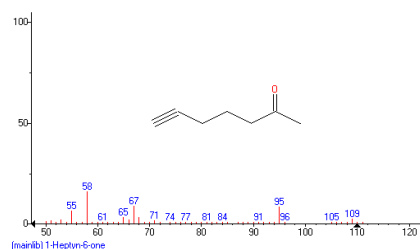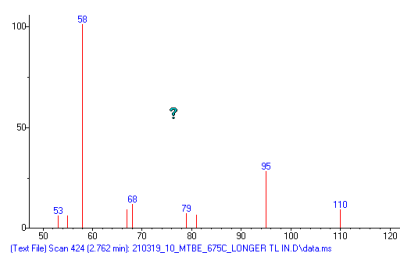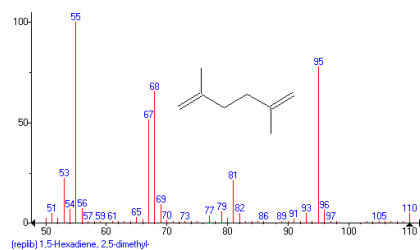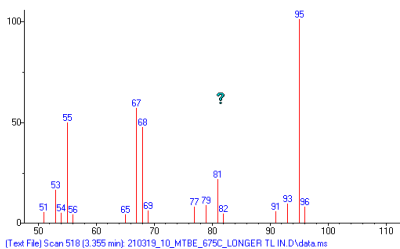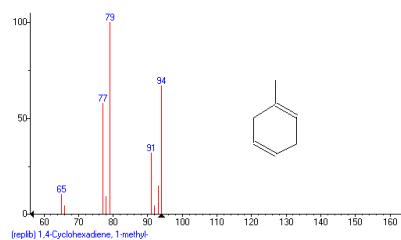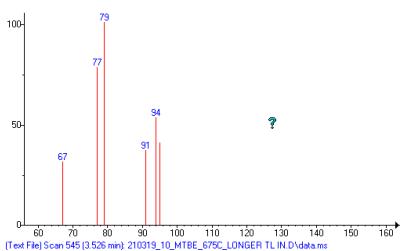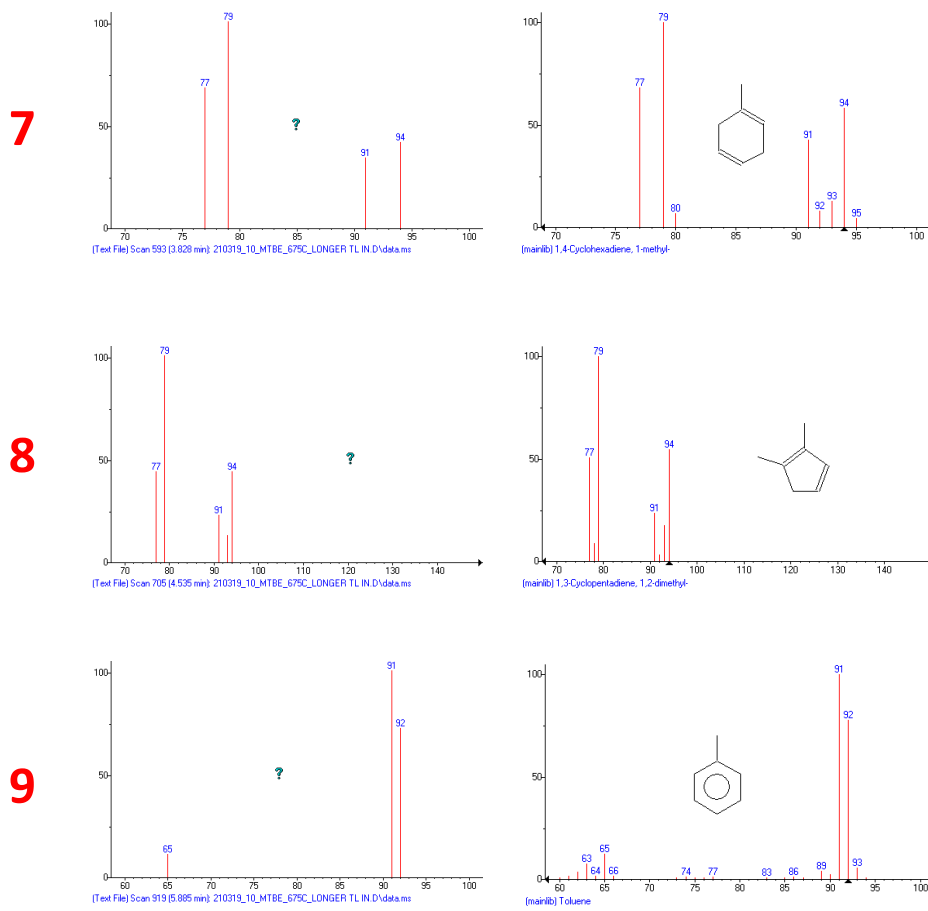
Figure 10.21 Proposed identification of MTBE 675°C pyrolysates.

Chapter 6: Appendix

Appendix A.6.1. ICE trap and *n*-alkane mix pilot experiment

Sigma-Aldrich 04070-1ML; C8-C20; 40mg/L
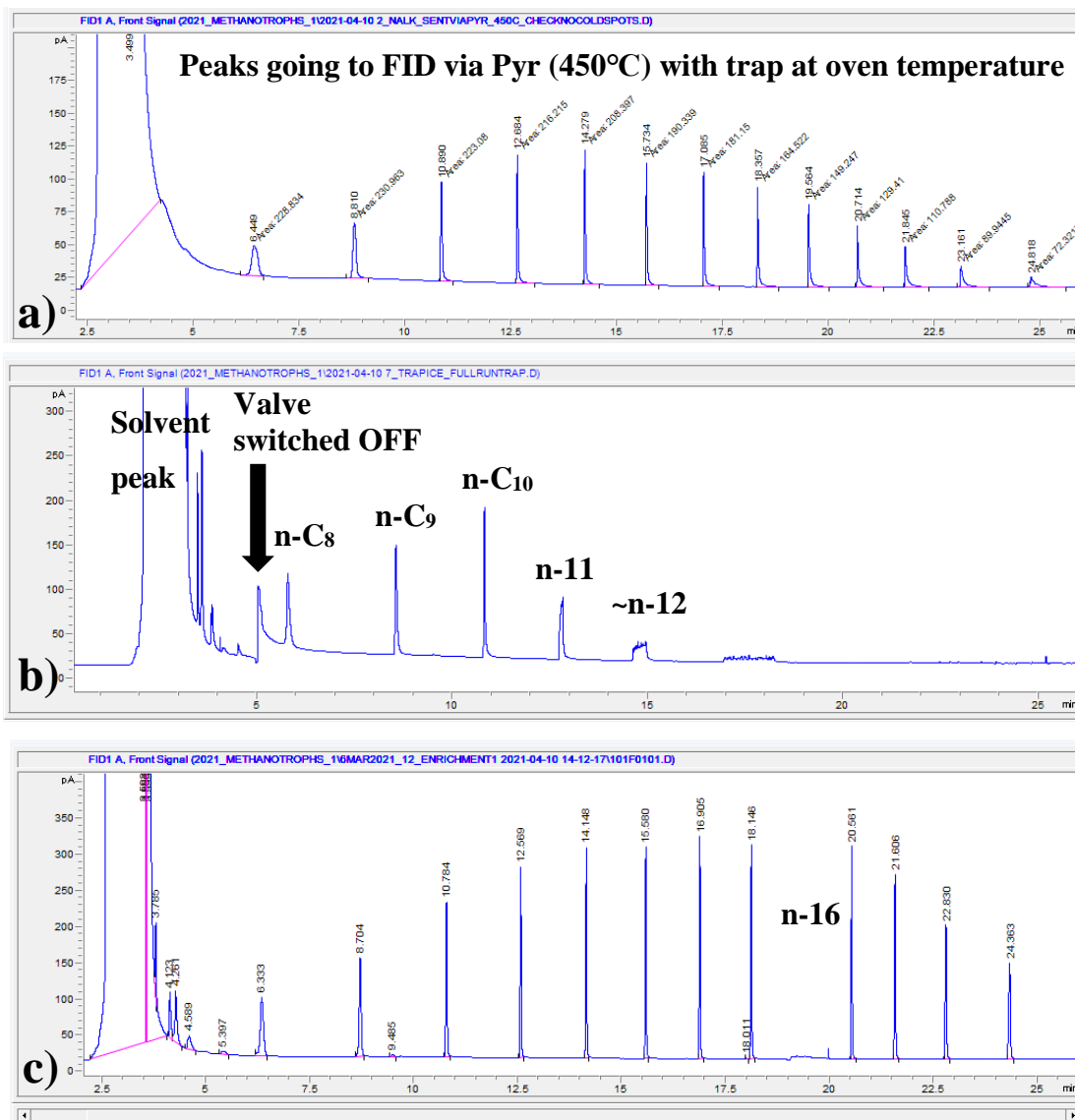
Figure 10.22 a) Retention times of integrated n-C$_8$ to n-C$_{20}$ compounds as they reach the FID via the pyrolyser and trap placed in oven (warm); b) The first 4 compounds have lower boiling points and lower trapping temperatures, below 2-4°C, and are escaping the cold trap. N-alkanes with more than 11 carbons are successfully trapped; c) n-C$_{16}$ heart-cutting using the ICE trap.

Appendix A.6.2. Mass spectra of compounds in Figure 6.14
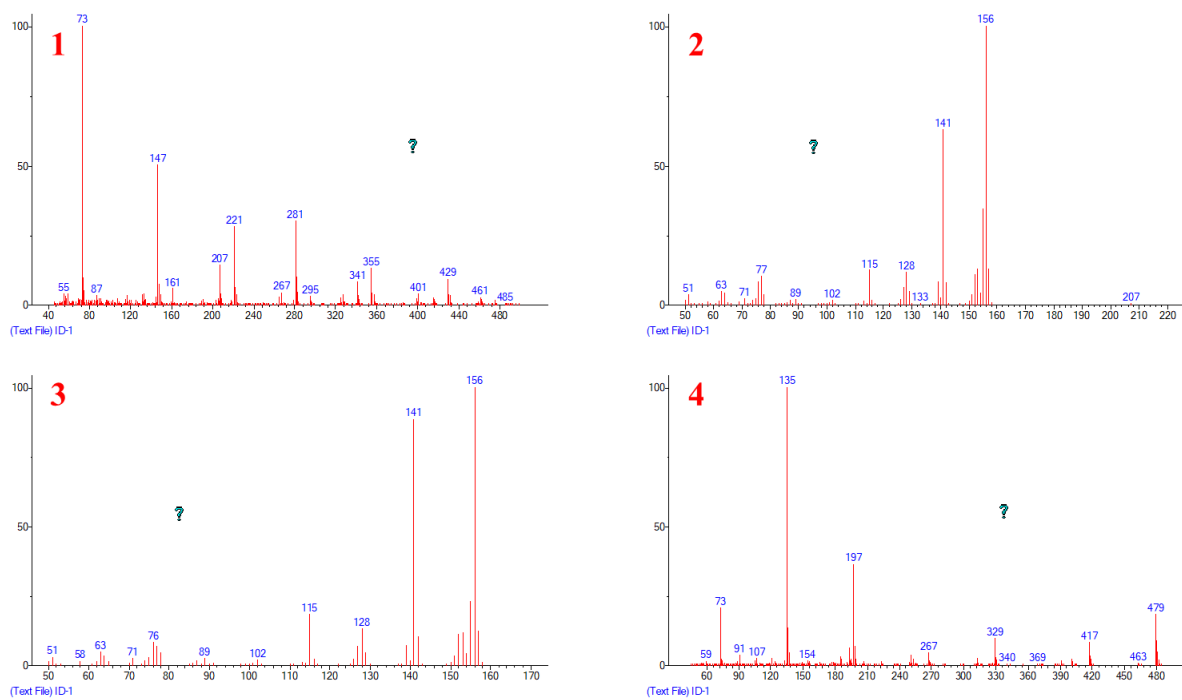
Figure 10.23 Mass spectra of compounds in Fig 6.14

Appendix A.6.3. Mass spectra of compounds of 2,3 DMN pyrolysis from Figure 6.17
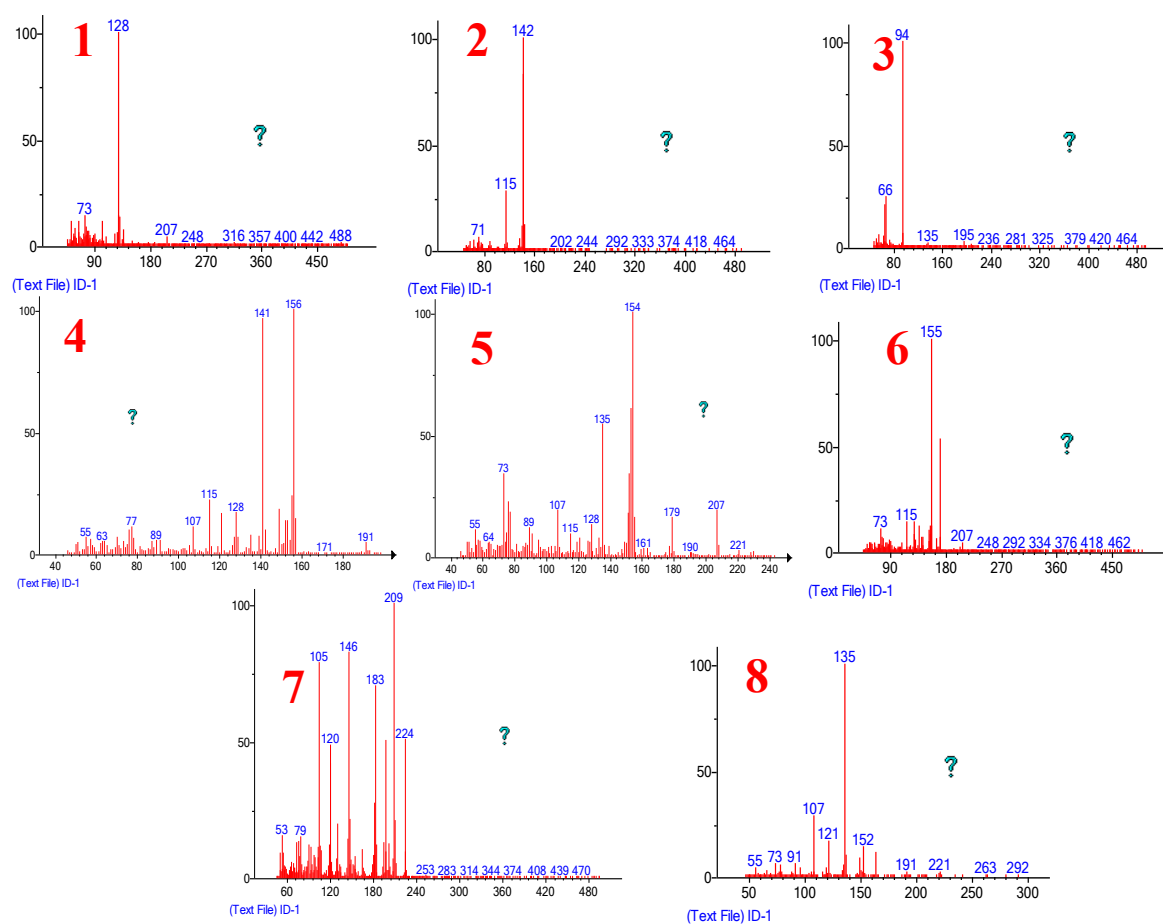
Figure 10.24 Mass spectra of 2,3 DMN pyrolysates.

Appendix A.6.4. ICE trap and release – lower oven ramp (10°C/min)
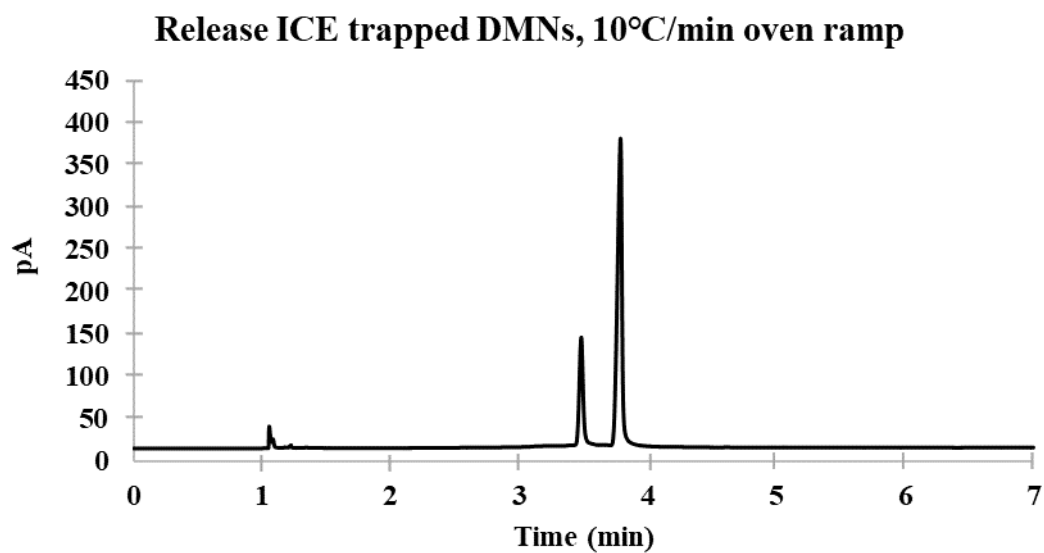
Figure 10.25 DMNs release order with slower oven ramp.

Method: 0.4 µL injection, 10:1, 1.5 mL/min, 60 m column, oven program: 80°C (1 min) →
10°C/min→140°C (0 min)

Appendix A.6.5. ICE trap pilot test – concentrated DMNs
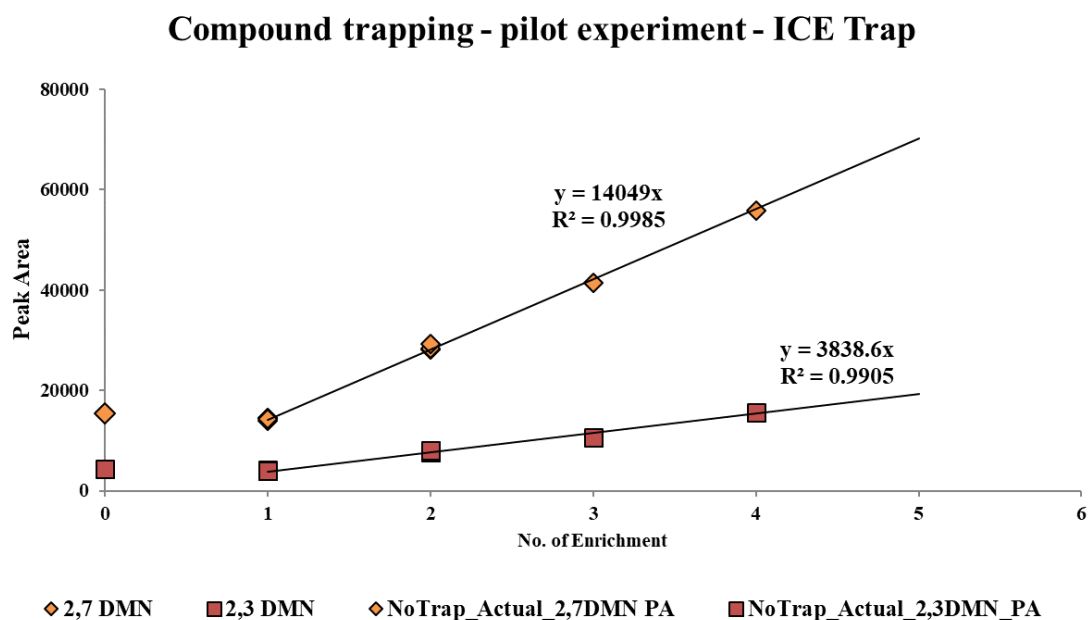
Figure 10.26 Compound concentration within the cold tube and quantification of released peaks (2 Methyl Naphthalenes). The number of concentrations refers to the number of times the compound was trapped (the number of injections). This was performed in triplicate for the trapping of one injection and for the trapping of 2 injections (i.e. injection-trap-injection-trap-release and quantification) and done only once when the compound was concentrated 3 and 4 times.

Chapter 7: Appendix

Appendix A.7.1. The effect of the valve box colder-spot on diploptene chromatography
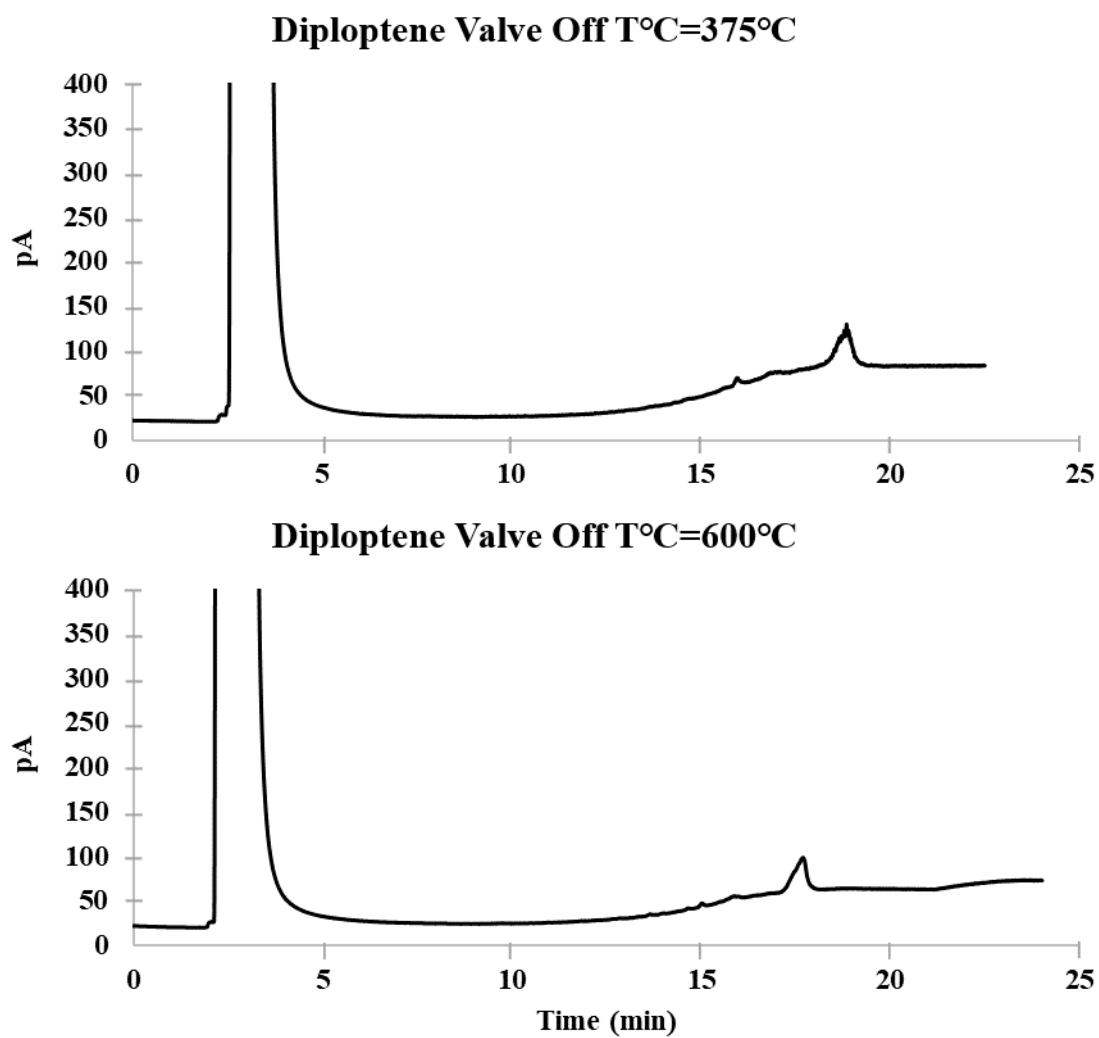
Figure 10.27 Diploptene chromatography with valve box cold-spot.

Appendix A.7.2. RMG diploptene pyrolysis at 750°C - reactions that lead to the formation of 2-isobutene pyrolysate. BDEs of 21.96 kcal/mol are required for this pyrolysate.
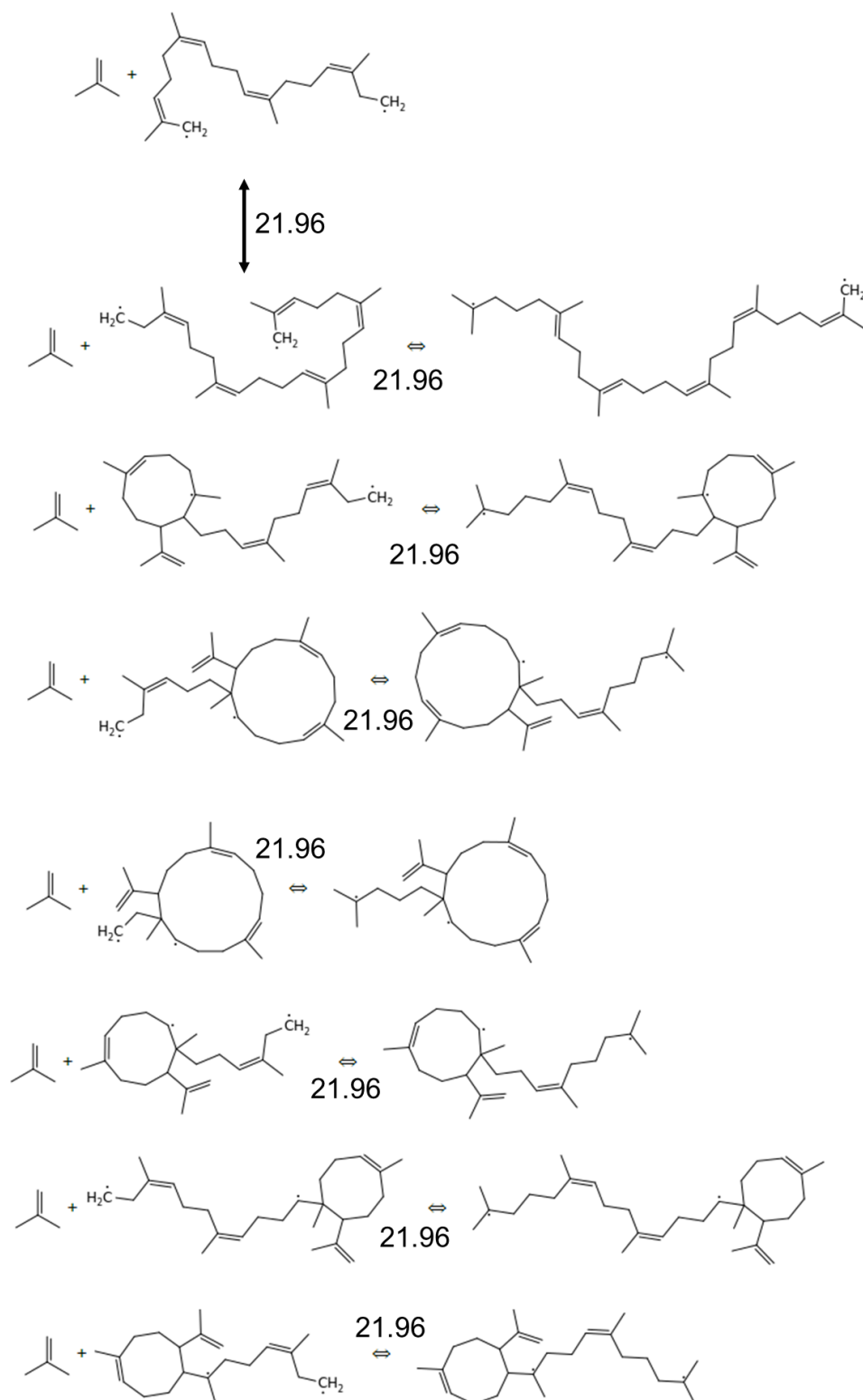
Figure 10.28 RMG diploptene pyrolysis at 750°C - reactions that lead to the formation of 2-isobutene pyrolysate.

Appendix A.7.3. RMG simulation providing BDEs for methyl radical cleavage from diploptene backbone
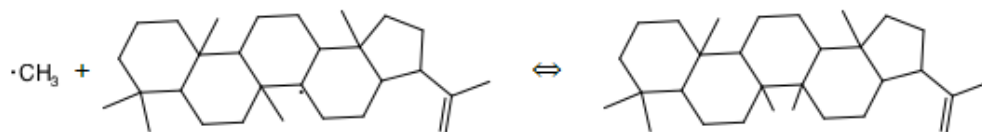
H298 (kcal/mol) = -87.09
S298 (cal/mol*K) = -46.41
G298 (kcal/mol) = -73.26
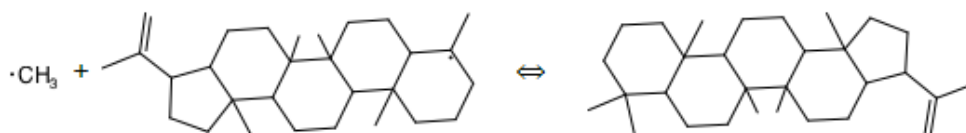
H298 (kcal/mol) = -87.09
S298 (cal/mol*K) = -46.41
G298 (kcal/mol) = -73.26
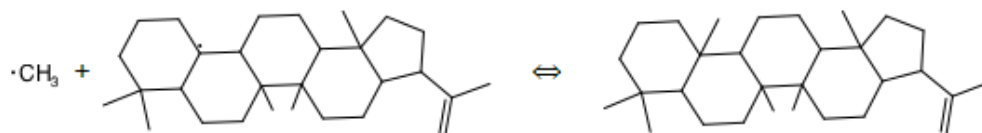
H298 (kcal/mol) = -87.09
S298 (cal/mol*K) = -46.41
G298 (kcal/mol) = -73.26

Figure 10.29 RMG provided data of methyl radicals BDEs, for comparison to lower BDEs values of backbone bonds.

Appendix A.7.4. Main pyrolysates and peaks of squalene experimental pyrolysis
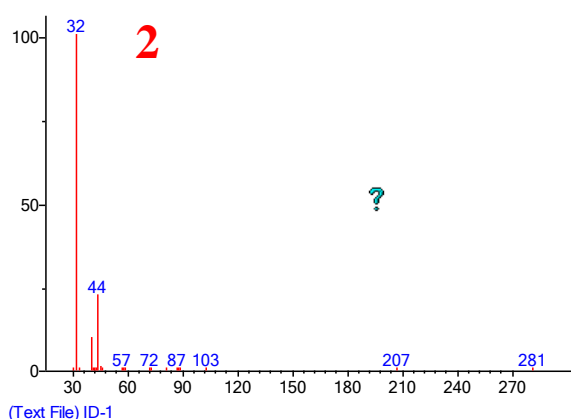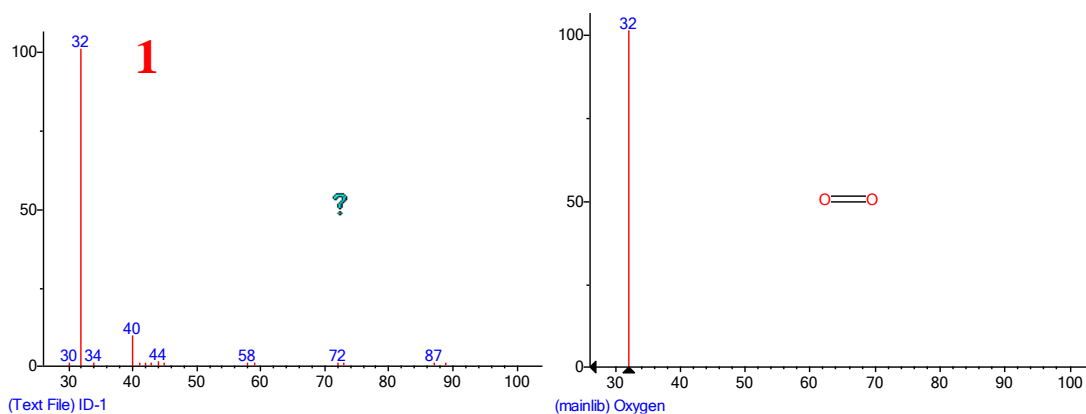
O_2 (mass 32) and CO_2 (mass 44) ?
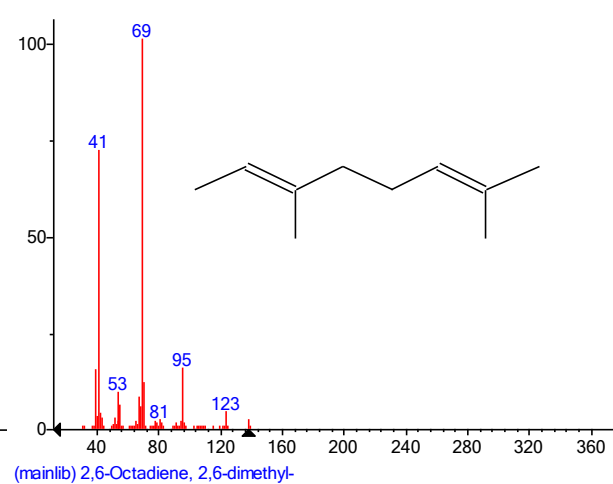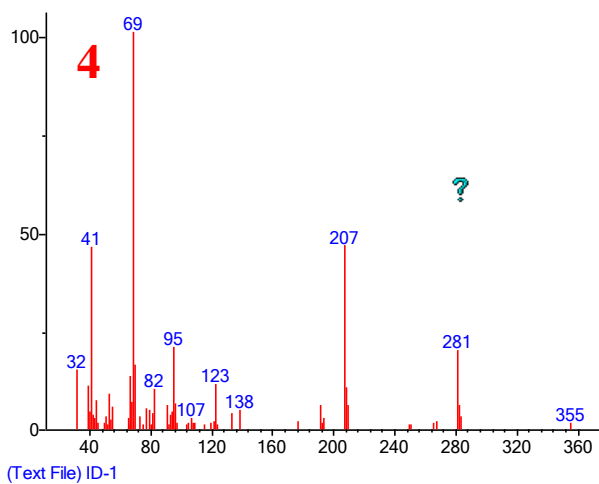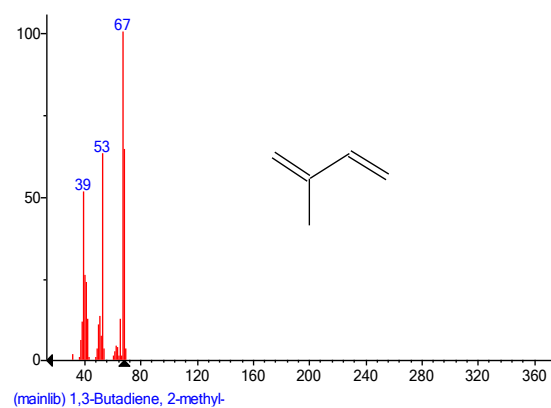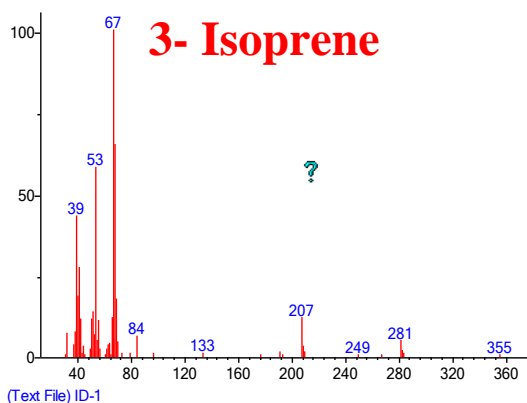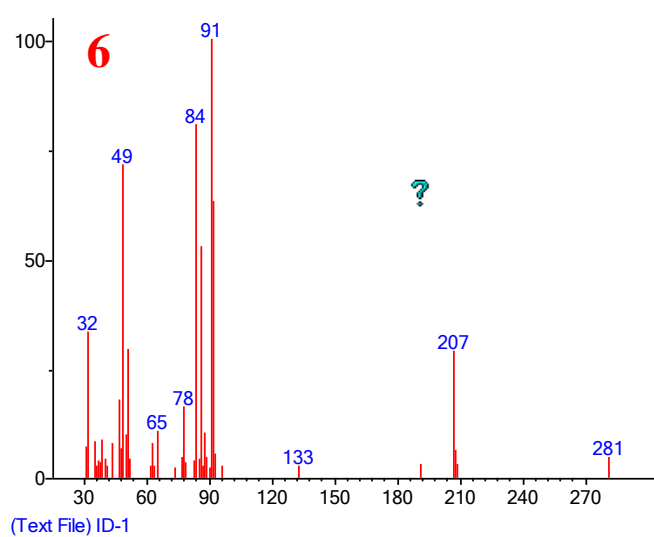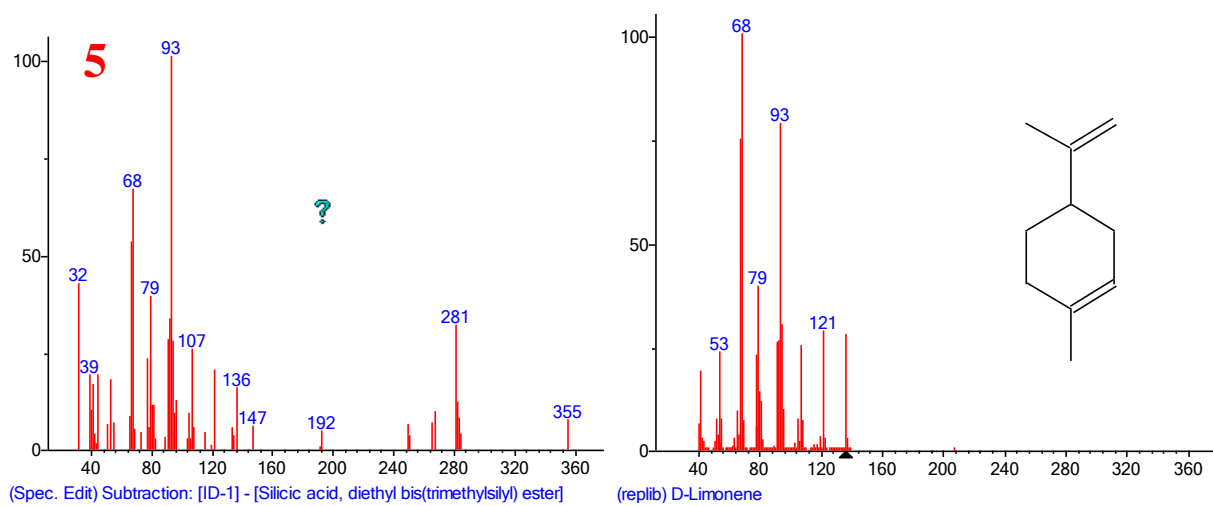
Most likely coelution between DCM and another monocyclic compound (benzene?).
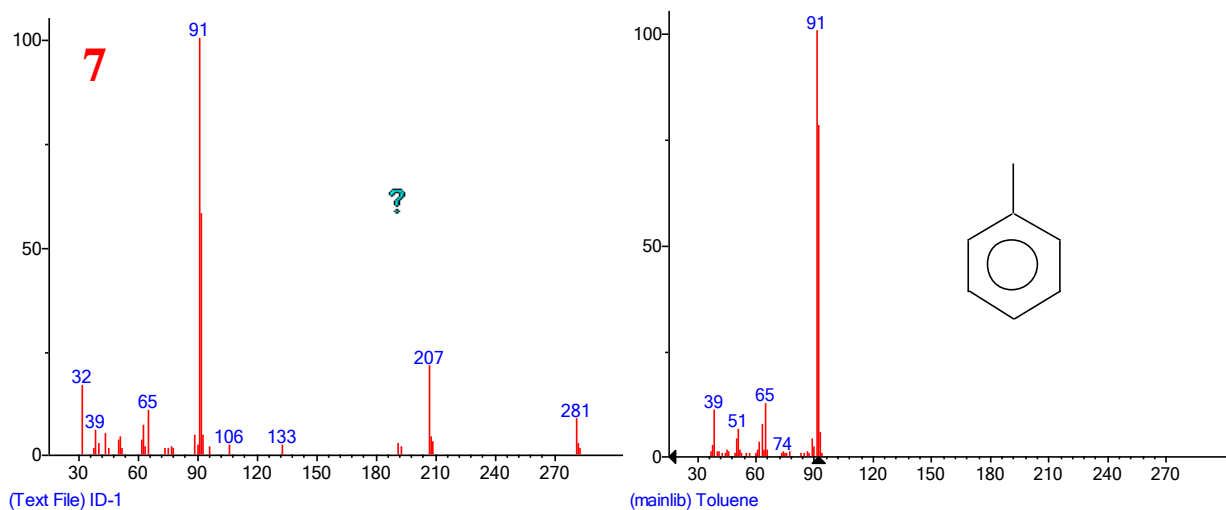
Figure 10.30 Squalene pyrolysates.

Appendix A.7.5. Isoprene 300°C late-eluting peaks, D-Limonene
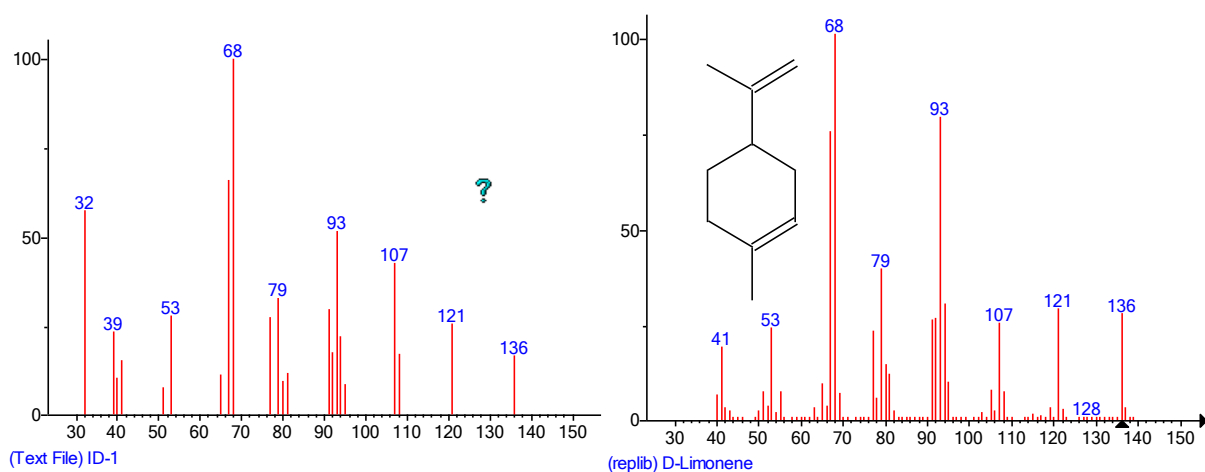
Figure 10.31 Isoprene D-Limonene contaminant peak mass spectrum.

Appendix A.7.6. Main pyrolysates and peaks of isoprene experimental pyrolysis

Main peak - isoprene
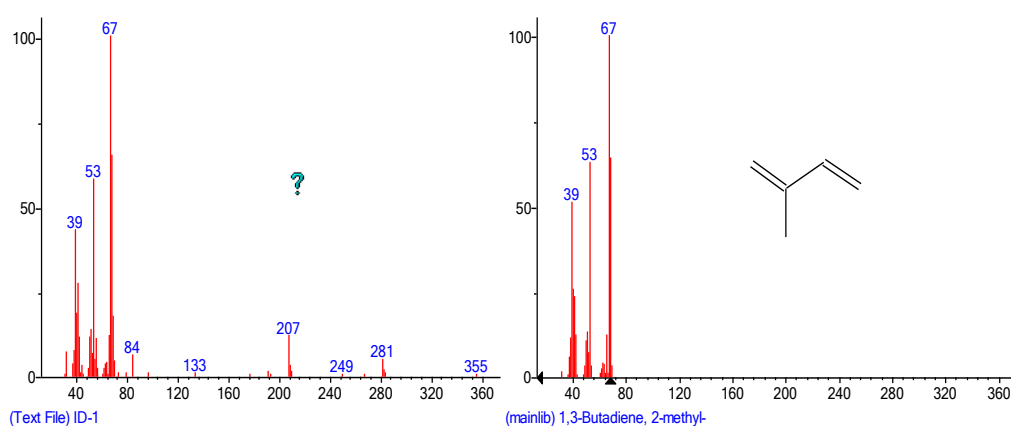
Figure 10.32 Isoprene main squalene peak mass spectrum.

Peaks 1 and 2
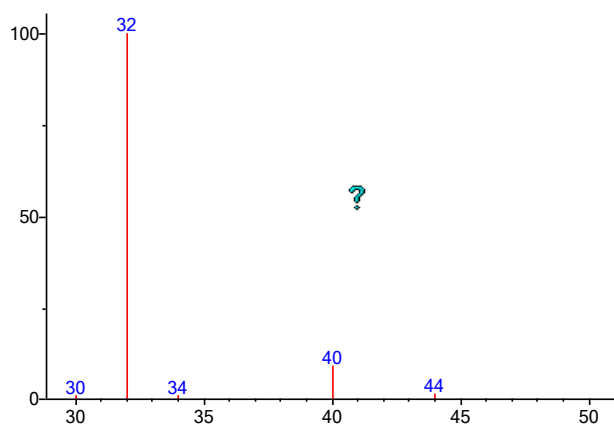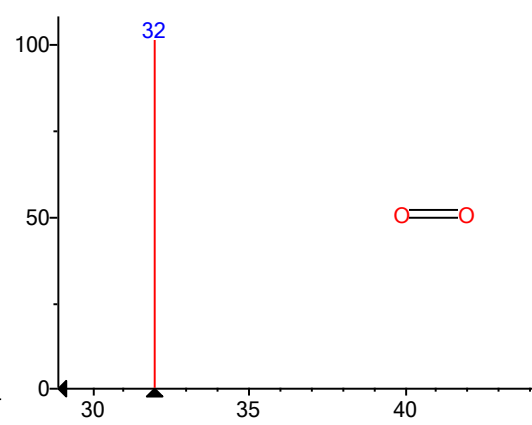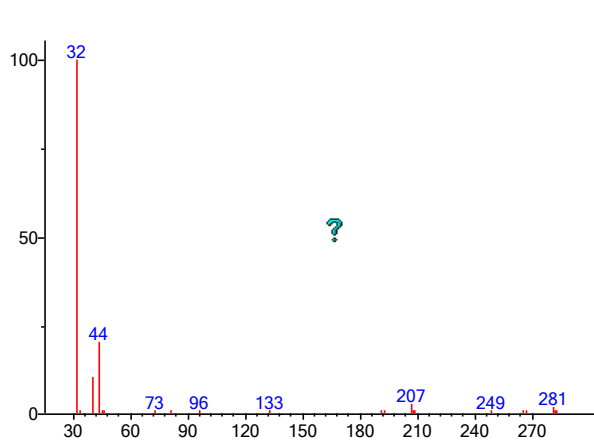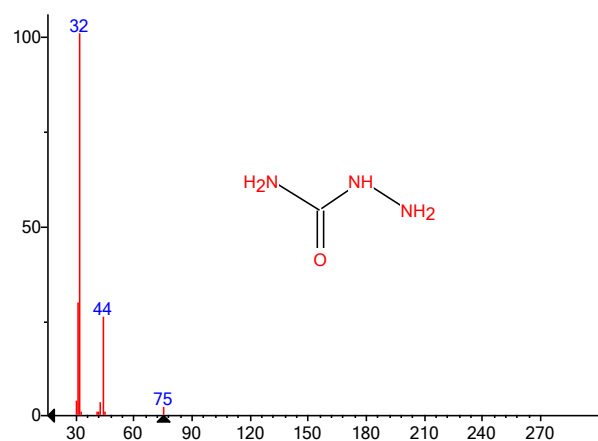
Peaks 3 and 4
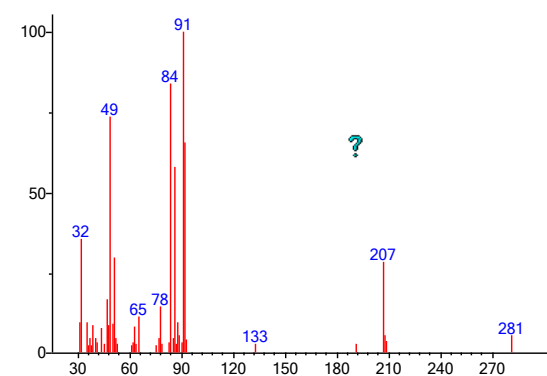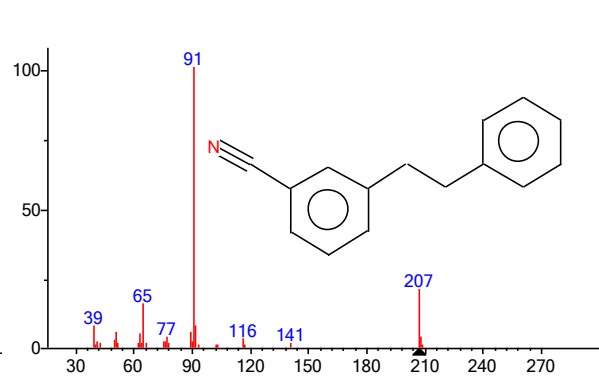
Figure 10.33 Main pyrolysates and peaks of isoprene experimental pyrolysis.

Appendix A.7.7. Diploptene pyrolysis of 5µL injections when the prep-GC had the valve box involved
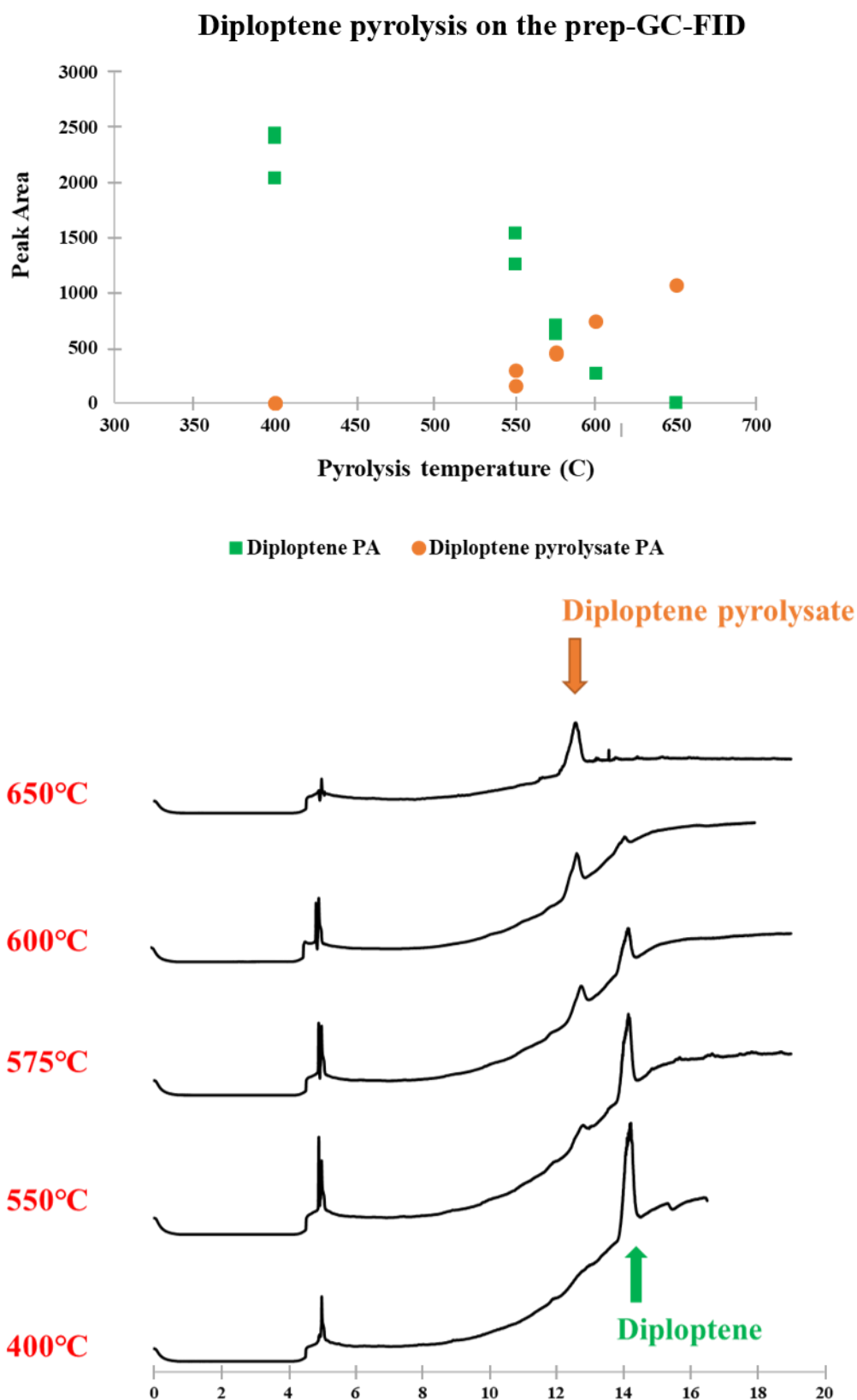
Figure 10.34 5µL diploptene pyrolysed with the valve box cold-spot connected to the prep-GC system. The pyrolysis breakdown takes place as previously seen, yet with poorer chromatography.

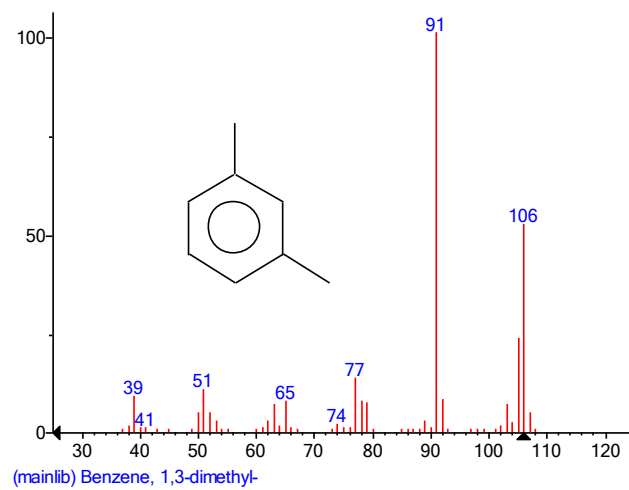## Appendix A.7.8. Diploptene trapped in stainless-steel tube and GC-MS 3 µL reinjection
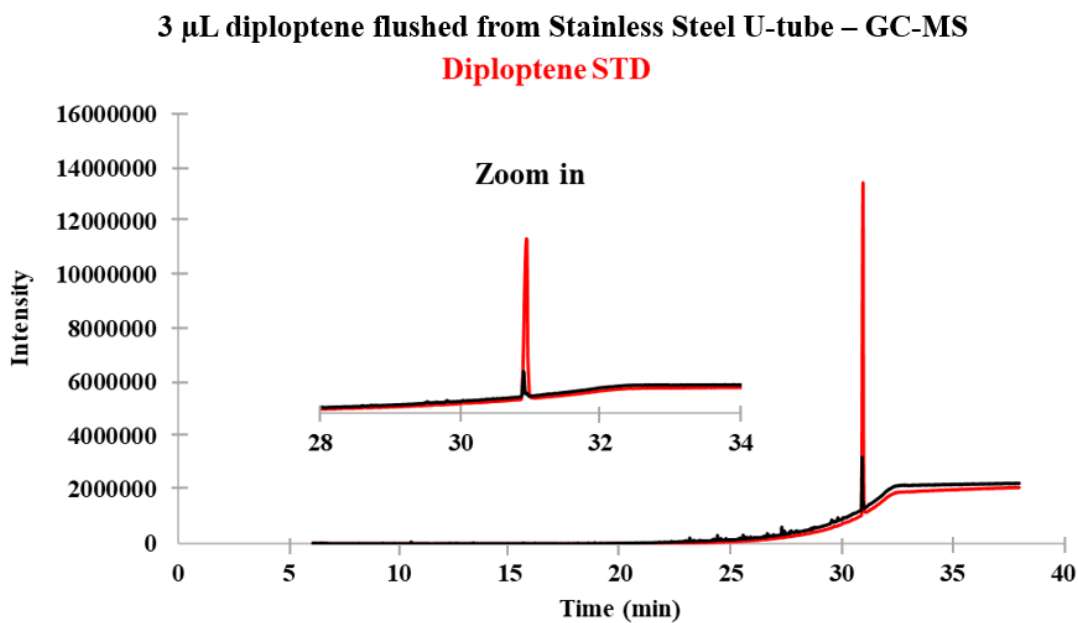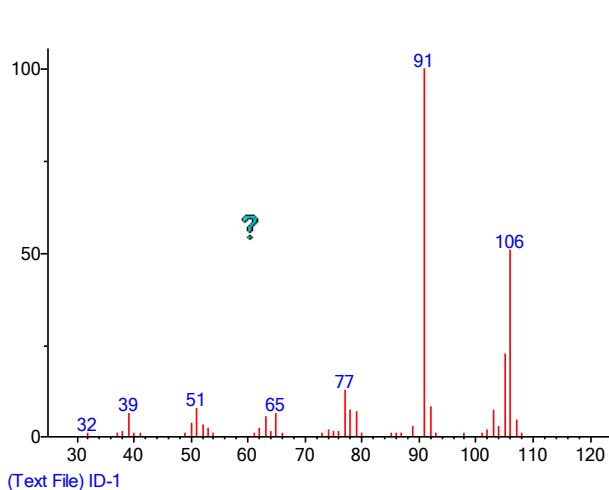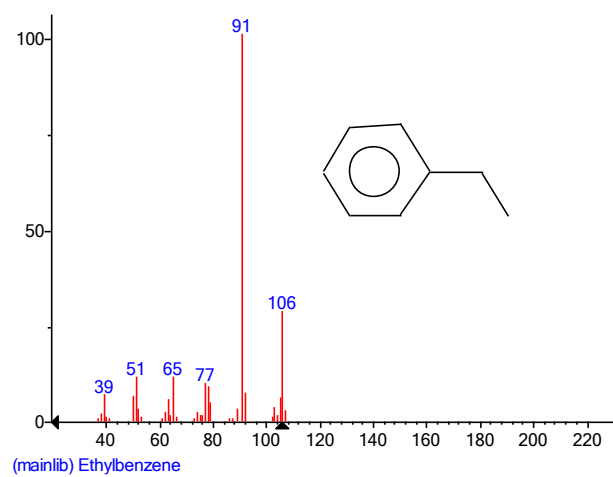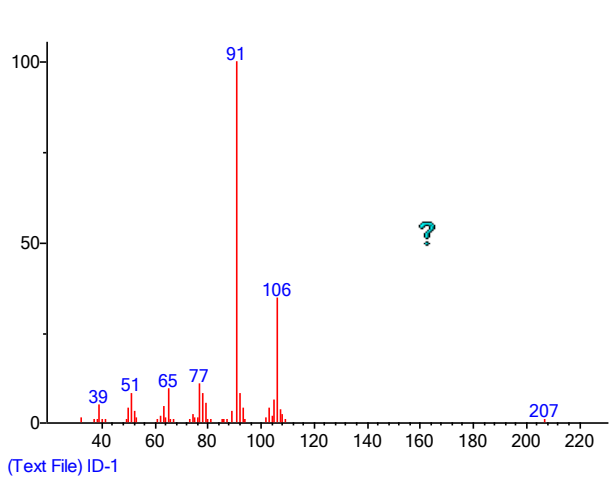

Figure 10.35 Diploptene trapped and flushed out of stainless-steel trap and injection of eluent on GC-MS. Multiple contaminants seen.

Appendix A.7.9. Figure 7.29 peaks, mass spectra and highest probability compound, 1-10,0

(Text File) ID-1

(replib) 1,3-Cyclohexadiene

(Text File) ID-1

(mainlib) Benzene

(Text File) ID-1

(replib) Toluene

(Text File) ID-1

(mainlib) Ethylbenzene

(Text File) ID-1

(mainlib) Benzene, 1,3-dimethyl-

(Text File) ID-1

(Text File) ID-1

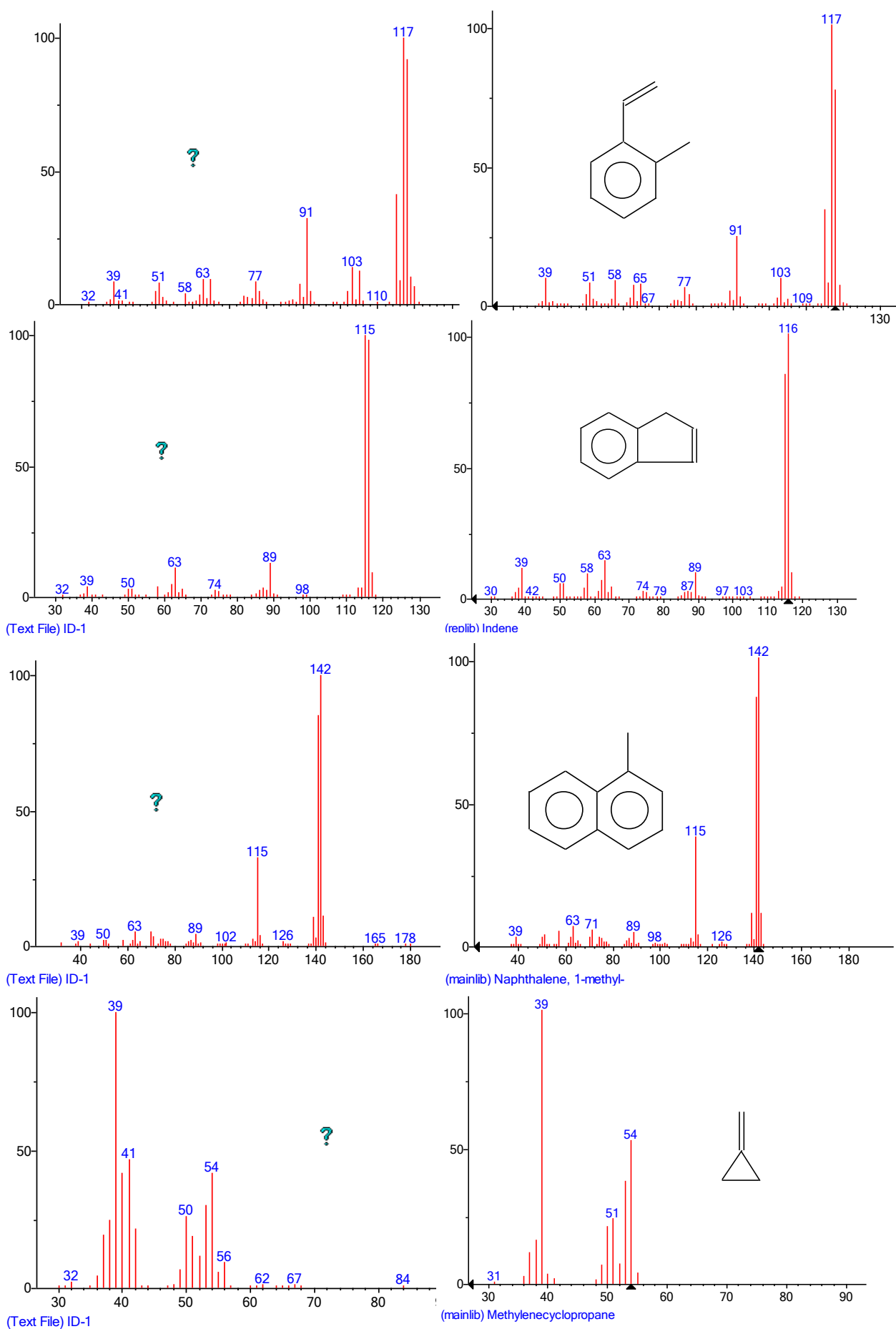(mainlib) Benzene, 1-ethyl-4-methyl-
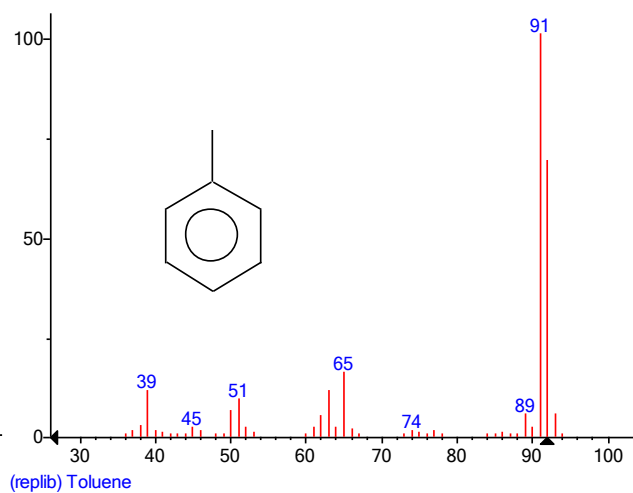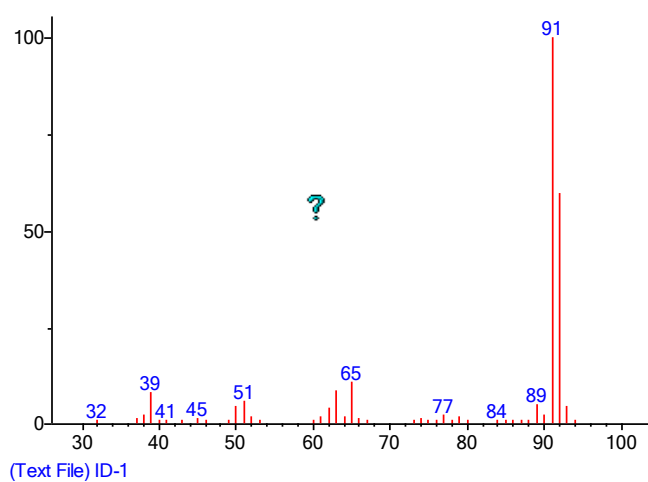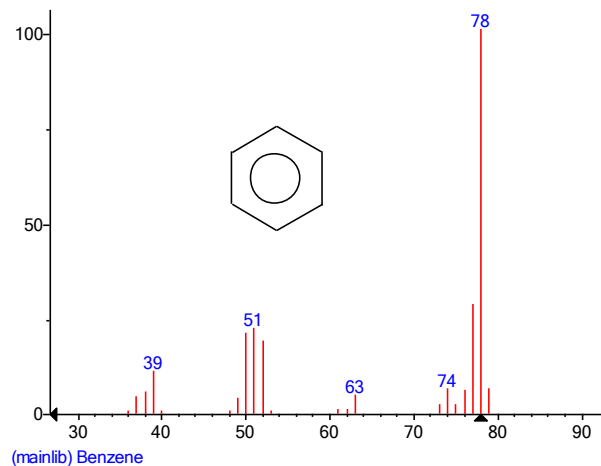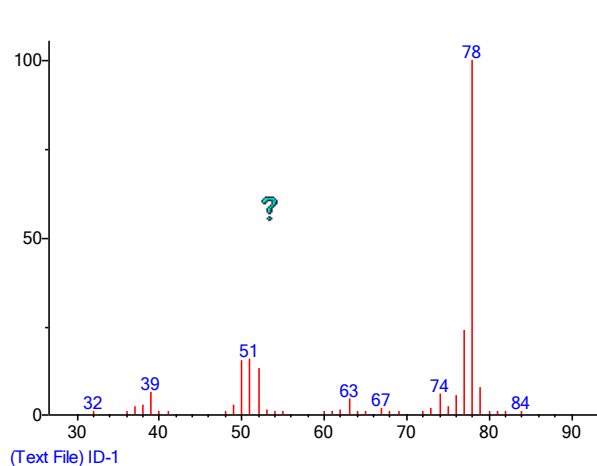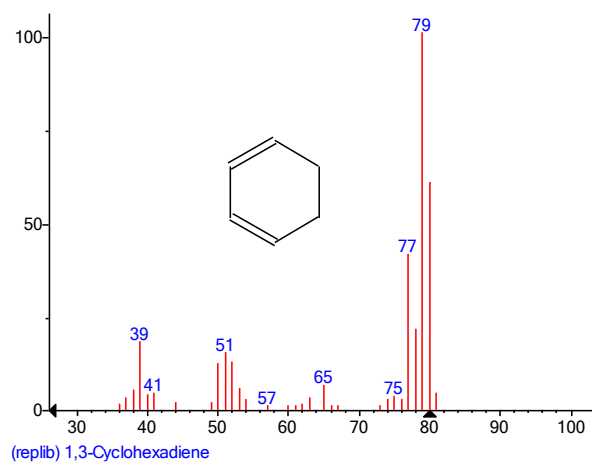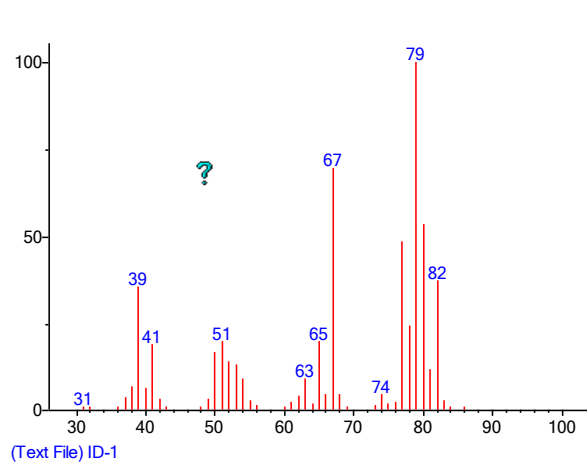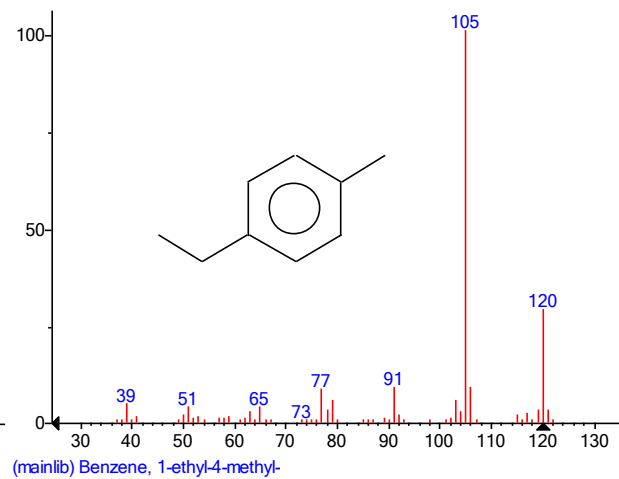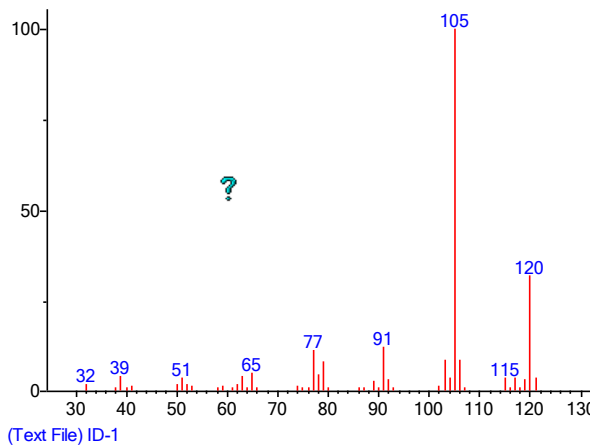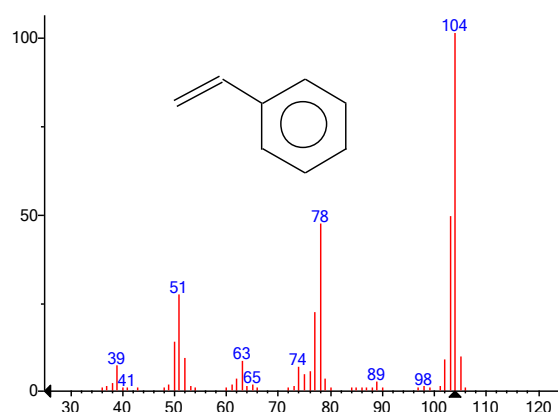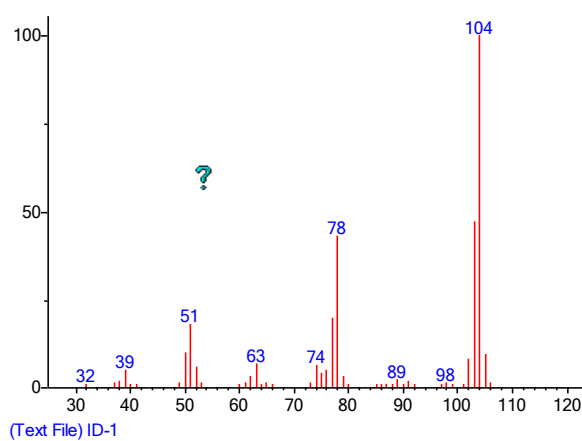
Figure 10.36 Peaks 1-10 and 0 of Figure 7.29, mass spectra and highest probability compound

Appendix A.7.10. Diploptene pyrolysis and initial GC-MS transfer-Ghost peaks
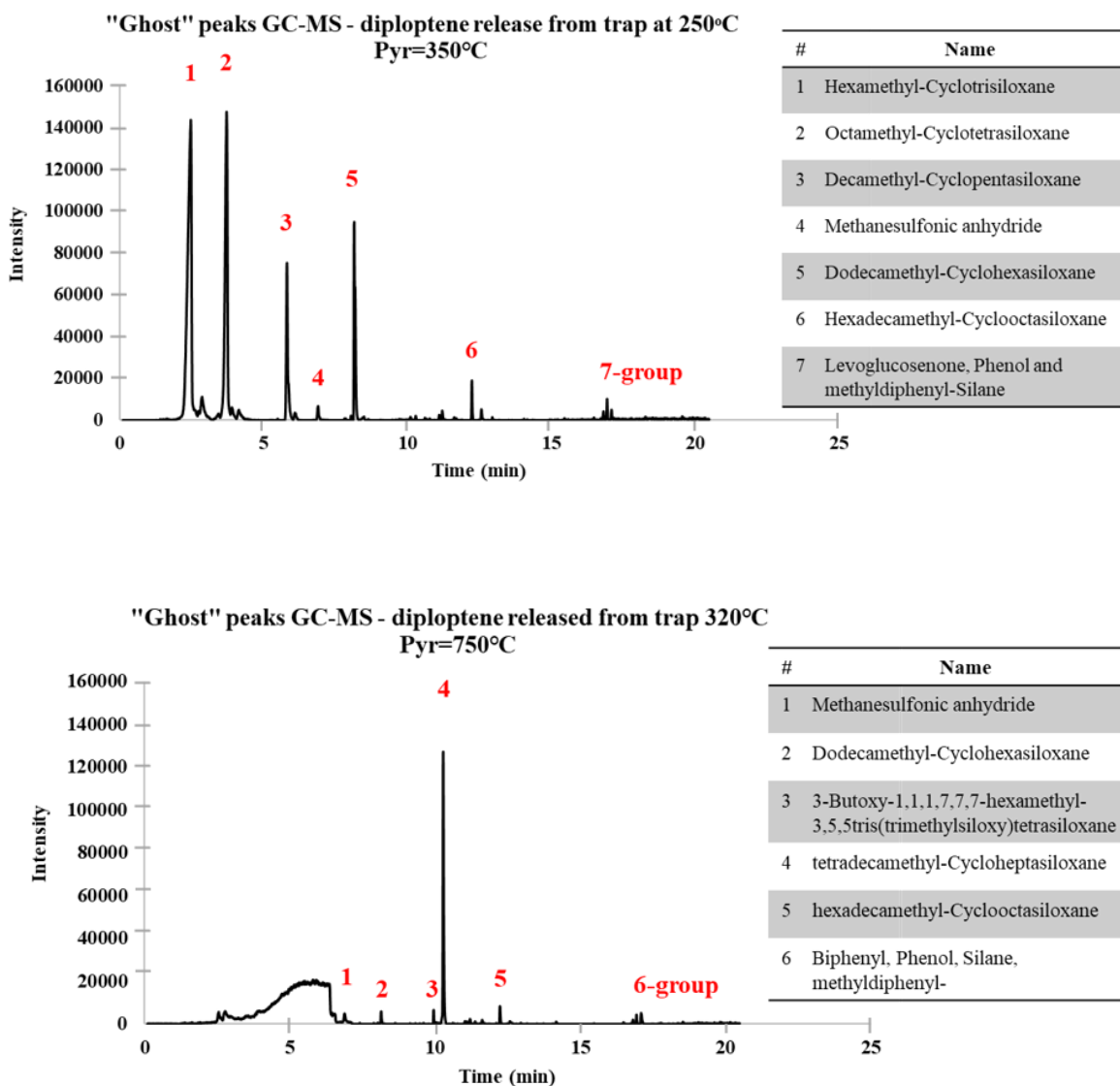

Figure 10.37 Diploptene pyrolysis transfer to GC-MS prior method development. All peaks identified as siloxanes, indicating capillary column breakdown.

Compound trapping, enrichment and transfer attempt (ghost peaks)

Initial trapping and enrichment of diploptene was done in the ICE trap. Runs of 1.5 µL of the analytical standard were injected in splitless mode in a 2-method sequence and trapped on a FS capillary placed in the ICE trap (SIM trap unavailable for this experiment). The HT-1 column was installed in the prep-GC defined as 30 m in length. During the **trapping method**, the oven was set at 240°C isothermal for 4 min and followed a 30°C/min oven ramp until 320°C were it was held for 10 min. The flow was set at 1.8 mL/min. The valve was switched OFF after 7 min, sending only the diploptene peak to the trapping capillary submerged in ice and water outside the oven.

For the release methods, the oven was brought down to 30°C and the capillary previously placed in the ICE trap was placed within the oven. The release took place in two stages, via two methods, and the peaks (trapped compounds and pyrolysates) were transferred to the GC-MS via the heated transfer line set at 200°C.

The first release stage involved a manual run and the oven program: 30°C (1 min), 30°C/min to 200°C (1 min), with a flow of 1.8 mL/min. The pyrolyser was set to 350°C and the transfer line was connected to the GC-MS for 5.5 min. The second release stage involved a manual start, with the oven starting at 200°C for 1 min followed by a ramp of 30°C/min until 320°C, where it was kept isothermal for 3 min. The pyrolyser was set at 750°C (based on first RMG simulation) and the pyrolysates of diploptene were transferred to the GC-MS via the heated transfer line set at 200°C.

Once the transfer line was connected to the GC-MS inlet, the GC-MS method was manually started. The ZB-WAX column was installed in the GC-MS oven and the oven program was: 35°C (2 min), 10°C/min to 200°C (2 min). The flow was of 1 mL/min and the scan range between 45-600 amu.

Appendix A.7.11. – Limitations and requirements for confirming isoprene pyrolysate

The prep-GC would require a high oven temperature to vaporize the low concentration diploptene analytical standard, a temperature at which isoprene would readily move through the system, and the injection of isoprene, with the highest inlet split ratio and lowest syringe volume, would still behave as a solvent peak and would elute in the first minute of the GC run when analysed using the same method as for diploptene. Retention times are of high importance and the system would have to separate the isooctane solvent from diploptene prior to pyrolysis. Pyrolysis would take place and the main pyrolysate would form. Isoprene would not require separation as the main compound of the following run, and it would reach the pyrolyser and detector in considerably shorter time given its low molecular weight and boiling point, when compared to the suspected isoprene pyrolysate produced via diploptene pyrolysis. Trapping in liquid N_2 and subsequent solvent flushing of the capillary would be possible yet, if isoprene is the suspected pyrolysate, it would be difficult to separate this pyrolysate from the solvent front as they would have similar low boiling points, and to confirm its identity by a post-pyrolysis injection onto a GC-MS. As transferring isoprene and its pyrolysates was demonstrated before via the transfer line (Subsection 7.3.5.), it would be possible to identify diploptene's main pyrolysate via this means and with the current prep-GC system.